DEGRADATION OF BISPHENOL-A AND 2-NITROPHENOL BY COMBINED ADVANCED OXIDATION TECHNOLOGIES

By

Jimoh Oladejo Tijani

B.Tech (Chemistry/Polymer Science), M.Tech (Analytical Chemistry) - Federal University of Technology, Minna, Nigeria

A thesis submitted in fulfillment of the requirements for the degree of Doctor of Philosophy in Chemistry in the Department of Chemistry, University of the Western Cape, South Africa

Supervisors: Prof. Leslie F. Petrik
Prof. Willem J. Perold
Dr. Ojo.O. Fatoba

December, 2015

KEYWORDS

Supported TiO_2 photocatalyst

Supported Ag doped photocatalyst

Dielectric barrier discharge system

Bisphenol-A

2-nitrophenol

Intermediate compounds

Polyethylene glycol stabilised zero valent iron particles

Photo-Fenton induced process

Jet loop reactor

Impingement

Free reactive species

Combined advanced oxidation technologies

ABSTRACTS

Emerging micropollutants such as bisphenol-A and 2-nitrophenol present a great threat in drinking water due to their adverse effects. Most conventional technologies in water and wastewater treatment are not designed to eliminate these xenobiotics; instead pollutants are merely transferred from one phase to another. Advanced oxidation technologies (AOTs) however, have been identified as suitable routes for the degradation of these potential damaging substances based on free radical mechanisms and use of less expensive chemicals. Moreover, due to the structural complexity of wastewater and the existence of pollutants as mixtures, no single advanced oxidation technology can convincingly remove all forms of contaminants and then most often than not, a combination of treatment processes is required for an effective purification process. Besides, the problem of adequate degradation of emerging contaminants in the environment, when AOT(s) are used individually, they present inherent problems. For instance, powder TiO_2 photocatalysts obstruct light penetration, thus prevent effective interaction of UV light with the target pollutants, and particulates present problems of post-filtration and recovery of catalyst particles after treatment. Additionally, TiO_2 has a high band gap energy, high electron-hole recombination rate, and is prone to aggregation of the suspended particles. Similarly, the dielectric barrier discharge (DBD) system produces ultra violet light and hydrogen peroxide within the plasma zone which is not fully maximised for the mineralization of persistent organic pollutants. Rapid oxidation and aggregation of nano zero valent iron particles in photo-Fentons process reduce the particles mobility and affect its performance. In the same vein, the jet loop reactor (JLR) system is characterised by low impingement yield, which is responsible for low mineralization rate. In light of this background, this research investigated the degradation of bisphenol-A and 2-nitrophenol in aqueous solution using the following combined advanced oxidation methods: DBD/supported TiO_2 or Ag doped TiO_2 photocatalysts, DBD/photo-Fenton induced process and JLR/UV/H_2O_2. The target was to assess the performance of each single system and then identify the best combined AOTs capable of significantly mineralizing the target compounds.

Firstly, two materials were developed namely supported TiO_2 and stabilized nano zero valent Fe. The TiO_2 photocatalyst supported on a stainless steel mesh was synthesised using sol-gel solution of 8 % PAN/DMF/$TiCl_4$. The influence of calcination temperature and holding time on the formation of nanocrystals was investigated. Afterwards, various amounts of metallic silver were deposited on the (optimum) supported TiO_2 photocatalyst using thermal evaporation. The catalysts were characterized by several analytical methods; HRSEM,

HRTEM, EDS, SAED, FTIR, TGA-DSC, UV-vis/diffuse reflectance spectroscopy, XRD, BET, and XPS. The photocatalytic activity of the prepared catalysts was determined using methylene blue as a model pollutant under ultra-violet light irradiation. Secondly, the TiO_2 photocatalyst and 2.4 % Ag doped TiO_2 nanocomposites obtained as optimums (in section 1) were combined with the DBD to decompose BPA or 2-NP in aqueous solution. Moreover, the photo-Fenton process was applied for degradation of the model pollutants, and different dosages of stabilized nZVI (in the range of 0.02 -1.00 g) were added to the DBD system to induce the photo-Fenton process and improve BPA or 2-NP degradation efficiency. Finally, a jet loop reactor (JLR) presenting advanced mixing by the "impinging effect" was explored to decompose BPA or 2-NP in aqueous solution as a function of inlet applied pressure, solution pH, and initial concentration of BPA or 2-NP. Subsequently, different concentrations of hydrogen peroxide (H_2O_2) were added to the JLR to enhance the mineralization process. Furthermore, a combination of JLR with in-line UV light and H_2O_2 were further utilised to decompose BPA or 2-NP in aqueous solution. The residual concentration of the model compounds and intermediates were analysed using high performance liquid chromatography (HPLC) and liquid chromatography mass spectrometry (LCMS). The concentration of the ozone, hydrogen peroxide and hydroxyl radicals generated by the DBD in the presence or absence of a catalyst was monitored using Ultraviolet-visible spectroscopy and Photoluminescence spectroscopy.

The results revealed that the optimal thermal conditions to obtain well supported uniformly grown, highly active crystalline TiO_2 catalysts with high specific surface area was 350 ºC at a 3 h holding time in N_2 atmosphere with a flow rate of 20 mL/min. Pyrolysis temperature and holding time played an important role on the crystalline nature and photocatalytic activity of the catalyst. Moreover, 2.4 % Ag doped TiO_2 nanocomposites exhibited higher photocatalytic activity for methylene blue degradation than the undoped supported TiO_2 nanocrystals. The results indicated that combining DBD with 2.4 % Ag doped TiO_2 nanocomposites achieved 89 % and 81 % removal efficiency for BPA or 2-NP compared to 67.22 % or 56.8 % obtain when using the DBD system alone. The 2.4 % Ag doped TiO_2 nanocomposites demonstrated excellent activity and offered photochemical stability after four repeated applications.

In the case of the photo-Fenton induced process, nano zero valent iron particles (nZVI) stabilized with polyethylene glycol were synthesised using a modified borohydride reduction method. The HRSEM, BET, XRD, and XPS analysis confirmed the formation of filamentous, high surface area iron nanoparticles in the zero valent state. Unlike combined DBD/Ag doped

TiO_2 nanocomposites, 100 % or complete removal of BPA or 2-NP in aqueous solution was achieved with DBD/nZVI system within 30 minutes compared to 67.9 % (BPA) or 56.8 % (2-NP) with DBD alone after 80 minutes. The removal efficiency was attributable to the production of an increased concentration of OH radicals as well as existence of a synergetic effect in the combined DBD/nZVI system.

Five new transformation products namely: 4-nitrophenol ($C_6H_5NO_3$), 4-nitrosophenolate ($C_6H_4NO_2$), 4-(prop-1-en-2-yl) cyclohexa-3,5-diene-1,2-dione, ($C_9H_8O_2$), 4-(2-hydroxylpropan-2-yl)cyclohexane-3,5-diene-1,2-dione ($C_9H_{10}O_3$), and 1,2-dimethyl-4-(2-nitropropan-2-yl)benzene ($C_9H_{10}NO_4$) were identified during the degradation of BPA. While, three aromatic intermediate compounds such as 2-nitro-1,3,5-benzenetriolate ($C_6H_2NO_5$), 2-nitro-1,4-benzoquinone ($C_6H_3NO_4$), and 2,5-dihydroxyl-1,4-benzoquinone ($C_6H_4O_4$) respectively were identified during the degradation of 2-NP for the first time in the DBD with JT14 or JT17 using LC-MS. These intermediate compounds have never been reported in the literature, thereby expanding the number of BPA or 2-NP intermediates in the data base in the DBD/JT14 or DBD/nZVI system. BPA degradation proceeded via ozonation, hydroxylation, dimerization, and decarboxylation and nitration step, while 2-NP proceeded via hydroxylation, nitration and denitration respectively.

Furthermore, maximum removal efficiency of BPA or 2-NP in aqueous solution using JLR alone under the optimum solution pH (3), inlet pressure (4 bar), flow rate (0.0007 m^3/s) was 14.0 % and 13.2 % respectively after 80 minutes. A removal efficiency of 34.9 % was recorded for BPA while 33.2 % was achieved for 2-NP using combined JLR/UV under the same conditions as JLR alone. For the combined JLR/H_2O_2 under optimum conditions of inlet pressure (4 bar), solution pH (3) and peroxide dosage (0.34 g/L), a 51.3 % and 50.1 % removal efficiency was achieved for BPA and 2-NP respectively under same conditions relative to JLR alone. Combination of JLR/UV/H_2O_2 achieved 77.7 % (BPA) or 76.6 % (2-NP) removal efficiency under the same conditions. The combined JLR/UV/H_2O_2 process was found to be most effective combination under the optimized operating parameters due to existence of a synergetic index value of 6.42 or 6.84. This implies that JLR should be coupled with UV and H_2O_2 to achieve greater mineralization efficiency instead of using the system individually. The obtained experimental data of these combined treatment processes fitted the pseudo-first order kinetic models. The combination of the JLR/UV/H_2O_2 was found to be energy efficient and could effectively degrade BPA or 2-NP in aqueous solution to a greater extent than the JLR, JLR/UV or JLR/H_2O_2 system. However, the total organic carbon (TOC)

reduction value by all combined DBD and JLR system recorded was not completely achieved due to the formation of recalcitrant intermediate compounds under the applied conditions.

In conclusion, this study is reporting for the first time a combination of supported 2.4 % Ag doped TiO_2 nanocomposites with dielectric barrier discharge system for BPA/2-NP degradation in aqueous solution; a combination jet loop reactor based on impingement with in-line UV lamp and H_2O_2 for successfully decomposing BPA or 2-NP in aqueous solution; as well as a combination of dielectric barrier discharge system and stabilised nano zero valent iron particles, which induced a photo-Fenton process for highly effective removal of BPA or 2-NP in aqueous solution. This study conclusively supports the hypothesis that combined advanced oxidation technologies offer a sustainable and highly efficient means of achieving partial or complete removal of BPA or 2-NP in aqueous solutions. Considering all the combinations of AOTs investigated in this study, the novel DBD/photo-Fenton-induced process under optimised operating parameters was found to be the most efficient in the elimination of BPA or 2-NP in aqueous solutions. The combination of DBD with photo-Fenton like process offers a promising advanced wastewater purification technology in the immediate future. Based on these findings, it is recommended that DBD should be re-designed to prevent loss of ozone and JLR system reconfigured to increase impingement and cavitational yield in order to have an effective combination treatment strategy for wastewater purification especially in large scale wastewater management.

.

DECLARATION

I declare that "*Degradation of bisphenol-A and 2-nitrophenol by combined advanced oxidation technologies*'' is my own work, that it has not been submitted before for any degree or assessment in any other university, and that all the sources I have used or quoted have been indicated and acknowledged by means of complete references.

Jimoh Oladejo Tijani November, 2015

…….

ACKNOWLEDGEMENTS

I wish to express my deepest sincere gratitude and appreciation to my supervisor Professor Leslie Petrik for giving me the opportunity to do my doctorate degree under her supervision. Your guidance, support, word of encouragement and constructive criticism during the proposal stage, experimental design and thesis writing are invaluable to me. I have seen myself grow to a level of being able to write a high quality scientific paper because of your openness, patience and encouragement. You are not just a supervisor but a mother to me and will forever grateful to you for this great accomplishment in my career.

I also wish to thank my co-supervisor, Prof. W. J. Perold, for allowing me to have direct access to the thermal evaporator facilities in his laboratory at University of Stellenbosch, South Africa. I am indebted to my co-supervisor Dr. Ojo.O.Fatoba for your kind-heartedness, technical inputs and insighful contribution to the thesis. Sir, I cannot thank you enough, you have been so kind to me since I know you.

I wish to sincerely appreciate Dr. Paul Eze, Dr. Godfrey Madzivire, and Dr. OO. Babajide for proof reading some chapters. Thanks very much, your constructive criticism have really improved the thesis. Special thanks to Averil Abbot, Ilse Wells, and Vanessa Kellerman for making the research easy for me via prompt raising of purchase order numbers.

This acknowledgment would not be completed without appreciating the following people that helped in analysing my samples: Prof.Weit Ross (XPS, Physics department, University of Free State), Dr Remy Bucher (XRD, ithemba Labs), Dr. Franscious Cummings and Dr. Subelia Botha (HRTEM, Physics department, University of the Western Cape (UWC), South Africa), Andrian Joseph (HRSEM, Physics department, UWC, South Africa), Dr. Wafeeq Davids (FTIR, South African Institute for Advanced Materials Chemistry (SAIAMC), UWC), Dr. Rudolph Erasmus (UV-Vis/diffuse reflectance spectroscopy, University of the Witwatersrand) Ilse Wells (BET and ICP, Chemistry department, UWC), Mr. Ogoneochukwu Oputu (HPLC and LCMS unit, Chemistry department, Cape Peninsula University of Technology, Cape Town).

Special thanks to all my colleagues in Environmental and Nano Sciences (ENS) Research Group for their support and assistance during this study. The social bonds we formed and living as people from one family made my life on campus even better.

My sincere appreciation goes to my employer, Federal University of Technology (FUT), Minna, Nigeria for granting me a study fellowship to do my PhD degree outside the shore of the country and for the support rendered to me. The financial assistance of the National Research Foundation (NRF) and Water Research Commission, South Africa towards this research is hereby acknowledged.

I would like to acknowledge Prof. J. Yisa, Prof. AM. Jinadu, Dr. AS Abdulkareem, Dr. Abdulfatai Jimoh, Dr. MM. Ndamitso, Dr. YA. Iyaka, Dr. Luqman Oyewobi, Mr. Femi Ibikunle, Mrs. L. Fadipe and Mrs MT Bankole of Federal University of Technology, Minna, Nigeria for your support and concern. Mallam Isa Lawal Usman and Emmanuel Ameh Alechine thanks for always being there for me.

Special thanks to my wonderful parents for their love, moral support and for believing in me throughout the programme. I love both of you so much, would not have gone far without your supports and prayers. To my family and friends, thanks for your supports. I appreciate you all.

To my loving and caring wife (Suliat Aduke Tijani) and my two lovely children (Abdulsalam and Mohammed), I owe you a lot and cannot thank for your perseverance and endurance throughout my PhD programme. This would not have happened without your understanding, encouragement, support and prayers during the thin and thick time. May God continue to strengthen our love and bless our children for us (amen).

TABLE OF CONTENTS

LIST OF FIGURES

LIST OF TABLES

LIST OF ABBREVIATIONS

AOT:	Advanced oxidation technologies
BET:	Brunauer Emmett-Teller
BPA:	Bisphenol-A
BP1-BP14:	By-products (1-14)
CEC:	Chemicals of emerging concern
CVD:	Chemical vapour deposition
DBD:	Dielectric barrier discharge
DMF:	N,N-dimethylformamide
DWA:	Department of Water Affairs
EDC:	Endocrine disrupting compounds
EDS:	Energy dispersive spectroscopy
FTIR:	Fourier Transform Infrared Spectroscopy
HRSEM:	High Resolution Scanning Electron Microscopy
HRTEM:	High Resolution Transmission Electron Microscopy
HPLC:	High Performance-Liquid Chromatography
JLR:	Jet loop reactor
JT1-17:	Jimoh Tijani photocatalyst 1 – 17
LC-MS:	Liquid Chromatography-Mass Spectrometry
MB:	Methylene blue
NDIR:	Non-dispersive infra-red
nZVI:	Nano zero valent iron particles
2-NP:	2-nitrophenol
OBP1-OBP9:	Oxidation by-products (1-9)
PAN:	Polyacrylonitrile
SAED:	Selected Area Electron Diffraction (SAED)
TGA/DSC:	Thermogravimetric analysis/Differential Scanning Calorimetry
TOC:	Total organic carbon
UNEP:	United Nations Environmental Programme
UV:	Ultra-violet light

WHO:	World Health Organization
WWTP:	Wastewater treatment plants
XPS:	X-ray photoelectron spectroscopy
XRD:	X-ray diffraction

ACADEMIC OUTPUTS OF RESEARCH REPORTED IN THIS THESIS

The output outlined below emanated from this study

Oral presentations

Jimoh O.Tijani, Ojo O.Fatoba, Emile S.Massima, Leslie F.Petrik. (2015). Degradation of 2-nitrophenol in aqueous solution by combination of dielectric barrier discharge and TiO_2 photocatalyst supported on stainless steel mesh. 7th SETAC Africa Conference and Horizon Scanning Project Workshop held at Anthene Conference Centre, Langebaan, South Africa, 5th-8th October, 2015 **(2nd Best Presenter)**

Jimoh O. Tijani, Ojo O. Fatoba and Leslie F. Petrik (2014). Photocatalytic activity of Ag doped TiO_2 nanocomposites MAM-14 International Symposium on Macro and Supramolecular Architectures and Materials: From Innovation to Commercialisation held at Emperor Palace Hotel Casino, Johannesburg, South Africa, 23rd - 27th November, 2014

Jimoh O. Tijani, Ojo O. Fatoba and Leslie F Petrik. (2013). Effect of pH on the photocatalytic degradation of Bisphenol-A by Ag-immobilized TiO_2 nanocomposites. 41st South African Chemical Institute National Convention held at River Park Conference Centre, East London, South Africa, 1st-6th December, 2013

Journal Publications

Jimoh O. Tijani, Ojo O. Fatoba., Omotola O. Babajide, and Leslie F. Petrik (2016). Pharmaceuticals, endocrine disruptors, personal care products, nanomaterials and perfluorinated pollutants: A review. *Environmental Chemistry Letters*, 14(1): 27-49

Emile S. Massima Mouele, **Jimoh O. Tijani**, Ojo O.Fatoba and Leslie F.Petrik (2015). Degradation of organic pollutants and microorganisms from wastewater using different dielectric barrier discharge configurations—a critical review. *Environmental Science and Pollution Research*, 22(23): 18345-18362

Jimoh O. Tijani., Ojo O.Fatoba, Godfrey Madzivire and Leslie F.Petrik. (2014). A Review of Combined Advanced Oxidation Technologies for the Removal of Organic Pollutants from Water. *Water Air Soil and Pollution*, 225:2102, DOI 10.1007/s11270-014-2102-y

Jimoh O. Tijani., Ojo O.Fatoba and Leslie F.Petrik. (2013). A review of pharmaceuticals and endocrine disrupting compounds: Sources, effects, removal and detections. *Water, Air and Soil Pollution.* 224:1770 DOI 10.1007/s11270-013-1770-3

In preparation

Jimoh O.Tijani, OjoO. Fatoba, Willem J. Perold, and Leslie F.Petrik (2015). Synthesis and photocatalytic activity of TiO_2 photocatalysts supported on a stainless steel mesh (Manuscript in preparation)

Jimoh O.Tijani, Ojo O. Fatoba, Willem J. Perold, and Leslie F.Petrik (2015). Enhanced photocatalytic activity of supported Ag doped TiO_2 nanocomposites prepared by combined sol-gel and thermal evaporation method (Manuscript in preparation).

Jimoh O.Tijani, Ojo O. Fatoba, Emile Massima, Willem J. Perold, and Leslie F.Petrik (2015). Application of dielectric barrier discharge and TiO_2 photocatalyst on stainless steel mesh for bisphenol-A degradation (Manuscript in preparation).

Jimoh O.Tijani, Ojo O. Fatoba, Emile Massima, Willem J.Perold and Leslie F.Petrik (2015). Enhanced 2-nitrophenol degradation using combination of dielectric barrier discharge and TiO_2 photocatalyst supported on stainless steel mesh (Manuscript in preparation).

Jimoh O.Tijani, Ojo O. Fatoba, Emile Massima, Willem J.Perold and Leslie F.Petrik (2015). Degradation of 2-nitrophenol in aqueous solution by combination of dielectric barrier discharge and stabilized nano zero valent iron particles (Manuscript in preparation).

Jimoh O.Tijani, Ojo O. Fatoba, Willem J. Perold and Leslie.F.Petrik (2015). Bisphenol-A and 2-nitrophenol degradation by jet loop reactor system: influence of hydrogen peroxide and ultra-violet light (Manuscript in preparation).

CHAPTER ONE

1 INTRODUCTION

This chapter presents a brief background on the global importance of clean water as well as the associated problems limiting availability of potable water. This chapter also contains information of emerging micropollutants in water. The background, problem statement, motivations, aims and objectives, research approach, research hypothesis including the scope, delimitations and thesis outline are also presented in this chapter.

1.1 Background of the study

Water sustains all life and needs to be preserved from pollution in order to maintain public health and pristine ecologies. The lack of sufficient, sustainable sources of clean drinking water has been linked to factors such as global climate change, industrialization, overpopulation and agricultural practices. It is worthy to note that despite the intervention by various governmental and non-governmental organizations globally, in 2013 United Nations Environment Programme (UNEP) and World Health Organization (WHO) reported that approximately 1.1 billion people do not have access to reliable drinking water. Another 2.6 billion people, mostly in Africa and Asia, lacked access to functional hygienic facilities while over 2.2 million children below the age of five die of waterborne epidemics annually. It is anticipated that more than two-thirds of the world population will be without access to clean drinking water by 2025 (Belgiorno et al., 2007; Fawell and Ong, 2012). In South Africa alone, close to 5.7 million people do not have access to safe drinking water while 17–18 million people lack access to adequate sanitary services (DWA, 2012). While there is growing concern about the persistent water crisis, the available potable water is often not completely suitable due to the presence of low quantities of persistent and emerging contaminants that are potentially harmful to humans and other living organisms (Boithias et al., 2014; Petrie et al., 2015; Steffen et al., 2011).

In the last couple of years, increased industrial and high-tech activities have contributed to improving gross domestic products and the standard of living. In spite of the increasing awareness and stringent environmental regulatory frameworks, environmental pollution has now become endemic thus demands urgent intervention. Furthermore, the direct discharge of untreated industrial and domestic wastewater which contains unpleasant odour, high pH, strong colour, high chemical oxygen demand (COD), biochemical oxygen demand (BOD),

total organic carbon (TOC), and other soluble substances into rivers continues to deplete the little available freshwater and impacts negatively on the water quality (Hussaini et al., 2013).These anthropogenic activities have forced many citizens to seek and use water from unconventional sources which have triggered health challenges among humans and other species.

While some previously used, harmful chemicals are being phased out of products, new chemicals are being manufactured and incorporated into products to meet human needs. These groups of chemicals are of great public health concern and are collectively called chemicals of emerging concern (CEC) (Richardson and Ternes, 2011; Kolle et al., 2013). According to the US Geological Survey, (2014), CEC are new chemicals without regulatory status which modulate the hormonal growth in the endocrine system and affect the physiological activities of endogenous hormones. In spite of the Stockholm Convention known as the Persistent Organic Pollutants Treaty of 2001 and the Berlaymont Declaration of 2013 to protect humans and aquatic species from risks associated with exposure to these chemicals, the number of exogenous chemicals particularly phenolic compounds and their metabolites are on the increase in environmental waters. Their perceived toxicity and environmental persistence have dominated public discussions especially among the experts in the field of water and wastewater management (Jiang et al., 2013; Trapido et al., 2014; Manickum and John, 2014). These chemicals which include bisphenol-A (BPA), 2-nitrophenol (2-NP), alkylphenols, nonylphenol, phthalates, ethinylestradiol, 17 β- Estradiol (E2) are introduced into the environment via different point and non-point sources such as industrial emission, direct disposal of untreated effluents containing drugs, human and animal medical care products amongst others (Magureanu et al., 2010).

With advances in analytical instrumentation and detection techniques, a sizeable number of CEC have been successfully identified and quantified at low concentrations in different water sources including drinking water by different scientists (Magureanu et al., 2010; Trapido et al., 2014). Furthermore, exposure to these chemicals via drinking water, or consumption of food irrigated with reclaimed water containing these substances have been reported to disrupt hormonal body functions and subsequently lead to cancerous tumours, early puberty, heart disease, obesity, birth defects, and other unpredicted abnormalities especially in aquatic species (Kolle et al., 2013; Tijani et al., 2013). While the health effect of BPA and 2-NP on human beings is still a subject of debate and needs further investigation, low sperm count, reduced fertility and reproductive malfunctions is on the increase in humans these days.

There are suspicions that most newly identified micropollutants, particularly BPA or 2-NP, may play a crucial role and perhaps be responsible for these manifestations.

Therefore, industrial wastewater containing endocrine-disrupting compounds must be treated prior to discharge into the environment. It is necessary from both the legal and ecological point of view to develop cost effective and long-term, sustainable purification techniques to be applied as a polishing step to tackle the ever increasing burden of emerging organic pollutants in water in order to prevent short and long-term health effects or impacts.

1.2 Rationale and Motivation

To date, studies still uphold advanced oxidation technologies (AOTs) as the most environmental friendly and promising techniques intensively studied for the decomposition of recalcitrant organic pollutants in water (Fabiola et al., 2010; Luiz et al., 2009). The degradation occurs in the presence of powerful oxidants especially hydroxyl radicals at ambient temperature and pressure (Chong et al., 2012; Oller et al., 2011). These free reactive species are short-lived, could exist alone or in a mixture, although very little information exists on the contribution made by the individual active species regarding the decomposition of the target pollutants. Among the chemically reactive species produced by AOTs, hydroxyl radicals remain the most powerful, reactive and non-selective species with the highest oxidation potential capable of oxidizing organic pollutants via hydrogen abstraction as well as electron transfer into harmless end products such as CO_2 and H_2O (Klavarioti et al., 2009). These free reactive species, particularly hydroxyl radicals, could be produced via most AOTs techniques such as the Fenton and photo-Fenton process, electrochemical oxidation, corona discharge, heterogeneous photocatalysis, photolysis/hydrogen peroxide, ozonation and cavitation, photolysis of hydrogen peroxide and ozone, wet oxidation, sonolysis among others.

The different advanced oxidation technologies mentioned above have been employed either individually or in combination to degrade the target pollutants (Bothias et al., 2014). However, due to the structural and chemical complexity of wastewater vis-a-viz the existence of pollutants as mixtures, no single technology manages to remove all the pollutants and most often a combination of treatment processes are required to effectively purify the water. To buttress this point, several studies have shown that combined treatment techniques are beneficial and more economical, offering greater efficiency than a single technology (Oller et al., 2011). Combined techniques allow the exploitation of each method's strength to provide

synergy, as well as supplementing each process in the overall interest of obtaining a sustainable treatment system. These synergistic effects could also enhance the generation of powerful oxidants, decrease mass transfer resistances and thus increase free radicals yield, shorten reaction time and lower the operational and maintenance cost. Based on the literature survey, the present research is conducted to identify the best combined advanced oxidation process capable of converting bisphenol-A and 2-nitrophenol into more readily biodegradable compounds or completely eliminate the two compounds in water. The following combined approaches such as dielectric barrier discharge/heterogeneous photocatalysis, dielectric barrier discharge/photo-Fenton process, and jet impingement/ UV/hydrogen peroxide system will be explored, in this study the survey of literature as far as could be ascertained indicates that little or no research has been conducted on the integration of combined advanced oxidation technologies for the removal of bisphenol-A and 2-nitrophenol from water.

1.3 Problem Statement

The production and use of chemically manufactured products have increased significantly due to the rapid population growth, industrialization drive and of course extensive agricultural activities. These activities are responsible for the presence and accumulation of different recalcitrant organic compounds in the environment. One class of compounds currently identified and detected in the global water cycle is endocrine disrupting compounds (EDCs). Among the EDCs, phenolic compounds such as bisphenol-A and nitrophenols have become a subject of considerable environmental concern and a public health issue. In fact, United States and European Environmental Protection Agencies categorized bisphenol-A and 2-nitrophenol as potential priority pollutants with different physicochemical and endocrine disrupting properties (Richardson and Ternes, 2011). The removal of phenolic compounds from contaminated matrices has been challenging and problematic due to their different lipophilic behaviour. These groups of chemical substances are highly mobile, toxic, non-biodegradable and persistent throughout conventional wastewater treatment, thus escape and are detected in water sources at ng/L to $\mu g/L$ levels. Additionally, chlorination technology widely used for disinfection purposes often accumulates disinfection by-products that are mutagenic and carcinogenic to public health. Problems such as further treatment, leading to extra costs and problems with solids disposal, and generation of large volumes of toxic sludge, and failure to decompose recalcitrant organic pollutants have been identified as drawbacks of conventional water/wastewater treatment technologies. Alternative treatment

based on advanced oxidation technologies have been developed and applied to degrade organic pollutants by many researchers (Tijani et al., 2014). Although advanced oxidation technologies appear promising there still exist limitations which impede their full implementation at commercial scale. These limits include incomplete destruction of recalcitrant pollutants, utilization of expensive but undesirable reagents, separation and recycling of sludge after treatment among others. For instance, direct application of ultraviolet light is limited by light scattering effects especially when dealing with highly turbid water (Chong et al., 2010). The high cost of the UV lamp, installation, and maintenance and electricity consumption also militate against the widespread use of this technique especially in developing countries where there is erratic power supply. Equally, heterogeneous photocatalysis which is most widely investigated, has some obstacles such as poor light penetration due to particulates, the need for post-filtration and recovery of catalyst particles from suspension after treatment, high electron-hole recombination rate, and aggregation of the suspended particles (Wankhade et al., 2013). In addition, application of powered TiO_2 for wastewater treatment increases solution turbidity and prevents the interaction of UV light with the target pollutants, thus reducing the photocatalytic potential of the material. These shortcomings limit its industrial scale application for wastewater treatment (Friedmann et al., 2010). The activity of the most common TiO_2 photocatalyst is mainly in the UV region. On the other hand, the dielectric barrier discharge (DBD) system produces ultra violet light and hydrogen peroxide within the plasma zone which is not fully maximised for the mineralization of persistent organic pollutants (Gao et al., 2013; Magureanu et al., 2011). The problem with DBD is high energy consumption, difficulty in scaling-up, thus affecting industrial utilization, despite being successful at laboratory scale. The problem of nano zero valent iron particles involves rapid oxidation and aggregation during synthesis which reduces the particles surface area and affects its performance (Shahwan et al., 2011). In the same vein, the jet loop reactor system is characterised by low cavitational yield occasioned by poor pressure recovery downstream of the constriction, which is responsible for low mineralization rate (Bokhale et al., 2014; Patil et al., 2014a)

Overall, it could be seen that the listed single advanced oxidation technologies are associated with some drawbacks and thus cannot operate individually and achieve the desired results. Thus, in order to overcome these drawbacks, development of combined advanced oxidation processes seems to be an attractive option. It is believed that application of combined advanced oxidation technologies will reduce the cost of treatment and increase the

mineralization efficiency of the pollutant. The present study is aimed at developing and comparing combined advanced oxidation processes for the efficient removal and degradation of bisphenol-A and 2-nitrophenol from water.

1.4 Aims and objectives of the study

Several conventional techniques have been applied but failed to decompose recalcitrant organic pollutants present in water. However various advanced oxidation processes have been identified as alternative solutions to achieve partial or complete mineralization of these emerging pollutants. In order to reduce the high operation and maintenance cost as well as energy consumption, a combinatory approach of different advanced oxidation processes was conceived. Therefore, the overall aim of this study is to evaluate and identify the best combined advanced oxidation technologies to achieve complete mineralization or partial degradation of bisphenol-A and 2-nitrophenol in water and to compare the efficiency of these combined system. This aim will be achieved through the outlined objectives:

- To prepare supported Ag doped TiO_2 nanocrystals via sol-gel and thermal evaporation method and study its photocatalytic activity using methylene blue as a model pollutant
- To synthesis and characterize stabilised nano zero valent iron particles to induce photo-Fenton process.
- To assess and evaluate the performance of combined DBD/supported TiO_2 or Ag doped photocatalysts and DBD/photo-Fenton induced process in the degradation of BPA or 2-NP in aqueous solution.
- To optimise the jet loop reactor system and establish the best optimum conditions for impingement.
- To establish the synergetic effect among the various combined advanced oxidation processes such as jet loop/UV, jet loop/H_2O_2, UV/H_2O_2, jet loop/UV/H_2O_2 system
- To identify any possible intermediate products formed during degradation, predict the mechanism of the degradation pathway and propose possible degradation pathways based on the generated free reactive species so as to have better understanding of the mechanism of removal of bisphenol-A and 2-nitrophenol

- To quantify the free reactive species produced by the optimized combined advanced oxidation technologies
- To establish or propose a suitable kinetic model for the degradation pathways of bisphenol-A and 2-nitrophenol.

1.5 Research questions

This study aim at providing answers to the following questions;

1. Is it possible to synthesis TiO_2 photocatalysts supported on a stainless steel mesh?
2. Does the deposition of plasmonic Ag reduce the band gap energy of TiO_2 and improve its photocatalytic ability?
3. Is the dielectric barrier discharge (DBD) system on its own capable of decomposing bisphenol-A and 2-nitrophenol? To what extent could UV and other reactive species generated by DBD enhance degradation?
4. Is the removal efficiency of the two compounds improved in the DBD system by incorporation of supported TiO_2 photocatalyst or Ag doped TiO_2 nanocomposites or nano zero valent iron (nZVI)
5. Are the OH radicals increased in the combined advanced oxidation system under optimised conditions?
6. Can the jet loop reactor alone remove and degrade the target pollutants due to impingement effect and effective mixing?
7. Does the jet loop system combined with in-line UV lamp, and hydrogen peroxide enhance the degradation rate?
8. Is there formation of any intermediate degradation products of bisphenol-A and 2-nitrophenol in either the single or combined AOT?
9. Which of the free reactive species are responsible for decomposition of the target compounds?

1.6 Research approach

Extensive literature review on the research topic was carried out to find potential AOTs routes to degrade bisphenol-A and 2-nitrophenol. The research approach employed to achieve the set aims and objectives of the study was organized in three sections as follows:

- **Section 1: Catalytic development, characterization and photocatalytic activity**

TiO_2 photocatalyst supported on a stainless steel mesh was developed via sol-gel method followed by dip coated and calcination at different temperatures (300 ºC, 350 ºC and 400 ºC using heating time of 1- 4 hr). Afterwards, various amounts of metallic silver were deposited on the (optimum) supported TiO_2 photocatalyst using thermal evaporation. Subsequently, the Poly ethylene glycol stabilized nano zero valent iron (PEG-nZVI) was synthesised using modified borohydride reduction method. The synthesised catalysts such as TiO_2, Ag doped TiO_2 nanocomposites and nZVI were characterized by several analytical methods such as High Resolution Scanning Electron Microscopy (HRSEM), High Resolution Transmission Electron Microscopy (HRTEM), Fourier Transform Infrared Spectroscopy (FTIR), Energy Dispersive Spectroscopy (EDS), Selected Areas Electron Diffraction (SAED), Ultraviolet and Brunauer Emmett-Teller (BET) Surface Area analysis, X-ray photoelectron spectroscopy (XPS), Thermogravimetric analysis/Differential Scanning Calorimetry (TGA/DSC), and X-ray diffraction (XRD). The photocatalytic activity of the supported Ag doped TiO_2 nanocomposites was conducted using ultra-violet light and methylene blue (MB) as a modelled pollutants and compared to baseline optimum supported TiO_2 nanocrystals without plasmonic metal.

- **Section 2: Degradation of bisphenol-A and 2-nitrophenol by DBD: influence of supported photocatalysts or stabilized nano zero valent iron particles**

An optimised DBD system was used to decompose bisphenol-A and 2-nitrophenol in water. Thereafter, supported TiO_2 nanocrystals, Ag doped TiO_2 nanocomposites or different dosage of nZVI were incorporated into the DBD reactor to improve degradation of the target pollutants. The influence of operating parameters such as solution pH, initial concentration of the target compounds, and radical scavengers on the degradation of BPA or 2-NP in water was investigated. The free reactive species (O_3, H_2O_2, $OH^{\bullet}$) produced by DBD in the presence or absence of catalysts were quantified using standard analytical methods. The oxidation products of bisphenol-A and 2-nitrophenol formed via DBD, DBD/supported photocatalysts and DBD/photo-Fenton induced process were identified and the mechanism of degradation equally proposed. The reaction kinetics of adding the various synthesised catalysts was studied in detailed. The residual concentration of the Bisphenol-A and 2-nitrophenol were determined using High Performance-Liquid Chromatography (HPLC). The

intermediate products were analysed using Liquid Chromatography-Mass Spectrometry (LCMS).

- **Section 3: Degradation of Bisphenol-A and 2-nitrophenol by Jet loop reactor: influence of UV light and Hydrogen peroxide**

A combined Jet loop reactor (JLR) system was designed and used to degrade bisphenol-A and 2-nitrophenol in water. Different combined advanced oxidation processes such as JLR/UV, UV/H_2O_2, JLR/H_2O_2 and JLR/UV/H_2O_2 were compared to degrade the target pollutants. The effect of the following operating parameters such as solution pH, inlet applied pressure, initial concentration of target compounds, concentration of radical scavengers was investigated. The synergistic index value of the BPA or 2-NP degradation via Jet loop reactor alone and other advanced oxidation technologies was determined. The residual concentration of the bisphenol-A and 2-nitrophenol were determined using High Performance-Liquid Chromatography (HPLC).

1.7 Research Hypothesis

These hypotheses are formulated based on extensive literature review.

- Thermal evaporated supported Ag doped TiO_2 photocatalyst will decolourised methylene blue solution.
- Dielectric Barrier Discharge (DBD) system will degrade bisphenol-A and 2-nitrophenol through free reactive species produced by the system
- The incorporation of supported TiO_2 or Ag doped TiO_2 photocatalyst or stabilized nano zero valent iron particles into DBD system will improve the overall degradation rate of the above mentioned pollutants.
- The jet loop reactor can degrade the target pollutants effectively due to impingement and effective mixing. The integration of the jet loop system with in-line UV lamp and hydrogen peroxide, can enhance the degradation rate of the target pollutants due to an increase in the concentration of hydroxyl radicals under the applied impingement conditions.

1.8 Scope and delimitation of the study

The current study focuses on the degradation of two phenolic compounds namely bisphenol-A and 2-nitrophenol, which have been widely detected in different environmental media. Their removal from water bodies has been problematic based on the application of single advanced oxidation technologies, which is often associated with low removal rates. This study therefore applied the following combined advanced oxidation technologies such as DBD/photocatalysts, DBD/nZVI and Jet loop system/UV/H_2O_2 to oxidise bisphenol-A and 2-nitrophenol in water. Simulated wastewater containing the modelled pollutants were used.

Delimitation

This research did not cover other combinations of advanced oxidation processes such as Jet loop reactor system with heterogeneous photocatalysis, Jet loop reactor system with ozonation process due to time constraint. The study only considered three types of persistent organic pollutants namely: methylene blue, bisphenol-A and 2-nitrophenol. Their selection was based on their level of persistency, stability and because they are not easily removed by conventional treatments, and are prevalent in the environment.

1.9 Thesis outline

This thesis comprises seven chapters which are outlined below:

Chapter 1: Introduction

This chapter outlines the introduction and gives a brief overview of the topic, motivation and objectives of the study, problem statement, research approach, hypothesis, scope and delimitations of the study together with thesis frame work.

Chapter 2: Literature review

This chapter deals with a review of the literature relevant to the study. An overview of emerging micropollutants and types, endocrine disrupting compounds, sources, effects, and environmental fate is provided. Critical appraisal of selected endocrine-disrupting chemicals is covered including critical evaluation of different water treatment techniques such as heterogeneous photocatalysis, photo-Fenton process, nano zero valent iron, dielectric barrier system and jet impingement process, and the gaps in literature will also be highlighted in this chapter. The methods of synthesising heterogeneous photocatalyst and nano zero valent iron

as well as applications of TiO_2 nanoparticles and nZVI are also appraised. The factors influencing the photocatalytic activity and impingement process as well as detection and quantification of free reactive species are also highlighted in this literature review. Finally, a critical overview is provided highlighting the gaps in the body of knowledge.

Chapter 3: Materials and Experimental procedures

This chapter will provide the detailed experimental procedures that were adopted to generate data needed to achieve the outlined aims and objectives of the study. This chapter will also include the materials and protocols that were used as well as a brief description of the analytical characterization tools that were employed in this study.

.

Chapter 4: Synthesis and characterisation of the catalysts

This chapter will present the results and discussion of the characterization of supported TiO_2 nanocrystals, Ag doped TiO_2 nanocomposites developed on stainless steel mesh as well as the non-stabilized and stabilised-nZVI. The characterization techniques that were used such as XRD, HRSEM, SAED, HRTEM, BET, XPS, TGA/DSC, FTIR, UV-vis/diffuse reflectance and EDS will also be presented. Furthermore, the chapter will also present results of the photocatalytic activity of Ag doped TiO_2 nanocomposites that were conducted under ultraviolet light as baseline before integration into DBD system.

Chapter 5: Degradation of bisphenol-A and 2-nitrophenol by dielectric barrier discharge: Influence of stabilized nano zero valent iron particles and heterogeneous photocatalysis

This chapter will provide the detailed discussion of the results that were obtained from the elimination and decomposition of bisphenol-A and 2-nitrophenol using the dielectric barrier discharge system. The discussion will also include the results that were obtained after incorporation of the supported heterogeneous photocatalyst or nano zero valent iron into the DBD system. The results of the quantification of free reactive species are given and intermediate degradation by-products were identified. The degradation pathways are proposed, presented and discussed in this chapter.

Chapter 6: Degradation of bisphenol-A and 2-nitrophenol by jet loop reactor and other advanced oxidation technologies

In this chapter, the optimization of the jet loop reactor system is presented as well as the trends that were observed for degradation of the target pollutants using the jet loop system. The comparison of the degradation of the target compounds by various combined approaches that were used in this study are presented. The results of the synergistic index value of the various combined treatment options are presented and discussed.

Chapter 7: Conclusion and Recommendations

In this chapter the overall findings of the study and recommendations for further studies based on the outcome of the research are provided.

CHAPTER TWO

2 LITERATURE REVIEW

2.1 INTRODUCTION

This chapter deals with a review of the literature relevant to the study. An overview of emerging micropollutants and types, endocrine disrupting compounds, sources, effects, and environmental fate is provided. Critical appraisal of selected endocrine-disrupting chemicals is covered including review of different removal techniques such as heterogeneous photocatalysis, photo-Fenton process, nano zero valent iron, dielectric barrier system and impingement or cavitations. The methods of synthesising heterogeneous photocatalyst and nano zero valent iron as well as applications of TiO_2 nanoparticles and nZVI are also appraised. The factors influencing the photocatalytic activity and jet impingement process as well as detection and quantification of free reactive species are also highlighted in this literature review. Finally, a critical overview is provided highlighting the gaps in the body of knowledge.

2.2 Emerging micropollutants

Emerging micropollutants or chemicals of emerging concern have no clear definition and no comprehensive list. Due to misconception among researchers the terms have been used interchangeably. Field et al., (2006) referred to emerging contaminants as a group of new chemicals found in the environment. The US EPA (United States Environmental Protection Agency, (2007) categorised emerging contaminants as new chemicals without regulatory status of which the impacts on the environment and human health are poorly understood or remain unknown. Houtman, (2010) opined that emerging contaminants do not only mean the newly developed and detected compounds in the environment but rather divided them into three different classes. The first class consists of chemical compounds recently released into the environment. The second class involves compounds that have been in the environment for a longer time but have recently been detected due to advances in analytical techniques. The third class refers to compounds whose associated adverse health effects is just now manifesting. Kümmerer, (2011) defined emerging contaminants as a more or less loosely defined sub-group of micro-pollutants present in the environment at low concentration with strongly variable chemical structures, properties, application ranges and effects. The United States Geological Survey (USGS, 2014) defines emerging micropollutants as any synthetic or

natural occurring chemical or microbial constituent that previously had not been detected or historically known or considered to be a contaminant, but interferes with hormonal body functions responsible for the maintenance of homeostasis, body growth and development.

2.2.1 *Types of emerging pollutants*

Different types of chemical containing products are currently manufactured to meet human basic needs in life ranging from cleansing agents, pharmaceuticals (prescribed and over the counter drugs), cosmetics, fragrances, and personal care products to mention but a few which are widely used globally. Basically, emerging contaminants are categorised into pharmaceuticals, personal care products, industrial chemicals, agricultural chemicals, disinfection by-products. Most of these chemical compounds such as bisphenol-A, 2-nitrophenol amongst others, possess endocrine activities that have generated public health concern. Today, thousands of emerging micropollutants have been identified and detected in virtually all environmental samples such as water, soil and even in human food. Due to the recalcitrant nature of these compounds, some bioaccumulate in living cells via the lipid layer and may be toxic to the organisms depending on the concentration and duration of exposure. It is predicted that these compounds may reach humans via food chain biomagnification.

2.2.2 *Endocrine disrupting compounds (EDCs)*

Endocrine systems control a large number of physiological activities in the body such as reproductive processes, embryonic development, sex differentiation, and metabolic development (Flint et al., 2012). However, there is available evidence that certain groups of compounds block or disrupt endocrine glands from functioning properly. These compounds are collectively known as endocrine-disrupting compounds (EDC). They are otherwise known as endocrine disrupting chemicals, or endocrine disruptors or environmental hormones or endocrine modulators. Diamanti-Kandarakis et al., (2009) referred to EDC as compounds that interfere with the synthesis, secretion, transport, binding, action, or elimination of natural hormones in the body that are responsible for development, behaviour, fertility, and maintenance of homeostasis (normal cell metabolism). EDC can be natural or man-made. Currently a full list of EDCs does not exist and it is anticipated that more chemicals may be recognized as endocrine disrupters in the nearest future (Richardson, 2012).

2.2.3 *Sources of endocrine disrupting compounds*

Endocrine disrupting compounds enter the receiving waters via different point and non-point sources such as agricultural, household discharge, industrial, sewage and municipal wastewater as shown in Figure 2.1. Most researchers have demonstrated that wastewater treatment plants are not designed to effectively degrade emerging contaminants due to their complex molecular structure and low concentration in the aqueous matrix (Baker and Kasprzyk-Hordern, 2013; Fawell and Ong, 2012). Subsequently, while many of these chemicals pass through the WWTP based on their hydrophobic nature, the remainder get absorbed onto the particulate matter and settle with bottom sediments and are accumulated continuously through electrostatic interaction (Michałowicz et al., 2014). Besides WWTP discharges, other identifiable sources include animal husbandry operations, recreational activities, transportation or wash-off from roadways, and atmospheric deposition (Rogers et al., 2013). Most of these contaminants are mobile, highly stable, and recalcitrant and partly decompose or persist throughout conventional wastewater treatment, thus escape, bioaccumulate and metabolise in living tissues causing considerable adverse effects on aquatic species or humans (Bell et al., 2011). Despite the fact that there is little epidemiological data regarding the impact of exposure to emerging contaminants on human health, there are increasing incidences of feminization, immune deficiency, neurological effects, bacterial resistance and cases of intersex alteration among alligators, frogs and fish upon exposure to endocrine disrupting chemicals (EDC) (Flint et al., 2012; Geens et al., 2011). With advances in qualitative and quantitative analytical and standardized detection techniques, endocrine disrupting compounds such as bisphenol-A and 2-nitrophenol have been identified in water, soil and even human food. This has attracted public attention due to their potential negative impacts on natural ecosystems and humans (Fawell and Ong, 2012). These chemicals compounds have been established to cause disruption of endocrine systems, yet they are still unregulated and discharged carelessly into the immediate environment especially in the developing countries where there is no stringent regulatory and legal frame work (Petrie et al., 2015). However, this problem has been known for more than a decade, yet little progress has been made to stem the tide of such pollutants from entering the global waterways. The main distribution pathways via WWTP to drinking water is depicted in Figure 2.1. In this study, two compounds namely bisphneol-A and 2-nitrophenol were selected based on a literature survey, industrial use, consumption habits, production output,

persistency level, poor biodegradability toxicity, bioaccumulation factor, frequent detection and prevalence in wastewater.

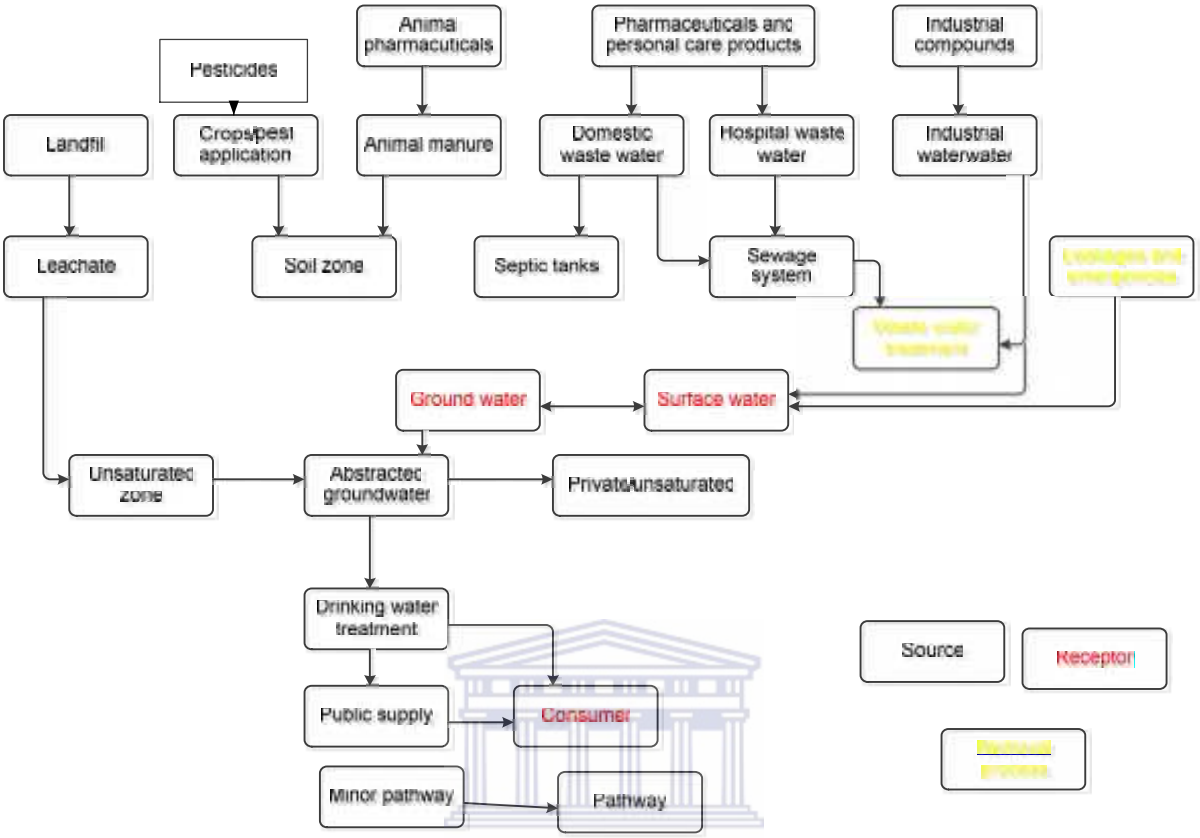

Figure 2.1: Potential sources and pathways of some emerging micropollutants to receptors and aquatic environment (Stuart et al., 2012).

2.2.4 *Mechanism of endocrine disruption compounds within the body system*

The mechanism of endocrine-disrupting compounds on the hormonal body system is a complex phenomenon and difficult to predict since compounds exist as mixtures. However, review of various studies (Olujimi et al., 2010, 2012) revealed that disruption can take place via multiple routes listed below:

- The contaminants can bind to the nuclear and hormonal receptor cells or sometimes block or mimic the chemical messengers in the body and cause considerable adverse ecological health effects. EDCs sometimes alter the response activity of genes. For instance, BPA can bind to oestrogen receptor β based on its lower affinity than estradiol (Rogers et al., 2013)
- The concentrations or level of the chemical messengers/hormones in the body may be affected via alteration of their metabolic or synthetic pathways (Olujimi et al., 2010)

- Interference with the hormonal-controlled physiological signals responsible for body homeostasis and development is often evident (Flint et al., 2012).
- Lastly, by modification or modulation of certain chemical messenger receptors within the cells responsible for the immune system (Michalowicz et al., 2014).

2.2.5 *Critical appraisal of selected endocrine-disrupting chemicals*

i. Bisphenol-A

Bisphenol-A (BPA) or 2, 2-Bis (4-hydroxyphenyl) propane belongs to the class of phenolic chemical compounds containing two hydroxyphenyl groups. BPA is a white solid, poorly soluble in water but is readily soluble in organic solvents. BPA has a molecular weight and molecular formula of 228.1 g/mol and $C_{15}H_{16}O_2$ respectively. BPA has a melting and boiling point of 156 ºC and 220 ºC with water-octanol coefficient value of 3.32. The water-octanol coefficient value expressed in logarithm suggests that BPA is readily soluble in fat and poorly soluble in water. The molecular structure is represented in Figure 2.2.

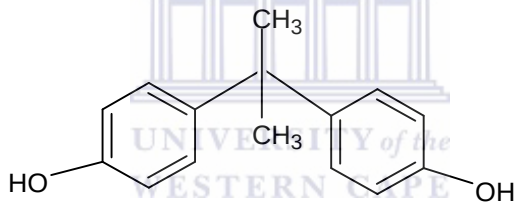

Figure 2.2: Structure of bisphenol-A

Historically, BPA was first synthesised by a Russian chemist (Alexander. P. Dianin) in 1891 via a condensation reaction of one molecule of acetone and two molecules of phenol in the presence of hydrogen chloride as a catalyst. Ever since then, BPA has been utilized as an intermediate in the production of polycarbonate plastics, polyesters, plasticizers, pesticides, thermal printing paper and epoxy resins (Geens et al., 2011; Rogers et al., 2013). Other products containing BPA include baby bottles, drinking water bottles, medical equipment, microwave dishes, food can linings and dental sealants (Tsai et al., 2009). An increase in the global consumption of plastic products has caused the production of BPA to rise by 6-8% annually (Fernandez, 2010; Huang et al., 2012). In the 80s, the production output was around 1 million; in 2003, over 3.2 million metric tons were produced globally (Tsai, 2006), USA alone produced approximately one-third of that figure (National Institute of Health, 2008) while EU produced 1.2 million tonnes, China also produced and used 670,000 tons of BPA

(Xu et al., 2007). In 2008 more than 3.2 million metric tonnes were utilised globally (Wang et al., 2012). In 2010, global consumption according to World Health Organization was over 5.2 million metric tonnes (Tsai, 2006). According to the US Environmental Protection Agency, (2010) over 1266 metric tons of BPA were discharged into the environment via manufacturing, incineration activities and wastewater treatment plants in 2008 alone. The global Industry Analysts has projected global production rate to rise to 6 million tons by the end of 2015. Currently, The USA, Taiwan, South Korea, China and Japan remained the highest producers of BPA in the world. With this geometrical increase and widespread use of plastics, BPA has been recognised as a problem globally, and its removal from wastewater has become a fundamental component of applied research.

BPA is a well-known antioxidant and ubiquitous synthetic xenooestrogen in the environment for modulating the activity of endocrine glands in humans and aquatic wildlife (Chang et al., 2011; Rocha et al., 2013). Apart from its known estrogenic activities on cells, bisphenol-A also is suspected to alter the immune responses in humans by acting as agonists or antagonists to nuclear-hormone receptors without significant toxicity (Michałowicz et al., 2014; Rogers et al., 2013). BPA as an endocrine-disruptors possesses oxidative, mutagenic and hypomethylation properties and thus exerts different harmful effects on animals and even humans (Ziv-Gal et al., 2013). As a result of the multidirectional effect of BPA on different receptors, the importation of infant food cans containing BPA such as baby feeding bottles have been strictly restricted in countries including China, North America, and Europe. Similarly, the South African Ministry of Health has also proposed draft regulations that will restrain the manufacture, sale, import and export of polycarbonate baby bottles containing BPA. Due to the absence of strong covalent bonds between chemical plastic components and BPA, fragmentation and leaching of BPA from the plastic products occur (Chen et al., 2010; Tsai, 2006). Exposure to BPA by humans and aquatic species could vary. According to United State Environmental Protection Agency, bisphenol-A is a known endocrine disruptor. A number of studies have identified drinking water, manufacturing effluents, dust inhalation, agricultural run-off, food, drinking, and beverage containers as possible exposure routes to this chemical (Bonefeld-Jorgensen et al., 2007; Sellin et al., 2009). At the moment, the main exposure route to BPA is via inhalation or oral ingestion (Geens et al., 2012). However recently, transdermal exposure has become a source of concern (Geens et al., 2012). Thermal paper coated with BPA is used for till slips which are daily touched and handled by millions

of people. BPA is regularly detected in municipal and industrial wastewater and its presence has been widely documented (Sanchez-Avila et al., 2009).

ii. Effect of BPA exposure

There is not enough available information from the literature regarding associated adverse environmental and health effects of BPA on human beings. Very recently, epidemiological studies conducted by Vandenberg et al., (2007) linked abnormalities namely polycystic ovarian syndrome, obesity, endometrial hyperplasia, heart diseases, repeated miscarriages, prostate and breast cancer, attention-deficit hyperactivity disorder, and infertility to human exposure to BPA (Teppala et al., 2012; Wang et al., 2012). Moreover, there have been documented health effects from exposure of aquatic species to BPA. It has been established that long term exposure to BPA could lead to transgenerational health effects on humans and wildlife (Dmitruk et al., 2008). BPA possesses estrogenic activity and alters metabolic kinetics and promotes DNA damage including chromosomal abnormalities. BPA is suspected to alter the immune responses in humans by acting as agonists or antagonists to nuclear-hormone receptors without significant toxicity (Rogers et al., 2013). BPA also prevents the endocrine hormones such as sex hormones, thyroxin, insulins and leptins from functioning properly and could result in immunotoxic, heptatoxic, carcinogenic and sometimes mutagenic effect (Michalowicz et al., 2014; Wang et al., 2015). Tay et al., (2012) opined that long term exposure to BPA can cause developmental toxicity, carcinogenicity, neurotoxicity, and estrogenic effect in humans and aquatic species. However, there is lack of reliable data and inconsistency on the neurotoxicity and tetratogenic effects of BPA on animals or humans (Michałowicz et al., 2014). It has also being established that exposure to BPA by aquatic species have led to a high predominance of early puberty, heart disease, obesity, low fertility, low sperm count, breast, ovarian and testicular cancer (Geens et al., 2012). Li et al., (2010a) reported that exposure to BPA by factory workers specializing in the production and packaging of epoxy resins in China was responsible for decrease in sexual desires, erectile and problems of ejaculation. Exposure to BPA during pregnancy has been found to overshadow some critical genes in the womb, thus retarding growth (Geens et al., 2011). In the same vein, the decline in fish populations is attributed to exposure to BPA (Deborde et al., 2008). Exposure to low doses of BPA can cause changes in body weight, cancers, abnormally early puberty, and disorders such as obesity, miscarriage predominantly among fish (Fan et al., 2013; Vandenberg et al., 2007). Considering the exposure rate to BPA, a

precautionary approach involving elimination and decomposition of BPA from contaminated water is considered necessary in order to safeguard potable water supplies as well as reduce potential threats.

iii. Fate of bisphenol-A in the environment

After the discharge and escape of persistent environmental pollutants from wastewater treatment plants, the need for a better understanding of their fate and impacts on the environment cannot be ignored. BPA enters the environment during manufacturing activities, transportation, processing, handling among others. In fact few places in the world are free of BPA (Rogers et al., 2013). The pathways of entrance into the environment could be air, water or sediment. However the most recognised source of entrance into the environment is via discharge of plastic products and household wastewater. Thus, the physico-chemical degradation of plastics causes leaching and volatilization of BPA which prompts the release of a substantial amount into the soil and lesser amounts into water and air respectively. BPA does not hydrolyse in water because of its chemical structure and as such more than 50 % BPA gets adsorbed or binds onto sludge/sediment, however it undergoes rapid photo-degradation in wastewater treatment plants and receiving waters. BPA is readily decomposed by bacteria under both aerobic and anaerobic conditions. BPA is therefore regarded as a pseudo-persistent pollutant with a short half-life between 2.5 to 4 days, though other conjugates or residual by-products are associated with longer half-lives of up to a month (Oehlmann et al., 2009). The concentrations of BPA differ appreciably in wastewater treatment plants depending on their location, plastic use patterns and sampling period. The fate and behaviour of the individual xenobiotic does not only depend on its hydrophobic-hydrophilic properties but also on environmental conditions such as water solubility, pH, adsorption coefficient, redox condition, temperature and bioaccumulation potential (Rahman et al., 2009). The quantity of residual pharmaceuticals and endocrine-disruptors in aquatic environments are frequently influenced by factors such as the amount of wastewater produced, the consumption patterns, geographical locations, lifestyle, appropriate treatment techniques, regulations and so on (Rogers et al., 2013).

i. 2-nitrophenol

2-nitrophenol (NP) is categorised as one of the three nitrated phenols with molecular weight and molecular formula 139.10 g/mol and $C_6H_5NO_2$ respectively. It is a yellow crystalline solid, readily soluble in water and moderately acidic upon dissociation in water. 2-nitrophenol is not naturally occurring in the environment. However it remains an integral components of industrial effluents, which has been identified in different urban and agricultural waste. It is mostly utilized in various industries as a reagent to manufacture organophosphate pesticides, herbicides, and explosives and as intermediate during the synthesis of dye (Ammar et al., 2007). The structure of 2-nitrophenol is shown in Figure 2.3.

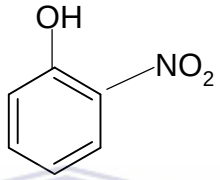

Figure 2.3: Structure of 2-nitrophenol

Due to the absence of stringent environmental regulatory frameworks, most phenolic compounds especially 2-nitrophenol (2-NP) have become environmental pollutants commonly detected in water sources, soil and industrial effluents (Ahmed et al., 2015; Amin et al., 2007). United State Environmental Protection Agency (USEPA, 2007) categorised 2-NP as a toxic and recalcitrant organic pollutant with considerable endocrine disrupting properties. The compound is a highly stable, non-biodegradable chemical compound which bio-accumulates over a long period of time in the environment. 2-nitrophenol is difficult to degrade in soil or water by conventional biological wastewater treatment processes and other treatment options (Oller et al., 2011; Pradhan and Gogate, 2010; Ribeiro et al., 2008). Also, 2-NP affects both the hormonal reproductive functions of male and female organisms (Ahmed et al., 2015). With their high level of persistency in the environment and the associated health risks due to exposure, USEPA recommended the tolerable level of this compound in natural water to be below 4.8 µg/L. So far, there are no identifiable natural sources of 2-NP in the environment. The presence of 2-NP in water also introduces an unpleasant odour and taste to available drinking water with a resultant adverse health impact on downstream users. The rate of toxicity of 2-NP in water is measured based on its dissociation mechanism in aqueous media at a specific solution pH. The dissociation

mechanism is linked to its toxicity level, thus a decrease in solution pH causes an increase in toxicity and promotes dissociation of the compound.

ii. Environmental effect of 2-nitrophenol

The short-term effect of exposure to 2-NP can cause skin irritation while continuous exposure can lead to severe skin disorders (Boehncke et al., 2000). Inhalation of 2-NP can lead to headaches, dizziness etc. Additionally, 2-NP has carcinogenic and mutagenicity effects on the target organisms. While there is limited or lack of reliable data regarding the genotoxicity effect of 2-nitrophenol on humans, exposure to 2-NP can influence catabolic metabolites in the body. For instance, the exposure of female rats and male rats to 2-NP can causes estrogenic and anti-androgen effects (Ahmed et al., 2015).

iii. Fate of 2-nitrophenol in the environment

The fate and behaviour of recalcitrant pollutants are quite diverse and complex depending on certain environmental factors, which complexity partly responsible for limited knowledge of their environmental fate. 2-nitrophenol may enter the environment via wastewater treatment plants. Other sources include industrial fugitive emission, vehicular exhaust emissions, and atmospheric photochemical reactions. In the environment, 2-NP evaporates from the topsoil within 10 days while less than 10 % decomposes slowly under aerobic conditions within 30 days inferring that 2-NP undergoes slow biodegradation (Ribeiro et al., 2008). In the terrestrial environment, the trio of photolysis, evaporation and biodegradation occurs while adsorption onto the particulate matter is not well defined. Because the pollutant does not adsorb onto soil, there is the possibility of leaching which may contaminate groundwater, although no monitoring studies have confirmed the presence of 2-NP in groundwater. Similarly, in the aquatic system, as a result of the low value of sorption constant characteristics (Koc) the pollutant did not adsorb onto particulate matter, instead certain fragments escaped during evaporation, photolysis and aerobic degradation (Boehncke et al., 2000). The fate of 2-NP in the aquatic environment depends on the intensity of sunlight, solution pH, nature of particulate matter, aerobic conditions, amongst others. While the atmospheric half-life of 2-NP remains relatively unknown, the half-life under photolytic and aerobic conditions varies depending on the nature of water. For instance, in a fresh water systems, the half-life ranged between 1-8 days, in sea water it was between 13-21 days, whereas in top soil, the half-life of 2-NP under aerobic conditions is close to 12 days. This

means that 2-NP undergoes slow photolysis under aerobic conditions. Finally, it is an indisputable fact that these compounds (BPA and 2-NP) are toxic in the environment and that it is only a matter of time before the levels build up to a point where human toxicity will be evident. Therefore, the precautionary principle may be a better route and it is suggested that South Africa follow the lead of other advanced countries and regulate the products containing these persistent organic compounds especially bisphenol-A and 2-nitrophenol until further notice as there is not enough capacity for continuously monitoring new compounds before their release into the market place and from there into the receiving environment.

2.2.6. ***Detection and quantification of BPA and 2-NP in environmental media***

BPA and 2-NP are present in the environment at low concentrations (ng/L to µg/L) and thus their detection requires advanced analytical techniques. The following analytical equipment namely liquid chromatography tandem mass spectrometry (LC-MS), liquid chromatography tandem mass spectrometry coupled with mass spectrometry (LC-MSMS), high-performance-liquid chromatography (HPLC), high-performance-liquid chromatography coupled with mass spectrometry (HPLC-MS), liquid chromatography coupled with electrochemical detection (LC-ED), capillary electrophoresis (CE), and gas chromatography coupled with mass spectrometry (GC-MS) have been widely used to quantify the concentration of the two compounds and other emerging micropollutants in various environmental samples (Nie et al., 2012; Verlicchi et al., 2012). Most of these methods usually require solid-phase extraction and derivatization of samples in the case of GC-MS prior to analysis. Furthermore, sensors are currently being considered as a potential substitute to those aforementioned instruments due to their ease of operation and the elimination of the pre-treatment steps, lower consumption time, higher sensitivity, and fast responses (Iwuoha, 2012). For instance, Wu et al., (2012) demonstrated that nanographene-based tyrosinase biosensor offered a more rapid response for the detection of BPA in tap water than conventional HPLC method. In the same vein, Zhu et al., (2015) developed Aptamer/Graphene oxide biosensor and found that the sensor can detect as BPA as low as 0.05 ng/mL over the concentration range of 0.1−10 ng/mL. According to the authors, the BPA recovery rate after spiking in real water samples was in the range of 96.0% - 104.5%. They concluded that the synthesised sensor was sensitive and can compete favourably with conventional HPLC, GC-MS, and immune-based sensing systems in the determination of actual concentration of BPA in real water systems. Apart from routine chemical analysis, BPA and 2-NP can be detected in environmental

samples via biological screening tools such as Enzyme-linked immunosorbent assay (ELISA), yeast estrogen screen (YES) bioassay (Manickum and John, 2014). Neng and Nogueira, (2014) applied the solid-phase extraction method followed by HPLC coupled with diode array detector to extract and quantify the levels of five phenolic compounds in surface water. The compounds included 3-nitrophenol, 4-nitrophenol, bisphenol-A, 4-n-octylphenol and 4-n-nonylphenol. The method showed good precision and accuracy with percentage recoveries of more than 88% when 25 mL of 10 $\mu g/L$ water sample was spiked. The detection limit of all the pollutants and the correlation coefficient were 0.25 $\mu g/L$ and 0.9904 respectively. Hou et al., (2013) employed dispersive liquid-liquid microextraction followed by HPLC to detect and quantify 4-nitrophenol, 2-naphthol and bisphenol-A in real water samples. Different detection limit were found for the three pollutants. For instance, 4-nitrophenol was 1.50 ng/mL while 2-naphthol and bisphenol-A were 0.10 and 1.02 ng/mL respectively. The relative recoveries of the pollutants varied with respect to water sample. The recoveries rate of the pollutants in tap water ranged between 85-105%, river water (98.3 – 110.0%), and spring water (98.6-109.0%).

2.3 Advanced oxidation technologies

Conventional wastewater treatment technologies comprising physico-chemical treatment and biological treatment have long been used to remove different contaminants that constitute a threat to public health and the environment. Nevertheless, the effectiveness or otherwise of these conventional treatment techniques such as biological treatment, coagulation/flocculation process, chlorination technology, ultrafiltration, reverse osmosis, activated carbon adsorption depend on the physicochemical properties of the compounds. For instance, recalcitrant organic pollutants are resistant to biological treatments. Coagulation/flocculation or activated carbon adsorption only change the pollutants' phases without necessarily removing or degrading them completely (Fabiola et al., 2010; Gao et al., 2013; Oller et al., 2011). Precipitation methods also produce sludge/flocs upon the addition of polymer coagulators or inorganic coagulants. Other methods such as reverse osmosis, nanomembrane, sedimentation and filtration are costly, and generate toxic by-products which need safe storage (Chong et al., 2010; Friedmann et al., 2010). Shortcomings of the filtration techniques include filter fouling that requires more energy, time and extra costs to clean, as well as the disposal of concentrates (Chong et al., 2010). These methods are not environmentally acceptable due to generation of large volumes of waste products/sludge,

which are toxic to humans and their environment. As a consequence of the shortcomings and challenges of conventional treatment technologies, alternative treatment methods are desired that will complement the existing ones.

Advanced oxidation technologies (AOTs) have been recognised as suitable pre or post treatment techniques for the degradation of toxic, recalcitrant organic pollutants in wastewater into innocuous or less toxic compounds (Gao et al, 2013; Magureanu et al., 2013). In advanced oxidation, the decontamination of persistent pollutants occurs in the presence of highly reactive molecular and radical species such as ozone, hydrogen peroxide, and hydroxyl radicals at ambient temperature and pressure (Oller et al., 2011). Among these species, hydroxyl radicals have higher oxidation potential than other known oxidizing agents such as potassium permanganate (Table 2.1).

Table 2.1: Comparison of various powerful oxidants in acidic media

Oxidising agent	**Oxidation potential (V)**
Fluorine (F_2)	3.03
Hydroxyl radical ($HO^{\bullet}$)	2.80
Atomic oxygen (O_1) or singlet oxygen (O_2*)	2.42
Ozone (O_3)	2.07
Hydrogen peroxide (H_2O_2)	1.78
Potassium permanganate ($KMnO_4$)	1.67
Hypobromous acid (HBrO)	1.59
Chlorine dioxide (ClO_2)	1.50
Hypochlorous acid (HClO)	1.49
Chlorine (Cl_2)	1.36
Oxygen (O_2)	1.23
Bromine (Br_2)	1.09

Source: Sharma et al., (2011)

The hydroxyl radical reacts non-selectively and fragments organic pollutants into harmless end products, CO_2 and H_2O. Despite being a short-lived species, the hydroxyl radical attacks organic pollutants through hydrogen abstraction, electron transfer, and formation of a double bond with the organic compounds as shown in the equations 2.01-2.03 below:

$$R + HO\bullet \rightarrow ROH \quad (2.01)$$

$$R + HO\bullet \rightarrow R\bullet + H_2O \quad (2.02)$$

$$R_n + HO\bullet \rightarrow R_{n-1} + OH^- \quad (2.03)$$

Advanced oxidation technologies are categorised into homogeneous and heterogeneous processes. The schematic representation of various types of advanced oxidation technologies, such as cavitations (ultrasound energy (US) irradiation, hydrodynamic cavitation (HC)), ultra-violet irradiation (UV), ozonation (O_3), hydrogen peroxide (H_2O_2) is shown in Figure 2.4.

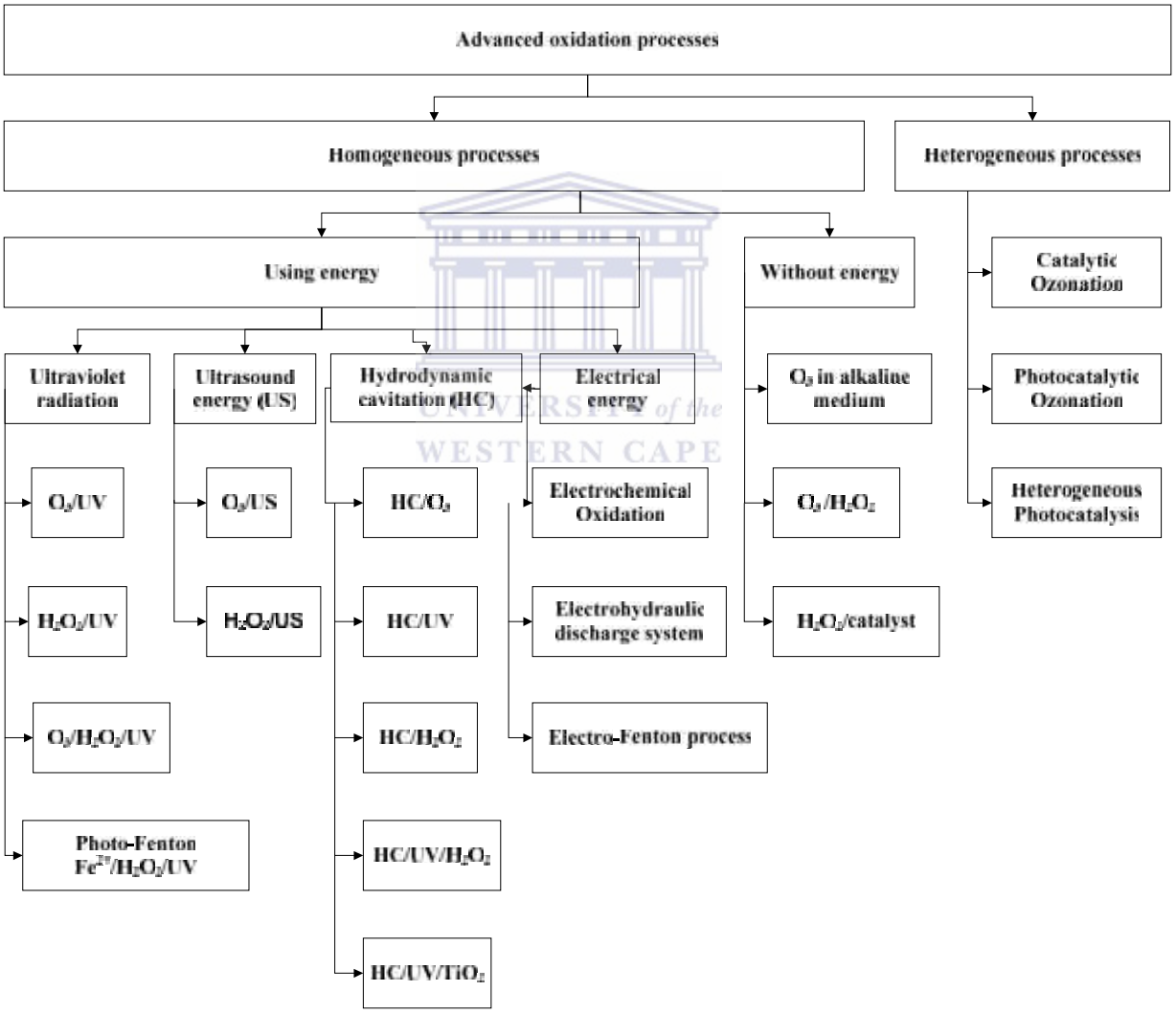

Figure 2.4: Various AOTs based on wastewater treatment technologies (Sources: Sharma et al., 2011)

Each of the aforementioned AOTs has been utilised to decompose organic pollutants in aqueous solution. However, the review of literature have shown that a single advanced oxidation technology is not capable of completely eliminating the pollutants, due to generation of intermediate by-products that are sometimes more toxic than the parent compounds (Oller et al., 2011). In order to improve the decomposition rate of persistent organic pollutants (POPs) present in wastewater, process combination rather than a single-technology system is required. This could allow synergy of the individual process strengths and may achieve the required degradation within a shorter reaction time and at a cheaper cost. This literature review will focus on photo-Fenton process, heterogeneous photocatalysis, dielectric barrier discharge and jet impinging process as well as mechanism of formation of OH radicals.

2.3.1 *Photo-Fenton process*

The photo-Fenton process has recently emerged as one of the more promising and feasible AOTs capable of mineralizing quite a wide range of organic and inorganic pollutants. The photo-Fenton process is unique and attractive due to the non-toxicity and relative abundance of iron. Apart from these advantages, the system is not expensive and is environmentally friendly (Machulek et al., 2013). The system encompasses using oxidizing agents such as hydrogen peroxide, with iron (Fe^{2+} or Fe^{3+}) as a catalyst (Trapido et al., 2014). It has been reported that the introduction of UV light to the dark Fenton reagent accelerated the formation of hydroxyl radicals and enhanced the degradation of the organic pollutants into harmless end-products (Elmolla and Chaudhuri, 2010; Trovo et al., 2008). The improved performance obtained when subjecting the pollutants to combined Fe^{3+}/H_2O_2/UV treatment may be due to the formation of more hydroxyl radicals as well as Fe^{3+} reduction to Fe^{2+} as shown below. The hydroxyl radicals with oxidation potential of 2.8 V were thus capable of reacting with almost all types of recalcitrant synthetic and natural organic pollutants resulting in their complete degradation into carbon dioxide and water (Magureanu et al., 2010). The reaction mechanism of the photo-Fenton process is described in the equations below

$$Fe^{3+}_{(aq)} + H_2O \xrightarrow{hv} Fe^{2+}_{(aq)} + OH\bullet + H^+ \quad (2.04)$$

$$OH^{\bullet} + OH^{\bullet} \rightarrow H_2O_2 \quad (2.05)$$

$$Fe^{3+} + H_2O_2 \rightarrow Fe\text{–}OOH^{2+} + H^+ \quad (2.06)$$

$$Fe\text{-}OOH^{2+} \rightarrow Fe^{2+} + {}^{\bullet}OOH \quad (2.07)$$

$Fe^{3+} + {}^{\bullet}OOH \rightarrow Fe^{2+} + O_2 + H^+$ (2.08)

$HO^{\bullet}$ + organics → intermediates + H_2O (2.09)

H_2O_2 + organics → intermediates + H_2O (2.10)

Intermediates + $^{\bullet}OH \rightarrow CO_2 + H_2O$ (2.11)

Studies have shown that degradation of organic pollutants are readily accomplished using the photo-Fenton process (Trapido et al., 2014). Despite successful outcomes concerning the use of photo-Fenton to remove organics, highly turbid wastewaters containing high COD concentration cannot be treated by photo-Fenton due to poor UV light penetration (Tamimi et al., 2010). Waste disposal is another serious issue due to inorganic sludge formation.

2.3.2 *Nano Zero Valent iron particles*

Nano Zero Valent Iron (nZVI) has recently emerged as a new water treatment nanomaterial. Although, this technology is relatively new, it has prospects of becoming a highly efficient and low-cost treatment technology compared to existing conventional remediation processes (Crane et al., 2011). The application of nano zero valent iron particles is otherwise known as "in situ passive method" and currently in use in some developed countries (Olson and Higgens, 2009). Zero-valent iron (ZVI) is elemental iron containing excess electrons with an overall zero charge. At zero charge, the iron nanoparticles act as an electron donor and thus become very reactive. The inner core consists of Fe^0 zero charge while the outer shell contains the +2 and +3 oxidized Fe ions represented in equation 2.12 and shown diagrammatically in Figure 2.5

$Fe^0 \rightarrow Fe^{2+} + 2e$ (2.12)

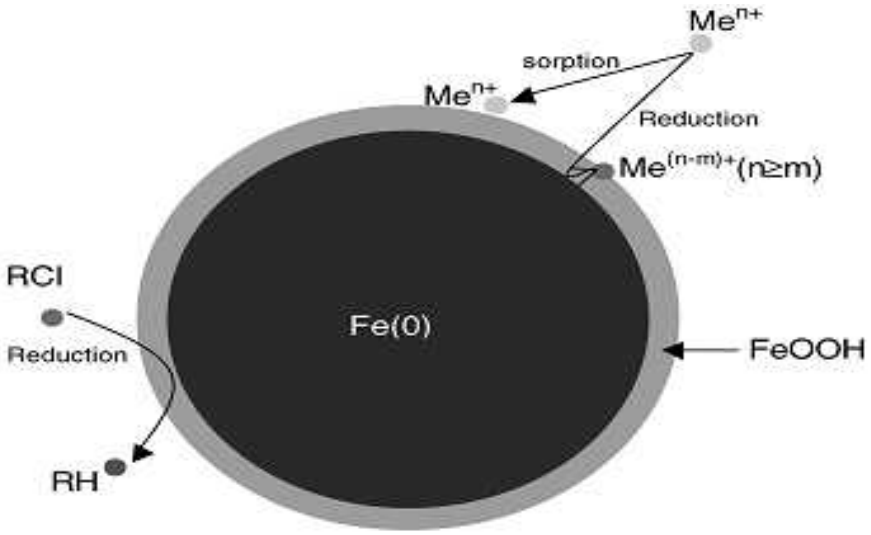

Figure 2.5: Core shell model of nano zero-valent iron showing various chemical mechanisms (Adapted from: Poursaberi et al., 2012) (RH= organic compound, RCl = $FeCl_3.6H_2O$, Me=Fe, n=+3 or m= +2)

However, rapid oxidation and aggregation of nZVI during synthesis due to electrostatic and magnetic forces of attraction and van der Waals forces between the particles reduces the surface area, limits long-term storage and affects its performance in terms of degradation of pollutants (Shahwan et al., 2011). Besides, non-stabilized nZVI often undergoes rapid reaction with air or water resulting in the loss of mobility and reactivity (Huang et al., 2015). In order to prevent rapid aggregation, improve the particles' mobility and its performance, different strategies have been exploited and reported in the literature. For instance, polymers, polyelectrolytes or as well as surfactants have been applied either a stabilizer or capping agents during or after synthesis to help prevent agglomeration through impartment of electrostatic repulsive force (Huang et al., 2015). Several authors have developed different strategies to modify and stabilise nano zero valent iron particles so as to enhance its performance. Some of these stabilization remedies include addition of polymers either before or after the synthesis of nZVI, as polymer stabilised nZVI have been reported to perform better than ordinary nZVI without a stabilizer or capping agents (Ayob et al., 2012).

i. Synthesis of nano zero valent iron (nZVI)

The quality of nano iron particles depends on the synthetic methods used. nZVI is commonly synthesised via electrochemical synthesis, micro emulsion based methods, sonication-assisted methods, sol-gel methods, laser pyrolysis techniques and microorganism or bacterial synthesis (Poursaberi et al., 2012). However, the most widely used method of producing

nZVI is by the reduction of aqueous ferric solution using a conventional reductant such as sodium borohydride or sodium hypophosphite, though this production technique is considered expensive (Pattanayak and Nayak, 2013a; 2013b).

ii. Applications of nano zero valent iron (nZVI)

The application of zero valent nano iron firstly appeared as a substantial standard technology for underground water treatment due to unique two-fold adsorption and reduction properties (Jabeen et al., 2011). Previously, granular iron was often engaged as permeable reactive barrier (PRB) materials in the treatment of underground contaminated water, but recently, nZVI was discovered as a potential candidate for the degradation of pollutants in water (Singh et al., 2011). Studies have shown that nanoscale metallic iron can effectively degrade a series of environmental contaminants such as halogenated compounds because of their higher surface area to volume ratio, small size and greater density of reactive sites compared to the granular counterpart (Boparai et al., 2013). The efficiency of nZVI particles to reduce the pollutants lies in its ability to oxidise to +2 and +3 valences (Figure 2.5). Stieber et al., (2011) explored zero valent nano iron to remediate pharmaceuticals present in water. Their findings showed clearly that zero valent iron nanoparticles reduced the concentration of pollutants to a satisfactory level. Because of the rapid aggregation and settling of nZVI, the nanometal loses surface area leading to poor mobility, loss of magnetism and dispersibility. In order to overcome these challenges, nZVI can be functionalized with chelating agents to improve the degree of stability in water systems (Singh et al., 2011).

2.3.3 *Heterogeneous photocatalysis*

The photocatalytic process is defined as the absorption of a photon of light by a catalysts to generate free reactive species (Klauson et al., 2010; Palominos et al., 2008). Heterogeneous photocatalysts are semiconductor oxides such as TiO_2, ZnO, SnO_2, GaP, CdS and ZnS which have been widely utilized for the decomposition of persistent emerging organic contaminants and produce more biologically degradable and less toxic compounds (Ahmed et al., 2011). Among the semiconductor metal oxides, nano-crystalline TiO_2 has received the greatest interest in both fundamental research and practical applications due to its low cost, electron band structure, photochemical stability, environmental friendliness, easy availability, strong oxidizing power among others (Dolat et al., 2012).

Titanium (IV) oxide, often referred to as titania, titanium white, titanic anhydride, or titanic acid anhydride occurs naturally as an oxide of titanium. It exists in four different polymorphs namely rutile, anatase, brookite and titanium (IV) oxide B. These crystal structures differ appreciably from one another through the bond angle distortion of the octahedral chains. And among the polymorphs, anatase is mostly preferred due to its high photocatalytic activity, photochemical stability and high surface area. Nevertheless rutile is the most thermodynamically stable phase. Anatase is sometimes mixed with rutile in order to decrease high photogenerated electron-hole recombination rate (Dalrymple et al., 2007). The application of TiO_2 as photocatalyst was started by Fujishima and Honda in 1972 (Fukushima et al., 2000; Kondo et al., 2008). These authors used a photo-electrochemical cell made up of a rutile titania anode and inert cathode to split water into hydrogen and oxygen. This achievement served as a turning point in the history of heterogeneous photocatalysis. Ever since then scientists all over the world have conducted research trying to understand the fundamental mechanism of heterogeneous TiO_2 photocatalysis. Far reaching research has been conducted on the application of titania or doped titania nanocomposites to destroy organic compounds (Malato et al., 2009). The photocatalytic degradation activity of the catalysts towards a particular pollutant depends largely on parameters such as solution pH, initial organic pollutants type and concentration, catalyst loading, dissolved oxygen, light wavelength and intensity, quantity of reactive oxygen species, temperature, absence of interfering ions and ionic profile of the polluted water (Friedmann et al., 2010). These parameters either raise or reduce the reaction rate depending on the pollutants' structural complexity and hydrophobic tendencies.

i. Limitations of heterogeneous photocatalysts

Shortcomings still exist in the use of TiO_2 photocatalyst which researchers are currently trying to address. One of these is the slow photocatalytic kinetics of TiO_2 in the visible region caused by high band gap energy, and the short-lived nature of electron-hole carriers linked to lower photon quantum efficiency. Most importantly, there is difficulty in light penetration of a solution containing suspended titania nanoparticles, and filtration of the suspended TiO_2 nanoparticles out of solution after the water treatment process, which is time consuming and creates additional costs. Other technical challenges include the agglomeration of nanoparticles, designing of a photocatalytic reactor, and difficulties in the reactor optimization (Ahmed et al., 2011; Chong et al., 2010).

2.3.3.1 Doping of TiO_2 nanoparticles

Studies have shown clearly that doping the crystal plane of the TiO_2 photocatalyst with either metal or non-metals will enhance the photocatalytic degradation rate of organic pollutants (Hintsho et al., 2014). Doping creates a defect level within the band gap causing reduction in the electron excitation of TiO_2 and possibly extends the absorption threshold to the visible region (Kuriechen and Murugesan, 2013). Several approaches for improving the photocatalytic activity of TiO_2 have been reported. One approach is doping of TiO_2 dielectric matrix with metal impurities such as Ag, Cu, Pd, Au, Pt, W or with non-metals such as C, N, and S. The dopants actually extend the optical absorption threshold to the visible region. Besides, the dopants acts as electron trappers and prevent high electron-hole recombination rates. Furthermore, doping of TiO_2 photocatalyst with plasmonic elements such as silver actually create a Schottky barrier and suppress the photogenerated electron-hole pairs and thus enhance the photocatalytic efficiency. A Schottky barrier represents a junction where reactive metal such as Ag come in contact with a semiconductor material like TiO_2. The junction can be rectifying or non-rectifying however the rectifying types between a metal and semiconductor is commonly referred to as the Schottky barrier. This parameter depends on the Schottky barrier height Φ_B of the junction which differs with respect to the nature of metal and semiconductor materials and the interfacial surface. A Schottky barrier height represents the differences between the interfacial conduction band edge and the Fermi level (E_F) of TiO_2 (Subrahmanyam et al., 2012). In this study, silver was selected as a dopant on titania due to its d–s band gap which is in the UV region. Silver acts by facilitating the electron capture and improves surface electron excitation via the creation of a local electric field. Apart from improving the photocatalytic activity, Ag often plays a crucial role during the charge transfer process throughout the catalyst/liquid interface interaction (Zhu and Zou, 2009; Hintsho et al., 2014).

2.3.3.2 Mechanism of heterogeneous photocatalysis

The basic mechanism of heterogeneous photocatalysis involves in-situ generation of powerful oxidants such as the hydroxyl radical under ambient conditions. In the heterogeneous photocatalysis process, the absorption of a photon of light either from sunlight or an illuminated light source by the semiconductor metal oxide such as titanium dioxide (TiO_2) causes the migration of a lone pair of electrons from the valence band to an empty conduction band, thus producing electron (e^-)-hole (h+) pairs within the bulk (Chong et al., 2010;

Wankhade et al., 2013). These eventually break-up into photoelectrons and photoholes in the conduction and valence band respectively. It should be noted that the photocatalytic reaction only becomes activated when the catalyst is able absorb sufficient photon energy that is equal or greater than its band gap energy. In a situation whereby the photons supplied have a lower energy than the catalyst band gap energy, energy degeneracy in the form of heat is usually evident. In the liquid solution, depending on the redox potential or energy level of the species (titanium and oxygen), the valence band becomes excited and oxidised while the conduction band of titanium dioxide accepts the transferred electron and is reduced. At this point, the semiconductor TiO_2 has become photo-excited. Under highly energetic energy source, the positive hole (h+) of the catalyst oxidises either the pollutant directly or oxidizes water molecules into hydrogen gas and hydroxyl radicals as shown diagrammatically in Figure 2.6 below and equations 2.13 - 2.23.

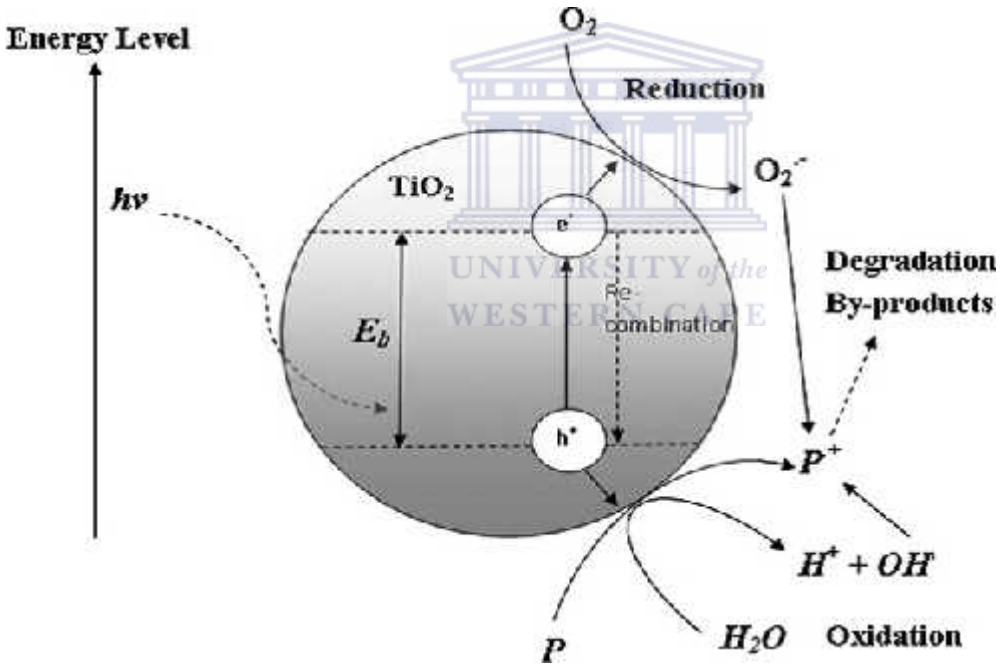

Figure 2.6: Mechanism of electron-hole pair formation in a TiO_2 particle in the presence of pollutants in water (Sources: Chong et al., 2010)

The negative-electron holes combine with oxygen molecules and produce superoxide radicals. During the electron transfer and electron acceptor process, the hydroperoxyl radical is produced which extends the life of photoholes (Wankhade et al., 2013). Furthermore, electron-hole recombination often occurs except when there is the availability of O_2 in the bulk to scavenge the electrons and produces the superoxide (O_2●-). Further reaction with

protons (H^+) produce hydroperoxyl radicals ($HO_2\bullet$-) and complete protonation gives hydrogen peroxide (H_2O_2) (Chong et al., 2010). These reactive species react with organic pollutants via direct electron acceptors to give intermediates and further oxidation produces CO_2 and H_2O. The step by step oxidation-reduction process leading to formation and decomposition of organic pollutants by the free reactive species is shown in equations 13-23 (Chong et al., 2010; Wandkade et al., 2013). The photocatalytic activity depends largely on the ability to prevent or reduce the electron-hole recombination rate on the catalyst surface. The literature survey has shown that more than 90 % of photogenerated electron-hole pairs recombined instantly after excitation, thus recombination is responsible for the low quantum yield of most semiconductor photocatalytic reactions (Friedmann et al., 2010). This reaction occurs within a femtosecond (10^{-15}) and the cycle continues as long as there is availability of energetic photons. In short, the decomposition of organic pollutants via the photocatalytic mechanism can be facilitated by both the holes and the hydroxyl radicals. The degradation pathways may not necessarily be the same but the same products in equal proportion are envisaged, thus making it extremely difficult to clearly discriminate between the two. The photo-induced redox process of TiO_2 is shown below (Dalrymple et al., 2007).

Photoexcitation: $TiO_2 + h\nu \rightarrow e^- + h^+$ (2.13)

Charge carrier trapping of e-: $e^-_{CB} \rightarrow e^-_{TR}$ (2.14)

Charge carrier trapping h^+: $h^+_{VB} \rightarrow h^+_{TR}$ (2.15)

Electron-hole recombination: $e^-_{TR} + h^+_{VB}\,(h^+_{TR}) \rightarrow e^-_{CB} + \text{heat}$ (2.16)

Photoexcited e^- scavenging: $(O_2)\,ads + e^- \rightarrow O_2\bullet$- (2.17)

Oxidation of hydroxyls: $HO^- + H \rightarrow HO^\bullet$ (2.18)

Photodegradation by $HO^\bullet$: $R\text{-}H + HO^\bullet \rightarrow R^\bullet + H_2O$ (2.19)

Direct photoholes: $R + h^+ \rightarrow R^+ \rightarrow S(s) \rightarrow$ final degradation products (2.20)

Protonation of superoxide: $O_2\bullet^- + H^+ \rightarrow HOO^-$ (2.21)

Co-scavenging of e-: $HOO^\bullet + e^- \rightarrow HO_2$- (2.22)

Formation of peroxide: $HOO^\bullet + H^+ \rightarrow H_2O_2$ (2.23)

From the above equations, the e^- denotes the conduction band while h^+ represent valence band electrons respectively. e^-_{TR} and h^+_{TR} depicts surface trapping valence band electrons and conduction band-holes respectively. While S represents the intermediate species. In fact, the mechanism of electron-hole pair formation on TiO_2 surface involves five key steps

namely: photo-excitation, diffusion, trapping, recombination, oxidation (Figure 2.8) which eventually generate powerful oxidants responsible for the degradation of target pollutants into carbon dioxide, water, and inorganic ions. The mechanism of generation of free reactive species such as OH, H_2O_2 depends on the nature of the pollutants and the photocatalysts (Friedmann et al., 2010). Lastly, the mineralization of recalcitrant organics can be achieved via the combined efforts of the semiconductor metal oxides, intense ultraviolet light and hydroxyl radicals.

2.3.3.3 Methods of synthesising TiO_2 nanoparticles

Nano TiO_2 can be synthesised via different techniques such as the sol-gel method, the solvo-thermal method, hydrothermal treatment, chemical vapour deposition, chemical precipitation methods sonochemical method, microwave method, electrodeposition amongst others (Chong et al., 2010). The synthesised TiO_2 material can be in the form of powder, crystals, or thin-films. Extensive review on most of these techniques, as well as the basic principle of heterogeneous photocatalysis particularly semiconductor TiO_2 have been widely reported in literature (Ahmed et al., 2011; Chong et al., 2010; Friedmann et al., 2012; Gaya and Abdullah, 2008; Nainani et al., 2012). Some of the commonly adopted procedure for the synthesis of unsupported and supported TiO_2 nanoparticles are briefly explained below:

i. Precipitation method

This is a reaction between two homogeneous liquid phases which prompts the physico-chemical transformation process and formation of a precipitate under the influence of temperature, solution pH, reactant concentration, solvent evaporation (Gupta and Tripathi, 2012).This synthetic approach predominately resulted in the formation of unsupported TiO_2 nanoparticles. In a typical precipitation process, two elementary steps such as nucleation and agglomeration occur concurrently within the liquid medium leading to formation of a solid phase. The rate of nucleation and agglomeration of particles in the homogeneous liquid phase medium can be regulated via slow drop wise addition of the anions and cations. This step promotes the precipitation of a monodisperse particle. Not only that, careful adjustment or optimization of the solution pH, reactant concentration, solution temperature often produces narrow size and uniformly dispersed nanoparticles. However, in the case of heterogeneous liquid phase, co-precipitation of oxides which are amorphous in nature often occur due to poor mixing within the liquid medium or slow precipitation rate. Further application of

hydrothermal treatment promotes the transformation of the amorphous precipitates to highly crystalline materials. In spite of this, several researchers have used the precipitation method to synthesis unsupported TiO_2 nanoparticles (Chong et al., 2010; Kostedt et al., 2008).

ii. Hydrothermal method

The hydrothermal technique involves the synthesis of unsupported TiO_2 using (titanium(IV) bis (ammoniumlactato) dihydroxide (TALH)) in an autoclave with or without Teflon liners under controlled conditions of temperature and pressure, where water acts as a catalyst and as a constituent of solid phases (Byranvand et al., 2013). The temperature can increase above the boiling point of water until it reaches the vapour saturation pressure. The internal pressure of the autoclave depends on the temperature and the quantity of the solution. Studies have shown that the size and shape of the synthesised TiO_2 via the hydrothermal method is dependent on temperature, time, pressure, solvent type, medium pH (Gupta and Tripathi, 2012). The technique is suitable for the synthesis of TiO_2 nanotubes, nanorods, nanowires and nanofibers.

iii. Solvo-thermal method

The solvo-thermal technique is closely related to the hydrothermal treatment method except that the former uses a non-aqueous solvent. Unlike in the case of hydrothermal treatment, the temperature is much higher due to the flexibility of different organic solvents. There is greater ease to control particle size, shape and crystallinity of TiO_2 nanoparticles than what is obtainable in the hydrothermal process. The technique is most versatile for the synthesis of nanorods, nanowires, nanotubes and nanocrystals of uniform but narrow size distribution and dispersity (Byranvand et al., 2013). Several researchers have utilised the technique to synthesize unsupported nanostructures TiO_2 of different particle sizes and shapes (Ahmed et al., 2011; Behnajady et al., 2011).

iv. Chemical vapour deposition method

The chemical vapour deposition (CVD) method involves the condensation of material in the vapour state usually in a vacuum to form a solid-phase on a support material. The technique is usually used to form a thin layer on a substrate so as to improve its mechanical, electrical, thermal, optical properties corrosion resistance, etc. In a typical CVD process, the gases in the coating chamber are heated by thermal energy which induces the deposition (Hintsho et

al., 2014; Byranvand et al., 2013). To achieve uniform deposition, process parameters such as flow rate, gas composition, deposition chamber geometry, deposition temperature and pressure need to be properly optimised. Typical examples of CVD are: electrostatic spray hydrolysis, diffusion flame pyrolysis, thermal plasma pyrolysis, ultrasonic spray pyrolysis, laser-induced pyrolysis amongst others.

v. Sol gel method

A sol-gel method involves the formation of a colloidal suspension or sol through inorganic polymerization reactions of titanium precursors in the presence of a solvent (Gupta and Tripathi, 2012). The titanium precursors can be inorganic metal salts ($TiCl_4$) or metal organic compounds {($Ti(OCH(CH_3)_2)_4$}. In a typical sol-gel process, four basic stages are involves specifically; hydrolysis, polycondensation, drying and calcination/annealing. The hydrolysis step basically involved the dissolution of titanium precursor in water or alcohol to form the colloidal solution or sol as shown in equation 2.24

$$Ti(OR)_4 + 4H_2O \rightarrow Ti(OH)_4 + 4\,ROH \quad (2.24)$$

where R represent the alkyl group.

Instead of using alcohol and water, TiO_2 nanoparticles can be prepared via acid-catalysed hydrolysis of a titanium precursor followed by condensation leading to the formation of a gel. Under the conditions of low water content and excess titanium precursor, the Ti-O-Ti bond is favoured. Under high hydrolysis rate and medium water content, $Ti(OH)_4$ is favoured (Behnajady et al., 2011). With excess water content, polymeric Ti-O-Ti chains are favoured. Thus, TiO_2 nanocrystals or thin-films can be obtained via dip or spin coating of the gel on a substrate (equation 2.25)

$$Ti(OH)_4 \rightarrow TiO_2 + 2\,H_2O \quad (2.25)$$

The obtained TiO_2 is dried temporarily in the oven and further subjected to calcination at higher temperature to remove the organic components. The sol-gel method can lead to formation of particulates TiO_2 nanoparticles or supported TiO_2 nanocrystals. The particle size of the synthesised TiO_2 nanoparticles can be altered by controlling the solution pH, temperature and solution composition. Depending on the synthetic routes employed, the calcination temperature applied serves to control the formation of nanostructured TiO_2. In fact, the structural phase transformation, degree of crystallinity, particle size and shapes are dependent on the calcination temperature (Chong et al., 2010). Calcination/annealing of TiO_2 gel/powder within the temperature range of 600-800 ºC leads to structural phase changes

from anatase phase to condensed rutile phase. Furthermore, calcination/annealing at higher temperatures promotes residual loss of water and volatile organic components, and may improve the crystallite growth. Studies have shown that photocatalytic activity of synthesised TiO_2 material at different calcination temperature varied and depended on several factors such as solution pH, nature of the surrogate model organic pollutants, interfering substances, light intensity amongst others (Ahmed et al., 2011, Chong et al., 2010). Of all methods, the sol-gel technique appeared most promising due to the production of nanoparticles with good homogeneity and high surface area at relatively low cost (Monreal et al., 2009). The advantages of the sol–gel deposition method are numerous and are briefly outlined by Bestetti et al., (2010) as follows: (i) application of sol-gel technique on different substrate materials; (ii) easily conducted with ordinary laboratory equipment; (iii) permits uniform coating of high contact areas and complex shapes; (iv) the properties of the resulting film can be easily manipulated and controlled via changing some parameters; and (v) dopants can be easily co-deposited. An interesting synthetic technique that could be used to control the size and the surface contamination of TiO_2 nanoparticles obtained via calcination is by the utilization of the polymeric precursor method. Mesoporous, thin-films, nanotubes, nanorods, dendrimer TiO_2 forms have been synthesised via the sol-gel method. Aside from that, the sol-gel technique has been used for the synthesis of doped nanomaterials of high surface area (Bestetti et al., 2010). Sol-gel method can be used to synthesise both unsupported and supported TiO_2 nanoparticles depending on the titanium precursor, solvent and nature of the binder. Farbod and Khademalrasool, (2011) synthesised TiO_2 nanoparticles using sol-gel method and investigated the influence of calcination temperature on the formation of particle size. They found that TiO_2 nanoparticles calcined at 550ºC having particle size of 55 nm achieved 80% removal of Congo red after 30 min.

2.3.3.4 Choice of TiO_2 support materials

The amount of TiO_2 nanoparticles in the bulk of liquid within the photochemical reactor determines the overall oxidation rate of organic pollutants. The increase in the TiO_2 loading initially accelerates the photocatalytic mineralization reaction rate of the organic pollutants and then decreases at high dosage values due to light scattering and screening effects (Friedmann et al., 2010; Gaya and Abdullahi, 2008). Beyond the optimal value, any further increase in the TiO_2 dose only mask the light penetration without any significant improvement in the mineralization rate, makes the solution highly turbid and leads to non-

uniform distribution of light intensity. In such a situation, the particles obstruct light penetration and limit the interaction with the pollutant, thus lowering the degradation efficiency. Excessive addition of TiO_2 nanoparticles in the bulk solution also leads to particle agglomeration which decreases the overall mineralization rate. Establishing the optimal dose is crucial but depends strictly on the solution pH and the nature of the pollutants. The survey of literature revealed that a catalyst dose in the range of 0.2 – 1.0 g/L is sufficient for complete oxidation of organic pollutants. The obtained results are however different due to differences in the reactor configuration, UV lamp intensity, wavelength, wattage, type of organic compounds amongst others. This is also an issue as methods are not standardized thus comparisons are difficult. Thus, the optimum catalyst dose should be determined for each photochemical reactor during wastewater treatment.

In spite of several unique characteristics of TiO_2 nanoparticles, the photocatalytic activity of TiO_2 is limited due to high band gap energy, electron-hole recombination rate from valence band to conduction band, and particles agglomeration. Besides the aforementioned, post-separation and recovery from wastewater after utilization constitutes major impediments to its full scale industrial applications. Based on the inherent shortcomings associated with the powder TiO_2 nanoparticles, immobilization of TiO_2 nanoparticles on a suitable substrate such as a glass, ceramic, polymers, activated carbon, wooden fibre cloth, carbon fibre, stainless steel mesh amongst others has received great attention in the field of heterogeneous photocatalysis. Several researchers have synthesized different supported TiO_2 nanoparticles which are reviewed as follows. Hänel et al., (2010) employed sol-gel method followed by a dip-coating technique to prepare pure and boron-doped TiO_2 nanoparticles supported on a glass beads. The authors found that the supported catalysts was stable and removed 33% phenol after three consecutive cycle, which suggests that the catalysts was re-usable. Shen et al., (2012) synthesized pure anatase TiO_2 nanoparticles supported on porous glass beads using in-situ ion exchange process. The prepared supported photocatalysts was found to exhibit excellent photocatalytic activity and successfully removed 65% methyl orange within 30 minutes. Habibi et al., (2012) prepared alumina supported TiO_2 nanoparticles using sol-gel method and found that under optimal conditions of calcination temperature (550ºC), refluxing temperature (66ºC) and calcination time (2 h), 61% degradation of acetaldehyde after 250 min. Wang et al., (2015) synthesized Cr-doped TiO_2 nanoparticles supported on a natural zeolite and found that 10% mol Cr-immobilized TiO_2/zeolite annealed at 400 ºC removed 41.73% methyl orange compared to undoped TiO_2/zeolite which only removed

17.9%. The authors attributed the improved removal efficiency to the doping effect of Cr, which prevented electron-hole recombination rate. Omri et al., (2015) synthesized TiO_2 nanoparticles supported on activated carbon made from Almond shell using combination of hydrothermal and sol-gel method. The authors found that the supported TiO_2 nanoparticles showed excellent photocatalytic activity with 94% TOC reduction from solution containing phosphoric acid after 300 min. Among the support materials upon which the TiO_2 catalyst may be developed, stainless steel mesh possesses unique qualities when compared to other supports which includes maintenance of structural integrity under the high heat treatment (during calcination of TiO_2). Other materials such as quartz glass deform and melt depending on the glass transition temperature. Also, stainless steel mesh is not susceptible to attack unlike others during the coating process. Nam et al., (2004) reported the diffusion of sodium from soda-lime glass onto the TiO_2 film which reduced the photocatalytic efficiency. Apart from the aforementioned, stainless steel mesh can be utilized in the electrochemical process while quartz and ceramics cannot be used due to their dielectric properties. At last, it can be easily used in complex shapes and has excellent mechanical properties (Chong et al. 2010).

2.3.3.5 Operating parameters influencing photocatalytic process

The photocatalytic process involving oxidation of organic pollutants in aqueous solution is strongly dependent on a number of parameters which influence the solution kinetics. These parameters include solution pH, initial organic pollutants type and concentration, pH of the catalyst, catalyst loading, light wavelength and intensity, quantity of reactive oxygen species, calcination temperature, radical scavengers and ionic profile of the polluted water. The next section provide detailed information on the influence of the some of the aforementioned parameters as related to the photocatalytic activity of TiO_2 nanoparticles.

i. Solution pH

The mineralization efficiency of organic pollutants in a typical heterogeneous photocatalytic water system is mostly governed by solution pH, which impacts on the catalyst surface charge and the ionization/dissociation state of the pollutant (Chong et al., 2010). The effect of solution pH can be explained on the basis of electrostatic interaction between the charged TiO_2 species in solution and the pollutant. This can be illustrated using the point of zero charge (PZC) of TiO_2 (Chong et al., 2009b, c). Thus any change in solution pH can affect the surface charge of most semiconductor metal oxides due to the fact that they are amphoteric in

nature. Specifically, the point of zero charge of TiO_2 is 6.0 - 6.5. When the pH of the solution is equal to the point of zero charge of TiO_2 (6.5), there is little interaction between the TiO_2 nanoparticles and the contaminant, due to lack of electrostatic forces of attraction. In such a situation, hydrated neutral species such as Titanol (TiOH) dominate. When the pH value is less than 6.5 (under acidic conditions) the TiO_2 surface is highly protonated and TiO_2 becomes a net positively charged species ($TiOH_2^+$) and exerts an electrostatic force of attraction upon the negatively charged organic contaminants in the solution. Such electrostatic attraction between the duo improve the photocatalytic reactions especially when the concentration of the anionic organic pollutant is low (Chong et al., 2010; Friedmann et al., 2012). At pH greater than the point of zero charge (under alkaline conditions), TiO_2 is deprotonated and becomes a negatively charged species (TiO^-) and thus exerts an electrostatic repulsion upon the anionic organic compounds in solution. Thus, the interactions between the surface charge of the TiO_2 nanoparticle and the electronic properties of the organic compounds are pH dependent. Additionally, at pH less than pZC (<6.5) radical scavengers such as HCO_3^-, Cl^-, SO_4^{2-} which are mostly present in water can react with the protonated species ($TiOH_2^+$) and reduce their efficiency. Conversely, at high pH, radical scavengers exert little influence due to strong electrostatic repulsion between the scavengers and OH^-. Thus, the photocatalytic efficiency is a measure of the adsorption of the organic pollutants onto the surface of the catalyst and the solution pH influences the surface charge and ionic state of pollutants which in turn alter the reaction mechanism.

ii. Initial concentration of the pollutant

The efficiency of the photocatalytic activity of TiO_2 nanoparticles is dependent on the initial concentration of the pollutant. Under the optimized conditions of solution pH, and TiO_2 dose, the photocatalytic degradation of organic pollutants increases with an increase in the initial concentration of the pollutant, until a certain level where the reaction rate begins to decrease (Pardeshi and Patil, 2008; Senthilnathan and Philip, 2010; Wei et al., 2009). However, as the concentration of the initial concentration of the pollutant increases, the surface active sites of TiO_2 nanoparticles become saturated. The free, available hydroxyl radicals reduce and thus affect catalysis performance, which in turn reduces the mineralization rate (Bahnemann et al., 2007). Additionally, photocatalytic degradation of higher concentrations of organic pollutants generate a series of transformation products which remain and deactivate the catalyst surface via slow diffusion, thus reduce the degradation rate. Therefore, the degradation reaction rate

depends on both the concentration and nature of the organic contaminants used during the TiO_2 photocatalytic experiment. The concentration of both the photocatalysts and organic pollutants determine the reaction rate and must be optimised accordingly (Chong et al., 2010).

iii. Light wavelength

The influence of ultraviolet light of different wavelengths on the reaction rate of the heterogeneous photocatalytic process depends on the nature and state of the TiO_2 nanoparticles. For instance, a light of wavelength $\lambda < 380$ nm is enough for the activation of the anatase phase of the commercial Degussa P-25 TiO_2 with a band gap of 3.2 eV while a light of wavelength close to 400 nm is required to activate the rutile TiO_2 nanoparticle of band gap 3.02 eV. This shows that catalysts with a smaller band gap require a higher wavelength for activation than catalysts with high band gap. Thus, the reaction rate is largely dependent on the light wavelength and the band gap of the catalyst. Furthermore, ultraviolet light is categorised into three classes based on its emitting wavelength and band gap, which include UV-A, UV-B and UV-C (Chong et al., 2010). UV-A has a light wavelength ranging between 320-400 nm with a corresponding band gap of 3.10- 3.94 eV. UV-B light wavelength ranges from 290-320 nm with a band gap of 3.94-4.43 eV. While the third category UV-C that is mostly used to kill bacteria or microorganisms, has a light wavelength that ranges between 100-290 nm and a band gap of 4.43-12.4 eV. Among the three, UV-A remains the most widely used due to the availability of photon energy to activate the catalyst (Ochuma et al., 2007).

iv. Interfering substances/radical scavengers

The performance of a photochemical reactor and in particular of the heterogeneous photocatalyst depends on the concentration of the inorganic species in the target water. Depending on the solution pH and the target organic compounds, inorganic adical scavengers influence the photocatalysis process via deactivation of the catalyst active sites (Chong et al., 2010). The competition between the inorganic species and organic pollutants for the active sites on the catalyst also cause photocatalytic surface deactivation. The adsorption of interfering substances onto the catalyst active sites hinders the formation of hydroxyl radicals and decreases the photocatalytic degradation efficiency. Furthermore, radical scavengers such as nitrate, phosphate, sulphate, chloride, and carbonate destroy the hydroxyl radical by

adsorbing the UV light and generating corresponding anionic radicals of lower oxidation potentials. Studies have also shown that NO_3^-, HCO_3^-, ClO_4^-, SO_4^{2-}, HPO_4^2 slow down the degradation rate via photocatalyst deactivation (Ahmed et al., 2011, Chong et al., 2010; Friedmann et al., 2010). Thus, a proper understanding of their roles and behaviours will assist in the design of an efficient photochemical reactor and help to ensure that their presence does not render the process ineffective.

v. Application of TiO_2 nanoparticles

In the late 1900's, the chemical industry substituted toxic lead oxides with titanium dioxide which was applied as a white pigment in paints, varnishes, papers and plastics. More than 80% of the world population consume products containing TiO_2. Apart from this, heterogeneous semiconductor TiO_2 has quite a wide range of applications such as in wastewater treatment, as part of dye-sensitized solar cells, as catalyst support, in gas sensors, in air purification, for the destruction of cancer cells and energy generation amongst others (Chanathaworn et al., 2012; Dolat et al., 2012). In this study, the synthesised supported TiO_2 nanoparticles were applied as photocatalysts to enhance the photocatalytic degradation rate of organic compounds. As a result of the uniqueness of TiO_2 vis-a-viz brightness and high refraction index value, TiO_2 has surpassed other materials and is currently used as a white pigment in most consumer products. The current figures indicates that more than 4.6 million tons of pigmentary TiO_2 containing products are used annually across the world (Chong et al., 2010). Similarly, TiO_2 acts as opacifier and imparts opacity to many consumer products namely plastics, coatings, toothpaste, and medicines among other. Even the whiteness of skimmed milk and its sensory acceptance score was ascribed to the presence of TiO_2. In the ceramic industry, TiO_2 is used to impart opacity and improve seed crystal formation.

Ever since the elucidation of the photocatalytic properties of TiO_2 by Fujishima and Honda in 1967 and 1972 respectively, there have been growing numbers of studies focusing on the application of TiO_2 for wastewater treatment. Several studies have shown that TiO_2 nanoparticles can be used to detoxify wastewater containing organic pollutants. Catalytic performance and behaviour towards organic pollutants depend on several factors such as light intensity, light wavelength, solution pH, photoreactor configuration, interfering substances amongst others (Behnajady et al., 2011). The photocatalytic efficiency of the catalyst can be improved via doping or immobilization of TiO_2 nanostructured materials with metals and non-metals. Furthermore, the incorporation of TiO_2 into outdoor building material helps to

reduce the concentration of atmospheric organic and inorganic pollutants such as CH_4 and NOx. More so, TiO_2 thin films or nanoparticles under energetic photons split water molecules into hydrogen and oxygen. This technology has been widely recognised as a clean and sustainable means of generating hydrogen fuel. The adsorption of high intensity ultraviolet light by TiO_2 molecules promotes reduction and oxidation reactions forming photo-generated electrons and holes. The oxidation of water molecules by the photo-holes produces oxygen while reduction by photo-electrons liberated hydrogen, which complete the splitting of water (Chong et al., 2010; Ochuma et al., 2007). The liberated hydrogen is stored and can be used as a fuel. The rate of conversion of water molecules to hydrogen can be improved via doping of TiO_2 with carbon. The doping causes a high level of disorderliness within the crystal structural layer of TiO_2, which allows infrared adsorption and enhances conversion rates (Friedmann et al., 2010). As a consequence of the characteristic features such as chemical and photochemical stability, TiO_2 nanomaterials are often utilised in both organic and inorganic bulk heterojunction photovoltaic cells to form antireflection/scattering layers, as well as interlayers in organic solar cells (Ahmed et al., 2011). Sometimes, TiO_2 nanoparticles are incorporated as an active component within dye-sensitized solar cells (DSSC) to act as electron transport material. The performance of the DSSC depends on the crystalline structure, morphology and size of the TiO_2 electrodes (Zhang et al., 2012). Electrodes made from TiO_2 nanocrystals have also been used in dye-sensitized solar cells (DSSC).

2.4 Dielectric barrier discharge system

Historically, the use of electrical energy to treat drinking and polluted water commenced in 1987 after Clements and co-workers demonstrated that high-voltage electrical discharge in water forming plasma could decolourise and decompose dye and phenol molecules (Jiang et al., 2014). Ever since then, underwater electrical discharges have continued to be investigated for medical, material functionalization, water treatment and disinfection processes (Bruggeman and Locke, 2013).The dielectric barrier discharge (DBD) system is regarded as a new approach in which a plasma is used for water and wastewater treatment specifically to inactivate microbes and degrade toxic or hazardous pollutants in aqueous solution (Jiang et al., 2014; Malik, 2010; Magureanu et al., 2010; Magureanu et al., 2011). Plasma is categorised as the fourth state of matter which can induced both the physical and chemical process. The physical process include the following strong UV light, local high temperature,

intense shockwaves. While the chemical process are made up of reactive atomic and molecular oxygen-based species such as $OH^{\bullet}$,O_3, $O_2^{\bullet-}$, $HO_2^{\bullet-}$, O, $H^{\bullet}$, H_3O^+ amongst other. Dielectric barrier discharge can be categorised as four processes in one system that comprises chemical, photochemical, ultrasonic irradiation and electrohydraulic cavitation process (Magureanu et al., 2011). The intensity of the electrical field determines the degree of ionization and formation of plasma. There are various forms of electrical discharge plasmas produced either above or within water or in the gas phase contacting the liquid (Krause et al., 2009; Marotta et al., 2012; Sato et al., 2008). For instance, corona discharge is applied above a water system, pulsed corona discharge (in water), dielectric barrier discharge (within wetted wall in water), and gliding arc discharge (within gas-liquid) (Jo and Mok, 2009; Malik, 2010). Each of these electrical wastewater treatments is associated with some challenges. The direct electrical discharge in water is affected by the liquid conductivity and the discharge electrode stability (Baroch et al., 2008). The electrical discharge in water promotes high-temperature channels and induces electrohydraulic discharge as well as supercritical water oxidation leading to the formation of short-lived molecular and radical species (Marotta et al., 2012). The plasma has strong oxidising impacts on the pollutants and that is what makes the technique more unique than conventional wastewater treatment technologies. The plasma indirectly provides reactive species such as ozone, hydrogen peroxide and UV that are needed for water treatment without necessarily contacting the liquid (Figure 2.7) (Bruggaman and Locke, 2013). The efficiency or reactivity of the plasma generation systems vary with respect to reactor configuration, energy yield and sometimes depend on the input energy, liquid properties and excitation voltage (Malik et al., 2010). Apart from the above factors, energy yield often depends on the electron density, pollutant molecular structure, nature and concentration of pollutants, temperature, electrode material, and the extent of transformed products, solution pH and sometimes conductivity (Jiang et al., 2014). The roles played by many of these factors are not clearly defined as most of them are strongly interrelated with respect to overall reactor performance. Currently, most studies are focusing on how to improve the energy yield of a plasma reactor. Although, the energy yield of each reactor varies over a wide range due to differences in the reactor configurations used by different research groups globally. Their findings indicate a dramatic variation in the efficiency of different types of plasma reactors and as such the difference is close to 5 orders of magnitude (Malik et al., 2010). In the same vein, limited data on the energy yield of plasma reactors exist because of the differences in the reactor type used by various research groups globally.

Another factor affecting the energy yield of different plasma reactors is the formation of intermediates as a result of degrading various organic pollutants. The physical and chemical effects produced by the plasma within the discharge convert the pollutants into various intermediates and secondary reactions often occur where the intermediates react or probably compete with the parent compound for the available reactive species. These intermediates differ according to the reactor and thus affect the energy yield.

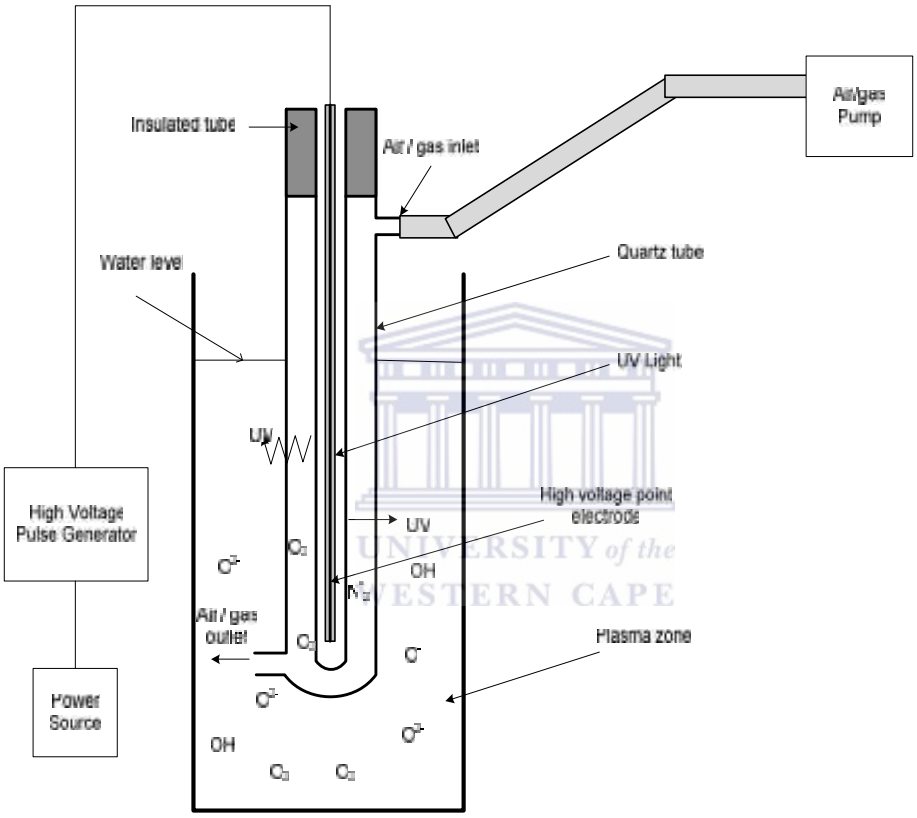

Figure 2.7: Schematic diagram of a typical dielectric barrier discharge system (Mouele, 2014)

2.4.1 *Mechanism of formation of free reactive species in DBD system*

Electrical discharge in liquid leading to the formation of free reactive species in DBD systems is not via a specific degradation mechanism but can be explained using bubble theory and direct ionization of liquids (Bruggaman and Locke, 2013). The liquid within the discharge channel of DBD reactor possesses a high particle density and electric field intensity. This means the movement of electrons is restricted due to short pathways.

Nevertheless the liquid still has higher ionization potential (Marinov et al., 2011). Within the discharge plasma zone, dissociation, ionization, photoionization, excitation as well as vibrational processes occur (Lukes et al., 2011). The discharge plasma can initiate both physical and chemical reaction mechanisms which eventually generate active species freely available within the bulk solution. The active species include the OH radical, O_3, H_2O_2, O, and O_2●- amongst others. The step by step formation of active species, which occurs simultaneously within the discharge zone is shown in the subsequent equations. Decomposition of water molecules by highly energetic electrons produces hydroxyl radicals (equation 2.26-22). Dimerization of hydroxyl radicals in the bulk liquid generates hydrogen peroxide (equation 2.30). Under intense ultraviolet light, hydrogen peroxide decomposes to the hydroxyl radical again (equation 2.31).

Dissociation

$$H_2O + e \rightarrow OH^{\bullet} + H^{\bullet} \quad (2.26)$$

Ionization:

$$H_2O + e \rightarrow 2e + H_2O^{+} \quad (2.27)$$

Dissociation:

$$H_2O^{+} + H_2O \rightarrow OH^{\bullet} + H_3O^{+} \quad (2.28)$$

$$H_2O + e- \rightarrow OH^{\bullet} + H^{\bullet} + e- \quad (2.29)$$

$$OH^{\bullet} + OH^{\bullet} \rightarrow H_2O_2 \quad (2.30)$$

$$H_2O_2 + hv \rightarrow 2OH^{\bullet} \quad (2.31)$$

$$OH^{\bullet} + H_2O_2 \rightarrow H_2O + HO_2^{\bullet} \quad (2.32)$$

$$HO_2^{\bullet} + H_2O_2 \rightarrow O_2 + H_2O + OH^{\bullet} \quad (2.33)$$

In addition to the formation of these aforementioned active species, other nitrogeneous species such as as NO_X are often also produced in the reactor zone. The formation of NO_X species depends on the source (air or oxygen). The mechanism of formation of NO, NO_2 and consumption of O_3 is represented below

$$O_2 + e \rightarrow 2O \quad (2.34)$$

$$N_2 + O \rightarrow NO + N \quad (2.35)$$

$$N_2 + e \rightarrow 2N + e \quad (2.36)$$

$$N + O_2 \rightarrow NO + O \quad (2.37)$$

$$NO + O \rightarrow NO_2 \quad (2.38)$$

$$NO + O_3 \rightarrow NO_2 + O_2 \quad (2.39)$$

$$2NO_2 + H_2O \rightarrow HNO_3 + HNO_2 \quad (2.40)$$

$$3NO_2 + H_2O \rightarrow 2H^+ + 2NO_3^- + NO \quad (2.41)$$

$$NO_2 + NO \rightarrow 2N_2O_3 + H_2O \rightarrow H^+ + NO_2^- \quad (2.42)$$

The concentration of these species varies and depends on the solution pH, electrical conductivity, applied discharge voltage, air flow rate, reactor configuration and the discharge magnitude (Shi et al., 2009). Shi et al., (2009) pointed out that the dielectric barrier discharge system in water is a combination of multi-advanced oxidation processes such as chemical reactions, photolysis, ultrasonic irradiation, electrical processes, as well as supercritical water oxidation. At the moment, very little information exists on the contribution made by the individual active species towards the decomposition of the target pollutants (Shi et al., 2009). Apart from that, the degradation mechanisms involving the breakdown of the primary compound through various intermediates to complete mineralization is difficult to predict. Joshi and Thagard, (2013) explained the fundamental mechanism of formation of reactive species responsible for the degradation of organic pollutants during electrical discharge in water. The question still remain which of the free reactive species was responsible for the decomposition or whether they act in concert. In DBD systems, the electrical discharge in liquid produces energetic electrons which dissociate the oxygen molecules via collisions into oxygen atoms (equation 2.43). Continuous reaction between the oxygen atom and oxygen molecules produce ozone (equation 2.44).

$$O_2 + e \rightarrow O + O + e \quad (2.43)$$

$$O + O_2 \rightarrow O_3 \quad (2.44)$$

Ozone is a powerful molecular species capable of mineralizing organic pollutants. In the DBD system, air or pure oxygen can be introduced into the reactor to produce ozone. It has been established that the presence of ozone within the plasma zone significantly increases the decomposition rate due to the formation of hydroxyl radicals formed by the reaction of UV light with ozone. In addition, the intensity of shock waves, UV light, the amount of bubbles, and reactive species generated varies with different reactor types. Ozone then undergoes a series of transformations within the solution compartment to different species. Ozone reacts with water to produce hydroxyl radicals (equation 2.45). In the presence of intense photon

energy within the reactor, ozone splits into oxygen and singlet oxygen respectively (equation 2.46). The singlet oxygen further reacts with water to liberate the hydroxyl radical (equation 2.47). Other reactions that occur within the solution compartment are represented in equation 2.48-2.49.

$$2O_3 + H_2O \rightarrow OH^{\bullet} + O_2 + HO_2^{\circ} \quad (2.45)$$

$$O_3 + h\nu \rightarrow O_2 + O \quad (2.46)$$

$$O + H_2O \rightarrow 2OH^{\bullet} \quad (2.47)$$

$$O_3 + HO_2^- \rightarrow HO_2^{\circ} + O_3^{\circ -} \quad (2.48)$$

$$O_3^{\circ -} + H_2O \rightarrow OH^{\bullet} + OH^- + O_2 \quad (2.49)$$

2.4.2 *Single and combined advanced oxidation technologies based on DBD system*

Studies have shown that DBD systems can remove and degrade priority pollutants (Locke et al., 2006; Magureanu et al., 2010; Krause et al., 2009; Sato et al., 2008). Available information from literature indicates that no single advanced oxidation technology on its own is efficient to remove all kinds of contaminants, and the current practice requires a combined approach (Bruggeman and Locke, 2013). Zhang et al., (2013) reported that combination of DBD system and heterogeneous photocatalysis will improve the degradation efficiency of organic pollutants. In trying to couple treatment processes, economic feasibility, system compatibility, and energy cost should be taken into consideration and comparative studies are needed with existing conventional methods. The DBD system can be coupled with catalysts, such as metal oxides, metal films and other catalysts to enhance free radical production and ultimately improve the overall process efficiency at a shorter time and overcome the shortcomings of individual processes (Jiang et al., 2014). However, the degradation efficiency of combined systems depend on the nature of the wastewater to be treated. Scott and Ollis, (1995) highlighted four categories of wastewater contaminants namely: recalcitrant compounds, largely biodegradable compounds, inhibitory compounds, and intermediate byproducts. In spite of the accelerated degradation rate, there are still challenges confronting the integrated approach in term of design, operational and installation cost.

Wang et al., (2008) applied glow discharge plasma to degrade bisphenol-A in aqueous solution. They observed that the BPA elimination rate as well as the rate of formation of H_2O_2 reduced in the presence of electrolytes such as sodium sulfate and phosphate solution, but increased in sodium chloride solution. Dobrin et al., (2013) utilized pulsed corona

discharge generated above liquid to degrade diclofenac in water. The results as presented indicated that, only 50 % of the compound decomposed after 30 min of exposure to plasma. Colombo et al., (2012) reported the decomposition of bisphenol-A in aqueous solution by combination of heterogeneous TiO_2 photocatalysis and ozonation. They observed 55 % mineralization efficiency for the combined system compared to (3 %) photolysis, (6 %) ozonation and (6 %) photocatalysis. In spite of achieving 55 % mineralization rate, the decomposition process was accompanied by the formation of intermediate compounds such as monohydroxylbisphenol-A ($C_{15}H_{16}O_3$) and kavalactone ($C_{15}H_{16}O_5$). Magureanu et al., (2010) applied dielectric barrier discharge to decompose pentoxifylline in water. The influence of pulse repetition rate and initial concentration of the pollutant on the pollutant degradation rate and degradation yield were explored. It was found that pentoxifylline degradation rate depends on the two parameters. 92.5% conversion rate with a corresponding degradation yield of 16 g/kWh was achieved after 60 minutes. Rong and Sun, (2013) reported the degradation of sulfadiazine in water by wetted-wall corona discharge. The effects of solution pH, initial concentration of the pollutant, H_2O_2, and radical scavengers on the decomposition rate of the compound were investigated. It was found that the above mentioned parameters influenced the pollutant rate of decomposition. The maximum degradation rate was obtained at a lower concentration of 10 mg/L and higher solution pH (11.04). In the same vein, Rong et al., (2014) demonstrated sulfadiazine degradation via water filling film dielectric barrier discharge system. The influence of solution pH, initial pollutant concentration, radical scavengers, and dosage of Fe^{2+} were explored. The authors observed 98% conversion rate for a 10 mg/L solution within 30 minutes at pH 9.10 in the presence of 1.0 mmol/L Fe^{2+} compared to 85% in the absence of Fe^{2+}. It was found that the presence of Fe^{2+} in the plasma zone enhanced the OH radicals and increase the mineralization rate. Liu et al., (2012) utilised dielectric barrier discharge alone to degrade carbamazepine in water. The authors achieved 100% pollutant removal rate via ex-situ discharge within 3 min. However, the degradation efficiency was affected by the formation of NOx, which consumed oxygen and reduced the solution pH. Furthermore, Lesage et al., (2013) applied both dielectric barrier discharge and gliding arc discharge to decompose 4-chlorobenzoic acid in water. The authors found that DBD exhibited greater degradation efficiency than gliding arc discharge with respect to the pollutant. The formation of NOx and corrosion of the brass plate reduced the pollutant removal rate. Lesage and colleague, (2013) revealed that gliding arc

discharge generated a high concentration of NOx, which affected the solution pH and O_3 concentration more than in the case of DBD.

Zhang et al., (2012) reported that combined technology involving pulsed plasma discharge with 24 kV discharge voltage and TiO_2 photocatalysis achieved 100 % phenol removal rate within 50 minutes compared to 88.8% removed by pulsed plasma discharge alone. The increase in the removal rate was attributed to the increase in hydroxyl radicals produced by the combined technology. Similarly, Zhang et al., (2013) demonstrated that combined pulsed plasma and TiO_2 nanotubes removed 98% phenol in water within 60 minutes with 20 kV discharge voltage compared to 60% removal rate by pulsed plasma alone. The authors ascribed the high removal rate to the existence of synergistic effect between the pulsed plasma and the photocatalysts. Qu et al., (2013) investigated the decomposition of phenol in water using combined plasma/TiO_2 photocatalysis. They found that the combined system with a discharge voltage of 24 kV removed 91.4 % phenol within 50 minutes compared to 60 % removed by the plasma system alone. They linked the high removal rate to the production of more hydroxyl radicals by the combined system than in a single plasma system. In the same vein, Hao et al., (2007) reported that combined plasma/TiO_2 photocatalysis system eliminated 90 % 4-chlorophenol in water within 60 minutes with 14 kV discharge voltage. Whereas, with the plasma system alone, only 74 % removal rate was achieved after 120 minutes. The increase in the removal rate by the combined system at a shorter time was attributed to the existence of a synergy between the plasma and TiO_2 photocatalysts. However, most studies that combined a plasma system with TiO_2 photocatalysts, utilised powder TiO_2 and also failed to investigate the performance of combined plasma with metal doped TiO_2 nanocomposites. The decomposition of carbamazepine, clofibric acid, and iopromide by corona discharge alone was accompanied by the formation of by-products (Krause et al., 2009). This occurred as a consequence of partial degradation; only 40 % degradation of iopromide was achieved while carbamazepine and clofibric acid degradation were close to 100. Similar trends were noticed during the degradation of carbamazepine, trimethoprim, meprobamate, primidone, and atrazine by non-thermal plasma discharge techniques (Gerrity et al., 2010). Wang et al., (2007) reported that pulsed corona discharge with a discharge voltage of 21 kV combined with TiO_2 supported on glass beads achieved 65% phenol removal within 60 minutes compared to 57% with pulsed corona discharge alone. The increase in the mineralization rate of phenol was ascribed to the existence of a synergistic effect between the two processes, which possibly increased the amount of OH

radicals, thus contributed to high degradation efficiency. It should be noted that, the difference in the removal efficiency reported by various authors can be attributed to several factors such as reactor configurations, applied voltage, initial concentration of pollutants, volume of aqeous solution, applied current to numerous to mention. The concentration of H_2O_2 produced by the combined system was 1.5 mmol/L compared to 1.0 mmol/L produced by pulsed corona discharge alone.The experiment was conducted as a function of gas bubbling type, solution pH and radical scavengers. In addition, Tang et al., (2013) utilized a combination of dielectric barrier discharge plasma and granular activated carbon (GAC) immobilised TiO_2 nanocomposites to decompose phenol in water. Tang and co-workers, (2013) found that combined DBD with TiO_2-GAC with input discharge voltage of 30 kV removed 88% phenol after 120 minutes compared to 69% obtained via DBD with GAC only. The 19% phenol removal rate was attributed to additional OH radicals provided by TiO_2. Neither of the individual systems was able to achieve complete degradation, but with an integrated system, complete elimination of the target pollutants was possible. Therefore, the combination of DBD system and heterogeneous photocatalysis offer hope for real applications in the near future.

2.5 Impingement and cavitation

The jet impingement process is becoming an increasingly important advanced treatment techniques in the water resources sector especially for the degradation of recalcitrant organic pollutants due to high mas transfer rate. Specifically, jet loop reactors have been utilised in fermentation, oil hydrogenation, synthesis of nanostructured particles and very recently in the treatment of wastewater containing high organic loads (Yildiz et al. 2005; Madzivire et al., 2015). It is a chemical free technique which operates on a continuous mode and involves rapid mixing and high mass transfer rate of liquids in a jet flow and orifice plate within the reactor cavity. The rapid and continuous mixing through a jet flow along the same axis but in the opposite direction within the reactor zone leads to collision. The collision effect of water molecules under high turbulence intensity within the reactor chamber produces impingement, which further resulted in the decomposition of water molecules and produced hydroxyl radicals. While cavitation involves generation, growth and eventual collapse of cavities/bubbles producing a significant amount of energy based on pressure field variation within milliseconds (Gogate, 2011). The collapse of the microbubbles generates highly reactive oxidizing species such as OH radicals and possibly H_2O_2 (Gogate and Patil, 2015).

The impinging device can be a circular orifice, throttling valve, slit or circular venturi or jet cavity (Gogate, 2008; Gogate, 2011). The liquid flow in a closed loop system driven by a suction pump increases the liquid velocity and kinetic energy value within the constriction zone at the expense of a local pressure. This action promotes expansion and then contraction of the liquid jet and produces vapourous cavities or bubbles. Under extreme flow rate, temperature and pressure, bubble-bubble interaction takes place to form spherical bubbles of different sizes and number (Arrojo and Benito, 2008). Consequently, the liquid jet expands reducing the average velocity and raising the pressure recovery rate leading to the collapse of the generated cavities (Gogate et al., 2008; Gogate, 2011).

There are different configurations of jet reactor namely free-surface jet, the submerged jet and the confined submerged jet. These device are of different shapes, and sizes and indeed their diameters have not been standardised. Their dimensions need to be properly optimised to obtain the needed impinging imparts and thus ultimately generate free radicals. However, the jet configurations of interest in this study is a submerged jet where the impingement of a similar liquid take places within the reactor cavity. The submerged jet configuration has been reported to have a higher heat transfer coefficient than other design due to rapid mixing on a continuous basis. The estimation of the heat transfer coefficient is rather complex and can be linked to several other factors such as Reynold's number, jet diameter, orifice diameter, consumption power among others (Yildiz et al., 2005).

The rapid mixing of liquid at optimum pressure leads to formation, collapse of cavities/bubbles and subsequently generation of highly reactive free radicals (Wang et al., 2008). The collision effect is accompanied with high turbulence and increase of the mass transfer rate in liquid/liquid mixing. The lifespan of produced cavities is very short (microseconds). The implosion of these micro and nano bubbles at very high energy densities produces physical and chemical effects leading to the generation of hydroxyl radicals and H_2O_2, shock waves and extreme shear forces (Bagal and Gogate, 2014b). The combined effects of these free reactive species is responsible for the improvement of the overall volumetric mass transfer coefficient and oxidation of most complex organic pollutants (Yildiz et al., 2005).

As the liquid flows through the cavitating devices, boundary layer adjustment at the bubble-liquid interface leads to considerable energy loss as well as swift pressure drop. The pressure drop and recovery rate determines the impingement or cavitational intensity, which in turn controls the cavitational yield. The cavitational yield measures the overall degradation

efficiency of the system. The yield depends on the degree of turbulence, pressure recovery rate, conditional liquid flow rate and geometry of the cavitational device (Bagal and Patil., 2014b). These parameters are independent of one another and are subject to changes within the cavitating device.

2.5.1 *Mechanism of radical formation in jet cavitation chamber*

The intense turbulence in a continuous flow system through the reactor zone produces implosion of nano and microbubbles with shear stresses and local hot spots at high temperature (10,000 K) and pressure (1000 bar). These conditions induce chemical and thermal effects that promote the eventual dissociation of water molecules into hydroxyl radicals and hydrogen (Gogate, 2008, Gogate, 2011). The generated hydroxyl radicals are non-selective, short-lived, relatively unstable but highly reactive, and attack the target pollutants, mineralizing/oxidising them into either toxic intermediates or innocuous, harmless, inorganic compounds such as CO_2 and H_2O

The decomposition reaction of water molecules under extreme conditions of temperature and pressure is shown in equation 2.50

$$H_2O \xrightarrow{Impingement} H^{\cdot} + OH^{\cdot} \quad (2.50)$$

As the reaction proceeds, hydroxyl radicals combine with each other or react with water to form hydrogen peroxide as shown in equation (2.51). Hydrogen peroxide is relatively stable, long-lived and thus accumulates in water.

$$OH^{\circ} + OH^{\circ} \rightarrow H_2O_2 \quad (2.51)$$

The two reactive species are continuously generated in a closed loop system and are thus individually or collectively responsible for the mineralization of the modelled organic pollutants. However, when hydrodynamic cavitation is coupled with other advanced oxidation strategies such as ultraviolet light, higher concentrations of hydroxyl radicals are obtained (Gogate, 2008). This synergistically improves the overall decomposition efficiency of the target compounds. The mechanism of a combined jet impingement/UV system involves dissociation of the generated hydrogen peroxide in the presence of ultraviolet light to hydroxyl radicals as indicated in equation (2.52).

$$H_2O_2 \xrightarrow{UV} 2\,OH^{\cdot} \quad (2.52)$$

Further reactions between the pollutant and the active species generates intermediates which ultimately decompose and yield carbon dioxide and water at room temperature.

OH^{o}+ organics → intermediates + H_2O (2.53)

H_2O_2 + organics → intermediates + H_2O (2.54)

Intermediates + ^{o}OH → CO_2 + H_2O (2.55)

It should be noted that an excessive amount of hydrogen peroxide in the bulk solution can moreover act as scavenger by consuming the available hydroxyl radicals (Bagal and Gogate, 2014a). There is the appearance and disappearance of hydroxyl radicals in the system and likewise hydrogen peroxide. This is expressed in equation 2.56 – 2.60

$^{\bullet}OH+H_2O_2 \rightarrow H_2O+HO_2^{\bullet}$ (2.56)

$^{\bullet}OH + HO_2^{\bullet} \rightarrow H_2O + O_2$ (2.57)

$HO_2^{\bullet} + H_2O_2 \rightarrow OH^{\bullet} + H_2O + O_2$ (2.58)

$OH^{\bullet} + OH^{\bullet} \rightarrow H_2O_2$ (2.59)

$H_2O_2 \xrightarrow{UV} 2OH^{\bullet}$ (2.60)

In fact, more free reactive species are continuously produced by the combined closed loop system, enhancing the degradation efficiency, which suggests the existence of a synergistic effect.

2.5.2 *An overview of single and combined hydrodynamic cavitation process*

Jet impinging system and/or hydrodynamic cavitation being a chemical free system has a great potential in wastewater treatment industries. Despite the simplicity of design and consumption of less energy compared to ultrasonic irradiation, jet impinging device system or hydrodynamic cavitation alone is rarely utilized as either municipal or industrial wastewater purification technique due to low yield of free reactive species. Studies have shown that combination of jet loop reactor or hydrodynamic cavitation with other advanced oxidation technologies are required to effectively purify wastewater. It is important to point out that little or information exist on the application of jet impinging system for degradation of organic pollutants. Thus, this section of the review will focus mainly on the application of hydrodynamic cavitation (HC) alone or the combined hydrodynamic cavitation process for wastewater treatment. Wang and Zhang, (2009) have explored hydrodynamic cavitation alone to degrade alachlor in aqueous solution. An increase in pressure and a simultaneous decrease in initial pollutant concentration significantly enhanced the degradation rate. The obtained pseudo-first rate constant k was found to be 4.90×10^{-2} min^{-1}. The rate of degradation was observed to depend on the temperature, pressure, initial concentration of alachlor and the solution pH. Madhu et al., (2014) reported hydrodynamic cavitation alone to decompose

malachite green and methyl violet solution. The authors reported that 98.42 % and 62.48 % removal rate of malachite green and methyl violet were respectively achieved with a 2 mm orifice plate. The rate of removing the two compounds an increase with increasing in solution pH and temperature. Zupanc et al., (2014) investigated the detoxification of wastewater containing clofibric acid, ibuprofen, naproxen, ketoprofen, carbamazepine and diclofenac by a shear-induced cavitating generating device. The influence of temperature, cavitation time and dose of hydrogen peroxide on the decomposition efficiency was explored. Under optimised conditions removal efficiencies of 54 % and 67 % of diclofenac and carbamazepine were observed when hydrodynamic cavitation was used as pre-treatment method to biological technique. This was high compared to 39 % and 54 % when hydrodynamic cavitation was used as a post-treatment method to biological treatment. Different combinations of hydrodynamic cavitation with other advanced oxidation processes have been widely exploited and satisfactory results reported in the literature. Patil et al., (2014a) investigated the efficiency of the hydrodynamic cavitation (HC), HC/H_2O_2 and HC/advanced Fenton process for the decomposition of a wastewater volume containing imidacloprid at an operating capacity of 4 L. Complete degradation of imidacloprid occurred within a short reaction time of 60 minutes for HC/advanced Fenton process compared to 120 minutes for the individual technique such as HC or H_2O_2. This was attributed to the rapid dissociation of hydrogen peroxide under the cavitating condition that perhaps enhanced the formation of more hydroxyl radicals. Raut-Jadhav et al., (2013) utilised combined hydrodynamic cavitation and hydrogen peroxide to decompose neonicotinoid in water. They found that under the optimised conditions, the combined system with synergistic index value of 22.79 more successfully removed the pollutant in water than with hydrodynamic cavitation alone. In the same vein, Saharan et al., (2012) utilized combined hydrodynamic cavitation with Fe-TiO_2 nanocomposites at an operating capacity of 15 L to degrade acid red 88 dye in aqueous solution. The degree of decolourization and mineralization increased with increasing initial dye concentration, though the rate of degradation was dependent on the solution pH. The degradation efficacy was further enhanced by the addition of hydrogen peroxide and catalyst (Fe-TiO_2). Thus, the degradation of recalcitrant organic pollutants using combined hydrodynamic cavitation based on free radical mechanism is identified as a sustainable wastewater purification process.

2.5.3 *Operating parameters in hydrodynamic cavitation process*

The performance of a hydrodynamic cavitation process depends on a combination of several factors. The optimisation of parameters identified as most important, require proper examination. These parameters include: inlet applied pressure, solution pH, initial concentration of the pollutant, temperature, additives such as H_2O_2, radical promoters and radical scavengers, geometry and size of the cavitating device (slit, circular orifice, venturi) (Gogate, 2008, Gogate, 2011). Some of these fundamental parameters which determine the efficiency of hydrodynamic cavitation process are reviewed below.

2.5.3.1 Influence of inlet applied pressure

The applied inlet pressure is a fundamental parameter which determined the rate of impingement and intensity within the reactor cavity in a jet loop impingement process. The impinging effects and intensity are related to the cavitation number δ, which reduces with an increase in applied inlet pressure regardless of the increase in the liquid flow and velocity. Cavitation number is expressed below as a function of the downstream, upstream and vapour pressure of a fluid (equation 2.61)

$$\delta = \frac{Pd - Py}{Pu - Pd} \approx \frac{Pd}{Pu} \qquad (2.61)$$

Where P_d, P_u and P_v represent the downstream, upstream and vapour pressure of the fluid respectively. Under the ideal situation when Pu»Pd»Pu, the value of δ at which cavitation will occur (C_v) is less than 1. C_v can be greater than 1 if suspended solids and dissolved gases make available extra nuclei for cavities to form (Bagal and Gogate, 2014b). In short, the rise in upstream pressure P_u reduces the cavitation number and increases the number of cavitation cavities which in the long run result in an increase in the decomposition rate of the pollutant depending on the cavitating device. On the other hand, a decrease in the cavitation number increases the density of cavities and causes total collapse of cavitation intensity. However, an increase in the number density and cavities continues until a point is reached where the cavities begin to coalesce, in such a situation the cavities are said to be choked or clouded. This condition is called choked cavitation and at this point, mineralization efficiency is usually low. Bagal and Gogate, (2014a) studied the effect of inlet pressure over the range of 2-4 bar on the decomposition of 20 ppm diclofenac sodium contained in a 5 L feed tank. The study showed that increasing the inlet pressure applied from 2 to 3 bar resulted in a corresponding increase in the degradation rate of the target compound. An inlet pressure of 3 bar was selected as the optimum value. With further increase in inlet pressure to 4 bar, a

decrease in the extent of mineralization rate was observed. The decrease in degradation efficiency despite the increase in applied pressure was due to choking of the cavitating region by excess liquid which produced large bubbles. The formation of large bubbles reduces the cavitational effects and intensity due to partial collapse of the cavities. Patil et al., (2014a) reported optimum pressure of 4 bar within the cavitation region, higher pressure of 5- 8 bar, there was the formation of numerous large bubbles and cavities within the constriction area which reduced collision rate and the number of free radicals. Thus, it is important to establish the optimum inlet pressure and avoid a situation of a cavity cloud which reduces the mineralization rate of a typical target compound.

2.5.3.2 Solution pH

An important operating factor widely studied in most advanced oxidation processes especially hydrodynamic cavitation is solution pH, which provides information on the solution physical and chemical properties. Optimum pH is often achieved by varying the pH value over a certain range via the addition of either acid or base and depends on several factors such as pollutant type, or pollutant dissociation pH constant. The degradation rate of pollutants differ in basic or acidic media; while higher pH values favour the decomposition of certain organic pollutants, others decompose better in the alkaline region regardless of whether hydrodynamic cavitation acted alone or in combination with other AOTs. Most researchers have demonstrated that higher oxidation rate of organic pollutant under acidic conditions than alkaline medium (Gogate, 2008; Patil and Gogate, 2012). Bagal and Gogate, (2014a) varied the solution pH over the range of 4 -7.5 during the hydrodynamic cavitation decomposition of diclofenac sodium. It was observed that the decomposition rate decreased as the solution pH increased. At pH values lower than the pKa value of diclofenac sodium (4.5), the pollutant exists in the molecular form, whereas at pH values greater than its pKa value, it exists in the ionic form. Diclofenac sodium being a hydrophobic salt was able to diffuse faster through the cavities containing gaseous-water and react with hydroxyl radicals. However, at higher pH values, most diclofenac in ionic form remained in the solution containing a lower concentration of hydroxyl radicals, which in turn affected the degradation rate.

2.5.3.3 Effect of initial concentration of the pollutant

The performance of the hydrodynamic cavitation process is measured in terms of the concentration of the pollutants in wastewater to be treated. The determination of the optimal concentration is a function of solution pH, and available free radicals (which depends on the cavitational intensity), in the bulk solution. The competition between the pollutant and the little available free reactive species makes the diffusion into the pollutant-liquid layer extremely difficult. Thus, total collapse of the radicals within the constriction zone is evident, which leads to lower degradation rate. Studies involving optimisation of the initial concentration of the pollutant include Basiri Parsa and Zonouzian, (2013) who studied the influence of the initial concentration of Rhodamine B over the range of 2-14 mg/L on the extent of mineralization via heterogeneous catalytic hydrodynamic cavitation. Basiri Parsa and co-worker established an inverse relationship between the duos, meaning that an increase in concentration of Rhodamine B resulted to decrease in mineralization efficiency, which is attributed to insufficient concentration of hydroxyl radicals within the constriction zone. It is thus possible to submit that high oxidation rate of organic pollutant based on the hydrodynamic cavitation process can be attained using a lower concentration of the pollutant, which can be determined through optimisation.

2.5.3.4 Influence of combination of hydrogen peroxide with impingement or cavitation process

One of the problems identified with hydrodynamic cavitation is generation of low cavitational intensity and hence of fewer hydroxyl radicals. The hydroxyl radicals can however be enhanced by adding a process intensifier such as hydrogen peroxide. Apart from oxidising the organic pollutants, hydrogen peroxide acts by preventing the recombination of electron-holes and dissociates under intense cavitation to hydroxyl radicals. The dissociation rate is faster in combination with ultraviolet light. The decomposition reaction is shown in the equation 2.62:

$$H_2O_2 \xrightarrow{UV} 2OH^{\cdot} \qquad (2.62)$$

Additionally, hydroxyl radicals formed via dissociation of water molecules under intense cavitation and impingement recombine in the bulk liquid or gas-liquid interface to form hydrogen peroxide, thus promoting decomposition of the contaminant. On the other hand, excess hydrogen peroxide in the solution can act as radical scavenger and consume the

available free generated hydroxyl radicals in the cavitation zone. The reaction is represented in the equation 2.63:

$$H_2O_2 + OH^{\cdot} \rightarrow HO_2^{\cdot} + H_2O \quad (2.63)$$

Furthermore, excess hydrogen peroxide beyond the optimum load contributes to the high COD level of water which is sometimes toxic to micro-organisms (Joshi and Gogate, 2012). Hydrogen peroxide thus plays a crucial role in the mineralization process of organic pollutants and it is imperative to establish the optimum dose (Bagal and Gogate, 2014b). Achieving the optimum dose of hydrogen peroxide during wastewater via individual treatment or combined AOTs is a critical task and depends on the nature of the pollutant (whether it is hydrophobic or hydrophilic), the initial concentration of the pollutant, cavitational intensity, reactor configuration and chemical composition of the effluent to be treated (Arrojo and Benito, 2008). Several researchers have investigated the influence of hydrogen peroxide on the extent of degradation of organic pollutants and have established the optimum value (Patil and Gogate, 2012; Patil et al., 2014a; Bagal and Gogate, 2014b). It has been demonstrated that beyond the optimum dose, further addition of hydrogen peroxide had scavenging effects on hydroxyl radicals, thus reduced the available hydroxyl radicals and hence lowered the oxidation rate. The authors also found that a higher concentration of hydrogen peroxide beyond optimal value in the solution caused vaporous cavities and reduced the cavitational intensity and yield. It appears that determining the optimal dose of hydrogen peroxide is important in the development of a less expensive but efficient combined process.

2.5.4 *Limitations of Advanced Oxidation Technology*

Advanced oxidation technologies are effective for the decomposition of organic pollutants due to the high oxidative potential and efficiency. However, high operational cost such as high energy consumption and chemical oxidants constitute a serious bottleneck limiting its municipal and industrial applications (Gogate and Patil, 2015). Moreover, the efficiency of advanced oxidation technologies is considerably reduced especially when treating raw environmental wastewater. This is because real wastewater are made up of different constituent one of which is the inorganic species. These organic species which includes bicarbonate, sulphates, phosphates, carbonates, chlorides, nitrates are commonly called radical scavengers (Bagal and Patil, 2014b). These ions acts by scavenging the oxidizing power of the hydroxyl radicals and ultimately decrease the efficiency of the process. The

matrix scavenging causes low oxidation efficiency of assimilable organic carbon formation given rise to the formation of unidentified transformation products. In order to avoid this problem, the interfering ions need to be removed—though will require more energy—thus causing additional costs and time. Advanced oxidation technologies cannot be used to treat large volume of wastewater unless pretreatment technique is applied. Furthermore, oxidation reactions via AOT often involve complex chemical and physical processes leading to generation of intermediate compounds (Gogate, 2011). These oxidation by-products are even more toxic than the original compounds and thus affect the quality of initial contaminated water. In order to reduce operational cost and achieve greater efficiency within a shorter time, integration of AOT with other treatment methods will go along way in obtaining a cost-effective, sustainable and advanced water purification system.

2.6 Quantification of free reactive species in AOTs

Molecular and radical species such as H_2O_2, O_3, $H^{\bullet}$ and $OH^{\bullet}$ obtained via heterogeneous photocatalysis, cavitation, and dielectric barrier discharge are powerful oxidants responsible for the physicochemical decomposition of organic contaminants. Over the years, the quantification of these active species has generated diverse interest and has become the subject of considerable investigation among experts in the field of advanced oxidation technologies due to their high selectivity and oxidation potentials. Different techniques such as electron spin resonance-spin trap, emission spectroscopy, chromatographic methods, chemical probes among others have been applied to quantify these species. However, most of these techniques are associated with one problems or the other. For instance, electron paramagnetic resonance (ESPR) technique which measures the spin adduct derivative after trapping is not sensitive and aside from that, the instrument is expensive and requires skilled personnel. This hinders its suitability for routine analysis. The measurement of aromatic hydroxylated derivatives based on the HPLC method is pH dependent due to the low concentration of OH radical (Jen et al. 1998). In the case of Fenton and photo-Fenton process, solution pH is adjusted to 3-4. It is therefore imperative to identify suitable chemical or physical methods to quantify the generated free reactive species.

2.6.1 *Hydroxyl radical*

Hydroxyl radicals are non-selective but highly reactive species with high oxidation potentials which are mostly responsible for the effective mineralization of organic pollutants. In the case of DBD system, the electrical discharge in water causes water ionization and production of O_3, H_2O_2 and OH radicals inside the streamer channel in a few hundred nanosecond (Kirkpatrick and Locke, 2005; Lukes and Locke, 2004). Procedures for quantifying the hydroxyl radicals have been widely reported in the literature, including salicylic acid dosimetry based on high performance liquid chromatography (HPLC), disodium of terephthalic acid dosimetry (fluorescence spectroscopy), formaldehyde dosimetry (HPLC), and dimethylsulfoxide (HPLC). The quantitative determination of the actual yield of hydroxyl radical in the aqueous media is important but never an easy task due to its transitory lifetime (Wang et al., 2009). The use of chemical probes has become a subject of debate simply because most chemical probes react with hydroxyl radicals and generate multiple products. The aromatic hydroxylation method involving chemical dosimetry probes such as salicylic acid, benzoic acid, para-chlorobenzoic acid, and coumarin-3-carboxylic acid based on gas-chromatography or liquid chromatography techniques is sensitive and convenient. Nevertheless, the method is associated with shortcomings such as poor solubility in water, formation of multiple reaction products, secondary formation of superoxide, thus making it difficult to prepare higher concentrations. In most cases, the concentration of the OH radical in the discharge channel may be higher than the concentration of the chemical probes, thus making quantification challenging. In the late 1990s, OH radicals generation rate was determined by following a pseudo steady-state approach based on liquid or gas-liquid pulsed corona discharge in the presence of phenol as a chemical probe and carbonate ion as a scavenger (Hoeben et al., 1997; Joshi et al., 1995). Hoeben et al., (1999) utilized 5,5-dimethyl-1-pyrroline N-oxide (DMPO) to trap OH produced by pulsed corona discharge. However, the spin-adduct DMPO-OH could not be detected by ESR due to decomposition by the pulsed corona reactor. Fluorescence spectrophotometry based on Coumarin-3-carboxylic acid (CCA) dosimetry was further utilized, nevertheless the generation of a large background signal in bulk solution relative to the prepared standards made OH quantification problematic (Sahn and Locke, 2006). Aside from that, there was the formation of multiple by-products, thus making it extremely difficult to distinguish between the fluorescence compound and the dye molecules. The physical and chemical properties of some chemical probes are indicated in Table 2.2.

Table 2.2: The physical and chemical properties of different chemical probes used for OH radical detection

Physical Parameters	Coumarine-3-carboxylic acid	4-Chlorobenzoic acid (pCBA)	Disodium salt of terephthalic acid	Dimethylsulfoxide (DMSO)
Chemical Formula	$C_{10}H_6O_4$	$C_7H_5ClO_2$	$C_6H_4(COONa)_2$	C_2H_6OS
Melting point	109.15524	240-243	-	19 °C
Boiling point	-	274-276	-	189 °C
Solubility	Poor	Poor	Very good	Highly water soluble
Reaction rate constant with OH radical	5×10^9 $M^{-1}s^{-1}$	5×10^9 $M^{-1}s^{-1}$	3.3×10^9 $M^{-1}s^{-1}$	$4.5 \sim 7.1 \times 10^9$ $M^{-1}s^{-1}$

Source: (Gupta, 2007)

Dimethyl sulfoxide is relatively water soluble and non-toxic even at higher concentration. It reacts with the hydroxyl radicals forming methanesulfinic acid (MSA), methyl radicals and formaldehyde as indicated in the equations below (Tai et al., 2004).

$$OH^{\bullet} + (CH_3)_2SO \longrightarrow CH_3SO_2H + {}^{\bullet}CH_3 \quad (2.64)$$

$${}^{\bullet}CH_3 + H\text{-}R \longrightarrow CH_4 + R \quad (2.65)$$

$${}^{\bullet}CH_3 + O_2 \longrightarrow CH_3COO^{\bullet} \quad (2.66)$$

$$2\,CH_3COO^{\bullet} \longrightarrow HCHO + CH_3OH + O_2 \quad (2.67)$$

Previously, spectrophotometric and HPLC measurement of the concentration of methanesulfinic acid was considered equivalent to generated hydroxyl radicals. Very recently, studies have shown that methane sulfinic acid is only an intermediate products which can still react with more hydroxyl radical to form methane sulfonic acid and sulfate (Gupta, 2007). Thus, the quantitative determination of the generated formaldehyde via DMSO/$^{\bullet}$OH reaction can be considered equivalent to the hydroxyl radical. In this study, the disodium salt of terephthalic acid (NaTA) was used as a chemical probe to trap and quantify the hydroxyl radicals produced by the dielectric barrier discharge system due to its high reaction rate constant (NaTA). Terephthalic acid (TA) is readily soluble in water containing NaOH, but its higher conductivity value impedes the streamer properties. Also, the reaction between NaTA and OH radical is not affected by the presence of other active species such as H_2O_2, $HO_2^{\bullet}$, $O_2^{\bullet}$. The reaction between the disodium salt terephthalic acid (NaTA) (non-fluorescent) and hydroxyl radical in the treated water produces a stable 2-

hydroxylterephthalic acid (HTA) which is fluorescent at 425 nm in a typical fluorescence spectrophotometer (Fang et al., 1996). The quantified peak intensity of the fluorescent compound (HTA) correspond to HTA concentration and is directly proportional to OH radicals in the solution. The reaction between NaTA and hydroxyl radical is represented in Figure 2.8

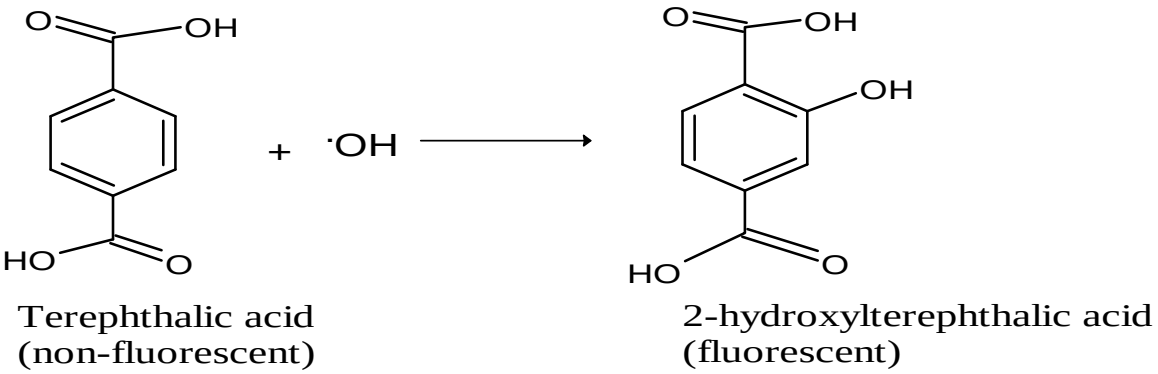

Figure 2.8: The formation of hydroxyterephthalic acid (HTA)

Sahni and Locke, (2006) quantified OH radicals in a pulsed corona discharge system using chemical dosimetry, Dimethyl sulfoxide (DMSO) and NaTA. It was found that the rate of formation of the OH radicals followed zero-order law irrespective of the applied voltage or the probes concentration. At 45 kV, the rate of formation of OH radical via DMSO and NaTA dosimetry were 1.2×10^{-7} Ms^{-1} and 1.67×10^{-8} Ms^{-1} respectively. The authors established a linear relationship between the OH radical and applied voltage over time. Sahni and Locke, (2006) concluded that the concentration of hydroxyl radical produced by a pulsed corona discharge depends on a plethora of factors such as chemical probes concentration, reactor configuration, electrode materials, solution pH, conductivity, applied voltage, air flow rate, additives amongst others. Jo and Mok, (2009) reported that the concentration of hydroxyl radicals produced by a dielectric barrier discharge system depended on the concentration of the electrolyte in the aqueous electrode, the applied voltage, the discharge power, and solution pH. Tahara and Okubo, (2012) employed (5, 5-Dimethyl-1-pyrroline N-oxide) (DMPO) as OH radical trapping chemical probe followed by ESR measurement. Surprisingly, no hydroxyl radicals were detected due to their short lifetimes. Instead the formation of H_2O_2 was confirmed. Further addition of Fe^{2+} prior to plasma discharge in the presence of H_2O_2 liberated hydroxyl radicals although at low concentration.

2.6.2 *Hydrogen peroxide (H_2O_2)*

Hydrogen peroxide is one of the most relatively stable, abundant powerful oxidants produced by the DBD reactor and as such plays a dual role in the decomposition of organic contaminants as well as the disinfection of water. It dissociates in the presence of ultra violet light into hydroxyl radicals ($OH^{\bullet}$), which in turn recombine with the bulk solution and form H_2O_2. Thus, quantification of the amount of H_2O_2 produced by the DBD is indirectly a determination of the amount of $OH^{\bullet}$. There are different methods for quantification of hydrogen peroxide. However, the colorimetric method is mostly reported in literature (Sahni and Locke, 2006). This involves the spectrophotometric measurement of the intense-yellow orange formed as a consequence of adding titanylsulphate to a solution containing hydrogen peroxide. The yellow colour is due to the formation of peroxotitanyl sulphonic acid shown in the reaction scheme below.

$$TiOSO_4 + H_2O_2 + H_2SO_4 \longrightarrow TiO_2(SO_4)_2^{2-} + H_2O + 2H^+ \quad (2.68)$$

The concentration of H_2O_2 produced by the DBD reactor is equivalent to the concentration of the peroxo titanyl sulphonic acid measured using UV-visible spectrophotometry at 410 nm. The substitution of the corresponding absorbance value at this wavelength into the Beer's Lambert formula allows calculation of the initial concentration of H_2O_2. Magureanu et al., (2013) quantified the amount of H_2O_2 generated by a pulsed corona discharge system and found that the concentration of H_2O_2 increased with an increase in the exposure time up to 200 mg/L in 30 minutes and thereafter decreased to 170 mg/L in the presence of methylene blue. The authors attributed the slight decrease to competition between the methylene blue and the intermediate compounds. Zhang et al., (2013) quantified the concentration of H_2O_2 produced by the dielectric barrier discharge at 20 kV in distilled water and phenol solution in the presence or absence of TiO_2. It was found that about 7.02 mg/L H_2O_2 was produced by the system in distilled water compared to the phenol solution, which further increased to 10.7 mg/L upon addition of TiO_2. The increase in peroxide concentration was attributed to an increase in the OH radical yield and dimerization of OH radicals in plasma and plasma/TiO_2 system. Whereas, in the phenol solution, there was suppression of OH radicals by both the phenol and other degradation products, which prevents OH radical recombination thus is responsible for lower H_2O_2 concentration. Manoj Kumar Reddy and Subrahmanyan, (2012) quantified the concentration of H_2O_2 produced in the DBD reactor at 18 kV in aqueous solution containing crystal violet. It was found that about 60 ppm of H_2O_2 was produced by the reactor within 25 minutes. Wang et al., (2008) reported a higher concentration of H_2O_2

(3.5 mmol/L within 60 minutes) in the combined pulsed discharge plasma and TiO_2 photocatalyst in distilled water compared to 0.75 mmol/L in phenol solution. The decline in H_2O_2 concentration in phenol solution was attributed to the consumption of the OH radical by the pollutant, which prevented recombination of the OH radical to form peroxide. Dobrin et al., (2013) utilized the indigo method and colorimetric method to quantify O_3 and H_2O_2 produced by a pulsed corona discharge in water and diclofenac solution. It was found that the concentration of O_3 produced (1.6 g/m^3) in water was slightly higher than in diclofenac solution, which was linked to ozone consumption by the pollutant. A linear relationship existed between the H_2O_2 concentration and the treatment time. In fact, within 30 minutes of discharge, 77 mg/L H_2O_2 was formed in water. Surprisingly, the concentration of the H_2O_2 formed in diclofenac within 15 minutes was 94 mg/L, which was higher than the value obtained in water. This was ascribed to the dissociation of hydroxylated aromatic rings present in DCF which enhanced the generation of more hydrogen peroxide in solution. Lei et al., (2007) employed the colorimetric and indigo methods to quantify the amount of H_2O_2 and O_3 produced by a pulsed corona discharge system. They found that the concentration of H_2O_2 and O_3 produced by a pulsed corona discharge system increased with an increase in discharge time and reached 0.64 and 0.029 mM within 60 minutes respectively. The values reported were less than the concentration of oxygen bubbled into the reactor. The authors ascribed lower concentration of H_2O_2 relative to oxygen bubbling (2.02 Mm) to the reaction between the active electrons and nitrogen. Whereas, the low concentration of ozone compared to oxygen (0.032 mM) was attributed to the reaction between oxygen and nitrogen atoms in the bulk solution.

2.6.3 *Indicator parameters used in wastewater treatment*

Wastewater comprises different constituents such as organic contaminants, inorganic species, and pathogenic agents amongst others. Organic species mostly identified in different water sources consist of pharmaceuticals, EDCs, pesticides, disinfection by-products (DBPs), metabolites, algae, and nutrients (Lessage et al., 2013). While the inorganic species includes heavy metals, trace metals, radioactive elements. These constituents are further classified into biodegradable and non-biodegradable species. The quality of potable drinking water or reuse water is measured based on the reduction of these constituents to within tolerable, permissible or acceptable limits using different indicator parameters (Rocha et al., 2013). These indicator parameters includes, total organic carbon (TOC), chemical oxygen demand (COD),

biochemical oxygen demand (BOD), biodegradable dissolved organic carbon (BDOC), colour, turbidity, alkalinity, pH, hardness, total dissolved solid (TDS), nitrogen and phosphorus content, chloride, faecal coliforms. Apart from chemical analysis, the biological assays involving the use of different Toxkits can also be conducted on the treated water to further confirm the purity level of such a water (Oller et al., 2011). Bioassays test would provide information on the toxicity level of the water. Different types of toxicity assays such as the anti-inflammatory test, nitrous test, daphnia test, Interleukin 6 (IL-6) assay have been conducted on treated water (Oller et al., 2011). Therefore, the overall water quality can be measured using both the chemical analysis as well as toxicity assays. In this study, the extent of mineralization of BPA or 2-NP was measured in terms of reduction in the total organic carbon.

2.6.3.1 Total organic carbon

Total organic carbon (TOC) is a measurement of the total non-purgeable chemically bonded organic carbon that is converted to CO_2. TOC includes the particulate organic carbon (POC) and dissolved organic carbon (DOC). It is an important indicator parameter mostly applied to measure the quality of water and the performance of drinking water purification as regards the presence of volatile and non volatile organic compounds (Oller et al., 2011). The determination of the TOC value basically involves two stages. The first stage deals with the conversion of the organic carbon to simple molecules such as CO_2. This can be achieved using any of the following processes: photodecomposition, thermal combustion, wet oxidation or a pyrolysis method (Fung et al., 1996). However, each of these methods has limitations. In the case of photodecomposition, TOC value of water that contains recalcitrant non-purgeable organic compounds cannot be determined. In addition, wet oxidation is limited to non-volatile organic compounds while the pyrolysis method cannot be used to determine low TOC value (1 mg/L) of a large volume of water. Whereas, the thermal method can decompose recalcitrant volatile and non-volatile organic compounds and can even be used for large volumes of water containing low TOC values (Anouzla et al., 2009). The second stage involves quantitative measurement of the CO_2 formed during the conversion of the organic bound carbon. The CO_2 measurement can be done using any of the following methods: nondispersive infrared (NDIR) absorption spectroscopy, thermal conductivity detector, ion exclusion chromatography (IC), nonsuppressed ion chromatography, acid/base titration, gravimetry amongst others (Fung et al., 1996; Oller et al., 2011). The first three techniques

required the use of analytical equipment while the last two do not. The extent of degradation of organic pollutants via DBD or jet loop reactor is measured either by measuring TOC or biological dissolved organic carbon (BDOC). It also involves determining the differences between the inorganic carbon and the total carbon content in the mixture. TOC cannot be conveniently used to distinguish between the biologically oxidizable constituents and inert organic matter. In this study, the extent of degradation of the modelled pollutants was measured using TOC as indicator parameter. The step by step conversion of the organic pollutant to CO_2 is shown in the equations below

$$R + O_2 \longrightarrow CO_2 + H_2O \quad (2.69)$$

$$R\text{-}N + O_2 \longrightarrow NO + CO_2 + H_2O \quad (2.70)$$

$$R\text{-}Cl + O_2 \longrightarrow HCl + CO_2 + H_2O \quad (2.71)$$

Where R represents carbonic substance.

2.7 Chapter summary and identified knowledge gaps

In this chapter, the sources, effects, environmental fate, as well as methods for detection and quantification of pollutants of bisphenol-A and 2-nitrophenol in water was reported. It is noted that the global production and demand for manufactured products containing BPA and 2-NP has increased tremendously. Consequently, higher concentration of BPA and 2-NP have been detected in water sources due to the systemic failure of wastewater treatment plants. Moreover, these compounds are not readily destroyed by conventional techniques. Alternative treatment methods are desired to maintain public health and improve environmental sustainability. The review of literature has shown that advanced oxidation technologies namely heterogeneous photocatalysis, dielectric barrier discharge systems, and hydrodynamic cavitation have been successfully utilized to decompose recalcitrant organic pollutants. Nevertheless, dielectric barrier discharge systems produce ultraviolet light and hydrogen peroxide (H_2O_2). Both the UV light and H_2O_2 are not maximally utilized, thus require adequate attention to improve efficiencies. In the same vein, most TiO_2 photocatalysts incorporated with DBD system are in powder form and not on a solid support, which prevents UV light penetration, and causes difficult post-separation of the catalyst, thus increasing treatment time and costs. Another research gap identified is related to rapid electron-hole recombination rate, high band gap energy of TiO_2 photocatalysts and low adsorption capacity which limits photocatalytic efficiency. It is also worth mentioning that particle agglomeration and stability affect the catalytic performance of nano zero valent iron

particles. Similarly, the concentration of OH radicals and yield of the jet loop reactor system alone is low thus reducing the mineralization rate. It is clear from the literature survey that the individual advanced oxidation technologies are associated with particular shortcomings which affect their overall performance and limit their full scale industrial applications. There is a need to provide answers to some of the unresolved identified problems in the literature. To overcome the identified associated shortcomings with regard to each treatment process, this research proposes a process integration to decompose recalcitrant organic pollutants. Thus, development of TiO_2 nanocrystals on a rigid support such as stainless steel mesh and subsequently doping with plasmonic Ag is considered research worthy of investigation. This will not only reduce the post-recovery problem but also prevent the electron-hole recombination rate and enhance the photocatalytic efficiency. Thus, the combination of DBD system and the supported Ag doped TiO_2 photocatalyst will be explored in detail. The combination of stabilized nano zero valent iron particles with DBD system to induce the photo-Fenton process constitutes another area that requires deeper understanding of the kinetics and degradation mechanisms. Furthermore, the degradation yield of the jet loop reactor may be enhanced via incorporation of in-line UV light and hydrogen peroxide. Researchers have demonstrated that combined advanced oxidation technologies remain ideal and sustainable ways for decomposition of recalcitrant organic pollutants. Combined techniques allow the exploitation of each method's strength to provide synergy, as well as supplementing each process in the overall interest of obtaining a cost effective and sustainable treatment system. These synergistic effects could also enhance the generation of powerful oxidants, decrease mass transfer resistances and thus increase degradation yield, shorten reaction time and lower the operational and maintenance cost (Golash and Gogate, 2012). However, limited studies have investigated combined advanced oxidation technologies in the literature. In fact, no studies have been conducted on the degradation of BPA and 2-NP in aqueous solution by combined DBD/supported Ag doped TiO_2 photocatalysts. Likewise, no information could be found on the decomposition of BPA and 2-NP in aqueous solution by DBD system and photo-Fenton induced process. And neither has the decomposition of the two modelled compounds by combined Jet loop reactor/in-line UV /hydrogen peroxide been reported in the literature. Although the individual treatment process had been effectively utilised to decompose emerging organic pollutants, however no studies have been conducted using the combinatory approach of the aforementioned systems to degrade BPA or 2-NP in water. Based on the gaps identified in the literature, the present

investigation is conducted to identify the best combined AOTs among the followings: DBD/supported photocatalysts, DBD/photo-Fenton induced process, JLR/UV/H_2O_2 that is capable of mineralizing BPA or 2-NP into innocuous or less toxic compounds. The next chapter provides detailed experimental protocols and analytical techniques used to achieve the outlined aims and objectives of the research.

CHAPTER THREE

EXPERIMENTAL AND ANALYTICAL TECHNIQUES

3 INTRODUCTION

The previous chapter of this study (Chapter two) focused on the review of literature. This chapter provides detailed descriptions of the experimental procedures used to generate the data needed to achieve the outlined aims and objectives of the study. It also sets out the materials, as well as the analytical characterization techniques employed in this study.

3.1 Materials

The name, molecular formula, supplier, grade/purity of the chemicals, solvents and acids used in this study are presented in Table 3.1 below. All the chemicals were used as received without further purification and the preparation of solutions is presented in section 3.1.1.

Table 3.1: Chemicals used in this study

Chemicals/Solvents/Acids	Molecular formula	Supplier/Source	Grade/Purity
Poly acrylonitrile (PAN)	$[C_3H_3N]n$	Sigma Aldrich	99 %
Titanium tetrachloride	$TiCl_4$	Sigma Aldrich	99 %
N,N-Dimethylformamide	$(CH_3)_2$ NC(O)H	Sigma Aldrich	99 %
Bisphenol-A (BPA)	$C_{15}H_{16}O_2$	Sigma Aldrich	99.5 %
2-nitrophenol (2-NP)	$C_6H_5NO_3$	Sigma Aldrich	97 %
Methylene blue	$C_{16}H_{18}N_3SCl$	Sigma Aldrich	98 %
Silver trioxonitrate (V) salt	$AgNO_3$	Merck	98 %
Pure silver metal	Ag	Kimix	99.8 %
Titanium(IV) oxysulphate	$TiOSO_4$	Sigma Aldrich	95.8 %
Disodium salt of terephthalic acid (NaTA)	$C_8H_6O_4$	Sigma Aldrich	>29 %
2-hydroxyterephthalic acid	$C_8H_6O_5$	Sigma Aldrich	98 %
Hydrogen peroxide	H_2O_2	Sigma Aldrich	97 %
Sulphuric acid	H_2SO_4	Sigma Aldrich	30 %
Sodium hydroxide solution	NaOH	Merck	98 %
Iron (III) chloride. hexahydrate	$FeCl_3.6H_2O$	Sigma Aldrich	50 %
Sodium borohydride	$NaBH_4$	Merck	99 %

Poly (Ethylene glycol)	$C_{2n}H_{4n+2}O_{n+1}$	Sigma Aldrich	99 %
Sodium chloride	NaCl	Sigma Aldrich	>99 %
Sodium tetraoxosulphate (VI)	Na_2SO_4	B and M Scientific	99%
Phosphoric acid	H_3PO_4	Sigma Aldrich	>85 %
Sodium trioxocarbonate(V)	Na_2CO_3	Sigma Aldrich	99.5 %
Di-sodium hydrogen orthophosphate	Na_2HPO_4	Sigma Aldrich	>99 %
Potassium indigo trisulfonate	$C_{16}H_7K_3N_2O_{11}S_3$	Sigma Aldrich	75%

3.1.1 *Preparation of simulated wastewater and reagents*

1000 ppm Methylene blue

1 g of methylene blue (MB) was accurately weighed into a 1 L volumetric flask containing purified water obtained from a milli-Q millipore system. The mixture was shaken until the methylene blue dissolved completely and thereafter made up to the 1 L mark with more millipore water. The working standard (10 ppm) was then prepared from the stock solution (1000 ppm) by serial dilution using the relationship below $C_IV_I=C_2V_2$. A freshly prepared 10 ppm solution was used for the photocatalytic experiment.

1 000 ppm Bisphenol-A

A standard solution of bisphenol-A (BPA) was prepared by accurately weighing 2 g into a 2 L volumetric flask containing millipore water and the mixture was shaken thoroughly to dissolve the BPA. After the complete dissolution which took several hours, the solution was made up to the 2 L mark with addition of more millipore water. Other working standards (10 -100 ppm) were prepared via the serial dilution method and the standard working curve based on mean HPLC peak areas was constructed for a concentration range of 10-100 ppm. The 10 ppm solution used for the degradation studies was obtained from 100 ppm via serial dilution using the relationship $C_IV_I=C_2V_2$, where C_I= 100 ppm, V_I = ?, C_2= 10 ppm, V2= 1500 mL. Thereafter 150 mL of 100 ppm was measured into 2 L volumetric flask and filled up to 1500 mL to give 10 ppm simulated solution of BPA.

1000 ppm 2-nitrophenol

2 g of 2-nitrophenol (2-NP) was accurately weighed into a 2 L volumetric flask containing millipore water and the mixture was shaken thoroughly to dissolve the 2-NP. After complete dissolution, the solution was made up to the 2 L mark with addition of more millipore water. Other working standards (10 – 100 ppm) were prepared via the serial dilution method. The 10 ppm solution used for the degradation studies was obtained from 100 ppm via serial dilution using the relationship $C_IV_I=C_2V_2$, where C_I= 100 ppm, V_I = ?, C_2= 10 ppm, V2= 1500 mL. Thereafter 150 mL of 100 ppm was measured into 2 L volumetric flask and filled up to 1500 mL to give 10 ppm simulated solution of 2-nitrophenol.

The structure of BPA, 2-NP and MB are shown in Figure 3.1.

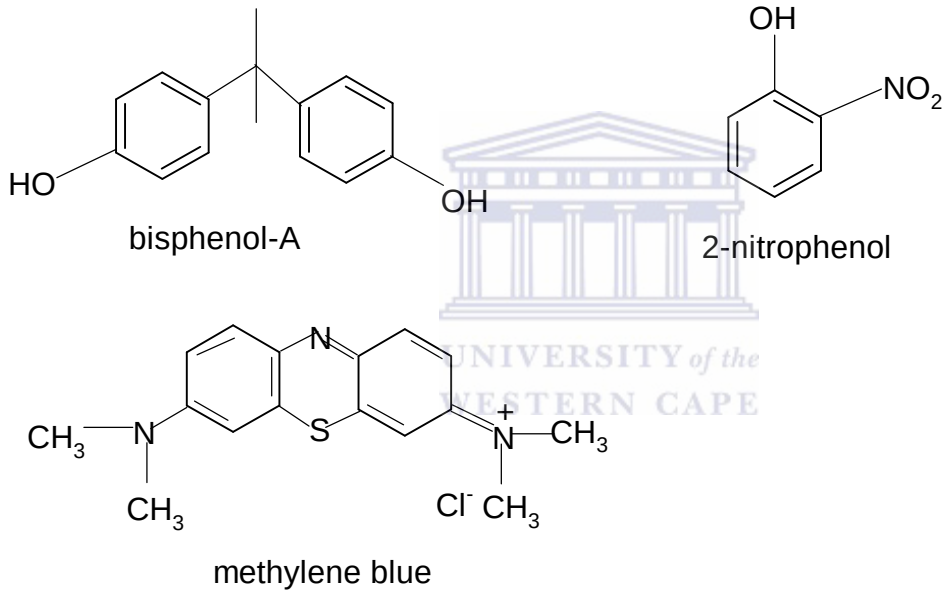

Figure 3.1: Chemical structure of bisphenol-A, 2-nitrophenol and methylene blue.

Indigo Solution-A

0.5 mL of phosphoric acid was mixed with 0.31 g of indigo trisulfanate in a volumetric flask and filled up to 500 mL with millipore water.

Indigo Solution-B

14 g of sodium dihydrogen phosphate was mixed with 17.5 g of H_3PO_4 (>85%) in a volumetric flask and filled up to 500 mL with millipore water.

1000 ppm 2-hydroxylterephthalic acid

A stock solution of 2-hydroxylterephthalic acid (HTA) was then prepared by dissolving 1 g of HTA, in a 1000 mL volumetric flask. The solution was made up to the mark with distilled-deionised water and other working concentrations (0.2 to 4 ppm) were prepared by serial dilution. The concentration range between 0.2 – 4 ppm was used to prepare the calibration curve.

0.2 mM disodium terephthalic acid

0.3323 g of disodium terephthalic acid (NaTA) and 0. 2 g NaOH were separately weighed and both dissolved in 1000 mL millipore water and was made up to the mark.

Phosphate buffer

A phosphate buffer (pH 7.4) was prepared by separately weighing and dissolving 0.588 g (KH_2PO_4) and 0.972 g (Na_2HPO_4) each in a separate 250 mL volumetric flask. The two prepared solutions were later mixed until pH 7.4 was achieved.

0.5 M NaOH

19.8 g of NaOH was accurately weighed and placed into a 1 L volumetric flask containing millipore water and the mixture was shaken thoroughly to dissolve the NaOH. After complete dissolution, the solution was made up to the 1 L mark with addition of more millipore water.

0.5 M H_2SO_4

27.8 mL of concentrated H_2SO_4 was accurately measured into a 1 L volumetric flask containing millipore water. The mixture was properly shaken and more millipore water was added to the diluted H_2SO_4 and made up to the 1000 mL mark.

1 M Na_2CO_3

104.9 g of Na_2CO_3 was accurately weighed and added into a 1 L volumetric flask containing millipore water and the mixture was shaken thoroughly to dissolve the Na_2CO_3. After complete dissolution, the solution was made up to the 1 L mark with addition of more millipore water. Other working standards (0.01 M-0.08 M) were prepared via the serial dilution method.

1M NaCl

57.85 g of NaCl was accurately weighed and added into a 1 L volumetric flask containing millipore water and the mixture was shaken thoroughly to dissolve the NaCl. After complete dissolution, the solution was made up to the 1 L mark with addition of more millipore water. Other working standards (0.01 M-0.08 M) were prepared via the serial dilution method.

1 M Na_2SO_4

139.18 g of Na_2SO_4 was accurately weighed into a 1 L volumetric flask containing millipore water and the mixture was shaken thoroughly to dissolve the Na_2SO_4. After complete dissolution, the solution was made up to the 1 L mark with addition of more millipore water. Other working standards (0.01 M-0.08 M) were prepared via the serial dilution method.

3.2 Experimental

The next section provides information on the experimental methodology used in addressing the identified research problems

3.2.1 *Experimental plan*

The experimental is divided into three sections. Section 1 describes the synthesis and characterization of the supported TiO_2 nanocrystals, Ag doped TiO_2 nanocomposites and stabilized nano zero valent iron particles. This section also contains methodology used for testing the photocatalytic activity of the supported TiO_2 nanocrystals and Ag doped TiO_2 nanocomposite using methylene blue as a modelled pollutant. Section 2 describes the methodology used for the degradation of bisphenol-A and 2-nitrophenol using supported photocatalysts and dielectric barrier discharge system, and also nano zero valent iron and dielectric barrier discharge system. Section 3 describes the methodology used for application of a jet loop reactor and other advanced oxidation treatment strategies to decompose the selected modelled pollutants. The flow charts showing the research approach, experimental and analytical techniques employed at different sections of the study are presented in Figures 3.2 and 3.3.

Section 1: Synthesis and characterization of catalysts

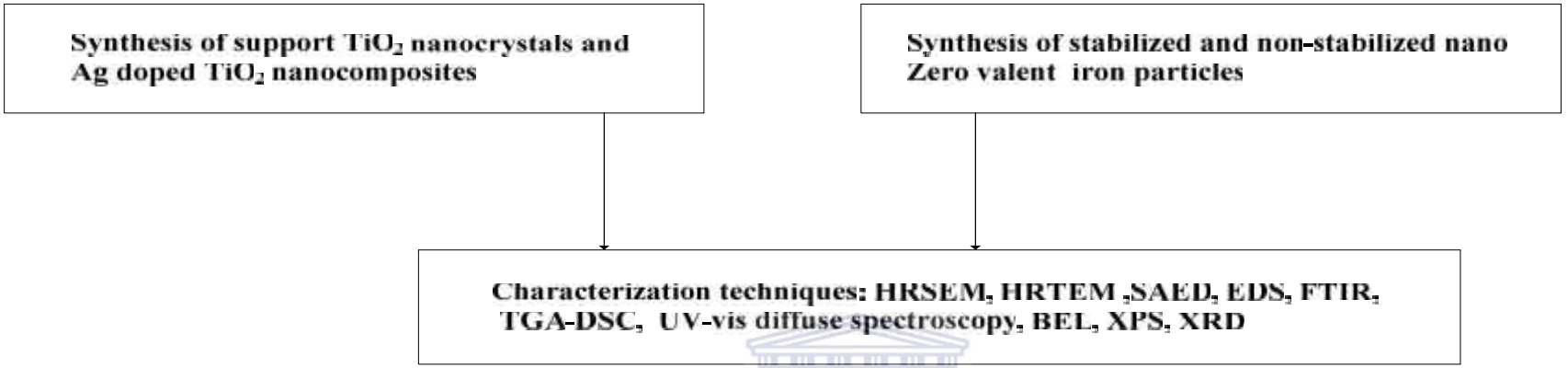

Section 2: Photocatalytic activity and application of catalyst with DBD

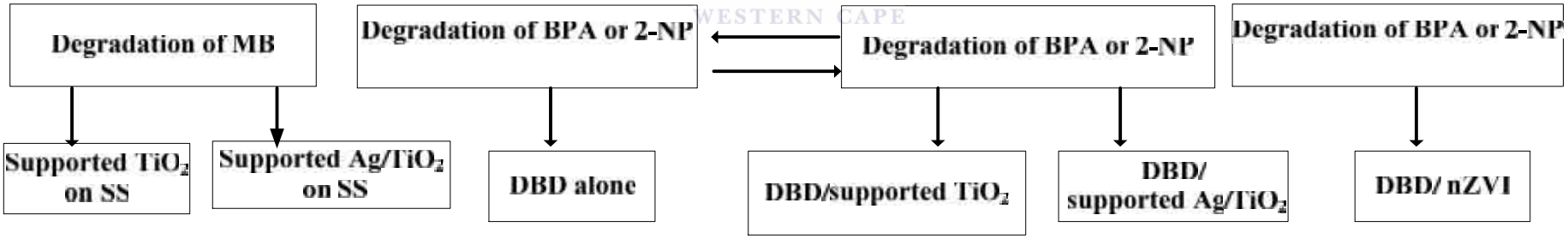

Figure 3.2: Flow chart of research plan based on synthesis, characterization; (section 1) and application with DBD (section 2) SS=stainless steel

Section 3

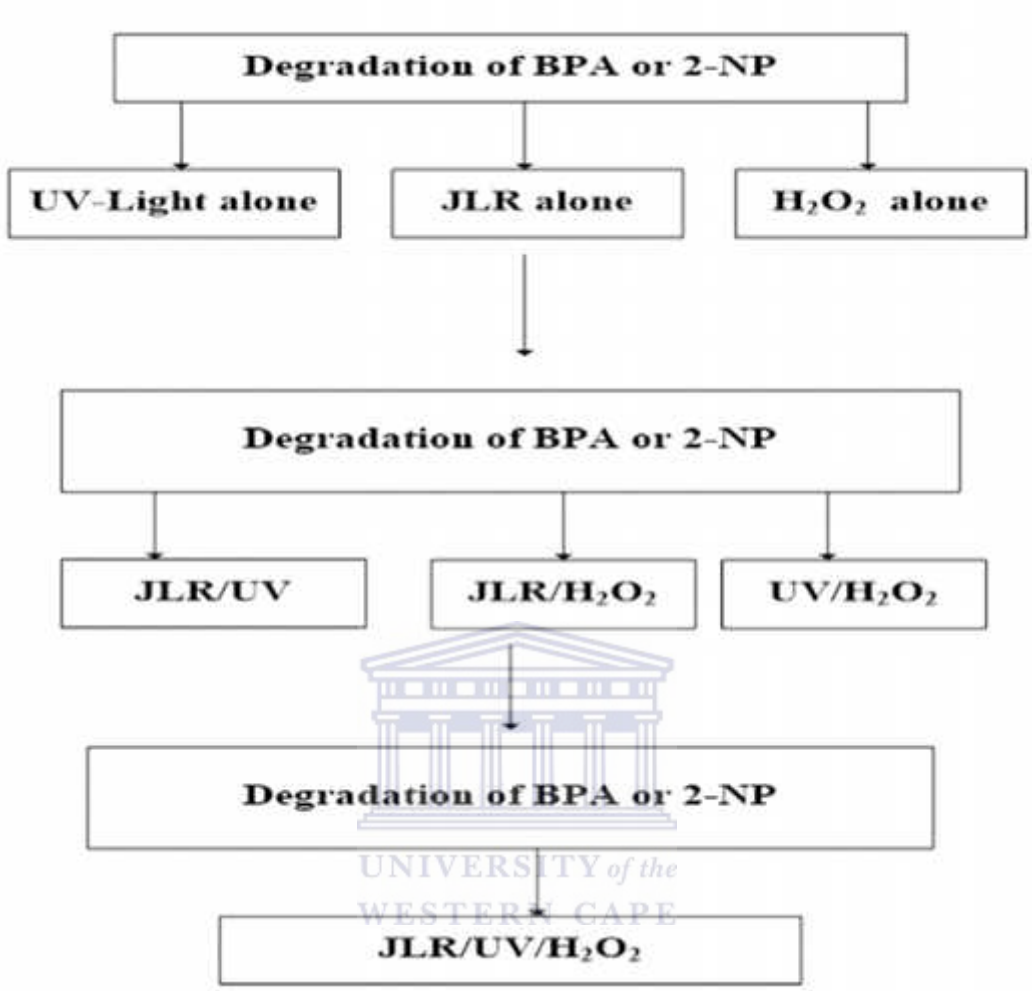

Figure 3.3: Flow chart of research plan based on application of combined advanced oxidation technologies to decompose BPA and 2-NP in aqueous solution.

3.2.2 *Synthesis of supported TiO_2 nanocrystals*

This section provides information on the methodology used to prepare the TiO_2 photocatalyst supported on a stainless steel mesh.

i. Preparation of PAN/DMF/$TiCl_4$ sol gel solution

Supported TiO_2 nanocrystals were synthesised via the modified sol-gel technique (Totito, 2014). To prepare the supported TiO_2 nanocrystals, 8 g of powdered polyacrylonitrile (PAN) was weighed and added to 92 g of dimethylformamide (DMF) making up 100 g of PAN and DMF. The mixture in a bottle open to air was then stirred on a magnetic stirrer at room temperature (25 ºC) for 12 hr. At the end of 12 hr stirring, a slightly transparent 8 % PAN/DMF viscous solution was obtained. From the solution, 50 mL of the mixture was placed in a separate bottle followed by slow drop wise addition of 6 mL of 0.09 M $TiCl_4$ at 25 ºC using magnetic stirrer with continuous stirring at 150 rpm. This step was conducted in a ventilated fume hood. During the addition of 6 mL of 0.09 M $TiCl_4$, the transparent solution rapidly became brownish yellow colour (Figure 3.4). The addition of 6 mL of 0.09 M $TiCl_4$ was accompanied by the release of a white fume of hydrochloric acid, and the stirring was continued for 15 min until the white fume disappeared. Prior to the addition of $TiCl_4$, the temperature of the sol was 20 ºC and after the addition of the titanium precursor, the temperature rose to 41 ºC. This implies that the reaction was purely exothermic. The formed gel solution was continually stirred until the white fume disappeared.

Figure 3.4: Solution A = 8 % PAN/DMF and Solution B = 8 % PAN/DMF/$TiCl_4$ sol gel

ii. Coating of stainless steel mesh with the 8 % PAN/DMF/$TiCl_4$ sol gel solution

Prior to manual coating, a 4 by 4 cm stainless steel mesh was washed with acetone, ethanol and water, and then dried in an oven at 90 °C. The reason for cleaning the mesh with acetone was to remove organic and inorganic contaminants. The cleaned stainless steel mesh was weighed and coated manually with the prepared sol gel formulation. A 3 mL plastic pipette was used to draw up 2.5 mL sol gel solution and uniformly disperse it until the sol-gel completely covered the stainless steel mesh. The coated mesh was air dried at room temperature in a fume cupboard for 10-15 minutes followed by pyrolysis in N_2 atmosphere at 300 °C, 350 °C or 400 °C in a Labfurn tube furnace shown diagrammatically in Figure 3.5. A heating rate of 50 ºC/min and holding time of 1 to 4 h was adopted. This step by step synthesis of nanocrystalline TiO_2 is illustrated in Figure 3.6. The procedure also included a flow of nitrogen gas through the inner tube at 20 mL/min in order to create an inert environment and to prevent side reactions such as hydrolysis.

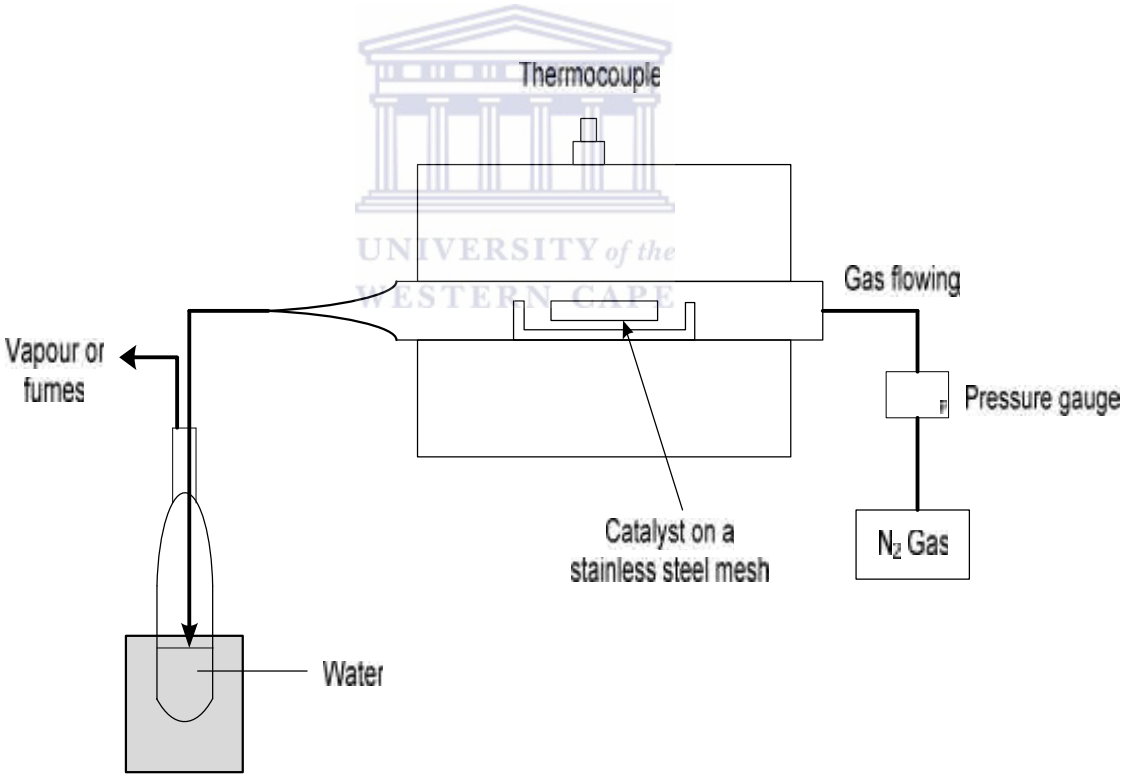

Figure 3.5: The schematic diagram of the tube furnace used for calcination

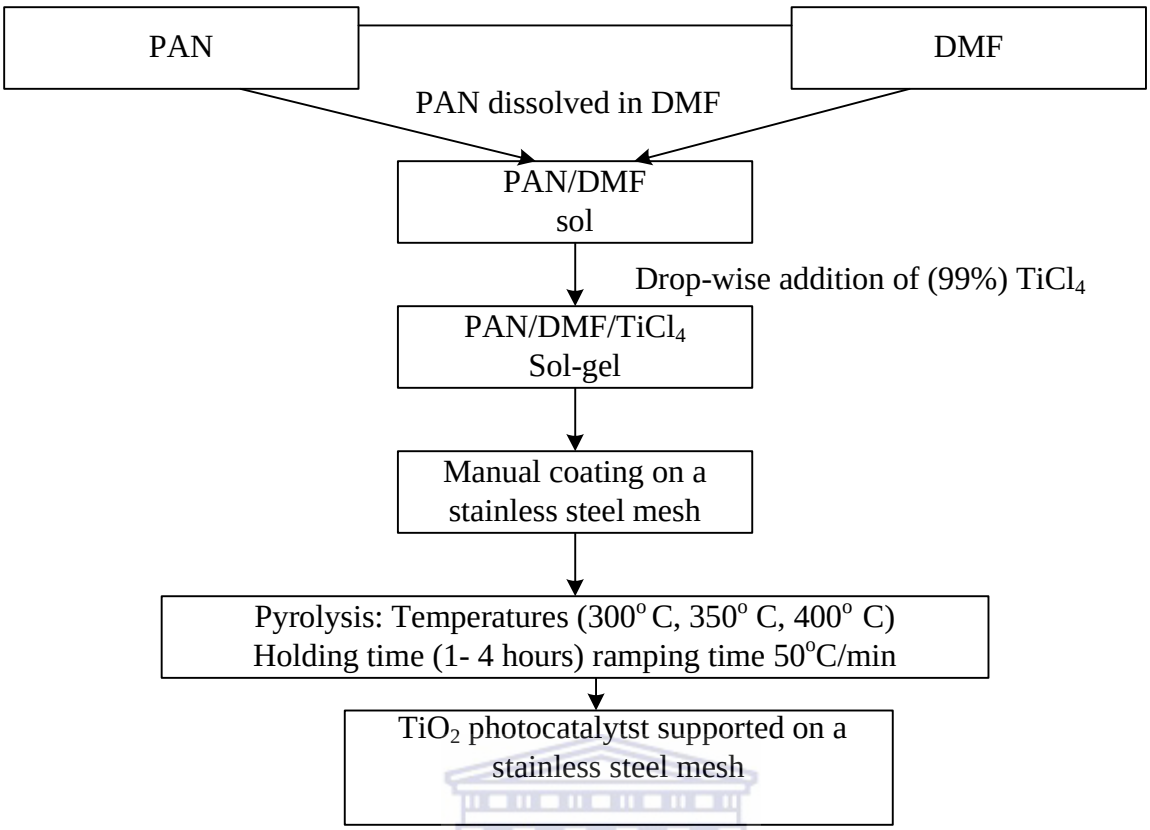

Figure 3.6: Flow chart representing the sol-gel method used for synthesising supported TiO_2 nanocrystals.

3.2.3 *Synthesis of Ag doped TiO_2 nanocomposites*

In this study, the post deposition of Ag onto supported TiO_2 nanocrystals was achieved via thermal evaporator method. Thermal evaporation technique is a form of physical vapour deposition involving deposition of a thin film of pure material usually metal, onto the surface of another substrate material. The film thickness is usually in the range of angstroms to microns. This technique is based on heating a metallic substrate using filament evaporation in a high vacuum chamber to produce metal vapour. This metal vapour stream traverses the chamber and eventually deposits on the substrate as a coating or film (Figure 3.7). The three steps involved in the thermal evaporation of plasmonic metal onto the TiO_2 surface are described below.

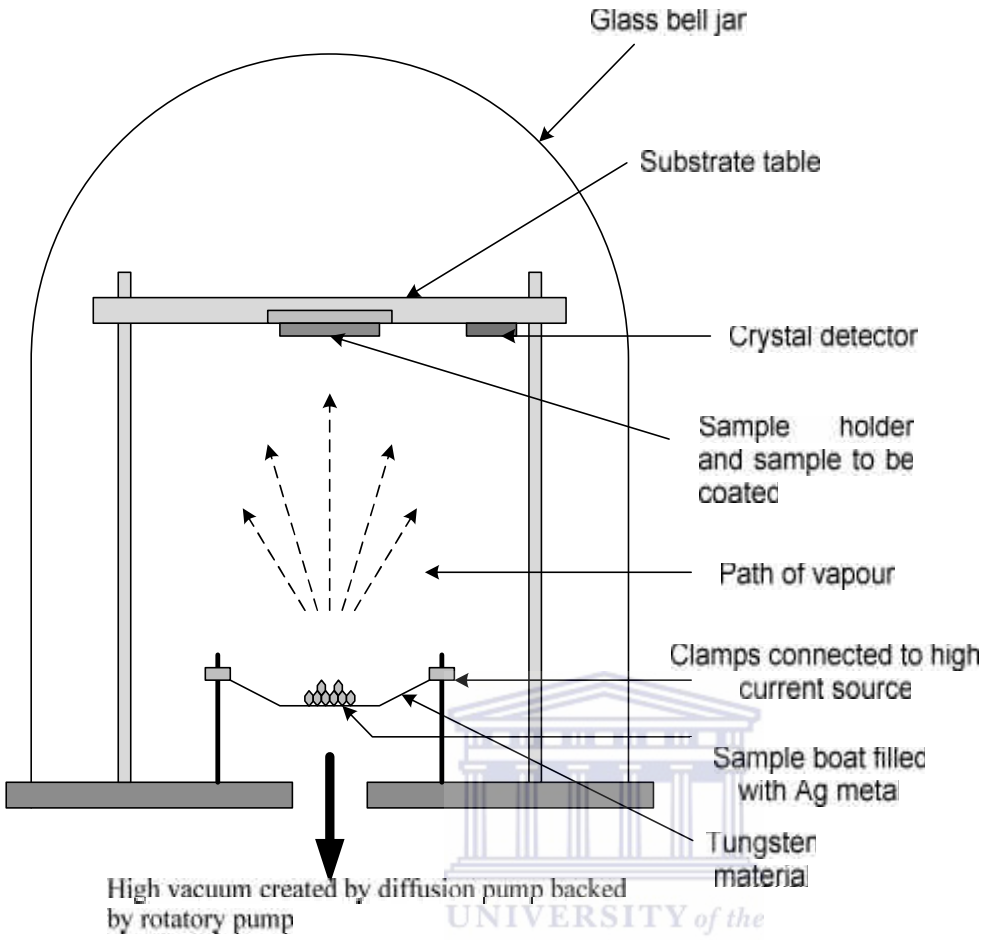

Figure 3.7: Schematic diagram of thermal evaporator used for depositing silver

The vacuum chamber was vented by opening the vent valve for approximately ten minutes after which the dome became loose. The dome was removed carefully. After this, the vent valve was closed and the samples (TiO_2 calcined at 350 ºC for 3 h) were loaded upside down into the sample holder while the source boat containing the plasmonic element (silver) was placed on the thermal source and covered with a shutter or swing-arm shield. The dome was then replaced and the mechanical vacuum pump switched on for about 10 minutes (Figure 3.7). A Pirani Cold Cathode Gauge was turned on to monitor the pressure. The pressure was allowed to build-up for approximately 30 minutes until the desired value of 2.5×10^{-5} mbar was reached. Prior to the deposition of silver, the Qpod laptop software was set up so that the sensor crystal frequency reading was displayed properly to the thermal plate holder connected to the high current source. Subsequently, the current of 100 A was slowly applied until the Ag begun to glow and evaporate. To achieve uniform deposition an evaporation rate of 0.5 Å/s was applied. The Qpod programme was executed and the shutter turned anticlockwise.

The desired amount of Ag was deposited using different deposition times (30, 45 and 60 sec) onto the TiO_2 surface by constant heating current of 44 A. Once the desired thickness was achieved, the shutter was closed, the Qpod programme was halted and gradually the current was reduced to zero. Thereafter, the vacuum pump and the cathode gauge was switched off, the water valve for sensor cooling was closed followed by a pause until the vacuum turbo pump stopped (Figure 3.7).

To remove the samples, the vent valve was switched on for 10 minutes to release the pressure for easy removal of the dome. The dome was removed and the loaded samples removed without touching the film surface. The various synthesised supported TiO_2 nanocrystals and Ag doped TiO_2 nanocomposites with their unique codes are represented in Table 3.2.

Table 3.2: Supported TiO_2 and Ag doped TiO_2 photocatalyst with code and conditions

Sample code	Temperature (ºC) at constant heating rate (50º C/min)	Holding time	Ag nanoparticles (w%)	Results (HRSEM and HRTEM images)
JT1	300	1		Figure 4.1 and 4.4
JT2		2		Figure 4.1 and 4.4
JT3		3		Figure 4.1 and 4.4
JT4		4		Figure 4.1 and 4.4
JT5	350	1		Figure 4.2 and 4.5
JT6		2		Figure 4.2 and 4.5
JT7		3		Figure 4.2 and 4.5
JT8		4		Figure 4.2 and 4.5
JT9	400	1		Figure 4.3 and 4.6
JT10		2		Figure 4.3 and 4.6
JT11		3		Figure 4.3 and 4.6
JT12		4		Figure 4.3 and 4.6
JT13	350	3	30 sec (1.8)	Figure 4.20
JT14	350	3	45 sec (2.4)	Figure 4.20
JT15	350	3	60 sec (3.5)	Figure 4.20

3.2.4 *Synthesis of nano zero valent iron*

In this section, iron nanoparticles were synthesized via a simple chemical reduction of iron chloride hydrate with sodium borohydride as a reducing agent. Two procedure were used as described below.

i. Synthesis of nano zero valent without stabilising agent

To prepare non-stabilized nano zero valent iron, two solutions (A and B) of equal volume were mixed together with vigorous stirring in a flask for 30 minutes. For solution A, 1.35 g of $FeCl_3.6H_2O$ was dissolved in 40 mL deionised water for a concentration of 0.125 M while for solution B, 0.28 g of $NaBH_4$ was dissolved in 50 mL deionized water to give 0.15 M. Thereafter, 60 mL solution B was added drop-wise to 40 mL of solution A under vigorous stirring in a fume hood until the solution turned dark and later completely black. The reaction is shown in the equation below.

$$Fe^{3+} + 3BH_{4-} + 9H_2O \rightarrow 4Fe^0 + 3H_2BO_{3-} + 12H^+ + 6H_2 \quad (3.1)$$

After the reaction, the black iron nanoparticles were separated from the aqueous solution with a bar magnet and washed three times with 20 mL ethanol to prevent immediate oxidation. After washing the synthesized iron nanoparticles were freeze dried at -55º C for four days and subsequently characterized. The non-stabilized nano zero valent iron (nZVI) was labelled JT16

ii. Synthesis of nano zero valent with stabilising agent

In order to prevent agglomeration of the nanoparticles during synthesis, a dispersing agent such as poly ethylene glycol was added to the solutions. The same procedure described in step i above was used to synthesis stabilized nano iron in zero valent state with the addition of poly ethylene glycol as a stabilising agent. The synthesis involved mixing solutions C and D together in a conical flask for 30 minutes. For solution C, 0.75 g $FeCl_3.6H_2O$ was dissolved in 20 mL deionized water and then mixed with 20 mL of 3.5 wt % poly ethylene glycol solution. The colour change of the $FeCl_3.6H_2O$ solution from yellow to orange was observed. For solution D, 0.28 g $NaBH_4$ was dissolved in 50 mL deionized water and was added drop by drop to solution C under vigorous stirring. There was the appearance of a black precipitate accompanied with bubble formation (H_2 release). The reaction was completed and iron nanoparticles were separated using a bar magnet. The synthesised iron nanoparticles were washed with ethanol prior to freeze drying and then labelled PEG-nZVI (JT17). The various

synthesised catalysts such as supported TiO_2 nanocrystals, Ag doped TiO_2 nanocomposites including stabilized and non-stabilized nZVI were characterized using the following analytical techniques: XRD, HRSEM, HRTEM, XPS, FTIR, UV-Vis diffuse reflectance, TGA-DSC, and BET surface area analyzer. These characterization techniques are presented in section 3.4.

3.2.5 *Photocatalytic setup*

The photocatalytic activity of sample JT1-JT15 were evaluated using methylene blue (MB) (concentration of 10 ppm) as a modelled pollutant. The experiment was conducted in a self-designed 500 mL beaker photo reactor containing 50 mL of MB solution (10 ppm concentration), pH of 6.8 and 30 mg of the supported catalysts. The amount of TiO_2 deposited on the stainless steel mesh was evaluated by subtracting the mass of the stainless steel mesh prior to coating from the amount retained by the stainless steel mesh after the pyrolysis in the furnace. It should be noted that the amount of TiO_2 deposited on the various samples of stainless steel was not entirely uniform due to differences in applied catalyst temperature and holding time. 30 mg of the supported photocatalyst and 50 mL of MB aqueous solution were placed in a beaker with continuous magnetic stirring at ambient temperature. The MB solution was irradiated with a 9 W UV-A low pressure lamp of wavelength of 315-400 nm. The light intensity of UV-A with wavelength 315-400 nm was 0.5 mW cm^{-2}. The UV lamp clamped on a retort stand was positioned at the centre of the beaker at a distance of 1 cm between the UV lamp and surface of MB. The supported catalyst was immersed in such a way that the incident UV light fell onto the surface of the catalyst. The photocatalytic experiment was conducted in a dark room to avoid interference with normal visible light.

3.2.5.1 Photolysis and adsorption blank control experiment

Prior to photocatalytic activity, control experiments involving the stainless steel support alone, was compared to stainless steel coated samples with an average value of 30 mg TiO_2 catalyst, and 50 mL of MB (10 ppm) were separately conducted in the dark with continuous stirring for 6 h using magnetic stirring at 150 rpm. A 2 mL solution was sampled periodically at every 1 h and immediately analysed using a UV-Visible spectrophotometer. This was done to establish whether that degradation or removal of methylene blue by the supported catalyst could occur via adsorption. Further control experiments were conducted by exposing the

methylene blue to UV-light without catalysts. These experiments were done to establish that % removal or mineralization of the MB at ambient temperature under UV light was only due to the agency of photocatalysis and not due to adsorption by the supported photocatalysts.

3.2.5.2 Photocatalytic activity of supported TiO_2 nanocrystals (JT1-JT12)

The supported catalyst immersed in MB solution was continuously stirred in the dark for 30 min to establish adsorption/desorption equilibrium. The concentration of the dye determined after adsorption saturation using UV-vis spectrophotometry and was taken as the initial concentration of the MB. Thereafter, the photo-reactor was closed; the UV lamp switched on for 6 hours to provide constant light intensity during the experiment and photocatalytic decolouration of MB was continuously monitored. At specific time intervals, 2 mL sample aliquots were withdrawn from the photoreactor. The absorption intensity of the solution was then measured using a Nicolette-Evolution 100 Ultraviolet spectrophotometer (Thermal Electron Corporation, UK) at 664 nm. The actual concentration of the MB was estimated from the calibration curve. Each experiment was repeated twice and an average experimental value was determined.

3.2.5.3 Photocatalytic activity of JT13-JT15

The photomineralization of the MB solution was further performed with the optimum supported TiO_2 nanocrystals (JT7) and various Ag doped TiO_2 nanocomposites (JT11-JT15). The solution pH was not adjusted. This experiment was also conducted in a self-designed 500 mL beaker photo reactor containing 50 mL each of MB solution (10 ppm concentration) and 30 mg catalysts as described in section 3.2.5.2. The mixture containing the supported catalysts was continuously stirred on a magnetic stirrer at 150 rpm for 5 h. At specific time intervals, 2 mL samples were withdrawn from the photoreactor and the absorption intensity of the solution was then measured using ultraviolet spectrometer at 664 nm.

3.2.6 *Data analysis*

The residual concentration of the MB solution after the photocatalytic degradation experiment was calculated from the absorption intensity of the MB solution measured at 664 nm by Nicolette-Evolution 100 Ultraviolet spectrophotometer in line with the calibration curve. The different concentrations and the calibration curve are shown in Table 3.3 and Figure 3.8 respectively.

Table 3.3: Different concentration of methylene blue used for the calibration curve

Concentration (ppm)	Absorbance
2	0.517
10	2.060
15	2.913
20	3.712
40	6.991

The residual concentration of each sample after the photocatalytic experiment was estimated from the calibration curve via extrapolation. Alternatively, the absorbance value was divided by the obtained slope from the calibration curve.

$$Residual\ concentration\ (in\ ppm) = \frac{Absorbance}{Slope\ of\ the\ calibration\ curve} \quad (3.2)$$

The percentage removal of MB by the photocatalyst was calculated using the equation (3.3)

$$\%\ removal\ efficiency\ of\ MB = \frac{Co - Ct}{Co} \quad (3.3)$$

Where Co and Ct represent the initial and the final concentration of MB solution respectively.

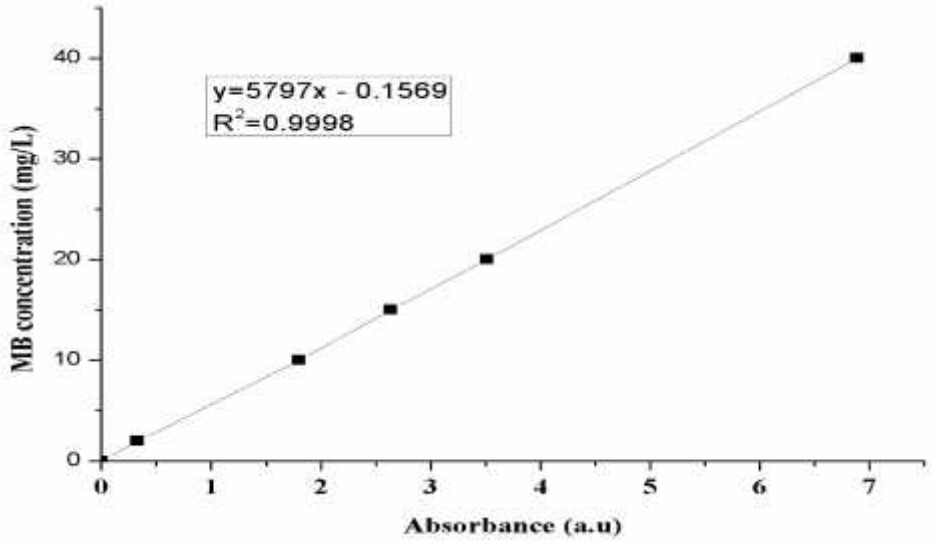

Figure 3.8: Calibration curve of the standard methylene blue solution

3.2.7 *Dielectric barrier discharge experimental section*

This section presents the degradation procedure of BPA and 2-NP by the dielectric barrier discharge (DBD) system. This also included integration of various synthesised catalysts with dielectric barrier discharge system to degrade BPA and 2-NP. In this section, the optimized DBD reactor was used as reported by Mouele, (2014).

3.2.7.1 Experimental set-up

Figure 3.9 represents the schematic diagram of DBD system used for the degradation of the recalcitrant organic contaminants. The device comprised a DBD reactor that generated powerful oxidants such as hydroxyl radicals, hydrogen peroxide, ozone and ultraviolet light, using an AC high voltage power supply, step down transformer, air flow meter, air pump, ground electrode and a reactor vessel containing the model wastewater.

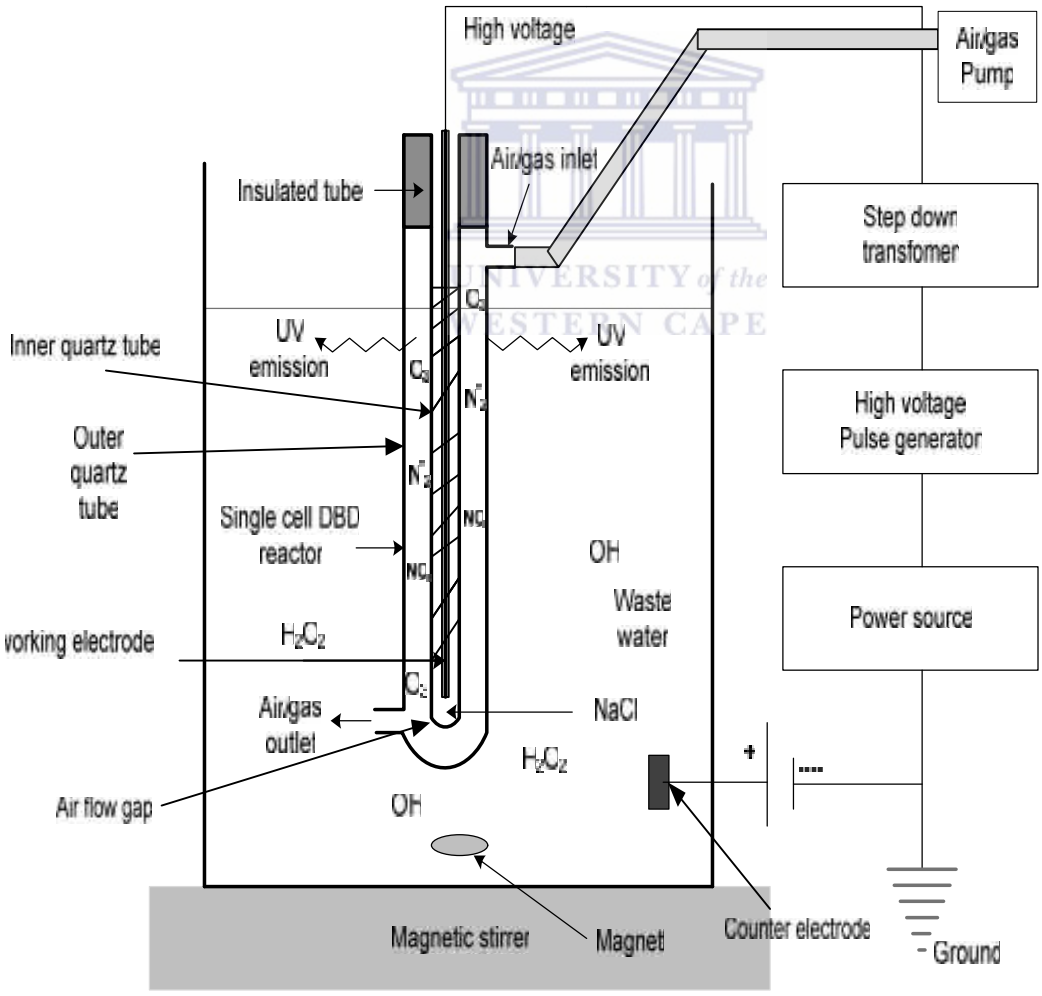

Figure 3.9: The schematic diagram of the dielectric discharge barrier system (Source: Moule, 2014)

The DBD reactor was a double quartz tube with a quartz inner tube and outer tube diameter of 1 mm and 7 mm respectively. The AC high voltage power supply was set at 25 V, delivering a current of 5 A and a power of 125 W, and was connected in series to a transformer and rectifier that steps the AC voltage up to a DC output voltage of ~8 kV. This potential was applied between the counter electrode in the DBD reactor and the working silver electrode held in the systems' inner quartz tube shown in Figure 3.9. The 0.5 mm silver electrode directly connected to the high voltage (output of the transformer) was immersed in a 50 g/L of sodium chloride electrolyte placed in the inner quartz tube of the single cell DBD reactor and was also earthed. Air was provided by an air pump with a high and low flow speed switch which was connected to both air flow meter and the single outer quartz cell reactor tube. An air-flow rate of 3.0 L/min was used through air flow gap. The DBD reactor was 23 cm long with an inlet and outlet for air circulation. All through the discharge, the powerful oxidants and UV/visible light produced, acted simultaneously to decompose the target compounds. The ozone generated by the DBD reactor was continuously and uniformly dispersed within the solution compartment by magnetic stirring of the BPA or 2-NP being treated.

3.2.7.2 DBD experimental method

The 10 ppm (4.4×10^{-5} M) solution of the prepared BPA or 2-NP as described in section 3.1.1 was used. 1.5 L of the simulated wastewater was measured and placed in a 2 L beaker. The original depth of the simulated organic wastewater in the reactor vessel was about 130 mm and later rose to about 135 mm due to the flow of air through the DBD which produced bubbles in the solution compartment. The electrical conductivity of the aqueous solution of BPA and 2-NP were measured to be 20.1 and 51.3 μS/cm with the aid of multi-parameter analyser C3010. The DBD experiment was conducted for 120 minutes at room temperature (20 ºC) and sampling was done at time intervals of ten minutes. The efficiency of the DBD process was determined by measuring the residual concentration of BPA or 2-NP as a function of treatment time using a high performance liquid chromatograph (HPLC) equipped with a Waters 2487 dual λ absorbance detector. The detailed HPLC methodology is provided in section 3.4.12.

3.2.7.3 Calibration curve of BPA and 2-NP

Standard solutions of BPA and 2-NP were prepared by diluting a 1000 ppm stock solution and a standard working curve based on mean HPLC peak areas was constructed for a concentration range of 10 – 80 ppm. The temperature was maintained at 26 °C throughout the analysis. Evaluation and quantification were made using a chromatography data system. The retention time for 2-NP and BPA was 8.2 and 13.3 minutes respectively. A calibration curve of standard solution against the peak area was plotted. The HPLC chromatograph of BPA and 2-NP at a retention time of 8.2 and 13.3 min is shown in Figure 3.10 and 3.11. The calibration curve of both 2-NP and BPA are shown in Figure 3.12 and 3.13 respectively.

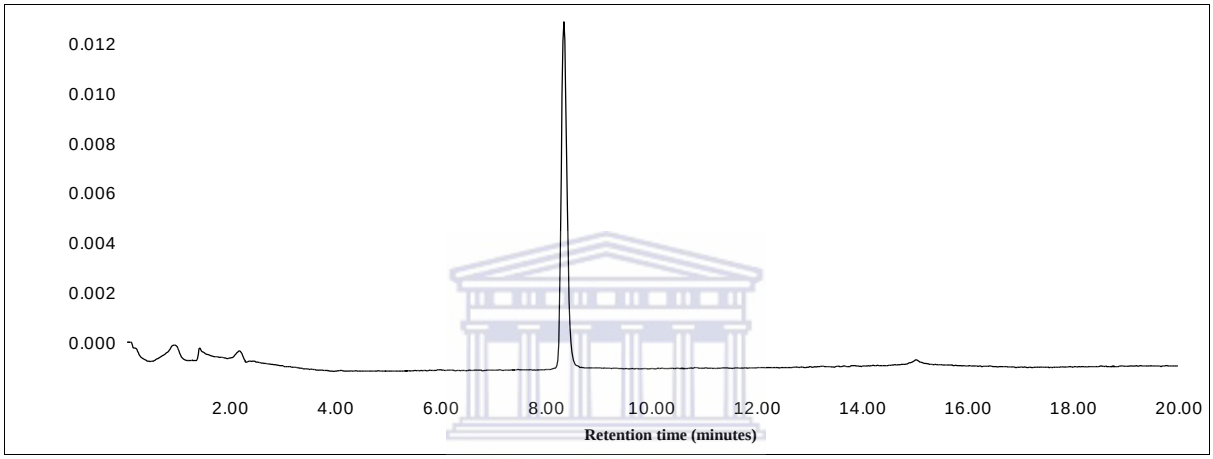

Figure 3.10: HPLC chromatogram of 2-nitrophenol standard solution

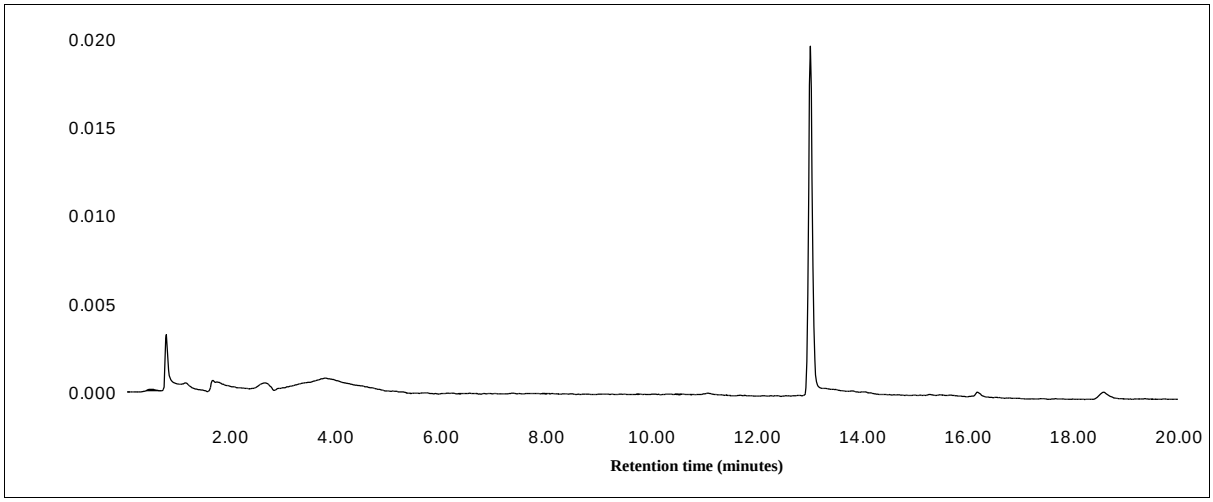

Figure 3.11: HPLC chromatogram of bisphenol-A standard solution

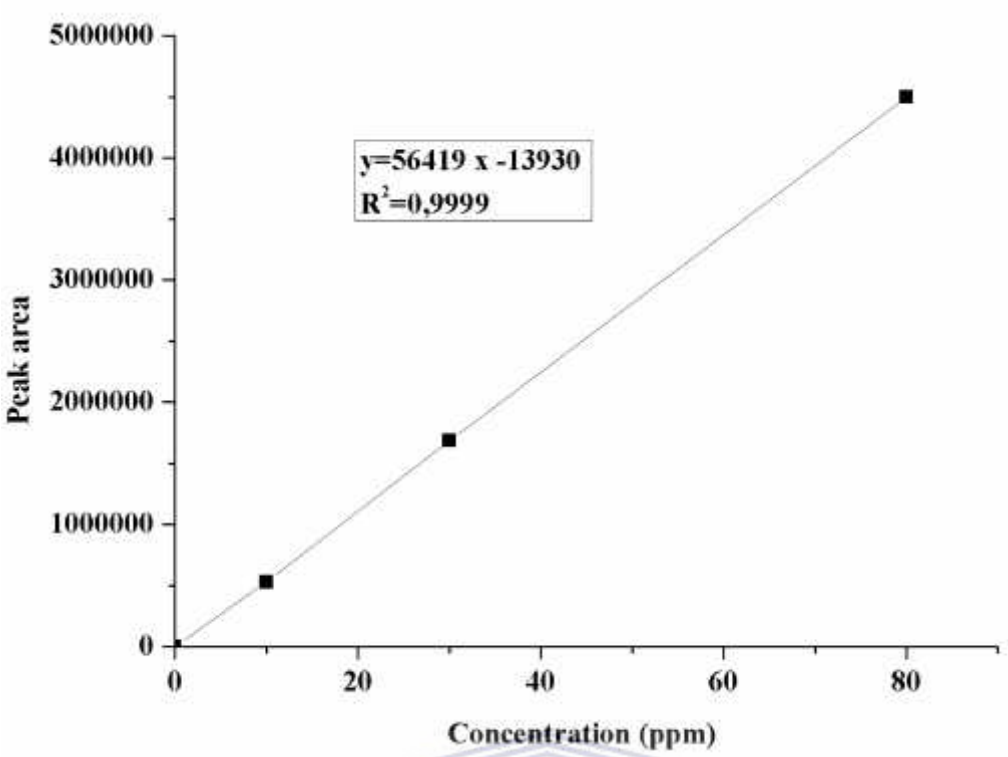

Figure 3.12: Standard calibration curve of 2-nitrophenol (HPLC)

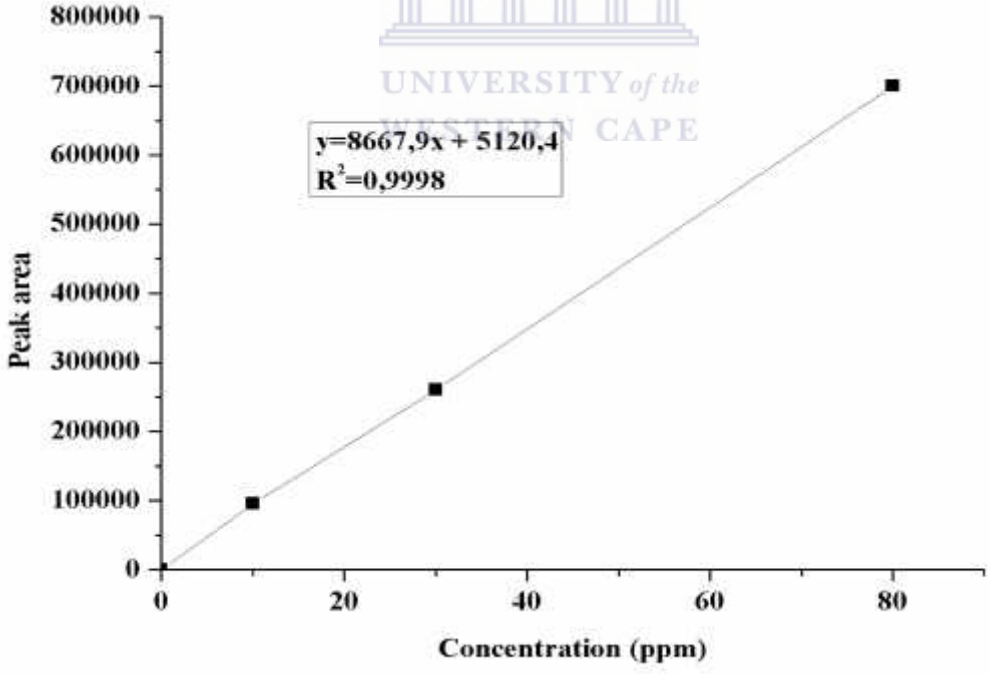

Figure 3.13: Standard calibration curve of bisphenol-A (HPLC)

3.2.8 *Investigating the influence of different experimental parameters on the oxidation rate of BPA or 2-NP via DBD system*

This section provides information on the experimental parameters studied using the DBD reactor only.

3.2.8.1 Effect of initial solution pH

In order to establish the optimum pH at which maximum degradation of the modelled pollutants occur, solution pH was investigated as a parameter. The initial solution pH was varied from 3 to 12 for 120 min by adding 0.5 M H_2SO_4 or 0.5 M NaOH dropwise until the desired pH was achieved. The solution pH was measured with a multi-parameter analyser C3010 and prior to that, the pH meter was calibrated based on the manufacturer's instructions. 1.5 L of 10 ppm BPA or 2-NP placed in 2 L beaker were treated with DBD system as explained in section 3.2.7. A 2 mL sample aliquot of the treated water was taken at each ten minutes interval and put in 2 mL glass vials, and then analyzed by HPLC equipped with a Waters 1525 binary HPLC pump and Waters 2487 dual λ absorbance detector.

3.2.8.2 Effect of initial concentration of the BPA and 2-NP

In order to determine the optimum concentration at which maximum removal of the modelled pollutants occurred using the DBD reactor on its own, the initial concentrations of BPA or 2-NP solution were varied in the range of 10 – 30 ppm maintained at optimum solution pH of 3. 1.5 L of the simulated organic wastewater was subjected to DBD treatment for 120 minutes and sampling was done at intervals of ten minutes during the reaction and 2.0 mL aliquots of the treated solution were withdrawn with a plastic syringe and analyzed by HPLC equipped with a Waters 1525 binary HPLC pump, and Waters 2487 dual λ absorbance detector set at 280 and 278 nm respectively.

3.2.8.3 Effect of radical scavengers

The presence of radical scavengers in solution affect the efficiency of advanced oxidation technologies due to inhibition and consumptions of free radicals. Among radical scavengers or inhibitors are inorganic species such as Na_2CO_3, Na_2SO_4, $NaHCO_3$, $Na_2B_2O_7$, $NaNO_3$, C_3H_9OH, t-C_4H_9OH, Na_3PO_4, and NaCl. In this study, the influence of separate addition of Na_2CO_3, Na_2SO_4 and NaCl on the removal rate of BPA or 2-NP in water by DBD system was examined. 60 mg/L each of (Na_2CO_3, Na_2SO_4, NaCl) solution were separately mixed with 1.5

L of BPA or 2-NP solution of known concentration (10 mg/L) at pH 3 in a 2 L beaker. The mixture was subjected to DBD treatment for 120 minutes and sampling was performed every 10 minutes. The residual concentration of BPA or 2-NP in the aliquot of samples withdrawn from the reactor were determined by HPLC equipped with a Waters 1525 binary HPLC pump, Waters 2487 dual λ absorbance detector AT set at 280 nm for both compounds respectively. A Waters Spherisorb C_{18} reversed-phase Liquid chromatography column dimension 150 by 4.6 mm, 5 µ was used for the analysis of BPA and 2-NP concentrations in the treated samples. The mobile phase was water: acetonitrile 85:15, (v/v) solution and the same components with 0:100 (v/v) for both compounds with a flow rate of 1 mL/min.

3.2.9 *Treatment of BPA and 2-NP by combination of DBD reactor and the supported photocatalysts*

The schematic diagram of the combined DBD/supported TiO_2 device used for the decomposition of BPA and 2-NP is shown in Figure 3.14

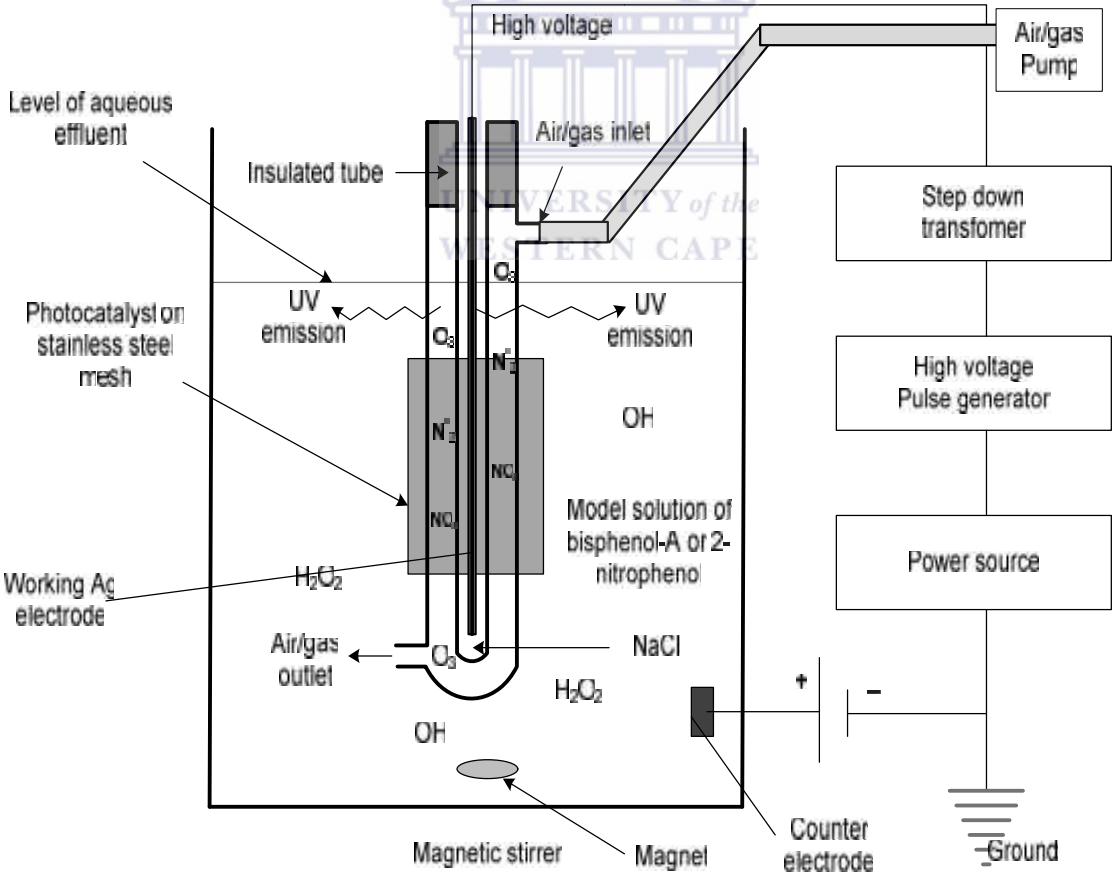

Figure 3.14: The schematic representation of the experimental device with supported photocatalyst

The AC high voltage power supply discharge system connected in series to the DBD reactor provided a constant potential of 8 kV across the working and counter electrodes in the DBD reactor vessel containing the simulated organic wastewater. Prior to testing the combined system, the BPA or 2-NP solution had earlier been treated with the DBD reactor alone for 120 min to determine the DBD degradation capability on its own (Section 3.2.7). The DBD reactor in Figure 3.14 is the same as shown in Figure 3.9 except that the DBD reactor was positioned at the centre of tubular arrangement of the sample JT7 and JT14. The whole unit was immersed in a 2 L beaker in order to utilize the ultra-violet light produced by the DBD reactor for photocatalysis. The dimension of the tubular supported catalyst was 19.5 cm by 2 cm which was equivalent to the length of the quartz tube. The rectangular pieces of mesh containing catalysts were joined together with a thread at the edge to form the tubular arrangement. The inner quartz tube was filled with 50 g/L NaCl solution and the electrode (silver) was then connected to AC high voltage. The aqueous NaCl solution in the inner tube acted as discharging electrolyte. In the course of this experiment, the passage of high voltage electrical discharge between the inner tube containing the silver electrode and the dielectric barrier produced powerful oxidants in the air gap as well as UV/visible light which were jointly responsible for the decomposition of the modelled pollutants (see Figure 3.14).

The gas flowing through the air gap could be air or oxygen, in this case air was used. The air flow rate was maintained at 3 L/min throughout the period. The counter electrode was equally immersed in the 2 L beaker containing 1.5 L of 10 ppm modelled pollutants. The initial concentration of the simulated organic compounds was 10 ppm and the pH of BPA or 2-NP solution was adjusted to 3 by adding a few drops of 0.5 M NaOH or 0.5 M H_2SO_4 respectively. Before the voltage was applied, the electrical conductivity of BPA and 2-NP solution was measured using a multi-parameter analyser C3010 and was found to be about 20.1 and 51.3 µS/cm respectively. The experimental set up was then switched on, air was fed into DBD reactor continuously and reactive species produced were uniformly dispersed within the solution compartment upon stirring. Sampling was done every ten minutes for 120 minutes. In order to prevent possible interference such as by indoor electrical light, the experiment was conducted in the dark, apart from the UV generated in situ. The residual concentration of 2 mL BPA or 2-NP sampled at 10 min intervals during the experiment was determined using an Agilent HPLC with a C_{18} column and ultraviolet detector operating at 278 nm or 280 nm. All experiments were replicated twice and the average residual concentration was noted.

The control experiment was conducted with ordinary supported TiO_2 nanocrystals without the DBD reactor in the dark using 10 ppm solution of BPA or 2-NP. 1.5 L of BPA or 2-NP aqueous solution were placed in a beaker with continuous magnetic stirring at ambient temperature. Sampling was done at 10 min interval and analysis using an Agilent HPLC with a C_{18} column and ultraviolet detector operating at 278 nm or 280 nm. For a comparison, 0.8 g powdery commercial titanium oxide (anatase, Degussa P-25) was uniformly dispersed into aqueous solution of BPA or 2-NP. The DBD reactor containing powder TiO_2 was run for 120 min. Sampling (2 mL) was done at 10 min interval and subsequently analysed using analytical technique described in section 3.4.12. Furthermore, the leaching or released of any metallic species such as Ti, Ag, Cr, Fe, Ni from both the catalyst and the support materials during the experiment were measured using ICP-OES. The detailed analytical measurement and conditions can be found in section 3.4.14.

3.2.9.1 Reusability and stability test

In order to investigate the reusability and stability potentials of the catalyst, the experimental procedure described in section 3.2.9 was repeated consecutively for four times using and sample JT14 combined DBD containing freshly prepared 10 ppm BPA or 2-NP solution. After each experiment, sample JT14 was cleaned with Millipore water and air-dried. The mineralogical integrity or stability of the catalysts after each experiment was examined using XRD. The surface morphology and adhesion of the catalysts upon the mesh before and after the experiment was checked using HRSEM. Detailed analytical characterization techniques and operating conditions are provided in section 3.4.1 and 3.4.2.

3.2.9.2 Treatment of BPA and 2-NP by combination of DBD reactor and the stabilized Nano zero valent iron (nZVI) particles

The set up used for the combined DBD/nZVI remained the same as for the DBD on its own except sample JT7 and JT14 were replaced with (0.02 - 0.1 g) poly ethylene glycol stabilized nano zero valent iron (PEG-nZVI) particles. As mentioned previously, the DBD system produces ozone, hydrogen peroxide, hydroxyl radicals, singlet oxygen and ultraviolet light. Thus, nano zero valent iron particles were added to induce the photo-Fenton process and enhance the generation of hydroxyl radicals which should in turn produce higher mineralization rate. The decomposition of BPA or 2-NP was conducted in a 2 L beaker filled with 1.5 L each of the 10 ppm modelled compounds. The experimental conditions remained the same as explained above except that the solution pH was adjusted to 3. This was because

the efficiency of photo-Fenton process has been reported to be higher at this pH value. The stirring speed of the magnetic stirrer remained 150 rpm. After 10 ppm of BPA or 2-NP solution was individually measured into the solution compartment, different amounts of PEG-nZVI (0.02, 0.04, 0.06, 0.08 and 0.1 g) were added corresponding to concentrations of 0.01, 0.03, 0.04, 0.05 and 0.07 g/L in the solution compartment. The degradation of BPA and 2-NP was achieved via continuous stirring and simultaneous introduction of dry air into the DBD for the production of ozone, hydroxyl radicals, hydrogen peroxide and UV-light. Sampling was done from the reactor vessel at time intervals of 10 min and the 2 mL aliquot was filtered with a 0.22 μm membrane filter and analysed using HPLC method shown in Table 3.10. The experiment was repeated twice and the average value was reported. The control experiment was carried out in the dark with ordinary PEG-nZVI using different dosage (0.02 – 1.00 g) at constant conditions of solution pH (3), volume of BPA or 2-NP (1.5 L) and concentration of BPA or 2-NP (10 ppm) while the DBD system was switched off.

3.2.9.3 Determination of Total Organic Carbon

The Total Organic Carbon content (TOC) is used an indicator parameter during wastewater treatment to provide information on the extent of conversion of organic pollutants in water to harmless inorganic species such as carbon dioxide and water. It is often used to assess the performance of wastewater treatment technique. In this study, the mineralization process of BPA or 2-NP was monitored in terms of the reduction in the amount of Total Organic Carbon (TOC) before and after the oxidation process using the adapted standard thermo-catalytic digestion followed by non-dispersive infra-red (NDIR) detection described by Fung et al., (1996). The detailed methodology is provided below.

Prior to analysis, 15 mL of treated water was pipetted into 25 mL volumetric flask and acidified with 3 mL of 0.2% (v/v) H_3PO_4. This was done to remove or purge the inorganic carbon (IC) such as CO_2 and CO_3^{2-}. The pH of the solution was reduced to 2 and was maintained under purging with purified O_2 for about 10 min at a rate of 100 mL/min^{-1}. The sample was then digested in an autoclave at a temperature of 116ºC for 2 h. Subsequently the digested sample was distilled over 10 g CuO catalyst at about 2-3 mL min^{-1} for 30 min in order to oxidize the volatile organic compounds. In the process of distillation, 0.03 g $K_2S_2O_8$ was also added to oxidize the nonvolatile organic compounds. Thereafter, the total non-purgeable chemically bonded organic carbon that is converted to CO_2 transported in the

purified oxygen streams was measured using nondispersive infrared analyser as the TOC value. The same procedure was repeated for a blank sample and 15 mL carbon-free water was used in place of the sample. The mineralization rate of BPA or 2-NP solution as a function of TOC was estimated using the relationship below

$$Mineralization\ rate = \frac{Initial\ TOC - Final\ TOC}{Initial\ TOC\ value} * 100 \quad \text{.....(3.4)}$$

3.2.9.4 Identification of transformation products

This experiment was conducted to identify the oxidation products of the target compound and to elucidate the degradation mechanism. The Agilent 6230 time of flight liquid chromatograph mass spectrometer (TOF LC-MS) in the negative ionization mode was used for qualitative identification of the intermediates formed during the decomposition of BPA or 2-NP by DBD reactor, DBD/JT14 and DBD/photo-Fenton induced process. Due to difficulty in the identification of the intermediate compounds at low concentration by LC-MS, 250 ppm each of BPA or 2-NP were separately subjected to DBD treatment. The combined system (of DBD/Ag/TiO_2 or DBD/0.06 g nano zero valent iron particles were further utilised to identify the oxidation products of BPA or 2-NP degradation in aqueous solution. The volume of the simulated organic wastewater was 1.5 L and the degradation of BPA or 2-NP into various fragments was monitored for a period of 2 h. Higher concentrations were selected for easy identification of the reaction intermediates and prediction of the degradation pathways. Sampling was done every 10 minutes when 2 mL aliquot was withdrawn into 2 mL bottles. The 2 mL vials were then sealed and the possible intermediate oxidation products were identified using Agilent 6230 TOF LC-UV and mass spectrometry at 280 and 278 nm respectively. A Thermo chromatographic system (pump + thermostated autosampler Surveyor) equipped with a diode array detector (Surveyor) and an ion trap mass spectrometer DECA XP Ion max was used. The separation of BPA or 2-NP into various fragments was accomplished using a symmetry C8 column and a gradient method with two mobile phases was used. Detailed of the gradient elution method is contained in section 3.4.12.

3.2.9.5 Quantification of free reactive species produced by DBD alone

The DBD reactor produced highly oxidative radicals, out of which, three reactive species namely H_2O_2, O_3 and OH were detected and quantified using suitable standard analytical procedures while in the combined system, only the concentration of hydroxyl radical was considered. The methodology adopted is detailed in the next section.

3.2.9.6 Hydrogen peroxide (H_2O_2) determination

The colorimetric method reported by Sahni and Locke, (2006) was adopted. This involves the spectrophotometric measurement of the intense-yellow orange formed as a consequence of adding titanylsulphate to a solution containing hydrogen peroxide. The yellow colour is due to the formation of peroxotitanyl sulphonic acid shown in the reaction scheme below.

$$TiOSO_4 + H_2O_2 + H_2SO_4 \longrightarrow TiO_2(SO4)_2^{2-} + H_2O + 2H^+ \quad (3.5)$$

The concentration of the H_2O_2 produced by the DBD reactor is equivalent to the concentration of the peroxo titanyl sulphonic acid measured using the UV-visible spectrophotometer at 410 nm. The substitution of the corresponding absorbance value at this wavelength into the Beer's Lambert formula produces the initial concentration of H_2O_2.

2.4 g of titanylsulfate (hydrate) was weighed and mixed with 100 mL of 20% H_2SO_4 in a volumetric flask and the remaining volume of the flask was made up to 500 mL with distilled-deionised water. 3 mL water sample containing BPA or 2-NP was taken from the DBD reactor and immediately mixed with 0.3 mL of the prepared titanylsulphate solution in a 20 mL volumetric flask which produced yellow pertitanic acid. The absorbance value of the resulting in the yellow colour of the pertitanic acid was measured at 410 nm. The concentration of the H_2O_2 generated insitu during the DBD treatment was calculated using the Beer's Lambert equation shown below (Sahni and Locke, 2006). The experiment was repeated with distilled-deionised water (as control) without BPA and 2-NP and the concentration of H_2O_2 was calculated accordingly. The DBD experiment was conducted for 2 h and sampling was done at 10 min interval.

$A = \varepsilon l C$, which implies that $C = \frac{A}{\varepsilon l}$ (3.6)

Where ε represent the molar extinction coefficient of H_2O_2 at 410 nm, which is 700 L $mol^{-1}cm^{-1}$, l is the optical path length usually 1 cm, A is the absorbance in (a.u), C is the concentration in (mol/L). The reaction pathways leading to formation of H_2O_2 in the DBD system can be found in section 2.4.1.

3.2.9.7 Quantification of dissolved ozone (O_3)

O_3 can be detected in either gas or liquid phase depending on the reactor configuration. In the current investigation, the Indigo method described by Bader and Hoigne, (1981) was adopted to quantify the amount of O_3 produced by the DBD in water. Indigo with a strong absorbance at 600 nm (ε = 20000 L $mol^{-1}cm^{-1}$) can easily be decolourised by one molecule of ozone and the decolourised products are rarely consumed further by ozone. It was also observed that H_2O_2 and OH did not interfere with the O_3 measurement. The reaction between ozone and indigo is shown in Fig. 3.15

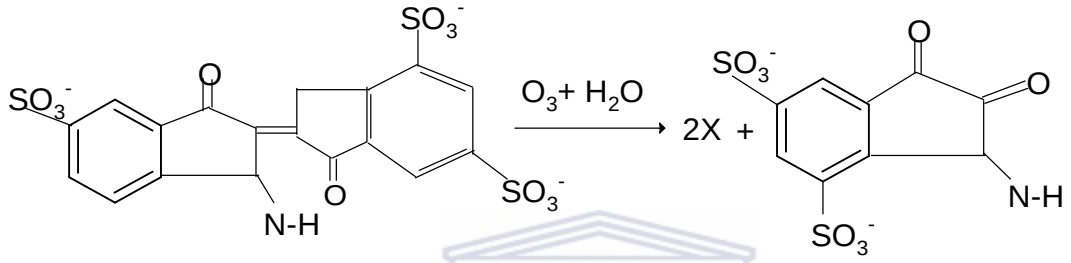

Figure 3.15: Reaction of ozone with indigo trisulfonic acid and formation of isatin sulfonic acid

The ozone produced by the DBD system was quantified using the Indigo method reported by Gupta, (2007). 2 mL each of solution (Indigo A and Indigo B) (in section 3.1.1) was mixed together in a volumetric flask and filled up to 25 mL with ordinary distilled-deionised water. The absorbance of this solution was measured with the UV-Vis spectrophotometer at 600 nm and recorded as a reference (blank absorbance count). In order to calculate the concentration of dissolved O_3 in aqueous solution containing BPA or 2-NP, 2 mL each of Indigo solution (A and B) was again mixed together in a 25 mL volumetric flask and the rest of the volume was made up with treated water BPA or 2-NP solution. Then the absorbance of the solution at 600 nm was measured and recorded as the sample absorbance. Sampling was done at 10 min interval for a period of 2 h. Thus, the O_3 concentration was calculated from the differences in absorbance between the blank solution and that of the DBD treated solution, where the molar absorptivity (ε) value of indigo solution was 20000 L mol^{-1} cm^{-1}. For the control experiment, ordinary distilled water without BPA or 2-NP was treated using DBD system for 2 h, sampling was done at 10 min interval. 2 mL of each indigo solution (A and B) was mixed together in a 25 mL volumetric flask and made up with ordinary distilled water subjected to

DBD treatment. The concentration of dissolved O_3 produced by DBD system in distilled water alone, BPA or 2-NP solution was calculated accordingly.

$$Concentration\ of\ (O_3)\left(\frac{mg}{L}\right) = \frac{At - Ao}{\varepsilon} * 48 * 1000 \quad (3.7)$$

Where A_t is the absorbance at different time, A_o is the absorbance of the blank, 48 g/mol is the molar mass of O_3, 1000 is the conversion factor from gram to milligram

3.2.9.8 Quantification of hydroxyl radical (OH•)

In this study, a disodium salt of terephthalic acid as dosimetry probe was used to trap and quantify the exact concentration of the OH radical produced by the DBD reactor. The reaction between the disodium salt terephthalic acid (TA) and hydroxyl radical in the treated water produces a stable 2-hydroxylterephthalic acid (HTA) which is fluorescent at 425 nm in a typical photoluminescence (PL) technique (Sahni and Locke, 2006). The concentration of HTA measured at 425 nm is proportional to the hydroxyl radical concentration produced by DBD. The reaction between TA and hydroxyl radical is represented in Figure 3.16.

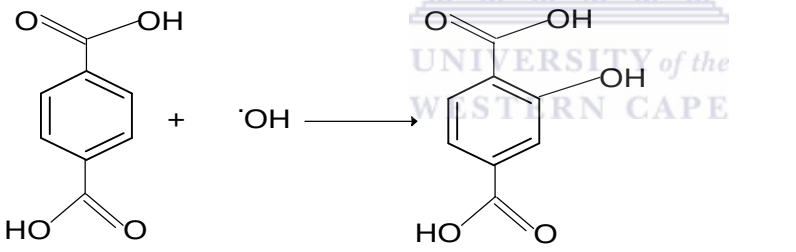

Terephthalic acid (non-fluoroscent)

2-hydroxylterephthalic acid (fluoroscent)

Figure 3.16: Formation of hydroxyterephthalic acid (HTA) through reaction of HA with OH radical

The DBD experimental set up and conditions as explained in (section 3.2.6.1) was used to generate the hydroxyl radicals. The solution pH and conductivity of the prepared 0.2 mM NaTA were adjusted to 7.4 and 105 μS cm^{-1} respectively. The pH was adjusted by adding a few drops of the phosphate buffer. Firstly, 1.5 L of distilled-ionised solution containing 0.2 mM NaTA was measured and poured into a 2 L beaker. The 2 L beaker was put on a magnetic stirrer and thereafter the DBD system was connected to the power source. First sample at time=0 was taken before the DBD system was switched on. Thereafter, the DBD

system was switched on and 2 mL samples were drawn from the reactor at 10 min for 2 h. The sample was introduced into a 2 cm cuvette and analyzed using photoluminescence (PL) technique. Photoluminescence technique measures the intensity of the HTA liberated from reaction between OH radicals and NaTA. Prior to the measurement, the excitation and emission slits were adjusted to 5 and 2.5 µm respectively while the excitation wavelength was set at 310 nm. Thereafter, the fluorescence spectra at a time equal to zero and 0.2 mM NaTA sampled every ten minutes, were collected in the range of 325 to 600 nm. This was considered as the blank experiment without the pollutants. This procedure was repeated separately with a wastewater containing 1 L of 10 ppm BPA plus 0.5 L of 0.2 mM NaTA. The same procedure was followed for 2-NP. Sampling (2 mL) was done every ten minutes and the intensity of HTA analysed accordingly using the analytical technique described in section 3.4.15. A calibration curve of known concentration of HTA solution in the range of 0.2 – 4 mM was prepared to determine the unknown concentration of hydroxyl radical produced by the DBD system. The standard HTA calibration curve is shown in Figure 3.17. The fluorescence intensity and HTA fluorescence yields were estimated.

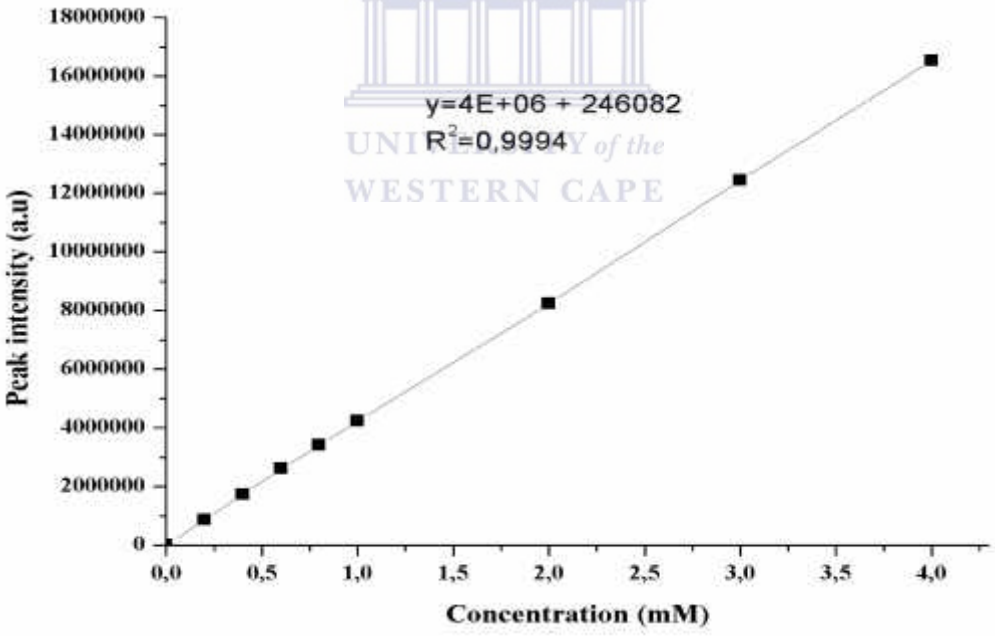

Figure 3.17: Standard calibration curve of HTA

3.2.9.9 Quantification of H_2O_2, O_3 and OH radicals produced by the combined system

This section describes the procedure used to quantify the amount of H_2O_2, O_3 and OH radicals generated in distilled water, BPA or 2-NP solution by either the combination of DBD/JT14 or DBD/0.06 g nZVI.

i. Quantification of H_2O_2, O_3 and OH radicals produced by DBD/JT14

The amount of H_2O_2, O_3 and OH radicals produced by the combined system (DBD with supported Ag doped TiO_2 nanocomposites) were determined using the methodology described in section 3.2.9 and 3.2.9.2 respectively.

ii. Quantification of H_2O_2, O_3 and OH radical produced by DBD/photo-Fenton induced process

In this case, the optimum nano zero valent iron particles dose (0.06 g) was introduced into the DBD system containing a 1L volume of 10 ppm BPA solution and 0.5 L 0.2 Mm NaTA in a 2 L beaker. The amount of H_2O_2, O_3 and OH radicals produced by the combined system (DBD/nZVI) were determined using the methodology described in section 3.2.9 and 3.2.9.2 respectively.

3.3 Degradation studies using Jet loop reactor

This section focuses on the application of the jet loop reactor and other advanced oxidation treatment strategies to decompose BPA or 2-NP. Detailed information on the varied operating parameters and the various combinatory approach are provided.

3.3.1 *Description of Jet loop reactor (JLR)*

In view of DBD system being difficult to scale up for industrial application, a Jet impinging reactor shown in the Figure 3.18 and 3.19 combined with other advanced oxidation processes such as UV light or hydrogen peroxide was explored to degrade the aqueous solution of BPA or 2-NP. The jet loop reactor system, otherwise known as jet impingement process has recently emerged as a chemical free process for degradation of refractory organic contaminants in wastewater. However, considering the chemical and structural complexity of wastewater, the jet impinging system alone cannot effectively decompose the complex organic pollutants due to the low yield of OH radicals. Thus, the combination of jet loop reactor with other advanced oxidation technologies has been considered to be a fundamental research area worthy of exploring. Jet impingement involves bringing together a liquid flow along the same axis but in opposite directions into collision, which causes the growth and subsequent collapse of cavities within the impingement zone occurring at ambient pressure and temperature. The application of a jet reactor accelerates the kinetics involved in these reactions. A brief description of the jet loop reactor is provided below. Table 3.4 contains the

essential components of the jet loop reactor. While Figure 3.18 and 3.19 shows the pilot scale set up and the block flow diagram.

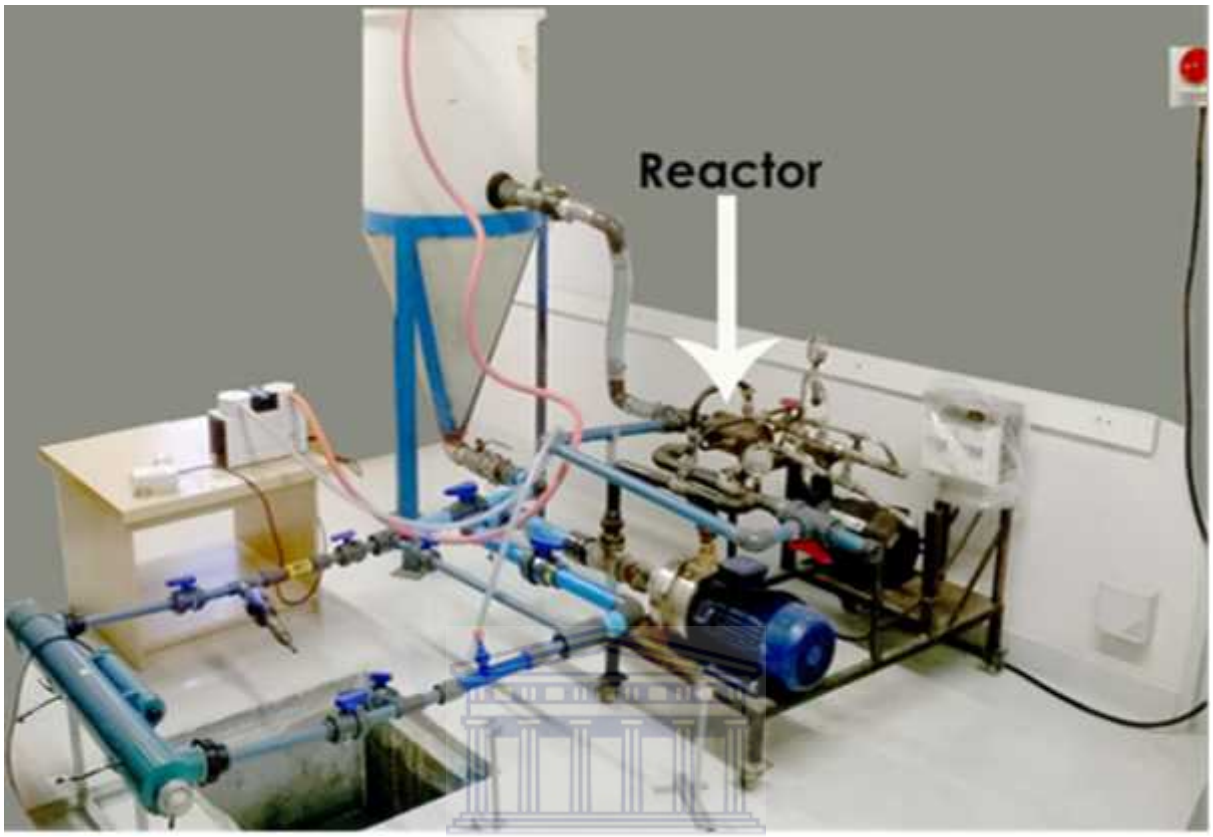

Figure 3.18: The schematic representation of the jet loop reactor with the in-line UV lamp

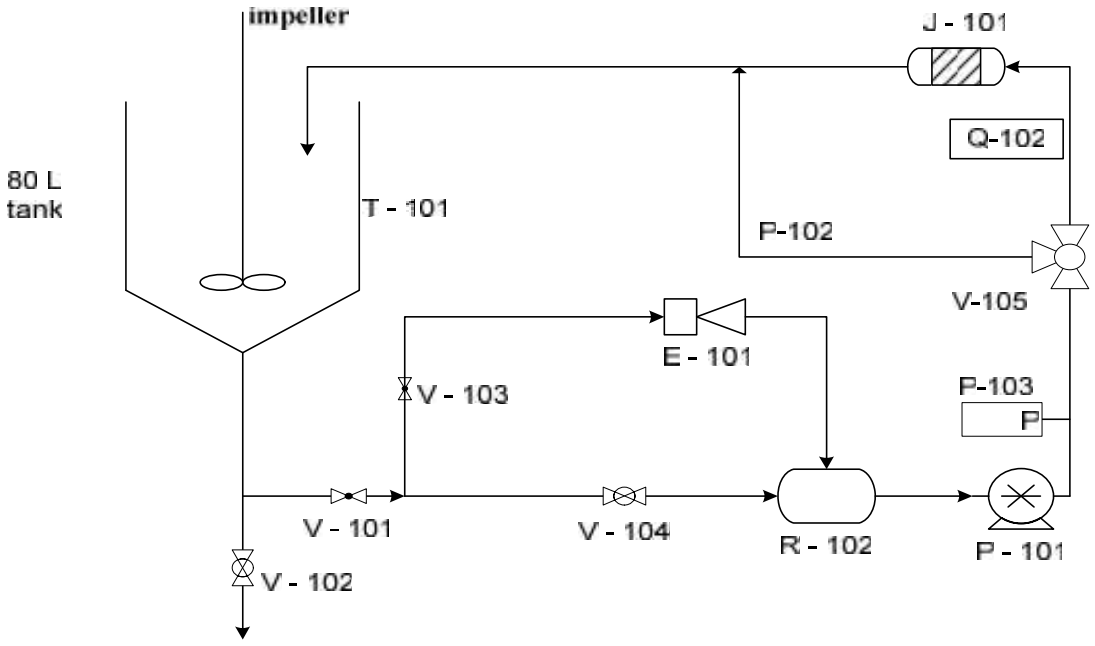

Figure 3.19: Process flow diagram of the Jet loop experimental set up

Table 3.4: List of all components described in Figure 3.19

Equipment	Description
E – 101	Sample collection point
J – 101	Jet Loop Reactor (Patent number ZA2009/07606)
P – 101	Displacement pump
R – 102	In-line UV lamp
T – 101	Holding Tank (80 L)
V – 101	Globe Valve
V – 102	Ball Valve
V – 103	Globe Valve
V – 104	Ball Valve
V–105	T-junction
P–102	Bypass line
P–103	Pressure gauge
Q–102	Main line

3.3.2 *Experimental setup*

The schematic diagram and the flow system of Jet loop reactor, in-line UV and hydrogen peroxide is depicted in Figure 3.18 and 3.19. The device essentially comprised a 100 L capacity holding tank with a piping layout as given above that has an integrated in-line UV lamp (55 W), displacement pump of power rating 2.5 KW, control valves, flanges to accommodate the multiple orifice and cavitating jet both of which form the cavitating device (Table 3.14). Figure 3.20 illustrates the inner view of the jet impinging device.

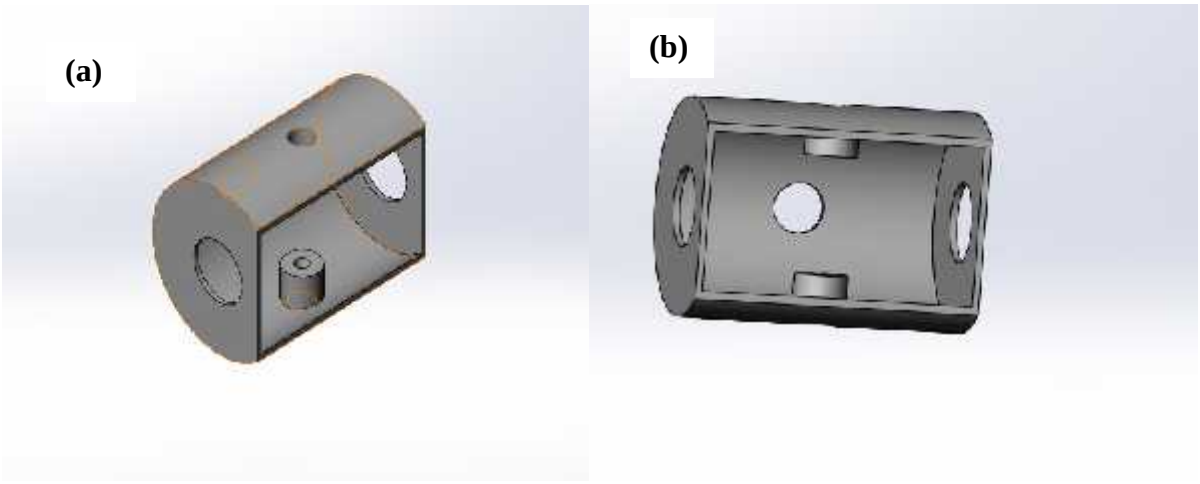

Figure 3.20: Jet reactor chamber (a) dimensions or specification (b) the inner view of the jet impinging device

The suction side of the pump (P-101) was connected to the bottom of the holding tank and the discharge pipe from the pump branched into two lines; the main line and bypass line. The main line consisted of a flange that held the impinging device comprised orifice and jet cavity otherwise known as impingement zone. While the diameter of the two impinging jets inside the jet loop reactor were 4 mm each. A pressure gauge was provided to measure the inlet pressure (P_1) was connected in between the discharge line of the pump and the feed tank. The in-line UV lamp is connected between the suction side of the pump and the bottom of the 80 L holding tank. Valves were used to control the flow rate through the main lines. The main line terminated inside the holding tank of the jet impinging reactor and below the liquid level to prevent induction of air into the liquid. By employing the jet loop reactor to treat wastewater the following activities occurred: (i) collision of similar streams of liquid with an equal flow rate in the jet reactor chamber and (ii) generation of free radicals through impingement within the jet reactor impinging chamber (iii) the possibility to add UV irradiation to the process to generate additional free radicals. The feed tank was separately filled with 60 L of the aqueous model solution at 10 ppm initial concentration of either BPA or 2-NP and the pump was started. The prepared aqueous solution was pumped from the holding tank into the reactor and distributed into the impinging devices as shown in Figure 3.20. In each jet the water was forced through orifice plate of 2 mm diameter. The water from the two sides of the jet reactor, collided with each other under high kinetic energy, a process called impingement. Due to the absence of a cooling device, it was difficult to maintain a

constant operating temperature. The temperature was monitored at 10 min each and measured using a thermometer.

3.3.2.1 Optimization of the jet loop reactor system

A set of experiments was conducted on the jet loop system under varied conditions using 60 L aqueous solution of BPA or 2-NP for a constant circulation period of 2 h. The experiments were conducted in order to determine the conditions under which maximum degradation of the studied pollutants occurred. The choice of 60 L of operating capacity was based on the pump's capacity in order to maintain the flow rate of (0.7 L/s) in the circulation loop and ensure generation of cavitating conditions. There was problem of overheating and incessant leakages of pipe when used volume below 60 L. The experiments involved the following steps to optimize the jet loop reactor system;

- To study of the influence of the UV lamp alone and establishing the synergistic effect between the combined JLR/UV systems.
- Investigation of the effect of hydrogen peroxide alone and JLR/H_2O_2, UV/H_2O_2 and
- To study the effect of the combined jet loop reactor/in-line UV/Hydrogen peroxide process on the extent of degradation of BPA and 2-NP solution.

The decomposition of the modelled compounds was analysed by observing the rate of degradation in the case of 2-NP as well as its complete mineralization. Degradation may be due to cleavage of chemical bonds by free radicals which were monitored as specified in section 3.2.9.5 while the rate of mineralization of BPA and 2-NP into CO_2 and H_2O was measured by TOC. The procedure for the determination of initial and final TOC value can be found in section 3.2.9.3. The parameters investigated including the detailed experimental procedures are provided below. The unit number/operation describing the important component of the JLR and in-line UV-light are represented in Table 3.4.

i. Effect of inlet pressure

The holding tank (T-101) was separately filled with 60 L of aqueous solution of 10 ppm initial concentration of BPA or 2-NP and the positive displacement pump (P-101) was started and the main line (Q-102) was controlled to be bubble free. The effect of inlet pressure (P-103) on the extent of degradation of the modelled compounds was investigated by varying the inlet pressure from 2 bar to 6 bar at the natural pH of the aqueous solution. However, the flow rate changes as the pressure increases. The inlet pressures was adjusted using the pressure

gauge (P–103) and the T-junction (V–105) was closed to allow easy flow of the water through the jet reactor (J–101) onto the holding tank (T–101). The continous flow of the aqueous solution of BPA or 2-NP into the holding tank via the JLR was allowed to continue for a period of 2 h and 2 mL samples were taken every 10 minutes The 2 mL aliquot of BPA or 2-NP solution was then analysed using the high performance liquid chromatography (HPLC) methodology described in section 3.4.12 at 280 and 278 nm wavelength respectively. The residual concentration of the contaminant was determined from the calibration curves prepared with solutions of known concentrations. Experiments were undertaken in duplicate to ensure that erroneous results were quickly identified within a series of samples. The optimum pressure was selected for the next set of experiments.

ii. Effect of initial solution pH

As described above, the holding tank (T-101) was separately filled with 60 L of aqueous solution of BPA or 2-NP of known concentration. The initial pH of the solution was varied over the range of 3-12 at constant inlet pressure of (4 bar) and flow rate 0.7 L/s.The solution pH adjustment was done with 0.5 M H_2SO_4 or 0.5 M NaOH until the desired pH value was obtained and thereafter the positive displacement pump (P-103) was started and and the aqueous solution of BPA or 2-NP passed through the main line (Q–102). The experiment was performed for 120 minutes and 2 mL samples were taken every 10 minutes. The 2 mL aliquot of either BPA or 2-NP was analysed using high performance liquid chromatography (HPLC unit having symmetry C_{18} column at 280 and 278 nm wavelength respectively. The concentrations were determined from the calibration curves prepared with solutions of known concentrations. The optimum pH (3) for 2-NP or BPA respectively and inlet pressure (4 bar) were selected for the next set of experiments.

iii. Effect of initial concentration of the modelled pollutants

The effect of initial concentration of BPA and 2-NP on the extent of decomposition was investigated by varying the concentration of BPA and 2-NP over the range of 10 – 30 ppm at constant inlet pressure of 4 bar, flow rate (0.7 L/s) and solution pH (3). Again, the holding tank (T-101) of the jet loop system was separately filled to 60 L capacity with aqueous solution of BPA or of 2-NP of known concentration. The pH adjustment was done with 0.5 M H_2SO_4 or 0.5 M NaOH. The optimum pH (3) and inlet pressure (P-103) (4 bar) obtained in step (i) and (ii) above was applied in this experiment and the pump (P-101) was switched on.

The flow path of aqueous solution of BPA or 2-NP was via the main line (Q–102) and not bypass (P–102). The reaction was allowed to proceed for 120 min during while sampling (2 mL) was done at intervals of 10 min for analysis of the extent of degradation. As usual the residual concentrations of BPA or 2-NP were analysed and determined using HPLC. The detailed HPLC conditions including the column and mobile phases have been outlined in section 3.4.12. The experiments were repeated twice and the average values reported.

iii. Effect of radical scavengers on the extent of degradation

The presence of radical scavengers in solution affect the efficiency of advanced oxidation technologies due to inhibition and consumptions of free radicals. Among radical scavengers or inhibitors are inorganic species such as Na_2CO_3, Na_2SO_4, $NaHCO_3$, $Na_2B_2O_7$, $NaNO_3$, C_3H_9OH, t-C_4H_9OH, Na_3PO_4, and NaCl. In this study, the influence of separate addition of Na_2CO_3, Na_2SO_4 and NaCl on the removal rate of BPA or 2-NP in water by JLR system was examined. 60 mg/L each of (Na_2CO_3 (0.0006 mol/L), Na_2SO_4 (0.0004 mol/L), NaCl (0.001 mol/L) were separately added to 60 L of aqueous solution of 10 ppm BPA or 2-NP in the holding tank (T-101). The pH adjustment was done with 0.5 M H_2SO_4 or 0.5 M NaOH. The experiment was conducted at optimum pH (3) and initial concentration for each pollutants (10 ppm), optimum inlet pressure (4 bar) and flow rate (0.7 L/s). The aqueous solution of BPA or 2-NP flow via the main line (Q–102) and not bypass (P–102). The positive displacement pump (P-103) was switched on and the reaction was allowed to proceed for 120 min during which sampling was done at intervals of 10 min for analysing the extent of degradation. As usual the residual concentration of BPA and 2-NP was analysed and determined using HPLC. The experiments were repeated twice and the reported values were the averages of two different experimental runs.

3.3.3 *Combined advanced oxidation technologies*

The experiments regarding process integration of the jet loop reactor system and different additives such as hydrogen peroxide and in-line UV lamp were performed under the set of optimized operating parameters. The main aim of the combination of jet loop reactor system with other advanced oxidation process was to maximise the extent of degradation of the modelled compounds using different integrated approaches explained in the next section.

i. Effect of ultraviolet light alone

In order to investigate the effect of the UV lamp alone (R–102), the valve to the main line (Q–102) pipe which held the JLR (J-101) was closed while the by-pass line valve (P–102) was opened. The in-line UV light (R–102) was positioned in between the displacement pump (P-101) and the holding tank (T-101). The mixing of the aqueous solution of BPA or 2-NP was by circulation through the holding tank (T–101) and bypass line (P–102) and not via the JLR (J–101). The holding tank (T–101) was filled with 60 L of aqueous solution of 10 ppm BPA or 2-NP while other parameters such as solution pH (3) for BPA, pH 3 for 2-NP, and inlet pressure (4 bar) (P-103) were kept constant. The diameter of the bypass line (P-102) was small compared to the main line (Q-102) and as such the flow rate was not measured. The positive displacement pump (P-101) was switched on and the experiment was run for 120 minutes. Sampling (2 mL) was done at intervals of 10 min for analysing the extent of degradation. As usual the residual concentrations of BPA or 2-NP were analysed and determined using HPLC. The experiments were repeated twice.

ii. Effect of hydrogen peroxide alone

The influence of adding a process intensifier such as hydrogen peroxide on the extent of degradation of BPA was explored. A similar procedure as described in step (i) above was adopted, the main line valve (Q–102) which linked the jet loop reactor (J-101) into the system was closed while the by-pass line valve (P–102) was opened for passage of the simulated wastewater. The mixing of the model solution of BPA or 2-NP was by circulation through the holding tank (T-101) and bypass line (P–102) and not via JLR (J-101). The experiment was carried out in a 60 L holding tank where different concentrations of H_2O_2 was added to 10 ppm aqueous solution BPA or 2-NP. The concentration of H_2O_2 added into the tank was in the range of 0.17 - 2.04 g/L. while solution pH (3) for BPA and for 2-NP, inlet pressure (4 bar) kept constant. Sampling (2 mL) was done at every ten minutes and subsequently analysed by HPLC. A similar procedure was repeated for the second pollutant.

iii. Effect of combined in-line UV and hydrogen peroxide

In order to investigate the combined effect of UV/H_2O_2 on the degradation efficiency of the simulated aqueous solution, the jet reactor system (J-101) was bypassed and the holding tank (T-101) was filled with 60 L of aqueous solution of 10 ppm initial concentration of BPA or 2-NP and the positive displacement pump (P-101) was initially switched off. Prior to adding

peroxide, the valve (V-101) at the bottom of the holding tank (T-101) was opened to allow the liquid to flow through and ensure a homogeneous mixture. The positive displacement pump (P-101) was then turned on and the liquid passed through the by-pass pipe (P–102) only without the JLR (J-101) system and the peroxide was dosed into the holding tank (T-101). The experiment was conducted at optimum solution pH (3) for BPA, pH 3 for 2-NP, and hydrogen peroxide concentration (0.34 g/L) were kept constant. The reaction was carried out for 120 min and samples (2 mL) were collected after every 10 minutes. Analysis of the treated solution was done using HPLC method (section 3.4.12) at 280 and 278 nm wavelength respectively and the residual concentrations of BPA or 2-NP were obtained from the calibration curve prepared from known concentrations.

iv. Effect of combined jet loop rector system with hydrogen peroxide

In another set of experiments, the jet loop system was combined with hydrogen peroxide without UV as the in-line UV lamp (R–102) was switched off and the bypassed line (P–102) was closed to bypass the UV. The effect of different concentrations of hydrogen peroxide was explored. Hydrogen peroxide as an additional source of hydroxyl radical was used in order to intensify the degradation efficiency using the jet loop reactor (J–101) system. Prior to adding peroxide, the valve (V-101) at the bottom of the holding tank (T-101) was opened to allow the liquid to flow through and ensure a homogeneous mixture. The positive displacement pump (P-101) was then turned on and the pressure (P-103) was regulated to 4 bar using a ball valve (V-102) and peroxide was dosed into the holding tank (T–101). The following parameters of optimum pH (3) for BPA or 2-NP, concentration of BPA or 2-NP (10 ppm), volume of BPA or 2-NP (60 L), flow rate (0.7 L/s), and inlet pressure (4 bar) were kept constant while the concentration of hydrogen peroxide was varied over the range of 0.17 – 2.04 g/L. The liquid passed from the holding tank (T-101) through the JLR (J-101) system where treatment took place. The reaction was carried out for 120 minutes and sample (2 mL) was collected every 10 minutes. Analysis of the treated solution was done using HPLC method (section 3.4.12) at 280 and 278 nm wavelength respectively and the residual concentrations of BPA and 2-NP were obtained from the calibration curve prepared from known concentrations. It is should mentioned that the temperature which was formerly 19ºC at zero min increased to 62ºC after 120 min.

v. Effect of combined jet loop reactor with in-line UV lamp

In order to study the effect of the combined process, the following optimum values of solution pH (3), inlet pressure (4 bar), flow rate (0.7 L/s), and concentration of 10 ppm were kept constant except that the jet loop reactor was combined with in-line UV light (55 W) of wavelength 278 nm. The in-line UV lamp (R-102) was connected to a power source and the same procedure as described above was followed. The 10 ppm of BPA or 2-NP was first passed via the jet reactor, followed by the UV light. The conditions applied were solution pH (3), flow rate (0.7 L/s) and optimum pressure (4 bar). The reaction was carried out for 120 minutes and samples (2 mL) were collected every 10 minutes. Analysis of the treated solution was done using HPLC method (section 3.4.12) at 280 and 278 nm wavelength respectively and the residual concentrations of BPA and 2-NP were obtained from the calibration curve prepared from known concentrations.

vi. Effect of combined jet loop reactor/in-line UV/Hydrogen peroxide

In order to study the effect of the combined jet loop reactor/UV/H_2O_2 process on the degradation of BPA or 2-NP an experiment was conducted at optimum pH for BPA and 2-NP (3), inlet pressure (4 bar), flow rate (0.7 L/s) and concentration of hydrogen peroxide (0.34 g/L). The holding tank (T–101) was filled with 60 L of aqueous solution of 10 ppm initial concentration of BPA or 2-NP and the pump (P–101) was switched off while the valve at the bottom of the holding tank (V–101) was opened to allow the liquid to flow through and ensure a homogeneous mixture before dosing H_2O_2. The pump (P–101) was then turned on and the pressure regulated to 4 bar using a ball valve (P–103) and H_2O_2 was dosed. The liquid passed through the main line pipe (Q–102), UV light (R–102) and the jet system (J–101) where treatment took place. The total duration of the experiment was 120 minutes and the sampling was done at an intervals of 10 minutes to monitor the progress of degradation. Analysis of the treated solution was done using HPLC method (section 3.4.12) at 280 and 278 nm wavelength respectively and the residual concentrations of BPA or 2-NP were obtained from the calibration curve prepared from known concentrations.

3.4 Analytical techniques

In this study, several analytical techniques were used to characterize the synthesised supported TiO_2, Ag deposited TiO_2 nanocomposites and nZVI. The different characterization techniques employed included: X-ray Diffraction (XRD), High Resolution Scanning Electron Microscopy (HRSEM), High Resolution Transmission Electron Microscopy (HRTEM), Energy dispersive spectroscopy (EDS), Selected area electron diffraction (SAED), Ultraviolet-visible spectrophotometry (UV-Vis), Ultraviolet-visible/diffuse reflectance spectroscopy, Thermal Gravimetric analysis (TGA)/Differential Scanning Calorimetry (DSC), Fourier Transform Infrared Spectroscopy, (FTIR), Inductive Coupled Plasma-Optical Emission Spectroscopy (ICP-OES) and Fluorescence spectrophotometry. The information derived from each of the analytical techniques including the sample preparation procedures are provided in the subsequent sections.

3.4.1 *X-ray Diffraction*

X-ray diffraction (XRD) is a powerful non-destructive analytical technique mostly utilized in solid state chemistry and material science for fingerprint characterization as well as phase identification of a crystalline material (Cullity and Stock, 2001). It is most often used in mineralogical identification and quantification including crystallographic structural determination of materials and more importantly crystallite size. Other information provided by XRD includes unit cell dimension, elemental phase identification, atomic spacing as well as identification of single and multiple phases of unknown materials. The principle of operation of XRD involves bombarding a single crystal or powder sample with X-rays photons which produce diffraction pattern (Okolo et al., 2004). These diffraction patterns are recorded and analysed to determine the nature of the crystal structure. The mineralogical phase characterization and estimation of the average crystallite size of the various synthesised materials were performed on a Bruker AXS D8 X-ray diffractometer system coupled with Cu-Kα radiation of 40 kV and a current of 40 mA. The λ for Kα was 0.1541 nm, scanning rate was 1.5º/min, while a step width of 0.05° was used over the 2θ range.

Sample preparation

The powder samples were placed and clipped into the rectangular aluminium sample holder. The diffractograms were recorded in the 2 θ range of 20^0 - 90^0 and the phase identification was done. Other operating and instrumental conditions are shown in Table 3.5

Table 3.5: Bruker D8 Advance XRD operating parameters

Operating parameters	Condition
Time constant	0.5 s
Radiation	Cu-Kα
Wavelength	1.542 Å
X-ray operating voltage	40 Kv
X-ray operating current	40 mA
Scanning angle range	$20^o<2\theta<90^o$
Scanning step	0.2^o
Scanning speed	60s/step

The Scherer equation shown below was used to determine the crystal size from half height peak width

$$d = \frac{k^{a}}{\cos} \quad \text{.....(3.8)}$$

Where d is crystallite size in nanometer, K= 0.94, λ is the wavelength of the X-ray which is 0.1541 nm, θ is the half-diffraction angle, β is the full width at half-maximum in radian.

3.4.2 *High Resolution Scanning Electron Microscopy*

High Resolution Scanning Electron Microscopy (HRSEM) is a characterization tool capable of producing high-resolution images of a sample surface and at the same time providing information regarding the surface structure and morphology as well as the degree of aggregation of micro and macro materials. Other information provided by HRSEM includes the crystalline nature of the scanned material. The bombardment of atoms present in the samples with beams of electrons give rise to different multiple signals such as back scattered electrons, X-rays secondary electrons among others which ultimately form an image of the samples surface (Egerton, 2005). The morphology and microstructure of the synthesised products was analysed using Zeiss Auriga HRSEM. HRSEM equipped with EDS was further used to determine the elemental composition of the synthesised catalysts. The method of sample preparation is described below

Sample preparation

0.05 mg of the synthesised materials were sprinkled on a sample holder covered with carbon adhesive tape wereand sputter coated with Au-Pd using Quorum T15OT for 5 minutes prior to analysis. The sputter coated samples were characterized using Zeiss Auriga HRSEM. The microscope was operated with electron high tension (EHT) of 5 kV for imaging. Other experimental parameters are outlined in Table 3.6

Table 3.6: HRSEM instrumental settings

Operating parameters	Condition
Current	10 mA
Magnification	Varies
Aperture	0.4 mm
Resolution	1 nm but sometimes varies
Emitter	Thermal field emission type
Working distance	4 - 10.4 mm
Voltage	5 kV
Signal A	Inlens

3.4.3 *High Resolution Transmission Electron Microscopy*

High Resolution Transmission Electron Microscopy (HRTEM) is a non-destructive electron microscope system that involves the interaction of an electron beam transmitted through a thin sample to produce an image that can be magnified and focused on a fluorescent screen or CCD camera. HRTEM is used for imaging the crystallographical structure of a material and remains the most viable characterization technique used to determine the properties of a crystalline material at nanoscale (Egerton, 2005). It is also utilized in studying the surface morphology as well as the distribution pattern of particle size in a material. Two distinct types of information that are provided by HRTEM about a sample are, a magnified image indicating the sample morphology and the degree of crystallinity via electron diffraction. Other information provided by HRTEM include chemical composition, porosity, structural defects and the crystal orientation of a material. The particle size and the crystalline nature of the synthesised catalysts was determined by Zeiss Auriga HRTEM. The procedure for sample preparation is described below.

3.4.4 *Energy dispersive spectroscopy*

Energy dispersive spectroscopy (EDS) is another useful non-destructive technique employed in determining qualitative and semi-quantitative elemental composition of an unknown sample. EDS involves the interaction of X-ray excitation (beam of electrons) with the sample atomic composition via a scanning microscopy to produce a unique spectrum comprising peaks corresponding to particular elements in the sample (Corbari, 2008). EDS provides the elemental distribution pattern in the form of a line scan which relates to particular peaks formed through X-ray emission. Invariably, EDS separates the X-rays of the individual elements into an energy spectrum and further characterizes the spectrum to give the relative abundance of each element in a material (Egerton, 2005). This is mostly coupled with HRSEM through scanning the selected area for a sufficient time to obtain the average weight of the elements.

3.4.5 *Selected area electron diffraction*

Selected area electron diffraction (SAED) is a type of electron diffraction technique that deals with the crystallographical as well as the structural orientation of a material. This provides information regarding the distribution pattern of the individual microscopic sized crystallites around the orbit (Corbari, 2008). Information such as degree of crystallinity is provided via a process diffraction computational program which indexes a reasonable number of crystals in a measurable pattern. This is mostly coupled with HRTEM and the scanned images are usually transferred to a SAED detector to establish the extent of crystallinity (Egerton, 2005).

Sample preparation for HRTEM analysis

Approximately 0.02 g of the synthesised products was suspended in 10 mL methanol and thereafter subjected to ultra-sonication until complete dispersion was achieved. One or two drops of the slurry was dropped onto a holey carbon grid with the aid of a micropipette and subsequently dried via exposure to photo light. After drying, the holey carbon 400 mesh copper grid was loaded onto the single-tilt sample holder and thereafter mounted onto the shaft of the electron microscope. The detailed instrumental settings/conditions are provided in Table 3.7.

Table 3.7: HRTEM experimental conditions

Operating parameters	Conditions
Illumination angle	15^{o}
Electron high tension	200 kV
Magnification	Varied
Resolution	0.24 nm
Spot size	3 nm
Gun lens	1 nm
Objective aperture	2 nm
Condenser aperture	3 mm
Emission current	54 µA
Extraction voltage	3950 V

Sample preparation for EDS analysis

0.05 mg of the synthesised materials sprinkled on a sample holder covered with carbon adhesive tape and were sputter coated with Au-Pd using Quorum T15OT for 5 minutes prior to analysis. The sputter coated samples were characterized using Zeiss Auriga HRSEM. The secondary electron mode is activated for imaging, and a homogeneous region on the sample identified. The microscope was operated with electron high tension (EHT) of 20 kV for EDS and then the elemental composition of the sample was determined with EDS.

3.4.6 *Brunauer-Emmett-Teller N_2 adsorption-desorption process*

Brunauer-Emmett-Teller (BET) is one of the most important and reliable analytical techniques employed to determine the actual surface area and the pore size distribution pattern of the synthesised catalyst. In 1940, the idea of multi-layer adsorption was conceived by Brunauer, Emmett and Teller (BET), where physical adsorption of gases such as nitrogen, argon or carbon dioxide on a solid surface was determined. The adsorption-desorption process is used to estimate the average pore size distribution and surface area of an unknown sample. It also provides information about the sample pore area and specific pore volume. The plot of the quantity of gas adsorbed at constant temperature against relative pressure is called the adsorption isotherm. The adsorption isotherms are classified into five and differ from each other depend on the nature of materials (Rouquerol et al., 2007).

Sample preparation

Prior to BET N_2 adsorption, about 100 mg of the sample in a sample tube was first degassed at 90º C for 4 hrs to remove residual water and other volatile components that were likely to block the pores. The BET surface area and average pore volume distributions were obtained from the plot of volume adsorbed (cm^3/g STP) against relative pressure. The N_2 adsorption-desorption isotherms were collected at -196º C using Micromeritics ASAP 2020 Accelerated Surface Area and Porosimetry analyzer.

3.4.7 *X-ray photoelectron spectroscopy*

X-ray photoelectron spectroscopy (XPS) is one of the sensitive analytical techniques utilized for the measurement of surface properties such as oxidation state, electronic state and the chemical environment of an element within a sample usually to a depth of approximately 10 nm (Ray and Shard, 2011). XPS profile of a sample can be obtained by bombarding the synthesised material with an X-ray electron beam causing the emission of core-level electrons from the sample, often localised at a specific binding energy position. In addition, XPS is a unique technique mostly operated under high or ultra-high vacuum (~10^{-8} or < 10^{-9} mbar). In this study, XPS PHI 5400 equipped with hemispherical sector analyzer operated using Alα K non-monochromated radiation with energy 1486.6 eV, at 300 W and 15 keV was used to examine the surface composition of the material. The energy scale was calibrated using the Au $4f_{7/2}$ at 83.95 eV and the linearity of the scan was adjusted to measure the Cu $2p_{3/2}$ at a position of 932.63 eV. All spectra obtained were energy corrected using the aliphatic adventitious hydrocarbon C (1s) peak at 284.8 eV. The XPS Peak 4.1 software was used for data analysis and fits. The various XPS signals were plotted as a function of the measured photoelectron intensity versus the binding energy.

Sample preparation

The Cu specimen holders were cleaned with alcohol and dried with nitrogen gas. A few micrograms of TiO_2 nanocrystals and Ag doped TiO_2 nanocomposites were mounted separately on Cu specimen holders. While nano zero valent iron particles was mounted on carbon tape with the same type of Cu specimen holder used for TiO_2 and Ag/TiO_2. Prior to that, to prevent further oxidation of iron nanoparticles, the nZVI particles were dried in a nitrogen-purged container at room temperature and then mounted into the sample cell directly. The instrumental operating conditions are provided in Table 3.8.

Table 3.8: XPS PHI 5400 operating conditions

Instrumental parameters	Conditions
Irradiation type	Non-monochromatized Al Kα source
Energy	1486.6 Ev
Power (voltage, current)	300 W (15 keV, 30 mA)
Scan rate	400 ms/step for 0.125 eV step-size
Hemispherical sector energy Analyser (CHA)	178.95 eV, 0.5 eV/step and 100 ms/step
Vacuum chamber	$< 10^{-9}$ mbar

3.4.8 *Ultraviolet-visible absorption spectroscopy*

Ultraviolet-visible absorption spectroscopy is one of the most versatile and commonly used analytical equipment to obtain the absorbance spectra and determine the concentration of a organic dye compound in a solution. The absorption spectroscopy in the UV-visible region is related to the Beer's Lambert law where the absorption of the solution in question is directly proportional to the concentration of the dye organic molecule in the solution (Skoog et al., 2007).

Sample preparation

In this study, the absorption intensity of the clear methylene blue solution at 664 nm in a quartz cuvette was measured using a Nicolette-Evolution 100 Ultraviolet spectrometer (Thermal Electron Corporation, UK). In order to determine the unknown concentration, a calibration curve of absorption intensity of methylene blue solution at 664 nm was recorded and plotted from different concentrations. The instrumental settings are provided in Table 3.9.

Table 3.9: UV-Vis instrumental conditions

Instrumental parameters	Conditions
Integration time	0.01 s
Lamp change	325 nm
Band width	2 nm
Cycles	1
Data mode	Absorbance
Fixed mode	Normal

3.4.9 *Fourier Transform Infrared Spectroscopy*

Fourier transform infrared spectroscopy (FTIR) is a non-destructive fingerprint characterization technique mostly used to identify absorption peaks corresponding to the vibrational frequencies of the respective bonds constituting the material. FTIR provides information regarding the chemical bonding, molecular structure and functional groups present in a material. The infrared spectra collected over certain wavelengths assist in the determination and identification of known and unknown functional groups in a mixture (Prati et al., 2010). Due to differences in the atomic arrangement of a materials, the infrared spectra of two materials are not the same. Pure samples normally give clear spectra with few functional groups whereas complex mixtures produce complex spectra with several absorption bands. Thus, infrared spectroscopy remains a viable tool to distinguish different positive materials.

Sample preparation

Perkin Elmer 100 FT-IR Spectrometer model "Spectrum Two" was used for the analysis with the following instrumental settings: Force gauge: 50, scan wavelength: 4000-400 cm^{-1}, scan number: 4, unit: % Transmittance was used for the analysis. The FTIR probe was first cleaned with ethanol and the baseline was run to guard against interference. Taking into cognisance the aforementioned instrumental conditions, a 0.005 g sample was placed directly under the probe. This was followed by scanning and spectra corresponding to each individual sample were collected after the peaks were smoothened.

3.4.10 *UV-Visible diffuse reflectance spectroscopy*

The UV-Visible spectrophotometer (Varian Cary 500 scan) coupled with a diffuse reflectance attachment was used to record and collect the reflectance spectra using $BaSO_4$ as a reference. The powder samples were loaded in a sample pan and spectra collected at a scanning rate of 120 nm/min in the the UV-visible range of 800 to 200 nm.

Sample preparation

A 25 mg sample of each supported catalyst was ground with 0.5 g of $BaSO_4$ and spread onto the sampling plate. Prior to the sample measurement, the background reflectance of $BaSO_4$ (reference) was measured. The Kubelka-Munk function F (R) was calculated as $F(R8) = (1–R_8)^2/2R_8$) where $R(8)$ is diffuse reflectance of the sample relative to the reflectance of a

standard according to the Kubelka-Munk theory. The % diffuse reflectance was then plotted against the wavelength.

3.4.11 *Thermogravimetric - Differential scanning calorimetry*

Thermogravimetric (TGA) otherwise known as thermogravimetry is a thermo analytical technique based on the measurement of residual weight loss with respect to temperature in a controlled environment. This loss in weight or mass may be due to thermal degradation, water loss or adsorption of oxygen. However, changes often occur in a substance that do not necessarily result in a weight change and such phenomenon can be readily observed using Differential Scanning Calorimetry (DSC) or Differential Thermal Analysis (DTA) (Farahany et al., 2012). While DSC is a thermo analytical technique that involves measurement of the amount of heat flow differences between the sample and the reference (empty pan). In the course of running the samples, the temperature of both sample and reference are often kept the same irrespective of differences between the two, allowing the heat capacity of both the sample and reference to be defined over the scanning temperature (Tao et al., 2009). The information provide by DSC is related to the amount of heat released or absorbed during transitions by observing the difference in heat flow between the sample and the reference. Sometimes, TGA/DSC are incorporated for simultaneous measurement of residual change in mass and the thermal behaviour of the synthesised catalyst. The thermal behaviour of air dried 8 % PAN/DMF/$TiCl_4$ was investigated with the aid of TGA-DSC techniques. The detailed sample preparation methodology is provided below.

Sample preparation

TGA-DSC analysis of the dried synthesised catalyst was performed in a Perkin Elma STA 4000. A 25 mg sample was placed in a sample pan and the thermal behaviour of the materials was performed from 30° to 800°C with a heating rate of 10°C/min. Over this temperature range, nitrogen operating at a flow rate of 20 mL/min was used as purging gas.

3.4.12 *High performance liquid chromatography*

High performance liquid chromatography (HPLC) is one of the analytical techniques employed in the separation, identification as well as quantification of constituents in a mixture. The principle of HPLC encompasses pumping and passage of pressurised liquid and sample mixture via a column containing adsorbents of different shapes and sizes. Within the

column, there is interaction among the sample components and the adsorbent, followed by separation and final flow out of the column (Wilfried et al., 2006). The level of interaction however depends on adsorbent particle size. The pressurised liquid, usually a mixture of solvents is referred to as mobile phase and the column is the stationary phase. However, the solvent composition and temperature determines the level of interaction or perhaps the separation process. Prior to separation, the temperature is regulated in the column oven. Different detectors such as UV/Vis photodiode array (PDA) and mass spectrometry are commonly employed to perform the analysis (Ferrer and Thurman, 2009). In spite of the advantages, the technique is very expensive, has low sensitivity to complex mixtures of certain compounds and often requires a large volume of expensive solvent.

HPLC instrumentation and chromatographic conditions

The residual concentrations of BPA and 2-NP were determined using a Waters high performance liquid chromatographic chromatograph equipped with a Waters 1525 binary HPLC pump, Waters 2487 dual λ absorbance detector, and Waters 2707 auto-sampler and running on the Breeze software. Separation was done with the aid of a Spherisorb C_{18} reversed-phase column and a gradient elution method involving two mobile phases was used. The optimized gradient program used for elution and quantification the target compounds is shown in Table 3.10.

Table 3.10: Chromatographic parameters used for analysis of BPA and 2-NP

HPLC parameters	**Conditions**		
Chromatograph	Waters		
Detector	UV		
Column	Spherisorb C_{18} (15mm, 3.9mm 5µ)		
Injection volume	20 mL		
Mobile phase	A: water,		B: Acetonitrile
Flow-rate	1 mL/min		
Gradient elution	Time	%A	%B
	0	85	15
	25	0	100
	28	0	100
	30	85	15
Temperature	26ºC		
Data Collection	Breeze software version 2		

3.4.13 *Liquid Chromatography-Mass Spectrometry (LC-MS)*

Liquid Chromatography-Mass Spectrometry (LC-MS) is an analytical technique which comprises both the physical separation potential of liquid chromatography (LC) and the mass scrutiny ability of the mass spectrometry (MS). The technique is selective and has many applications especially in the identification of molecular mass from a complex mixture with less clean-up, determination of elemental isotopic composition. The principle of LC-MS methods is similar to high performance liquid chromatography (HPLC), where the samples in liquid form (mobile phase) at relatively high pressure is made to pass through a column containing uniform or irregular shaped particles (Ferrer and Thurman, 2009). The column is often referred to as the stationary phase. The separation of the charged particles or constituent occurs in the stationary phase. In short, LC-MS provides information on the mass-to-charge ratio (m/z) of charged particles in the sample, elemental composition and perhaps elucidation of molecular structures of the compounds. The liquid sample loaded onto the MS instrument goes through a vapourization step followed by electrospray ionization by beams of electron to produce charged particles, which are separated by the column in a mass analyser based on their mass-to-charge ratio. The mass analysers are of different categories namely single or triple quadrupole, ion trap, time of flight (TOF), and quadrupole-time of flight (Q-TOF). In this study, LC-MS tandem with time of flight mass analyser was used. However, the technique is expensive, and lacks mass spectral libraries and suffers from matrix effects (Ferrer and Thurman, 2009).

LCMS determination of BPA and 2-NP

The intermediate products of BPA and 2-NP were separated and identified using a liquid chromatograph coupled to a mass spectrometer (Agilent 6230 TOF LC-MS). The Agilent 1260 Infinity series used comprise a binary pump, an auto-sampler and an 1100 diode array detector (DAD). Operating program was Mass Hunter software version 3.0. Mobile phase were water (0.1 % formic acid) and acetonitrile (0.1 % formic acid). Ionization of BPA intermediates was by electron spray ionization (ESI) and ions were captured in the negative mode while ionization of 2-NP was captured in the positive mode. The optimized gradient program used for elution and identification of intermediates on the LC-MS is shown in Table 3.11

Table 3.11: LC-MS parameters for identification of intermediates

HPLC parameters	Conditions		
Chromatograph	Agilent 6230 TOF LC/MS		
Detector	Agilent DAD 1100		
Column	Waters Symmetry C_8 15mm, 3.9mm 5µ		
Injection volume	5 µL		
Mobile phase	A: water (1% formic acid)		
	B: Acetonitrile (1% formic acid)		
Flow-rate	0.4 mL/min		
Gradient elution	Time	%A	%B
	0	85	15
	35	0	100
	47	0	100
	50	85	15
Temperature	26 ºC		
Data Collection	Mass Hunter		

3.4.14 *Inductive Coupled Plasma-Optical Emission Spectroscopy*

Inductive Coupled Plasma-Optical Emission Spectroscopy (ICP-OES) is an analytical technique mostly used in the determination of trace elements/metals in different sample matrices sometime at very low levels (parts per billion). The principle of operation involves emission of photons from excited atoms or ions in a radio frequency discharge. While liquid and gas can be injected directly into the instrument, solid samples should be digested first in such a way that the analyte of interest will be present in aqueous solution. The injected solution is converted to an aerosol and thereafter moved to the central compartment of the argon plasma and vapourised at approximately 10, 000 K (Dussubieux and Van Zelst, 2004). The analyte elements in the gaseous form are produced as free atoms. Further collision of atoms within the argon plasma zone cause promotion of atoms to excited states. There is also a significant amount of energy readily available to assist in the conversion of atoms to ions and eventual promotion of ions to the excited state (Dussubieux and Van Zelst, 2004). The emission of photons leads to relaxation of excited atoms and ions to the ground state. These photons possess unique energies determined for the atoms and ions using the quantized energy level structure. Thus the wavelength of the respective photons is then used to deduce the elements. The concentration of the elements in that particular sample is related to the number of photons from each element.

Sample preparation

The concentration of Ag, Ti, Fe, Cr and Si in the leacheate from the supported catalyst on a stainless steel mesh was determined using a Varian 710-ES ICP-OES instrument. Prior to that, the sample was filtered using a 0.22 µm membrane filter paper and the instrument was calibrated. The 8 mL of the sample was further diluted with 2 mL of 2% HNO_3. The sample was injected into the single-pass cyclone spray chamber via a high sensitivity glass and conical nebulizer using argon gas. The sample was then passed through the argon plasma and the respective wavelengths released for the individual elements were detected with a CCD detector. The sample were run through the instrument several times to check the variability of the results and average value were reported.

3.4.15 *Photoluminescence (PL) technique*

Photoluminescence technique otherwise called spectrofluorometry belongs to a category of electromagnetic spectroscopy which analyses fluorescence from a sample. The principle of FS is based on the excitation of electrons in a molecule of a specific compound under the influence of a beam of light (usually ultraviolet light) which causes the compound to emit a typical visible light (Vivian and Callis, 2001). The following light sources can be used as excitation sources: lasers, LED, and lamps; xenon arcs and mercury-vapour lamps. The light produced by the excitation source strikes the sample after passing through the monochromator. While a portion of the incident light gets absorbed by the sample, the remaining molecules in the sample fluoresce and this fluorescent light is emitted in all directions. The fluorimeter measures the intensity of the fluorescence. FS provides information on the electronic and vibrational state of a species under investigation (Caputo and London, 2003). The drastic loss of vibrational energy causes the molecule to drop down to the vibrational levels of the ground electronic state again. In the process of dropping, a photon comprising characteristics energies and frequencies is emitted. Thus, spectra of the different vibrational levels can be collected by analysing the frequencies of the emitted light alongside their relative intensity.

Sample preparation

Fluorescence spectrometry requires no special sample preparation. 4 cm^3 water sample containing 0.2 mM of 2-hydroxyl terephthalic acid was placed in a 4 cm^3 and their Fluorescence spectra recorded. The instrumental settings are shown in Table 3.12

Table 3.12: Photoluminescence (PL) technique operating parameters

Instrumental parameters	Conditions
Detector	S2
Excitation wavelength	350 nm
Entry slit	5 nm
Exit slit	5 nm lateral
Integration time	0.1s
Gratenc	1200/500

3.5 Chapter summary

The materials, experimental protocols including the characterization techniques have been provided in this chapter. The next chapter (Chapter four) contains the results and discussion on the various synthesised catalysts. The results of the preliminary investigation on the photocatalytic activity of the supported TiO_2 nanocrystals and Ag doped TiO_2 nanocomposites using MB as a pollutant will be presented and discussed respectively.

CHAPTER FOUR

SYNTHESIS, CHARACTERIZATION AND PHOTOCATALYTIC ACTIVITY

4 INTRODUCTION

This chapter presents the results and discussion of the characterization of the supported TiO_2 nanocrystals as well as Ag doped TiO_2 nanocomposites. Subsequently, the characterization results of the polymer stabilised and non-stabilised nano zero valent iron particles are also presented and discussed. Different analytical techniques such as X-ray diffraction (XRD), High resolution scanning electron microscopy (HRSEM), high resolution transmission electron microscopy (HRTEM), Selected Area Electron Diffraction (SAED), Electron Dispersion Spectroscopy (EDS), Ultraviolet-vis (UV-vis)/diffuse reflectance, X-ray diffraction (XRD), X-ray photoelectron spectroscopy (XPS), BET, the thermogravimetric analysis/differential scanning calorimetry (TGA/DSC), and Fourier transform infrared spectroscopy (FTIR) were utilised to characterise the synthesised catalysts. The results of the photocatalytic activity of the supported TiO_2 nanocrystals and Ag doped TiO_2 nanocomposites using methylene blue as a modelled pollutant are also presented in this chapter.

4.1 Characterization of the supported TiO_2 nanocrystals

High resolution scanning electron microscopy (HRSEM) was used to determine the morphology of the synthesised supported catalysts. The catalysts microstructure and average particle sizes were determined by high resolution transmission electron microscopy (HRTEM). Fourier transform infrared spectroscopy (FTIR) was utilized to identify functional groups in the synthesized materials. Selected Area Electron Diffraction (SAED) and Electron Dispersion Spectroscopy (EDS) were used to identify the nature of crystallinity and elemental composition of the catalyst, respectively. Ultraviolet-vis (UV-vis)/diffuse reflectance spectroscopy was used to acquire the diffuse reflectance spectra (DRS) of the catalysts while the thermal behaviour of the catalysts was investigated using thermogravimetric analysis/differential scanning calorimetry (TGA/DSC). X-ray diffraction (XRD) was used to identify the mineral phase and crystallite size. The specific surface area, pore size distribution of the as-synthesised catalyst were evaluated using BET and the surface chemical state was determined with XPS. The detailed sample preparation of the supported carbon doped TiO_2 nanocrystals was outlined in Chapter three, Section 3.2.2 and the results of the

characterization by HRSEM of the supported TiO_2 nanocrystals synthesised via the sol-gel method are presented as follows:

4.1.1 *The HRSEM results of the synthesised supported TiO_2 nanocrystals*

High resolution scanning electron microscopy (HRSEM) was used to monitor the crystal distribution and the morphology of the synthesised supported TiO_2 nanocrystals prepared via the sol-gel method described in Section 3.2.2. The HRSEM analysis was conducted according to the procedure described in Section 3.4.2. The sol-gel solution coated stainless steel mesh was treated in a furnace using a heating profile of 50 ºC/min from room temperature to either 300 ºC, 350 ºC or 400 ºC and held at this temperature for holding time between 1 to 4 hr under N_2 atmosphere of flow rate 20 mL/min. The pyrolysis was done under free flow N_2 because, it was discovered that under calcining air the TiO_2 nanocrystals separated and were not firmly attached to the stainless steel mesh. This is due to complete combustion of PAN in air versus pyrolysis of PAN in N_2. Figures 4.1 – 4.3 illustrates the HRSEM micrographs of the supported TiO_2 catalysts ramped at 20 ºC to 300 ºC, 350 ºC or 400 ºC respectively in N_2 atmosphere with a holding time of 1 to 4 hr at constant heating rate of 50 ºC/min. The catalyst code and synthesis conditions have been described in Table 3.2.

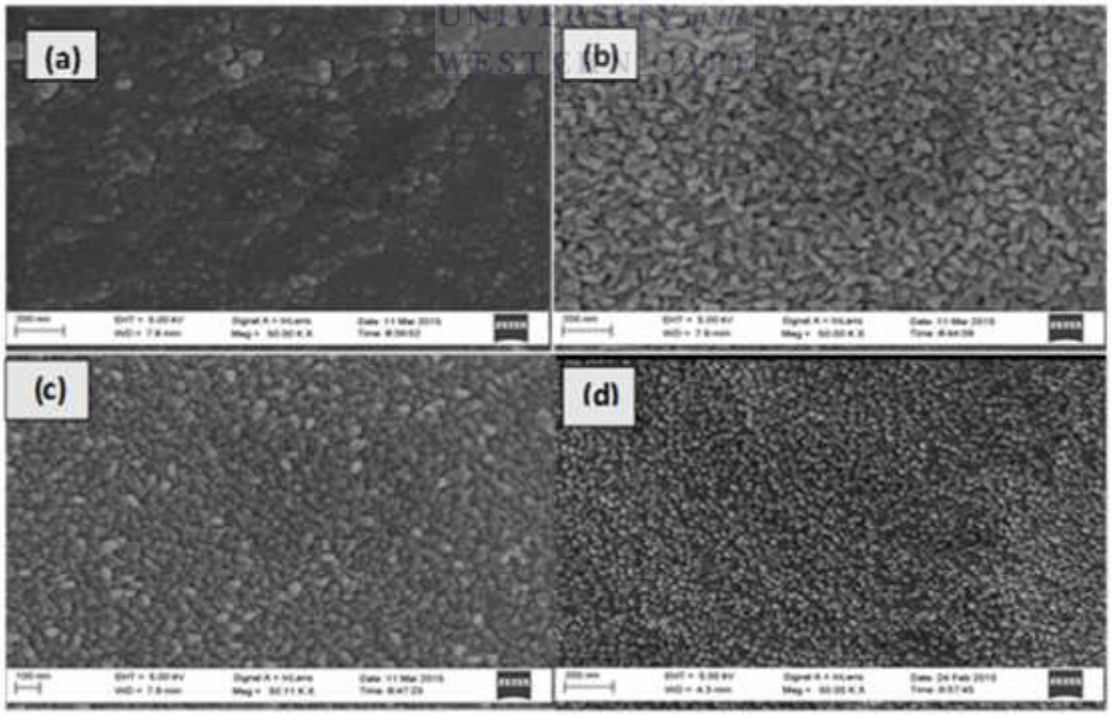

Figure 4.1: HRSEM image of catalyst prepared at 300 ºC: (a) JT1 (1 hr) (b) JT2 (2 hr) (c) JT3 (3 hr) (d) JT4 (4 hr) at constant heating rate of 50 ºC/min

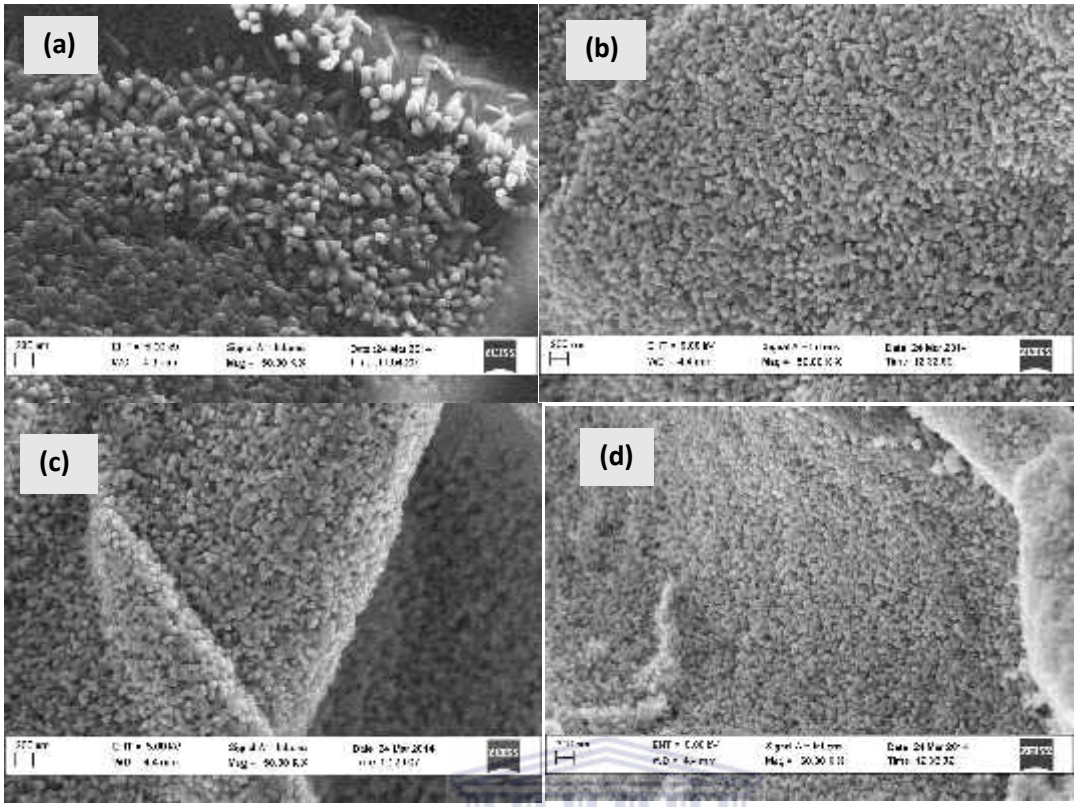

Figure 4.2: HRSEM image of catalyst prepared at 350 ºC: (a) JT5 (1 hr) (b) JT6 (2 hr) (c) JT7 (3 hr) (d) JT8 (4 hr) at constant heating rate of 50 ºC/min

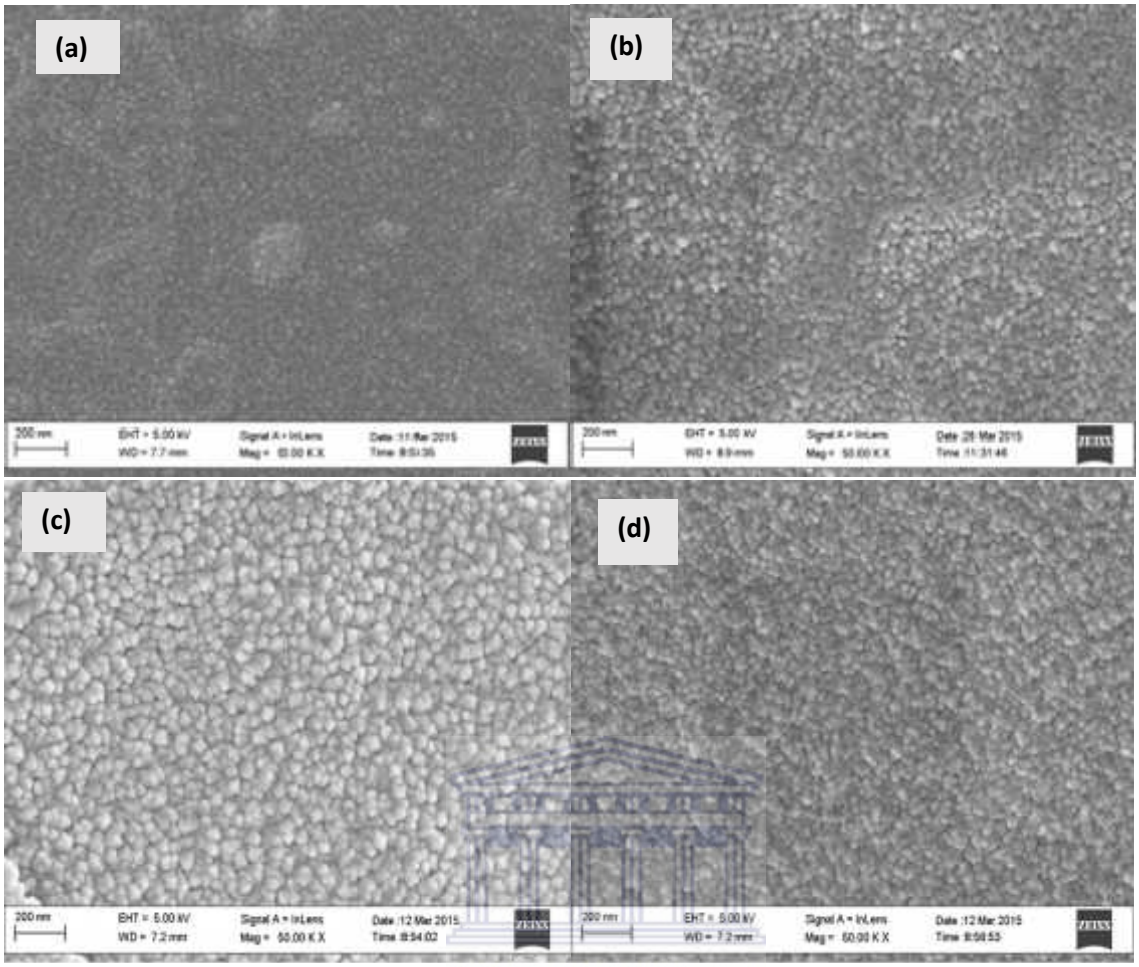

Figure 4.3: HRSEM image of catalyst prepared at 400 ºC: (a) JT9 (1 hr) (b) JT10 (2 hr) (c) JT11 (3 hr) (d) JT12 (4 hr) at constant heating rate of 50 ºC/min

Figure 4.1 depicts the HRSEM micrographs of the synthesised supported TiO_2 catalysts pyrolyzed at 300 ºC between 1 to 4 hr. The HRSEM image of JT1 (Fig. 4.1a), indicated the formation of irregular and scattered nanocrystals. This suggested pyrolysis of PAN since it is not stable above 200 ºC followed by initiation of crystallization of the $TiCl_4$ precursor into TiO_2 under the set conditions. It is important to mention that, in-situ crystallization process commenced immediately $TiCl_4$ was added to the PAN/DMF in a ventilated fume hood. During the stirred addition of 6 mL of 0.09 M $TiCl_4$, there was a sudden disappearance of the transparent solution and the appearance of a highly viscous brownish yellow colour (oxidation reaction). The sudden change of colour from transparent to brownish yellow under excessive air in a ventilated fume hood indicated oxidation reaction, this is $TiCl_4$ is known to oxidise to TiO_2 upon contact with air and subsequently released HCl as in the equation 4.1.

$$4{\sim}C_3H_3N + 4C_3H_7O + TiCl_4 \xrightarrow{excess\ air(\ O_2)} 4\,C_3H_3N - CO - NC_2H_6 + TiO_2 + 4HCl \uparrow \ldots\ldots(4.1)$$

Besides, there was a substitution of the oxygen atom in DMF by chlorine from $TiCl_4$ and subsequent replacement of the chlorine by oxygen resulting in the formation of TiO_2 nanoparticles. This was also evident with the release of a white fume of hydrochloric acid with a temperature increase, implying that the reaction was purely exothermic. Prior to the addition of $TiCl_4$, the temperature of the sol was 20 ºC and after the addition of the titanium precursor, the temperature rose to 41ºC. This indicated that oxygen in DMF or free oxygen in the ventilated fume hood displaced the chlorine in the $TiCl_4$ to yield TiO_2. After the manual coating of the sol-gel onto the stainless steel mesh, the coated mesh was air dried at room temperature in a ventilated fume cupboard for 10-15 minutes. The brownish colour later turn to black. The colour changes may be due to exposure to air. According to Rahaman et al., (2007) the phemenon and mechanism of appearance or disappearance of colour is complex and not fully understood. Nevertheless, the authors ascribed the black colouration of PAN on exposure to air to the formation of ladder ring structure due to conversion of the C≡N to C=N. The second reaction was the thermal pyrolysis of the PAN into carbon during the heating period inside the programmable tube furnace and complete formation of TiO_2 nanocrystals as shown in equation 4.2.

$$4\,C_3H_3N - CO - NC_2H_6 + TiO_2 \xrightarrow{heat\ (300-400^{\circ}C)\ in\ N_2\ atmosphere} 4C_2H_2O + 4C_2H_6N + 4HCN + 4C + TiO_2 \ldots\ldots(4.2)$$

At 2 hr holding time of JT2 (Fig. 4.1b), there was a sudden colour change from brown to black upon visual inspection, possibly due to pyrolysis and carbonization of the PAN polymer, or perhaps due to the decrease in the nitrile bond strength. The 2 hr heating period resulted in the formation of uniformly distributed and densely agglomerated TiO_2 nanocrystals. The shape and sizes of the TiO_2 crystals were not uniform and remained unchanged even at 3 hr holding time as shown in the HRSEM image of JT3. At this time (3 hr), PAN is undergoing pyrolysis and carbonization process leading to the disappearance of PAN peaks (see Figure 4.8 and 4.11). At 3 hr JT3 (Fig.4.1c), homogeneous, evenly distributed TiO_2 nanocrystals were observed. At 4 hr JT4 (Fig.4.1d), some nanocrystals fell off the mesh which could due to the prolonged holding time, which resulted in complete loss of carbonaceous species causing weak interaction between the stainless steel mesh and the TiO_2 nanocrystals. It is important to stress that PAN and its pyrolysis or decomposition

products acts as an adhesive that stick the TiO_2 crystals together onto the stainless steel mesh. However, when the holding time is too long or the temperature too high all the PAN and carbon burns away and the TiO_2 crystals fall off the mesh. Despite their loss off the mesh, the imaged crystals were still homogeneous, spherical, less agglomerated and loosely bound to each other.

In Figure 4.2 (a), at 1 hr holding time at 350 ºC (JT5), the formation of both TiO_2 nano rods and densely packed aggregated TiO_2 nanocrystals that stick to the stainless steel mesh were observed. At 2 hr (Fig.4.2b, sample JT6), the TiO_2 nano rods disappeared and thereafter transformed completely to fully grown, closely packed, identical TiO_2 nanocrystals. It was noticed that, there were no clear differences in the HRSEM micrographs of Fig. 4.2(b), (c) and (d) despite an increase in the holding time, all samples had a uniform particle size and longer holding times did not alter the spheroidal spherical crystal morphology. Again, uniformly monodispersed, spherical and agglomerated TiO_2 nanocrystals were evident. Also, during the photocatalytic activity, there was loss of crystals off the mesh at 4 hr holding time. This was plausibly due to structural changes of the polymer to carbon and complete conversion of titanium precursor to oxide which produced TiO_2 nanocrystals of identical samples and sizes in the inert environment. Abdo et al., (2013) had earlier reported that the carbonization process of PAN in air atmosphere at temperature of 600 ºC to 1000 ºC for 1 h at heating rate of 4.5 ºC/min was associated with release of more than 90% carbon and other volatile compounds such as HCN, H_2O, and N_2. Furthermore, a similar trend was observed at 400 ºC irrespective of the holding time (Fig. 4.3).The appearance of agglomerated spherical TiO_2 nanocrystals which showed some degree of homogeneity can be ascribed to extensive decomposition of PAN as the holding time increased. Although the shape and size of the nanocrystals were not uniform, it can be seen that the pyrolyzed temperature (300 ºC, 350 ºC and 400 ºC) and holding time (3 hr) had an effect on the size and the shape of the TiO_2 nanocrystals and upon their adhesion. Ba-Abbad et al., (2012) reported that temperature had a profound effect on the particle size, shape and catalytic activity of the TiO_2 nanoparticles synthesised via sol-gel method made up of titanium tetra isopropoxide (TTIP), ethanol and water.

Generally irrespective of the temperature, it was observed that at higher holding time specifically 4 hr, all the PAN decomposed and the TiO_2 crystals fell off the mesh. Based on this, 3 hr holding time was selected as the optimum holding time required to achieve uniform

crystals growth for the three temperatures. Beyond 3 hr holding time, there was a noticeable loss of the binding force between the stainless steel mesh and the TiO_2 nanocrystals, which ascribed to the extensive decomposition of PAN.

From the results presented (Figure 4.1 - 4.3), it is apparent that the supported TiO_2 nanocrystals are of different shapes and sizes, which occurred due to the heating conditions applied. In summary, two important reactions occurred during the synthesis of supported carbon doped TiO_2 nanocrystals: (i) oxidation of $TiCl_4$ to TiO_2 (in-situ crystallization mechanism as shown in equation 4.1): This took place prior to pyrolysis in the furnace. The crystals growth commenced immediately $TiCl_4$ precursor was added to the PAN/DMF solution in a ventilated fume hood. (ii) Thermal combustion of PAN in the furnace to different carbonaceous species (equation 4.2). It should be noted that the TiO_2 nanocrystals was strongly adhered onto stainless steel support using carbonaceous species resulting from pyrolysis of PAN. This was further substantiated by FTIR and XPS results shown in Figure 4.11 and 4.15 respectively.

4.1.2 *HRTEM-SAED analysis of the synthesised supported TiO_2 nanocrystals*

HRTEM and SAED was utilized to further examine the microstructure, morphology, crystalline nature and possible particle size of the supported TiO_2 catalyst prepared by pyrolysis at 300º, 350º, or 400º C for 1-4 hr. The detailed experimental protocol for the synthesis of supported TiO_2 nanocrystals via the sol-gel method is described in Section 3.2.2. The HRTEM analysis was conducted according to the procedure described in section 3.4.3. The HRTEM operated at 200 kV was employed to obtain the images (see Table 3.7). The HRTEM characterization results of the supported TiO_2 nanocrystals pyrolyzed at 300 ºC, 350 ºC or 400 ºC in N_2 atmosphere at 20 mL/min between 1-4 hr are represented in Figure 4.4 – 4.6.

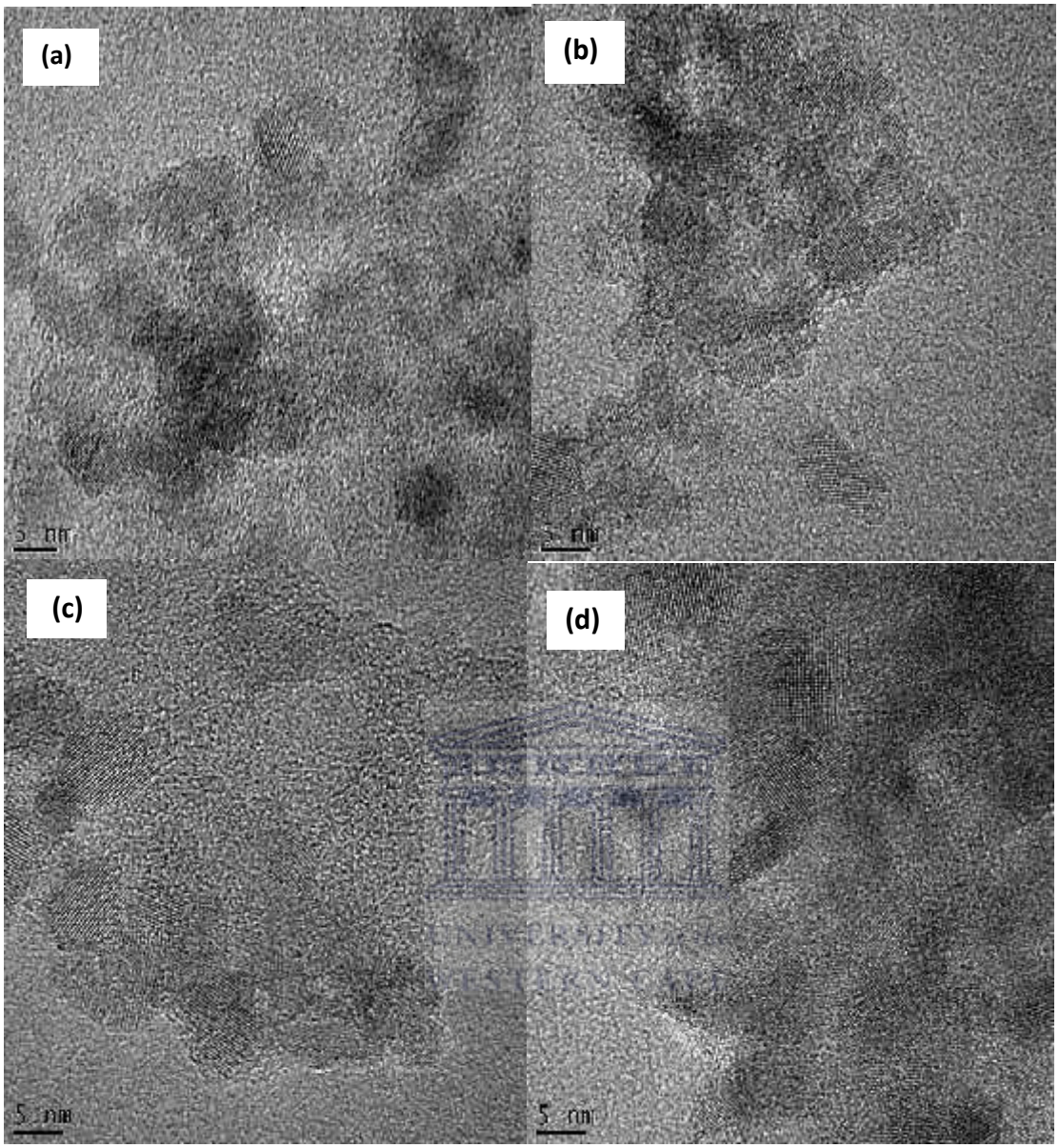

Figure 4.4: HRTEM image of catalyst prepared at 300 ºC: (a) JT1 (1 hr) (b) JT2 (2 hr) (c) JT3 (3 hr) (d) JT4 (4 hr) at constant heating rate of 50 ºC/min

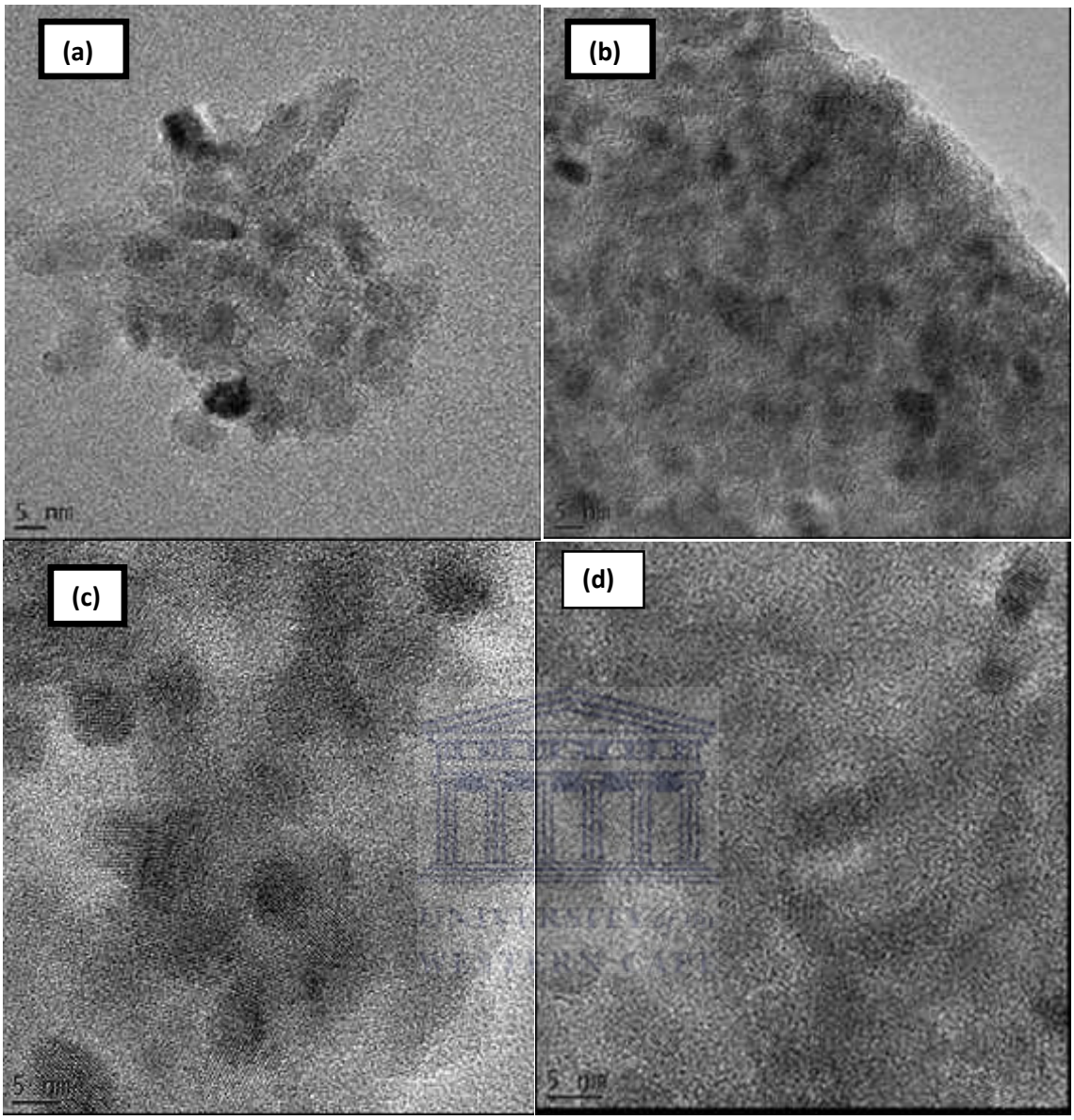

Figure 4.5: HRTEM image of catalyst prepared at 350 ºC: (a) JT5 (1 hr) (b) JT6 (2 hr) (c) JT7 (3 hr) (d) JT8 (4 hr) at constant heating rate of 50 ºC/min

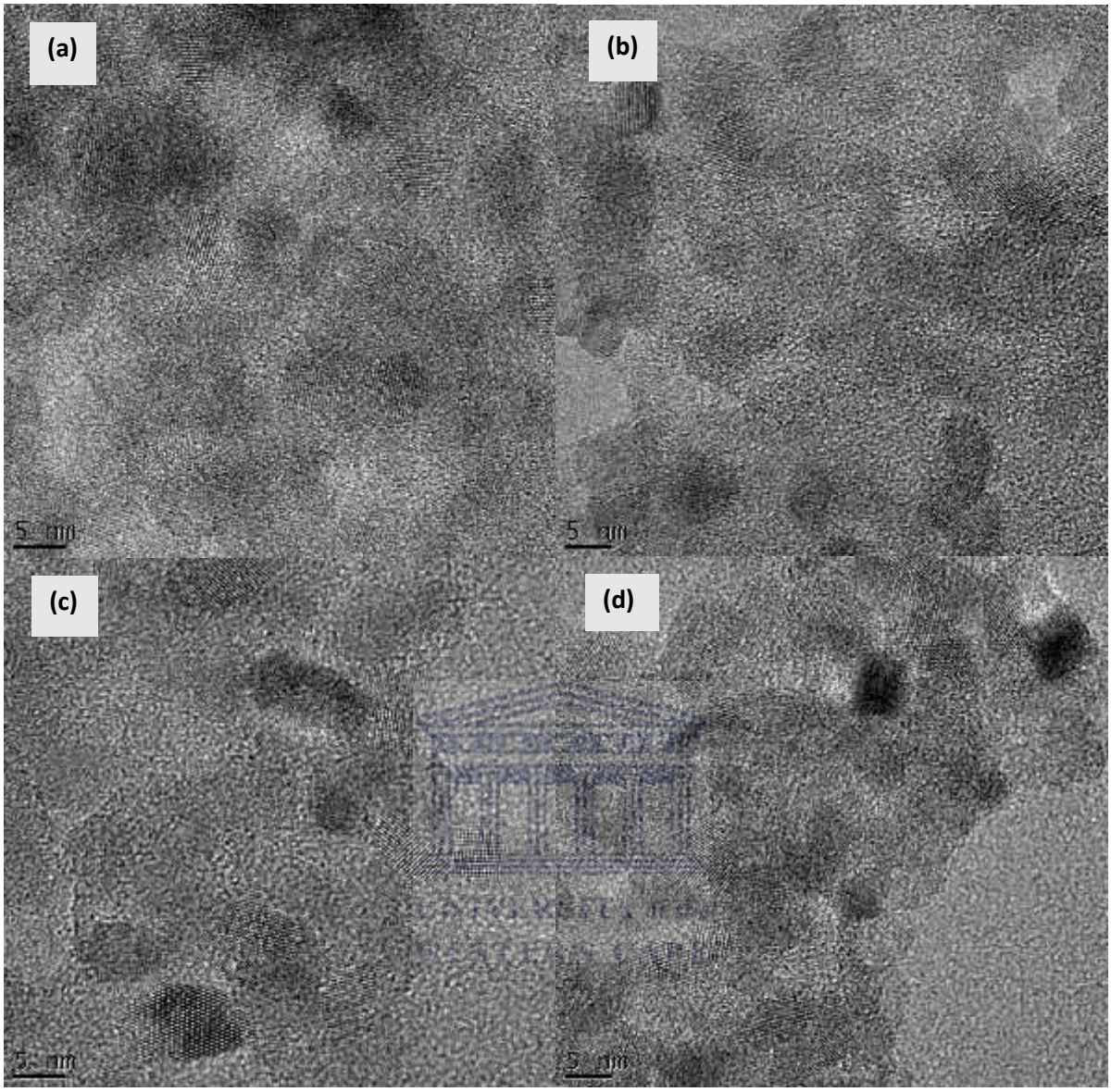

Figure 4.6: HRTEM image of catalyst prepared at 400 ºC: (a) JT9 (1 hr) (b) JT10 (2 hr) (c) JT11 (3 hr) (d) JT12 (4 hr) at constant heating rate of 50 ºC/min.

Figure 4.4 shows the HRTEM images of supported carbon doped TiO_2 nanocrystals prepared by pyrolyzed in N_2 atmosphere at 300 ºC between 1-4 hr. At 1 hr, sample JT1 (Fig.4.4a), there was an appearance of small crystal lattice fringes. The indistinct TiO_2 crystals at 300 ºC for 1 hr, indicates that some of the $TiCl_4$ precursor was still embedded in the slowly decomposing PAN polymer. With the increase in the holding time to 2 hr (Fig.4.4b), there were small TiO_2 crystallites which could be attributed to further decomposition of PAN. The TiO_2 lattice fringes became more clearly visible at 3 hr holding time (Fig.4.4c). Further increase in the holding time to 4 hr (Fig.4.4d) produced well resolved TiO_2 lattice fringes with interplanar spacing of about 0.35 nm, which agreed well with the lattice index of the

(101) crystallographic plane of anatase TiO_2 (Chang et al., 2009). The formation of a well-defined lattice fringes suggests high crystallinity (Cao et al., 2011). Figure 4.5 and 4.6 show the structural characteristics of the supported catalysts calcined at 350 ºC and 400 ºC for 1-4 h respectively. HRTEM micrograph of JT1 (a) and JT2 (b) indicates TiO_2 grains with no clear defined particle size while the HRTEM image of sample JT3-JT12 showed clear and well-resolved crystal lattice fringes of isolated particles with interplanar spacing of 0.352 nm. The SAED pattern of the supported TiO_2 nanocrystals pyrolyzed at 300ºC between 1-4 h are shown in Figure 4.7.

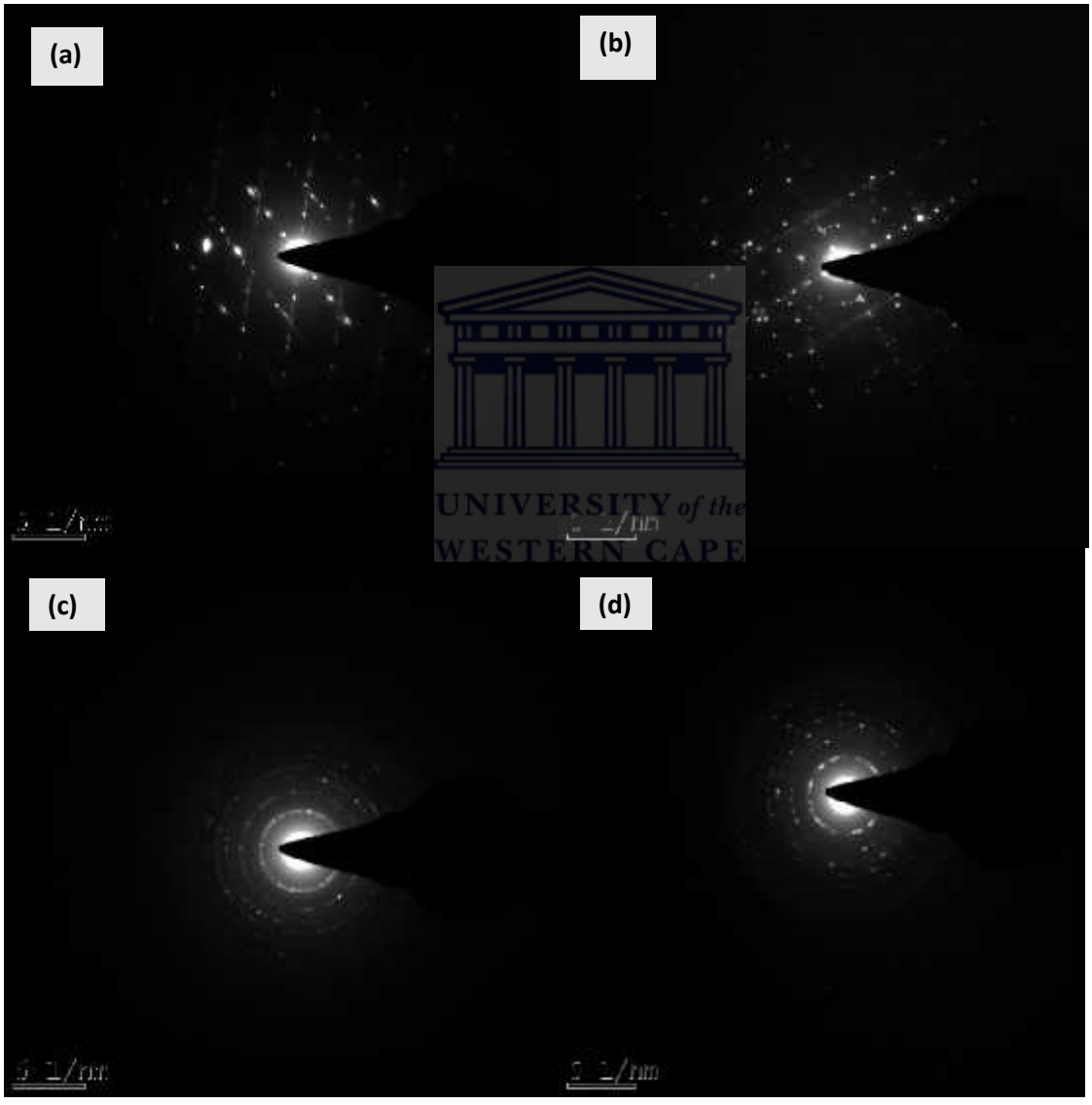

Figure 4.7: SAED of catalyst prepared at 300 ºC: (a) JT1 (1 hr) (b) JT2 (2 hr) (c) JT3 (3 hr) and (d) JT4 (4 hr) at constant heating rate of 50 ºC/min

The SAED image of sample JT1 (Fig.4.7a) and sample JT2 (Fig.4.7b) indicates the formation of overlapping crystal planes, but no polycrystallinity. With the exception of the SAED image of sample JT1 and JT2, other supported TiO_2 nanocrystals (not shown) exhibited a strong homogeneous polymorphic ring pattern with small dotted lines, which is an indication that the materials were very small polycrystalline particles irrespective of pyrolyzed temperature and holding time. Similarly, apart from what was observed in Fig. 4.7a and 4.7b, other reflections in the SAED pattern indicated lattice spacing distance of 0.354 nm corresponding to (101) crystal plane of a pure anatase phase, which is corroborated by the XRD results presented in Figure 4.11- 4.13. These results support previous studies conducted by Shirke et al., (2011) on the synthesis of pure anatase TiO_2 nanoparticles via microwave assisted sol–gel method, in which the SAED pattern of the synthesised material was polycrystalline in nature. This observations support the findings of Luo et al., (2012) who synthesised neat TiO_2 nanoparticles using a combination of polyacrylonitrile pre-oxidised in air at temperature of 200-300 ºC followed by modification with titanium dioxide nanoparticles.

4.1.3 *EDS result of the supported TiO_2 nanocrystals*

The EDS analysis was done to investigate the elemental composition of the supported carbon doped TiO_2 nanocrystals pyrolyzed at 300 ºC, 350 ºC and 400 ºC between 1-4 hr. The experimental procedure has been described in section 3.2.2 and the sample analysis was done following the steps explained in Section 3.4.4. The samples were coated with Pd and Au to prevent charging during SEM analyses, which can distort images. The weight percentage of each element as revealed by EDS is present in sample JT1-JT12 is represented in Table 4.1.

Table 4.1: Energy dispersive spectroscopy (EDS) spectrum of supported TiO_2 nanocrystals in atomic percentage at different pyrolyzed temperatures and holding time

Samples name	Elemental composition (Wt%)						
	Ti	O	C	Cr	Fe	Ni	Cl
JT1	25.21	31.35	19.73	7.15	8.12	3.92	3.52
JT2 Ti:O ratio (1:1)	27.78	32.11	17.98	5.74	7.21	3.54	5.64
JT3	37.14	31.56	14.17	4.04	7.64	2.87	2.58
JT4	39.45	29.76	10.54	7.29	8.23	2.52	2.21
JT5	43.56	30.37	10.34	4.41	7.45	2.53	1.34
JT6 Ti:O ratio (1:2)	44.88	28.75	8.86	5.45	7.50	3.45	1.11
JT7	45.13	26.94	8.23	4.49	7.92	3.40	3.89
JT8	43.55	30.30	7.81	5.33	6.97	2.88	3.16
JT9	45.57	27.50	5.32	6.28	8.19	4.12	3.02
JT10 Ti:O ratio (1:2)	45.38	32.80	5.25	5.52	6.02	2.61	2.42
JT11	54.89	22.64	4.41	6.19	6.80	2.09	2.98
JT12	68.04	10.32	2.31	6.88	7.56	1.38	3.51

According to Table 4.1, the supported TiO_2 nanocrystals contained the following elements: Ti, O, C, Cr, Fe, Ni, and Cl in different proportion irrespective of temperature and holding time. The values presented in Table 4.1 symbolised average of three spots scanned, which indicated that the values were representative. The weight percentage of Ti and O in each samples varied with pyrolyzed temperature and holding time. Even though, the EDS analysis is not a quantitative measure of the concentration of each elements in the sample, it can provide information on the type of elements in the sample. Thus, the presence of Ti and O confirmed the formation of TiO_2 nanocrystals via the sol-gel method. It can be seen from Table 4.1 that the ratio of Ti to O at 300 ºC was 1:1 and was 1:2 when the temperature

increased to 350 ºC and 400 ºC at a longer holding time of 3 hr. The observed ratio 1:1 suggested dilution by PAN at a lower temperature (300 ºC), which corroborates the XRD result shown in Figure 4.11, where graphitic carbon peaks were prominent. As the temperature increases, the Ti:O increases, which was an evidence of thermal pyrolysis and decomposition of PAN. The slow oxidation of $TiCl_4$ to TiO_2 during pyrolysis may be due to changing ratio of Ti to O. In the same vein, it can be seen in Figure 4.8 that, the weight percentage of carbon content decreased from 19.73 observed at 300 ºC for 1 hr to 2.13 at 400 ºC for 4 hr holding time. There was a clear decreasing in carbon content as temperature (300º - 400ºC and holding time (1 to 4 hr) increases, which suggested the partial and extensive decomposition of PAN. The decrease in the carbon content as evident in the EDS results corroborates the XRD results shown in Figure 4.11 - 4.13. This further confirmed direct carbon doping and the adhesion role the products of pyrolysis played.

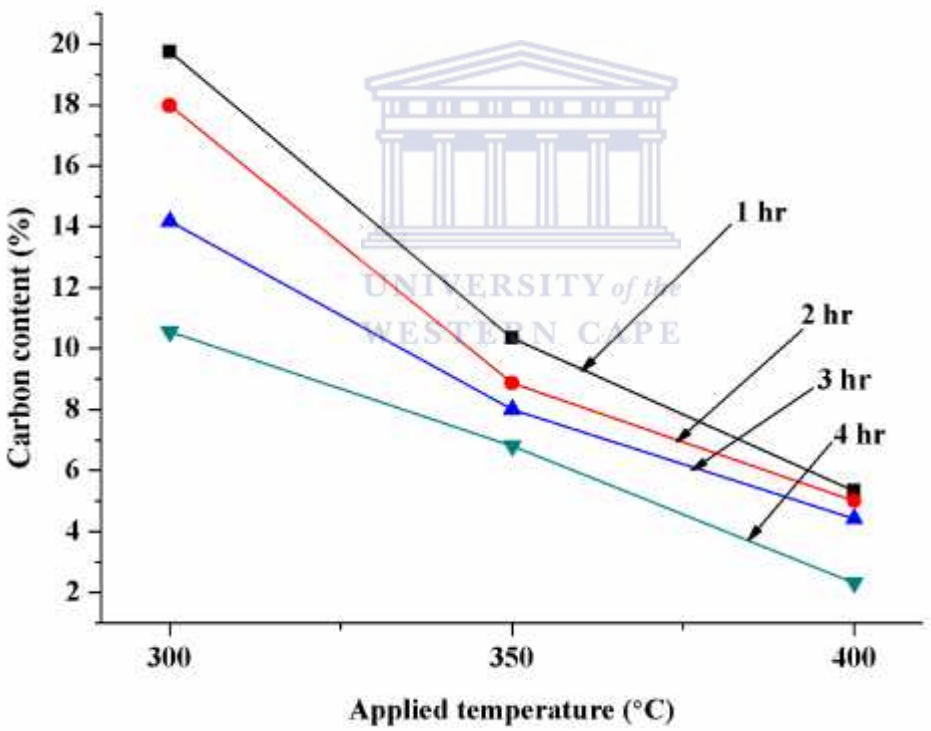

Figure 4.8: Carbon content in the supported TiO_2 nanocrystals prepared at different temperature and holding time.

Since the samples were not coated with carbon, the probable sources of carbon in the sample could be traced to the PAN or holey grids. However, XPS analysis carried out on the samples further confirmed that the amount of carbon in the catalysts did not come from holey

carbon grids but rather from PAN precursor (see Figure 4.24 a). In addition, Abdo et al., (2013) had earlier reported that carbonization process of PAN is associated with release of more than 90 % carbon and other volatile compounds such as HCN, H_2O and N_2. The presence of carbon in the EDS results suggests that PAN decomposed to carbon that was present in the supported TiO_2 nanocrystals, which is in agreement with the XPS results shown in Figure 4.14 - 4.17. Furthermore, the EDS spectra also indicated the presence of Fe, Cr and Ni, which originated from the stainless steel mesh owing to the thermal effect. The presence of chlorine could be linked to the titanium precursor used $TiCl_4$. The thermal treatment caused the diffusion of Fe, Cr, Ni from the stainless steel mesh onto TiO_2 layer according to their ionic radii. These elements (Fe, Cr and Ni) have been reported to also act as a dopant for titania (Fernández et al., 1995). Similar phenomenon was reported by Fernández et al., (1995) during the synthesis of TiO_2 photocatalysts on rigid supports such as stainless steel. The authors synthesised TiO_2 nanoparticles by dissolving 1 g of commercial TiO_2 (Degussa) in 100 mL acetone and subsequently utilised electrophoretic method to deposit TiO_2 particles onto the stainless steel. The supported TiO_2 nanoparticles were calcined in N_2 atmosphere at 700º C for 4 h and 8 h respectively. They found that Fe, Si, Cr from stainless steel diffused into titania lattice structure during thermal treatment.

4.1.4 *Thermal Gravimetric Analysis/ Differential Scanning Calorimetry (TGA-DSC) analysis*

The Thermal Gravimetric Analysis/ Differential Scanning Calorimetry (TGA-DSC) plots shows the physico-chemical structural changes such as loss of moisture and other volatile organic compounds present in the sample. The wet sol-gel solution (8% PAN/DMF/$TiCl_4$) obtained via the protocol described in Section 3.2.2 was subjected to thermal treatment process described in section 3.4.10. The results of the heat-profile of raw 8% PAN/DMF/$TiCl_4$ are presented in Figure 4.9. This was done in order to determine the temperature at which PAN starts decomposing.

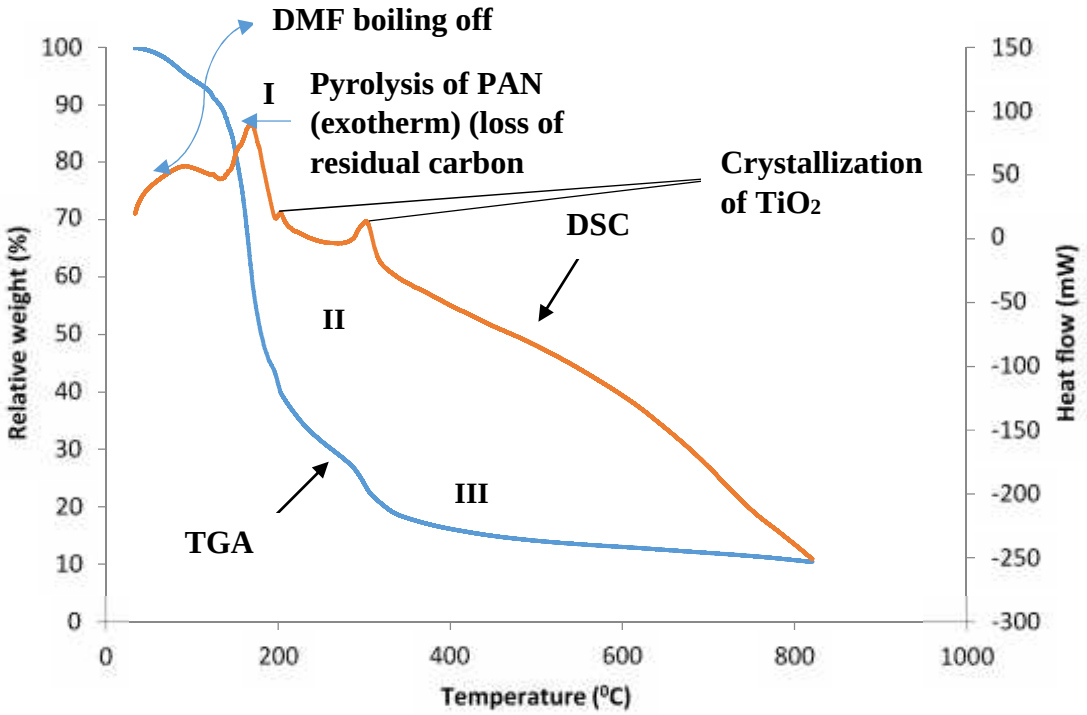

Figure 4.9: TGA-DSC curves of the wet sol-gel solution (8%PAN/DMF/$TiCl_4$) measured at a heating rate of 10°C/min in nitrogen atmosphere with a purging rate of 20 mL/min

The results presented in Figure 4.9 showed an increase in weight loss as the temperature increased. Substantial weight loss was observed before 350 °C after which the TGA curve remained nearly flat till 800 °C. There are three prominent weight losses as shown in the TGA curve. The first residual weight loss of ~10.2 % observed from 30-150 °C, was attributed to the dehydration of adsorbed DMF embedded within the PAN or bound to the PAN backbone. The second weight loss of ~50.8 % observed between 172 and 330 °C could be ascribed to the pyrolysis of unhydrolyzed PAN which was accompanied by a peak (exotherm) 172 °C. This is because PAN is not stable above 200 °C. Further weight loss of ~19.51 % before 350 °C could be due to decomposition of other residual intermediates carbonaceous species in the PAN as products of pyrolysis before complete carbonization. The DSC curve showed an endothermic peak localised at 137.7 °C, and two sharp exothermic peaks at 172°C and 300°C. A slight endothermic peak localised in the DSC curve at 137.7°C may be due to volatilization of DMF. The exothermic peaks between 172 °C and 300 °C may be linked to pyrolysis of PAN or reaction of oxidation of $TiCl_4$ to TiO_2 respectively. The TGA-DSC results are in good agreement with the XRD results shown in Figure 4.11. It is noteworthy mentioning that, lack of further exothermic peaks and very gradual or slight weight loss between 400 °C and 600 °C in DSC-TGA curve connoted complete decomposition of carbon precursor such as PAN or volatilization of residual carbon but no

phase changes from anatase to either rutile or brookite. Instead, the heat-treatment process enhanced the oxidation of $TiCl_4$ and formation of pure anatase TiO_2 phase, which was relatively thermally stable. No phase evolution or transformation occurred in the as-synthesised TiO_2 nanocrystals in spite of an increase in calcination temperature, which could be attributed to the particles size (see Table 4.3). However, the stability and formation of a specific polymorph of TiO_2 depends on surface free energy, surface stress and most importantly on the particle size (Leong et al., 2014; Miao et al., 2012). Li et al., (2007) had reported that the anatase polymorph of TiO_2 with particle size less than 14 nm was more thermodynamically stable than rutile or brookite. Abdo et al., (2013) reported exothermic reaction for typical PAN/Ag particles in the temperature range of 200 ºC and 350 ºC. The authors ascribed the exothermic peaks at 300 ºC to cyclization of the nitrile groups of PAN and loss of HCN, N_2 and others. This also agrees with the submission of Miao et al., (2012) and Suwarnkar et al., (2014) which independently linked the exothermic peaks localised at this temperature range to the degradation of organic residues or moieties.

4.1.5 *FTIR of the supported TiO_2 nanocrystals*

The structural elucidation vis-a-viz the functional groups/absorption peaks formed during the chemical interaction, stabilization and pyrolysis process of PAN/DMF/$TiCl_4$ was investigated using the FTIR technique as described in section 3.4.9. The preparation of the supported TiO_2 nanocrystals via mixing of PAN and DMF with $TiCl_4$ followed by thermal treatment was presented in section 3.2.2. Figure 4.10 illustrates the FTIR profile of PAN, PAN/DMF and 8% PAN/DMF/$TiCl_4$. While Figure 4.11 shows the FTIR spectra of supported TiO_2 nanocrystals pyrolyzed at 300 ºC, 350 ºC and 400 ºC for 3 hr. The distinctive absorption bands of PAN, PAN/DMF, 8% PAN/DMF/$TiCl_4$ and supported TiO_2 photocatalyst pyrolysed at different temperature and holding time is provided in Table 4.2.

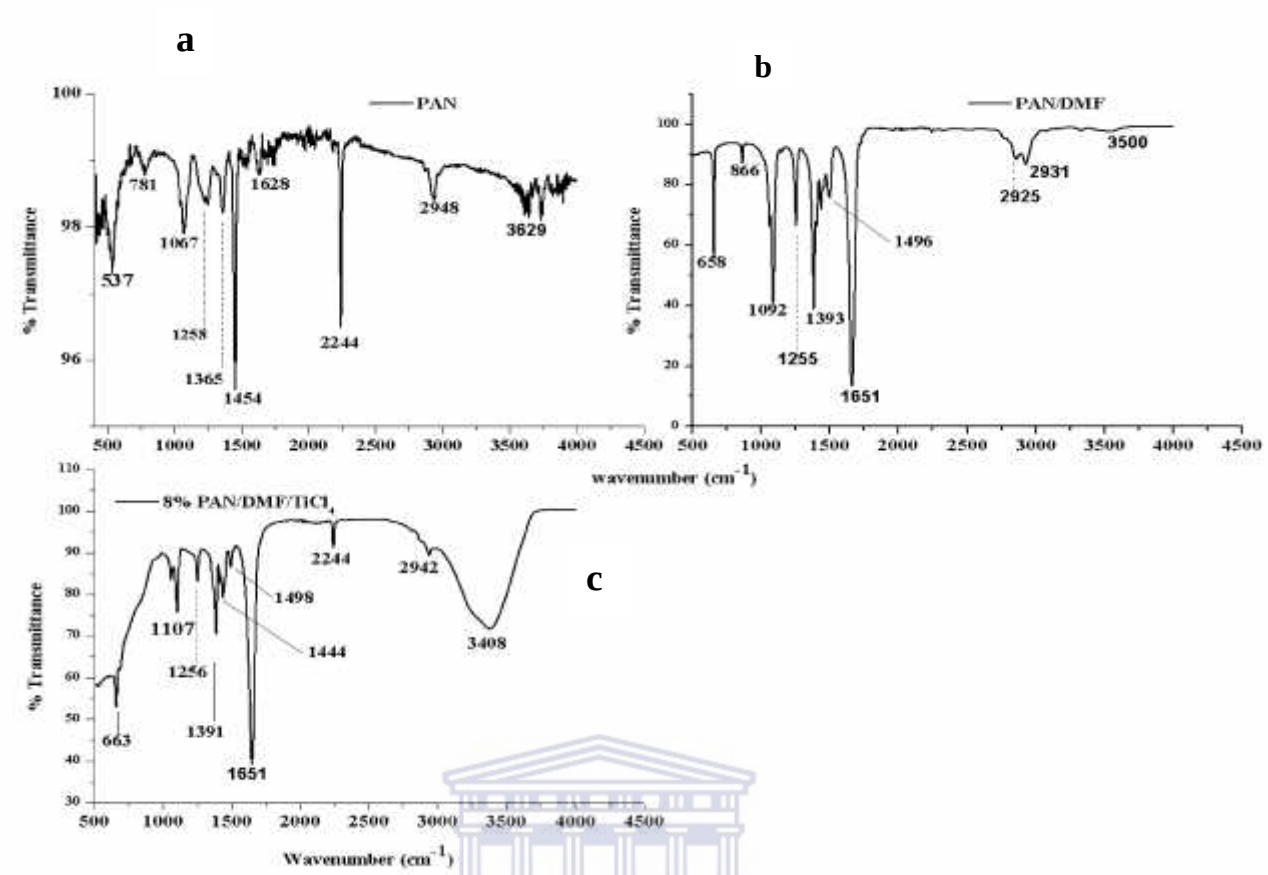

Figure 4.10: FTIR spectra of: (a) ordinary PAN (b) sol PAN/DMF (c) 8% sol-gel solution of PAN/DMF/$TiCl_4$ prior to pyrolysis in the programmable tube furnace

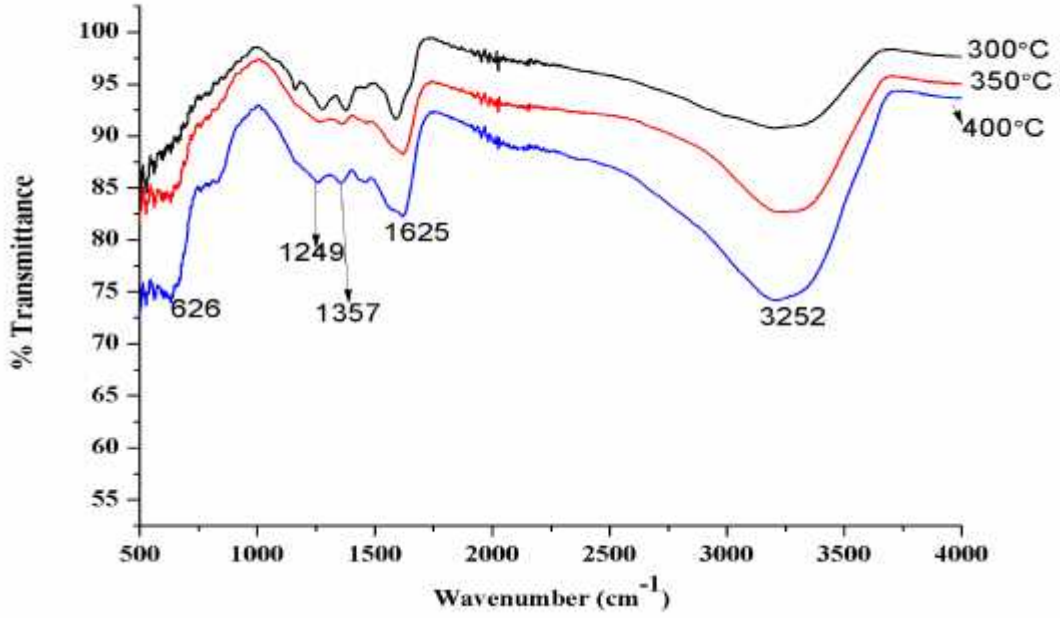

Figure 4.11: FTIR spectra of (i) JT3 (300 °C for 3 hr) (ii) JT7 (350 °C for 3 hr) (iii) JT11 (400 °C for 3 hr)

Table 4.2: Characteristic absorption bands and strength of PAN, PAN/DMF, 8% PAN/DMF/$TiCl_4$ and supported TiO_2

Absorption bands/ constituents	Functional groups						
	-C≡C or C-C	**Aliphatic group CH, CH_2, CH_3**	**Carbonyl group C=O, C=C, C-O**	**O-H(bending)**	**Nitrile stretching C≡N**	**N-H wag**	**C-H stretching**
Absorption band characteristics (cm^{-1})	610-700	1395-1200 1465-1405 2950-2850	1750 - 1590	1650-1630	2260 – 2220	910-665	3500 - 3200
PAN	Nil	Strong strong strong	Medium	Nil	Strong	Nil	Nil
PAN/DMF	strong	Medium Strong	Nil	Strong	Weak	strong	weak
8% PAN/DMF/$TiCl_4$	medium	Strong	Nil	Strong	Medium	medium	strong
JT3	Nil	Weak	Nil	Medium	Nil	Nil	weak
JT7	Weak	Nil	Nil	Medium	Nil	Nil	weak
JT11	Weak	Nil	Nil	Medium	Nil	Nil	medium

According to Figure 4.10 (a), the FTIR spectra of PAN revealed the presence of the following absorption bands at 3629, 2948, 2244, 1628, 1454, 1365, 1258, 1067 and 537 cm^{-1} respectively. Out of which, four absorption peaks observed at 2244 (C≡C), 1454 (C-C) and 1365 cm^{-1} (C-H) and 2948 cm^{-1} had strong intensity (see Table 4.2). The absorption band at 2948 cm^{-1} is normally assigned to C≡N.

DMF is one of the polar solvent mostly used to dissolve PAN as such the dissolution of PAN by DMF resulted in formation of strong intermolecular attraction and new functional groups. The FTIR spectrum of PAN/DMF is shown in Figure 4.10 (b), the following distinct absorption bands appeared at 3500, 2931, 2925, 1651, 1496, 1393, 1255, 1092, 866 and 658 cm^{-1} respectively. Of all the absorption peaks, the following had strong absorption peaks: 1651 cm^{-1}(C=O), 1393 cm^{-1}(C-H), 1255cm^{-1}(C-N), and 658 cm^{-1}(N-H) appeared for a typical PAN/DMF (see Table 4.2). According to Zhang et al., (2011), three of the absorption peaks such as 1651, 1393 and 658 cm^{-1} corresponded to a typical DMF spectrum with absorption band C=O, C-N and N-H respectively. With the dissolution of PAN by DMF, there was a complete disappearance of absorption peaks observed at 2244 and 1457 cm^{-1} observed in PAN. Besides, the intensity of the absorption band at 2948 cm^{-1} reduced and new adsorption bands at 2931 and 2925 cm^{-1} with medium intensity were observed in PAN/DMF. These new absorption bands was assigned to C-H. Also noteworthy of mentioning was the slight appearance of a weak absorption band at 3500 cm^{-1} in PAN/DMF, which was assigned to N-H.

With the drop-wise addition of $TiCl_4$ to PAN/DMF solution (Figure 4.10 (c), there was a complete disappearance of absorption peak at 866 cm^{-1} (C-C) in DMF and a significant decrease in the strength of the following absorption bands: 1393, 1255, 1093 and 658 cm^{-1}. The intensity of absorption bands at 2244 and 2942 cm^{-1} (C≡N) observed in PAN equally reduced (see Table 4.2). There was formation of a broad O-H at 3408 cm^{-1} bond upon the addition of $TiCl_4$ to PAN/DMF. This may be due to substitution effect of oxygen in DMF with chlorine in $TiCl_4$ and replacement of chlorine with oxygen (oxidation step) as shown in equation 1.

Furthermore, the pyrolysis of 8% PAN/DMF/$TiCl_4$ produced supported TiO_2 nanocrystals, which was accompanying by volatilization of the solvent (DMF) and decomposition of PAN.

The volatilization of DMF during heating in a furnace at different temperatures resulted in the complete disappearance of the following absorption peaks: 1651, 1444, 1498, 1391, 1256 and 1107 cm^{-1} which indicated the loss of N_2, HCN and other volatile compounds. While the carbonization process of the PAN was accompanied with the loss of absorption peaks at 2244 and 2942 cm^{-1} (C≡N) and formation of new absorption peaks in the sample JT3, JT7 and JT11 shown in Figure 4.11. After the carbonization process, most peaks identified in PAN were however absent in the supported TiO_2 nanocrystals. This further confirms thermal pyrolysis and decomposition of the PAN. The FTIR of sample JT3, JT7 and JT11 indicated formation of both weak and medium absorption peaks at 3252 (O-H), 1625 (C=C) and 625 cm^{-1} (C≡C) respectively. The strength of these peaks varies with the catalysts, which can be attributed to difference in the applied pyrolysis temperature. Complete disappearance of the absorption peak at 2243 cm^{-1} assigned to C≡N was due to the thermal pyrolysis and decomposition of PAN in nitrogen environment. This further agrees with the DSC results (Figure.4.9). The weak absorption band at 625 cm^{-1} is related to the C≡C or Ti-O-C bond. Ti-O-C point towards interaction between the Ti-O, and the C=O and C-O groups present in the PAN. This was an indication of residue of carbon doping on TiO_2 nanocrystals, which also suggested carbon being doped onto the TiO_2 lattice structure. This further supports the XPS results (see Figure 4.18). Additionally, when comparing the FTIR spectra of the calcined supported TiO_2 nanocrystals with the starting materials PAN and DMF, it is evident that, there was a complete disappearance of most identified peaks in PAN, suggesting complete thermal decomposition of the polymer during pyrolysis.

4.1.6 *XRD analysis*

X-ray diffraction (XRD) was used for phase identification and estimation of the average crystallite sizes of the synthesised supported catalysts at 300 ºC, 350 ºC and 400 ºC for different holding time of 1- 4 hr in N_2 atmosphere at 20 mL/min as previously noted. The obtained supported TiO_2 nanocrystals after pyrolysis was further characterized using XRD. The detailed experimental protocol, sample preparation and instrumental conditions for measurement has been described in Sections 3.2.2 and 3.4.1 respectively. The results of the XRD analysis of the supported TiO_2 nanocrystals pyrolysed in the furnace at different temperature and holding time are displayed in Figure 4.12 – 4.14.

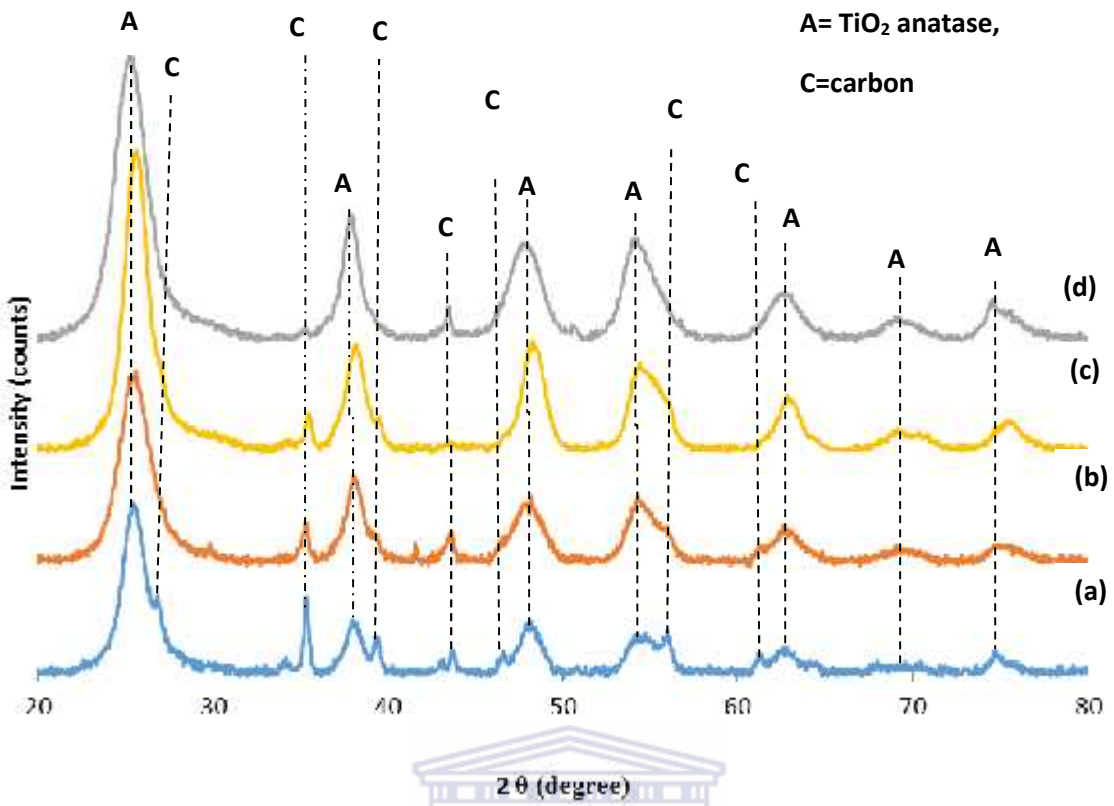

Figure 4.12: XRD pattern of the catalysts: (a) JT1 (300 ºC for 1hr) (b) JT2 (300C for 2 hr) (c) JT3 (300 ºC for 3 hr) and (d) JT4 (300 ºC for 4 hr)

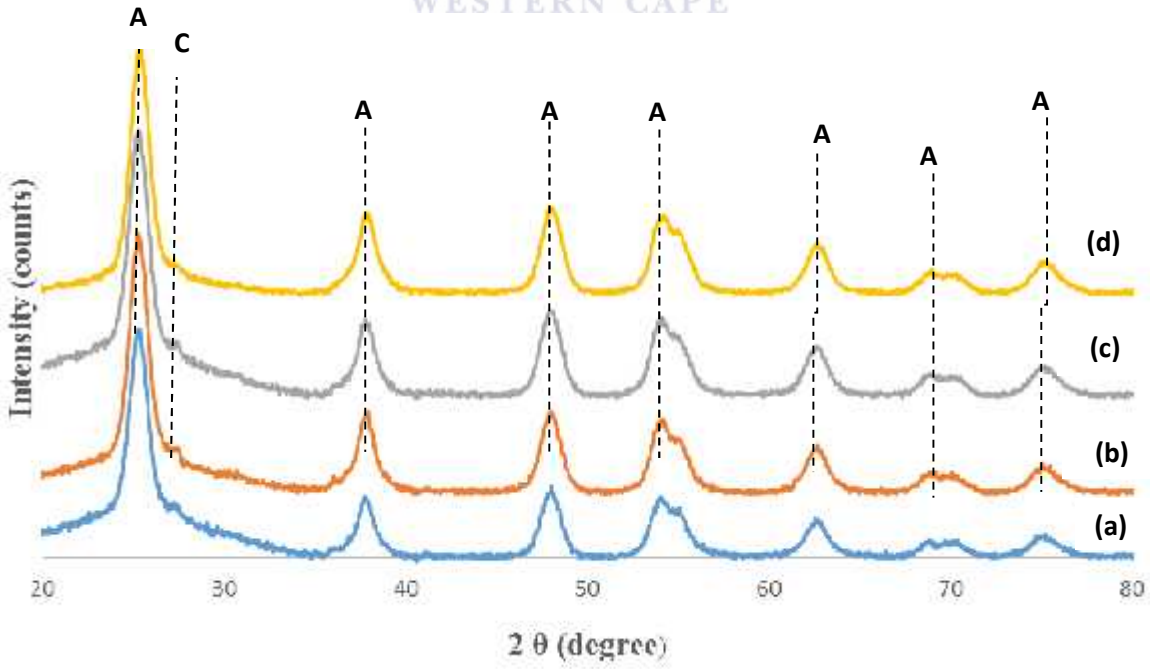

Figure 4.13: XRD pattern of the catalysts: (a) JT5 (350 ºC for 1 hr) (b) JT6 (350 ºC for 2 hr) (c) JT7 (350 ºC for 3 hr) and (d) JT8 (350 ºC for 4 hr)

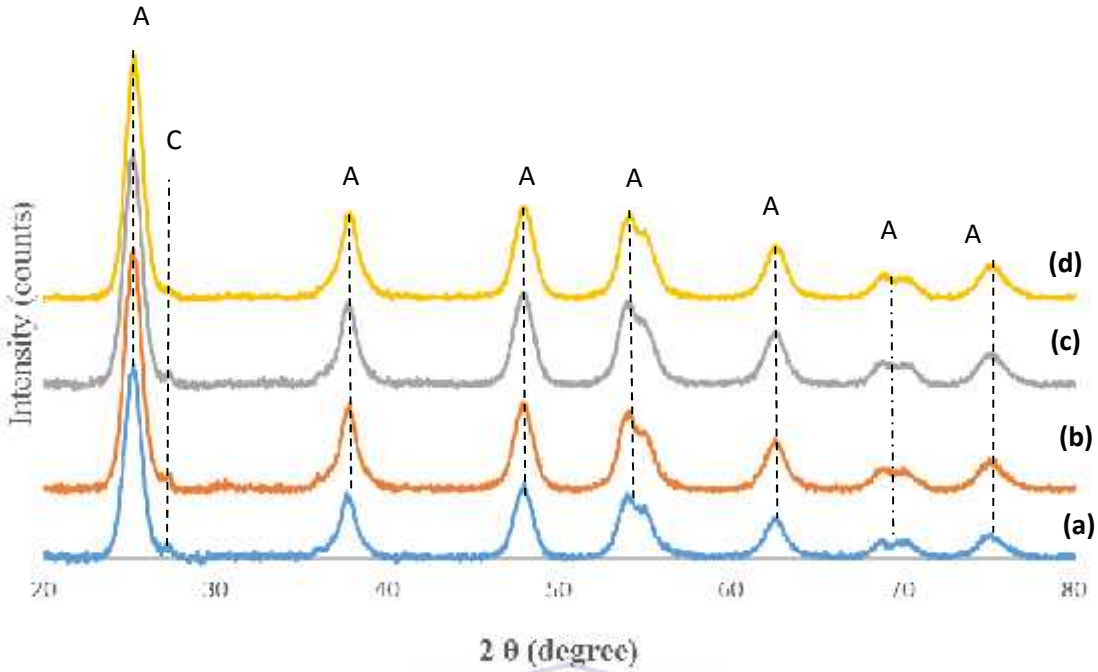

Figure 4.14: XRD pattern of the catalysts: (a) JT9 (400 ºC for 1 hr) (b) JT10 (400 ºC for 2 hr) (c) JT11 (400 ºC for 3 hr) (d) JT12 (400 ºC for 4 hr)
A=anatase, C=carbon

Figures 4.12 - 4.14 depict the X-ray diffraction patterns of the supported catalysts pyrolyzed at 300 ºC, 350 ºC or 400 ºC for holding times between 1-4 hr. All the XRD patterns except Figure 4.12 (a-c) clearly demonstrated strong, sharp and relatively intense diffraction peaks at 2 thetha values of 25.3º, 37.8º, 49.55º, 55.10º, 62.60º, 68.8º, and 75.70º irrespective of the holding time. These diffraction peaks indicate the presence of following crystal planes (101), (004), (200), (211), (204), (220), and (215). For each holding time, the XRD patterns indicated the formation of pure anatase polymorph of TiO_2 (JCPDS: No 21-1272). There were no rutile or brookite phases detected within the x-ray detection limit at each holding time. In contrast, the XRD pattern at 300ºC for 1 h (Figure 4.12a), exhibited weak diffraction peaks at 26.3º, 36.1º, 39.2º 41.8º, 45.4º, and 60.5º, which corresponded to crystal plane (002), (111), (100), (200), (204) and (220) of a typical carbon species originating from PAN. At this holding time, it was shown that PAN was pyrolysis and oxidation of $TiCl_4$ precursor into TiO_2 occurred concurrently. Additionally, at 300 ºC for 1 h, diffraction peaks at 72.4º, which corresponded to crystal plane (220) was yet to develop, which suggested slow growth of TiO_2 crystallites. Furthermore, as shown in Figure 4.12(a-c) the diffraction peak intensity at 36.1º

of the crystal plane (110) decreased significantly with an increase in holding time from 1 to 3 h. This might be ascribed to further decomposition of PAN. More so, as the holding time increased from 2-3 h at 300 ºC, the diffraction peak of (220) became more intense indicating crystal growth while several other carbon peaks that had been identified at 1 h holding time disappeared. The intensity of the diffraction peak at (220) increased up to 4 h holding time. Furthermore, after 3 h holding time, the peak corresponding to crystal plane (110) disappeared completely and this suggests pyrolysis of graphitic species derived from PAN. In spite of the broad diffraction peaks and presence of carbon species, the synthesised supported TiO_2 nanocrystals were still dominated by pure anatase crystallite phase. This result is in accordance with Shirke et al., (2011) who also obtained pure anatase phase for unsupported TiO_2 nanoparticles synthesised via microwave assisted sol–gel method, calcined at 300 ºC for 1 h. Conversely, Li and co-workers (2002) did not obtain peaks corresponding to anatase phase for TiO_2 nanoparticles annealed at 300ºC for 1 hr. Instead they found a mixture of rutile and brookite phases dominated. Leong et al., (2014) had reported that during thermal treatment of a sol-gel solution containing titanium precursor at different calcination temperature, the Ti-O-Ti bonds in the sol-gel crystallize into TiO_2, and the heat results in residual water loss and loss of other volatile organic components. Thus, the complete morphological transformation observed by HRSEM (Fig. 4.2 to 4.3) at 350 ºC and 400ºC irrespective of holding time suggested that all $TiCl_4$ precursor species were converted to form TiO_2. Furthermore, the XRD pattern of the supported catalyst annealed at 350 ºC and 400 ºC (Figure 4.13 - 4.14) for different holding time are similar. It is should be noted that the peak at 26.3º, which was attributed to carbon species was common to all samples especially at 350º and 400 ºC. This suggests the existence of Ti-O-C bond and substitutional effect of oxygen in TiO_2 by a carbon species from PAN precursor. This corroborated XPS results shown in Figure 4.14. The calcined samples at (350 – 400 ºC) demonstrated a pure anatase crystalline phase as shown in the HRTEM (Figure 4.5 to 4.6) and XRD patterns (Figure 4.13 to 4.14) where the peak intensity increased monotonically with holding time and the full width at half maximum (FWHM) of the peaks became narrower. The sharp and more intense diffraction peak observed irrespective of the holding time was attributed to heat treatment which increase the crystallinity and average crystallite size. This is, however, different to the broad diffractograms observed at 300 ºC as shown in Figure 4.12. Critical evaluation of the relative intensity of the characteristics diffraction peaks (Figure 4.12 - 4.14), for all the synthesised catalysts, indicates that the TiO_2 crystallization process was promoted by both pyrolyzed

temperature and holding time (see Table 4.3). The average crystallite size for the intense anatase peak (101) in the synthesized TiO_2 nanocrystals was calculated using Debye-Scherrer equation as shown in equation 4.3.

$$d = \frac{k^{a}}{\cos} \quad \text{.....(4.3)}$$

Where d is crystallite size in nanometer, K= 0.94, λ is the wavelength of the X-ray which is 0.1541 nm, θ is the half-diffraction angle, β is the full width at half-maximum in radian of 2 θ value (25.30). Using the above equation, the average crystalline size for each applied condition was estimated and the obtained value is shown in Table 4.3. The 2 θ value (25.30), θ (12.65) and cos θ (0.9757) at 300 ºC, 350 ºC or 400 ºC were the same irrespective of the holding time.

Table 4.3: Crystallite size of the synthesised supported TiO_2 pyrolyzed at 300ºC, 350 ºCand 400 ºC for holding time 1- 4 h

Samples	Width in half-high/º	Width/radian	Particle size (nm) (XRD)
300 ºC			
JT1	1.70	0.0296	4.05
JT2	1.90	0.0333	5.01
JT3	1.30	0.0227	6.51
JT4	1.20	0.0209	7.09
350 ºC			
JT5	0.81	0.0140	10.6
JT6	0.75	0.0130	11.4
JT7	0.66	0.0114	13.0
JT8	0.65	0.0114	13.3
400 ºC			
JT9	1.1	0.0191	11.2
JT10	0.80	0.0139	13.6
JT11	0.75	0.0131	14.2
JT12	0.60	0.0104	14.3

According to Table 4.3, it can be seen that the longer the pyrolysis time at each temperature, the larger the crystals. Also, the higher the temperature the larger the crystal size. The average particle size increases with increasing holding time especially for samples JT5-JT8 and JT9-JT12 (Table 4.3). This suggests that the particle size and crystalline phase depends on the pyrolysis temperature as well as the holding time. Comparing the particle size of the various synthesised TiO_2 nanocrystals at different temperatures and holding times, it is obvious from Table 4.3 that the particle size of the supported TiO_2 nanocrystals pyrolyzed at 300 ºC (Figure.4.12) for 1-4 h increased from 5.01 nm to 7.09 nm as holding time increases. The small nanoparticle size was shown by peak broadening caused by growth/nucleation of TiO_2 crystals during extended heating. Thus, thermal treatment of 8% PAN/DMF/$TiCl_4$ in N_2 atmosphere at different temperature and holding time had a significant impact on the nature of TiO_2 and determined the average crystallite sizes. This study further demonstrated a way to control the particle size of TiO_2 directly during supporting procedures in one step. Luo et al., (2012) had reported similar behaviour on the PAN/TiO_2 nanoparticles synthesised from pre-oxidized PAN/DMF solution containing titanium precursor in normal air. Gupta et al., (2013) showed that calcination of unsupported TiO_2 powder in air at 450 ºC for 30 min increased both the crystallinity and its photocatalytic activity. Their results however contradict the findings of Dong et al., (2011) who reported that thermal treatment of unsupported TiO_2 nanoparticles prepared from a mixture of $Ti(SO_4)_2$, $C_{12}H_{22}O_{11}$ and H_2O followed by calcination at 100, 200, 300 ºC for 2 h had no effect on the average crystals size of TiO_2 nanoparticles.

4.1.7 *X-ray photoelectron spectroscopy (XPS) analysis*

The XPS measurements were conducted to determine the electron structure and surface valence states of each element contained in the supported catalyst synthesised via sol-gel method. Sample JT7 (prepared at 350 ºC for 3 hr) was selected due to its higher photocatalytic activity compared to others (see Section 4.20). The detailed XPS sample preparation and instrumental operating conditions have been described in section 3.4.7. Figure 4.15 represents the general XPS survey of supported TiO_2 nanocrystals calcined at 350 ºC for 3 h (JT7), which indicated the presence of Ti, O, C, Fe, Cl and N. Figure 4.16-4.18 represents the XPS spectrum of individual elements namely Ti 2p, O 1s, C 1s, N 1s, Cl 2s or 2p, and Fe 2p or 3p in the following order of binding region Ti 2p (459.2 eV), O 1s (465 eV), C 1s (284.6 eV). Other elements such as N 1s, Cl 2s or 2p, and Fe 2p or 3p are explained below.

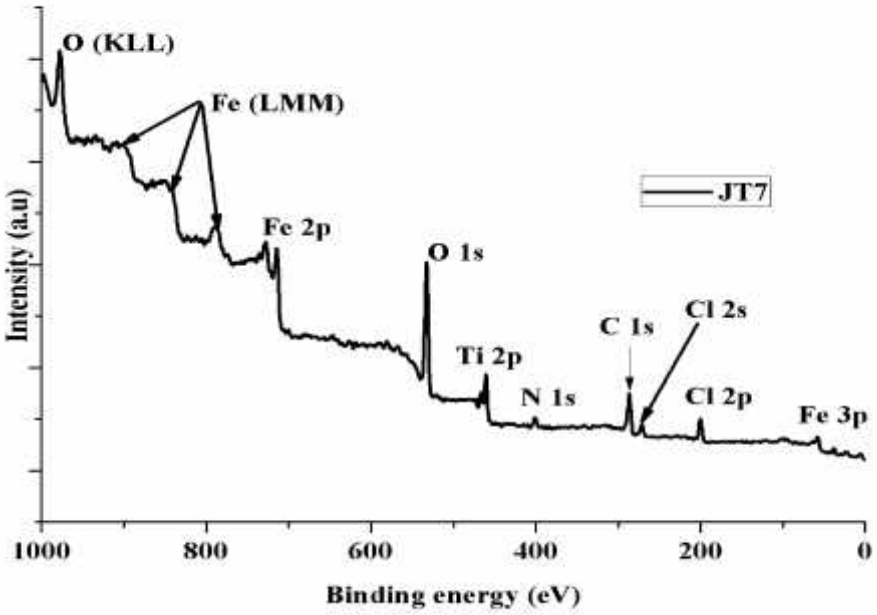

Figure 4.15: General XPS survey of sample JT7 indicating elements within the detection limit.

According to Figure 4.15 which represents the general survey of the synthesised sample JT7, there are presence of Ti 2p and O 1s peaks in binding energy regions of 459.12 and 530.6 eV respectively. Additionally, the magnified Ti 2p shell shown in Figure 4.16, had two peaks in the binding energy region of 459.2 and 465.7 eV.

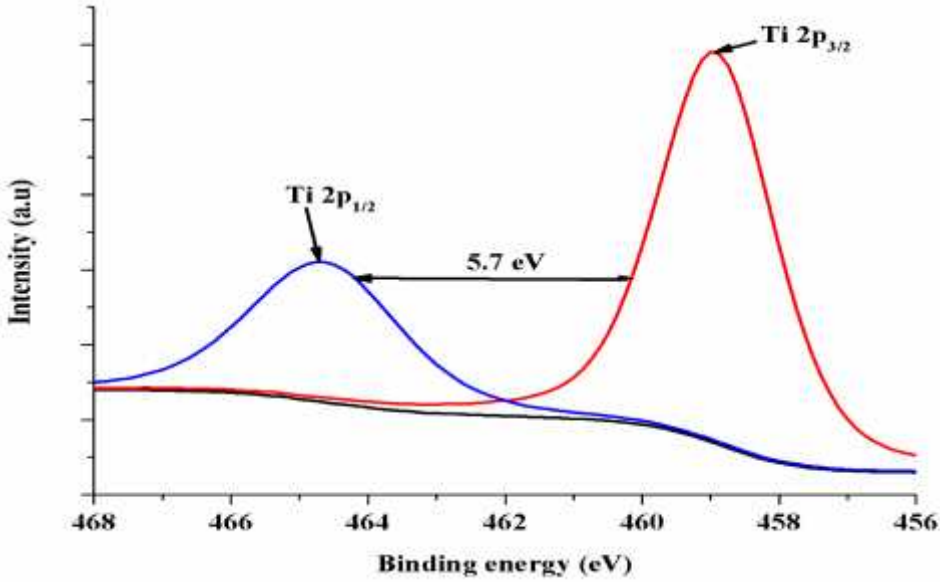

Figure 4.16: Detail XPS scan of Ti 2p enveloped in JT7

Furthermore, the presence of broad and sharp narrow peaks at the binding region of 459.3 and 465 eV suggested the existence of Ti and Ti^{4+} species in the sample. In Figure 4.15, the normalized count rate in the Ti 2p shell region was dominated by a sharp peak belonging to Ti $2p_{3/2}$, this mean that Ti occurred in one chemical state. Besides, the splitting between the binding energies values of Ti $2p_{3/2}$ and Ti $2p_{1/2}$ was 5.7 eV. There was no binding energy values which corresponded to Ti^{3+}, which means that Ti in this case existed as Ti^{4+} in the as-synthesised TiO_2 nanocrystals. Mostly the chemical state of Ti reported in the XPS studies in the literature for typical pure anatase TiO_2 nanoparticles was Ti^{4+}. The obtained binding energies for Ti and O corroborated XPS data reported in literature for typical TiO_2 nanoparticles (Aziz et al., 2013; Dhabbe et al., 2014; Leong et al., 2014; Rodríguez-González et al., 2010).

According to the XPS spectrum of O 1s shown in Figure 4.17, the peaks assigned to oxygen could be found in the binding energy region of 530.6, 531.7 and 532.9 eV, which were related to Ti-O, O-C and C=O bond respectively.

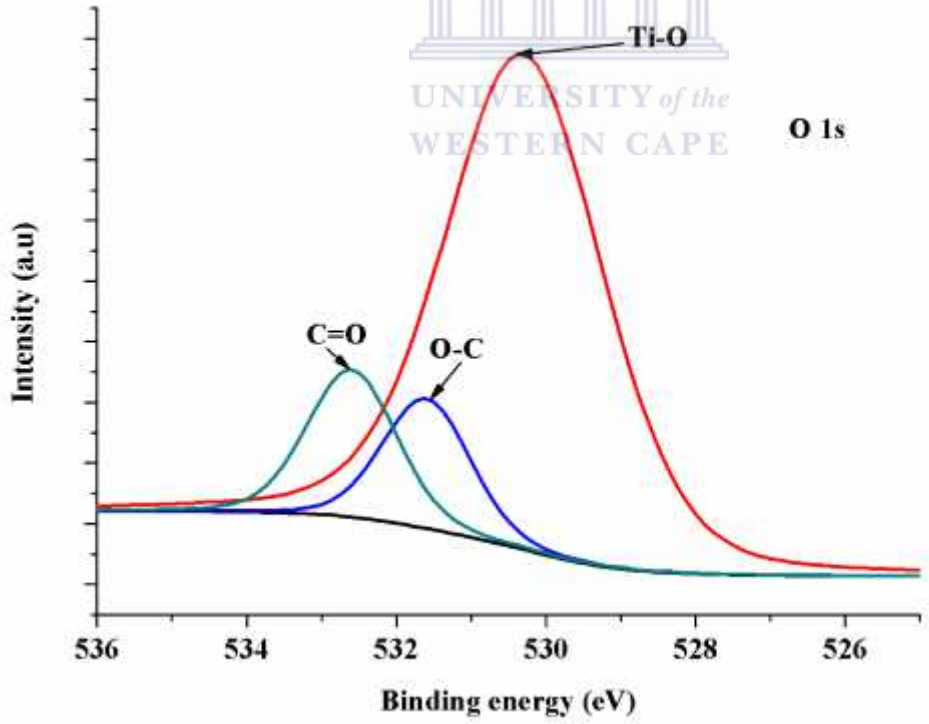

Figure 4.17: The XPS spectrum of O 1s enveloped in sample JT7

Of all three options, the most abundant or prominent peak was observed in the binding energy region of 530.6 eV, which corresponded to the Ti-O bond of TiO_2, thus suggesting that the titanium atom was bonded to oxygen. Other noticeable peaks at 531.6 and 533.6 eV correspond to C-O and C=O respectively. Comparing the normalized count rate of Ti 2p and O 1s in Figure 4.16 and 4.17, the bulk of the titania nanocrystals lattice structure was dominated by Ti-O.

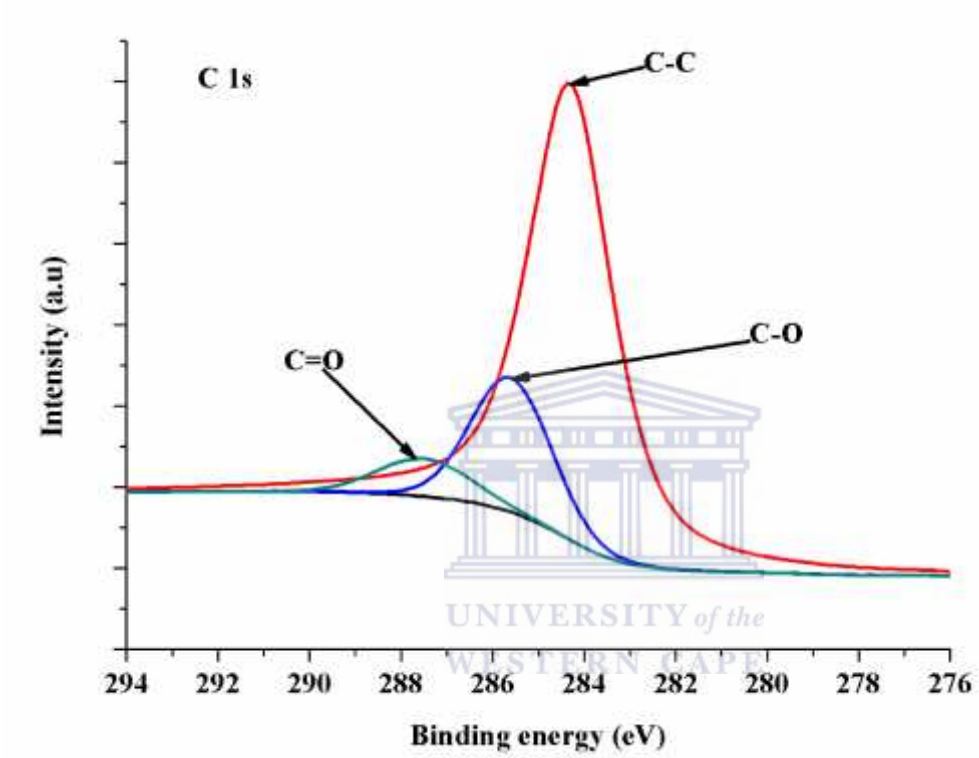

Figure 4.18: High resolution-XPS scan of C 1s enveloped in sample JT7

In order to determine the states of carbon in the supported TiO_2 nanocrystals (JT7), the C 1s shell was measured and the scanned results shown in Figure 4.18. In Figure 4.18 three prominent peaks which corresponds to C-C or C=C, C-O and C=O or COO bonds were observed in the binding energy region of 284.6, 286.2 and 288.2 eV respectively. Specifically the signal observed at binding energy value of 284.6 eV was categorised as adventitious elemental carbon (C=C). The presence of elemental carbon may be attributed to the pyrolysis of polymer precursor (PAN) to carbon. There was no noticeable peak for Ti-C bond in the binding region of 281.0 eV, which suggests non-existence of Ti-C bonds in the synthesised supported material. Studies have shown that the carbonization process of PAN contributed about 90% carbon to the synthesised Ag/PAN nanoparticles (Abdo et al., 2013). Ren et al., (2007) ascribed the two peaks observed at 284.8 and 288.6 eV to formation of carbon-doped

TiO_2 nanoparticles. Nevertheless, comparatively the combined XPS spectra of Ti 2p, O 1s and C 1s indicated the formation of Ti-O-C due to pyrolysis of PAN and transformation of $TiCl_4$ during the heating process. Furthermore, the presence of C-C, C-O and C=O or COO bonds in the TiO_2 crystals indicates that carbon was doped onto the TiO_2 nanoparticles. Furthermore, the doping effect of carbon species on TiO_2 nanocrystals by PAN might be responsible for the smaller particle size (see XRD result Figure 4.12). Cong et al., (2011) reported similar observation during the synthesis of carbon doped TiO_2 coated on multi-walled carbon nanotubes. The authors ascribed the formation of Ti-O-C bond to the close interaction between the TiO_2 lattice structure and the multi-walled carbon nanotubes. On the contrary, Ren et al., (2007) linked the formation of Ti-O-C bond to the substitution effect of carbon on the lattice titanium atom and not on oxygen atom. In addition, the presence of impurities or contamination such as Fe in the general XPS spectra (Figure 4.15) may be ascribed to the heating of the stainless steel mesh, which may have caused the diffusion of ions, mostly Fe onto the TiO_2 lattice structure. The presence of other elements such as Cl and N possibly are remnants of the titania and polymer precursor. These elements had earlier been identified during EDS analysis shown in Table 4.1. Therefore, the EDS analysis is in agreement with the XPS results. Luo et al., (2012) ascribed the element C and N detected in the XPS spectra of as-synthesised TiO_2/PAN nanoparticles to PAN molecules and PAN chain respectively. Fernández et al., (1995) had earlier reported the presence of Fe^{3+}, Cr^{3+}, and Si^{4+} in the TiO_2 nanoparticles developed on a stainless steel via electrophoretic deposition method. The supported TiO_2 nanoparticles was pyrolysed in N_2 atmosphere at 700 ºC for 30 min and the authors attributed the existence of these heterocations to the thermal treatment which promoted the diffusion of some ions (Fe^{3+}, Cr^{3+}, Si^{4+}) from the stainless steel into the TiO_2 layer..

4.1.8 *BET Surface area of the as-synthesised supported TiO_2 nanocrystals*

The textural properties of the as-synthesised supported TiO_2 nanocrystals was investigated using Micrometrics ASAP 2020 surface area and Porosity Analyzer. The N_2 adsorption–desorption isotherms of the supported TiO_2 nanocrystals pyrolysed in the furnace at 300 ºC, 350 ºC and 400 ºC for 3 h (JT3, JT7, JT11) are depicted in Figure 4.19. The detailed catalysts preparation procedure has been described in section 3.2.2. The BET analysis was conducted using sample preparation and instrumental settings conditions stated in 3.4.6. The BET surface areas, pore diameter, pore volume and pore area of the as-synthesised TiO_2

nanocrystals as determined by BET and Barrett-Joyner-Halenda methods are indicated in Table 4.4.

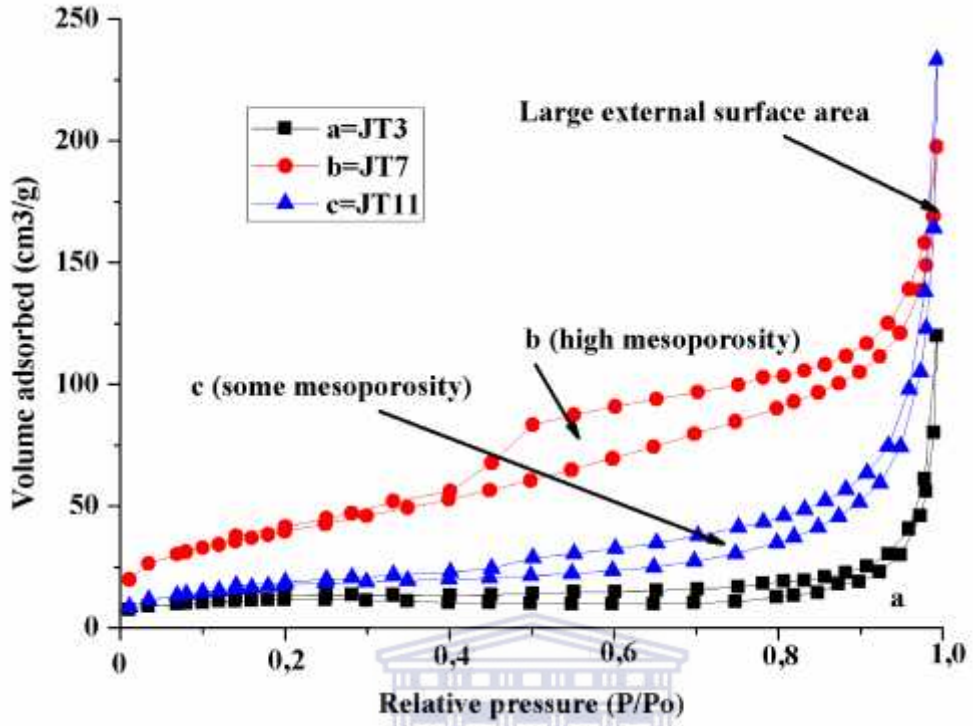

Figure 4.19: N_2 adsorption-desorption isotherms plot of: (a) JT3 (300 ºC for 3 hr) (b) JT7 (350 ºC for 3 hr) (c) JT11 (400 ºC for 3 hr)

Table 4.4: Specific surface area and micropore area for the supported as-synthesised carbon doped TiO_2 nanocrystals compared to commercial powder Degussa P25

Samples	BET surface area (m^2/g)	Micropore area (m^2/g)
P25 (commercial TiO_2)	56	18
JT3 (300 ºC for 3 hr)	107	24
JT7 (350 ºC for 3 hr)	152	35
JT11 (400 ºC for 3 hr)	132	31

According to the IUPAC nomenclature, the adsorption-desorption branch of the JT3, JT7 and JT11 can be categorised as a typical type IV isotherm, which belongs to a hysteresis loop type III of the aggregated particles of a purely mesoporous material with small pore sizes. The adsorption type IV indicates capillary condensation of gases within the mesopores, as the relative pressure (P/Po) approaches unity. The hysteresis loop consist of both sloping adsorption and a moderately sharp desorption branch even at high relative pressure (P/Po)

range. Table 4.4 showed that JT7 had the highest BET surface area and micropore area of 152 m^2/g and 35.3 m^2/g respectively. The formation of a relatively small micropore area could be due to the agglomeration of the TiO_2 nanocrystals as evident in the HRSEM images (Figure 4.1- 4.3) or formation of larger mesopores which would reduce surface area during the pyrolyzed process. According to Table 4.3, it was found that particle size increased with an increase in calcination temperature and holding time. Specifically, the particle size of samples JT3, JT7 and JT11 were 6.51 nm, 13.0 nm and 14.2 nm respectively. On the contrary, the trend was observed with the BET surface area of these samples did not follow a similar trend as the particle size. In the formation of pores, it is possible that gaseous species formed during pyrolysis or volatilization of the PAN breakdown products would create porosity in the carbon. This was evident in the TGA result shown in Figure 4.9, which showed that carbon still remain in the supported TiO_2 nanocrystals even after 350 ºC. As shown in Table 4.4, BET surface area of JT3 was 107 m^2/g, JT7 (152 m^2/g) and JT11 (132 m^2/g), the differences in the BET surface area can also be related to the amount carbon and the carbon state in the samples. At 300ºC for 3 h (JT3), PAN precursor had not pyrolysed completely, which means certain PAN chains or fragments still blocked the TiO_2 pores, thus may be responsible for the lower BET surface area and particle size. At 350ºC for 3 h (JT7), it was found that PAN precursor had pyrolyzed more extensively which resulted in the creation of a greater porosity in the TiO_2 layers. However, further increase in calcination temperature to 400 ºC for 3 h (JT11) resulted in the coalescence of the TiO_2 hollow structures thus resulting in the decrease BET surface area. The obtained BET surface areas for all the samples are however much higher than the 56 m^2/g reported for the commercial TiO_2 nanoparticles in the literature (Sheikhnejad-Bishe et al., 2014). The increased specific surface area might be attributed to the pyrolysis temperature and possibly the doping effect of carbon from PAN. The supported TiO_2 nanocrystals pyrolyzed at 350 ºC for 3 h (JT7) had higher surface area compared to samples made at other temperatures. It was evident that at 300 ºC for 3 h (JT3), the PAN was still partially stable as most nanocrystals were still embedded in the polymer as shown by HRSEM results in Figure 4.1. At 300 ºC, the adsorption-desorption isotherms were nearly flat with the hysteresis loops becoming smaller as the relative pressure approached unity. The low mesoporosity could be related to the smaller BET surface area. With an increase in the temperature to 350ºC, extensive pyrolysis of the bulk PAN occurred and high mesoporosity was observed due to formation of gaseous species during volatilization of PAN and fully grown TiO_2 crystallites were observed. Further increasing in

the pyrolyzed temperature to 400 ºC led to reduction in the BET surface area and lower mesosity. A study conducted by Chen et al., (2013) reported a decrease in the specific surface area and pore volumes of TiO_2 nanoparticles as calcination temperatures increased from 400º to 500ºC, in which the reduction was attributed to uncontrollable destruction of porous structure. In addition, Leong et al., (2014) and Sheikhnejad-Bishe et al., (2014) independently ascribed the decline in the surface area to the gradual increase in particle size during calcination.

4.1.9 *Section summary*

In summary, TiO_2 nanocrystals could be supported easily on stainless steel mesh and was robust. PAN pyrolysis instead of calcination allowed controlled carbon content and mesoporosity could be tailored by applied temperature. Carbon doping was achieved and carbon residues improved adherence to stainless steel mesh. FTIR analysis revealed the presence of functional group associated with a typical TiO_2 nanoparticles while the DSC/TGA confirmed the carbonization process of the PAN precursor. The EDS, XRD and XPS results complemented one another and affirmed the presence of carbon species in or on the TiO_2 layer, and XPS suggested the substitutional effect of oxygen in TiO_2 by carbon. It is possible to conclude that supported TiO_2 nanocrystals prepared by pyrolysis at 300 ºC, 350 ºC and 400 ºC for 3 h was actually supported carbon doped TiO_2 nanocrystals and that PAN/DMF/$TiCl_4$ offers a facile sol-gel related route for preparing supported carbon doped TiO2 nanocomposite in one step.

4.2 Characterization of the supported Ag doped TiO_2 nanocomposites

This section discusses and presents the results of the characterization of the supported Ag doped TiO_2 nanocomposites using HRTEM, XRD, XPS, UV-Vis diffuse reflectance spectrophotometer, and EDS. Sample JT7 was modified with different Ag contents using thermal evaporator operated at a desired value of 2.5×10^{-5} mbar and evaporation rate of 0.5 Å/s. Layers of Ag nanoparticles were deposited at different time intervals onto the TiO_2 surface by constant applied current of 100 A. The detailed experimental protocol on the surface modification of sample JT7 with Ag was described in section 3.2.3.

4.2.1 *HRTEM of supported TiO_2 nanocrystals and Ag doped TiO_2 nanocomposites*

HRTEM analysis was conducted on the Ag doped TiO_2 nanocomposites to confirm the possible deposition or presence of Ag nanoparticles on the TiO_2 nanocrystals. The detailed experimental protocol for the synthesis of supported Ag doped TiO_2 nanocomposites via the

thermal evaporation method is described in Section 3.2.3. The HRTEM analysis operated at 200 kV was conducted according to the procedure described in section 3.4.3. The deposited layers, which apparently appeared in the form of nanoparticles on the surface of TiO_2 nanocrystals were expressed in angstroms and converted to nanometer. The deposition were carried out at constant pressure of 2.5×10^{-5} mbar, deposition rate of 0.5 Å/s, current (100 A), distance between the supported catalyst and the boat (15 cm), however deposition time differs (30 - 60 sec), for instance with sample JT13, the deposition time was 30 sec, and JT14 (45 sec) while JT15 was (60 sec). The relative wt % of the silver content deposited on TiO_2 layer according to EDS ranged from 1.8% to 3.5%. The Ag doped TiO_2 nanocomposites at deposition time of 30 sec, 45 sec and 60 sec were labelled as: JT13 (1.8%), JT14 (2.4%), and JT15 (3.7%). The HRTEM images of the sample JT7 and JT13-JT15 are shown in Figure 4.20.

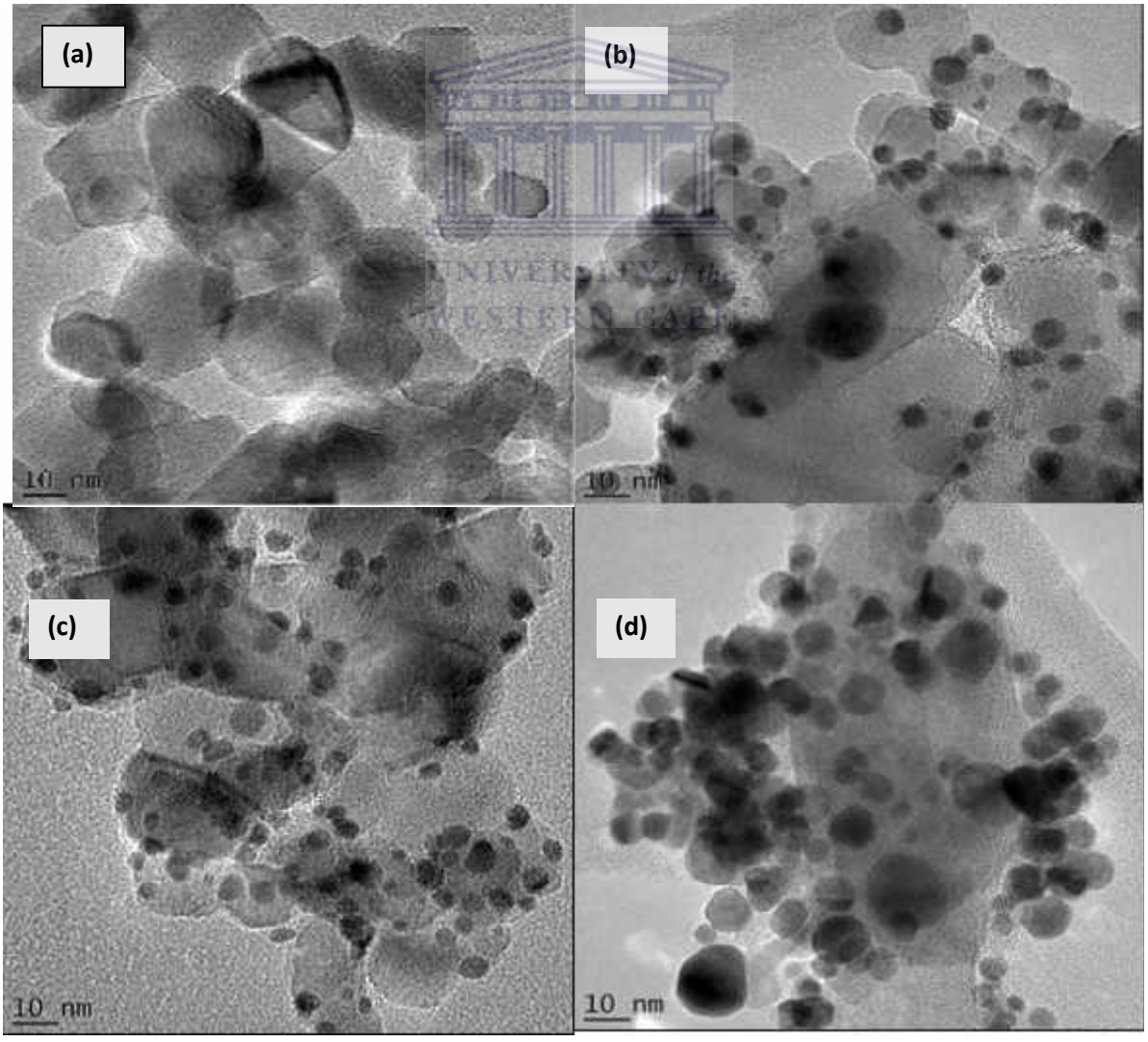

Figure 4.20: HRTEM images of: (a) JT7 (b) JT13 (c) JT14 (d) JT15

With the exception of sample JT7 (Figure 4.20 a), it can be seen that Ag-NPs were present and widely distributed on the TiO_2 surface (Figure 4.20 b-d). The dark spots within the composite micrograph depict the Ag nanoparticles deposited upon the TiO_2 nanocrystals. The Ag-NPs were spherical in shape and homogeneously distributed without significant aggregation as the deposition time increased from 30 – 60 sec at constant applied current of 100 A. It is noteworthy mentioning that the particle size of Ag nanoparticles are not completely uniform as evident in the Figure 4.20 b-d. In fact, the Ag nanoparticles appear to have covered the whole surface containing TiO_2 when deposition time was increased to 60 sec (Figure 4.20d), which may likely obstruct UV or visible light from interacting with the TiO_2. The degree of the TiO_2 surface coverage increases with Ag deposition time. Further analysis of the Ag doped TiO_2 nanocomposites, precisely sample JT14 with XPS (section 3.4.7) showed that Ag-NPs were firmly deposited on the titania surface without being inserted into the TiO_2 lattice framework due to its large ionic radius compared to titania. The SAED was further employed to establish the degree of crystallinity of the supported TiO_2 nanocrystals after the deposition of different layers of Ag. The SAED patterns of JT13-JT15 shown in Figure 4.21 demonstrated that the nanocomposites consist of TiO_2 and Ag-NPs nanoparticles, which corresponded to crystal planes (101) and (111) of anatase TiO_2 and Ag nanoparticles with interplanar distance of 0.35 nm and 0.23 nm respectively.

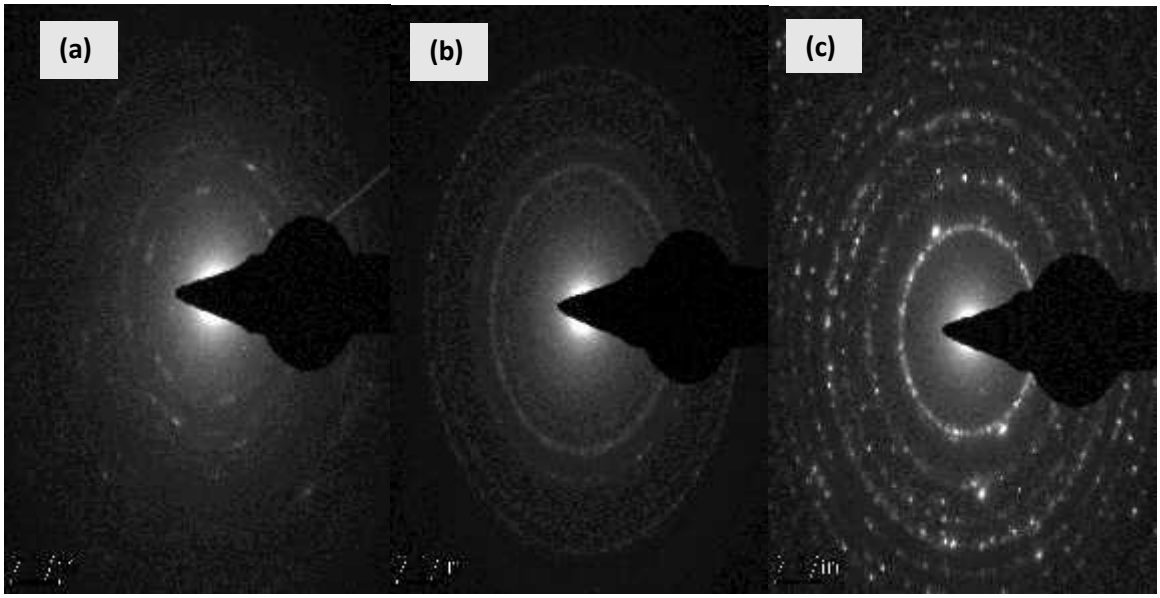

Figure 4.21: SAED pattern of: (a) JT13 (b) JT14 (c) JT15

It should be noted in Figure 4.21 that as the deposition time increases from 30-60 sec, the extent of bright reflections of Ag nanoparticles also increased, which was evidence of poly-crystallinity of Ag nanoparticles. The SAED results matched well with the HRTEM and XRD result shown in Figure 4.20 and 4.22 respectively. In spite of the deposition of different layers of Ag, the supported Ag/TiO_2 nanocomposites were still polycrystalline in nature.

4.2.2 *Elemental analysis of Ag doped TiO_2 nanocomposites*

The EDS analysis was carried out to determine percentage elemental composition in the prepared catalysts. Prior to analysis, the samples were coated with Pd and Au to prevent charging, which frequently distorted images. The experimental procedure was described in section 3.2.3 and the qualitative estimate of the composition and relative wt% of each element present in sample JT13-JT15 is represented in Table 4.5.

Table 4.5: Energy dispersive X-ray spectroscopy (EDS) spectrum of sample JT7, JT13-JT15 (number of replicates = 2)

Sample names	**Elemental composition (Wt%)**								
	Ti	**O**	**C**	**Ag**	**Cr**	**Fe**	**Ni**	**Cl**	**TOTAL**
JT7	46.13	30.50	11.94	Control	1.88	3.94	2.17	3.44	100
JT13	46.21	29.94	10.73	1.8	1.75	3.93	1.86	3.78	100
JT14	45.76	28.47	9.90	2.4	2.27	3.95	2.35	4.90	100
JT15	44.94	28.94	8.37	3.5	2.56	3.85	2.67	5.17	100

According to Table 4.5, the presence of Ti, O, C, Ag, Cr, Fe, Ni, and Cl was noted in in different proportion in the samples. On the other hand, Pd and Au detected in samples were the elements used for coating to prevent charging during analyses, which often distorted images. The weight percentage of Ag as shown in Table 4.15 increased with an increase in deposition time and sample JT15 exhibited the highest Ag percentage, with JT13 having the lowest amount. The presence of other elements such as Cr, Fe, Ni and Cl in the EDS spectra and the possible explanation for their occurrences have been explained in Section 4.2.3. It is important to mention that the carbon present in this sample did not originate from the holey carbon grid but rather from PAN precursor. Studies have shown that carbonization process of

PAN precursor was accompanied by the release of N_2, HCN and H_2O and increased carbon content by more than 90% (Abdo et al., 2013). According to Table 4.5, it can be seen that PAN and pyrolysed species of about 8-12% still remained in the sample despite applied temperature of 350 ºC. Thus, the presence of carbon is due to PAN precursor and not holey carbon grid and further corroborated by TGA and XPS results shown in Figure 4.9 and 4.15 respectively. The presence of Ag in the EDS further demonstrated that a controlled amount of Ag actually deposited on the TiO_2 surface depending on the applied thermal evaporation conditions, which agreed with the XPS results shown in Figure 4.25. Previous studies conducted by Suwarnkar et al., (2014) reported the presence of 0.25 mol% Ag in the EDS spectra of unsupported Ag doped TiO_2 nanocomposites prepared via microwave assisted method containing a controlled amount 0.1 M Titanium tetra-isopropoxide and 0.05 M silver nitrate in 100 mL of absolute ethanol at pH 8.

4.2.3 *XRD pattern of Ag doped TiO_2 nanocomposites*

Particle sizes and the mineralogical phases of supported Ag doped TiO_2 nanocomposites was examined by XRD. The XRD patterns of sample JT7 and JT13-JT15 presented in Figure 4.17 were obtained using the procedure described in Section 3.2.3. This was done to investigate if the deposition of Ag on the supported TiO_2 nanocrystals via thermal evaporation will influence the mineral phases. The instrumental settings and conditions used for the measurement of sample JT7, JT13-JT15 has been described in Section 3.4.1. To further clarify the peaks, in Figure 4.22, the peaks corresponding to anatase TiO_2 were marked A and Ag as Ag accordingly.

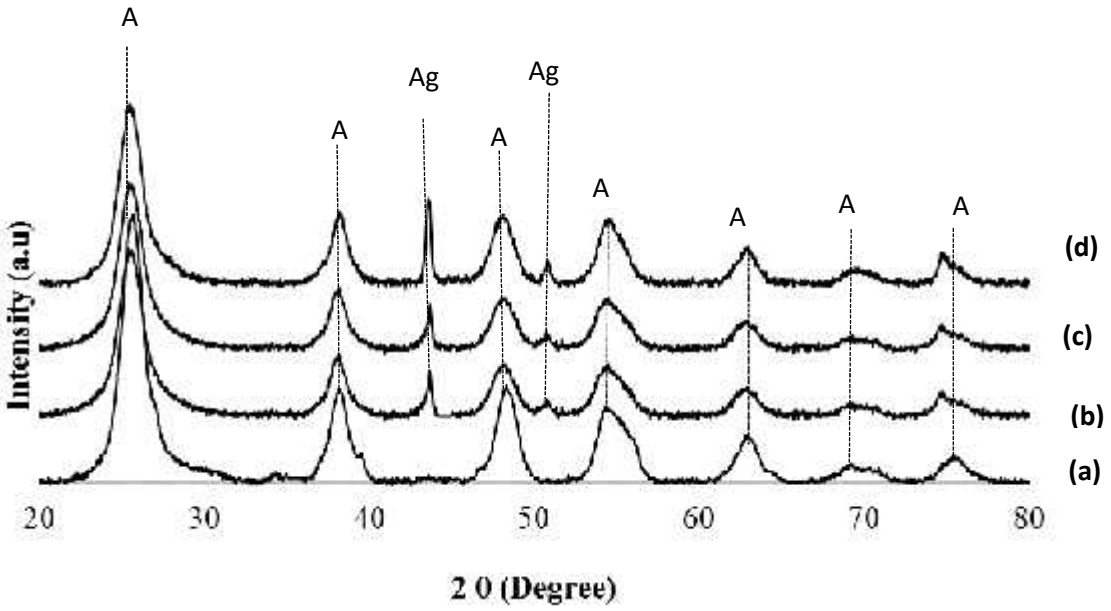

Figure 4.22: XRD pattern of: (a) JT7 (b) JT13 (c) JT14 (d) JT15

As shown in Figure 4.22, the XRD patterns of supported TiO_2 nanocrystals corresponded to anatase phase present in the nanocomposites except for two additional peaks at 2 thetha values of 44.32º and 53.21º which corresponded to face-centered cubic (fcc) crystal planes (200) and (200) of Ag. This confirms the presence of metallic silver (JCPDS card no.04-0783). No detectable peaks corresponded to silver oxide (AgO), rutile or brookite were observed. It is noteworthy that, there was a slight decrease in the diffraction peak intensity when Ag was deposited compared to the baseline supported TiO_2 nanocrystals. This indicates that there was a slight anatase peak shifts compared to JT7 especially at 2θ values of 25.3º and 76.7º respectively. When the deposition time of Ag nanoparticles was 30 and 45 sec, the intensity of Ag peaks still remained the same however the TiO_2 peaks became less intense. The intensity of Ag peak increases, which was indication of more Ag or bigger sizes of Ag nanoparticles and not necessarily more crystallinity. This agreed with the HRTEM and EDS results shown in Figure 4.20 and Table 4.5 respectively. This According to the Bragg's law ($n\lambda=2d\sin\theta$) the lower the value of sinθ, the greater the d spacing, which suggest slight distortion TiO_2 nanocrystals by Ag. This means that the silver coating obscured the TiO_2 since XRD penetration depth is small. As a consequence, peak shifts of anatase phase to lower angles was an evidence of TiO_2 lattice distortion by Ag. Studies have shown that the distortion of TiO_2 crystals lattice by Ag is not easy due to the differences in the ionic radius and valence state of the metal (Pham and Lee, 2014). The ionic radius of Ag^+ is (126 Å) is considerably greater than that of Ti^{4+} (68 Å). Complete substitution or replacement of Ti with

Ag was not likely. Instead, a small amount of Ag could diffuse and induce distortion of TiO_2 lattice structure while a significant amount of Ag is merely dispersed on the TiO_2 surface as revealed by HRTEM analysis shown in Figure 4.20. This observation is similar to what had earlier been reported by Pham and colleague, (2014) during the deposition of Ag on glass supported TiO_2 nanoparticles. In comparison to the previous studies, the various Ag loaded carbon doped TiO_2 nanocomposites obtained in this study were polycrystalline as revealed by SAED shown in Figure 4.21. With an increase in the deposition time of Ag to 60 sec (3.5% wt% Ag), the relative peak intensity corresponding to Ag crystal planes increased, which is an indication of larger Ag crystals as was also evident in HRTEM shown in Figure 4.20. In spite of the deposition of Ag onto TiO_2 nanocrystals, the structural integrity of a typical anatase phase observed in TiO_2 nanocrystals was still maintained. This is in accordance with the studies conducted by Nainani et al., (2012) who also found that the incorporation of different concentration of Ag did not change the anatase TiO_2 to rutile. Previous studies carried out by Cao et al., (2008) on the synthesis of Ag doped TiO_2 nanoparticles also established that Ag^+ cannot diffuse onto TiO_2 crystal plane due to larger ionic radius value than Ti^{4+}. This suggested that metallic Ag was mainly deposited on the TiO_2 surface without necessarily diffusing into the lattice structure. Behnajady, (2008) and Choi et al., (2010) had both demonstrated that due large differences in the ionic radius of Ag over Ti, Ag particle are merely deposited on the TiO_2 lattice layer.

4.2.4 *UV-vis/diffuse reflectance spectroscopy analysis of supported TiO_2 and Ag doped TiO_2 nanocomposites*

UV-vis/diffuse reflectance analysis of supported TiO_2 nanocrystals (JT7) and various Ag doped TiO_2 nanocomposites (JT13-JT15) was conducted to measure the transmission and reflectance spectra of both undoped and Ag doped TiO_2 nanocomposites and hence estimate the band gap energy. The UV-Vis/diffuse reflectance spectra of sample JT 7 and JT13-JT15 in Figure 4.22 was obtained using the procedure described in Section 3.4.10. While detailed experiment protocol on the surface modification of sample JT7 with Ag was described in section 3.2.3. On the other hand, Figure 4.23 or 4.24 shows the Taut plot of $(\alpha hv)^{1/2}$ against photon energy (hv). The optical band gap was estimated using equation 4.4

$$\alpha hv = R(hv - Eg)^n \quad \text{.....(4.4)}$$

Where α is the absorption coefficient or Kubelka-Munk transformation constant, hv is the photon energy (eV), R represents the reflectance (%), Eg (band gap energy) while n stands

for the type of transition, which may be direct or indirect. For TiO_2 nanoparticles, the transition was direct and as such n=0.5 (Dhabbe et al., 2014).

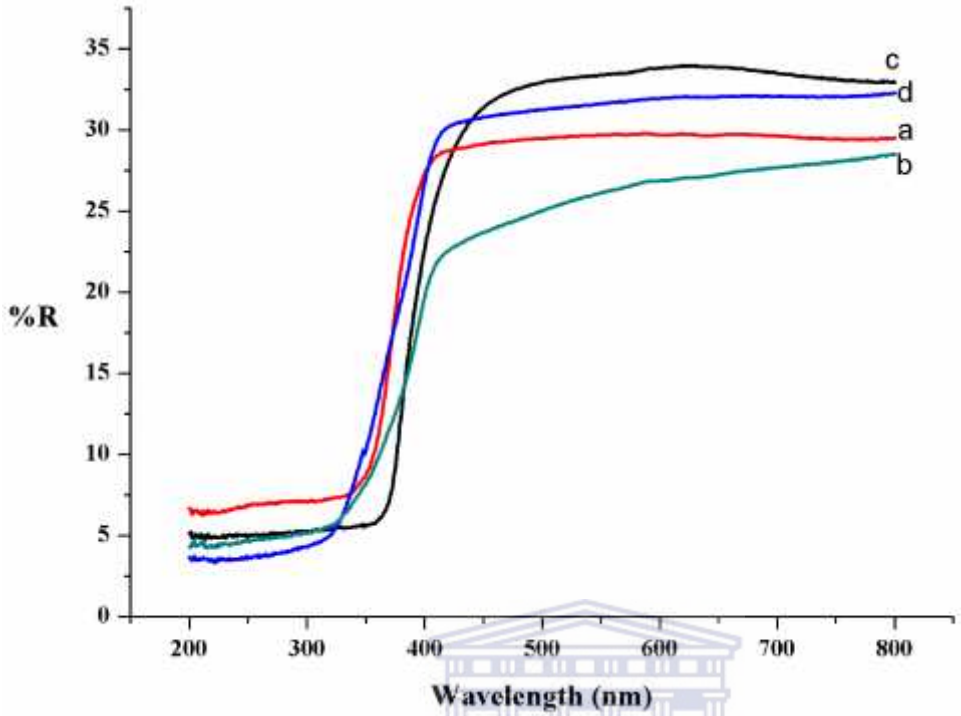

Figure 4.23: UV-Vis diffuse reflectance spectra of: (a) JT7 (b) JT13 (c) JT14 (d) JT15

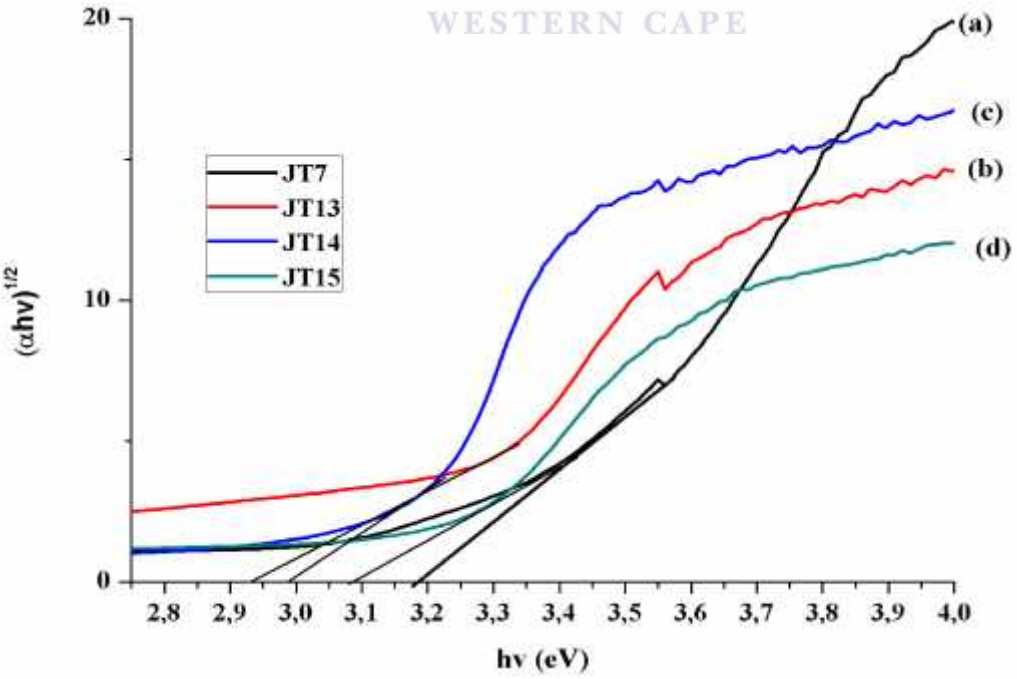

Figure 4.24: Taut plot showing Variation of $(\alpha hv)^{1/2}$ as a function of photon energy (hv): (a) JT7 (b) JT13 (c) JT14 (d)JT15

As shown in Figure 4.23, the sample JT7 had an absorption band at 325 nm. Whereas, the absorption bands of the Ag deposited samples JT13, JT14, and JT15 were 340 nm, 370 nm and 327 nm respectively. A slight shifting in the absorption band towards the visible region was observed with sample JT14 (2.4% wt% Ag) showing the highest shift and sample JT15 (3.5% wt% Ag) having the lowest shift. It can also be seen in Figure 4.23 that the optical band gaps of samples JT7 without Ag was 3.18 eV, which was however narrowed to 2.94 eV upon doping with metallic Ag for JT13. In the same way, the band gap energy of JT15 was higher than JT13 and JT14, but slightly lower than JT7. The band gap energy shifting due to deposition of Ag onto supported TiO_2 layer (JT7) in comparison with commercial powder Degussa P25 is shown in Table 4.6.

Table 4.6: The estimated band gap energy of supported TiO_2 and Ag doped TiO_2 nanocomposites in comparison with commercials powder Degussa P25

Samples	Band gap energy (eV)
Commercial powder Degussa P25	3.20
JT7	3.18
JT13	2.98
JT14	2.94
JT15	3.08

Thus, a slight shift in the absorption bands and decrease in band gaps may be attributed to surface plasmonic effect of the deposited Ag. Subsequently, this caused the electron transfer from metallic Ag onto TiO_2 surface since pure Ag has a lower Fermi level than that of TiO_2. In addition, the reduction in the band gap energy of TiO_2 nanocrystals was not only due to the plasmonic effect of Ag alone but rather carbon species provided by PAN during the pyrolysis process in the furnace. The shift observed for JT7 (PAN/TiO_2 at 350 ºC for 3 hr) was 325 nm. The presence of carbon in JT7 was confirmed by XRD, XPS and EDS analysis (see Figure 4.12, 4.15 and Table 4.1) The formation of Ti-O-C as established by FTIR (see Figure 4.11) and XPS analysis (see Figure 4.15), further demonstrated the substitutional effect of oxygen in the TiO_2 crystals with carbon. The substitutional effect relative to commercial powder

Degussa P25 and PAN/TiO_2 samples may have resulted in the formation of absorption bands in the binding energy region of 284.6 eV (see Figure 4.17). Therefore, the narrowing of band gap energy of JT7 from 3.18 eV to 2.94 eV in the case of JT14 can be ascribed to the combined effect of both C and Ag doping. The lowest absorption edge value and higher band gap energy noticed in sample JT15 can be attributed to the presence of large non-homogeneous silver clusters on the TiO_2 layer, which could prevent or block light from reaching the TiO_2 surface as evidenced in HRTEM shown in Figure 4.20d (JT15). Furthermore, large silver clusters were probably responsible for non-absorption of light by the samples as was seen in the UV-vis diffuse spectrometry. Pham and Lee, (2014) had earlier observed that a high amount of Ag clusters on the TiO_2 lattice structure could retard both the plasma resonance and electron-hole separation of TiO_2, and as well reduce visible light penetration. The obtained band gap energy for the synthesised supported TiO_2 nanocrystals (JT7) in this study is however lower than the reported value in the literature for a typical commercial powder Degussa P25 anatase phase. The differences are ascribed to the carbon precursors and nature of the polymer (PAN). Band gap energy values of 3.2 eV have been reported in the literature for pure anatase phase (Leong et al., 2014; Wu et al., 2013; Ba-Abbad et al., 2012). The band gap energy value of 2.94 eV obtained in this study for JT14 (2.4% Ag doped TiO_2 nanocomposites) was greater than 3.26 eV reported for Ag doped TiO_2 film prepared via sol-gel and photochemical impregnation method by Rodríguez-González et al., (2010). The differences may ascribed to the nature of titanium and Ag precursor, calcination temperature and method of synthesis. Subrahmanyam et al., (2012) reported an absorption peak of 420 nm for Ag doped TiO_2 nanoparticles and a decreased in band gap energy of unsupported TiO_2 nanoparticles from 3.20 eV to 2.98 eV. The authors attributed the shifting in absorption peak and reduction of band gap energy to the surface plasmonic effect of Ag. However, the highest absorption band observed in this study was 370 nm, which is lower than that reported by Subrahmanyam et al., (2012) and Suwarnkar et al., (2014). This differences may be due to the amount of Ag doped, time of deposition or deposition method.

4.2.5 *X-ray photoelectron spectroscopy (XPS) analysis of supported Ag doped TiO_2 nanocomposites*

In order to further confirm the nature of Ag deposited on the surface of supported carbond doped TiO_2 nanocrystals via the thermal evaporation technique, the as-synthesised sample JT14 was further characterized using XPS. Sample JT14 was chosen among others due to its highest photocatalytic activities under UV-light during the preliminary test using methylene

blue as a model pollutants (see Section 4.4.3). Sample JT14 also had the lowest band gap among other catalysts. The detailed experimental protocol for the sample preparation as well as instrumental conditions of analysis were described in section 3.2.3 and 3.4.7 respectively. Figure 4.25 presents the general XPS measurement of sample JT14 while Figure 4.26 - 4.29 represents the high resolution XPS profiles of the individual elements such as Ag 3d, Ti 2p, O 1s and C 1s spectra respectively.

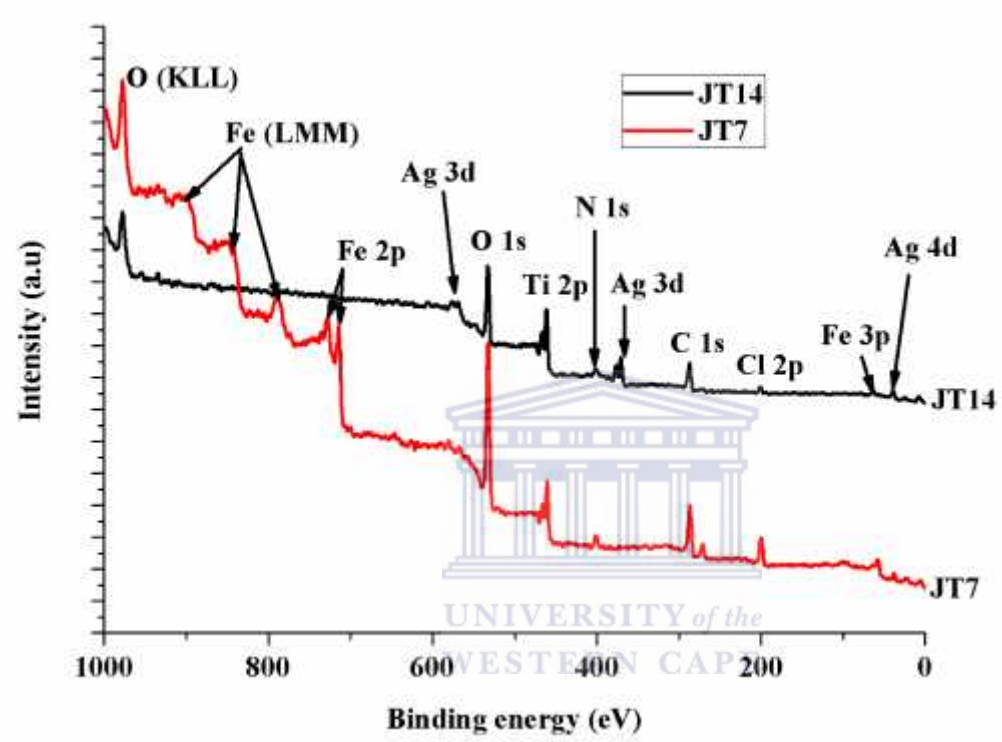

Figure 4.25: General XPS survey of JT14 superimposed on JT7 indicating elements within the detection limit.

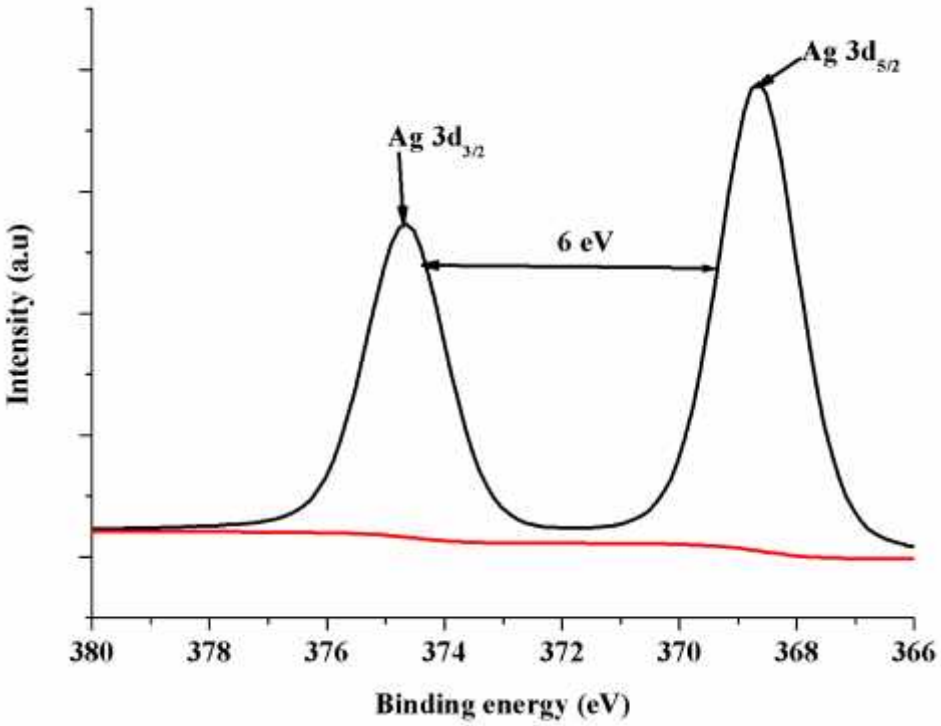

Figure 4.26: High resolution XPS spectra of Ag 3d peaks in JT14

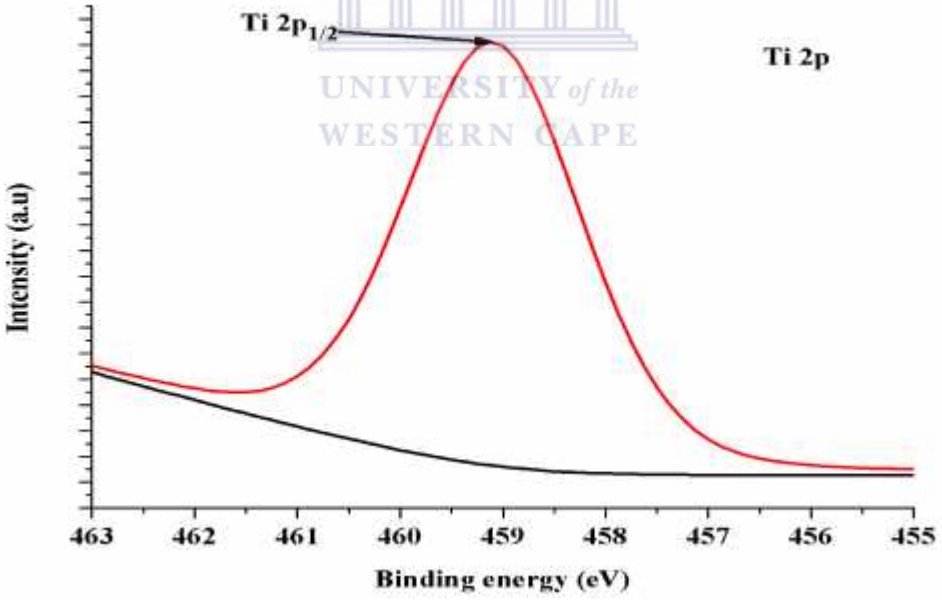

Figure 4.27: High resolution XPS spectra of Ti 2p peak in JT14

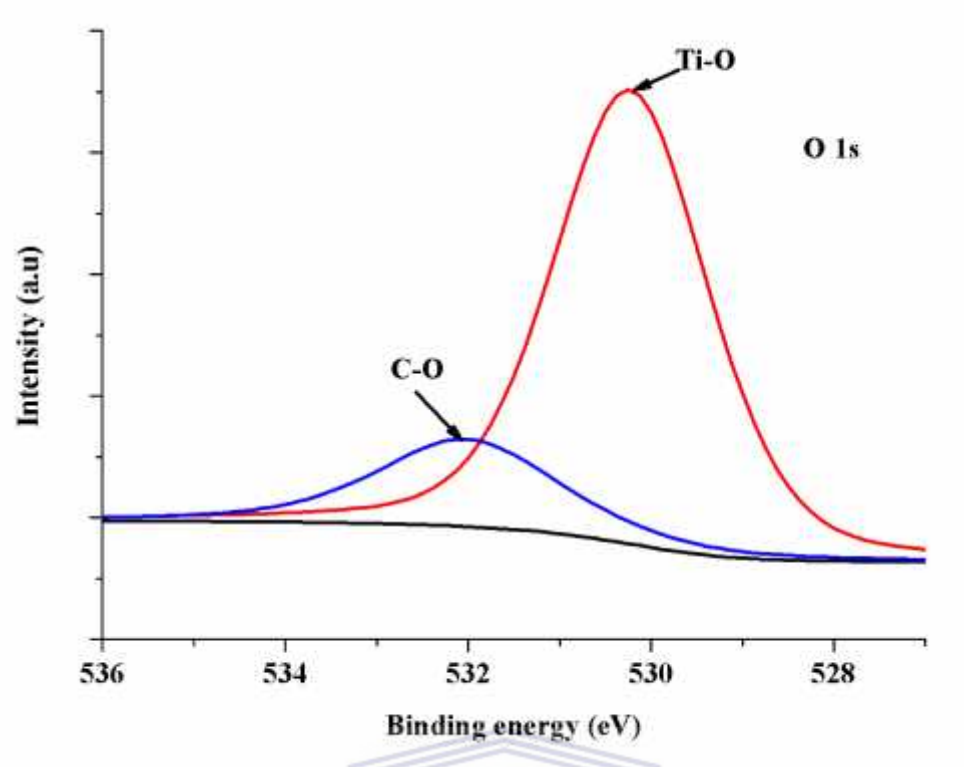

Figure 4.28: High resolution XPS spectra of O 1s peaks in JT14

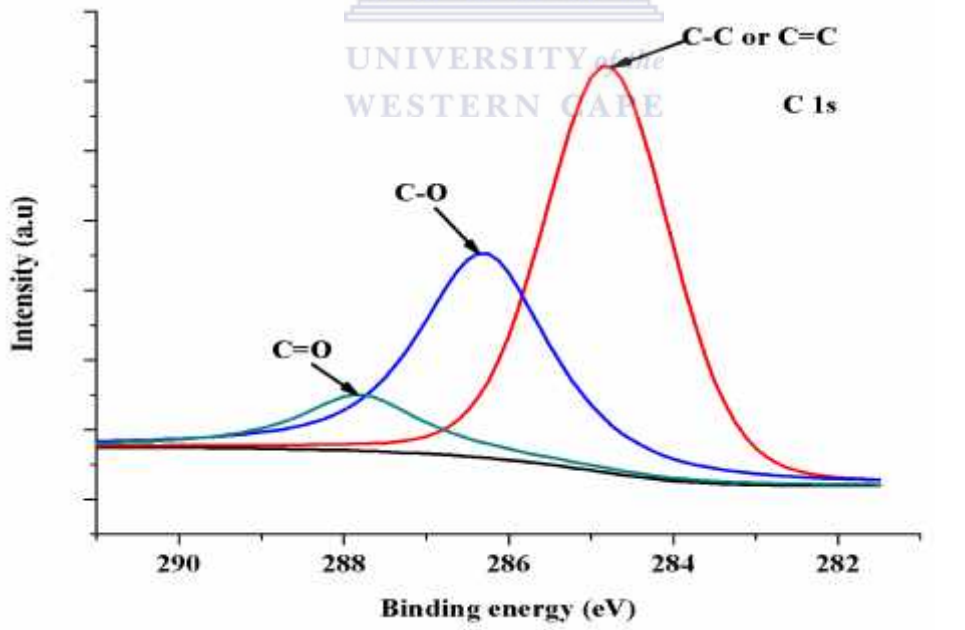

Figure 4.29: High resolution XPS spectra of C 1s peaks in JT14

The general XPS profile of Ag doped TiO_2 nanocomposites (Figure 4.25) revealed that the prominent elements present on the surface of the sample were titanium, oxygen, carbon, silver, chlorine and nitrogen. It was obvious that metallic Ag was located mainly on the

surface of the nanocomposites. The detailed explanation on the XPS analysis of Ti, O, C (shown in Figure 4.26 - 4.29) which constituted the undoped TiO_2 nanocrystals (JT7) have been provided in section 4.1.7. However, it is worth mentioning here that the XPS spectra of Ti 2p shell of Ag loaded carbon doped TiO_2 nanocomposites (JT14) is quite different from Ti 2p spectra of ordinary supported carbon doped TiO_2 nanocrystals in the sense that only one sharp peak of Ti 2p appeared in the former. Whereas, in the case of bare TiO_2 nanocrystals (JT7), two different peaks which corresponded to Ti $2p_{3/2}$ and Ti $2p_{1/2}$ orbital shells were observed. Thus, the presence of one relatively sharp Ti 2p peak in Ag doped TiO_2 nanocomposites showed that Ti existed in only one valency state, which is Ti^{4+}. The appearance of only one sharp peak in Ti 2p suggested that a relatively small proportion of TiO_2 could have been distorted by Ag. In Figure 4.26, two peaks were observed in the binding energy region of 368.5 and 374.5 eV, which corresponded to Ag $3d_{5/2}$ and Ag $3d_{3/2}$ respectively. The appearance of two sharp peaks broadly distributed in the binding energy region of 368.5 and 374.5 eV indicated the presence of metallic Ag. The binding energy values of 368.5 and 374.5 eV that were assigned to Ag $3d_{5/2}$ and Ag $3d_{3/2}$ have been reported in the literature for a typical Ag^0 (Rodríguez-González et al., 2010; Yu et al., 2011). Furthermore, no peak corresponded to either AgO or Ag_2O nanoclusters. The difference in the binding energy as a result of the doublet splitting energy of Ag 3d orbital into $3d_{5/2}$ and $3d_{3/2}$ was roughly 6.0 eV. This differential binding energy value revealed that a significant amount of Ag in the zero valent state was deposited on the TiO_2 surface. This result was in accordance with the outcome of Dhabbe et al., (2014) who reported a differential binding energy value of 5.97 eV between the peak of metallic Ag $3d_{5/2}$ and $3d_{3/2}$ located at 367.73 and 373.7 eV respectively. Thus, it is possible to suggest that reduced metallic silver particles were successfully dispersed on the surface of the supported TiO_2 with no evidence of chemical bond formation with TiO_2. In spite of the deposition of Ag, the binding energy and chemical state of Ti did not change. This indicates that silver deposition did not affect the Ti 2p shell.

4.2.6 *Section summary*

It can be seen in this section that different amount of metallic Ag was successfully deposited on the TiO_2 layer under applied thermal evaporation conditions. High dispersion of Ag was confirmed by HRTEM and a band gap shifts due to plasmonic effect of Ag was evidenced. In spite of the deposition of different amount of Ag onto TiO_2 lattice structure, the anatase phase

of TiO_2 was not affected. The next section focuses on the characterization of nano zero valent iron particles.

4.3 Characterization of the synthesized nano zero valent iron particles

In this section, several analytical techniques mentioned in section 4.1 were utilised to characterise the prepared nano zero valent iron particles. The results obtained via each analysis are presented as follows:

4.3.1 *HRSEM analysis of non-stabilised and stabilised nano zero valent iron particles*

High resolution scanning electron microscopy (HRSEM) was used to monitor the crystal distribution and the morphology of the JT16 and JT17 prepared via the modified borohydride reduction method described in Section 3.2.4.1. and 3.2.4.2. The HRSEM analysis was conducted according to the procedure described in section 3.4.2.. The HRSEM images of the prepared non-stabilized (JT16) and polyethylene glycol-stabilised nano zero valent iron particles (JT17) of different magnification is depicted in Figure 4.30.

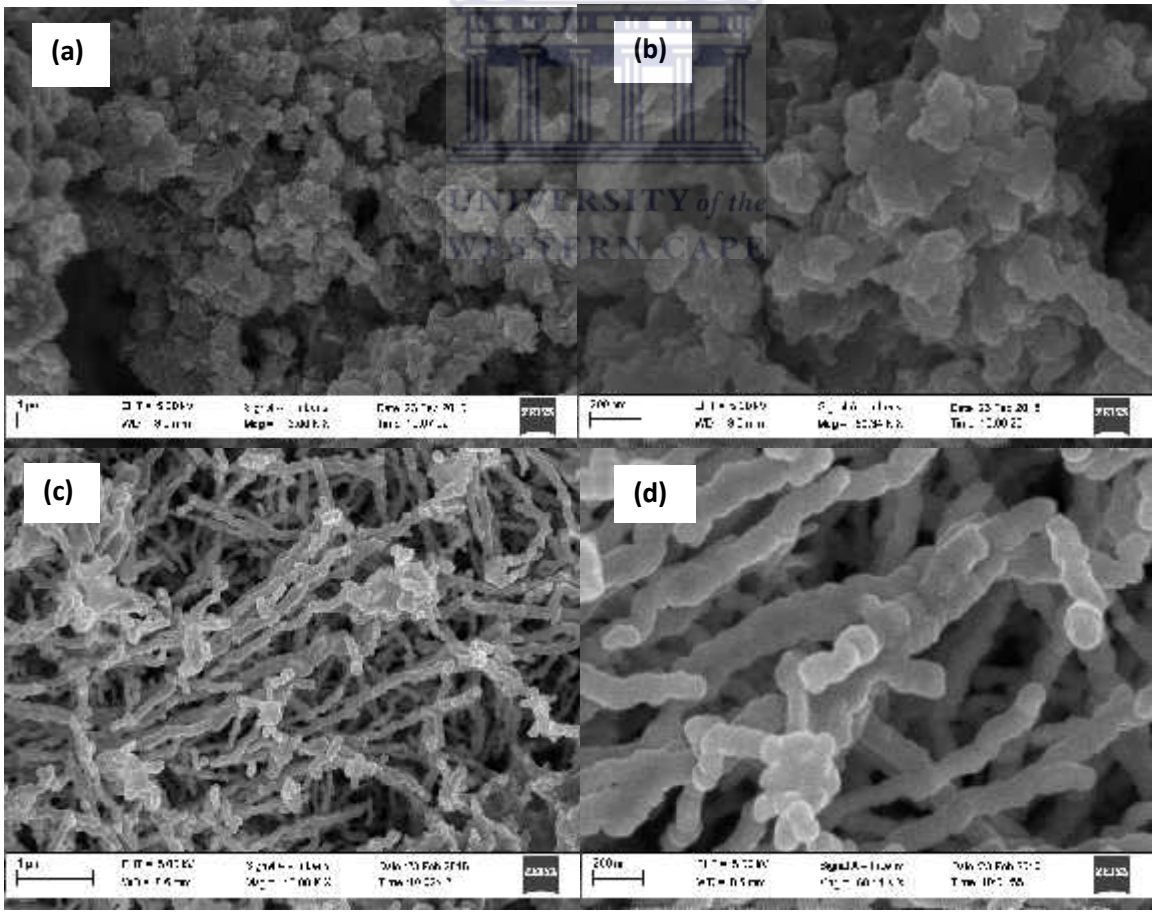

Figure 4.30: HRSEM micrograph of JT16 (a) at low magnification (b) high magnification and JT17 (c) at low magnification (d) high magnification

The HRSEM images of sample JT16 at low and high magnification are shown in Figure 4.30 (a and b). While HRSEM images of sample JT17 at low and high magnifications are represented in Figure 4.30 (c and d). The HRSEM results showed that the JT16 (a) did not resemble a discrete particles but rather appeared in the form of agglomerated and densely packed particles with uneven surface morphologies. The formation of agglomerated particles may be as a result of high surface area and magnetostatic attractions among the individual particles. In addition, the particles were deposited on one another forming nanoclusters, which is evident in JT16 (b). Thus, the morphology of JT16 at high magnification was irregular. On the other hand, JT17 (c and d) did not produce agglomerated nanoparticles. Instead, the particles are threadlike forming long uniform wires or beads on a string filaments. In spite of dominant chain-like morphology, the nanoparticles were still spherical in nature (JT17). Thus, the formation of filamentous morphology may be due to the strong intrinsic magnetostatic force of attraction between the Fe nanoparticles. The observed structure in JT17 (c and d) may be also due to the stabilization effect of polyethylene glycol which prevented the iron nanoparticles from agglomeration into clusters or being oxidised by oxygen in air. These filamentous network of iron nanoparticles had been previously observed and reported by others (Chingoua et al., 2012; Fan et al., 2010; Park et al., 2012).

4.3.2 *HRTEM-SAED of non-stabilised and stabilised nano zero valent iron particles.*

HRTEM and SAED analysis was performed on the synthesised nano zero valent iron particles to determine the crystalline nature and perhaps particle size of the prepared samples. The detailed experimental protocol for the synthesis of nano zero valent iron particles via the borohydride reduction method is described in Section 3.2.4.1. and 3.2.4.2. respectively. The HRTEM analysis was conducted according to the procedure described in section 3.4.3. The HRTEM operated at 200 kV was employed to obtain the images (see Table 3.7). The HRTEM images of samples JT16 and JT17 at different magnification are displayed in Figure 4.31.

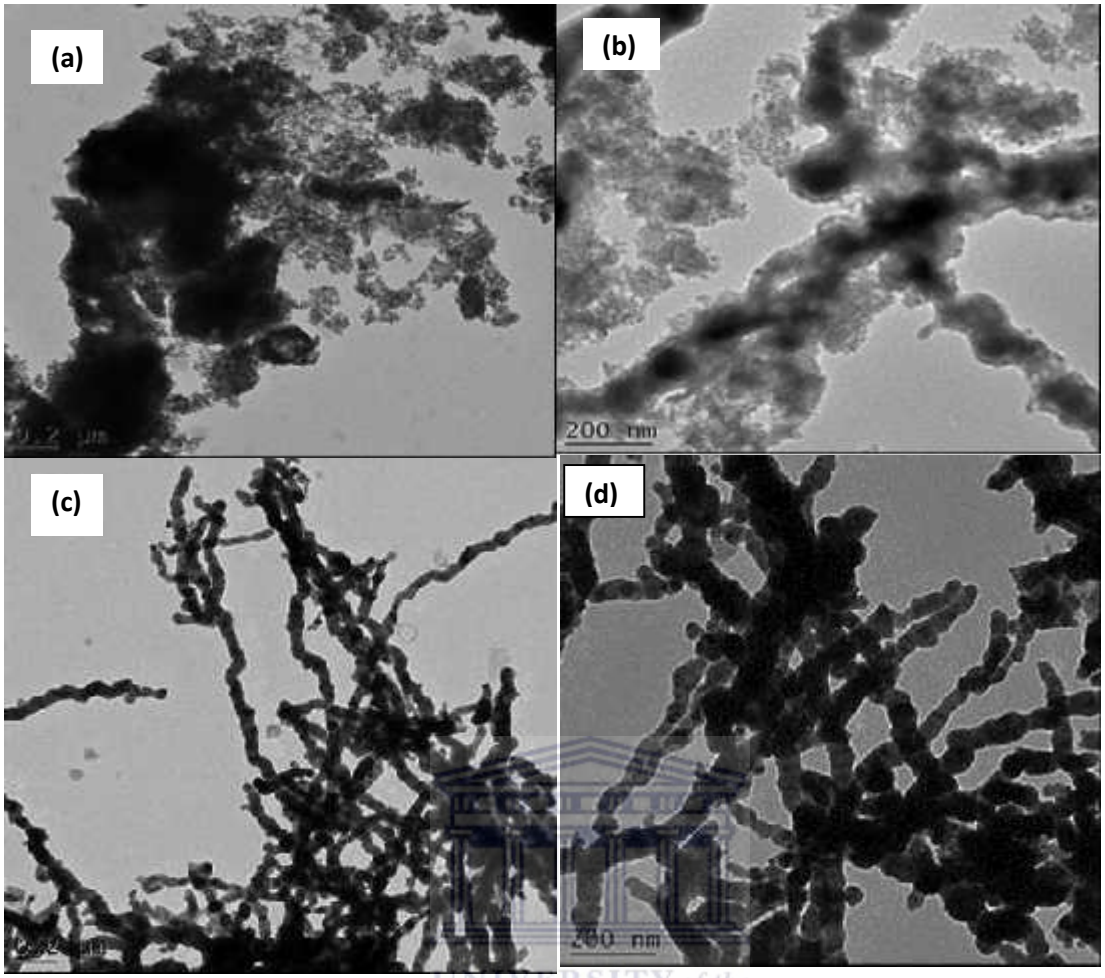

.

Figure 4.31: HRTEM micrograph of JT16 (a) at low magnification (b) high magnification and JT17 (c) at low magnification (d) high magnification

In the absence of polyethylene glycol (sample JT16 (a and b)), the unstabilized nanoparticles were spherical with a slight linearity in the aggregated structure especially in Figure 4.31 (b). The observed spherical morphology as well as linear network of aggregates confirmed the observation in the HRSEM results (Figure. 4.30). In constrast, the HRTEM micrographs of JT17, Figure 4.31 (c) and (d) demonstrated clearly visible filamentous aggregates. It should be noted that in the case of the stabilized particles the degree of particle agglomeration observed in Figure 4.31 (c and d) was less compared to that displayed in Figure 4.31 (a and b) (prepared without a stabilizer). This gives evidence of the stabilising effect of the polyethylene glycol chains. The observed spherical and chain-like morphology has been reported for a typical nZVI by several researchers (Üzüm et al., 2008; Xi et al., 2010). The crystalline nature of the non-stabilized and stabilised nZVI particles was further examined by SAED as shown in Figure 4.32.

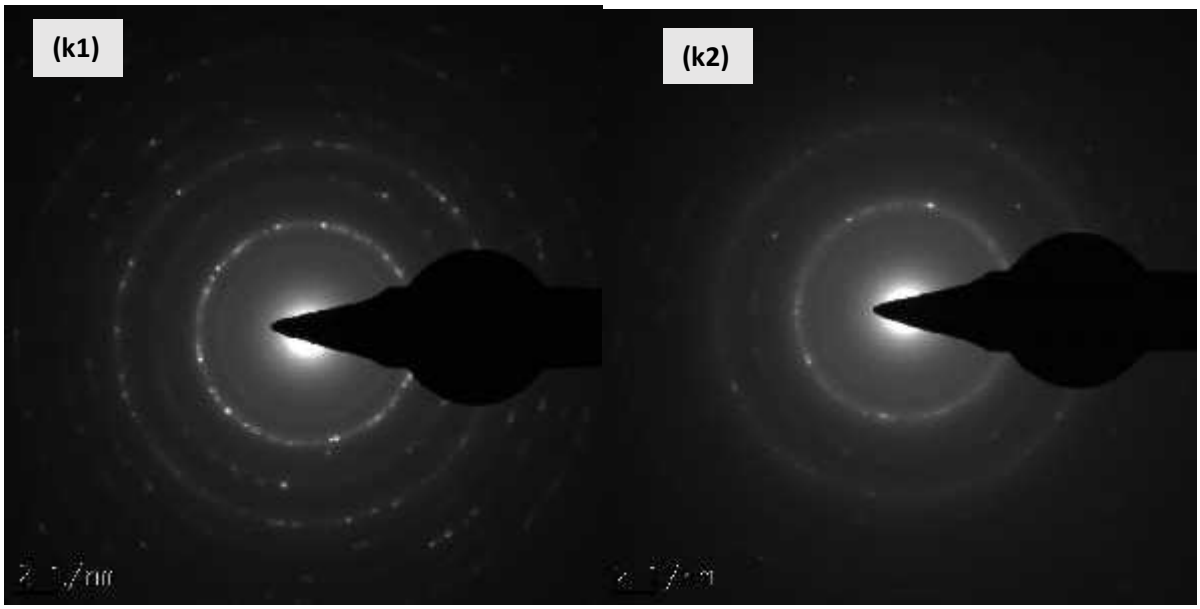

Figure 4.32: SAED pattern of: (k1) JT16 (k2) JT17

The SAED pattern of non-stabilised and stabilised nZVI in Figure 4.32 shows polycrystalline nature of the nanoparticles by the bright homogeneous polymorphic ring with small bright reflection of polycrystalline grains. The dotted lines with interplaner distance of 0.222 nm according to image J software corresponded to the crystal plane crystal plane (110), which indicates the formation of a typical nano zero valent iron particles. This result is in accordance with the findings of Jabeen et al., (2013) who synthesised nano zero valent iron-graphene composite. They found that the interplaner distance of the synthesised graphene containing nano zero valent iron particles containing graphene was 0.202 nm which corresponded to the crystal plane (110).

4.3.3 *EDS analysis of non-stabilized and stabilized nano zero valent iron*

The EDS analysis was done to investigate the elemental composition of the non-stabilised and stabilised nano zero valent iron particles. Detailed experimental protocol for the synthesis of sample JT16 and JT17 via the modified borohydride reduction method is described in Section 3.2.4.1. and 3.2.4.2. respectively. Sample JT16 and JT17 were coated with Au and Pd prior to analysis to prevent charging, which often distorts imaging during measurement. The detailed procedure was explained in Section 3.4.3. The weight percentage of each element present in JT16 and JT17 is presented in Table 4.7.

Table 4.7: Energy dispersive X-ray spectroscopy (EDS) spectrum of JT16 and JT17 in weight percentage

Samples	Elements (weight percentages)				
	Fe	**O**	**C**	**Na**	**B**
JT16	69,32	26,99	-	1.66	2,03
JT17	71,92	22,74	5,34	-	-

According to Table 4.7, it can be seen that both samples (JT16 and JT17) mostly contained Fe and O in different proportion. No carbon peak was detected in sample JT16 but carbon was present in JT17. The carbon peak in sample JT17 was linked mostly to the stabilising agent (polyethylene glycol). The greater atomic percentage of Fe as shown in Table 4.7 suggested that Fe remains the most abundant and integral component of the nZVI. Apart from the strong signals in the Fe region, other peaks such as Na and B were also identified in non-stabilized nZVI which may be ascribed to the reducing agent ($NaBH_4$) used. These peaks (Na and B) were however not detected in the stabilized nZVI, which may be due to the smaller quantity of the individual element. The presence of Fe, O, and C on the surface of JT17 was further confirmed by XPS (see Figure 4.34).

4.3.4 *FTIR analysis of non-stabilized and stabilized nZVI*

The structural elucidation and vibrational state of non-stabilised (JT16) and stabilised nZVI particles (JT17) formed via modified borohydride reduction method were examined using FTIR technique described in section 3.4.9. The FTIR spectra of both samples are shown in Figure 4.33.

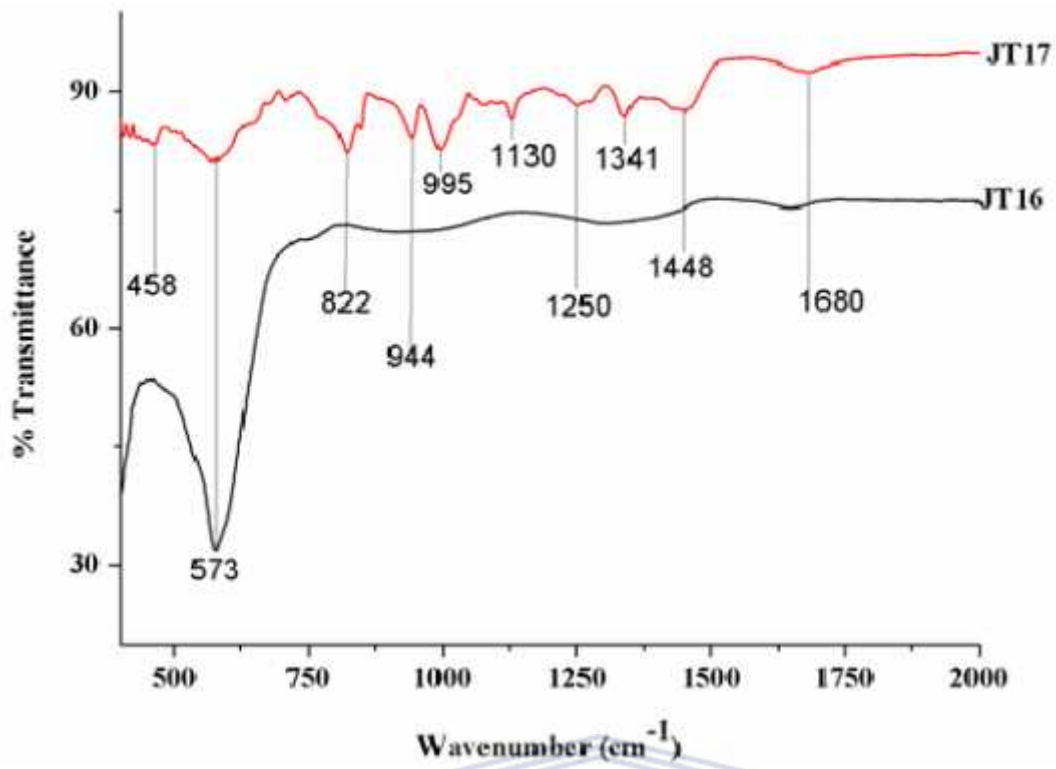

Figure 4.33: FTIR spectra of sample JT16 and JT17

Figure 4.33 represents the FTIR spectra of sample JT16 and JT17 respectively. Only one prominent absorption band was observed in JT16 at 573 cm^{-1}, which was also identified in JT17, although the intensity was not as strong as in the case of JT16. The absorption peak at 573 cm^{-1} observed in JT16 and and JT17 corresponds to the Fe-O bond. This absorption peak (573 cm^{-1}, Fe-O) was also observed by Ayob et al., (2012) for polyacrylic acid stabilised nano zero valent iron particles prepared using ultrasonic irradiation method. This prominent peak has been widely reported for typical nano zero valent iron particles (Madhavi et al., 2013; Singh et al., 2011). The small absorption bands in the stabilized nZVI at 3336 and 1680 cm^{-1} were ascribed to OH stretching and bending vibration of the surface adsorbed water (Singh et al., 2011). The OH functional group may possibly have emanated from the polyethylene glycol. The characteristics IR band at 1343 and 1448 cm^{-1} were ascribed to C-H bending vibration and aliphatic C-H stretching respectively. The absorption bands observed at 1130 and 1252 cm^{-1} arise from C-O-H bend and C-O stretching vibrations of nZVI particles in polyethylene glycol media according to Shameli et al., (2012). The observed characteristics band at 822, 944 and 995 cm^{-1} were ascribed to the binding of the nZVI to isolated C-H, C-C-O or C-O-H groups on the polyethylene glycol. The presence of these

functional groups further confirmed that the surface of nZVI had been stabilised with polyethylene glycol.

4.3.5 *X-ray diffraction analysis*

An X-ray diffractometer with Cu-Kα radiation operated at 40 kV voltage and 40 mA current was used to determine phase composition and particle size of the synthesised nano zero valent iron nanoparticles. The detailed experimental procedure have been described in section 3.4.2.1 and 3.4.2.2. The iron nanoparticles were placed in a glass holder and the diffractograms were run from 10º to 80 º at a scanning rate of 2 º/min as explained in section 3.4.1. The XRD diffractogram of freshly synthesised stabilised and non-stabilised nZVI is depicted in Figure 4.34.

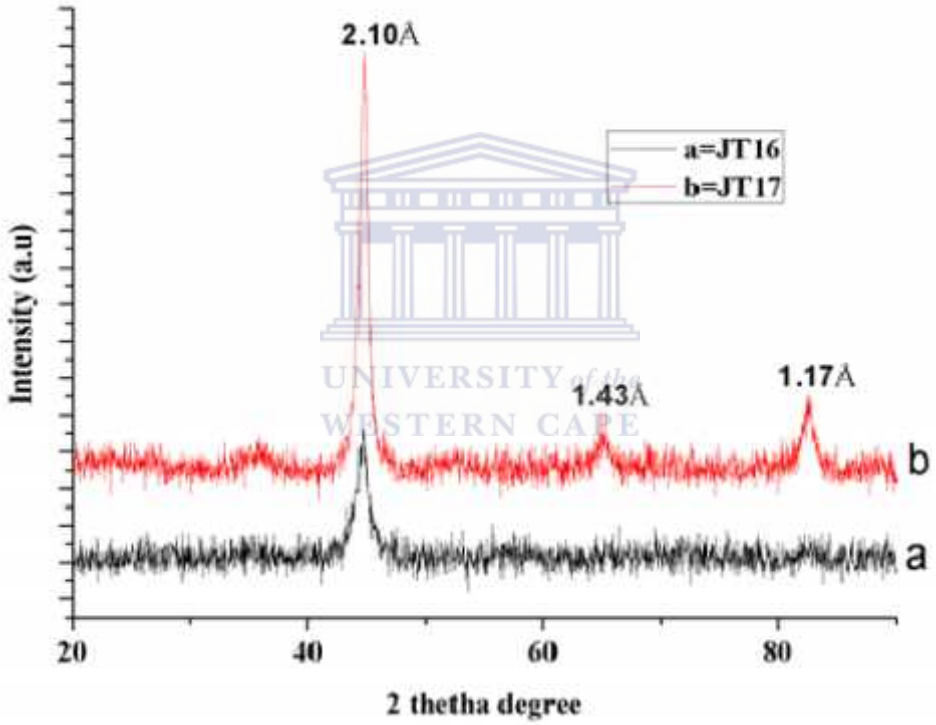

Figure 4.34: XRD spectrum of sample: (a) JT16 and (b) JT17

The XRD spectra of both the non-stabilized (JT16) and polyethylene glycol stabilized nZVI (JT17) are illustrated in Figure 4.34. The broad intense diffraction peak at 2 θ values of 44.77º which correspond to reflection plane of 110 (2.01 Å) revealed the formation of iron in zero valent state, which matched well with JCPDS (00-006-0696). The average particle size was calculated using the Debye Scherer's equation shown in equation (4.3) above. From the calculation, it was revealed that the particle sizes of non-stabilized and stabilized nZVI were 19.5 nm and 22.6 nm respectively. Similarly, diffraction peaks in both cases indicate the

crystalline nature of the nZVI particles. Apart from the broad diffraction peaks observed at 2 θ values of 44.77º, there were two additional low intensity diffraction peaks at 2 thetha value of 65.2º and 82.6º in the stabilized nZVI. These diffraction peaks corresponded to a reflection plane 200 (1.43 Å) and 211 (1.17 Å). Therefore, the presence of the three prominent peaks in the XRD pattern of the stabilized iron particles at a 2-thetha value of 44.7º, 65.2º and 82.6º agrees with typical nano zero-valent iron particles. Furthermore, the core shell of the iron nanoparticles is predominantly metallic α- Fe with body centre cubic (bcc) structure in zero state and no other shell or peak corresponded to contain iron oxide (FeO; Fe_2O_3, Fe_3O_4). This results corroborates the XPS analysis shown in (Figure 4.36 b), where metallic Fe in zero state was observed at 707.5 eV. Kushwaha et al., (2014) had earlier shown that nano Fe particles may have core–shell structure, Fe^0 (core) and iron oxides (shell). This result is in accordance with the findings reported by Sun et al., (2012) who synthesised nano-Fe^0 encapsulated in carbon spheres. They demonstrated the formation of a pure zero valent iron particles with a body-centered cubic (bcc) crystalline structure possessing crystal plane (110) and (200) respectively. Jabeen et al., (2013); Singh et al., (2011) and Wang et al., (2015) ascribed the observed diffraction peak at 45.1º to the formation of nano-Fe in zero valent state. The differences in particle size of JT16 (19.5 nm) and JT17 (22.6) could be attributed to the stabilization effect of the polyethylene glycol which prevented rapid particle agglomeration. The results agreed with the previous findings reported in the literature (Singh et al., 2011; Sun et al., 2006; Xi et al., 2010).

4.3.6 *XPS analysis of Polyethylene glycol stabilized nano zero valent iron particles*

XPS analysis of the polyethylene glycol-stabilized iron nanoparticles was done to examine the surface composition of the samples. XPS PHI 5400 equipped with hemispherical sector analyzer operated using Alα K non-monochromated radiation with energy 1486.6 eV, at 300 W and 15 keV was used to examine the surface composition of the material. The detailed instrumental conditions and measurements are described in Section 3.3.7.1. Figure 4.35 represents the full XPS profile of polyethylene glycol stabilized nano ZVI particles (JT17) while Figure 4.36 - 4.38 depicts the photoelectron measurement of individual elements present in the sample namely: Fe 2p, O 1s and C 1s respectively.

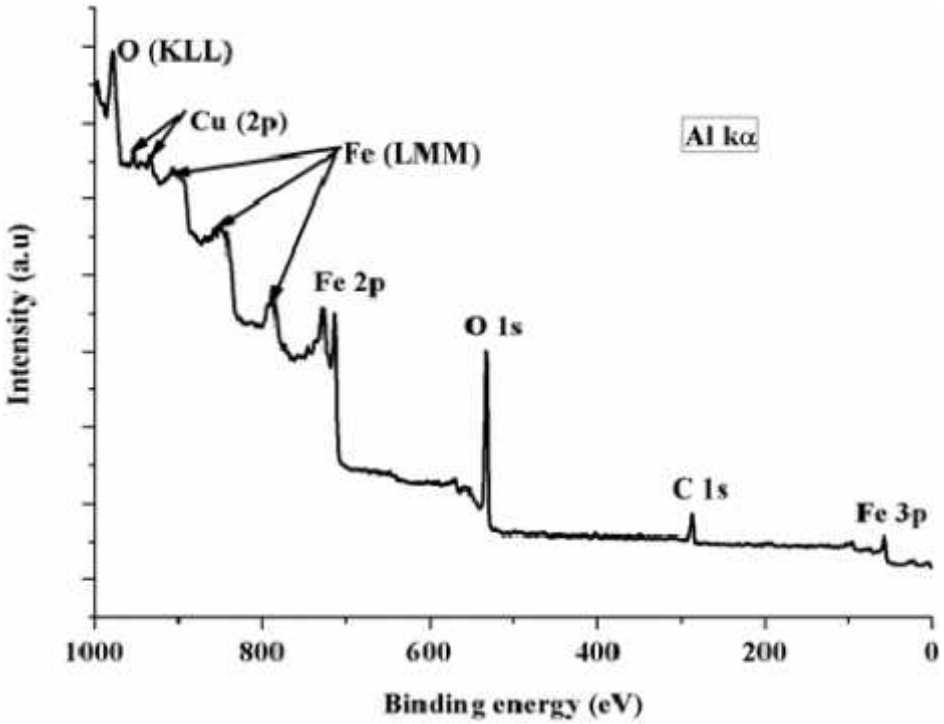

Figure 4.35: General XPS survey of sample JT17

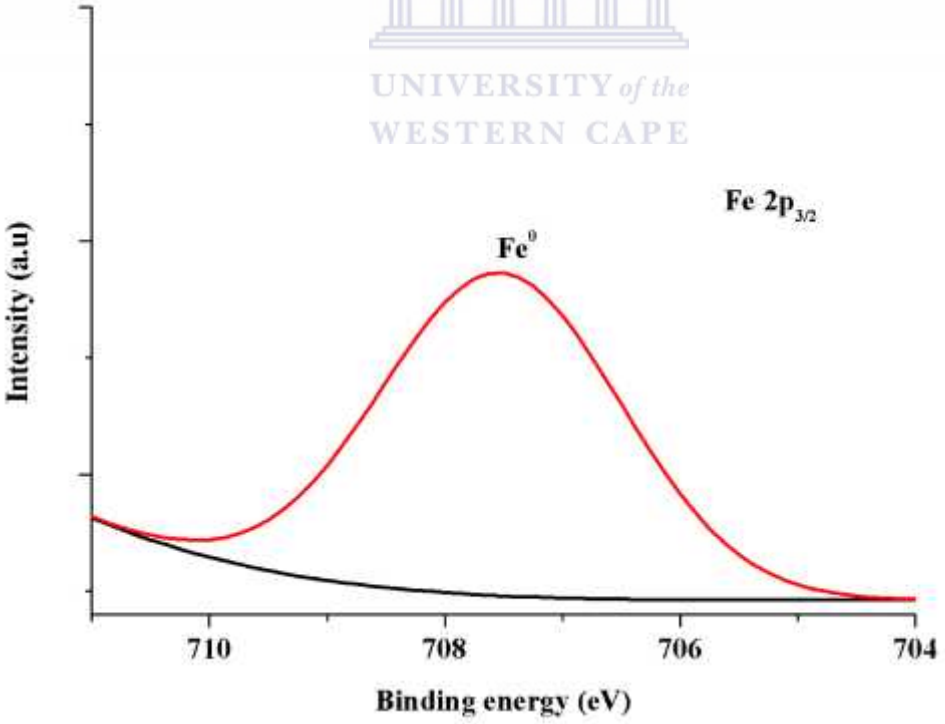

Figure 4.36: High resolution XPS profile of Fe 2p in JT17

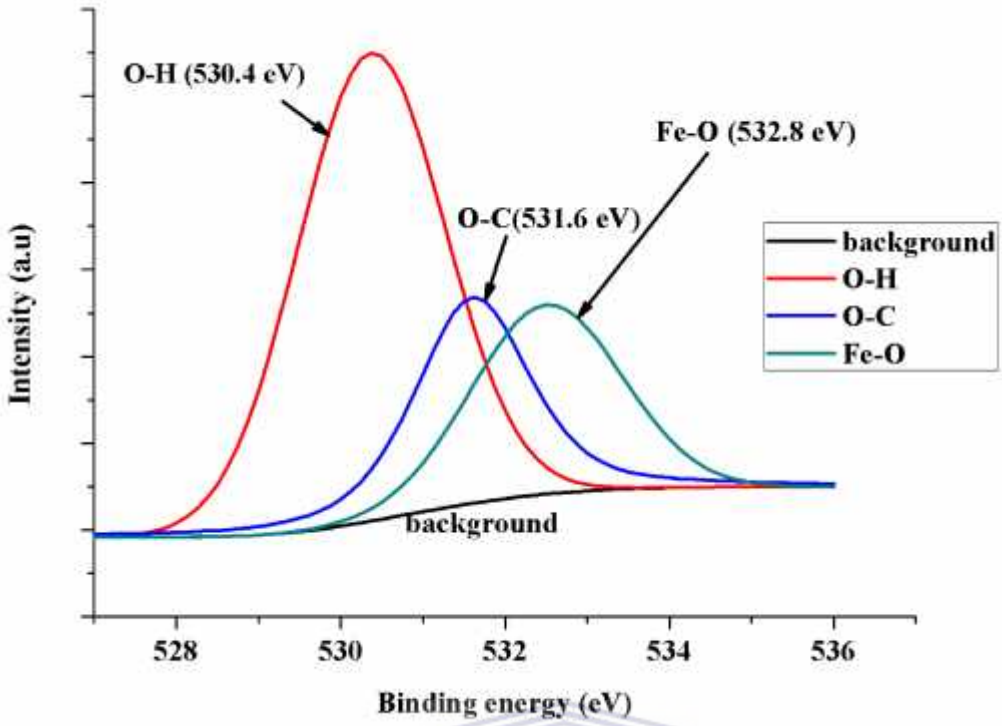

Figure 4.37: High resolution XPS measurement of O 1s in JT17

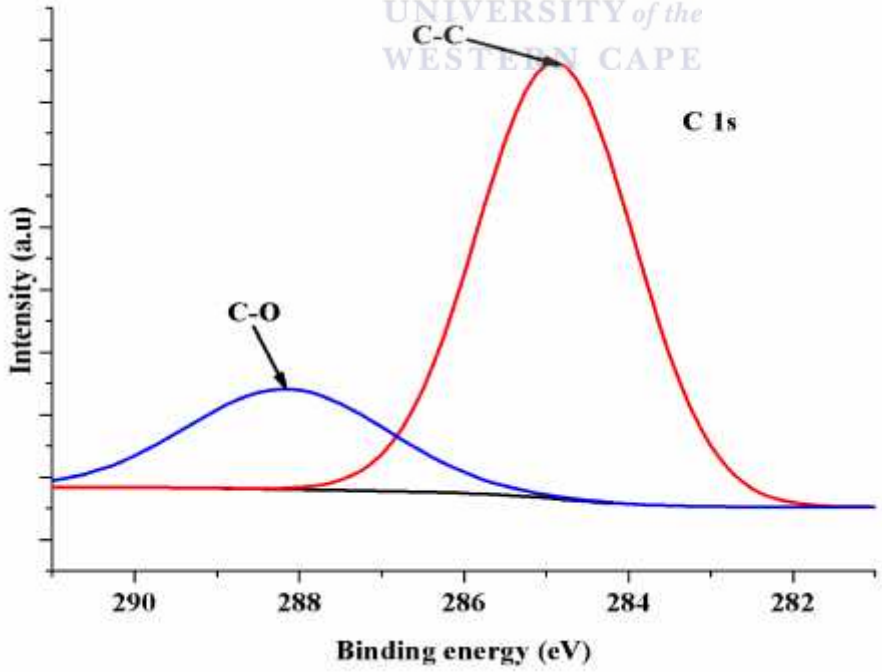

Figure 4.38: The high resolution XPS scan for the C 1s envelope in JT17

In Figure 4.36, the peak located at 707.5 eV corresponded to Fe $2p_{3/2}$ in the zero valent state. Besides Fe in the nanoparticles, additional elements identified by the XPS included O 1s and C 1s. The XPS profile of O 1s shown in Figure 4.37 revealed three prominent peaks in the binding energy positions of 530.4, 531.6 and 532.8 eV respectively. The O 1s peak at 530.4 eV corresponded to OH group present in the polyethylene glycol chain while the observed value in the binding energy region of 531.6 eV was assigned to O-C. The O-C suggests bonding of oxygen to carbon which indicates the existence of carbon species from polyethylene glycol in the sample JT17. The observed peak in the binding energy region of 532.8 eV was assigned to O in FeO, which confirmed the existence of Fe oxide particles. In Figure 4.38, three different carbon peaks were located separately in the binding energy region of 284.8, 286.4 and 288.0 eV , which corresponded to C-C, C=C and C-OH. The carbon signals must be originating from the polyethylene glycol used a stabilizing agent. The XPS spectrum of the JT17 agreed with the XRD result (see Figure 4.34), although FeO was not detected in the XRD probably due to its generally amorphous nature. Similar observation on the presence of Fe^0 and iron oxides was reported by Xi et al., (2010) on nano zero valent iron particles synthesised from $FeCl_3.6H_2O$ and $NaBH_4$. The existence of zero valent iron in the binding energy position of 706.99 or 707.5 eV has been widely reported in the literature (Jabeen et al., 2013; Sun et al., 2006). The Cu shown in Figure 4.34 originated from the Cu sample holder. Furthermore, it is worth mentioning that most elements identified in the EDS analysis (JT17) were also observed in the XPS spectra, which shows that two results complement each other.

4.3.7 *BET surface area of JT16 and JT17*

The surface area and pore size distribution patterns of sample JT16 and JT17 were investigated using Micrometrics ASAP 2020 surface area and Porosity Analyzer. The detailed experimental procedure for the synthesis of samples JT16 and JT17 haS been described in Section 3.3.4.1 and 3.2.4.2. The BET analysis of the samples was conducted according to the instrumental conditions described in Section 3.3.6.1. The results of N_2 adsorption-desorption isotherm of JT16 and JT17 as well as pore size distribution are presented in Figure 4.39 and 4.40.

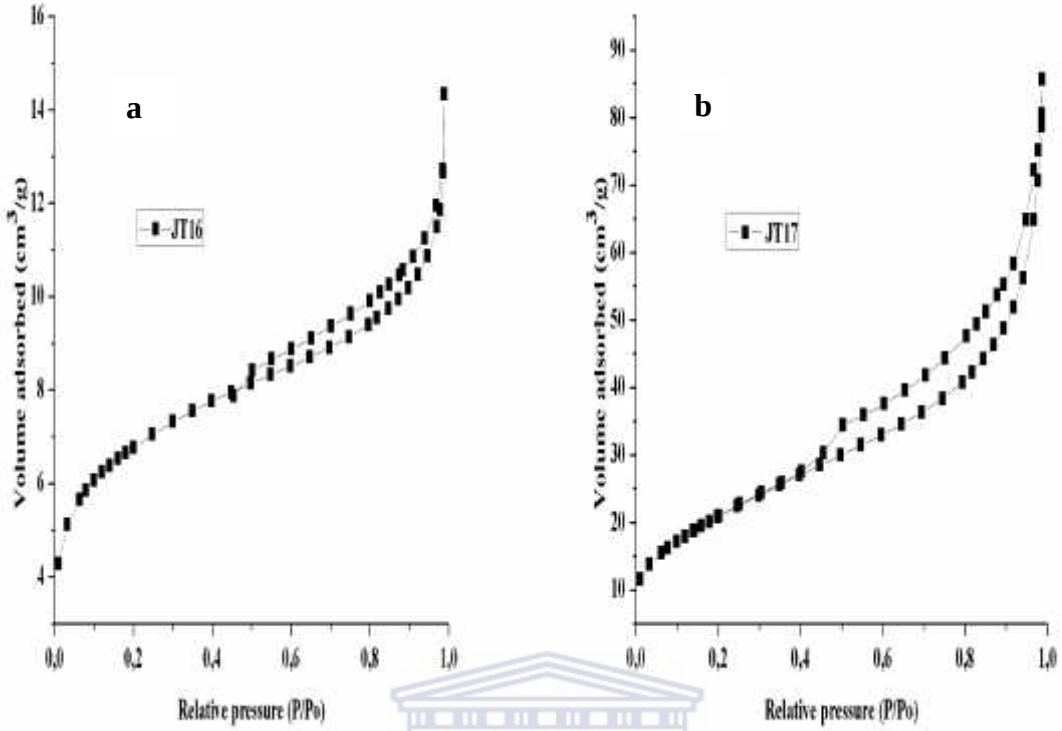

Figure 4.39: N_2 adsorption-desorption isotherm plot of: (a) JT16 (b) JT17

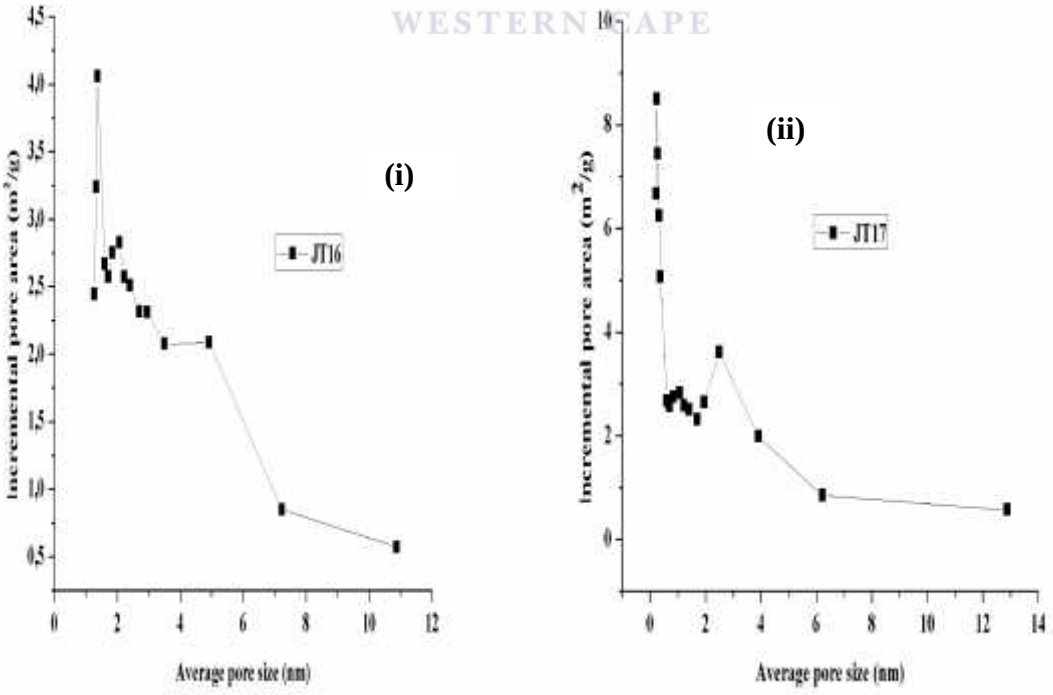

Figure 4.40: Pore size distribution of: (i) JT16 (ii) JT17

The BET surface area of JT16 and JT17 as obtained from N_2 adsorption-desorption were 28.82 and 76.77 m^2/g respectively. The BET surface area of JT17 was three time more than JT16, which can be attributed to the use of polyethylene glycol as a stabilizer which prevented aggregation of the individual particles (see HRSEM images shown in Figure 4.30 (c) and (d)). According to the International Union of Pure Applied Chemistry (IUPAC) nomenclature, the adsorption isotherms of both samples were type IV isotherms. Sample JT17 exhibited a strong H3 hysteresis loop characteristics of cylindrical shaped pores with wider bodies, which is a characteristic of a mesoporous structure. The mesoporous structure of sample JT17 exhibited a bimodal pore size distribution at relative pressure range of 0.46 - 1.0. The bimodal pore size distribution was not clearly defined in the case of JT16, which may be as a result of agglomerations of individual particles. The obtained value was far greater than BET surface area of 0.11 m^2/g reported for commercial ZVI (Xi et al., 2010). It was observed from Figure 4.40 that the incremental pore area of JT16 and JT17 were 4.05 and 8.49 m^2/g respectively. In addition, the pore sizes of JT16 and JT17 were closely related with a narrow distribution range of 1.07 -10 nm and 1.22 – 12.8 nm respectively. The two samples (JT16 and JT17) had a major peak located below 3 nm. This narrow pore size distribution curve suggested that both samples had very even pores in the mesoporous region. The narrow pore size distribution pattern can be linked to intra-agglomeration among the particles. These results were similar to the findings of Sun et al., (2012) who reported adsorption isotherm type IV of H3 hysteresis loop for typical nZVI encapsulated in microcarbon spheres. Lastly, the HRSEM, HRTEM, EDS, XRD and XPS analysis complement one another and confirmed the formation of nano zero valent iron particles.

4.3.8 *Section summary*

In this section, nano zero valent iron particles with higher specific surface area than the commercial nZVI reported in the literature due to the stabilising effect of polyethylene glycol was synthesised using the modified borohydride reduction method. Both HRSEM, HRTEM, XRD, and XPS analysis demonstrated the formation of filamentous iron nanoparticles in zero valent state.

4.4 Photocatalytic degradation of methylene blue by supported TiO_2 nanocrystals

TiO_2 photocatalyst has been widely utilised in the treatment of contaminated liquid either in the powder or in immobilised form upon a rigid substrate materials. For instance, powder TiO_2 photocatalyst has high surface area, and is uniformly dispersed in the solution thus enables easy interaction with the pollutants. On the other hand, the use of powder TiO_2 still has some associated shortcomings which limits its industrial applications such as post-separation and recovery after treatment, high electron-hole recombination rate, inhibition of UV light penetration and interaction with the pollutants, which limits the catalytic efficiency. Conversely, supported TiO_2 nanoparticles in spite of restricted surface area compared to powder TiO_2 do not require post-separation and there is no interferences with UV-light in a photocatalytic reactor. Thus, the photocatalytic activity of the various supported TiO_2 nanocrystals prepared by calcination at 8% PAN/DMF/$TiCl_4$ solution at different temperatures (300 ºC, 350 ºC and 400 ºC) for holding times ranging from 1-4 h (JT1-JT12) using MB as a model pollutant under UV-light is presented. The PAN precursor acted as binder between the stainless steel mesh and the TiO_2 nanocrystals. The detailed synthesis protocol and photocatalytic experimental set-up have been described in section 3.2.2 and 3.5.2 respectively. The supported TiO_2 nanocrystals with the highest photocatalytic activity (JT7) was selected and different size of metallic Ag were deposited on JT7 (section 3.2.3). The photocatalytic activity of the Ag doped TiO_2 nanocomposites (JT13-JT15) in comparison with the optimum supported TiO_2 nanocrystals (JT7) were equally evaluated and results presented. Detailed information on the samples synthesis conditions and sample codes can be found in Chapter three Table 3.2.

4.4.1 *Effect of pyrolysis temperature on MB removal rate*

It was shown that pyrolysis temperature had an effect on the characteristics of the synthesised materials in section 4.1. In this study, TiO_2 photocatalysts supported on a stainless steel mesh prepared by the sol-gel method were pyrolysed in a furnace at different temperatures (300 ºC, 350 ºC and 400 ºC) for holding times ranging from 1 to 4 hr. The results of the effect of the pyrolysis temperature used during preparation of the catalysts on the photocatalytic activity toward MB by various supported catalysts (JT1-JT12) are presented in Figure 4.41. Figure 4.41 - 4.43 depict the MB removal rate using stainless steel mesh supported TiO_2 nanocrystals pyrolysed at 300 ºC, 350 ºC and 400 ºC for 1-4 hr. The photocatalytic experiments were conducted in a self-designed 500 mL beaker photoreactor containing 50 mL of 10 ppm MB solution (pH 6.8) and 30 mg of the supported catalysts as described in

Section 3.2.5. Prior to the photocatalytic measurements, control or blank experiments were carried out on MB solution in the absence of the supported catalysts. The solution was magnetically stirred under UV light in the absence or presence of catalyst in the dark for 6 h. Furthermore, each catalyst was later exposed to UV light and the MB removal rate was monitored for 6 h. The experiment was repeated twice (n= 2) and average experimental values were determined. The obtained results are presented in Figure 4.41 - 4.43. The time given in the legend represent the exposure time of each sample to UV light. While the label on the X axis represents the conditions applied during the synthesis procedure.

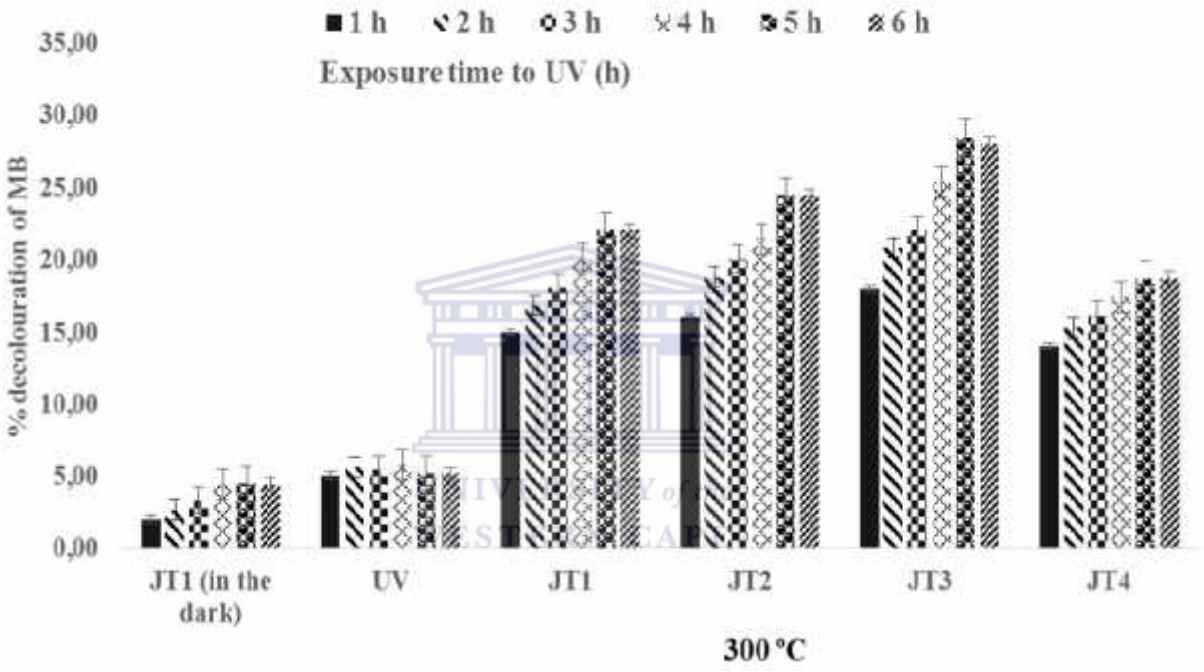

Figure 4.41: Percentage decolouration of MB by JT1-JT4. (MB concentration (10 mg/L), pH 6.8, catalyst dose 30 mg, UV lamp (9W), solution volume (50 mL), irradiation time (1-6 h), stirring speed 150 rpm), number of replicates=2

Figure 4.41 represents both the control experiment and the photocatalytic activity of supported TiO_2 nanaocrystals prepared using pyrolysis at 300 ºC for 1-4 h (JT1-JT4) and then tested for photocatalytic activity using MB as a model pollutant. The % MB decoloration was estimated using the formula provided in section 3.2.5.6. The result in Figure 4.41 (TiO_2 without UV) in the dark thus demonstrates clearly that only 4.4 % of the MB was decoloured in the dark over 6 h due to adsorption of the dye onto the surface of the catalyst. Likewise in Figure 4.42-4.43, the MB adsorption onto the catalyst monitored in the dark never exceeds 5.2 % of the initial concentration of MB. It is obvious that the high degree of elimination of

MB achieved for the differently prepared samples was not based on adsorption phenomenon only simply because the supported catalysts did not show a strong degree of adsorption towards the target compound. No significant change was observed over the irradiation time thus the result of adsorption can be considered negligible. In the same vein, the direct photo-mineralization of the MB solution under UV irradiation in the absence of the supported catalysts (Figure 4.41 - 4.43) indicates that only 5.2 % MB was decoloured at the end of 6 h, which is not significant when compared to the amount of MB decoloured when irradiated by UV light in the presence of the catalyst and can be considered negligible. The supported catalyst prepared by pyrolysis at 300 ºC for 3 h (JT3) had highest MB removal decolouration percentage while the catalyst prepared at 4 h holding time (JT4) had the lowest value As shown in Figure 4.41, with sample JT1, the percentage decolouration of MB increased from 15 % - 22 % with an increase in UV irradiation time up till 5 h and thereafter reduced at 6 h. For JT2 and JT3, MB decolouration percentage increased from 16 % - 24 % and 18 %-28 % respectively under the same conditions as JT1. On the contrary, the percentage decolouration of MB in the presence of JT4 under intense UV-light slightly increased from 14% -18%. This value is however lower than that obtained with JT1-JT3. This showed that for the catalysts prepared at 300 ºC and holding time longer than 3 h with an UV exposure time of 5 h, the MB decolouration efficiency decreased. The increment in the MB decolouration efficiency correlated with the holding time for each catalyst and could be attributed to the time of pyrolysis at 300 ºC applied in the preparation of the catalyst. As a matter of fact, at 300 ºC most TiO_2 nanocrystals were still embedded/ entrapped within the polymer as demonstrated in the HRSEM/XRD results (see Figure 4.1 and 4.12). The lower MB decolouration efficiency observed for JT4 can be attributed to weak adhesion between the catalyst and the stainless steel mesh, which resulted in loss of most of the catalyst from the mesh during photocatalyst. Only a small quantity was retained and that was perhaps responsible for its low activity towards MB. Similar trends were observed in Figure 4.42 and 4.43. This shows that the time of pyrolysis during catalyst preparation required careful control to remove sufficient PAN to expose the catalyst but not to lose the adhesive PAN component completely.

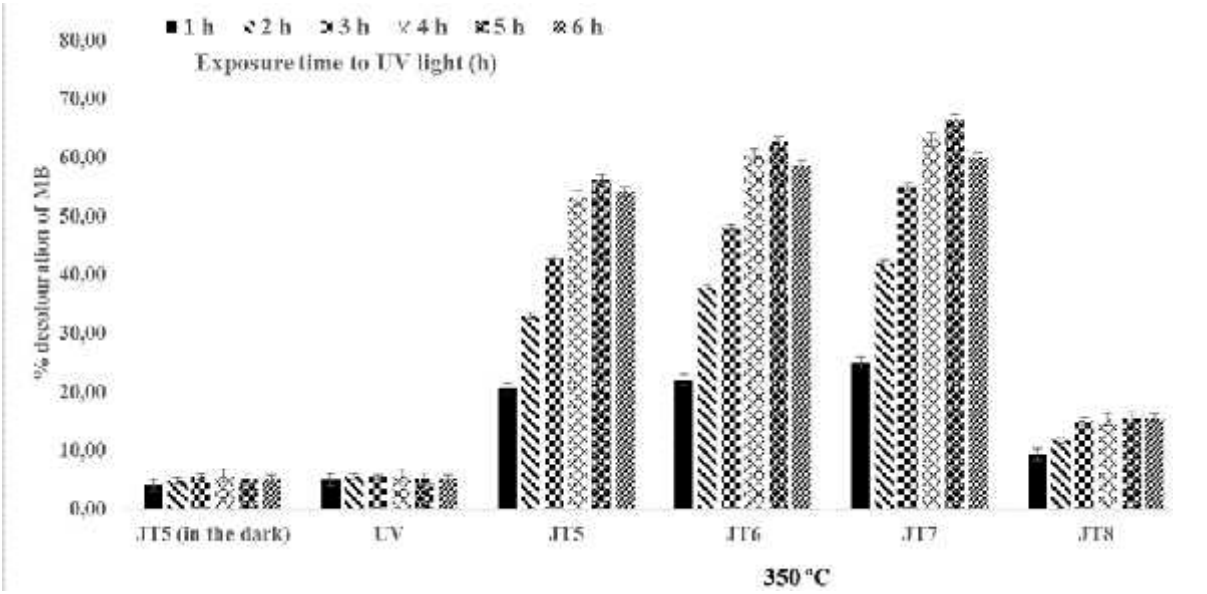

Figure 4.42: Percentage decolouration of MB by JT5-JT8. (MB concentration (10 mg/L), pH 6.8, catalyst dose 30 mg, UV lamp (9 W), solution volume (50 mL), irradiation time (1-6 h), stirring speed 150 rpm, number of replicates=2

In Figure 4.42, the photocatalyst prepared at 350 ºC showed relatively high removal of approximately 70 % of the dye molecule compared to those prepared at 300 ºC. The slight decolouration in the absence of the catalyst is partially due to the interaction of the photonic energy from UV light with the carbon-carbon bond in the MB resulting in chromophore cleavage and mineralization. Furthermore, the MB decolouration efficiency observed for each sample as the UV irradiation time increases from 1 - 5 h were as follows: JT5 (20.6 % - 56.2 %), JT6 (22.4 % - 62.6 %), JT7 (25.1 % - 66.7 %), and JT8 (9.3 % -15.1 %) respectively. It is obvious that sample JT7 had approximately 67 % MB decolouration efficiency after 5 h of irradiation while sample JT8 had the lowest MB removal efficiency of 15.1%. Jia et al. (2012) had earlier demonstrated that incident light of lower wavelength in the range of 253.7 and 289 nm possessed high photonic energy which was capable of decomposing the organic carbon framework by itself. Additionally, organic dyes such as MB with two unsaturated benzene rings structure that show strong absorption of short-wave UV light. Thus, exposure of MB without catalyst to UV light of short wavelength obviously caused some MB removal. In the case of TiO_2 in the dark, the decolouration of MB was ascribed to adsorption of the MB onto TiO_2 due to surface attractive forces. The two control experiments showed that only limited MB decolouration occurred in either case and the overall performance of the TiO_2 catalyst did not depend on adsorption alone. Similar results have been reported in the

literature on the performance of TiO_2 photocatalysts in the dark and under UV irradiation alone (Ba-Abbad et al., 2012; Carlucci et al., 2014; Leong et al., 2014).

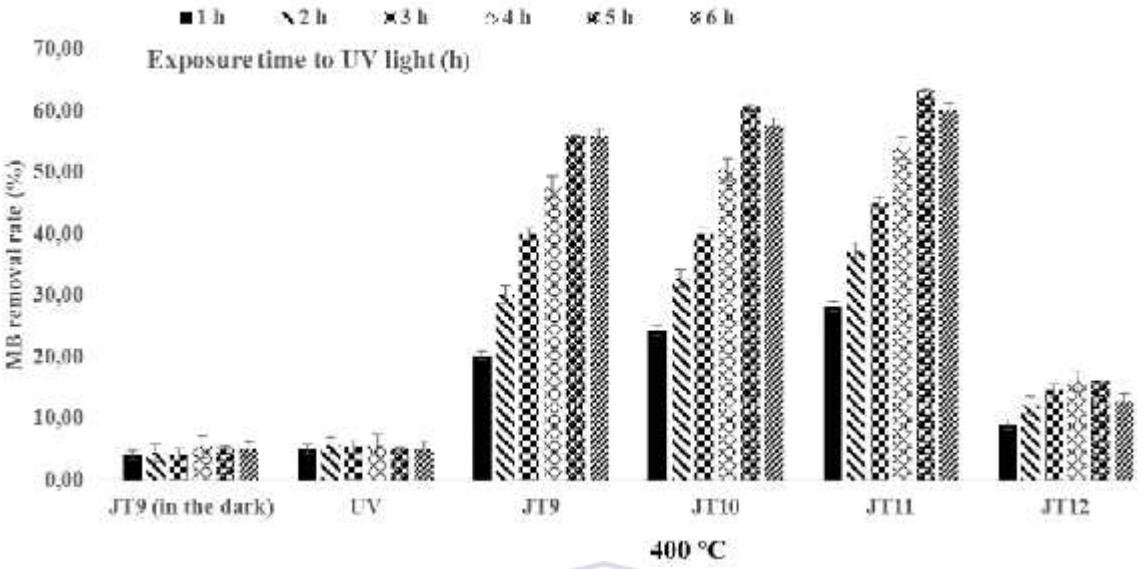

Figure 4.43: Percentage decolouration of MB by JT9-JT12 (MB concentration (10 mg/L), pH 6.8, catalyst dose 30 mg, UV lamp (9 W), solution volume (50 mL), irradiation time (1-6 h), stirring speed 150 rpm, number of replicates=2

In Figure 4.43, the photocatalyst prepared at 400 ºC showed relatively low removal of approximately 60% of the dye molecule compared to those prepared at 350 ºC. According to Figure 4.42 and 4.43, the MB decolouration percentage increased with an increase in UV irradiation time till 5 h for catalyst JT5-JT8 and JT9-JT12 respectively. It should be pointed out that, the percentage decolouration of MB by sample JT8 and JT12 was low compared to other catalysts (JT5-JT7) and (JT9-JT11). Furthermore, the MB decolouration efficiency observed for each sample as the UV irradiation time increases from 1- 5 h were as follows: JT8 (9.3 % -15.1 %), JT9(20.2 % - 55.0 %), JT10 (24.3 % - 60.5 %), JT11(25.2 % - 64.2 %) and JT12(8.9%-16.1%) respectively. Approximately 67% MB decolouration efficiency after 5 h of irradiation was observed for JT7 (350 ºC for 3 h), which was similar to 64.2 % MB decolouration efficiency obtained with sample JT11 (400 ºC for 3 h) compared to 28 % decolouration in the case of JT3 (300 ºC for 3 h). The higher percentage MB decolouration seen for catalysts made at 350 ºC temperature may be due to improve crystallization of TiO_2 and mesoporosity. The high photocatalytic activity at 350 ºC and 400 ºC may also be linked to the anatase nature of TiO_2 as evidence in the XRD results shown in Figure 4.13 and 4.14 respectively. Whereas, low MB decolouration efficiency observed with catalyst synthesised

at 300 ºC (JT1-JT4), may be ascribed to the effect of incomplete decomposition of PAN as evident in the TGA results (see Figure 4.9) causing low mesoporosity as noticed in BET results (see Figure 4.19).

According to Figure 4.41 - 4.43, it can be seen that the percentage MB decolourized upon exposure to UV light increased with an increase in holding time (1-3 h) during preparation and pyrolysis temperature (300 ºC – 400 ºC). This indicates that photocatalytic activity of the synthesised supported catalysts was dependent on both catalyst calcination temperature and holding time. The percentage MB decolouration efficiency increased with an increase in UV irradiation time in the following order; JT7 (350 ºC) > JT 11 (400 ºC) > JT3 (300 ºC). The supported TiO_2 nanocrystals pyrolysed at 350ºC for 3 h (JT7) exhibited greater activity while TiO_2 calcined at 300 ºC for 3 h (JT3) had the least activity possibly due to high carbon content as shown in Figure 4.8. It is noteworthy mentioning that, since no significant increment was observed at 6 h, the optimum UV irradiation time was 5 h irrespective of the catalyst and the calcination temperature. This may possibly due to diffusional constraints and change in pH or due to strong competition between MB and the degradation by-products. The differences in the photocatalytic activity of the catalyst can also be due to different particle size shown in Table 4.3. It is noteworthy mentioning that the pyrolysis temperature and not holding time had a noticeable effect on the photocatalytic activity of the prepared TiO_2 materials. In summary, TiO_2 nanocrystals supported on a stainless steel calcined at 350ºC for 3 h (JT7) exhibited the highest photocatalytic activity towards MB than other conditions.

4.4.2 *Comparison of photocatalytic activity of the supported photocatalyst at optimum irradiation time*

Critical analysis of Figure 4.41 - 4.43 indicates that the percentage MB decolourised by the three samples JT3, JT7 and JT11 after 5 h were higher than other samples. Thus, Figure 4.44 represents the correllation between percentage MB decolourised and BET surface area at optimum UV irradiation time of 5 h using JT3, JT7 and JT11 respectively.

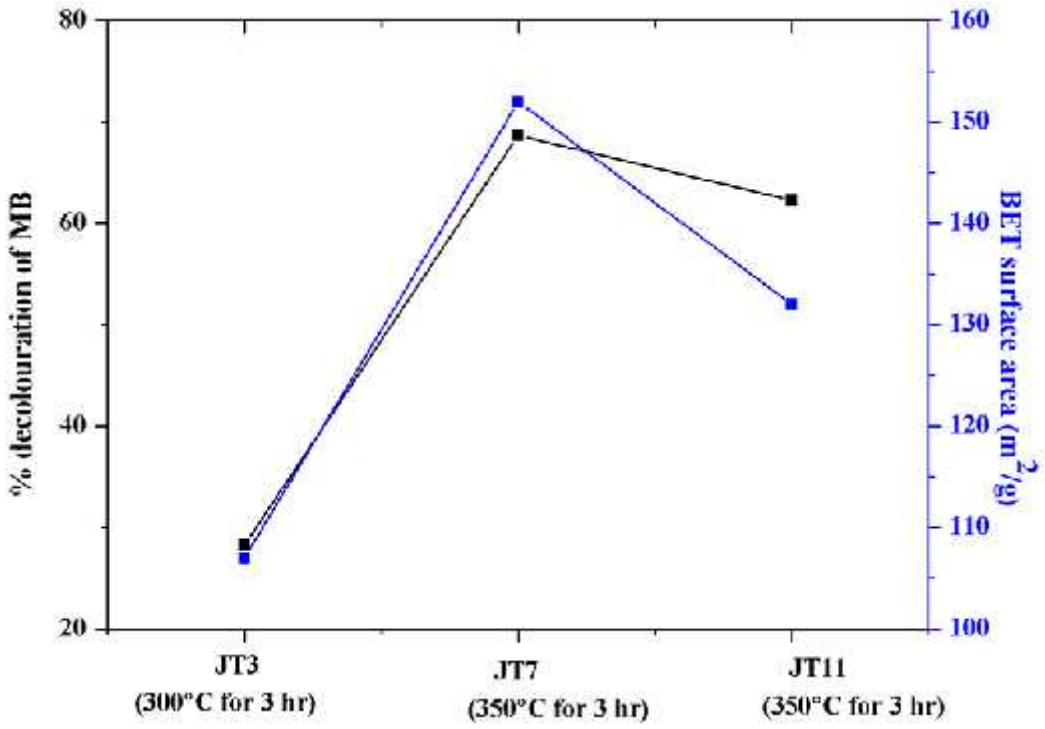

Figure 4.44: Comparison of percentage MB decolourised after 5 h irradiation time using JT3, JT7 and JT11 (Experimental conditions same as in Figure 4.41-4.43)

According to Figure 4.45, sample JT3 with BET surface area of 107 m^2/g had the lowest MB decolouration efficiency of 28% after 5 h under UV light. Whereas, JT7 and JT11 with BET surface area of 152 and 132 m^2/g respectively had MB decolouration efficiency of ~70 % and 63% respectively. By and large, among the three catalysts, sample JT7 had higher photocatalytic activity than others, where approximately 70 % MB molecules were decolourised within 5 h. Also, the photocatalytic activity of the JT3, JT7 and JT11 was dependent upon their BET surface area (see Figure 4.19 and Figure 4.45). The larger the surface area, the more the number of active sites, and the better the photocatalytic activity. Therefore, the difference in the percentage MB decolourised was partially attributed to higher surface area of 152 m^2/g compared with TiO_2 nanocrystals pyrolysed at 400 ºC with surface area of 132 m^2/g as shown in Figure 4.45. The low photocatalytic activity efficiency observed at 400 ºC was attributed to loss of the mesoporous surface area and decreased BET surface area.

The differences in the percentage MB removed by JT3, JT7 and JT11 can also be explained in terms of residual carbon content doped on the TiO_2 layer. The residual carbon content of sample JT3, JT7 and JT11 with respect to percentage MB removed after 5 h exposure to UV

light is shown in Figure 4.46. It can be seen that percentage MB removed was dependent on the amount of carbonaceous species on the TiO_2 layer. It was found that the photocatalytic activity of sample JT7 with 8 % carbon content was the highest followed by JT11 and JT3 containing 4 % and 14 % carbonaceous species. This indicated that the optimum amount of carbon content introduced more active sites on the sample JT7, which made catalyst to adsorb more reactive species than sample JT3 and JT11.

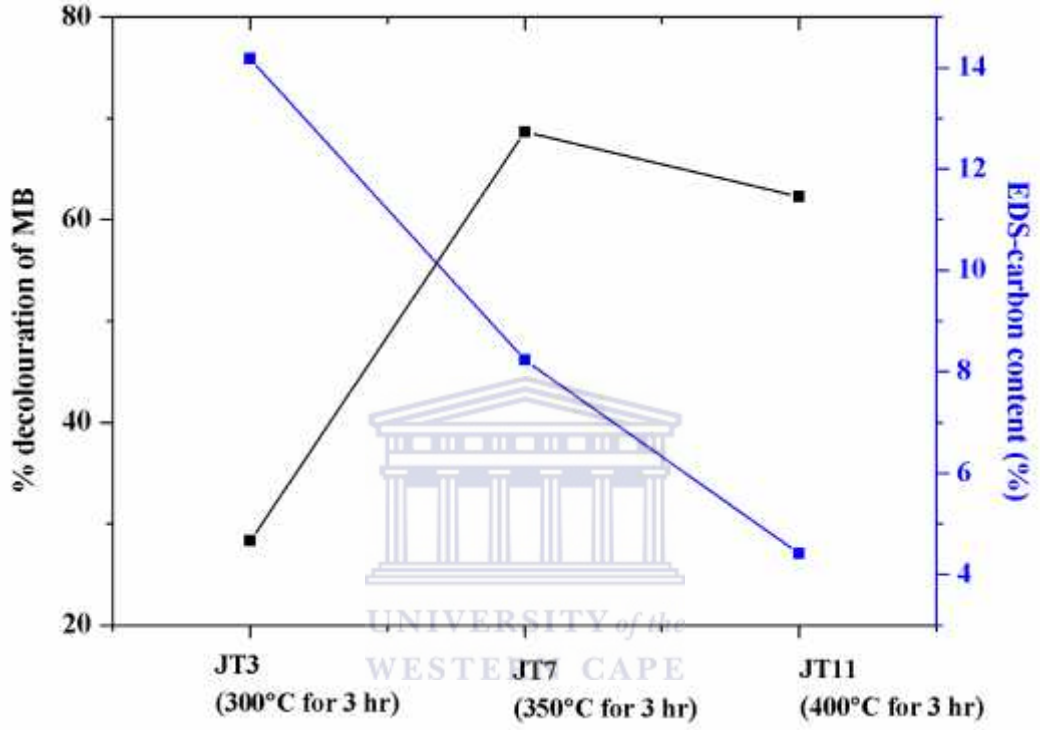

Figure 4.45: Comparison of the MB removal efficiency as function of carbon content using JT3, JT7 and JT11 (Experimental conditions same as in Figure 4.41- 4.43)

The doping effect of the substituted carbon on sample JT7 created more active sites, and prevented electron–hole pairs recombination and hence improved the photocatalytic activity. On the other hand, excessive or under doping of TiO_2 with carbon resulted in high rate of electron–hole recombination and as such reduced the photocatalytic efficiency. Thus, the low photocatalytic activity of sample JT3 and JT11 compared to JT7 as shown in Figure 4.46 can be attributed to excessive doping of sample JT3 or or under doping of JT11 with carbonaceous species. Thus, photocatalytic activity of JT3, JT7 and JT11 was found to depend on the carbon content, and JT7 with optimum dosage showed better photocatalytic performance than JT3 or JT11. Additionally, the percentage MB removed by the JT7 and JT11 within 5 h were closely related. This is due to the fact that the two materials are purely

anatase phase, which have been reported to be more thermodynamically and photocatalytically active than other phases (Ahmed et al., 2011).

Previous studies conducted by Kuriechen and Murugesan, (2013) on the photocatalytic activity of carbon-doped TiO_2 Nanoparticles using Azo dyes under Visible Light showed that the photocatalytic performance of TiO_2 depends on the amount of carbon content. The authors demonstrated that 5 % carbon-doped TiO_2 nanoparticles achieved 79 % decolouration efficiency for azo dyes compared to 2.5 % or 7.5 % carbon doped TiO_2 nanoparticles that managed to remove 59 % and 55 % respectively after 60 min. Zhao et al., (2009) ascribed a sharp decrease in the photocatalytic activity of TiO_2 nanoparticles at higher calcination temperature to excessive crystallite growth or collapse of hollow structures. Whereas, He et al., (2014) demonstrated that TiO_2 nanoparticles heat-treated at 250 ºC exhibit a greater photocatalytic activity than at 450 ºC. He and colleague, (2014) attributed the observed high photocatalytic activity to an improved crystallization process and reduced crystal defects. Literature survey shows that TiO_2 nanoparticles heat-treated at high temperature (400 – 600 ºC) usually have high photocatalytic activity due to an increase of crystallite size and stability of the anatase phase. Based on the results presented in Figure 4.45 and 4.46, pyrolysis temperature and not the holding time had the most significant effect on the catalytic activity. Thus, sample JT7 (supported TiO_2 nanocrystal prepared by calcination at 350 ºC for 3 h) which exhibited highest photocatalytic activity due to high BET surface area was selected for the next set of experiments, in which silver was added as plasmonic metal.

4.4.3 *Photocatalytic activity of supported Ag doped TiO_2 nanocomposites*

The photocatalytic activity of Ag doped TiO_2 nanocomposites was evaluated using MB as a model compound under UV irradiation at room temperature. The amount of metallic Ag loaded on JT7 was varied with deposition time at constant current of 40 A according to the procedure described in Section 3.2.3.The supported Ag doped TiO_2 nanocomposites prepared as a function of deposition time were labelled as JT13 (1.8 % Ag), JT14 (2.4 % Ag) and JT15 (3.5 % Ag). For comparison purposes, undoped supported TiO_2 nanocrystals (JT7) and Ag loaded carbon doped TiO_2 nanocomposites (JT13-JT15) were subjected to the photocatalytic experiments. The detailed photocatalysis procedure used to test JT7 and JT13-JT15 under UV irradiation was described in Section 3.2.5. The residual concentration of MB was determined using UV-vis spectrophotometry as described in Section 3.4.8. The results of the photocatalytic removal was determined from the residual concentration of MB, and the

percentage decolouration efficiency of MB by JT7, JT13-JT15 is represented in Figure 4.47 and 4.48.

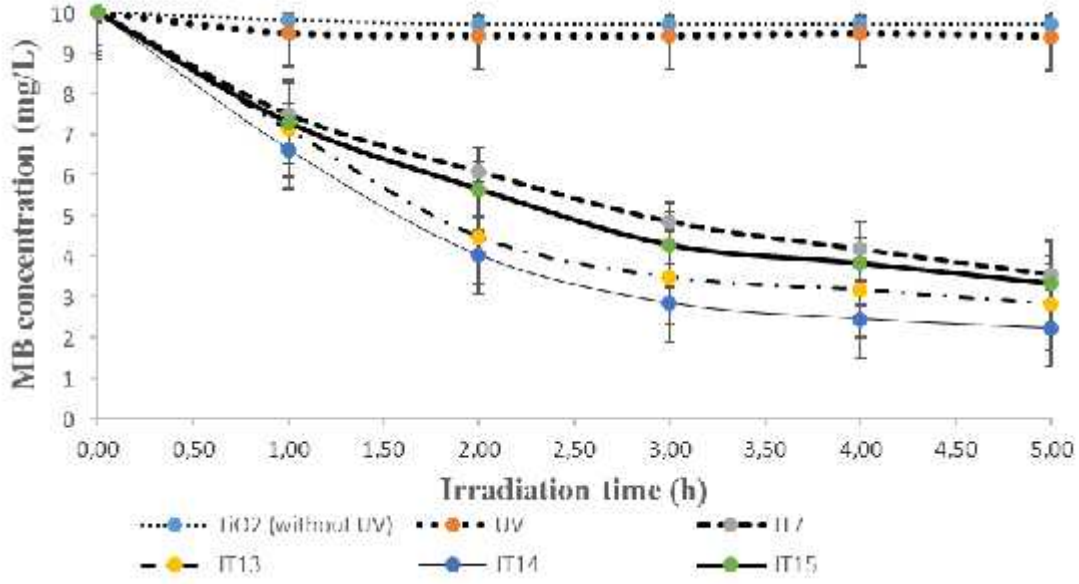

Figure 4.46: Photocatalytic activity of JT7 and JT13-JT15 using MB under UV irradiation. Experimental conditions: Concentration of MB (10 mg/L), catalyst dose 0.35 mg, volume of MB 50 mL and irradiation time 5 h, number of replicates n=2

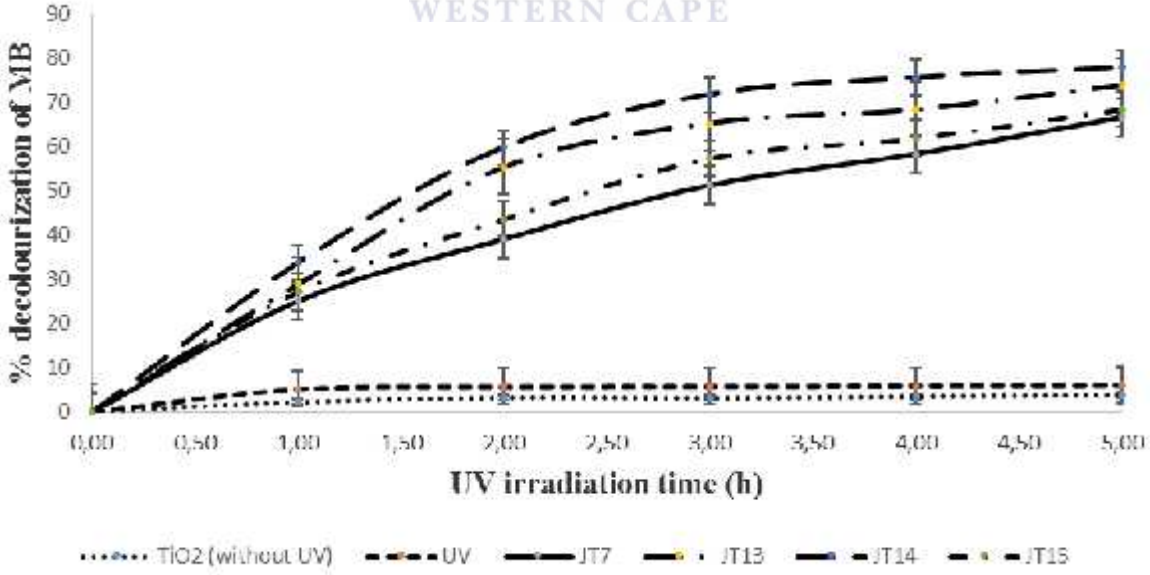

Figure 4.47: Percentage MB decolourized using JT7, JT13-JT15. Experimental conditions: Concentration of MB (10 mg/L), catalyst dose 0. 35 mg, volume of MB 50 mL, and irradiation time (1- 5 h) number of replicates n=2

Prior to the photocatalytic experiment, sample JT7 was immersed in MB solution and magnetically stirred in the dark for 5 h. At the end of 5 h interaction between the catalyst and MB in the dark, about 3.3 % MB was removed (Figure 4.47 and 4.48), which was attributed to the adsorption behaviour of the catalyst. By direct ultra-violet irradiation of MB solution alone in the absence of JT7, only 5.9 % MB removal rate was achieved within 5 h of treatment as discussed previously in Section 4.4.1 (see Figure 4.41 – 4.43). The results of the blank experiments demonstrated that no catalytic activity took place instead the slight MB removal was ascribed to the adsorption behaviour of the catalyst and photolytic reaction induced by UV. This observation has been reported by different studies on TiO_2 photocatalysts (Carlucci et al., 2014; Jia et al., 2012; Leong et al., 2014). Generally, the mechanism of photocatalytic efficiency of TiO_2 nanocrystals is based on the excitation of electrons from the valence band to conduction band upon UV-light irradiation. The photogenerated electrons may be utilised in the degradation of MB. According to the results shown in Figure 4.47 and 4.48, it can be seen that all UV irradiated samples possessed photocatalytic activity in the decolouration of MB compared to the blank experiments. It was shown that the photocatalytic efficiency (MB decolouration efficiency) of sample JT7 increased with an increase in plasmonic Ag loading (JT13-JT15). Maximum MB decolourization efficiency after 5 h by JT7 was approximately 67 %. While that obtained for samples JT13, JT14 and JT15 were 73.4 %, 77.8 % and 68.4 % respectively. The trend of percentage MB decolourized were: JT14 > JT13 > JT15 > JT7, which indicates that sample JT14 (2.4 % Ag) had the highest percentage MB decolourization efficiency of 77.7 % after 5 h and sample JT7 (no Ag) had the lowest value. Thus, the optimum Ag loading on sample JT14 enhanced the MB decolouration efficiency by 10.8 % relative to sample JT7. The higher photocatalytic activity of JT13, JT14 and JT15 above JT7 could be explained in terms of the differences in work function (Φ) value of Ag and TiO_2. The work function of TiO_2 was 4.2 eV whereas that of Ag was 4.6 eV. With the deposition of Ag, an interfacial layer was formed, which accelerated the transfer of electrons from TiO_2 to Ag. The transferred electrons were trapped and separated by Ag on the TiO_2 surface region and thus enhanced the photocatalytic activity by reducing or preventing recombination of holes and electrons, because the Ag deposited on TiO_2 may have created a Schottky energy barrier, which could have reduced electron-hole recombination rate and produced more surface hydroxyl radicals, and thus accelerated the photocatalytic process. This was also evident from the reduction of band energy of JT7 from 3.18 eV to 2.94 eV upon the deposition of Ag as as

shown in Figure 4.24. Therefore, another possible reason for the higher photocatalytic activity of sample JT13, JT14 and JT15 over JT7 could be due to the reduction of the band gap energy of JT7 from 3.18 eV to 2.94 eV by surface plasmon metallic Ag (see Table 4.6). Besides. Also, the MB decolouration efficiency of JT13 was slightly higher than JT15. The enhanced photocatalytic activity of JT13 and JT14 compared to JT15, may be linked to the free electron from metallic Ag which acted as electron trappers and suppressed the electron-hole pair recombination rate. The reduction in activity by sample JT15 could be linked to the complete coverage of TiO_2 surface with Ag as evident in the HRTEM (Figure 4.20 d) thus shadowing the catalyst plus preventing UV irradiation of the surface. Furthermore, the higher amount of Ag on the TiO_2 surface may constitute a barrier for the dye to contact the surface and act as recombination centre for most photo-generated holes thereby inhibiting interaction between TiO_2 and MB. Furthermore, excessive Ag often enlarges the diffusional distance which would affect the formation and interaction of hydroxyl radicals and subsequently decrease the photocatalytic activity (Cao et al., 2008). Studies have shown that too high an amount of Ag particles on the TiO_2 surface may possibly accelerate the hole capture, create interfacial barriers, affect the charge separation and decrease the photocatalytic efficiency of TiO_2 (Subrahmanyam et al., 2012). It is possible to conclude from this study that, high photocatalytic activity of supported Ag doped TiO_2 nanocomposites depends on the optimum amount of silver (2.4 %) added as shown by these results.

4.4.4 *Mineralization kinetics of MB*

The mineralization kinetics of MB by JT7 and JT13-JT15 could be explained using the Langmuir- Hinshelwood first-order kinetics model. The Langmuir–Hinshelwood first order kinetic model demonstrated the relationship between the reaction rate constant and the residual MB concentration for photocatalytic phenomenon taken place at the solid–liquid interface (Fenoll et al., 2015). The Langmuir-Hinshelwood kinetic model is shown in equation 4.5 below

$$r = \frac{-dC_{dye}}{dt} = \frac{k.K.C_{dye}}{1+K.C_{dye}} \quad \text{.....(4.5)}$$

r represents the rate of disappearance of MB, C_{dye} is the equilibrium MB concentration, t (reaction time), K stand for the equilibrium constant of the adsorption behaviour of the catalysts, while k is the reaction rate constant. In the case of low MB concentration dye, KCdye value become small and approach 1, which means KCdye can be ignored or neglected. Thus, the integration of equation (5) taken into cognisance the assumptions with

respect to time t can be reduced to a pseudo first order kinetic equation (4.6) represented below

$$ln\frac{C}{Co} = -kat \quad \text{.....(4.6)}$$

Where C_o represents the initial concentration of MB and C was the concentration at different time interval t, ka represents the first-order reaction rate constant (h^{-1}), which is a product of k.K. The pseudo first-order reaction rate constant depends only on the concentration of the MB in solution at constant dosage of the catalysts. Figure 4.48 represents the graph of ln C/C_o against the irradiation time.

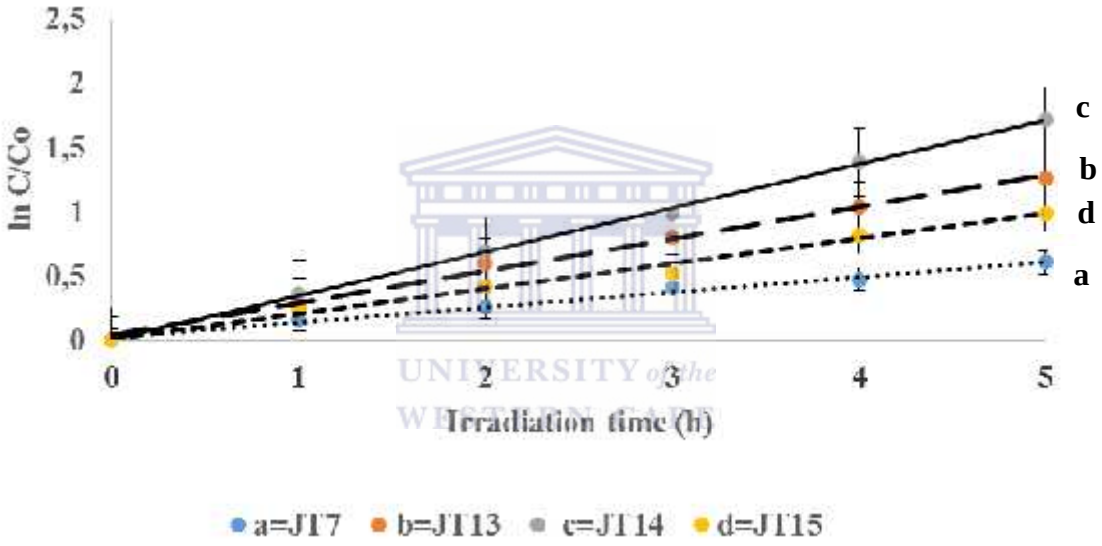

Figure 4.48: The kinetics of MB mineralization using supported TiO_2 nanocrystals and Ag deposited TiO_2 nanocomposites. (Experimental conditions: MB concentration (10 mg/L), MB volume 50 mL, catalyst dose 0.35 mg and irradiation time 5 h, number of replicates n=2

The photodecomposition reaction of MB of all catalysts demonstrated a linear relationship between the MB concentration and irradiation time. The regression coefficient (R^2) value as indicated in Table 4.7 was close to one ($R^2 > 0.98$) signifying that the photo-oxidation reaction of MB fitted well to pseudo-first order. Salehi et al., (2012) reported pseudo-first order kinetics on the photocatalytic activity of MB by TiO_2 nanoparticles. Several other authors have reported first-order kinetics for MB photomineralization using TiO_2 nanoparticle and Ag doped TiO_2 nanocomposites (Xu et al., 2012).

Table 4.8: The photocatalytic reaction rate constant of MB: Initial concentration of MB, 10 mg/L, catalyst dosage 30 mg, irradiation time 5 h

Catalysts	Rate constant (k) (h^{-1})	Rate constant (k) (min^{-1})	Linear regression equation	Regression coefficient (R^2)
JT7	0.1183	0.000197	lnC/Co= -0.1183t	0.9903
JT13	0.2498	0.00416	lnC/Co= -0.2498t	0.9940
JT14	0.3423	0.00571	lnC/Co= -0.3423t	0.9989
JT15	0.1960	0.00327	lnC/Co= -0.1960t	0.9878

According to the information provided in Table 4.7, it was noted that the photo degradation rate constants of samples JT13, JT14 and JT15 were higher than undoped TiO_2 nanocrystals without Ag (JT7). The apparent pseudo-first order reaction rate constant (k) for supported TiO_2 nanocrystals was found to be 0.1183 h^{-1} or 1.97 x 10^{-3} min^{-1}, which however increased with an increase in the loading of Ag upto an optimum of 2.4 %. The apparent degradation rate constant of JT14 was 2.9 times greater than that obtained with JT7, which indicated that the rate of decolouration of MB was faster using JT14 than JT7. The enhanced photocatalytic activity was linked to the electron trapping potential of Ag, which suppressed the photon-generated hole and e- recombination rate. The obtained apparent rate constant (k) was higher than to 0.0019 min^{-1} reported by Kerkez and Boz, (2013) for the photocatalytic degradation of MB with TiO_2 nanorods. Apparently, sample JT15 did not substantially fitted pseudo-first order kinetic plot as evidenced in the correlation coefficient value of 0.9878. The possible reason for slight deviation from the pseudo-first order kinetics was explained in section 4.43. However, the obtained rate constant in this study is lower than 0.024 min^{-1} reported by Salehi et al., (2012) on the photocatalytic performance of TiO_2 nanoparticles on MB. The lower degradation rate constant in this study suggests slow photocatalytic kinetics. The possible reasons for the different values may be ascribed to different experimental conditions such as TiO_2 dosage, UV lamp intensity, irradiation time, and wavelength and MB concentration

amongst others. Nevertheless, the higher rate constant of 0.3423 h^{-1} or 5.705 x 10^{-3} min^{-1} for Ag/TiO_2 nanocomposites compared to ordinary supported TiO_2 nanocrystals indicated the potential for higher photocatalytic performance by Ag deposition. Xu et al., (2012) attributed the enhanced photocatalytic activity of Ag/TiO_2 film to strong local electric field induced by Ag on TiO_2 film.

4.5 Chapter summary

In this chapter, a route is described in which TiO_2 photocatalyst was supported on a stainless steel mesh synthesis using a sol-gel solution of 8 % PAN/DMF/$TiCl_4$. The influence of pyrolysis temperature and holding time on the formation of nanocrystals was investigated. Subsequently different amounts of metallic nano silver particles were deposited on the optimum supported TiO_2 photocatalyst by the thermal evaporation technique. Based on the results obtained the following conclusions are drawn:

XRD analysis complemented by HRSEM, HRTEM, EDS, SAED, and XPS confirmed the formation of a pure anatase TiO_2 phase. PAN precursor did not only act as a binder between the stainless steel mesh and TiO_2 nanocrystals but acted as a carbon doping source as shown by EDS, TGA/DSC and XPS. Thus, the supported TiO_2 nanocrystals was rather termed supported carbon doped TiO_2 nanocomposites according to EDS, XRD and XPS analysis. Among the TiO_2 photocatalysts, TiO_2 nanocrystals prepared by calcination at 350 ºC for 3 hr exhibited higher activity compared to others due to higher mesoporosity and BET surface area, good crystallinity and optimum carbon content as revealed by BET, XRD and EDS analysis. The weak or low photocatalytic activity of the catalyst prepared at 300º and 400 ºC for 3 h was due excess PAN at the lower temperature and too little carbon remaining at 400 ºC. It was found that the TiO_2 crystals fell off at 400 ºC and contributed to loss of catalyst. The most influential parameter during the photocatalyst preparation was temperature and not holding time. Furthermore, 2.4 % Ag doped TiO_2 nanocomposites demonstrated higher photocatalytic activity than the supported TiO_2 nanocrystals without silver and enhanced the MB decolouration efficiency by 10.3 %. The excellent photocatalytic activity of 2.4 % Ag doped TiO_2 nanocomposites was attributed to the coupling effect of Ag and C which suppressed the band gap energy from 3.18 eV to 2.94 eV. The optimum supported carbon doped TiO_2 nanocrystals (JT7) and Ag/C co-doped TiO_2 nanocomposites (JT14) described in this chapter will be incorporated into the dielectric barrier discharge system in Chapter five.

In addition, the synthesised nano zero valent iron particles had specific surface area than the commercial nZVI reported in the literature due to the stabilising effet of polyethylene glycol. The HRSEM, HRTEM, XRD and XPS analysis the formation of filamentous iron nanoparticles in zero valent state. The stabilized nano zero valent iron particles will also be incorporated to DBD in Chapter five to induce photo-Fenton reaction. The extent of mineralization of bisphenol-A and 2-nitrophenol by the integrated system (DBD/supported photocatalysts and DBD/nZVI will be evaluated.

CHAPTER FIVE

DEGRADATION OF BPA OR 2-NP BY DIELECTRIC BARRIER DISCHARGE SYSTEM: INFLUENCE OF SUPPORTED PHOTOCATALYSTS AND STABILIZED NANO ZERO VALENT IRON PARTICLES

5 INTRODUCTION

This chapter focuses on the removal and degradation of bisphenol-A (BPA) and 2-nitrophenol (2-NP) by dielectric barrier discharge (DBD) system, combined DBD/photocatalysis and DBD/photo-Fenton induced process. The identified intermediate compounds, the degradation pathways or routes followed by BPA or 2-NP via DBD alone and the various combined systems are presented and discussed. Subsequently, the description of the experimental data by pseudo-first order kinetic model as well as the quantification of free reactive species responsible for the oxidation process are presented and discussed in this chapter.

5.1 Background

The growing numbers of endocrine disruptors such as bisphenol-A and 2-nitrophenol and their metabolites in the aquatic environment due to industrial activities, population growth and individual consumption habits have attracted serious public concern. Thus, the removal of these xenobiotics from the environment, particularly water sources, has become necessary considering their associated health effect on humans and aquatic species. As stated in Chapter one, these contaminants are, toxic, stable, mobile and resistant to conventional wastewater treatment techniques (WWTT) such as coagulation/flocculation, activated carbon adsorption, ultrafiltration, precipitation, chlorination technology amongst others. Thus, development of alternative advanced treatment techniques is worthy of exploring. Advanced oxidation technologies such as dielectric barrier discharge (DBD) is considered effective in the conversion of refractory emerging organic pollutants into inorganic compounds such as carbon dioxide and water. According to the initial hypothesis, bisphenol-A and 2-nitrophenol could not be completely decomposed with DBD alone as demonstrated in Section 5.2. Therefore, combined advanced oxidation technologies such as DBD/supported photocatalysis and DBD/photo-Fenton induced process were utilised to degrade BPA and 2-NP in water. It is important to mention that, dielectric barrier discharge (DBD) system produces intense ultraviolet (UV) light and hydrogen peroxide which are not effectively utilised. In order to

properly maximise the UV-light and hydrogen peroxide being produced by the DBD system, the stabilized nano zero valent iron particles was added to the DBD system to enhance the mineralization efficiency of the contaminants (see Chapter three Section 3.2.7.6.). Similarly, TiO_2 nanocrystals and Ag doped TiO_2 nanocomposites supported on a stainless steel mesh were incorporated into the DBD system for the purpose of making the best use of the UV-light. The influence of the following experimental parameters on degradation efficiency of selected compounds was investigated: solution pH, initial pollutants concentration and addition of radical scavengers. High pressure liquid chromatography and Liquid chromatography mass spectrometry were used to quantify and identify the intermediate degradation by-products. The next section focuses on the influence of different operating parameters on the extent of degradation of BPA or 2-NP by the DBD system on its own.

5.2 Investigating the influence of different experimental parameters on the oxidation rate of BPA or 2-NP via DBD discharge

5.2.1 *Effect of initial pH on the removal of bisphenol-A or 2-nitrophenol*

The pH of the solution is one of the important parameters that influences the oxidation of organic compounds in advanced oxidation technologies such as DBD system. Solution pH also affects the oxidative strength of the reactive species such as H_2O_2, O_3, $^{\bullet}O$ and OH^{o} amongst others. Based on this background, the influence of variation of solution pH in the range of 3-12 on the removal of BPA or 2-NP by the DBD system was explored. The desired solution pH value was adjusted by 0.5 M NaOH or 0.5 M H_2SO_4 solution (experimental procedure and conditions have been described in section 3.2.8.1). The residual concentration of BPA or 2-NP in aqueous solution was determined using analytical techniques described in Section 3.4.12. The results showing the influence of solution pH on the removal of BPA or 2-NP are presented in Figures 5.1 and 5.2 respectively. Figure 5.1 (a) shows the effect of pH on the removal of BPA degradation with time, (b) change in solution pH during the plasma discharge experiment. While Table 5.11 shows the pseudo-first order kinetic constant (k), correlation coefficient (R^2) and maximum removal efficiency of BPA or 2-NP at 80 minutes via DBD discharge.

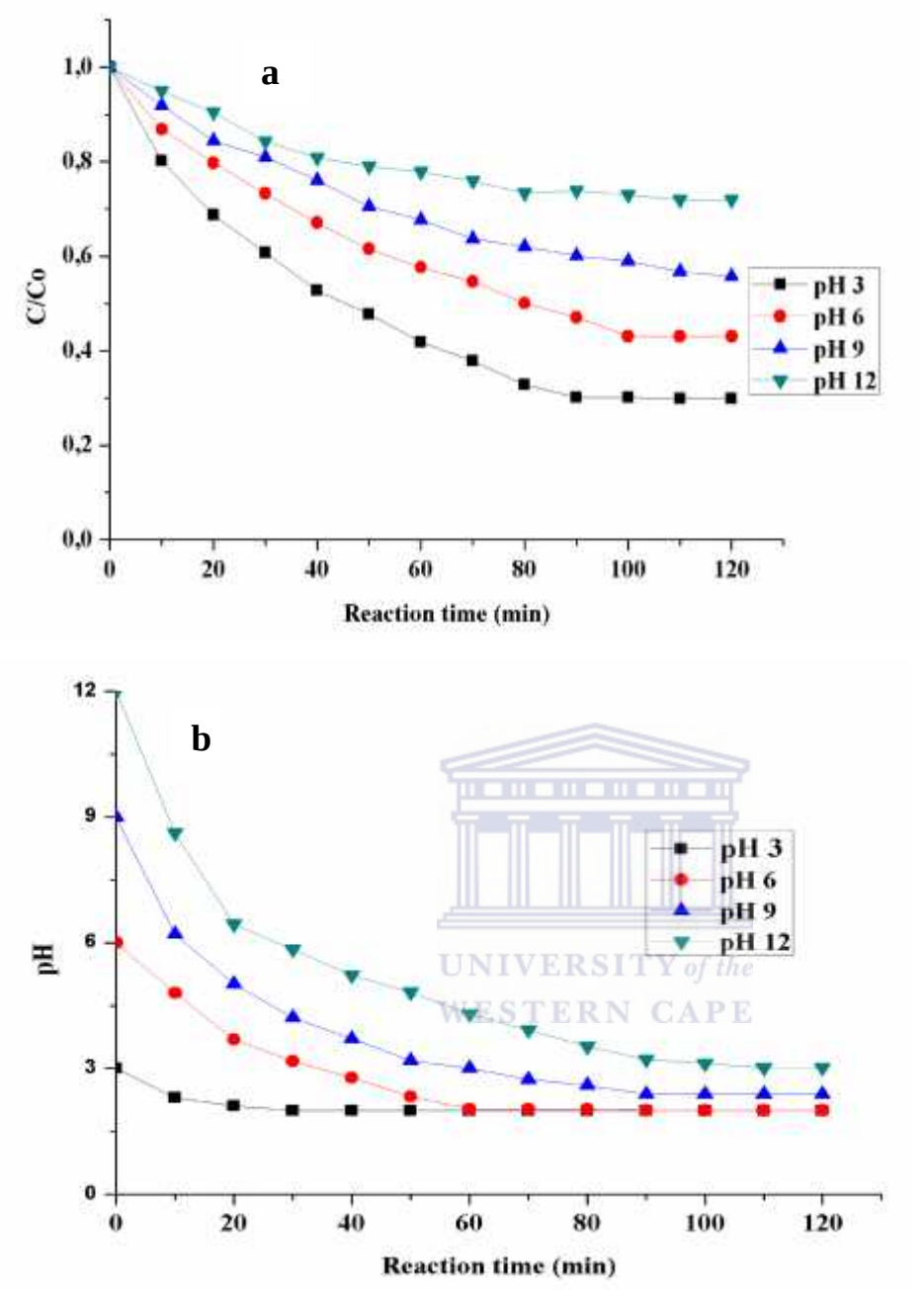

Figure 5.1: Effect of (a) the initial pH value on the degradation of BPA (b) decrease in solution pH values during DBD. Conditions: discharged voltage 8 kV, volume of BPA 1.5 L; air flow rate 3 L/min; electrode (silver); electrolyte NaCl (50 g/L); concentration of BPA (10 ppm), number of replicates n=2

While, Figure 5.2 represents (a) 2-NP degradation with treatment time (b) change in solution pH during the DBD plasma discharge experiment.

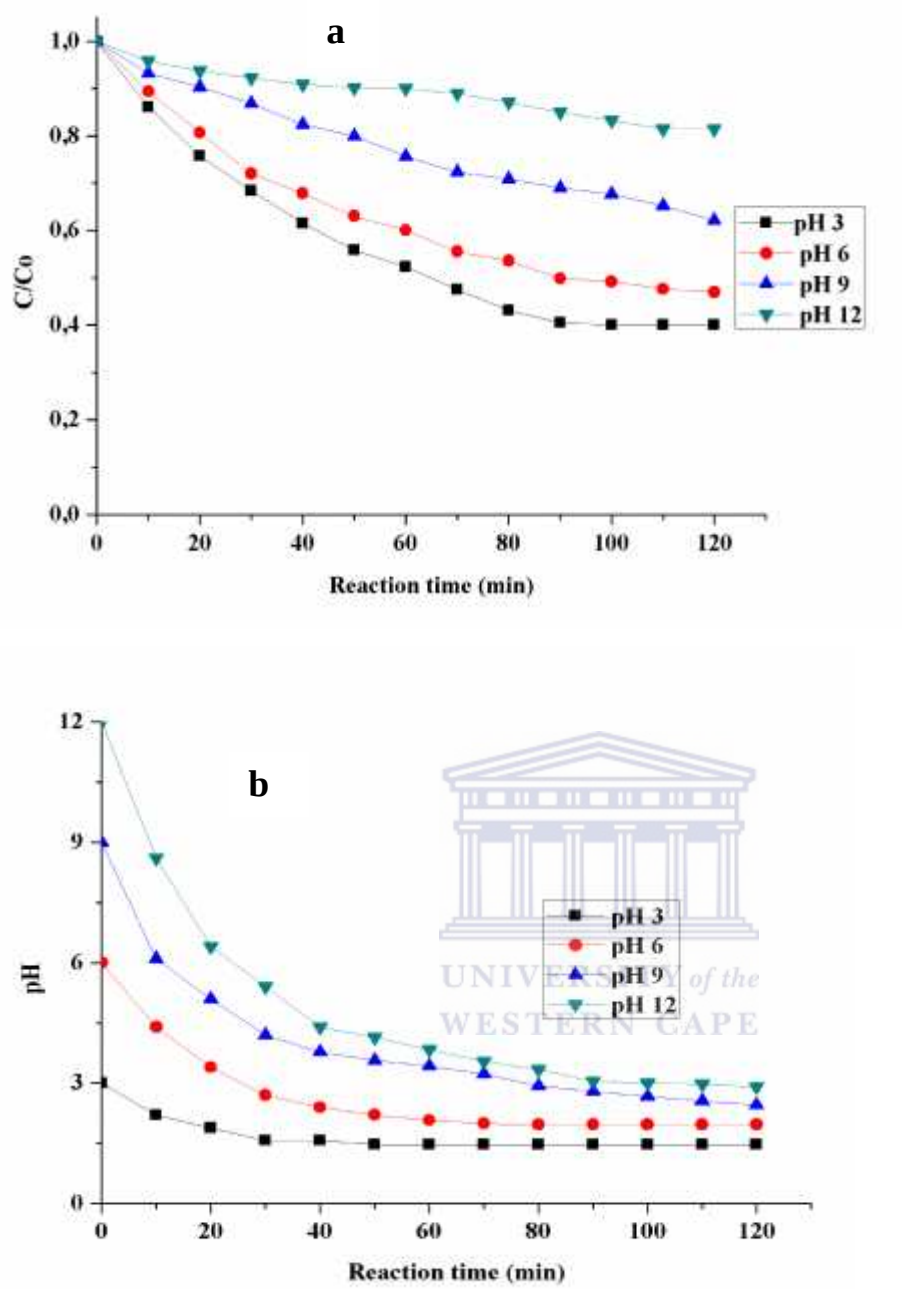

Figure 5.2: Effect of (a) the initial pH value on the degradation of 2-NP (b) decrease in solution pH values during DBD. Conditions: discharged voltage 8 kV; volume of 2-NP 1.5 L; air flow rate 3 L/min; electrode (silver); electrolyte NaCl (50 g/L); concentration of 2-NP (10 ppm), number of replicates n=2.

Table 5.1: The rate constant and correlation coefficient at different pH values (Experimental conditions as in Figure 5.1 and 5.2)

Pollutants	pH	Rate constant (min^{-1})	Correlation coefficient (R^2)
	3	0.0136	0.9896
BPA	6	0.0083	0.9888
	9	0.0060	0.9877
	12	0.0038	0.9589
	3	0.0079	0.9878
2-NP	6	0.0062	0.9858
	9	0.0038	0.9982
	12	0.0016	0.9216

As shown in Figure 5.1 (a), it can be seen that the removal efficiency of BPA was faster at lower pH than at higher pH. The removal efficiency of BPA at pH 3, 6, 9 and 12 was found to be 70.2 %, 57 %, 45 % and 28.1 % respectively after 120 minutes (Figure 5.1 (a)). A similar trend was observed for 2-NP with the lowest removal efficiency observed at pH 12 and the highest at pH 3 (Figure 5.2 (a)). Besides, the removal efficiency of each pollutant by DBD, the obtained experimental data obtained within 10-80 minutes at different pH values were fitted to the pseudo-first order kinetic model (see Appendix 1-2). The obtained results are shown in Table 5.1. From Table 5.1, it can be seen that the apparent reaction rate constant (k) of BPA (k =0.0136 min^{-1}, R^2=0.9896) at low pH (pH 3) reduced to (k=0.0038 min^{-1}, R^2=0.9589) at pH 12. Similarly, the apparent rate constant of 2-NP declined abruptly from 0.0079 min^{-1} (R^2= 0. 9783) at pH 3 to 0.0016 min^{-1} (R^2=0.9116) at pH 12. This means that acidic conditions favoured the removal and degradation of BPA rather than the alkaline medium.

At low pH, O_3 is stable and remains the dominant species and as such was assummed to be responsible for the mineralization of BPA or 2-NP in solution in the acidic conditions. Instead of O_3, OH^o radicals with higher oxidation potential in acidic conditions, or perhaps H_2O_2, were responsible for the observed high removal efficiency. This is becaused substantial

amount of O_3 generated by the DBD escaped from the surface of the solution because the DBD was not a closed system (see Figure 3.10). The open DBD system reduced the concentration of O_3 interacting with the target compounds compared to OH^o. The other possibility may be due to the consumption of oxygen by nitrous (NO) and nitric oxide (NO_2) which consequently reduced the concentration of O_3 in the system (see Chapter two Section 2.4.1). The removal efficiency at different pH values can also be linked to the ionization behaviour of the compounds in solution, which can also be explained in terms of their acid dissociation constant value. BPA exists in two forms in solution, as either anionic or dianionic species, with different acidic dissociation constant values of pKa1=9.59 and pKa2=10.2 respectively. Whereas, the pKa value of 2-NP in solution is 6.80. At low pH (when pH <pKa), the two compounds exist as molecular or undissociated species and due to their hydrophobic nature at lower pH, the BPA or 2-NP molecules can readily diffuse into the gas-water interface and react with the electrophilic OH^o. Whereas at higher pH value (pH >pKa), the compounds exist in ionic form due to the deprotonation of the hydroxyl group and their highly hydrophilic nature. Thus, the possibilities of being attacked by OH^o in the solution is reduced, which in turn resulted in lower removal efficiency at higher pH.

In addition, studies have shown that OH^o with higher electrophilic and oxidation potentials attacked the organic pollutants at 10^6-10^9 time faster than ozone (Rong et al., 2014). However, due to the loss of a significant amount of O_3 from the system, acidic conditions favoured the generation of the hydroxyl radicals and were responsible for higher removal efficiency than the alkaline region. It should be noted that the two pollutants exhibited similar removal pattern at different pH values, with BPA having higher removal efficiency than 2-NP. This was because BPA has several points of attack where OH^o, O_3 or H_2O_2 can abstract protons compared to 2-NP with only a few points of attack in the aromatic rings. This showed that BPA was more susceptible to attack and decomposed faster than 2-NP in solution.

Furthermore, the extent of removal of the non-coloured pollutant (BPA) was higher than a coloured pollutant (2-NP) irrespective of the solution pH. This observation could be attributed to the inhibitory effect of colour pigment on the formation of reactive species. Very recently, Zhang et al., (2013) found that non-coloured pollutants such as phenol, microcystin-LR degraded much faster than a coloured organic compound methyl orange. They argued that

coloured organic pollutants inhibited UV-light produced by a plasma system thereby affecting the formation of reactive species in solution.

At a higher pH (basic region), the formation of OH^{o} was expected to predominate and accelerate the oxidation of BPA or 2-NP molecules. On the other hand, lower removal efficiency of both pollutants were observed. The most possible reason for low removal efficiency under strongly alkaline conditions (high pH) could perhaps be linked to the generation of CO_2 during the oxidation of BPA or 2-NP, which perhaps formed carbonate ions (CO_3^{2-}) and HCO_3^{-}. These carbonate species (CO_3^{2-} and HCO_3^{-}) are known as radical scavengers and consume OH radicals owing to their high rate constant value. The decrease in the amount of OH radicals in solution would then have affected the removal efficiency. Similar observations were reported by Wang et al., (2007) who found that the OH^{o} produced via radical-type chain reaction of O_3 in the basic medium was consumed by carbonate species and reduced the removal efficiency of phenol. Zhang et al., (2003) found that the H_2O_2 dissociated under alkaline conditions to hydroperoxyl radical (HO_2-). The formation of hydroperoxyl radical reduced the OH^{o} in solution and affected the degradation rate of 4-NP.

The outcome of this study is however contrary to the findings reported by Lee et al., (2003) and Tay et al., (2012) on BPA oxidation via ozonation process. The two authors found that BPA degradation rate increased with the increase in solution pH from 2-12. The reason for the inconsistency in the result reported by the two authors and the outcome of this study was that, radical scavengers (t-BuOH) was added by those authors to scavenge and consume available OH^{o}. This action eliminated the stronger competition between OH^{o} and O_3 for the organic pollutants. Thus, it was demonstrated that only O_3 reacted with BPA. Whereas in this study, radical scavengers were not added to the DBD system to consume OH, thus creating room for stronger competition among O_3, OH^{o} and H_2O_2 for the organic pollutants. It was found that, at low pH, the concentration of OH^{o} was higher than that of O_3 due to significant loss of O_3 from the open system. In addition, Ku et al., (2006) studied the influence of solution pH over the range of 3-11 on the degradation of 2-NP by ozonation and the combined UV-ozonation process. The authors found that alkaline conditions favoured the decomposition of 2-NP more than acidic or neutral conditions and attributed such to conversion of dissolved ozone in the solution to OH^{o}. Contrary to the results obtained by Ku et al., (2006), under acidic conditions, in this study predominately OH^{o} or H_2O_2 favoured the degradation of 2-NP, due to the loss of a significant amount of O_3 in the system. The

significant loss of O_3 facilitated the formation of H_2O_2 and OH^o under acidic conditions in the presence of UV light and favoured the decomposition of the two compounds.

Figure 5.1 (b) and 5.2 (b) represents variation in solution pH monitored during the oxidation process. It was found in both cases that the initial pH values reduced significantly on exposure to plasma discharge especially at higher pH values as the reaction time increases. The decrease in the solution pH upon exposure to plasma generated via dry air may be due to the formation of carboxylic and mineral acids. Furthermore, the release of NO_2 by 2-nitrophenol or phenolic fragments by bisphenol-A during the oxidation process may also contribute to the solution acidity and low pH. The detailed reaction mechanisms involved in the formation of nitrogen oxides (NO, NO_2), nitrous and nitric acid during plasma discharge in water and are shown in Chapter two Section 2.4.1. The presence of OH^o in the solution may also have accelerated the formation of NO and NO_2 to HNO_2 and HNO_3 respectively, thus contributed to the solution acidity index value. A similar decrease in solution pH of sulfadiazine or carbamazepine was reported by Liu et al., (2012) upon exposure to plasma and Rong et al., (2014). Such a decrease in pH was attributed to the formation of nitrogenous oxides (NO, NO_2), which dissolved in water forming nitrate ion (NO_3-) and nitrite ion (NO_2^-). Further reaction of the nitrate and nitrites ions formed nitric acid (HNO_3), nitrous acid (HNO_2) and sometimes peroxynitrous acid (ONOOH). Based on the experimental data, the optimal degradation pH for both compounds was found to be 3.0, thus subsequent experiments were carried out at this pH value.

5.2.2 *Effect of initial concentration of BPA or 2-NP*

The influence of different initial concentration of BPA or 2-NP on the degradation efficiency and yield in the range of 10 – 30 mg/L under the optimal conditions of pH 3.0, discharge voltage 8 kV, air flow rate 3 mL/min were investigated. The detailed experimental procedure and conditions have been described in section 3.2.8.2. The residual concentration of BPA or 2-NP in aqueous solution was analysed using HPLC technique described in section 3.4.12. The removal efficiency and degradation yield of BPA as a function of reaction time is shown in Figure 5.3 (a) and (b). Figure 5.4 (a) and (b) illustrates the degradation efficiency and 2-NP degradation yield as a function of reaction time.

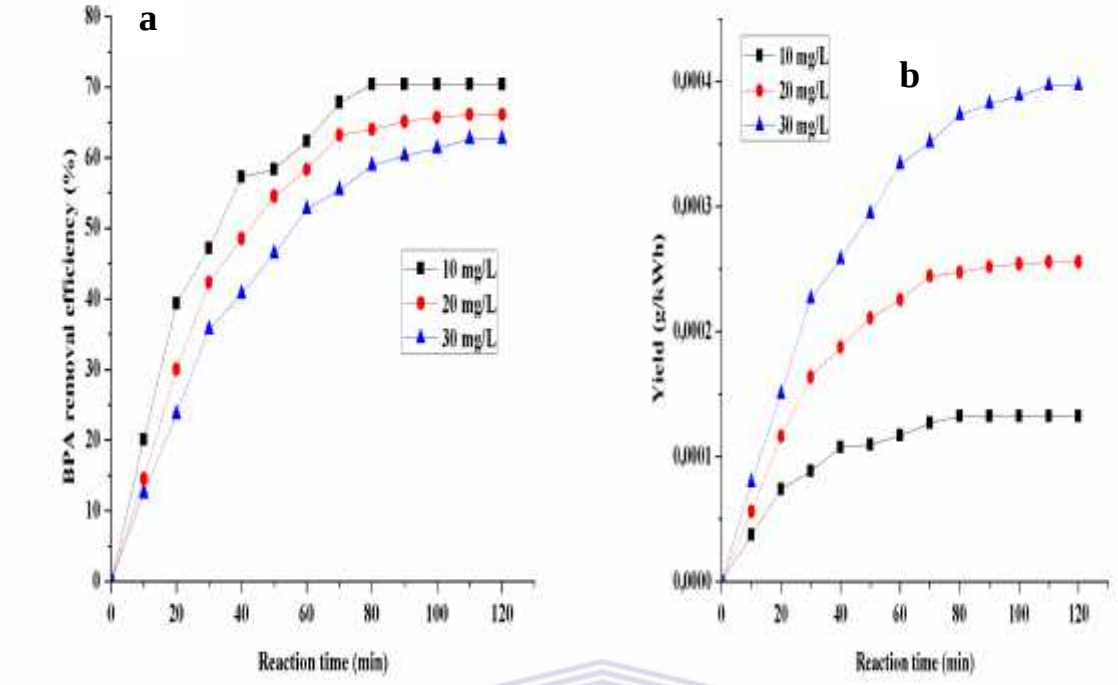

Figure 5.3: Effect of (a) BPA initial concentration (b) BPA degradation yield at different concentration values by the DBD system at discharge voltage 8 kV; pH 3; air flow rate 3.0 mL/min; electrolyte NaCl (50 g/L); volume of BPA (1.5 L); electrode (silver).

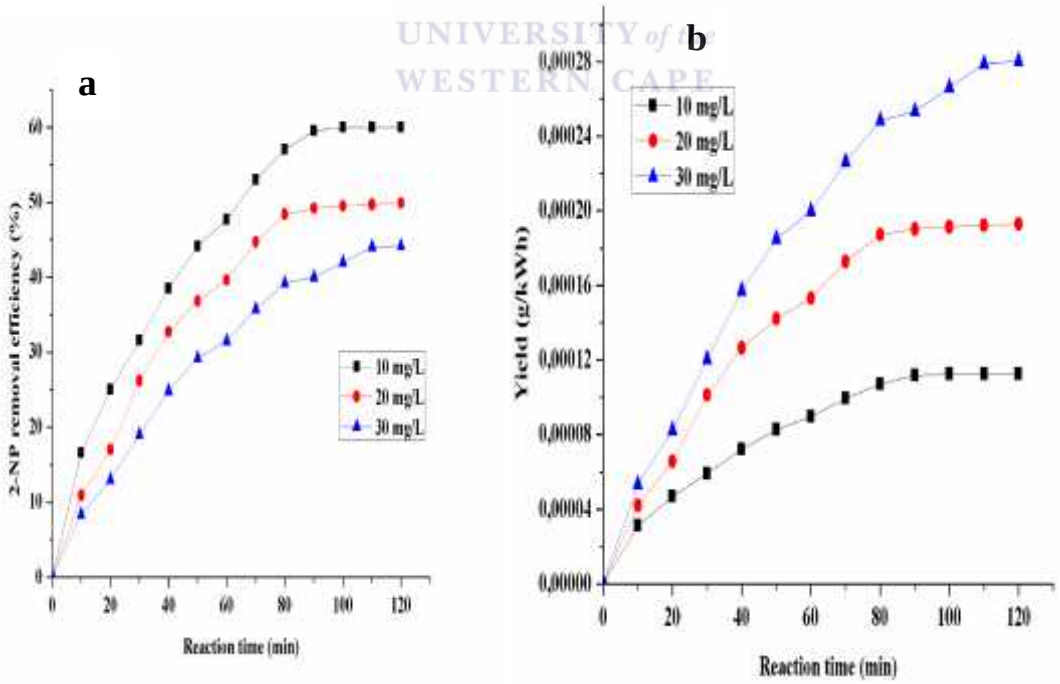

Figure 5.4: Effect of (a) 2-NP initial concentration (b) degradation yield of 2-NP at different concentration values by the DBD system at discharge voltage 8 kV; pH 3; air flow rate 3.0 mL/min; electrolyte NaCl (50 g/L); volume of BPA (1.5 L); electrode (silver), number of replicates n=2

As shown in Figure 5.3 (a), the BPA removal efficiency after 80 minutes reaction time at 10 mg/L concentration and at pH 3 and discharge voltage 8 kV was 70.4 %, and however reduced to 58.9 % as the BPA concentration was increased to 30 mg/L. Similar trends were observed with 2-NP in Figure 5.4 (a), where the removal efficiency of 2-NP reduced significantly from 57.6 % to 39.2 % as the concentration was increased at the applied experimental conditions. As expected, the removal efficiency of BPA or 2-NP was greater at lower concentration than at higher concentrations. According to Figure 5.3 (a) and 5.4 (a), it can been seen that at every treatment time, the percentage removal efficiency of BPA or 2-NP decreases with an increase in the initial concentrations of the BPA or 2-NP. This could be attributed to the relative number of BPA or 2-NP molecules competing with the DBD generated reactive species during the plasma discharge.

On the other hand, at higher pollutant concentration, the number of BPA or 2-NP molecules at the fixed conditions applied increased without a corresponding increase in the concentration of the DBD generated free reactive species. As a result, the concentration of available oxidant species was lower and could not effectively mineralize large numbers of BPA or 2-NP molecules into harmless compounds. This resulted in lower removal efficiency as seen at higher concentration of the pollutants. The other possibility for lower removal efficiency could be due to the formation of refractory secondary transformation products at higher pollutant concentrations, which may have strongly competed with the original BPA or 2-NP compound for free reactive species (see Figure 5.17 and 5.30). The competition between the intermediates and initial compound may have prevented further degradation of the original compound and thus have caused the lower degradation efficiency. It is obvious that the removal efficiency of BPA or 2-NP was strongly affected by the pollutant concentration. This observation is in agreement with previous studies reported by researchers on endocrine disruptors in the literature in spite of the differences in the configuration of the DBD (Gao et al., 2013; Li et al., 2014; Rong and Sun, 2013).

Furthermore, the removal efficiency of BPA or 2-NP can equally be explained in terms of degradation yield as shown in Figure 5.3 (b) and 5.4 (b), which represents the rate of oxidation of the pollutants per unit energy consumed during the process as expressed in equation (5.1)

$$Y\,(g/kWh) = \frac{C(g/L) * V(L) * 1/100 * conversion(\%)}{P(kW) * t(h)} \quad \text{.....(5.1)}$$

Where C(g/L) represents initial concentration of the pollutants, V is the volume of the aqueous solution in Litre, P is the average power dissipated in kW, which is expressed as the product of the discharge voltage (V) and applied current (A), t is the treatment time, while the conversion (%) is the same as removal efficiency at each treatment time (Magureanu et al., 2010).

According to equation (1), the degradation yield of BPA or 2-NP was estimated using discharge voltage of 8 kV and applied current 5A. These values change during the oxidation process and depended on the concentration of the pollutants. Figures 5.3 (b) and 5.4 (b) illustrate the degradation yield of BPA and 2-NP at different initial concentrations. Contrary to the trend observed in Figure 5.3 (a) and 5.4 (a), the degradation yield of BPA or 2-NP increased with increasing pollutant concentrations. According to Figure 5.3 (b), the degradation yield of 10 mg/L BPA solution after 80 minutes treatment time was 1.32×10^{-4} g/kWh, which however increased to 3.73×10^{-4} g/kWh as concentration increased to 30 mg/L. Similarly, the degradation yield of 2-NP increased from 1.07×10^{-4} g/kWh to 2.48×10^{-4} g/kWh under the same reaction conditions. According to Figure 5.3 (b), the degradation yield of 30 mg/L solution of BPA was 3 and 1.55 times greater than that obtained with 10 mg/L and 20 mg/L solution of BPA under the applied experimental conditions. Similarly, the degradation yield of 30 mg/L solution of 2-NP was 2.47 and 1.45 times greater than that obtained using 10 mg/L and 20 mg/L solution of 2-NP under the same experimental conditions. Contrary to observed trend in Figure 5.3 (a) and 5.4 (a), it is obvious that the increase in the degradation yield at higher pollutant concentration did not depend on the amount of free reactive species in the DBD but on the number of molecules taking part in the reactions. It should be noted that, higher concentration of BPA or 2-NP implies higher number BPA or 2-NP molecules, which means that a higher amount of energy is required to achieve complete degradation. Contrary to what was obtained with removal efficiency at higher concentration of BPA or 2-NP, it was found that increases in the concentration of BPA or 2-NP resulted in the corresponding increase in the discharge energy and hence the degradation yield. This observation supported previous investigation reported for different

organic pollutants: 17 β-Estradiol (Gao et al., 2013), 4-chlorobenzoic acid (Lesage et al., 2013), pentoxifylline (Magureanu et al. 2010). These authors attributed the increase in the degradation yield with increasing concentration of organic pollutants to consumption of more energy overtime by the DBD syetm

The obtained degradation yield in this study was lower than 17×10^{-3} and 15×10^{-3} g/kWh reported for clofibric and phenol by Krause et al., (2009). At the same time, also lower than 4.5 and 48 g/kWh for phenol and methylene blue reported by Grabowski et al., (2006) and Grabowski et al., (2007) respectively. Lesage et al., (2013) reported degradation yield value of 0.87 g/kWh and 0.16 g/kWh for 4-chlorobenzoice acid decomposed by DBD and gliding arc discharge. It can be seen that different degradation yields were reported by different researchers, and the yields depended on several factors such as the nature and structure of organic pollutant, types of DBD, discharge power of the DBD, nature of the feed gas (air or oxygen), and flow rate, amongst others (Magureanu et al. 2008). Thus, considering the fact that the removal efficiency was faster and consumed less energy at a lower concentration, 10 mg/L was selected as the optimal initial concentration for both compounds in this study.

5.2.3 *Effect of the addition of radical scavengers*

The presence of radical scavengers in solution affect the efficiency of advanced oxidation technologies due to inhibition and consumptions of free radicals. Among radical scavengers or inhibitors are inorganic species such as Na_2CO_3, Na_2SO_4, $NaHCO_3$, $Na_2B_2O_7$, $NaNO_3$, C_3H_9OH, t-C_4H_9OH, Na_3PO_4, and NaCl (Ahmed et al., 2011). In this study, the influence of addition of 60 mg/L each of (Na_2CO_3 (0.0006 mol/L), Na_2SO_4 (0.0004 mol/L), NaCl (0.001 mol/L) on the removal rate of BPA or 2-NP in water by the DBD system was examined. The detailed experimental methodology has been provided in section 3.2.8.3. The residual concentration of BPA or 2-NP in aqueous solution was analysed using HPLC technique described in Section 3.4.12. The results of the influence of radical scavengers such as Na_2CO_3, Na_2SO_4 and NaCl on the removal efficiency of BPA or 2-NP are presented in Figure 5.5 (a) and 5.6 (a). While Figure 5.5 (b) and 5.6 (b) illustrate the pseudo-first order kinetic model plot of ln (C/Co) against the reaction time for BPA or 2-NP respectively.

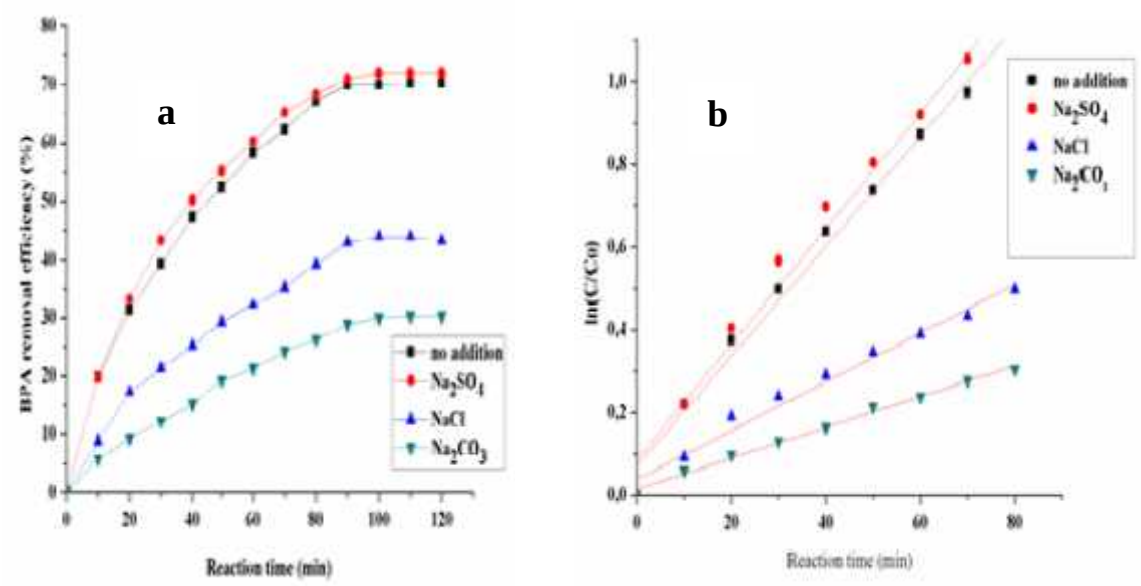

Figure 5.5: Effect of (a) radical scavengers on the removal efficiency of BPA (b) degradation kinetics of different radical scavengers on BPA (Discharge voltage 8 kV; BPA concentration 10 mg/L; BPA volume 1.5 L; radical scavengers concentration 60 mg/L; air flow rate 3 mL/min; solution pH 3; electrolyte, NaCl (50 g/L); electrode (silver), number of replicates n=2

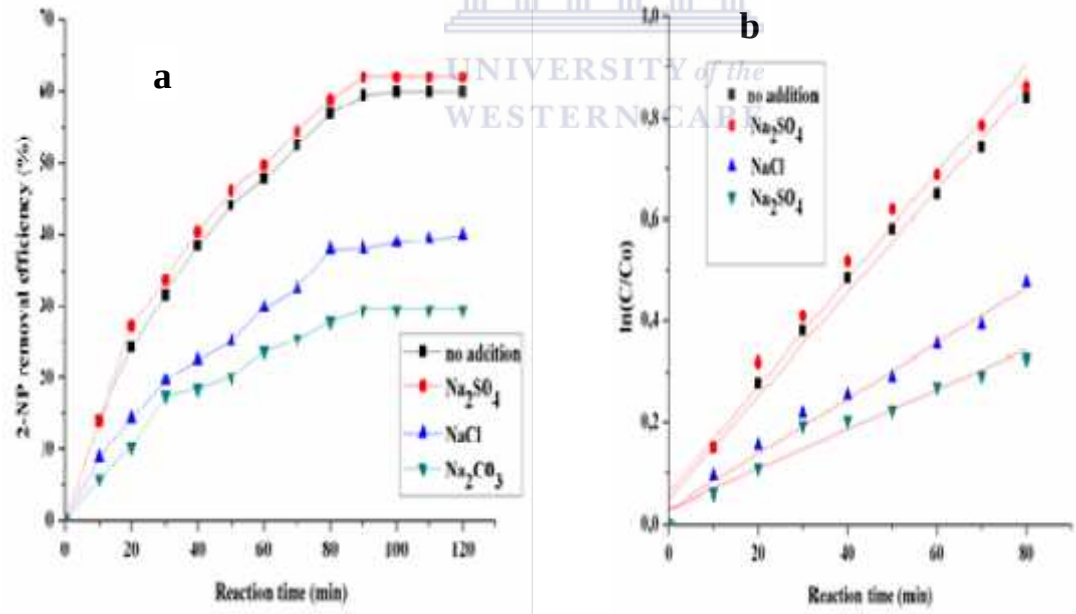

Figure 5.6: Effect of (a) radical scavengers on the removal efficiency of 2-nitrophenol and (b) degradation kinetics of different radical scavengers on 2-NP (Discharge voltage 8 kV; 2-NP concentration 10 mg/L; Volume of 2-NP, 1.5 L; radical scavengers concentration 60 mg/L; air flow rate 3.0; electrolyte, NaCl (50 g/L); electrode (silver), number of replicates n=2

As shown in Figure 5.5 (a) and 5.6 (a), the BPA or 2-NP removal efficiency decreased in the presence of Na_2CO_3 and NaCl and slightly increased in the presence of Na_2SO_4. The BPA removal efficiency was 27.0 % and 40 % upon the addition of NaCl and Na_2CO_3 after 80 minutes treatment time. Similarly, 2-NP removal efficiency was 22.1 % and 30.5 % under the same conditions. On the other hand, with the addition of Na_2SO_4, the degradation efficiency of BPA and 2-NP was 71.9 % and 61.6 % respectively. The addition of Na_2SO_4 slightly enhanced the removal efficiency of BPA or 2-NP by 1.9 % and 2.0 % respectively.

Notably, among the three radical scavengers, Na_2CO_3 considerably inhibited the removal efficiency of BPA or 2-NP. The decrease in the removal efficiency gives an indication of a rapid consumption and conversion of the hydroxyl radicals into non-active species by the carbonate ionS in solution. In contrast, the slight improvement in the removal efficiency of BPA or 2-NP upon Na_2SO_4 could be attributed to the formation of $SO_4^{-\bullet}$ due to reaction of SO_4^{2-} with the hydroxyl radicals. The formation of $SO_4^{-\bullet}$ during the oxidation process is shown in the equation (5.2)

$$SO_4^{2-} + OH^{\bullet} \longrightarrow SO_4^{-\bullet} + OH^- \quad \text{.....(5.2)}$$

Manoj Kumar Reddy et al., (2013) had earlier reported that $SO_4^{-\bullet}$ with oxidation potential of 2.6 V was more reactive than OH^o with oxidation potential value of 2.8 V. Therefore, the preference or selectivity for $SO_4^{-\bullet}$ by BPA or 2-NP over OH^o may be based on the contribution of $SO_4^{-\bullet}$ to the electron transfer reaction. This reaction occurred between the pollutant and $SO_4^{-\bullet}$ rather than with the OH^o, which were perhaps involved in hydrogen abstraction or addition reactions. Manoj Kumar Reddy et al., (2013) observed similar selectivity behaviour of $SO_4^{-\bullet}$ over OH^o by methylene blue during the oxidation process by dielectric barrier discharge reactor, where Na_2SO_4 served as a radical scavenger. The increase could also simply be as a result of the presence of both OH^o and $SO_4^{-\bullet}$ radicals in the system.

Furthermore, the experimental data obtained during investigation of the effect of radical scavengers on BPA or 2-NP removal rate were further fitted into the pseudo-first order kinetic plots as illustrated in Figure 5.5 (b) and 5.6 (b) respectively. Table 5.2 represents the rate constant and correlation coefficient of the different radical scavengers.

Table 5.2: The rate constant and correlation coefficient with different radical scavengers (Experimental conditions as in Figure 5.5 and 5.6)

Pollutants	Radical scavengers	Rate constant (min^{-1})	Correlation coefficient (R^2)
	Na_2SO_4	0.0139	0.9434
BPA	NaCl	0.0049	0.9512
	Na_2CO_3	0.0031	0.9641
	No addition	0.0136	0.9421
	Na_2SO_4	0.0083	0.9507
2-NP	NaCl	0.0040	0.9204
	Na_2CO_3	0.0029	0.9041
	No addition	0.0079	0.9393

According to Table 5.2, the apparent rate constant (k) of BPA in the presence of Na_2SO_4 was 0.0139 min^{-1}, which was greater than 0.0049 min^{-1} and 0.0031 min^{-1} obtained with NaCl and Na_2CO_3. Similarly, the apparent degradation rate constant (k) for 2-NP upon the addition of 60 mg/L of Na_2SO_4, NaCl and Na_2CO_3 were 0.0084 min^{-1}, 0.004 min^{-1}, 0.0029 min^{-1} respectively. The obtained reaction rate constant (k) for Na_2SO_4 in the presence of BPA or 2-NP was three and four times greater than that observed for NaCl and Na_2CO_3. The higher BPA or 2-NP removal efficiency in the solution containing NaCl compared to Na_2CO_3 may be linked to the formation of oxidative species such as $Cl_2\bullet$- or $ClOH^{\bullet-}$ which are of higher oxidation potential value than CO_3^{2-}. The reaction mechanism of formation of $ClOH^{\bullet-}$, is shown in equation 5.3 – 5.4.

$$Cl^- + OH^{\cdot} \rightarrow Cl^{\cdot} + OH^- \rightarrow ClOH^{\cdot-} \quad (5.3)$$

$$Cl^{\cdot} + Cl^- \rightarrow Cl_2^{\cdot-} \quad (5.4)$$

Thus, the removal efficiency of BPA or 2-NP by the DBD in the presence of radical scavengers followed the order Na_2SO_4 > NaCl > Na_2CO_3. Zhu et al., (2007) also found that the removal rate of phenol oxidised via pulsed corona discharge decreased from 80 % to 30 % upon the addition of 60 mg/L radical scavenger Na_2CO_3. The authors ascribed such a significant reduction to rapid reaction between the carbonate ion and the OH radicals, which resulted in the termination of the oxidation process. Wang et al., (2007) reported phenol

removal efficiency of 63.2 % in the presence of 0.5 mmol/L Na_2CO_3, and 77.5 % removal efficiency in the absence of a radical scavenger by pulsed corona discharge. Zhang et al., (2003) reported that the addition of 10 mM sodium hydrogen carbonate (IV) to a solution containing 4-nitrophenol decreased the degradation rate constant of the compound by a factor of 0.48 compared to 0.29 by Cl^-. The authors attributed the decrease in the degradation rate of 4-NP to a decrease in the concentration of OH^o and consumption of H_2O_2 by sodium hydrogen carbonate (IV). This study shows that radical scavengers such as Na_2CO_3 and NaCl could influence the removal efficiency of BPA or 2-NP in water.

The next section focuses on the incorporation of the supported carbon doped TiO_2 nanocrystals (JT7) and Ag doped TiO_2 nanocomposites (JT14) into the DBD reactor using the optimum conditions of solution pH and initial pollutant concentration established in Sections 5.2.1 and 5.2.2.

5.3 Degradation of BPA or 2-NP by combined DBD and supported TiO_2 or Ag doped TiO_2 photocatalyst

The objective of this section of the study was to assess the removal and degradation efficiency of BPA or 2-NP by DBD combined with supported TiO_2 nanocrystals (JT7) or Ag doped TiO_2 nanocomposites (JT14). Based on the results presented in Chapter four Section 4.4.3 on the photocatalytic activities of Ag doped TiO_2 nanocomposites on MB, the optimal supported catalysts were incorporated into the DBD reactor to enhance the BPA or 2-NP mineralization efficiency. In this regard, the removal efficiency of BPA or 2-NP in aqueous solution was investigated using six different approaches. The experiment was conducted using the optimum solution pH and initial concentration of the pollutant obtained in Section 5.2.1 and 5.2.2. The residual concentration of BPA or 2-NP in aqueous solution was determined using gradient elution method described in Section 3.4.12. The detailed experimental procedure and conditions have been described in Section 3.2.9. The removal efficiency of BPA or 2-NP via DBD alone or DBD with supported photocatalysts are represented in Figure 5.7 (a) and (b) respectively.

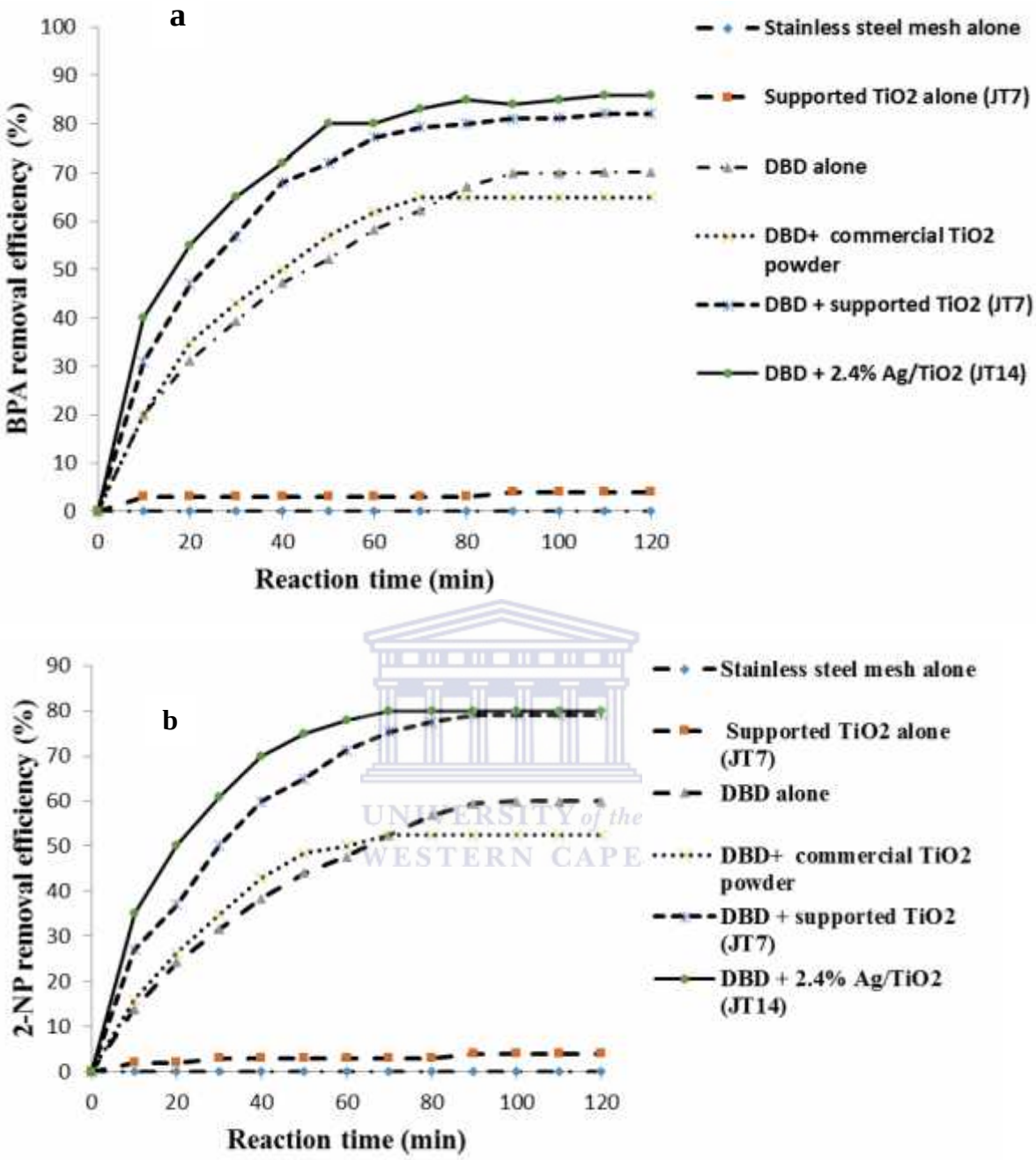

Figure 5.7: Removal efficiency of (a) BPA (b) 2-NP by combined DBD and supported carbon doped TiO_2 (JT7) and Ag loaded carbon doped TiO_2 nanocomposites (JT14). (Experimental conditions, BPA or 2-NP volume 1.5 L; BPA or 2-NP concentration 10 mg/L; discharged voltage 8 kV; air flow rate 3 mL/min; solution pH 3; electrode (silver); NaCl electrolyte concentration 50 g/L; mass of supported TiO_2 catalyst 0.8 g; mass of commercial TiO_2 (0.8 g), number of replicates n=2

It is apparent from Figure 5.7 (a) and (b) that there was no appreciable removal efficiency for every measurement using stainless steel mesh alone. This indicates that the removal efficiency of BPA or 2-NP did not depend on the support material. In the same vein, the experiment conducted in the dark with the aid of TiO_2 supported nanocrystals, showed only a slight removal efficiency of about 4% for both compounds over the treatment time. This observation could be attributed to adsorption of BPA or 2-NP by the supported TiO_2 photocatalyst rather than photo-oxidation. The removal efficiency at this stage was low despite having higher BET surface area of 152 m^2/g (see Figure 4.44). This suggests that high BET surface area value did not contribute to the adsorption of BPA or 2NP on the TiO_2 surface. Thus, adsorption phenomenon in the dark did not improve the degradation of BPA or 2-NP in water.

It can also be seen from Figure 5.7 (a) and (b) that the removal efficiency of BPA or 2-NP by the DBD alone at 80 minutes of reaction time was 67.22 % and 56.8 % respectively. When 0.8 g commercial powder TiO_2 was added to the DBD system, the BPA or 2-NP removal efficiency was 65.1 % and 52.2 % within same treatment time as DBD system. With the incorporation of the supported TiO_2 photocatalyst (JT7) into the DBD reactor, the BPA removal efficiency was 80 % while 77.5 % of 2-NP was removed under the same experimental conditions. According to the results, there was an improvement in removal efficiency of BPA or 2-NP in the presence of irradiated supported TiO_2 photocatalyst than commercial TiO_2 powder without support. This shows that the prepared supported TiO_2 photocatalyst exhibited higher photocatalytic activity than the standard titania (P25) photocatalyst. Primarily, this was due to the shadowing effect of the particulates of the unsupported P25 catalyst. Studies have also shown that the photocatalytic activity of TiO_2 is governed or largely depends on the specific surface area, microstructure and crystallite size (Chong et al., 2010). Additionally, TiO_2 exists in three different polymorphs namely anatase, rutile, and brookite with anatase phase exhibiting higher photocatalytic activity than others. Besides, the commercial powder TiO_2 used in this study comprises 80 % anatase and 20 % rutile with a specific surface area of 56 m^2/g. Whereas, in this study, the synthesized supported TiO_2 photocatalyst (JT7) was purely anatase with specific surface area of 152 m^2/g (see Table 4.4). Thus, the pure anatase phase, high mesoporosity and relative high BET specific area of the synthesized TiO_2 may be responsible for such higher photocatalytic activity compared to the commercial powder TiO_2. Furthermore, the presence of carbon residues from PAN precursor (see Figure 4.8) may have prevented recombination or have

introduced more active sites on the supported TiO_2 photocatalyst, and in turn could be responsible for the observed enhanced photocatalytic activity. The doping effect of carbon on the surface lattice layers of the supported TiO_2 may possibly have played a role during the oxidation process of BPA or 2-NP in aqueous solution. The interaction of the supported catalyst (JT7) with the UV light produced by the DBD, increased the concentration of OH radicals and enhanced the removal efficiency (see Figure 5.41 b). Apart from the formation of OH radicals, hydrogen peroxide can also decomposed in the presence of ultra-violet light to give OH^o as shown in equation (5)

$$H_2O_2 + hv \rightarrow 2OH^{\cdot} \quad (5.5)$$

The OH radicals and other reactive species reacted non-selectively to degrade the contaminants, when the supported TiO_2 photocatalyst was irradiated by the UV generated by the DBD system.

With the incorporation of Ag doped TiO_2 photocatalysts (JT14) with the DBD system, BPA or 2-NP removal efficiency at 80 min was 89.02 % or 81 % respectively. This shows that the incorporation of supported Ag doped TiO_2 photocatalysts (JT14), further enhanced BPA or 2-NP removal efficiency by 21.8 % and 24.2 % compared to DBD alone (see Figure 5.7 (a) and (b)). The BPA or 2-NP removal efficiency was improved by 9.02 % or 3.5 % using combined DBD with Ag supported TiO_2 nanocrystals (JT14) compared to combined DBD with supported TiO_2 photocatalysts (JT7). This further corroborates the initial hypothesis that incorporation of supported photocatalysts into the DBD reactor will improve the removal efficiency of BPA or 2-NP. The enhanced BPA or 2-NP removal efficiency by DBD/JT14 compared to DBD/JT7 may be explained as a result of a combination of several factors. These factors include the suppression of the electron-hole recombination rate by the Ag or carbon on the TiO_2 surface which could possibly be responsible for the enhanced removal efficiency. Secondly, the trapping of photo-induced electrons as a result of Schottky barrier created by C or Ag could facilitate the transfer of electrons to oxygen molecules adsorbed on the surface of TiO_2 layer and possibly generate more surface hydroxyl radicals, which enhanced BPA oxidation rate. Thirdly, the uniform deposition of Ag nanoparticles on the TiO_2 layer as revealed by HRTEM (Figure 4.20 c), allowed effective interaction and activation of the catalyst by UV-light, leading to generation of more hydroxyl radicals and improved removal rate.

The BPA or 2-NP removal efficiency obtained using combined DBD with 0.8 g commercial powder TiO_2 was lower than the removal obtained via the DBD alone. The decrease in the pollutant removal efficiency may be linked to the turbid nature of the solution caused by the powdery TiO_2, which inhibited the ultraviolet light penetration and reduced the amount of free reactive species. This observation was supported by the findings of Mok et al., (2007) who had earlier demonstrated that addition of 0.5 g/L powder TiO_2 into DBD reactor containing Acid Red 27, reduced the removal efficiency of the pollutant from 60 % to 40 %. Mok and colleague, (2007) submitted that utilization of powdery TiO_2 made the solution turbid and affected the UV light penetration lowering the production of free radicals, resulting in lower degradation efficiency. The obtained (80 % - 85 %) removal rate especially for BPA by the combined DBD and supported 2.4% Ag doped TiO_2 photocatalysts was greater than 50 % BPA removal reported for a combined $UV/O_3/TiO_2$ system reported by Colombo et al., (2012). Unfortunately, data and results comparison are complicated due to different experimental conditions such as UV-light intensity, type and initial concentrations of pollutants, reactor configuration, concentration of free reactive species, discharge voltage, solution pH amongst others. Thus, the differences in the reported removal efficiency could be linked to some of the aforementioned factors.

Besides the aforementioned, studies have shown that the free reactive species such as O_3 and H_2O_2 inhibited the electron-hole recombination rate on the TiO_2 surface and increased the concentration of OH radicals (Tang et al., 2013). Therefore, the improved BPA or 2-NP removal rate may be attributed to the existence of a synergetic effect between the two system (DBD and JT14) which produced more OH^{o} and other reactive species than the DBD alone. The increase in BPA or 2-NP removal efficiency via the combined approach used this study was greater than the 5% increment observed for phenol removal with combined pulsed corona discharge/TiO_2 photocatalysis reported by Wang et al., (2007). The possible reasons for the difference may be explained in terms of free radical production, where the combined system used by Wang et al., (2007) produced OH radicals and H_2O_2 only as compared to the combined DBD/$AgTiO_2$ system used in this study which produced hydroxyl radicals, O_3, and H_2O_2 (see Section 5.8). In spite of the incorporation of supported 2.4 % Ag doped TiO_2 photocatalysts (JT14) to the DBD, 100 % BPA or 2-NP removal efficiency was not achieved in the time on stream under the applied conditions. Therefore, with the current combined DBD system, extension of reaction time may be needed, or an increase input discharge voltage or perhaps it is necessary to re-configure the DBD reactor by using a closed system to

prevent loss of ozone. The next section focus on the stability and reusability of the supported Ag doped TiO_2 nanocomposites (JT14).

5.3.1 *Leaching test on the catalyst support material*

One of the shortcomings of powder TiO_2 nanoparticles is post-filtration or recovery of powder after treatment, this can however be remedied via the development of the catalyst on a suitable support materials. However, the stability of the supported catalyst during photocatalytic environment depends on the integrity of the substrates in this case, the stainless steel mesh. Stainless steel mesh contains Fe, Cr, and Ni (Bassioni et al., 2015) and it is imperative to determine whether or not these toxic elements leach or are released into the solution on exposure to plasma discharge during the degradation experiment. Prior to this, a control experiment was conducted using DBD alone without the TiO_2 photocatalyst supported on a stainless steel to determine background value of these elements in the treated sample. ICP-OES was used to quantity the concentration of Ti, Cr, Fe, Ni and Ag that leached or was released into the solution. The detailed experimental procedure can be found in Section 3.4.4.1. While the sample preparation and instrumental conditions have been described in Section 3.4.14. The results obtained using DBD alone without combining with the supported photocatalyst is presented in Table 5.3 (see appendix 3). While the amount of the metallic species leached into the solution as well as solution pH measured at respective time intervals is presented in Figure 5.8

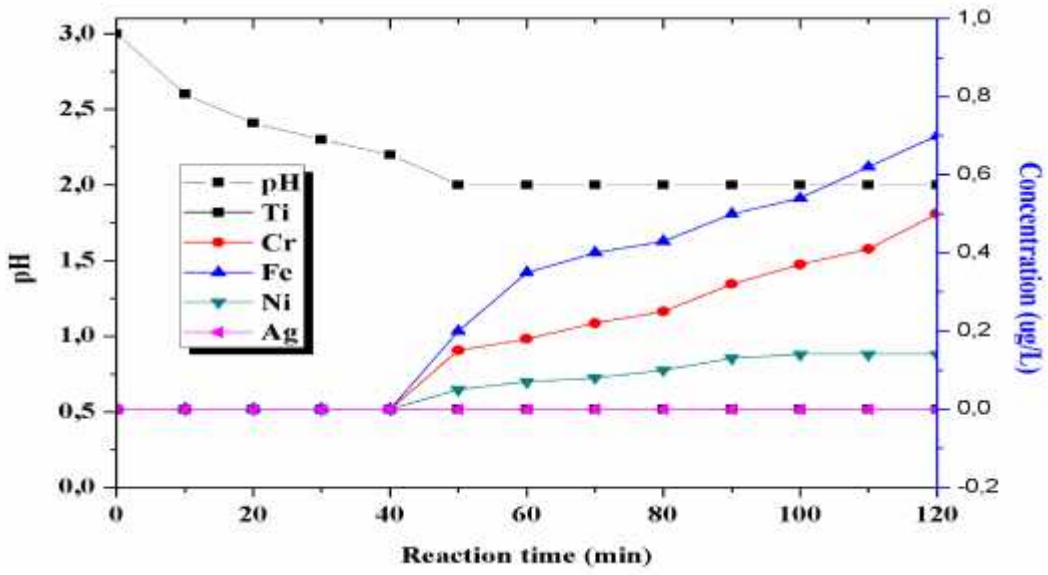

Figure 5.8: Concentration of elements and solution pH at different reaction time during oxidation of BPA by DBD/JT14 (Experimental conditions, same as Figure 5.7 or 5.8).

It can be seen from Figure 5.8 that the amount of metallic elements in the DBD treated BPA solution was insignificant and in most cases below the detectable limit (see Appendix 3). Also, as shown in Figure 5.8, there was no leaching of any metallic species from the substrate within the first 40 minutes upon continuous exposure to the supported catalyst (JT14) to plasma discharge. The only noticeable effect was a slight decrease in solution pH which may be due to formation of intermediate compounds. Non-leaching within this reaction time probably indicated strong adherence of the catalysts onto the support material. However, after 50 minutes, leaching of Fe, Cr and Ni was evident and concentration differ appreciably in the solution. It is obvious that, Fe leached at a higher rate than others elements followed by Cr and Ni whereas Ag + Ti did not leach. The Ni released from the stainless steel mesh was between 0.001 and 0.16 $\mu g/L$. The concentration of Fe and Cr increased linearly from 0.2 – 0.7 $\mu g/L$ and 0.22- 0.5 $\mu g/L$ at a lower pH value of 2.0. According to Figure 5.8, leaching of the elements started when pH reached 2.0. Comparing Table 5.3 and Figure 5.8, the concentration of Fe, Cr, Ni was higher in the combined DBD with supported JT14 than DBD alone without a stainless steel supported photocatalyst. This means that the leaching of Fe, Cr, Ni really emanated from the stainless steel mesh and the metal release rate was dependent on the solution pH. The leaching of Fe, Cr and possibly Ni into the solution may be linked to the acidic nature of the solution, owing to the formation of nitrous and nitric acid at low pH in water during the plasma discharge (Lesage et al., 2013). It is important to mention that, only one side of the stainless steel mesh was covered with titania and silver layer while the other side was uncoated. Remarkably, there was no leaching of Ti and Ag during the oxidation process, and non-detection of Ti and Ag in solution suggested strong adhesion between the stainless steel mesh and the catalyst. Sometimes, non-detection of elements during analysis depends on the instrument detection limit, thus it may be that the concentrations were too low for the instrument to detect. Since no leaching of Ag and Ti was observed from the coated side, it is possible to conclude that the leaching of Fe, Cr, and Ni emanated from the uncovered side of the mesh. The leaching or release of Fe, Cr and Ni from uncoated side of the stainless steel substrate as a consequence of corrosion during the DBD discharge may be ascribed to the corrosive effect of the mineral or organic acids generated during the discharge on the stainless steel mesh. The leaching of Fe, Cr and Ni agrees with the findings of Lesage et al., (2013) who observed the leaching of Cu and Zn from a brass plate during oxidation of 4-chlorobenzoic acid by DBD. The authors attributed the leaching

of the two metallic species to corrosion effect caused by the formation of NO_2^- through reaction of NO_3^- and H^+ in the solution. The presence of NOx and possibly NO_3^- increased the solution acidity level and caused corrosion and consequently leaching of toxic metallic species (Lesage et al., 2013). According to Lesage et al., (2013), NO_x and NO_3- are radical scavengers, and inhibit or consume OH radicals, O_3 and H_2O_2, thus could have reduced the degradation of the organic pollutants. Bagheri et al., (2014) also attributed the leaching of metallic species to weak interaction between the support materials and the catalyst. Studies have shown that the leached metallic species (Fe, Cr, Ni) sometimes compete with Ti^{4+} based on ionic radii differences and reduce the performance of the photocatalyst, which in turn decreases the degradation efficiency (Fernández et al., 1995). This might probably be part of the reason for not achieving complete removal BPA or 2-NP with DBD despite the incorporation of the various supported photocatalysts in this study. To buttress this fact, Lesage et al. (2013) revealed the occurrence of a secondary reaction between the leached Cu, Zn from a brass plate and reactive species produced by DBD in solution. The secondary reaction reduced the degradation efficiency from 64% in the absence of a brass plate containing Cu, Zn to 20% in the presence of Cu and Zn. Their results confirmed that corrosion of a support material affected the process efficiency. The authors recommended reduction or complete removal of NOx species in the DBD system, since the nitrogenated species consumed the reactive species produced by the DBD. Furthermore, the leaching of Fe, Cr and Ni from the stainless steel mesh into the treated water may be lethal to human health. Although, the amount of Fe, Cr and Ni detected in the treated water was lower than 0.2 mg/L (Fe), 0.05 mg/L (Cr) and 0.02 mg/L (Ni) European Union permissible limit for drinking water. Nevertheless, long-term consumption of the treated water should be avoided.

5.3.2 *Reusability of the supported Ag doped TiO_2 nanocomposites*

One of the fundamental aspects of heterogeneous photocatalysis that cannot be ignored is the concept of the reusability and the stability of a synthesised catalyst. The stability and reusability of the catalyst contribute considerably to the reduction of operational treatment cost. In this regards, the supported 2.4 % Ag doped TiO_2 nanocomposites (JT14) which enhanced the removal efficiency of BPA or 2-NP by 21.8 % and 23.2 % compared to the DBD reactor was re-used. The detailed experimental procedure on the removal efficiency of BPA or 2-NP using DBD with freshly prepared JT14 and the re-used JT14 was explained in section 3.2.9.1. The residual concentration of BPA or 2-NP in aqueous solution was

determined using HPLC techniques described in section 3.4.12. The results of the reusability test of the DBD with supported Ag doped TiO_2 nanocomposites (JT14) are presented in Figure 5.9. Figure 5.9 (a) and (b) represents the removal efficiency of BPA or 2-NP by combined DBD with fresh and re-used supported Ag doped TiO_2 nanocomposites (JT14).

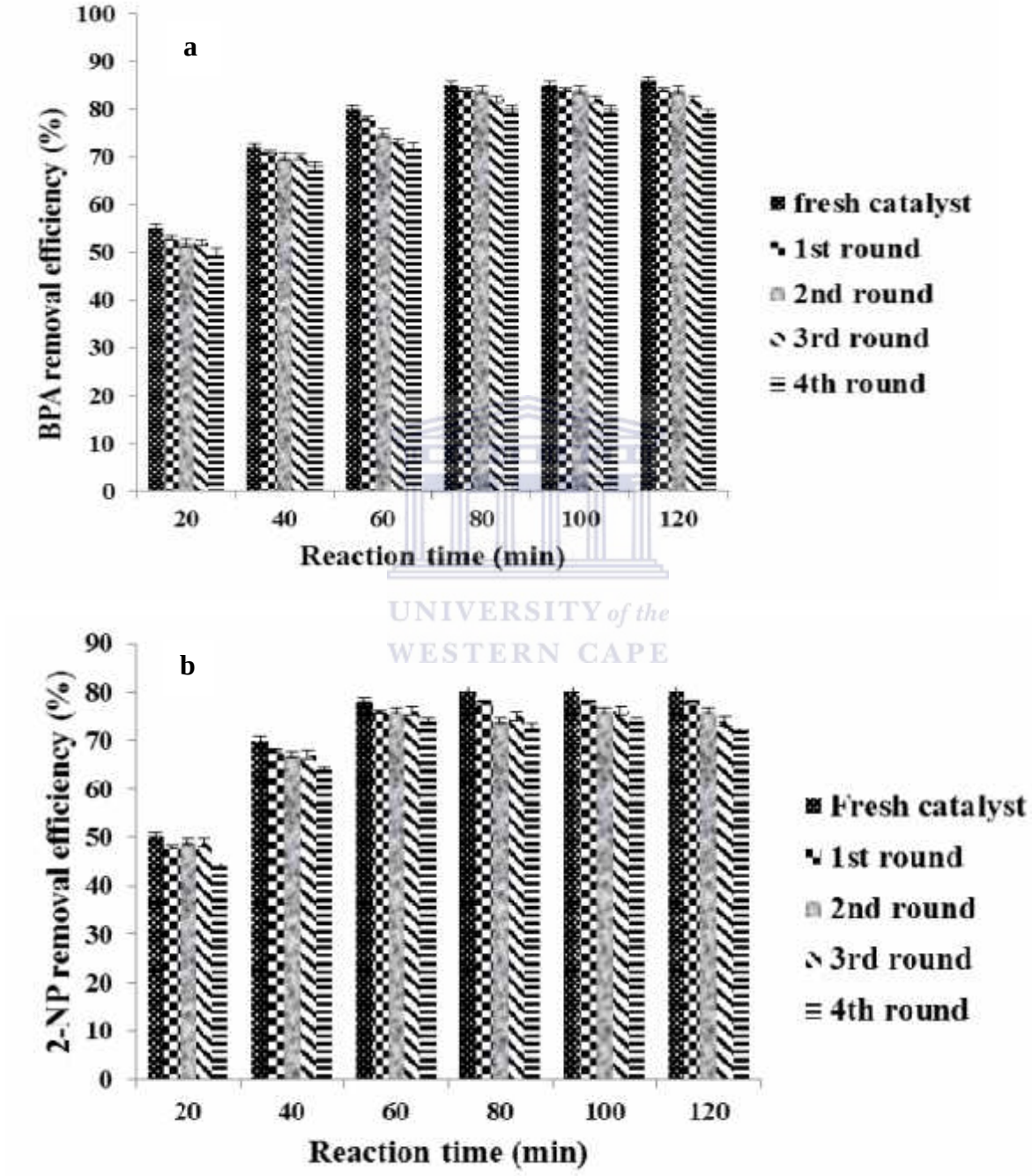

Figure 5.9: Removal efficiency of (a) BPA (b) 2-NP using combined DBD with fresh and re-used supported Ag doped TiO_2 nanocomposites (JT14). (Experimental conditions, same as Figure 5.7 or 5.8), number of replicates n=2

As shown in Figure 5.9 (a) and (b), the % removal of BPA or 2-NP at 20 min reaction time was 55 % or 50 % using combined DBD with the freshly prepared catalyst JT14. At 40 min, the % removal efficiency of BP or 2-NP increased to 72 % and 69 % respectively using combination of DBD and the freshly prepared JT14. This increase in the removal efficiency of both pollutants was consistent till 80 minutes and no significant increase was observed beyond 80 minutes. When the catalyst JT14 was re-used for the first time with the DBD, the % removal of BPA or 2-NP at 20 minutes was 53 % and 47 % respectively, which suggested a slight decrease of 2 – 3 % relative to the fresh catalyst. A similar trend was observed when the catalyst was re-used for the second and third times at each reaction time of 40 -120 minutes. This showed that the freshly prepared and re-used supported Ag loaded carbon doped TiO_2 nanocomposites (JT14) exhibited similar or catalytic activity with regard to the removal of BPA or 2-NP after three consecutive applications. This indicated that the re-used catalyst competed favourably with freshly prepared catalyst, since the BPA or 2-NP removal efficiency remained high after three consecutive applications. When the catalyst was re-used for the fourth time irrespective of the reaction time, % removal of BPA or 2-NP was reduced by less than 10 % with respect to the freshly prepapred catalyst. It is also obvious that BPA or 2-NP removal rate was rapid for the first 20 minutes and increased with treatment time. This suggested that the catalyst was still stable, not deactivated by the pollutants or intermediates and remained strongly adhered on to the stainless steel mesh. It further demonstrates that the supported Ag doped TiO_2 photocatalyst (JT14) was not affected by the discharge and as such the catalyst can be used for a long time. The slight decrease of less than 10 % after four repeated applications suggested the catalyst to be reusable. The decrease in the removal efficiency after four repeated applications may be linked to accumulation of low molecular carboxylic acids or intermediate compounds on the TiO_2 surface resulting to partial blockage of the catalytic active sites. Khan et al., (2013) reported similar stability and photocatalytic activity for both freshly prepared and recycled unsupported Ag/TiO_2 nanocomposites with MB removal. Similar findings were reported by Also, Álvarez et al., (2010) ascribed the loss of catalytic activity of the re-used catalyst to mass losses during separation and possibly leaching of support materials such as Fe from TiO_2/Fe_3O_4 nanocomposites. In this study, no mass loss was observed even after four repeated applications as evident in the catalytic efficiency of the original and recycle catalysts. The next section showed the XRD and HRSEM results of the fresh and re-used catalysts.

5.3.3 *Stability of the supported Ag doped TiO_2 nanocomposites after treatment*

The stability of a photocatalytic material is considered an essential parameter from both practical and economical perceptives. Based on this, the stability of Ag doped TiO_2 nanocomposites after four repeated applications with plasma discharge for the degradation of BPA or 2-NP was examined using XRD and HRSEM. The detailed experimental procedure on the catalyst preparation and sample analysis have been described in Section 3.2.3, 3.4.1 and 3.4.2 respectively. Figure 5.10 shows the XRD patterns of the original catalyst (JT14) before plasma discharge and after re-use for four times.

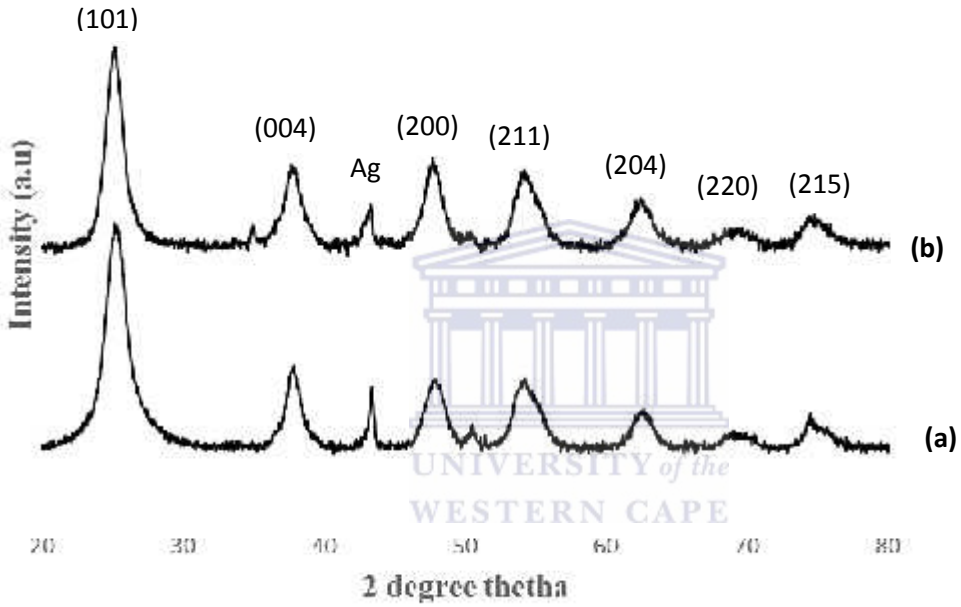

Figure 5.10: XRD patterns of: a) freshly prepared JT14 (b) JT14 after four repeated applications

As shown in Figure 5.10, the XRD pattern of the freshly prepared Ag/TiO_2 supported catalyst (JT14) matched well with the reused Ag doped TiO_2 nanocomposites after four successful applications. This shows that reused catalyst still maintained the same crystalline nature and pure anatase polymorph as the freshly prepared catalyst. There was no detection of additional peaks, except a slight decrease in the peak intensity of Ag in the re-used catalyst, which was due to high intense shock wave by DBD created within the bulk solution. This shows that the supported catalyst is photo-irradiation stable and not subject to photo-corrosion in spite of long term DBD discharge. Khan et al., (2013) also reported similar observations with the reused unsupported $Ag@TiO_2$ nanocomposites after two consecutive applications.

Furthermore, the HRSEM images of the fresh catalyst before discharge and reused supported catalyst after discharge is presented in Figure 5.11.

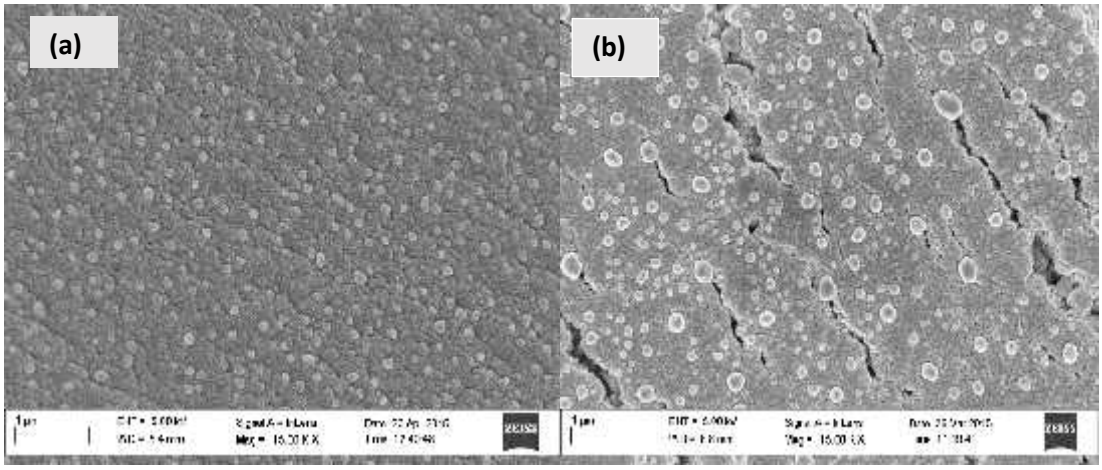

Figure 5.11: HRSEM images of 2.4 % Ag doped TiO_2 nanocomposites (JT14): (a) before plasma discharge (b) after four repeated applications

As shown in Figure 5.11, it is evident that the particle morphological arrangement were not destroyed or changed after four repeated discharge except slight cracks or voids. This may be linked to intense shock wave, exposure to UV light, discharge plasma which perhaps resulted to occasional spark discharge between the DBD reactor and the immersed catalyst. Continuous exposure to plasma discharge often erodes the catalyst surface and created holes or cracks. Zhang et al., (2012) attributed the formation of holes on the catalyst surface during plasma discharge to intense shock waves caused by high-voltage discharge. The next section focuses on the integration of the synthesised stabilised nano zero valent iron particles with the DBD system, which produces UV and H_2O_2.

5.4 Degradation of BPA or 2-NP by combined DBD and photo-Fenton induced process

The DBD reactor produces a large amount of H_2O_2 and intense ultraviolet light which are not maximally utilized. Thus, in order to induce photo-Fenton process and enhance the degradation rate of BPA or 2-NP, different dosage of polyethylene glycol nano zero valent iron (nZVI) particles in the range of 0.02 - 0.1 g was added to the DBD reactor. The detailed experimental procedure is provided in Section 3.2.9.2 while the residual concentration of BPA or 2-NP was determined using HPLC technique in Section 3.4.12. The BPA or 2-NP

removal efficiency with respect to different dosage of nZVI added to the DBD reactor with the reaction time is illustrated in Figure 5.12 and 5.13 respectively.

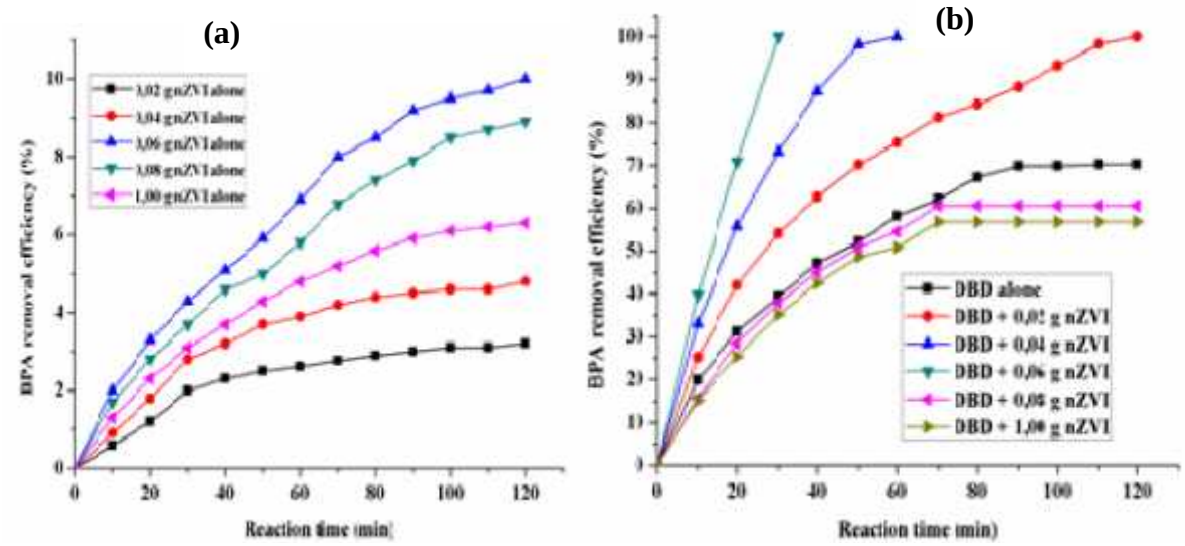

Figure 5.12: Removal efficiency of (a) BPA by different dosage of stabilized nZVI alone (JT17) (b) BPA by DBD combined with different dosages of nano zero valent iron (Experimental conditions: BPA volume 1.5 L; BPA concentration 10 mg/L; discharged voltage 8 kV; air flow rate 3 mL/min; solution pH 3; NaCl electrolyte concentration 50 g/L; electrode (silver), number of replicates=2

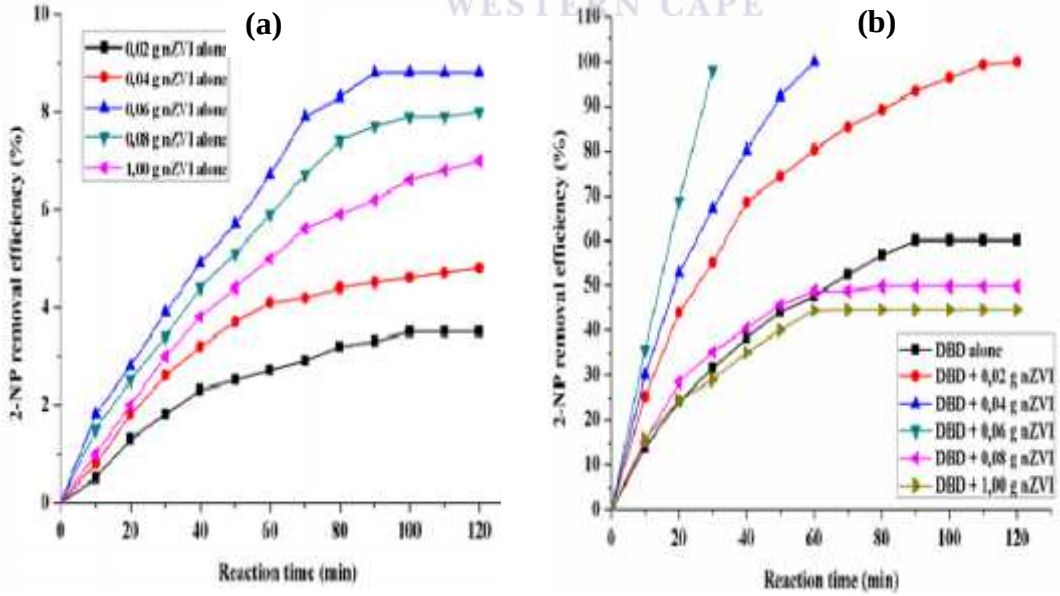

Figure 5.13: Removal efficiency of (a) 2-NP by different dosage of stabilized nZVI alone (JT17) (b) 2-NP by DBD combined with different dosages of stabilised nano zero valent (Experimental conditions same as in Figure 5.12), number of replicates=2

Figure 5.12 (a) and 5.13 (a) shows the control experiment conducted using different dose of nZVI sample (JT17) alone without the DBD system at optimum solution pH of 3, initial concentration of BPA or 2-NP (10 mg/L), volume of BPA or 2-NP (1.5 L) and discharged voltage (8 kV). It can be observed from Figure 5.12 (a) and 5.13 (a) that the removal efficiency of BPA or 2-NP using nZVI sample JT17 alone was in the range of 5 - 10% after 2 h. This slight percentage decrease of BPA or 2-NP in aqueous solution was attributed to the adsorption phenomenon of the catalyst, which can be ignored when compared to the removal efficiency obtained either by DBD alone or combined DBD/nZVI. Also from Figure 5.12 (b) and 5.13 (b), it was found that BPA or 2-NP removal efficiency at 30 min via DBD system alone was 39.3 % and 31.5 % and the removal efficiency increased till 90 min. Beyond 60 min, there was no further increase in the removal efficiency of BPA or 2-NP, which can be ascribed to the resistance of transformation products formed via the degradation process.

With the addition of 0.02 g nZVI, the pollutants removal efficiency was rapid reaching 57.1 % or 54.1 % at 30 min reaction time. This was probably due to an increased concentration of hydroxyl radicals, which accelerated the oxidation of BPA or 2-NP. When 0.04 g nZVI (JT17) was added to the DBD reactor, the removal effiency of BPA or 2-NP at 30 min was 73 % and 67.3 % respectively. With the addition of 0.06 g nZVI to the DBD system containing BPA or 2-NP, 100 % or complete removal of BPA or 2-NP was achieved at 30 min. The increase in removal efficiency during the initial stages of combined DBD and photo-Fenton induced reaction compared to DBD alone may probably be attributed to the presence of UV/H_2O_2 in solution which probably facilitated the photoreduction of hydroxylated ferric ion (Fe-OOH^{2+}) leading to formation of ferrous ion (Fe^{2+}) and OH^o radicals (equations 5.6 -5.8).

$Fe^{2+} + H_2O_2/UV \rightarrow Fe^{3+} + OH^o + OH^-$ ……..(5.6)

$Fe^{3+} + H_2O_2 \rightarrow Fe–OOH^{2+} + H^+$ ……..(5.7)

$Fe–OOH^{2+} + UV \rightarrow Fe^{2+} + OH^o$……....(5.8)

Additionally, the rapid oxidation reaction of Fe^0 to Fe^{2+} and subsequent reaction of Fe^{2+} with UV/H_2O_2 produced more OH radicals (equation 5.9).

$Fe^0 + H_2O_2 + UV \rightarrow Fe^{2+} + 2\,OH^o$……..(5.9)

The two additional sources of OHº may perhaps be responsible for such initial higher removal efficiency and complete elimination observed at a short reaction time of 30 minutes. Therefore, nZVI exhibited best catalytic activity at dosage of 0.06 g. The possible explanation for this trend could be that with the addition of 0.02 and 0.04 g nZVI, the amount of Fe^{2+} in solution required to react with UV/H_2O_2 to induce photo-Fenton reaction and liberate OHº was small. The low yield of OHº in the solution may be responsible for the lower removal efficiency compared to 0.06 g nZVI. Thus, with addition of 0.06 g nZVI to the DBD reactor, it is believe that more of Fe^{2+} was able to react with UV/H_2O_2 to produce OH radicals and Fe^{3+} (equation 5.10).

$$Fe^{2+} + H_2O_2/UV \rightarrow Fe^{3+} + OH^{o} + OH^{-} \quad \text{.....(5.10)}$$

Therefore, complete BPA or 2-NP removal achieved with 0.06 g nZVI/DBD system in less than 40 minutes may be ascribed to higher yield of OHº and Fe^{3+} in the reaction mixture (see Section 5.8.3). This assumption corroborated the earlier studied conducted by Wang et al., (2007) who demonstrated that the presence of Fe^{3+} in the glow discharge plasma accelerated the oxidation of BPA. The authors pointed out that BPA degradation by glow discharge plasma was mainly by hydroxyl radical attack involving either hydrogen abstraction or electrophilic and resulted in the formation of intermediates. These intermediates equally act as a reducing agent and reduced the Fe^{3+} to Fe^{2+}. The regenerated Fe^{2+} further reacted with UV/H_2O_2 in solution to produce OHº, thus responsible for the mineralization of BPA. Thus, it is possible to conclude that complete removal of BPA or 2-NP observed within 30 min could be linked to the sustainable and continuous oxidation-reduction reaction between Fe^{0} and Fe^{3+} within the bulk solution which produced Fe^{2+}. At every reaction time, it was noticed that more BPA molecules were removed than 2-NP. The reason for such have earlier been discussed in Section 5.1.1. Comparing the efficiency of combined DBD with respect to different dosage of nZVI as presented in Figure 5.12 (b) and 5.13 (b), it can be seen that 0.06 g nZVI demonstrated stronger catalytic activity, and enhanced the overall removal efficiency of BPA or 2-NP within short reaction time than higher or lower dosages of nZVI. This showed that successful elimination of BPA or 2-NP can be achieved via integrated approach and demonstrated existence of a synergetic effect between DBD and nZVI. This further validates the initial hypothesis that addition of nZVI to DBD to induce photo-Fenton process will improve rate of elimination of BPA or 2-NP in water.

Conversely, with the addition of 0.08 g and 0.1 g, the BPA or 2-NP removal efficiency decreased abruptly. In fact, the removal efficiency in both cases was lower than the removal rate obtained with alone DBD alone. This may be due to the fact that, at higher nZVI dosage beyond 0.06 g, made the solution highly turbid. The high level of turbidity impeded the UV-light intensity and penetration path leading to light scattering and thus pollutants were not decomposed by free radicals. In addition to the shielding effect which affects UV light penetration, the reaction between Fe^{2+} and H_2O_2/UV that leads to the formation of OH^o was affected. Thus, low concentration of OH^o may also be responsible for lower removal efficiency of BPA or 2-NP. Goi and Trapido, (2002) and Trapido et al., (2014) independently submitted that the effectiveness or performance of a photo-Fenton process regarding decomposition of refractory organic pollutants depends on the dosage of Fe^{2+} invariably Fe^0. The authors affirmed that the photo-Fenton process would be less effective in a solution containing excess Fe^{2+}. It was also found that BPA and 2-NP exhibited similar removal pattern via the combined DBD/nZVI, which suggest that the two compounds may likely be attacked by the same free reactive species. Manoj Kumar Reddy and Subrahmanyam, (2012) also found that addition of 0.5 g/L Fe^{2+} to DBD increased crystal violet removal rate from 85 % to 99 % within 25 min. Their results were however lower than what was obtained in this study with just 0.06 g nZVI, where 100 % BPA or 2-NP removal rate was achieved in less than 40 min. Manoj Kumar Reddy et al., (2013) reported that MB removal rate was enhanced by 35 % upon the addition of 60 mg/L $FeCl_2$ to the DBD reactor within 25 min. The authors attributed the improved degradation efficiency to the synergetic effect between the two processes which contributed to higher concentration of hydroxyl radicals in the solution. Jiang et al., (2013) found that BPA was completely degraded within the same reaction time when different doses of nZVI (5 mg-15 mg) was added to activated persulphate ($S_2O_8^{2-}$). The authors attributed such complete BPA oxidation to continuous and sustainable electron transfer from Fe^0 to Fe^{2+} in the presence of O_2.

5.5 The kinetic model for BPA or 2-NP oxidation

In order to further demonstrate the effectiveness of combined DBD/supported photocatalysts and DBD/photo-Fenton induced process over DBD alone on the removal efficiency of BPA or 2-NP, the obtained experimental data shown in Section 5.3 and 5.4 were fitted to the pseudo- first order kinetic model shown in equation (5.11).

$$ln\frac{Cp}{Cpo} = -kt \quad \text{.....(5.11)}$$

Where t represents the reaction time (min), C_p connotes initial at time t=0, while C_{po} is the concentration at a given time t. The pseudo-first order kinetic plot of experimental data obtained via the degradation of BPA or 2-NP oxidation process by combined DBD/supported photocatalyst and DBD/photo-Fenton induced reaction are shown in Figure 5.14 and 5.15 respectively. The experimental data obtained up to 80 min reaction time were used for the kinetic plots since no significant improvement in the BPA or 2-NP removal efficiency were noticed after this time. The slopes of the individual fitted straight line corresponds to the reaction rate constant (k'), which are indicated in Table 5.3 and 5.4 respectively.

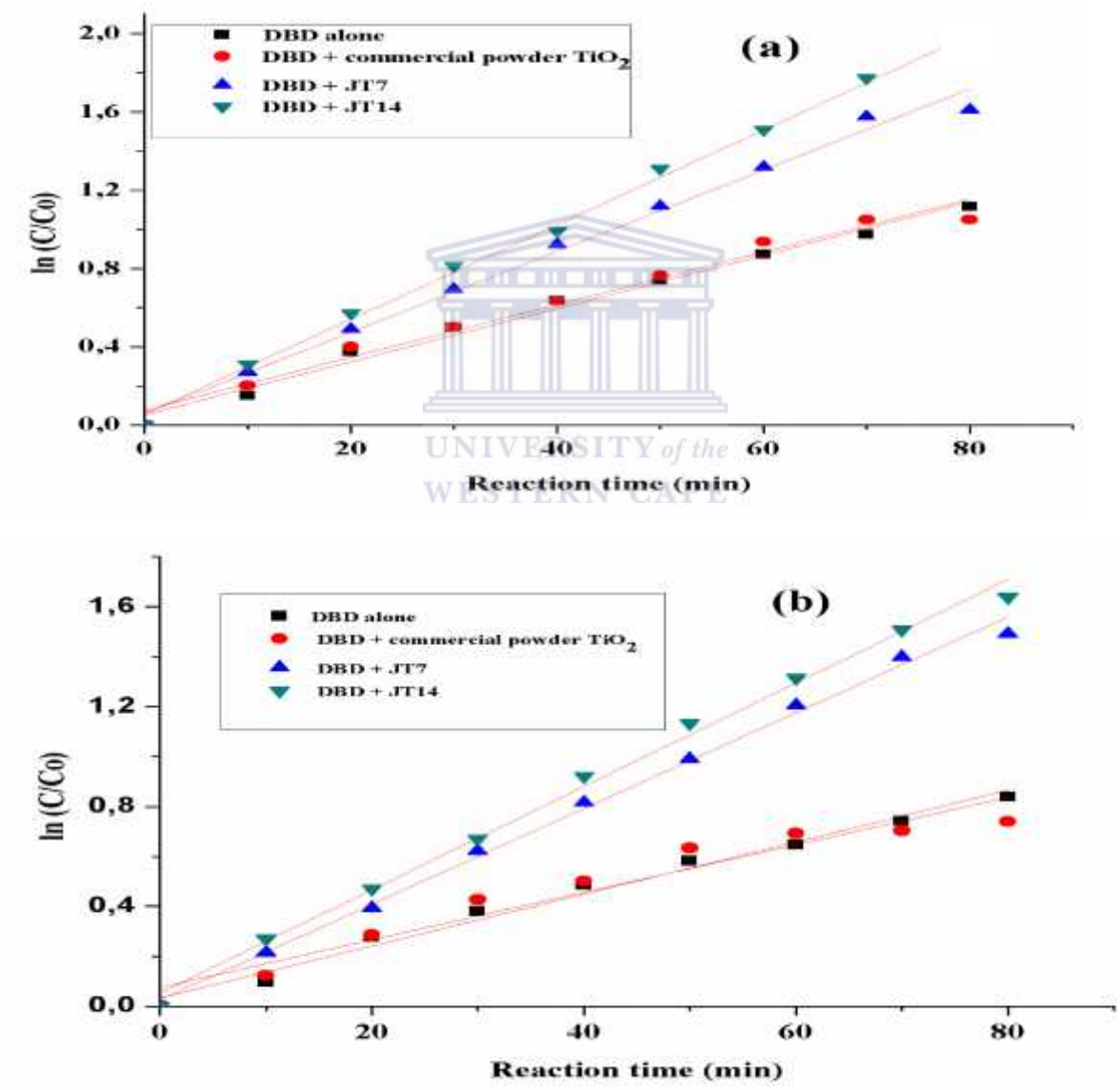

Figure 5.14: Pseudo-first-order plots for the degradation of (a) BPA (b) 2-NP by combination of DBD/JT7 and DBD/JT14. The experimental conditions are the same as in Figure 5.7 and 5.8

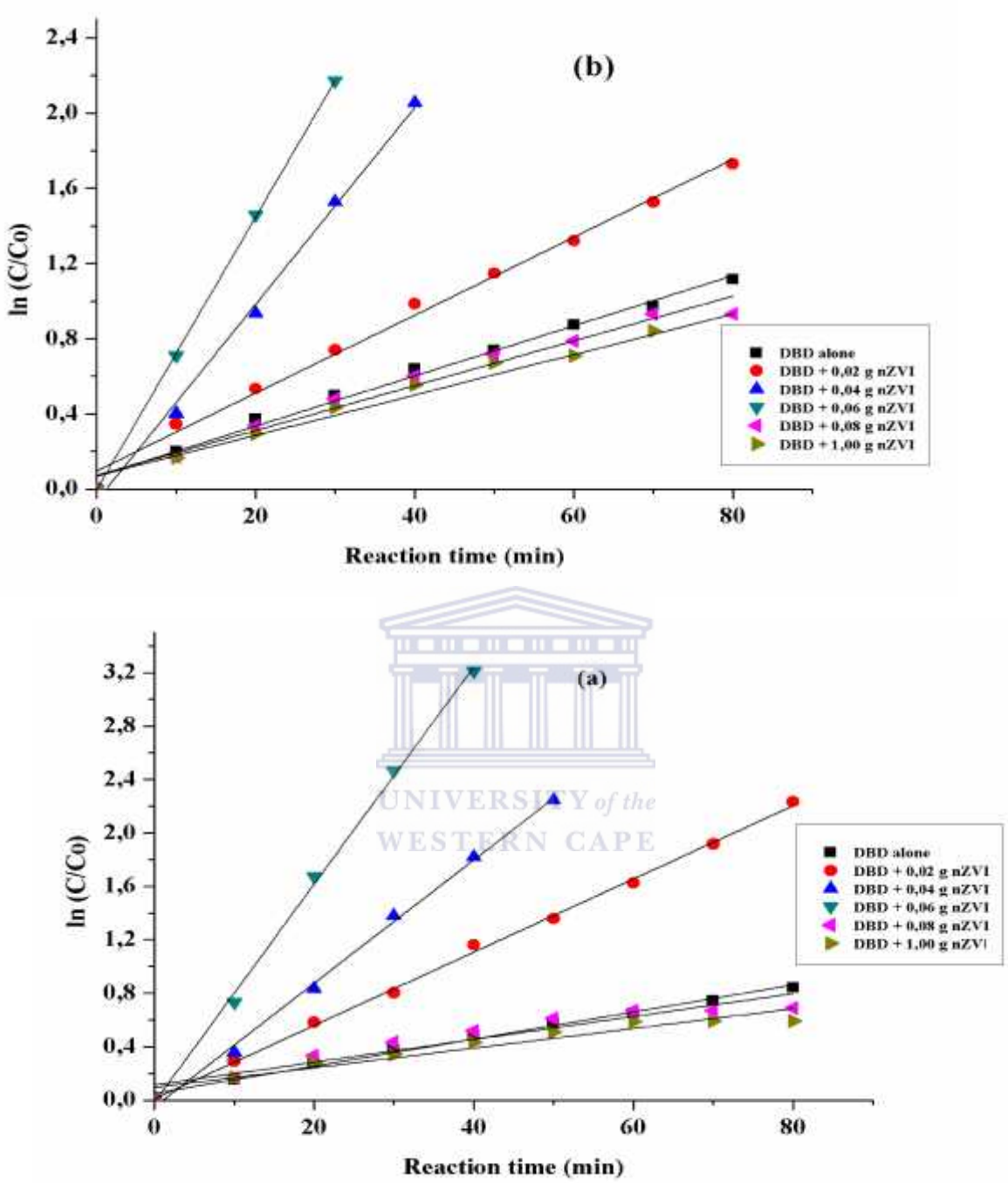

Figure 5.15: Pseudo-first-order plots for the degradation of a) BPA b) 2-NP by combination of DBD with different dosage of nZVI (JT17). The experimental conditions are the same as in Figure 5.12 and 5.13

The pseudo-first order rate constants (k) and the correlation coefficient (R^2) of the combined DBD/JT7 or DBD/JT14 on the degradation of BPA or 2-NP are shown in Table 5.3.

Table 5.3 : The pseudo-first rate constant and correlation coefficient value for BPA or 2-NP degradation via combined DBD/JT7 and DBD/JT14 (Experiment conditions as in Figure 5.7 and 5.8)

Pollutants	Treatment process	Rate constant (min^{-1})	Correlation coefficient (R^2)
BPA	DBD alone	0.0103	0.9921
	DBD + commercial TiO_2 powder	0.0090	0.9919
	DBD + JT7	0.0207	0.9946
	DBD + JT14	0.0242	0.9967
	DBD alone	0.0079	0.9913
	DBD + commercial TiO_2 powder	0.0061	0.9905
2-NP	DBD + JT7	0.0192	0.9932
	DBD + JT14	0.0207	0.9946

As shown in the Table 5.3, it is apparent that the rate constant (k) of BPA by combined DBD/JT14 and DBD/JT7 were 0.0242 min^{-1} and 0.0207 min^{-1} respectively. The rate constant of DBD was 0.0103 min^{-1} while that obtained using DBD/powder commercial TiO_2 was 0.0090 min^{-1}. The obtained rate constant for 2-NP removal via each process were as follows: DBD alone (0.0079 min^{-1}), DBD/powder commercial TiO_2 (0.0061 min^{-1}), DBD/JT7 (0.0192 min^{-1}), DBD/JT14 (0.0207 min^{-1}) respectively. It was found that the rate constant for removal of BPA using DBD/JT7 was 2.3 times higher than using DBD alone. In the same vein, the first order kinetic constant for 2-NP removal by the integrated DBD/JT14 was 3.4 times greater than DBD alone. The rate constant obtained using DBD alone was slightly greater than obtained using combined DBD/powder commercial TiO_2. It is obvious that the rate constant obtained for BPA using DBD with JT7 or JT14 was 2.3 or 2.7 times greater than that obtained via DBD with powder commercial TiO_2. A similar trend was observed for rate constant of 2-NP removal obtained using DBD/JT7 or DBD/JT14 compared to DBD/powder commercial TiO_2. The possible explanation for the observed higher reaction rate constant for both pollutants using DBD/JT7 or DBD/JT14 may be linked to fast reaction kinetics between the pollutants and the free reactive species in the solution in the combined system than DBD alone. This was also an indication of the existence of a synergetic effect between DBD and supported photocatalyst. The result agreed with the earlier hypothesis that incorporation of

supported TiO_2 photocatalyst could enhance the BPA or 2-NP mineralization rate more than TiO_2 without support. Similar observations were reported by Zhang et al., (2012) during the degradation of phenol by integrated pulsed corona discharge and TiO_2 nanotube films. The authors demonstrated reaction rate constant (k) of 0.00304 min^{-1} for phenol degradation by combined system and 0.00124 min^{-1} for pulsed corona discharge alone. Comparing the rate constant (k) values reported by Zhang et al., (2012) either in the presence or absence of TiO_2 catalyst and the rate constant obtained in this study, it is clear that the DBD in this study exhibited higher pollutant removal efficiency, especially in the integrated system with supported TiO_2 photocatalysis than what was obtainable by Zhang and colleagues, (2012). This further affirmed that incorporation of supported TiO_2 to the DBD system enhanced the degradation of organic pollutants. The rate constant obtained in this study was smaller than 0.03 and 0.05 min^{-1} reported by Zhang et al., (2013) for phenol degradation via pulsed corona discharge and combined pulsed corona discharge with TiO_2. A possible explanation for such difference may be attributed to the pollutant type as well as different reactor type and applied conditions such as discharge voltage. In the case of studies conducted by Zhang and co-workers, (2013) point-to-plate pulsed discharge system of 16 kV discharge voltage with TiO_2 film was used compared to the DBD system used in this present study which could only deliver 8 kV discharge voltage. The discharge voltage of the pulsed corona system used by Zhang et al., (2013) was double the value used in this study. Zhang et al., (2013) attributed the high kinetic constant to excess H_2O_2 in the integrated system, which in turn was responsible for more OH radicals and ultimately high degradation rate.

However, no significant difference was observed in the rate constants obtained for BPA or 2-NP removal by DBD and DBD with powder commercial TiO_2. The reason for such a close value despite the addition of the powdered TiO_2 may be attributed to the fact that powder TiO_2 in solution made the solution turbid, and caused an increase in the opacity and thereafter inhibited UV-light intensity. This reduced the interaction of the pollutants with free radicals, causing slower kinetics and low degradation rate. Furthermore, the rate constant and correlation coefficient of the DBD/photo-Fenton induced process degradation of BPA or 2-NP were determined and represented in Table 5.4.

Table 5.4: The pseudo-first rate constant and correlation coefficient value for BPA or 2-NP degradation via combined DBD/photo-Fenton induced process (Experimental conditions as in Figure 5.12 and 5.13)

Pollutants	Treatment process	Rate constant (min^{-1})	Correlation coefficient (R^2)
BPA	DBD alone	0.0103	0.9921
	DBD + 0.02 g nZVI	0.0274	0.9984
	DBD + 0.04 g nZVI	0.0462	0.9974
	DBD + 0.06 g nZVI	0.0815	0.9999
	DBD + 0.08 g nZVI	0.0075	0.9335
	DBD + 0.1 g nZVI	0.0073	0.9227
	DBD alone	0.0079	0.9913
	DBD + 0.02 g nZVI	0.0207	0.9931
2-NP	DBD + 0.04 g nZVI	0.0523	0.9960
	DBD + 0.06 g nZVI	0.0617	0.9999
	DBD + 0.08 g nZVI	0.0119	0.9741
	DBD + 0.1 g nZVI	0.0108	0.9693

According to Table 5.4, it is apparent that addition of different dose of nZVI in the range of 0.02 – 0.06 g DBD system enhanced the degradation rate constant from 0.0274 min^{-1} to 0.0815 min^{-1} for BPA and 0.0207 min^{-1} to 0.0617 min^{-1} for 2-NP respectively. The degradation reaction rate constant of both pollutants were eight times greater with the addition of 0.06 g nZVI to the DBD system than with the DBD alone. The experimental data could be better described using pseudo-first order kinetics as evident in the correlation coefficient (R^2) value that was closed to unity. This showed that addition of nZVI at optimum dose increased the concentration of hydroxyl radicals in the solution, which in turn enhanced the degradation efficiency of the two compounds. Similar result was reported by Rong and Sun, (2013) on the decomposition of sulfadiazine (SDZ) by wetted-wall corona discharge. The authors found that addition of Fe^{2+} to corona discharge improved the SDZ degradation rate by four times. On the contrary, further addition of nZVI dosage beyond 0.06 g resulted in the reduction of the reaction rate constant. A slight deviation from pseudo-first plot was observed with the increase in dosage of nZVI from 0.08 to 0.1 g as revealed by the correlation coefficient value (R^2). This showed that beyond the optimal value of 0.06 g, other

obtained experimental data precisely from 0.08 g to 0.1 g poorly fitted the pseudo-first order kinetics. This means that further addition of nZVI to DBD increased wastewater turbidity level, and inhibited the UV-light intensity. Aside from that, the formation of free reactive species was limited and the interaction between the pollutants and oxidants affected, thus responsible for such lower rate constant. Very recently, Rong and Sun, (2013) found that higher concentration of Fe^{2+} in solution did not translate to higher pollutant mineralization rate due to stronger competition between organic pollutants and excess Fe^{2+} in the solution for free radicals such as OH radicals. Additionally, Chen et al., (2009) reported the decreased in pollutant removal efficiency from solution at higher dosage of Fe^{2+} during plasma discharge. According to the authors, an excessive amount of Fe^{2+} in solution increased solution conductivity which inhibited the plasma discharge activities.

According to Table 5.4 and 5.5, it is obvious that the rate constants obtained for BPA or 2-NP via DBD/photo-Fenton process at optimum dosage were greater than that obtained by DBD/supported photocatalyst. The significant improvement in the degradation rate constant by DBD/photo-Fenton induced reaction may be explained as follows: firstly high surface area to volume ratio nanoparticles, allowed easier interaction of the particle with the pollutants. Secondly, continuous and sustainable production of Fe^{2+} by Fe^{0} accelerated the formation of more hydroxyl radicals in the solution as shown in equations 5.6 -5.9. Travido et al., (2014) attributed the higher reaction rate constant for ibuprofen and diclofenac removal via photo-Fenton process to the additional OH radicals provided via UV-light interaction with complex $Fe\text{-}OOH^{2+}$. In the case of DBD/JT7, although the support materials assisted to overcome the post-filtration problem, reaction rate constants was low compared to DBD/photo-Fenton induced process. This indicates that photocatalytic activity was not rapid due to restriction of catalyst surface areas on a support materials, which limited the mass transfer rate. Very importantly, the presence of cationic impurities such as Fe, Cr and Ni on the TiO_2 layer may have inhibited or interfered with the photocatalytic activity of TiO_2, simply because their ionic radii are similar to that of Ti^{4+} Also, the rate constants (k) for BPA was greater than slightly greater than that of 2-NP irrespective of the treatment process, this possibly suggest the higher recalcitrance of 2-NP towards the reactive species compared to BPA. Another reason for higher degradation of BPA may be linked to the number of possible points of attack by O_3 or OH^{o}. For instance, O_3 or OH^{o} react non-selectively with BPA either by hydrogen-abstraction on the CH_3 group or electrophilic attacked on the C=C double in the

aromatic rings. Whereas, these species can only react with 2-NP via electrophilic attacked on C=C in the aromatic ring alone.

5.6 Identification of intermediates or transformation compounds

The identification of intermediates compound or oxidation by-products formed on exposure of organic pollutants to free radicals is somehow tricky and complex. This however depends on several operational factors such as pollutant concentration, oxidant dosage and reaction times. Besides, intermediates compounds are unstable and present at a concentration below a limit detectable by analytical techniques. In this study, the higher concentration approach was adopted to identify the intermediate compounds and predict which of the reactive species was responsible for BPA degradation. Dielectric barrier discharge (DBD) alone, DBD/JT14 and DBD/0.06 g nZVI, were utilized to decompose BPA or 2-NP in water, where the degradation experiment was monitored for 2 hr. The detailed experimental procedures and analytical detection techniques can be found in Section 3.2.9.4 and 3.4.13 respectively. The Agilent 6230 Time of Flight Liquid Chromatograph Mass Spectrometer (TOF LC-MS) in the negative ionization mode was used for qualitative identification of the intermediates at every 20 minutes. The intermediate compound formed during the degradation of BPA or 2-NP via DBD, DBD/supported photocatalysts (JT14) and DBD/photo-Fenton induced process are explained in the next section.

5.6.1 *BPA and BPA oxidation by-product*

Figure 5.15 (a) illustrates the mass spectra (MS) of BPA standard solution or starting material measured in the electrospray ionization (ESI) negative mode, which contained a sharp peak of deprotonated molecular ion $[M-1]^-$, m/z at 227.10 within 6.5 min. The means that the original mass of BPA was 228.29 but was measured to be 227.10. The LC-UV spectra as shown in Figure 5.15 (b) indicated that BPA had a maximum absorption band at 278 nm.

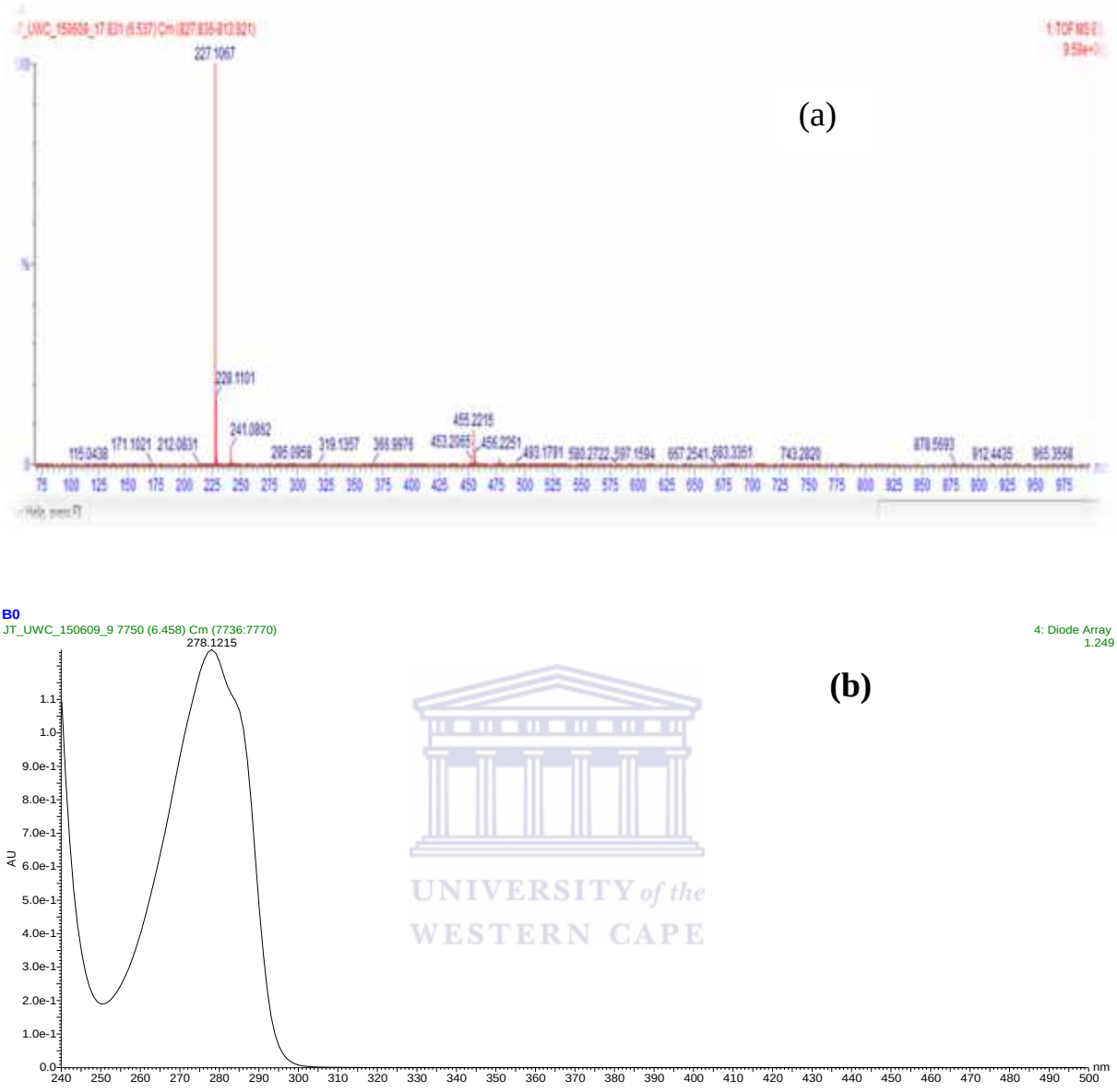

Figure 5.16: (a) LC-MS chromatograph and (b) LC-UV of standard BPA solution prior to oxidation process either by DBD alone, DBD/JT17 or DBD/photo-Fenton induced process.

After the exposure of BPA to plasma discharge or radical environment (using either DBD alone, combined DBD/JT14 or DBD/photo-Fenton induced process) several other prominent peaks of different relative molecular masses (m/z) were noticed in the aliquot with retention time in the range of 1.9 min to 5.8 min (see Figure 5.18). The lower retention time indicates formation of more polar compounds than BPA. Although, retention times greater than 5.8 min were also noticed which suggested the formation of high molecular weight species, which could result from secondary reactions among the oxidation by-products of BPA. The LC-MS chromatograph revealed the mass fragmentation pattern (m/z) and relative abundance

(%) of identified intermediate compounds via the three treatment approaches as shown in Table 5.4. All the intermediate compounds formed via the three processes are summarised with their proposed chemical structure in Table 5.6. The chemical structures were proposed using the MS library.

Table 5.5: Transformation products of BPA via the three treatment methods

Compounds	Molecular formula	Molecular mass (g/mol)	Theoretical mass [M-H]	Observed fragment ion at m/z value (% abundance)	Acquisition or retention time
Bisphenol-A	$C_{15}H_{16}O_2$	228.29	228.26	227.107 (100)	6.5
BP1	$C_{15}H_{16}0_5$	276. 28	276.24	275.09 (97.50)	4.8
BP2	$C_{14}H_{16}0_3$	232.28	232.24	231.10 (97.50)	4.6
BP3	$C_{30}H_{32}O_{10}$	552.55	552.46	551.19 (97.50)	9.9
BP4	$C_{13}H_{16}O$	188.23	188.26	187.10 (84.5)	4.5
BP5	$C_6H_5NO_3$	139.10	139.09	138.01 (45.62)	4.4
BP6	$C_{15}H_{16}O_3$	244.28	244.25	243.10(97.57)	5.8
BP7	$C_{15}H_{14}O_3$	242.27	242.23	241.89(66.5)	5.0
BP8	$C_{13}H_{14}O_5$	250.24	249.19	249.07 (94.07)	4.3
BP9	$C_{13}H_{14}O_3$	218.24	218.21	217.08 (57.80)	4.0
BP10	$C_{12}H_{14}O_3$	206.21	206.24	205.08 (66.7)	3.9
BP11	$C_9H_{10}NO_4$	196.11	196.18	195.9 (77.8)	3.2
BP12	$C_9H_7O_2$	147.11	147.15	146.9 (14.2)	2.5
BP13	$C_9H_{10}O_3$	166.06	166.14	165.01(82.7)	2.8
BP14	$C_6H_4NO_2$	122.10	123.09	121.02(52.3)	1.9

BP= by-product

Furthermore, the obtained transformation products during the oxidation of BPA via three degradation systems namely: DBD alone, DBD/supported photocatalysts, and DBD/photo-Fenton induced reaction are illustrated in the time based scheme in Figure 5.17

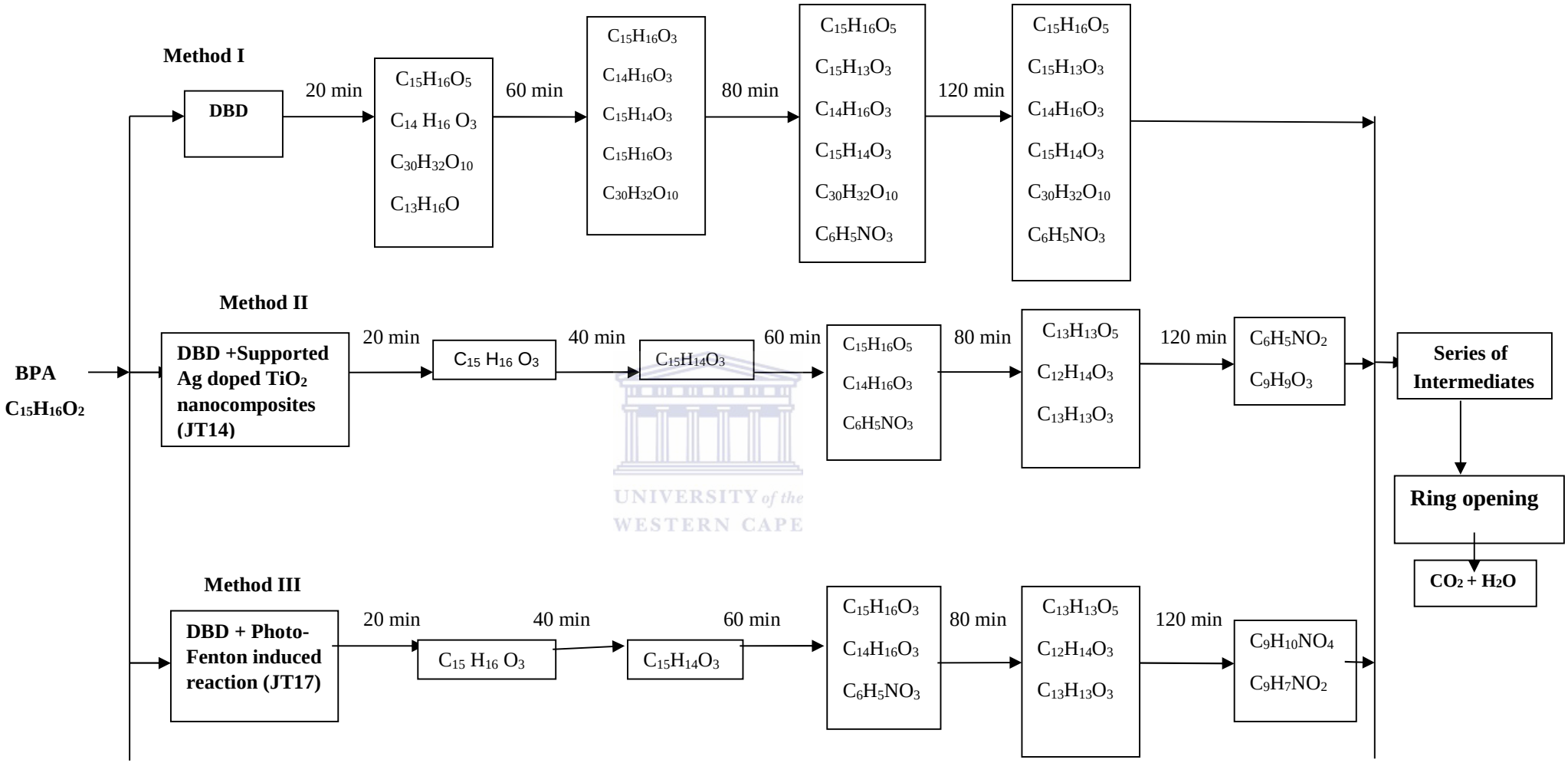

Figure 5.17: Time based identification of BPA intermediates via DBD alone, DBD/JT14 and DBD/photo-Fenton induced reaction

Within the first 20 minutes using DBD alone, BPA oxidised to five by-products with main fragment (m/z) value of 275.09, 231.10, 187.10 and 551.19 and 112.98. However, the intermediates with mass fragment ion at m/z 112.98 could not be detected by MS possibly due to low concentration. The LC-MS and LC-UV spectra of the four intermediates are shown in Figure 5.18

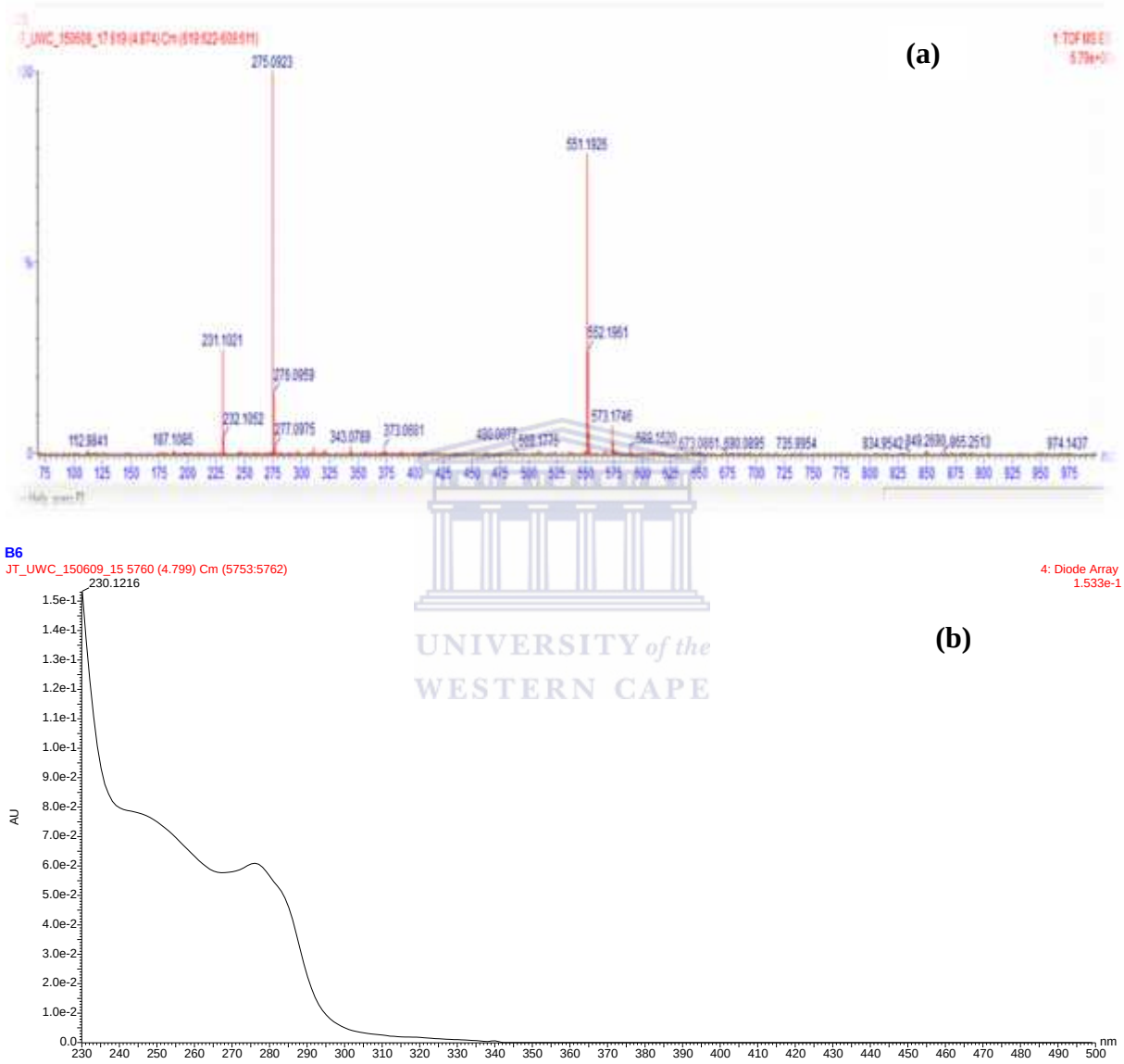

Figure 5.18: (a) LC-MS and (b) LC-UV chromatograph of the intermediates products formed via DBD alone within 20 minutes reaction time.

Comparing the LC-UV spectra of ordinary BPA shown in Figure 5.17 (a) with that of Figure 5.18 (b), it can be seen that the intensity of the earlier observed absorption band at 278 nm decreased significantly, which suggested transformation of BPA. Besides, there was an appearance of a weak absorption band in the range of 240-250 nm, and 280 nm which

possibly confirmed the identified intermediates compounds. The retention time of three oxidation products shown in Table 5.6 was less than 4.9 min. This means the intermediates that originated from BPA were polar as polar oxidation-byproducts were found to elute faster from the non-polar (C_8) chromatographic column than BPA. The mass difference between 275.09 and fragment ion at m/z 231.10 was 44, which corresponded to the losses of CO_2. While the mass differences between 275.09 and 187.10 was 88, which indicated two consecutive loss of CO_2. The fourth intermediate compound with a higher molecular weight having a fragmentation pattern (m/z) at 551.19 was suspected to be a dimeric or an oligomeric compound. This was a result of secondary reactions between two molecules of 275.09. Based on the obtained fragmentation patterns as demonstrated in the MS spectra and available MS library, the following chemical structure were predicted for BP1, BP2, BP3 and BP4 : 275.09 ($C_{15}H_{16}O_5$), 231.10 ($C_{14}H_{16}O_3$), 187.10 ($C_{13}H_{16}OH$) and 551.19 ($C_{30}H_{30}O_{10}$) respectively using BPA ($C_{15}H_{16}O_2$) as a starting compound.

Furthermore, there was no difference in the range of intermediate compounds formed after 40 minutes using DBD alone (MS spectra not shown), which showed that the compounds were stable and resistant. With DBD alone, at 60 minutes, a new by-product (BP5) with mass fragment ion at m/z 138.01 was observed with other intermediates still in solution (Figure 5.19 (a)).

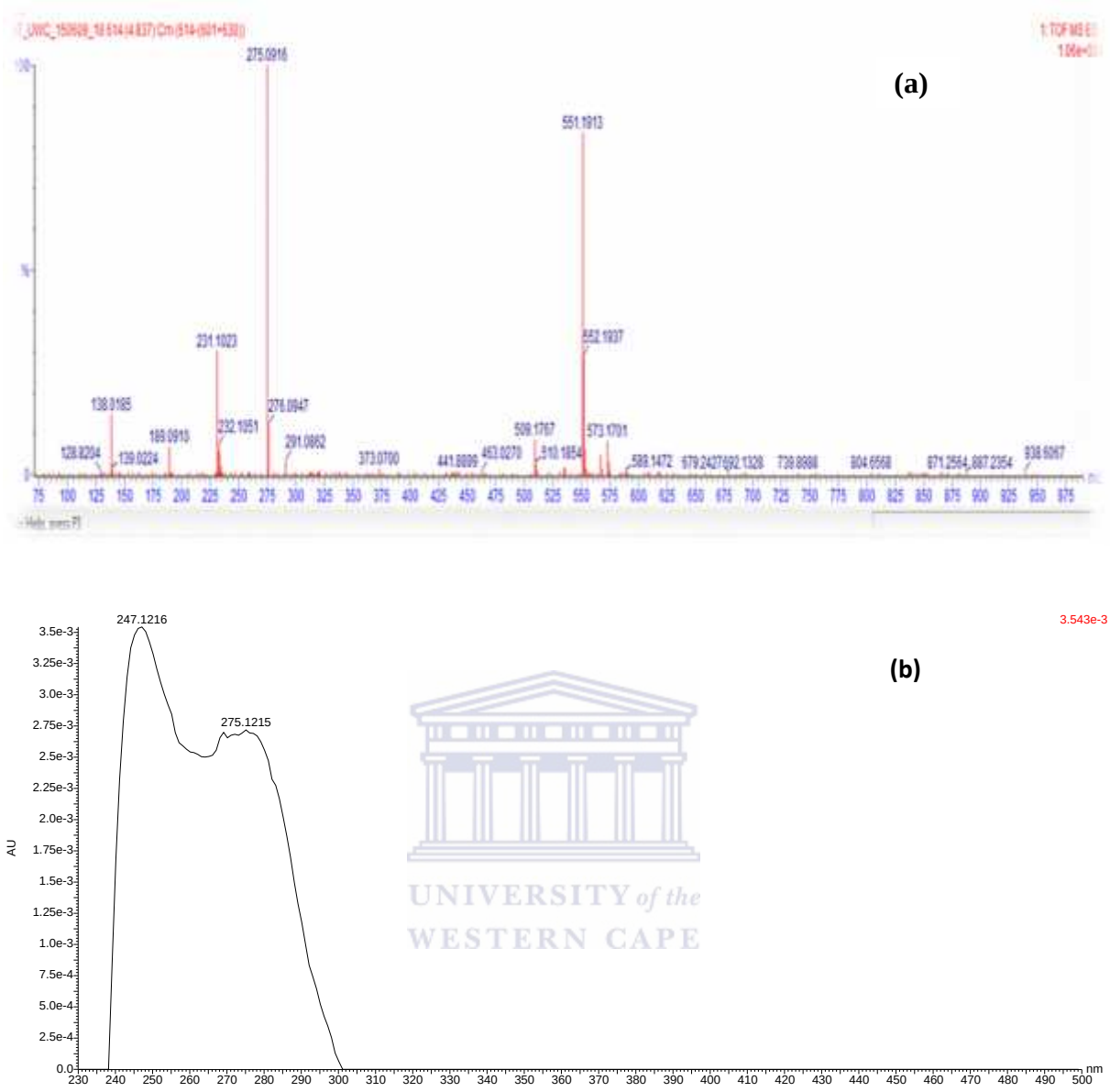

Figure 5.19: (a) LC-MS and (b) LC-UV chromatograph of the intermediates products formed via DBD alone at 60 minutes reaction time

The LC-UV spectrum of the intermediates having maximum absorption band at 247 and 275 nm is shown in Figure 5.19 (b). The observed fragmentation pattern at m/z 138.01 indicated cleavage of C-C bond of one of the two aromatic rings in BPA molecules into smaller moieties. The cleavage of one of the two aromatic rings suggested hydrogen abstraction from the methyl group (CH_3) by OH radicals. It should be noted that electron-donating species such as OH^o increase the electron-density of the aromatic rings and made the double bonds more susceptible to subsequent attacks. Based on the available MS library database, the chemical formula of BP5 with fragment ion at m/z 138.01 was predicted to be $C_6H_5NO_3$ (4-nitrophenol). It had earlier been pointed out that DBD produces nitrogenous species such as

nitrous and nitrite oxide, which emanated from the feed dry air. The formation of a nitrogeneous species suggested reaction of phenolic moieties with NOx in the solution. It should be mentioned that similar intermediate compounds observed in solution at 60 min were still the same as those found at 120 min. This suggested that the intermediates were persistent or resistant to further oxidation by the reactive species. The detailed degradation pathways or reaction mechanism are provided in section 5.6.2.

5.6.2 *Intermediates compound obtained via DBD/JT14 and DBD/photo-Fenton induced process*

On the other hand, when combined DBD/JT14 and combined DBD/photo-Fenton induced process was applied to decompose BPA, unlike what was obtained with DBD, only one intermediate compound was formed within the first 20 minutes. The obtained intermediate compound (BP6) with fragmentation pattern at (m/z) 243.10 is shown in Figure 5.20 (a). Comparing compound BP6 with the parent compound BPA ($C_{15}H_{16}O_2$), it was found that the compound (BP6) has one more additional oxygen which corresponds to an OHº. Based on this, the chemical structure of BP6 is proposed to be $C_{15}H_{16}O_3$ (mono-hydroxylbisphenol-A) which strongly agreed with UV-spectra shown in Figure 5.20 (b).

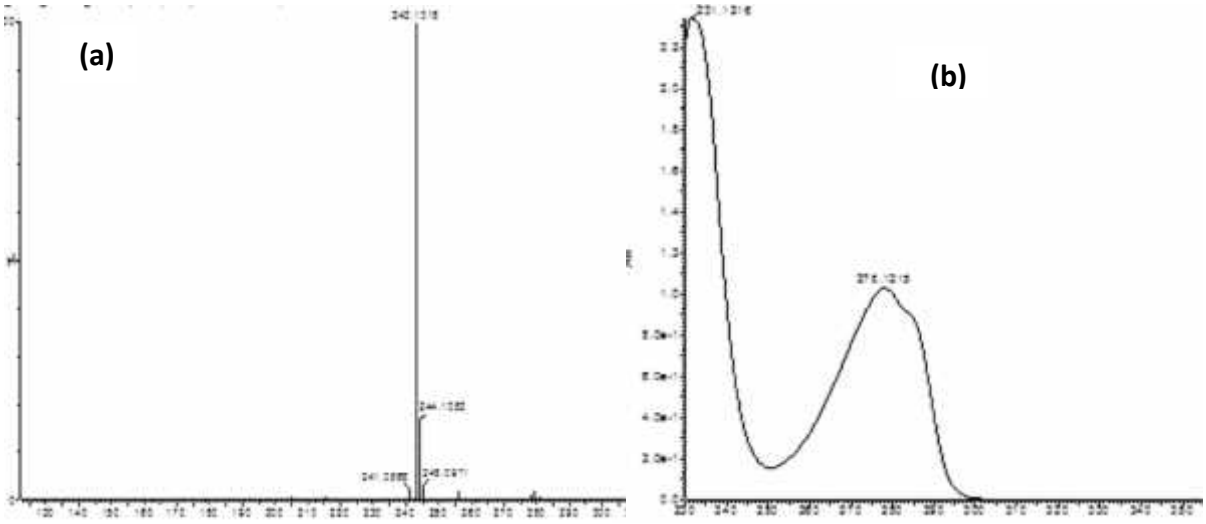

Figure 5.20: (a) LC-MS and (b) LC-UV chromatograph of the intermediates products formed via DBD/JT14 and DBD/photo-Fenton induced reaction (JT17) within 20 minutes reaction time

At 40 minutes, the MS spectra revealed only one peak (not shown), with mass fragment pattern at m/z 241.89. This corresponded to the loss of hydrogen molecules due to oxidation when compared to 243.10. According to the fragmentation patterns, $C_{15}H_{14}O_3$ is proposed as the chemical formula of the BP7. At 60 minutes, three different deprotonated molecular ions were observed on the MS spectra at m/z value of 275.09, 231.10, and 138.01 as shown in Figure 5.21. This corresponds to BP1, BP2 and BP5 which had been previously observed with DBD alone.

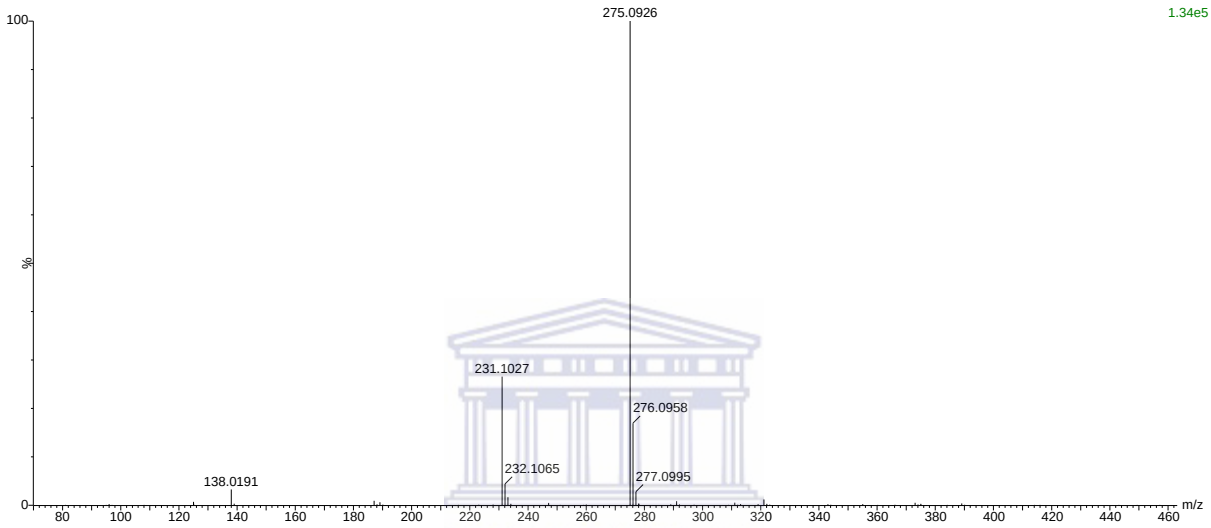

Figure 5.21: LC-MS of the intermediates products formed via DBD/JT14 and DBD/photo-Fenton induced reaction at 40 minutes reaction time

At 80 minutes, three fragmentation patterns at m/z 249.07, 217.06 and 205.08 labelled BP8, BP9 and BP10 were found on the MS spectra and the UV-spectra in Figure 5.22 (a) and (b) respectively.

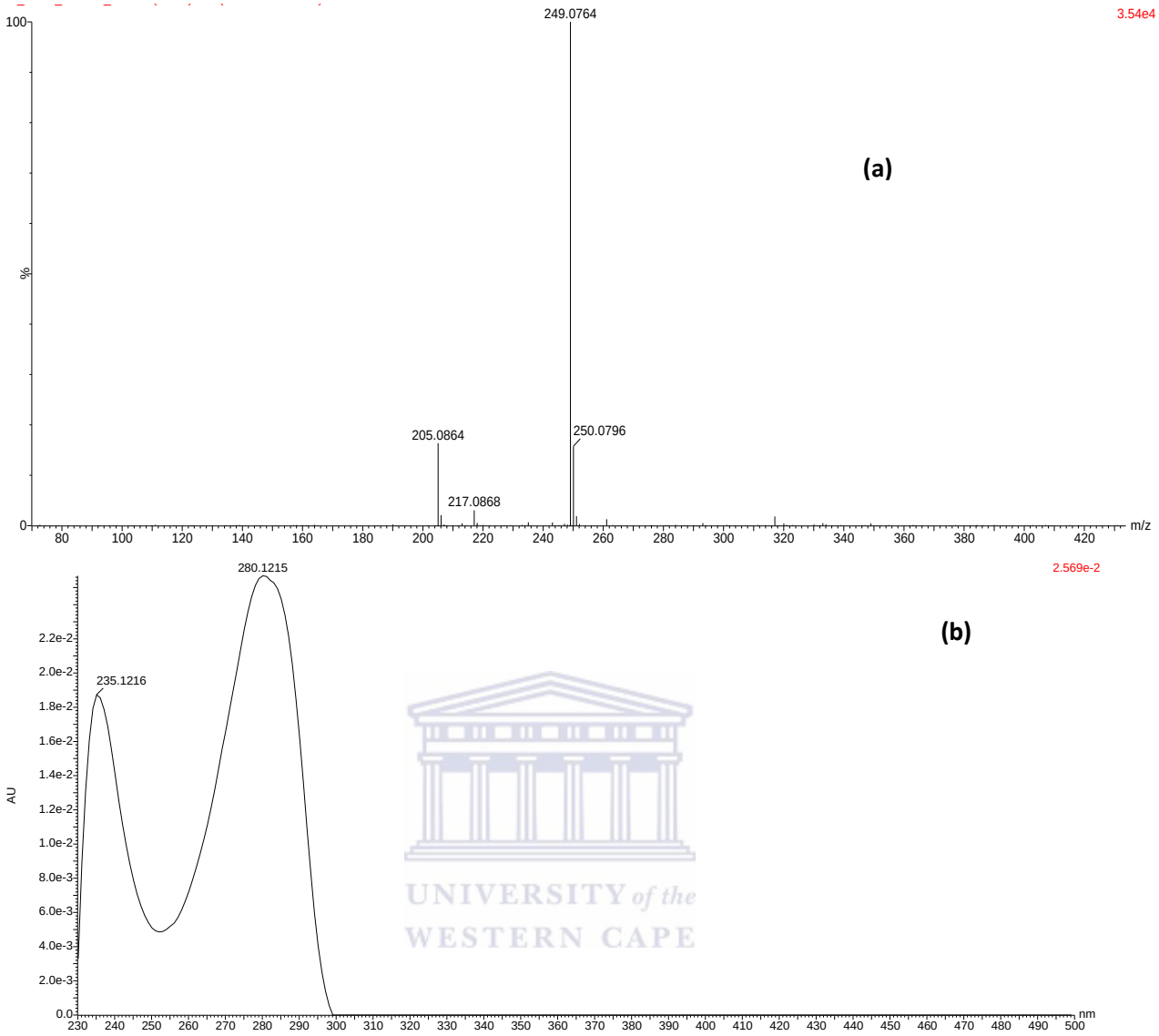

Figure 5.22: (a) LC-MS and (b) LC-UV chromatograph of the intermediates products formed via DBD/supported photocatalyst (JT14) and DBD/photo-Fenton induced reaction (JT17) within 80 minutes reaction time

The fragmentation pattern at m/z 249.07 corresponded to loss of the carbonyl group (CO) by a compound with m/z value of 275.09. While the elimination of carbon dioxide (CO_2) by an intermediate with fragmentation pattern at m/z 249.07 produced compound BP10 with m/z at 205.08. As regards the fragmentation patterns at m/z 217.06, the difference between this fragmentation pattern and 249.07 was 32, which corresponded to loss of oxygen molecules. The following chemical formulas are proposed for BP8 ($C_{13}H_{14}O_5$), BP9 ($C_{13}H_{13}O_3$) and BP10 ($C_{12}H_{14}O_3$). At 120 minutes, with combined DBD/supported photocatalyst (JT14) system, only two mass fragmentation patterns at m/z 165.01 and 121.02 were noticeable as shown in Figure 5.23. While in the case of combined DBD/photo-Fenton induced reaction as

shown in Figure 5.24, three prominent deprotonated molecular ions appeared at m/z 241.89, 196.6 and 146.96. However, the molecular formula of fragment ion at 103.92 could not be identified by the LC-MS instrument probably because it was below detectable limits. The presence of low molecular weight compounds at 120 minutes for the two combined systems suggests the cleavage of the two aromatic rings into a smaller moiety. According to the MS library, the following molecular formula are proposed: 195.9 ($C_9H_{11}NO_4$), 165.01 ($C_9H_{10}O_3$), 146.9 ($C_9H_8O_2$) and 121.02 ($C_6H_5NO_2$).

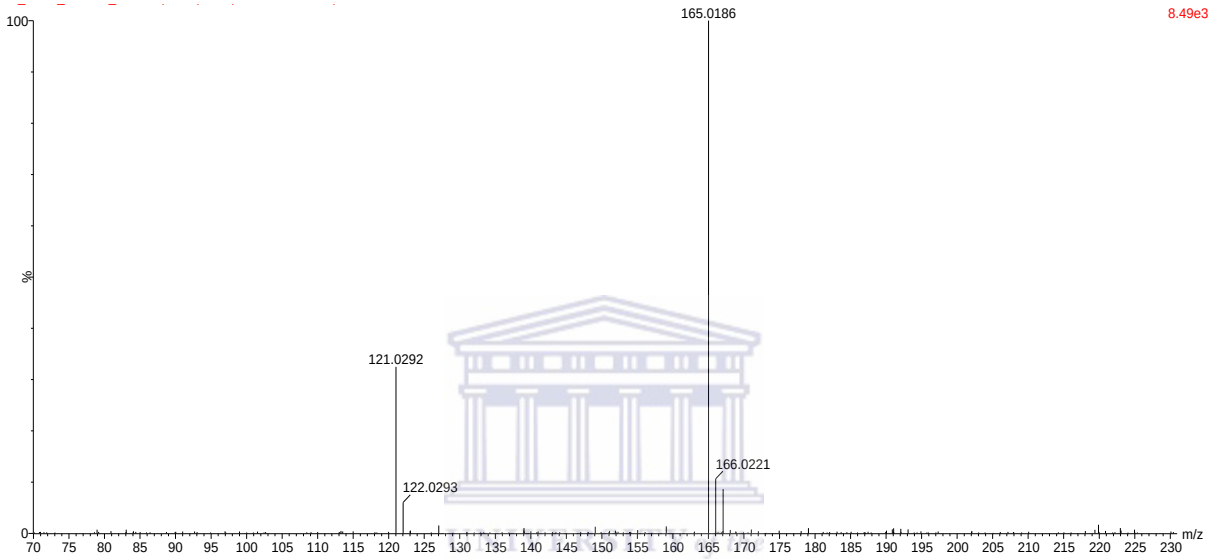

Figure 5.23: LC-MS chromatograph of the intermediates products formed by DBD/supported photocatalysts (JT14) within 120 minutes

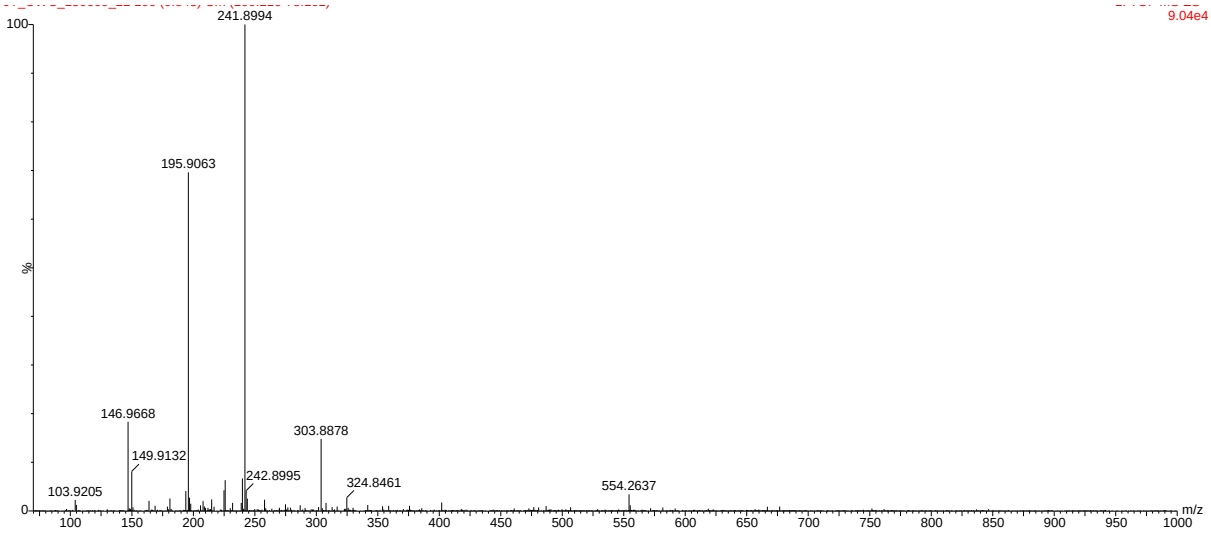

Figure 5.24: LC-MS chromatograph of the intermediates products formed using DBD/photo-Fenton induced process within 120 minutes reaction time

As demonstrated in the time scheme experiment shown in Figure 5.17, it is evident that the transformation products obtained via three degradation systems were different. The differences in the number of intermediates also demonstrated that BPA followed different degradation routes or pathways. It should be noted that a higher number of stable and persistent intermediates were obtained via DBD alone, which suggests a high level of persistency or stability of intermediates and can be ascribed to the low concentration of free reactive species generated in the DBD system (See section 5.8). On the contrary, similar and fewer intermediate compounds were detected in the two combined systems (DBD/supported photocatalyst (JT14) and DBD/photo-Fenton induced process (JT17) except at 120 minutes. The low number of intermediates in the combined systems compared to DBD alone suggested fast reaction kinetics between the BPA and the reactive species. Most of the persistent intermediates in the DBD system were successfully mineralized into a small fragment ions by the two combined integrated system. Also worthy of mentioning is that the same number and type of intermediates were obtained in the two combined systems. The similarities in the intermediates showed that the degradation in the two integrated systems proceeded via a common degradation route despite the differences in the intermediates at 120 min. This suggested that BPA was likely to be attacked by the same free reactive species. This also suggested a higher concentration of the reactive species in the combined systems than in DBD alone, which were responsible for formation of low molecular weight intermediates (see Section 5.8). Thus, the higher BPA mineralization rate by the combined systems indicated the existence of synergetic effects. This observation is supported by findings of Wang et al., (2007) who found that a higher number of phenolic intermediates were generated via pulsed discharge system alone compared to combined pulsed plasma discharge and TiO_2 photocatalyst. Wang and colleagues, (2007) attributed formation of a low number of intermediates in the combined system to a higher concentration of hydroxyl radicals which enhanced the mineralization efficiency. The next section focuses on the detailed degradation pathways or routes via the three degradation systems and also on the identification of the reactive species responsible for BPA degradation.

5.6.3 *Proposed degradation pathways for the obtained oxidation products from BPA degradation via DBD, DBD/JT14 and DBD/photo-Fenton induced reactions*

It is a well-known fact that DBD produces hydroxyl radicals, ozone, and hydrogen peroxide UV light among others, which reacted with BPA according to their oxidation potential values. Based on the obtained intermediates shown in Table 5.6, a route for the degradation of BPA to BP4 was proposed and illustrated in the Figure 5.25.

i. Formation of BP1-BP4

The degradation mechanism of BPA which resulted in the formation of BP1-BP4 within 20 minutes is shown in Figure 5.26. As earlier shown in Figure 5.18, the number of oxygen increased to 5 when compared to the starting compound with two oxygen, which means three oxygens were added, thus suggests that the step I in the oxidation of BPA by DBD was ozonation by an electrophilic substitution reaction. This indicates that BP1 ($C_{15}H_{16}O_5$) was formed by direct electrophilic substitution reaction of ozone with BPA to give an ozonide derivative. The ozonide derivative further undergoes intramolecular rearrangement to yield BP1. Step II involved the loss of CO_2 by BP1 ($C_{15}H_{16}O_5$) to give BP2 ($C_{14}H_{16}O_3$), which otherwise is known as a decarboxylation reaction. The third oxidation by-product (BP3) was obtained directly via a double decarboxylation reaction on BP1 ($C_{15}H_{16}O_5$) (Step III). BP4 was a product of dimerization reaction involving two similar intermediate compounds. Since the m/z was 551.19 ($C_{30}H_{32}O_{10}$), it was possible to conclude that the step IV was addition of two $C_{15}H_{16}O_5$. The proposed mechanism has demonstrated that oxidation of BPA proceeds via ozonation, decarboxylation, double decarboxylation and dimerization reaction to produce recalcitrant intermediate compounds BP1-BP4. The formation of BP1-BP3 via ozonation and photocatalytic process has previously been reported in the literature with exception of BP4 (Colombo et al., 2012: Deborde et al., 2008; Tay et al., 2012).

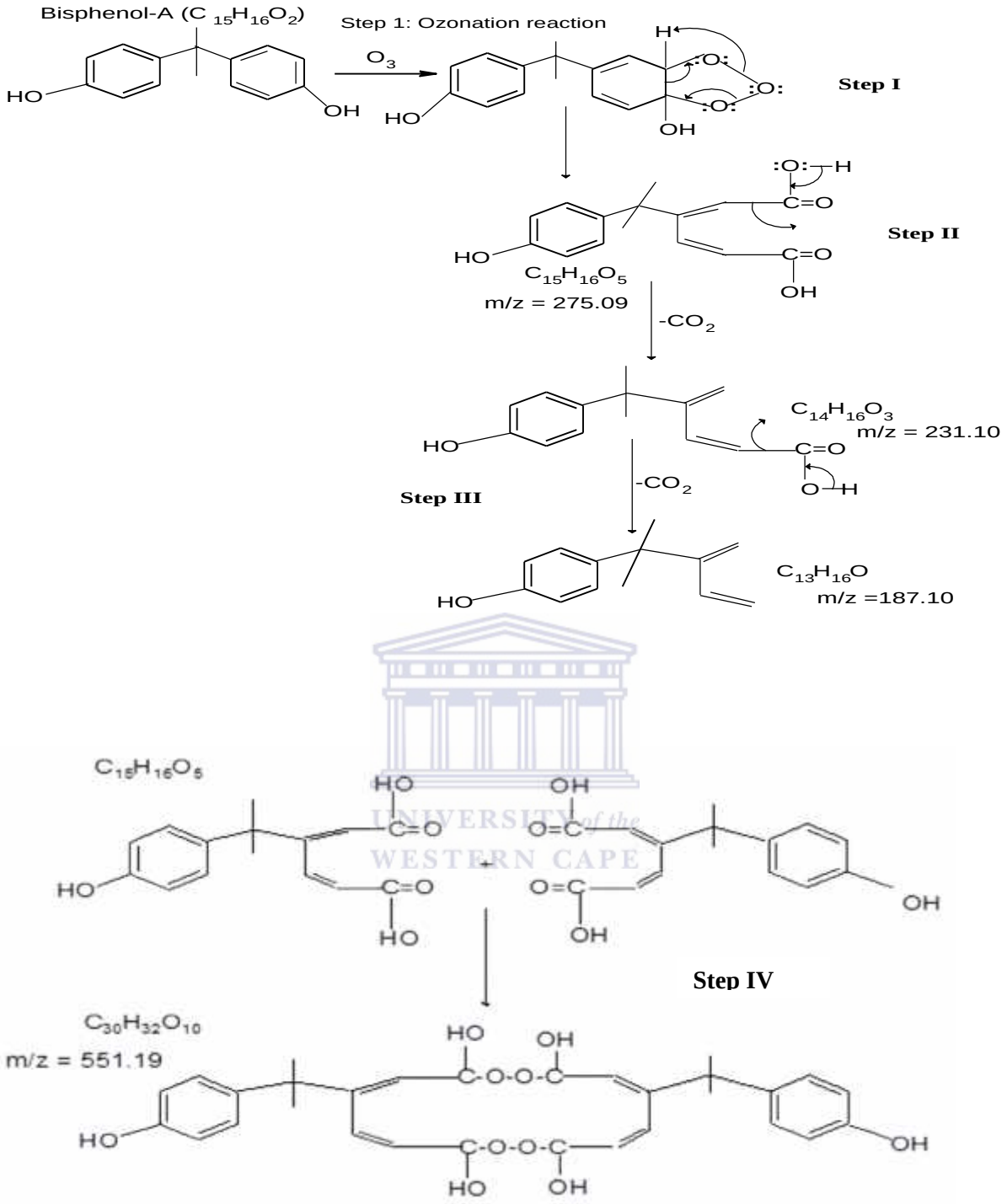

Figure 5.25: Proposed degradation pathways for the formation of BP1 – BP4 from BPA using DBD alone.

ii. Formation of BP5-BP7

Furthermore, the proposed degradation pathways for compounds BP5-BP7 is shown in Figure 5.26. As shown in Figure 5.26, it is obvious that compound BP6 ($C_{15}H_{16}O_3$) was formed via two degradation routes: via a hydroxylation step or direct electrophilic substitution of ozone on the aromatic rings of BPA. This indicated that the two reactive species produced by the

DBD were probably responsible for the formation of BP6. This corroborates previous studies where it was demonstrated that the mechanistic formation of BP6 proceeds through both hydroxylation and ozonation reactions (Tay et al., 2012). In the same vein, Cardoso da Silva et al., (2013) and Colombo et al., (2012) reported similar intermediate compound during the photodegradation and combined $TiO_2/UV/O_3$ treatment of BPA. The two authors established that BPA undergoes a hydroxylation reaction to produce the monohydroxylated compound ($C_{15}H_{16}O_3$). Deborde et al., (2008) also reported a similar molecular formula for BP6 during ozonation process of BPA. The oxidation of BP6 (which is removal of hydrogen) by either hydroxyl radicals or ozone produced BP7 ($C_{15}H_{14}O_3$). The attack by hydroxyl radicals on the methyl group (CH_3) in between the two aromatic rings resulted in hydrogen abstraction and C-C bond cleavage, which later produced the phenolic moiety and other residual intermediate compounds. Subsequently, the attack by the nitrogen oxides (NO_2 or NO) produced by DBD on the phenolic moiety, formed 4-nitrophenol as illustrated in Figure 5.26.

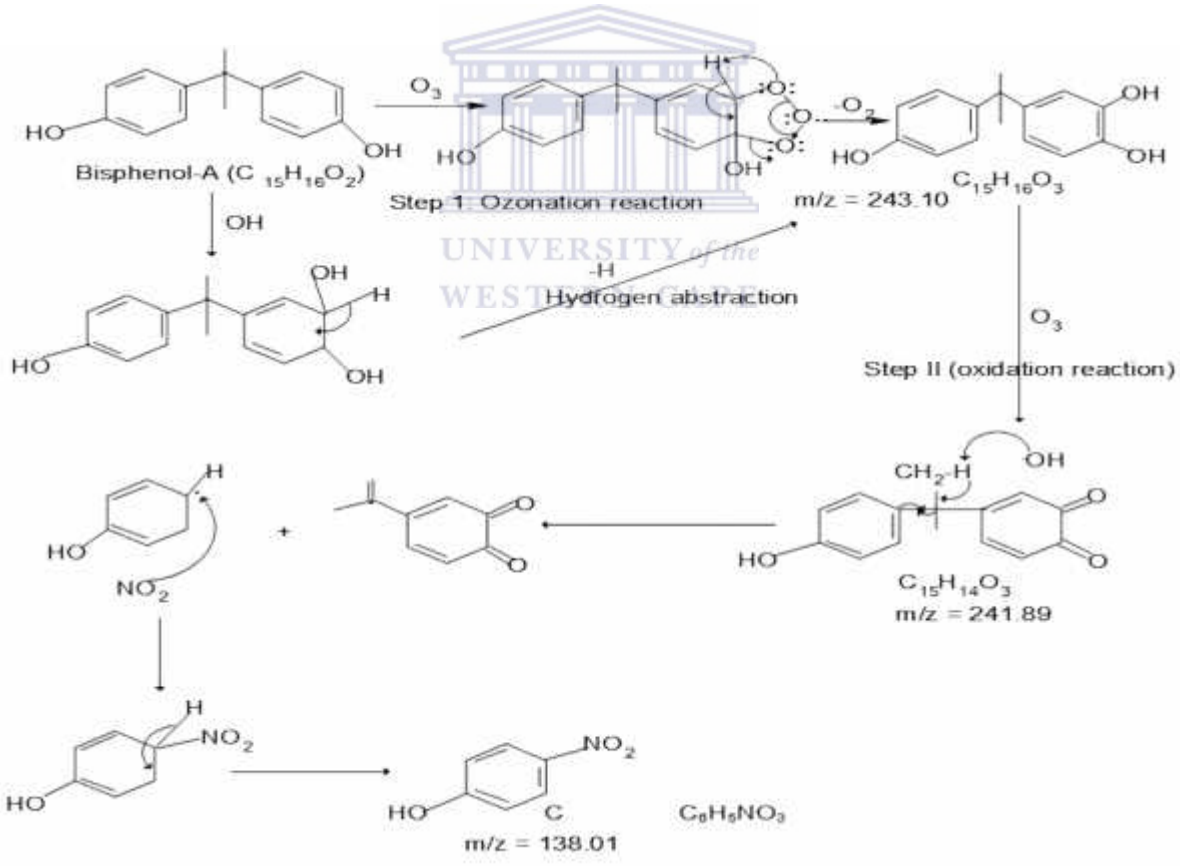

Figure 5.26: Proposed degradation pathways for the formation of BP5 – BP7 from BPA using DBD alone and combined DBD/JT14 or DBD/photo-Fenton induced process.

iii. Formation of BP8-BP10

In addition, the degradation routes of BPA leading to the formation of BP8-BP10 is illustrated in Figure 5.27. The step by step attack of BPA molecules by hydroxyl radicals produced mono, bi and polyhydroxylated BPA. The polyhydroxylated BPA undergoes intramolecular rearrangement leading to C-C bond cleavage, loss of H_2 molecules thus forming BP1 ($C_{15}H_{16}O_5$).

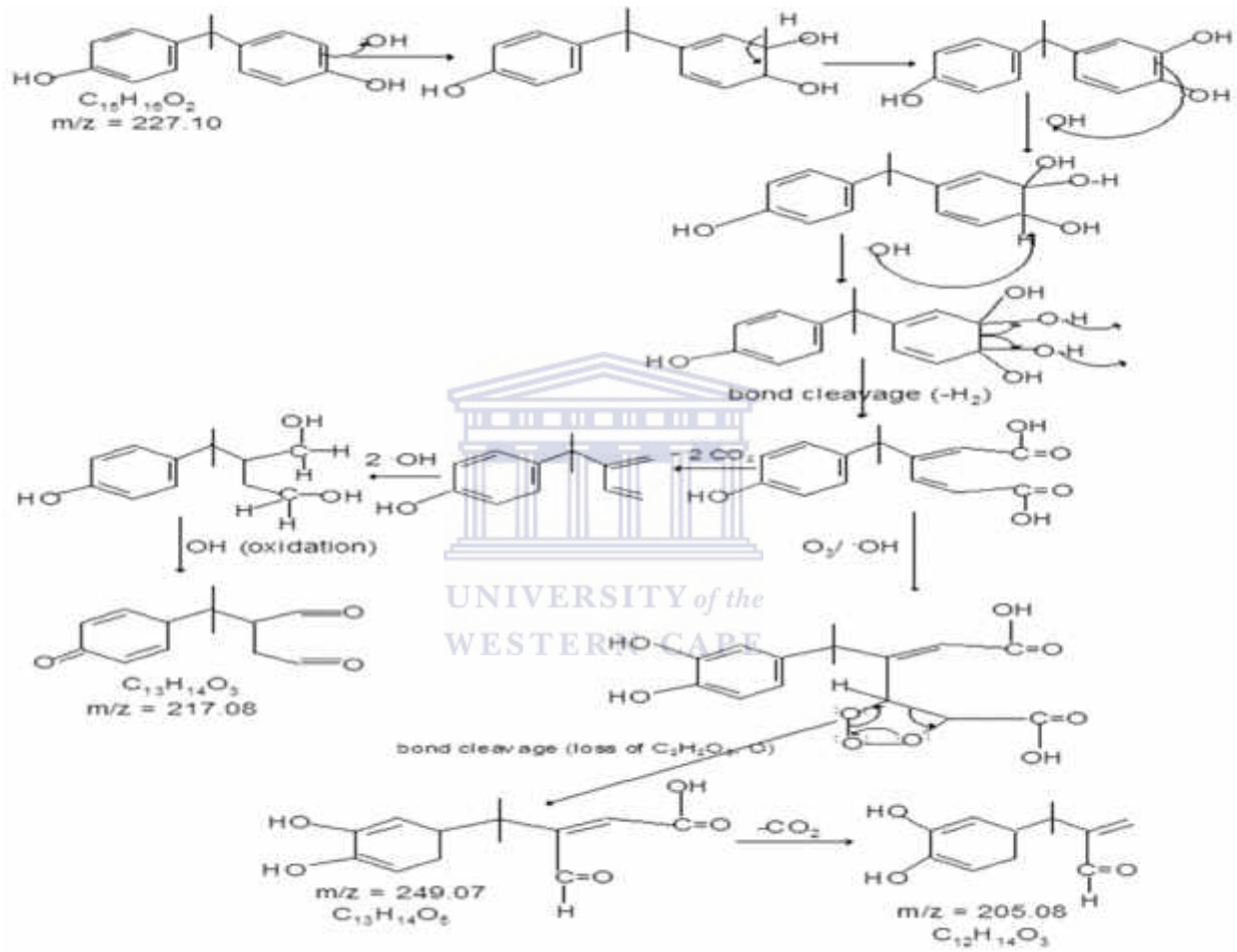

Figure 5.27: Proposed degradation pathways for the formation of BP8 – BP10 from BPA using combined DBD with either supported catalyst or photo-Fenton induced reaction

More so, oxidation of BP1 in the presence of O_3/OH radicals or perhaps H_2O_2 in solution produced BP8 with molecular formula ($C_{13}H_{14}O_5$). This reaction was accompanied with loss of $C_2H_2O_3$ and atomic oxygen (O). Two consecutive CO_2 eliminations from BP1 and further oxidation in the presence of O_3/OH^o yields compound BP9 ($C_{13}H_{14}O_3$). According to Deborde et al., (2008) compound BP9 was categorised as 3-formylacrylic acid derivative.

While BP10 ($C_{12}H_{14}O_3$) was obtained from BP8 via CO_2 elimination as illustrated in Figure 5.27.

iii. Formation of BP11-BP14

The formation of BP11-BP14 starting with BP6 is presented in Figure 5.28.

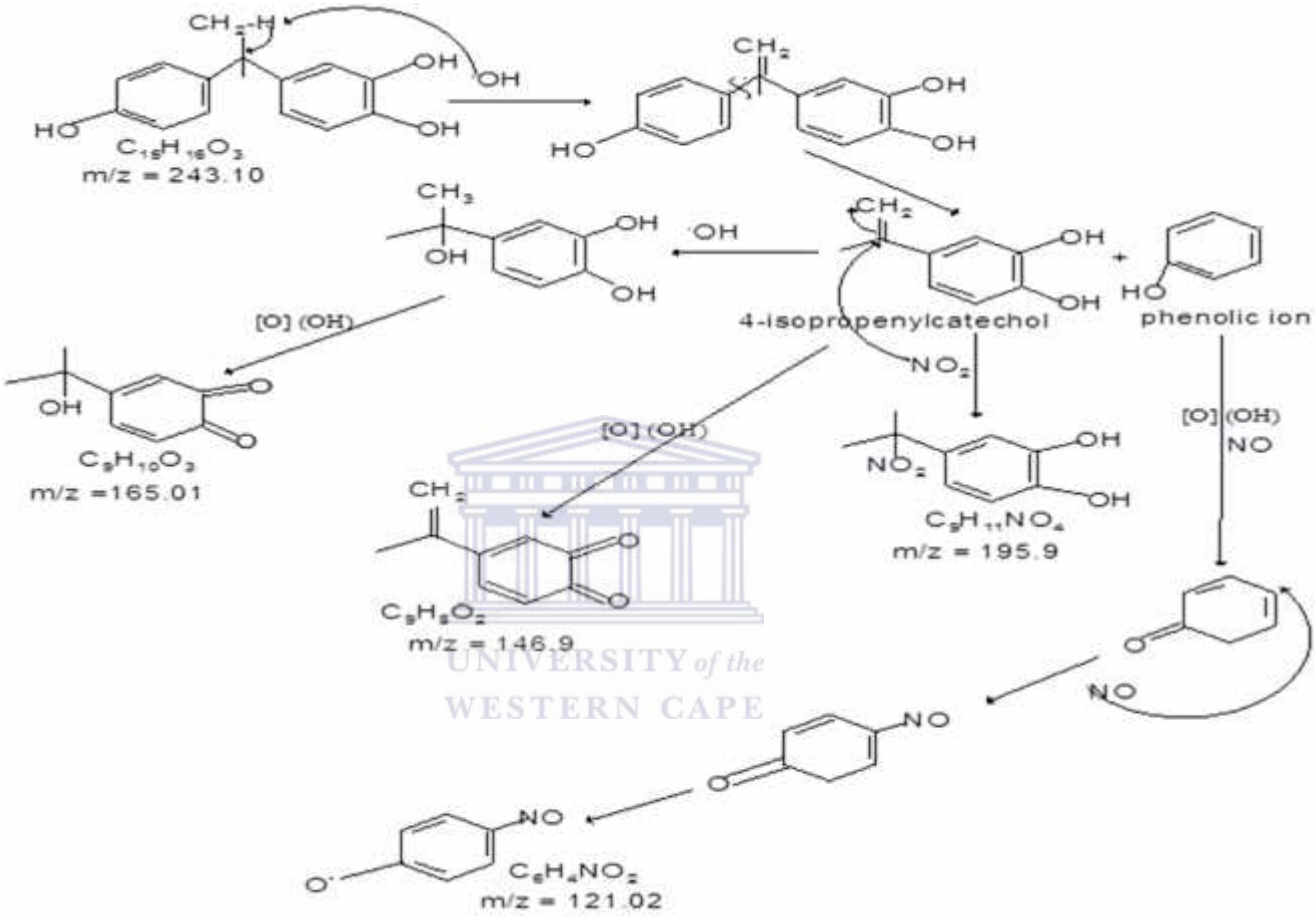

Figure 5.28: Proposed degradation pathways for the formation of BP11 – BP14 from BPA using combined DBD with either supported catalyst or photo-Fenton induced reaction

As shown in Figure 5.28, The initial hydroxylation of BP6 by hydroxyl radicals or direct attack by OH on the methyl group (CH_3) in between the two aromatic rings, resulted in hydrogen abstraction and subsequently ring cleavage leading to formation of smaller fragments (4-isopropenylcatechol and phenolic ion). The substitution on 4-isopropenylcatechol by one of the nitrogenous species (NO_2) yielded compound BP11 with molecular formula ($C_9H_{11}NO_4$). Likewise, the substitution of nitrous oxide (NO) on the phenolic ion liberated compound BP14 with chemical structure $C_6H_4NO_2$ (4-

nitrosophenolate). The presence of nitrogenous oxide as part of the oxidation-products was a result of dry air used to generate ozone in the DBD system as nitrogen is a component of air. Detailed information of NO and NO_2 in the DBD can found in Chapter two section 2.4.1 Also, oxidation of 4-isopropenylcatechol involving loss of hydrogen in the presence of $O_3/OH^o/H_2O_2$ produced compound BP12 ($C_9H_8O_2$). Further hydroxylation of BP12 by hydroxyl on the methylene group (CH_2) formed compound BP13 with molecular formula $C_9H_{10}O_3$.

Fourteen major transformation products including oligomeric compound were identified during BPA oxidation by single and combined advanced oxidation technologies. The following intermediates: BP1-BP4, BP6-BP7 have been extensively reported in the literature (Cardoso da Silva et al., 2014; Colombo et al., 2012; Deborde et al., 2008; Tay et al., 2012). While BP5, BP8, BP9-BP14 have not been reported in the literature. The differences in the intermediates proposed in this study compared to other studies may be attributed to the applied oxidation process and perhaps the types of free reactive species produced by the DBD system. The DBD produced O_3, H_2O_2, OH^o, where air containing nitrogen was used as a source of ozone generation. Studies conducted by Tay et al., (2012) and Deborde et al., (2008) used the ozonation process alone, Colombo et al., (2012) combined $TiO_2/UV/O_3$ while Cardoso da Silva et al., (2014) utilized powder commercial TiO_2 with UV to decompose BPA. It is clear from the previous studies that different advanced oxidation processes produce different free radicals and definitely result in different intermediate compounds. Critical analysis of the intermediates showed that BPA decomposed via ozonation step in the DBD while most intermediates in the combined system were proposed via hydroxylation and nitration steps respectively. In all, the degradation of BPA followed different steps: ozonation, hydroxylation, decarboxylation, and dimerization, double decarboxylation and nitration reaction. It is important to mention that unlike DBD alone (see Figure 5.25), no dimeric or high molecular weight compounds was formed as intermediates in the two combined systems. This is in accordance with the results reported by Wang et al., (2007) where there was no formation of oligomeric compounds during the degradation of phenol by combined pulsed plasma discharge and TiO_2 photocatalyst. Additionally, the most of the intermediates obtained with the combined system were of lower molecular mass compared to high molecular weight intermediates obtained with DBD alone. This further demonstrated that the incorporation of supported photocatalyst or nano zero valent iron with DBD enhanced the mineralization of BPA much more than with DBD alone. Complete

mineralization of BPA into CO_2 and H_2O was not achieved via the three approaches, which may be attributed to the DBD reactor type.

5.6.4 *The obtained intermediates from 2-NP degradation via DBD, DBD/JT14 and DBD/photo-Fenton induced reactions*

In this study, the different intermediates of 2-NP obtained via the three treatment processes (DBD alone, DBD/JT14 or DBD/photo-Fenton induced reactions) were qualitatively analysed by LC-MS TOF Agilent. The detailed experimental procedure and analytical techniques can be found in section 3.2.9.4 and 3.4.13 respectively. The LC-MS and LC-UV spectra of the standard 2-nitrophenol solution recorded in the electrospray ionization (ESI) negative mode, revealed a deprotonated molecular ion $[M-1]^-$, m/z at 138.1087 within 5.7 min (Figure 5.29 (a)). This indicates that the original mass of 2-NP was 139.11 but was measured to be 138.1087, indicating loss of a proton (H). The UV spectra of 2-NP shown in Figure 5.29 (b) revealed a slight, sharp and broad absorption band at 232, 276 and 349 nm respectively.

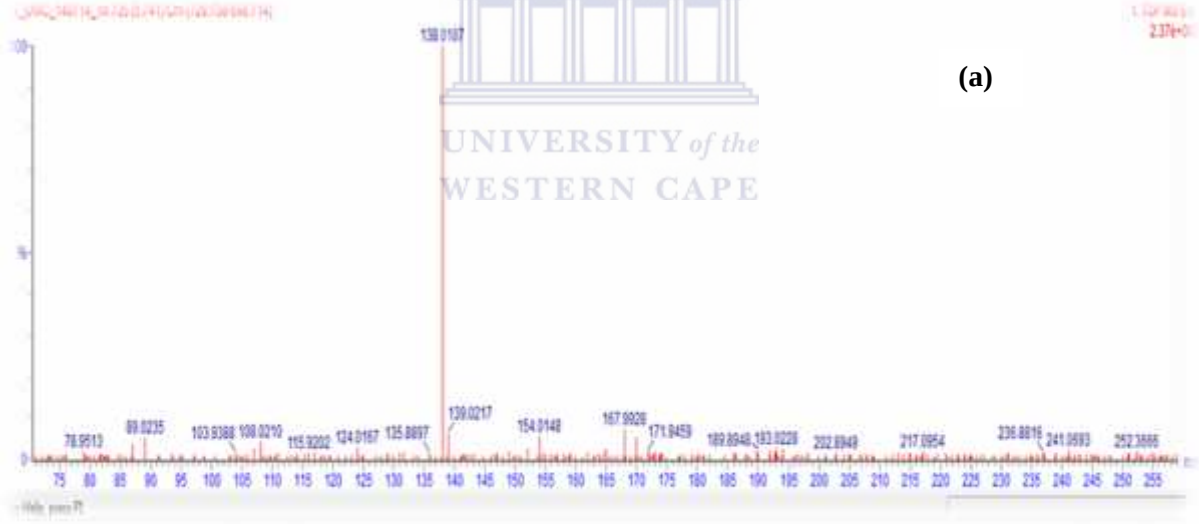

(a)

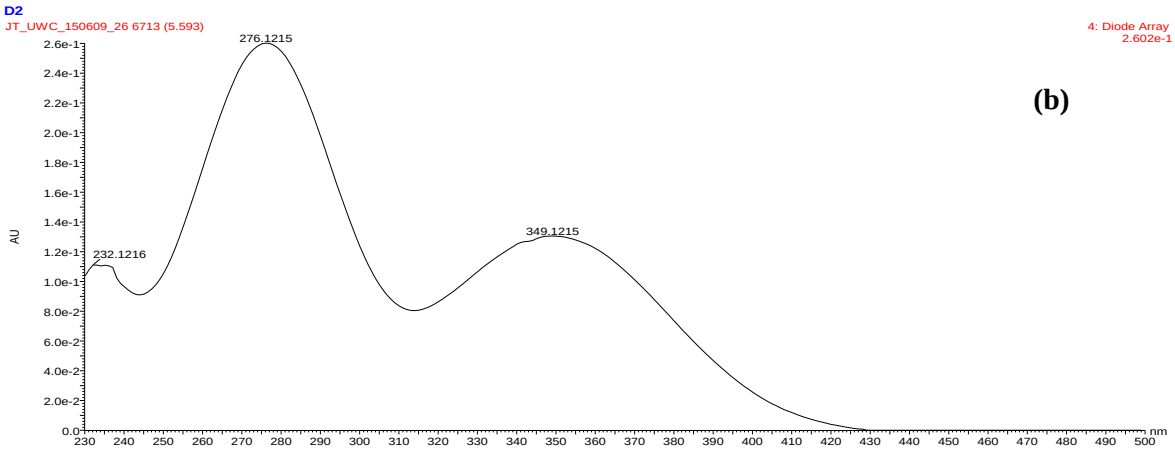

Figure 5.29: (a) LC-MS (b) LC-UV spectra of standard 2-nitrophenol solution prior to degradation experiment

Table 5.7 also contains the mass fragmentation pattern (m/z), relative abundance (%) and proposed chemical structure of the identified organic intermediates. The chemical structure of the identified compounds are proposed and compared with the LC-MS library databases.

Table 5.6: Transformation products of 2-NP via the three treatment methods

Compounds	Molecular formula	Molecular mass (g/mol)	Theoretical mass [M-H]	Observed fragment ion at m/z value (% abundance)	Acquisition or retention time
2-nitrophenol	$C_6H_5NO_3$	139.11	139.08	138.02 (99.89)	5.7
OBP1	$C_6H_5NO_4$	155.10	155.08	154.01 (100.0)	4.4
OBP2	$C_6H_5NO_5$	171.11	171.04	170.00(100.0)	3.4
OBP3	$C_6H_2NO_5$	168.08	168.05	167.99(98.64)	3.2
OBP4	$C_6H_4O_4$	140.1	140.06	140.00(100.0)	2.9
OBP5	$C_6H_4N_2O_5$	184.11	184.07	183.00(99.99)	5.5
OBP6	$C_6H_3NO_4$	153.09	153.07	152.99 (97.50)	4.2
OBP7	$C_6H_6O_2$	110.11	110.09	110.01(96.07)	1.5
OBP8	$C_6H_5O_3$	125.10	125.08	124.01 (97.30)	4.5
OBP9	C_6H_5OH	94.11	94.09	92.05(66.5)	1.0

OBP= Oxidation by-product

As shown in Table 5.7, nine different transformation products mostly nitrogenous compounds were obtained via the three degradation systems namely: OBP1 ($C_6H_5NO_4$, 2-nitroresorcinol),

OBP2 ($C_6H_5NO_5$, 2-nitrobenzene-1,3,5-triol), OBP3 ($C_6H_2NO_5$, 2-nitro-1,3,5-benzenetriolate), OBP4 ($C_6H_4O_4$, 2,5-dihydroxyl-1,4-benzoquinone), OBP5 ($C_6H_4N_2O_5$, 2,4-dinitrophenol), OBP6 ($C_6H_3NO_4$, 2-nitro-1,4-benzoquinone) OBP7 ($C_6H_5O_3$, 3,5-dihydroxylphenolate), OBP8 ($C_6H_6O_2$, hydroquinone), OBP9 (C_6H_5OH, phenol). The retention time of all the by-products shown in Table 5.6 were less than that of 2-NP, which suggests that most of the intermediates were more polar than the 2-NP. The time based scheme of the intermediates generated by DBD, DBD/supported photocatalyst (JT14) and DBD/photo-Fenton induced process is presented in Figure 5.30.

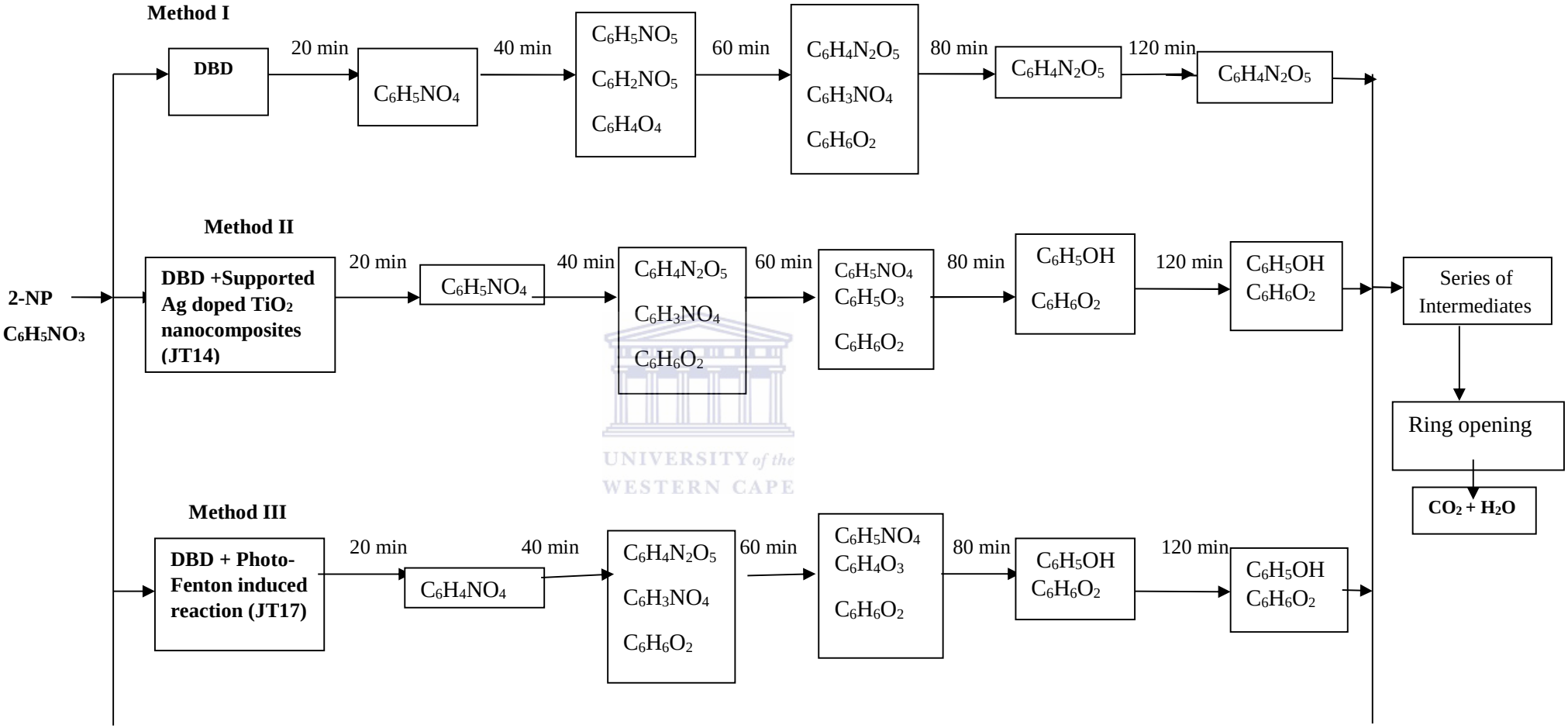

Figure 5.30: Time based identification of 2-NP intermediates via DBD alone, DBD/supported photocatalyst and DBD/photo-Fenton induced reaction

As shown in Figure 5.30, it is evident that the intermediate compounds formed either via the DBD or the two combined systems were similar except at 80 minutes. During the oxidation experiments, some of the intermediates disappeared completely while some remained stable and resistant to further degradation. It is also noteworthy mentioning that, $C_6H_4O_3$ and C_6H_5OH were not detected in the DBD alone but were identified with the two combined systems. Additionally, there was a high level of resemblance in the intermediates generated by the two combined systems, which suggest that 2-NP was attacked by the same free reactive species. Hydroquinone ($C_6H_6O_2$) remained the most persistent among all the intermediates irrespective of the treatment process. This is consistent with the findings of Zhang et al., (2003) who had earlier recognised hydroquinone as one of the most predominant and stable intermediates during the oxidation of p-nitrophenol by UV/H_2O_2. It is important to mention that hydroquinone is unstable and readily oxidised to benzoquinone by the hydroxyl radical. Although, benzoquinone was not detected in this study nevertheless hydroquinone undergoes complete oxidation to form OBP8.

According to the time based scheme shown in Figure 5.30, similar intermediate compounds were formed via all the three applied processes at 20 minutes. This indicates the possibility of 2-NP being attacked by the same free reactive species. As a matter of fact, 2-NP disappeared completely within 20 minutes and transformed into a compound with a fragment ion at m/z 154.01 shown in Figure 5.31 (a). No other peaks were detected by mass spectrometry. Very importantly, the mass difference between 154.01 and 138.01 was 16, which showed that the decomposition of 2-NP was initiated by OH radicals. Thus, the first step during the oxidation process of 2-NP either by the DBD or the combined system was hydroxylation (OH radicals) and not both hydroxylation and ozonation observed with BPA. This observation corroborated previous investigations where researchers have demonstrated hydroxylation reaction as the first step during the degradation process of nitrophenols via advanced oxidation technologies (Quiroz et al., 2014; Wei et al., 2011). Based on the available MS library, the chemical structure of the compound is proposed to be 2-nitroresorcinol ($C_6H_5NO_4$,), which agreed with the UV-spectrum shown in Figure 5.31 (b).

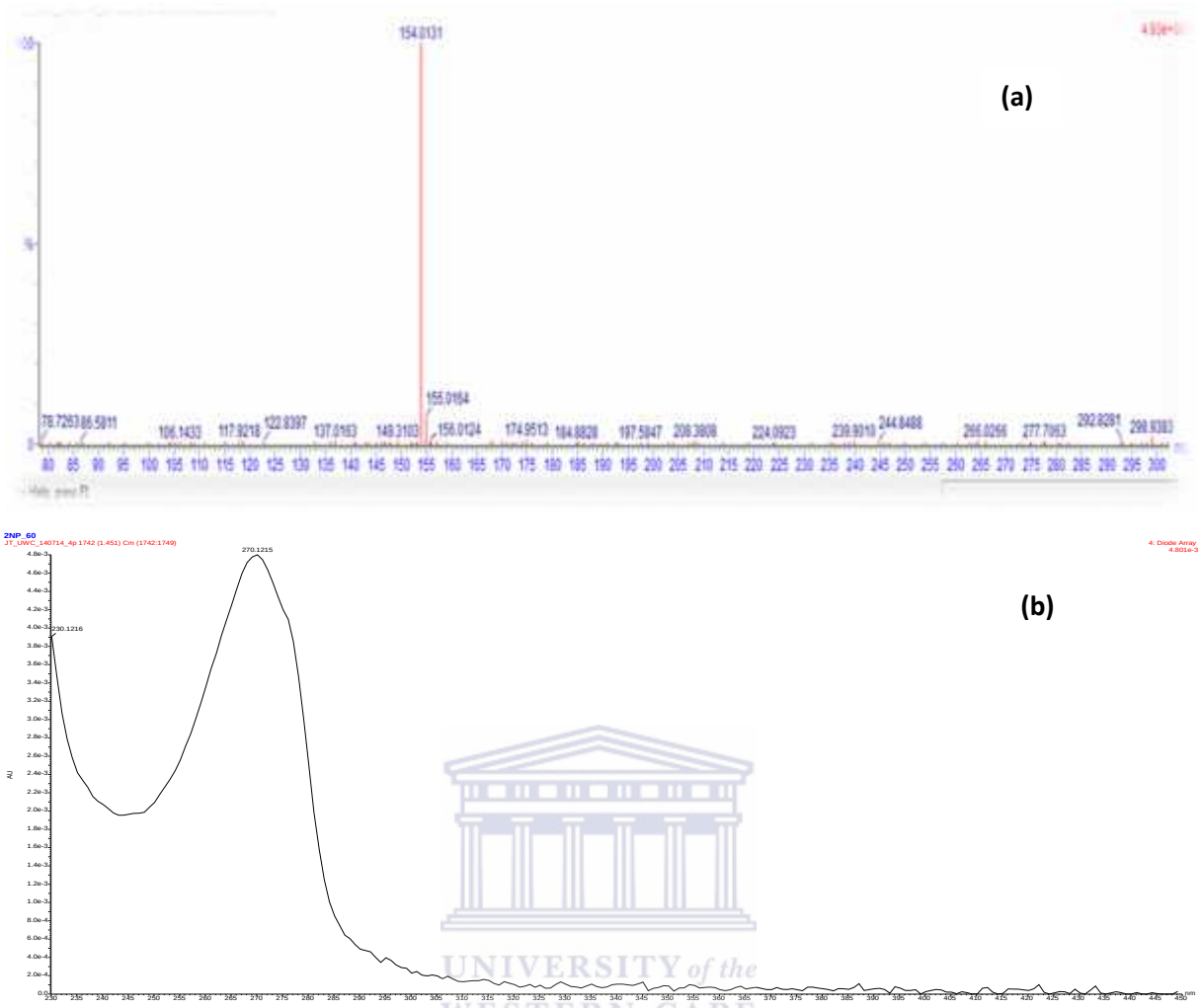

Figure 5.31: (a) LC-MS and (b) LC-UV chromatograph of the intermediates products formed via DBD, DBD/supported photocatalyst and DBD/photo-Fenton induced reaction within 20 minutes reaction time

i. Formation of 2-nitrobenzene-1,3,5-triol ($C_6H_5NO_5$), 2-nitro-1,3,5-benzenetriolate ($C_6H_2NO_5$) and 2,5-dihydroxyl-1,4-benzoquinone ($C_6H_4O_4$)

Figures 5.32 (a) and (b) represent the LC-MS and LC-UV chromatograph of the intermediates obtained via DBD alone after 40 minutes. There was a disappearance of the peak observed at 20 minutes and formation of four additional new peaks with the following mass fragment ions at m/z (170.00, 167.99, 151.99 and 140.00). The deprotonated molecular ion at 170.00 corresponded to addition of OH radical to the earlier identified OBP1 having m/z (154.01). This implies a repetitive attacked of the hydroxyl radical on OBP1. The chemical formula $C_6H_5NO_5$ is proposed for OBP2 based on the MS library. Further oxidation of OBP2 vis-a-viz removal of hydrogen certainly resulted in a compound with fragmentation

pattern at m/z 167.99. The chemical structure of OBP3 is proposed to be ($C_6H_2NO_5$, 2-nitro-1,3,5-benzenetriolate).

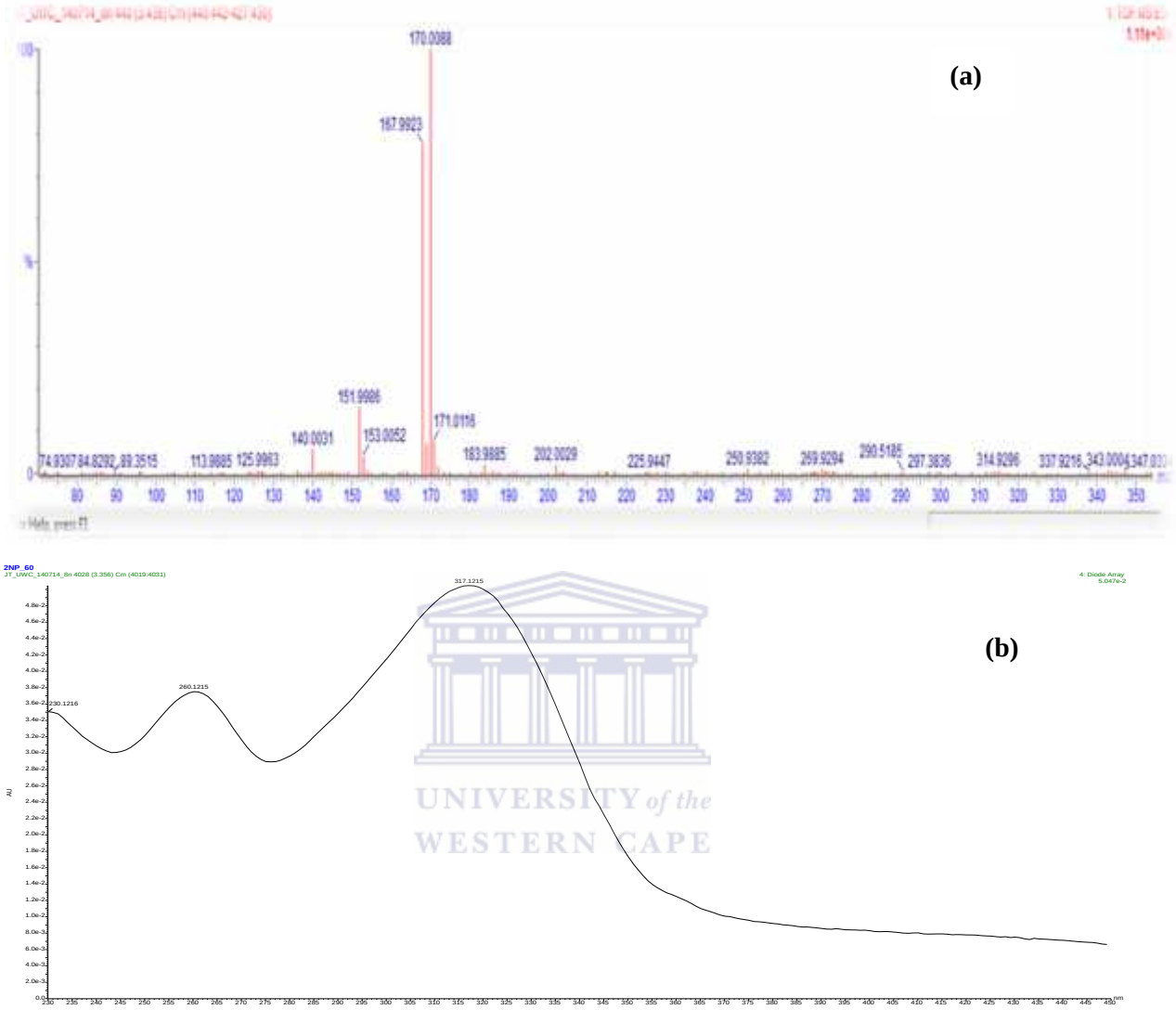

Figure 5.32: (a) LC-MS and (b) LC-UV chromatograph of the intermediates products formed via DBD after 40 minutes reaction time

The fragmentation spectrum at m/z 140.00 corresponded to elimination of an electron withdrawing group (NO_2) from OBP2 by direct attack by the highly electrophilic OHº. This was followed by the electrophilic substitution or replacement of a NO_2 group by the OHº, which showed NO_2 as a good leaving group. The chemistry of the formation of OBP4 basically involved the attacked of OH at the ortho position of the benzene ring. It is important to mention that the electrophilic OH radical with high redox potential attacked a carbon atom with the highest electron density within the benzene ring forcing the NO_2 to leave. The presence of both OH and NO_2 groups in 2-NP created a strong electron density on the carbon

atom in the para- and ortho- position relative to the OH group. OH group as an electron-donating substituent is known to be an *ortho* (o) and *para* (p) director while NO_2 (electron-withdrawing group) is equally referred to as *meta* (m) director. Therefore, the OH radical increases the electron density at these two positions in the benzene rings, and because of the ortho/para directory effect, the subsequent attack can occur at either (o) or (p) position, forcing the NO_2 at (o) position to leave and be substituted by the OH^o. Further oxidation (removal of hydrogen) of two phenolic groups attached to the (o) and (p) positions yield the intermediate OBP4. The phenomenon of denitration and hydroxylation are widely reported and considered to be the dominant degradation pathways for 2-NP (Wei et al., 2011). Based on the available MS library, the chemical formula of OBP4 is proposed to $C_6H_4O_4$. However, the chemical structure of the fragment ion at m/z 151.99 could not be established at 40 minutes, probably due to low concentration but however it manifested at 60 minutes. At 60 minutes, some of the intermediates observed at 40 minutes had disappeared and new ones with MS and UV pattern at m/z (183.01, 152.99 and 112.99) were noticed as shown in Figure 5.33 (a) and (b).

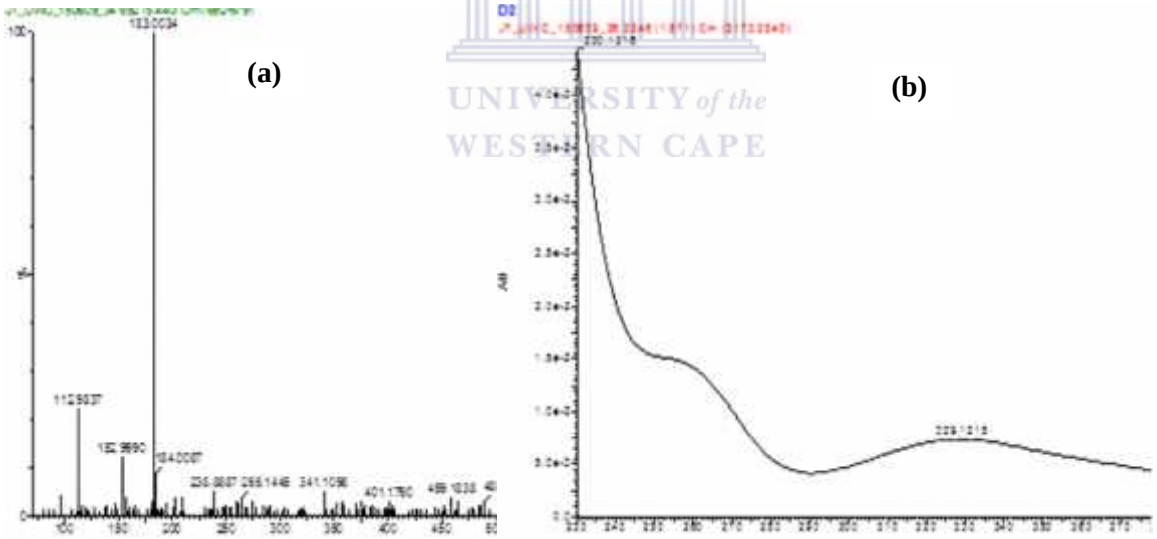

Figure 5.33: (a) LC-MS and (b) LC-UV chromatograph of the intermediates products formed via DBD after 60 minutes reaction time

The mass difference between fragmentation patterns observed at m/z of 183.00 and 138 was 45, which corresponded to the addition of a nitro group (NO_2) at the ortho position. Based on the available MS library, a chemical structure ($C_6H_4N_2O_5$, 2,4-dinitrophenol) is proposed for OBP5. Oxidation of the two phenolic groups in OBP1 ($C_6H_5NO_4$) (removal of hydrogen) in

the presence of $OH^o/O_3/H_2O_2$ resulted in OBP6 with a molecular formula of $C_6H_3NO_4$. The de-nitration or removal of the nitro group from OBP1 produced OBP7 with chemical formula $C_6H_6O_2$ (hydroquinone). More so, at 80 and 120 minutes, only OBP5 was identified, which indicates that the compound was stable and resistant to further oxidation (Figure 5.34).

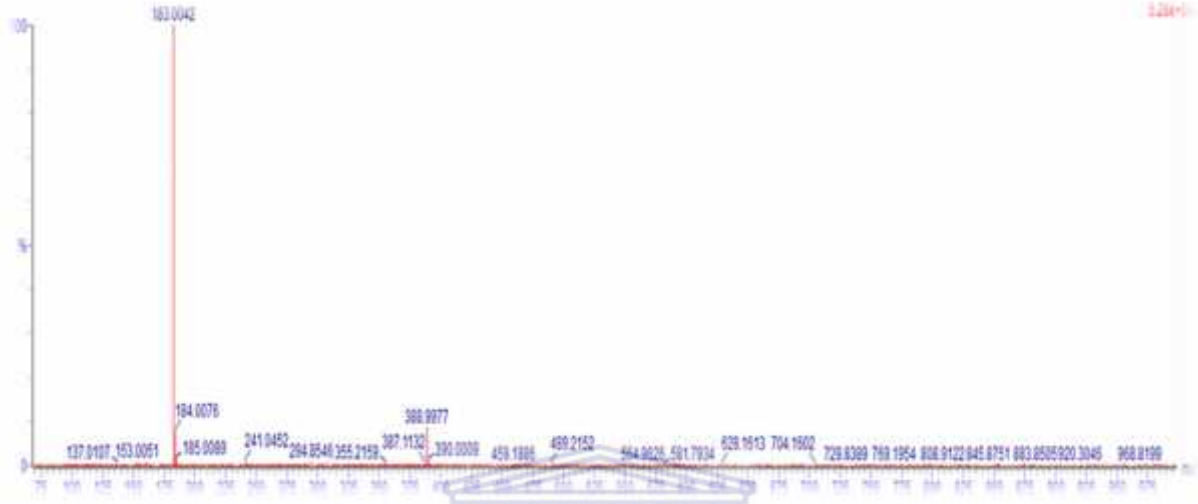

Figure 5.34: LC-MS of the intermediates products formed via DBD after 80 minutes reaction time

ii. Formation of hydroquinone ($C_6H_6O_2$) and phenol (C_6H_5OH).

Critical analyses of the three treatments' performance based on the obtained intermediates enumerated in Figure 5.30 indicated that 2-NP was better decomposed via the two combined system than DBD alone. This may be due to the higher concentration of reactive species in the combined systems. The only difference was the formation of intermediates OBP8 and OBP9 at 60 and 80 minutes respectively in the two combined systems. While OBP8 was formed at 60 minutes, a small fragment of OBP9 was detected at 80 minutes and persisted in solution till 120 minutes. The molar mass of the two compounds were lower in the combined system than the original compound (2-NP) unlike with DBD alone, thus suggested addition of the catalyst enhanced the free reactive species in solution and was perhaps responsible for the appearance of peaks with lower m/z value. Also, the final oxidation product obtained via DBD alone was hardly oxidized further after 80 minutes but oxidized into a lower fragment ion with the addition of catalysts. The LC-MS spectrum of the two intermediates are shown in Figure 5.35 (a) and (b).

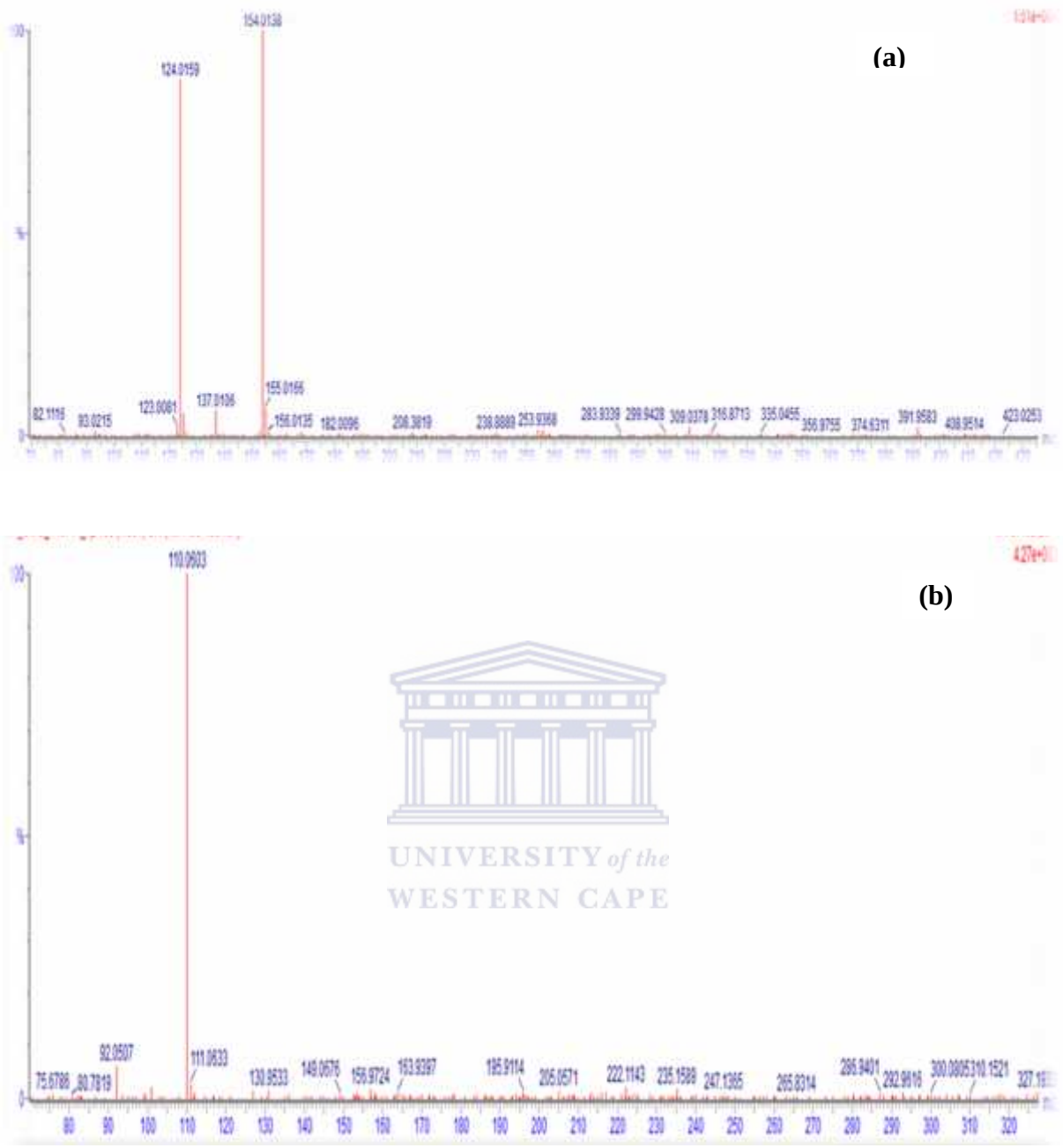

Figure 5.35: LC-MS chromatograph of (a) OBP8 (b) OBP9 formed via combined DBD/photocatalyst or DBD/photo-Fenton induced process at 60 and 120 minutes

As illustrated in Figure 5.35 (a), two fragmentation peaks at m/z 154.01 and 124.01 were observed. The fragmentation pattern at m/z 154.01 was assigned to OBP1, which was explained earlier (see Figure 5.31). The elimination of NO_2 at the ortho position from OBP1 and substitution by the OH group and further oxidation of the two phenolic OH groups at the ortho and para position formed compound OBP8. The denitration of 2-NP without further substitution and oxidation of the OH group produced a small phenolic fragment shown in Figure 5.35 (b) and labelled as OBP9. The chemical structure of OBP8 and OBP9 is proposed

to be $C_6H_4O_3$ and C_6H_5OH with the aid of MS library. Detailed degradation mechanisms are provided in the next section.

5.6.5 *Proposed degradation pathways or routes for 2-NP via DBD alone, DBD/JT14 and DBD/photo-Fenton induced process*

As mentioned in Chapter Two section 2.4.1, the DBD system produces different reactive species namely OHº, O_3, H_2O_2, O, NO_2, NO and OOH, which are directly or indirectly responsible for the degradation of organic pollutants. In this study, the degradation pathways for 2-NP were proposed based on the obtained intermediates and it was possible to identify which of the reactive species were responsible. Therefore, the degradation mechanism of each intermediate is shown in Figure 5.36.

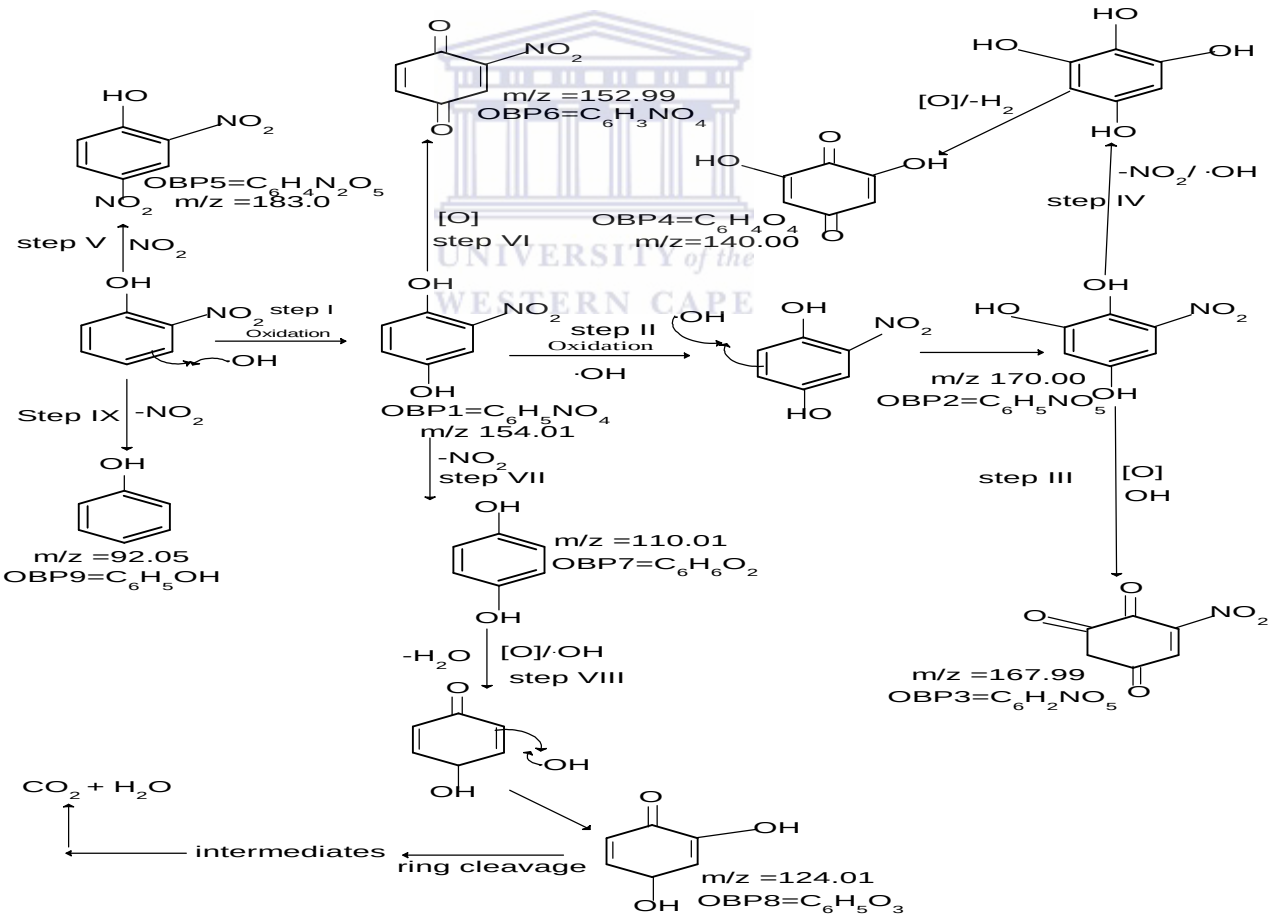

Figure 5.36: Proposed routes for 2-NP degradation by DBD, DBD/supported photocatalysts (JT14) and DBD/photo-Fenton-induced reaction (JT17).

Three major pathways or routes were identified during the oxidation of 2-NPs namely hydroxylation, nitration and denitration. As demonstrated in Figure 5.36, step I, II, III, IV, VI and VIII, which led to the formation of the intermediates OBP1-OBP4, OBP6, OBP8, corresponded to the hydroxylation reaction. While Step VII and IX which produced OBP7 and OBP9 proceed with the loss of a nitro group, often called the denitration step. Step V represents the nitration step. Notably, the intermediate compounds obtained via step VII, VIII and IX ARE similar to those reported by Cañizares et al., (2004) who identified benzene derivatives such as phenol and hydroquinone as organic oxidation by-products during oxidation of nitrophenols via electrochemical methods. Furthermore, the oxidation of OBP9 would lead to ring cleavage and formation of carbonyl compounds and carboxylic acid, which in turn would mineralised into CO_2 and H_2O. However, carboxylic acids such as acetic acid, malonic acid, oxalic acid, and glyoxylic acid which have been previously reported (Ammar et al., 2007; Kavitha and Palanivelu, 2005) as part of 2-NP degradation oxidation by-products were not detected in this study. Irrespective of the nature of the intermediate compounds, the degradation mechanism of 2-NP via the three treatments followed hydroxylation, nitration and denitration step. Based on the proposed mechanism and the identified intermediates, the hydroxyl radical remained the most prominent oxidant responsible for the mineralization of 2-NPs compared to BPA where both OH^{o} and O_3 played a crucial role. It is imperative to mention that despite the incorporation of different catalyst, complete conversion of the BPA or 2-NP to CO_2 and H_2O was not achieved. This may be attributed to a stronger competition between the various intermediate compounds and original BPA or 2-NP molecules for the free reactive species. Another possible explanation has to do with the nature of the intermediates, as shown in Figure 5.17 and 5.30, some of these compounds were persistent and resistant to further oxidation and undergoes recombination reaction forming oligomeric compound in the case of BPA. The intermediates compounds were somehow similar despite different treatment process, suggesting that 2-NP was decomposed by the same reactive species possibly by hydroxyl radicals. Similar observations were reported by Ammar et al., (2007) during the oxidative degradation of 2-NP via electro-Fenton process. Kavitha and Palanivelu, (2005) applied the Fenton and the photo-Fenton process to mineralize 2-nitrophenol in water. The authors identified nitrodihydroxylbenzene and nitro-p-benzoquinone as intermediates compounds. Wei et al., (2011) reported tetrahydroxylbenzene as one of the intermediates formed during the electrochemical oxidation of p-nitrophenol.

5.7 Mineralization of BPA or 2-NP

In order to compare the effectiveness of DBD alone, with DBD/supported photocatalyst (JT14) or DBD/photo-Fenton induced process (JT17) for the degradation BPA or 2-NP, the mineralization rate was measured in terms of Total organic carbon (TOC). The detailed experimental protocol has been described in section 3.2.9.3. The TOC removal efficiency was evaluated using equation 5.12

$$TOC\ removal(\%) = \frac{To - It}{To} \times 100 \quad \text{.....(5.12)}$$

The results of TOC removal of BPA or 2-NP by DBD/supported photocatalysts (JT7 and JT14) is presented in Figure 5.37

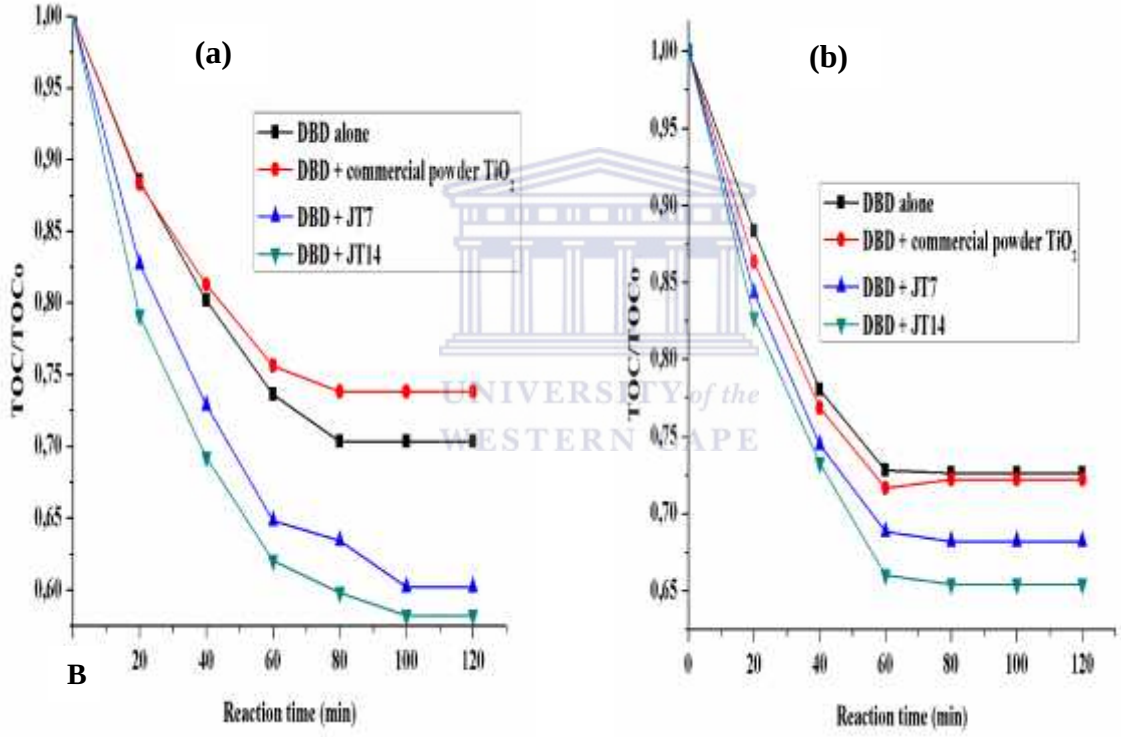

Figure 5.37: Mineralization of (a) BPA (b) 2-NP by DBD and DBD/supported photocatalyst: solution pH 3, discharge voltage 8 kV, concentration of BPA or 2-NP 10 ppm, powder TiO_2 dosage 0.8 g, supported catalyst dosage 0.8 g, solution volume 1.5 L

According to Figure 5.37, it can be seen that the TOC removal for BPA was only 29.7 % after 80 minutes treatment time with DBD alone which however increased to 39.8 % or 41.8 % when DBD was integrated with either supported carbon doped TiO_2 nanocrystals (JT7) or 2.4 % Ag loaded carbon doped TiO_2 nanocomposites (JT14) under the same conditions. Also, in Figure 5.37, the TOC removal rate of 2-NP by DBD alone was 27.4 % at 80 minutes, and

increased to 32.2 % and 35.4 % in the presence of supported carbon doped TiO_2 nanocrystals (JT7) or 2.4 % Ag loaded carbon doped TiO_2 nanocomposites (JT14) respectively. The TOC value of the solution reduced with increasing treatment time in the presence or absence of a catalyst. The decrease in TOC value demonstrated partial decomposition and elimination of some organic compounds from the pollutants as evident in the degradation routes shown in Figure 5.17 and 5.30 respectively. It was difficult to compare the TOC values obtained in this study with the literature due to differences in the applied experimental conditions such as pollutant initial concentration, applied discharge voltage, volume of the aqueous solution, concentration of the free reactive species, solution characteristics amongst others, since most of these parameters obviously influence the pollutant mineralization rate. Nevertheless, the obtained TOC value in this study is higher than 23 % TOC removal rate of sulfadiazine by wetted-wall corona discharge reported by Rong and Sun, (2013). The difference in the reported TOC value may be linked to the type of the reactive species. The DBD used in this study produced OH^{o}, O_3 and H_2O_2 while corona discharge reactor used by Rong and co-worker, (2013) produced OH^{o} alone. The differences in the TOC value may be based on the number of free reactive species generated by each system. Furthermore, the 29.4 % or 27.4 % TOC removal rate of BPA or 2-NP by DBD alone reported in this study is lower than 48 % TOC removal percentage of crystal violet by dielectric barrier discharge reactor reported by Manoj Kumar Reddy and Subrahmanyan, (2012). The difference in the obtained TOC value may be attributed to the concentration of the pollutants used, discharge voltage, air flow rate. In fact, the discharge voltage and air flow rate of the DBD used by Manoj Kumar Reddy and colleague was 18 kV and 200 mL/min compared to 8 kV and 3 mL/min used in this study. Studies have shown that discharge voltage and air flow rate determine the yield of free radicals, which in turn determine the mineralization rate. Thus, higher mineralization reported by Manoj Kumar Reddy and co-worker, (2012) may be linked to the impact of the aforementioned parameters. However, for the combined DBD/supported TiO_2 nanocrystals (JT7) or DBD/supported 2.4 % Ag doped TiO_2 nanocomposites (JT14), the TOC removal rate was 31.8 % and 34.6 % respectively. The reason for the increase of TOC removal rate by supported Ag doped titania nanocomposites over the undoped supported titania nanocrystals is similar as what was discussed in section 5.3. Surprisingly, there was no significance difference between the TOC value obtained with DBD alone and that of combined DBD with commercial powder TiO_2. In fact, the TOC value with DBD alone was slightly higher than the latter. This was because the powdered TiO_2 particles inhibited or hindered UV-light

penetration intensity produced by the DBD, thus reduced the amount of free radicals in solution and hence affected the pollutants mineralization rate. The TOC value gives a quantitative measure of the remaining organics whereas LC-UV and LC-MS are both qualitative methods. The TOC proves that despite intermediates forming there was actually a quantitative overall reduction in the loads of pollutants in the water. Furthermore, the change in TOC value of BPA or 2-NP as a function of treatment time upon the addition of different dosage of nZVI is illustrated in Figure 5.38

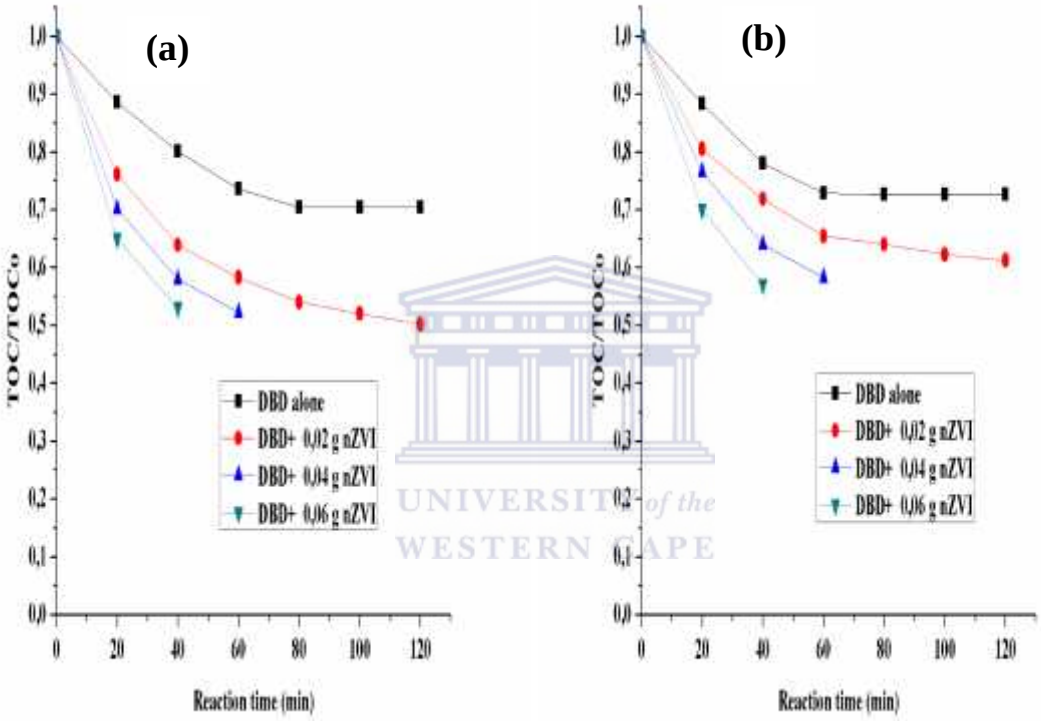

Figure 5.38: Mineralization of (a) BPA (b) 2-NP by DBD and DBD/photo-Fenton induced process: solution pH 3, discharge voltage 8 kV, concentration of BPA or 2-NP 10 ppm, solution volume 1.5 L

As shown in Figure 5.38 (a), the TOC removal rate of BPA increased with an increasing dosage of nZVI. For the DBD containing 0.02, 0.04 and 0.06 g nZVI, the TOC removal rate of BPA were 37.2 %, 41.9 % and 47.5 % as compared to 20% by the DBD alone after 40 minutes. In the same vein, under the same experiment conditions as BPA, 28.8 %, 36.8 % and 43.1 % TOC removal rate of 2-NP relative to 19.3 % removal rate by DBD alone were observed. The TOC removal rate increased with increasing dosage of nZVI for both compounds. The argument put forward for such increment upon the addition of nZVI has

been discussed in Section 5.3. The TOC removal rate of BPA and 2-NP upon addition of 0.06 g nZVI were 47.5 % and 43.1 % respectively at 40 min. This demonstrated a slower mineralization rate when compared to 100 % removal rate of BPA or 2-NP achieved within 40 minutes using DBD with 0.06 g nZVI (see Figure 5.12 and 5.13). The possible explanation for the slower mineralization rate may be due to formation of persistent and stable intermediates which resisted further degradation. Nevertheless, the combined system significantly increased TOC removal rate compared to the DBD alone, as was also evident in the number of intermediates generated via each treatment process. The lower TOC removal rate by the DBD correlated well with the number of intermediate compounds generated. The higher TOC value of the combined DBD with different dosages of nZVI may due to the existence of synergistic effects between the combined systems. It is also important to mention that the TOC removal rate of BPA is higher than that of 2-NP. The lower TOC removal rate of 2-NP suggested the formation or presence of more persistent and stable intermediates in 2-NP compared to BPA as obtained in this study (see Figure 5.17 and 5.30). The TOC value of 47.5 % or 43.1 % in this study was greater than 33% TOC removal rate reported by Rong et al., (2014) during oxidation of sulfadiazine by dielectric barrier discharge reactor containing powder ferrous ion. The improvement in the TOC removal rate in this study over the outcome reported by Rong et al., (2014) may be due to small size, high surface area, and enhanced reactivity of nZVI than ferrous ion. Comparing Figure 5.37 and 5.38, it was found that the mineralization rate of BPA or 2-NP was much faster via the combined DBD/photo-Fenton process (JT17) than in the case of combined DBD with various supported TiO_2 photocatalysts. This is mainly ascribed to high surface coverage or dispersion of the nZVI, which would promote high electron transfer, both of which were responsible for high pollutant mineralization rate compared to TiO_2 constrained on a stainless steel mesh. This study has demonstrated that the degradation of BPA or 2-NP can easily be achieved using a combinatory approach involving DBD with either photocatalysts or nZVI compared to DBD alone.

5.8 Quantification of free reactive species

The role played by the free reactive species such as O_3, H_2O_2 and OH^o during oxidation of BPA or 2-NP via DBD system cannot be underestimated. Based on the results presented so far, it has been demonstrated that BPA or 2-NP conversion rate was higher in the DBD system containing catalysts than DBD without catalysts. The improved removal efficiency

was attributed to higher yield of the free reactive species in the combined systems than in the DBD system alone. Therefore, it was deemed imperative to detect and quantify the amount of the free radicals produced by each system namely: DBD alone, DBD/supported photocatalyst (JT14) and DBD/photo-Fenton induced process. This would assist in establishing and drawing valid conclusions about which system produced the highest yield of the molecular and atomic oxidative species and which oxidant species influenced the pollutant degradation rate most. This section focuses on the detection and quantification of free reactive species such as O_3, H_2O_2 and OH^o in the DBD, DBD/JT14 and DBD/photo-Fenton induced process. The measurement of the free radicals was done using the following experimental conditions: discharged voltage 8 kV, air flow rate 3 L/min, electrolyte concentration NaCl (50 g/L), electrode (silver), BPA or 2-NP concentration (10 mg/L), BPA or 2-NP volume 1.5 L, mass of nano zero valent iron (0.06 g), mass of supported 2.4% Ag doped TiO_2 nanocomposites (JT14) (≈ 0.8 g). Each of the reactive species were separately quantified as outlined in the experimental procedures and analytical technique described in section 3.2.9.5.

5.8.1 *Quantification of Ozone*

Ozone is one of the most widely recognized powerful oxidizing agents responsible for the mineralization of organic compounds in wastewater. It reacts non-selectively with organic pollutants via direct molecular reaction or indirect chain reaction types, which sometimes occur simultaneously. Therefore, considering the significance or influence of ozone during the oxidation reaction of BPA or 2-NP via DBD or DBD with catalysts, the measurement of the amount of O_3 generated by the DBD in the presence or absence of catalysts is critical. The amount of ozone generated by the DBD alone or when combined with catalysts were measured either in distilled water which served as a blank or the aqueous solution containing BPA or 2-NP. The measurement of the amount of O_3 in the DBD and DBD combined with catalyst was carried using the experiment procedure described in Section 3.2.9.7. The concentration of O_3 was measured using a UV-visible spectrometer as described in Section 3.4.8. Thus, the results of the concentration of O_3 produced by the DBD in the distilled water or BPA or 2-NP solution in the presence or absence of catalyst as a function of discharge time is presented in Figure 5.39. Figure 5.39 (a) illustrates the formation of O_3 in distilled water and BPA or 2-NP solution by DBD alone. Figure 5.39 (b) and (c) represents the concentration of O_3 formed in distilled water, BPA or 2-NP solution by combined DBD/JT14 or DBD/photo-Fenton induced process respectively.

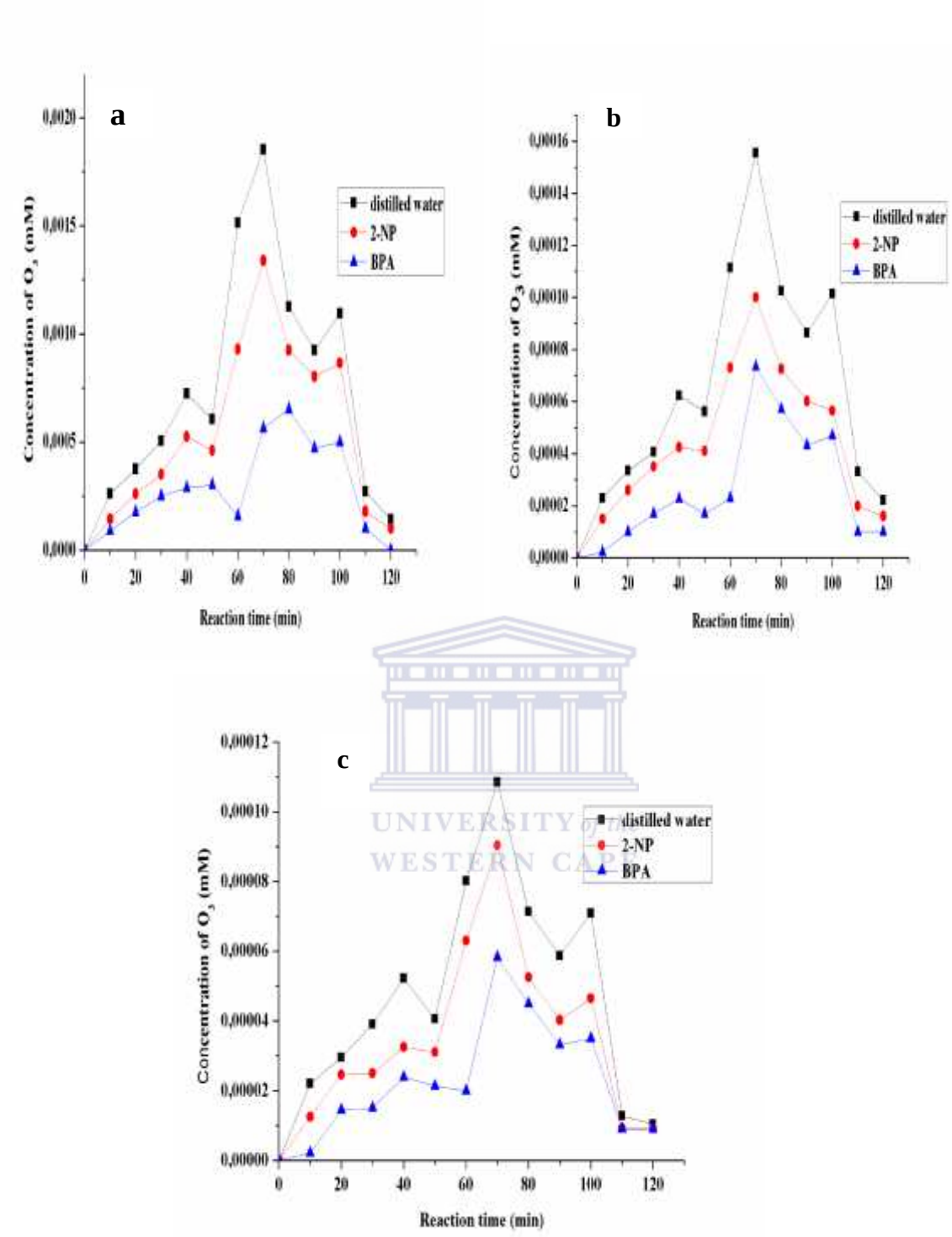

Figure 5.39: Concentration of O_3 produced by (a) DBD alone (b) DBD/JT14 (c) DBD/photo-Fenton induced process (JT17) in distilled water or BPA or 2-NP solution. (Conditions: solution pH 3, dosage of JT17, 0,06 g, mass of catalyst JT14 (0,8 g), discharge voltage 8 Kv, concentration of BPA or 2-NP 10 ppm, solution volume 1.5 L)

As shown in Figure 5.39, the maximum O_3 concentration was produced by the DBD in distilled water and reached 0.0185 mM in 70 minutes compared to 0.00134 mM and 0.00056 mM in 2-NP and BPA solution respectively. While in the case of combined DBD/JT14, the ozone concentration in distilled water, 2-NP and BPA solution were 0.000155 mM, 0.0001 and 0.00007 mM respectively at 70 minutes. Similarly, the amount of O_3 detected in distilled water, 2-NP and BPA solution via combined DBD/photo-Fenton induced process were 0.000115 mM, 0.00009 mM and 0.000052 mM respectively under the same time. It is obvious that DBD alone produced a significantly greater amount of ozone in distilled water or the aqueous solution of BPA or 2-NP at every treatment time than DBD with catalysts. While DBD with photo-Fenton induced process produced the least amount of O_3. The higher concentration of O_3 in distilled water was expected since there was no competition between the pollutants and the free reactive species. Additionally, the UV light intensity in the distilled water was stronger, that possibly enhanced the O_3 concentration since other species such as singlet oxygen (O) moves freely in the solution without being consumed thus easily recombined to form more O_3 which cannot be ruled out. It is clear that the concentration of ozone was higher in the distilled water followed by 2-NP and then BPA solution in both the DBD and the DBD with catalysts. Thus O_3 consumption rate varies with the types of pollutants and the treatment system. The concentration of O_3 depicted in Figure 5.39 (b) and (c) was lower than that of Figure 5.39 (a), which means that ozone concentration detected in distilled water or BPA or 2-NP using the DBD system was higher than the amount generated by the two combined systems. Unlike the linear trend observed with H_2O_2 and OH radicals (see Figure 5.40 and 5.41), the concentration of O_3 in all three systems fluctuated during the experiment as the plasma discharge time increases. This was because most of the gaseous ozone generated by the DBD escaped from the surface of the solution since the DBD design used was not a closed system. Due to the escape of this species, the amount of O_3 involved in the degradation process was small compared to OH radicals or H_2O_2 and was not utilized fully. The gaseous O_3 is difficult to dissolve in water due to low solubility and large bubbles size thus needs improvement. Besides, the lower concentration of O_3 in the solution may be due to the decomposition of O_3 into other species such as singlet oxygen (O), OH radicals, OOH among others within the plasma discharge zone. The declined in the concentration of O_3 in the DBD or DBD with catalysts can equally be explained in terms consumption of oxygen by the nitrogeneous species such as nitrous (NO) and nitric oxide (NO_2) formed

during the plasma discharge. The consumption of oxygen by these species affected the O_3 formation in the plasma zone.

Nevertheless, the lower yield of O_3 in the BPA solution indicates effective interaction of available O_3 with the pollutant as demonstrated in degradation pathways shown in Figure 5.25. It was found that BPA decomposed via ozonation and hydroxylation within the first 40 minutes (see Figure 5.26 and 5.27). It is important to mention that the electrophilic attack of O_3 on organic pollutants is dictated by the nature of the substituent group on the aromatic rings. If the substituent group is an electron donating species such as OH or NH_2, O_3 would attack at the ortho or para position. However, if the substituent group is an electron withdrawing species such as NO_2, O_3 would be expected to attack at the meta position. In the case of 2-NP, the OH radical was the main substituent while NO_2 was a leaving group and as such O_3 was expected to attack and displace NO_2 at the ortho position. But, this never happened as demonstrated in Figure 5.36, instead 2-NP was attacked by OH^o at the para position. Based on the LC-MS profile of intermediate compounds shown in (Figure 5.36) and the quantification results (see Figure 5.39), it is possible to conclude that the 2-NP reactivity towards O_3 was slow compared to BPA or simply put, that 2-NP was refractory towards ozone. Lesage et al., (2013) also found that 4-chlorobenzoic acid exhibited slower reactivity towards ozone. Ku et al., (2006) also reported that 2-nitrophenol was recalcitrant or refractory towards ozone.

The decreased concentration of O_3 in the combined DBD/JT14 can be ascribed to the conversion of O_3 to OH radicals. These findings could be explained as follows: The UV-light produced by the DBD caused the activation of TiO_2 catalyst resulting in the movement of electrons from the valence band to conduction band. The energetic electron (e-) in the conduction band reacted with the O_3 and formed ozonide radical ($O_3^{\cdot-}$). The ozonide radical reacted with the positive hole (h+) on the conduction band to form $HO_3^{\cdot}$, and later decomposed to OH^o and O_2. The reaction mechanism is represented in equation 5.13-15

$$e^- + O_3 \rightarrow O_3^{\cdot-} \quad \text{.....(5.13)}$$

$$O_3^{\cdot-} + H^+ \rightarrow HO_3^{\cdot} \quad \text{.....(5.14)}$$

$$HO_3^{\cdot} \rightarrow {}^{\cdot}OH + O_2 \quad \text{.....(5.15)}$$

Furthermore, the lower concentration of O_3 in the combined DBD with nano-zero valent iron particles can be explained on the basis of conversion of O_3 to OH^o via reaction with nZVI. The oxidation of Fe^0 in the acidic media (pH 3) vis-a-viz interaction with the O_3 produced

FeO^{2+}, and FeO^{2+} further reacted with more H_2O molecules to give the OH^{o} as shown in equation 5.16 – 5.18.

$$Fe^{0} + 2H^{+} \rightarrow Fe^{2+} + H_2 \quad \text{(5.16)}$$

$$O_3 + Fe^{2+} \rightarrow FeO^{2+} + O_2 \quad \text{(5.17)}$$

$$FeO^{2+} + H_2O \quad \text{(5.18)}$$

The lower concentration of O_3 in the two combined systems in this study was similar to the outcome reported by Zhang et al. (2013) on the O_3 production rate in phenol solution via combined pulsed discharge system and TiO_2 film. The reduction in the concentration was linked to O_3 conversion to OH radicals. The concentration of O_3 produced by DBD with or without catalysts in the range of (0.000115 mM – 0.0185 mM) is small compared to (1.6 g/m^3) that was reported by Dobrin et al., (2013) during the oxidation of diclofenac by pulsed corona discharge. The difference in the results may be ascribed to experimental conditions. For instance, Dobrin and co-workers, (2013) utilized pure oxygen to generate ozone which eliminated the formation and perhaps interference of nitrogenous species. The lack of such interferences coupled with other factors such as air flow rate (600 sccm, reactor volume (200 mL) among others were responsible for such higher O_3 concentration. Additionally, the DBD reactor used was sealed and no substantial O_3 loss was reported unlike the present study where the greater amount of O_3 escaped as gas from the surface of the solution because the DBD design was not sealed. Very importantly, in this study, dry air which contained nitrogen was used to generate O_3, and there was the formation of nitrogenous species such as NO and NO_2 which consumed oxygen as shown in equation 1-9. The formation of active species also depends on the geometry of the DBD, input power and other factors. DBD with co-axial configurations with discharge voltage of 20 kV was used in their study compared to this study using a DBD with double cylindrical configuration with discharge voltage of 8 kV.

However, the obtained O_3 concentration (0.0185 mM) via DBD alone in distilled water in this study is closely related to 0.029 mM reported by Lei et al., (2007). The slight difference in the values may be attributed to the input discharge voltage as Lei and co-workers utilised DBD with input discharge voltage of 16 kV which is double the discharge voltage used in the present study. In addition, the lower concentration of O_3 in the aqueous solution of BPA or 2-NP than distilled water is consistent with the findings of other researchers who have equally demonstrated a lower concentration of O_3 in solutions containing organic pollutants. Magureanu et al., (2011) found that the concentration of O_3 in distilled water produced by

DBD was 1.5 g/m^3 that however reduced to 0.8 g/m^3 and 0.2 g/m^3 in solutions containing amoxicillin, oxacillin or ampicillin respectively. The decrease in the concentration was linked to the consumption of O_3 by the antibiotics and their intermediates. Zhang et al., (2013) reported O_3 concentration of 0.0005 mM produced by combined DBD and TiO_2 film containing phenol solution. Their reported value is however low compared d to 0.0185 mM produced by the DBD alone in this study. This further showed that free radicals production via DBD depends on several factors such as discharge voltage, reactor geometries among others. Generally, as demonstrated in Figure 5.36 and Figure 5.39, it is clear that O_3 did not contribute substantially to the degradation of the two pollutants instead most O_3 produced in all the three systems was probably converted to OH radicals and in most cases H_2O_2 or escaped in the form of gas. The next section involved the quantification of H_2O_2 in the three systems.

5.8.2 *Quantification of H_2O_2*

The degradation of BPA or 2-NP via DBD or the two combined systems occurred in the presence of reactive species such as hydrogen peroxide, formed via recombination reaction of OH radicals. Thus, the determination of the concentration of H_2O_2 formed during oxidation process was deemed crucial as it gives an understanding into how much OH radicals is being produced by the DBD system. The concentration of H_2O_2 generated by DBD in distilled water and BPA or 2-NP solution with or without catalyst as a function of plasma discharge time was quantified using the colorimetric method. The detailed experimental procedure is described in section 3.2.9.6. The concentration of H_2O_2 was measured using UV-visible spectrometry technique described in Section 3.4.8 and the obtained results are shown in Figure 5.40. Figure 5.40 (a) illustrates concentration of H_2O_2 produced by DBD alone in distilled water or aqueous solution of BPA or 2-NP. Figure 5.40 (b) and (c) indicates the yield of H_2O_2 produced by DBD/supported photocatalyst (JT14) or DBD/photo-Fenton induced process (JT17) respectively.

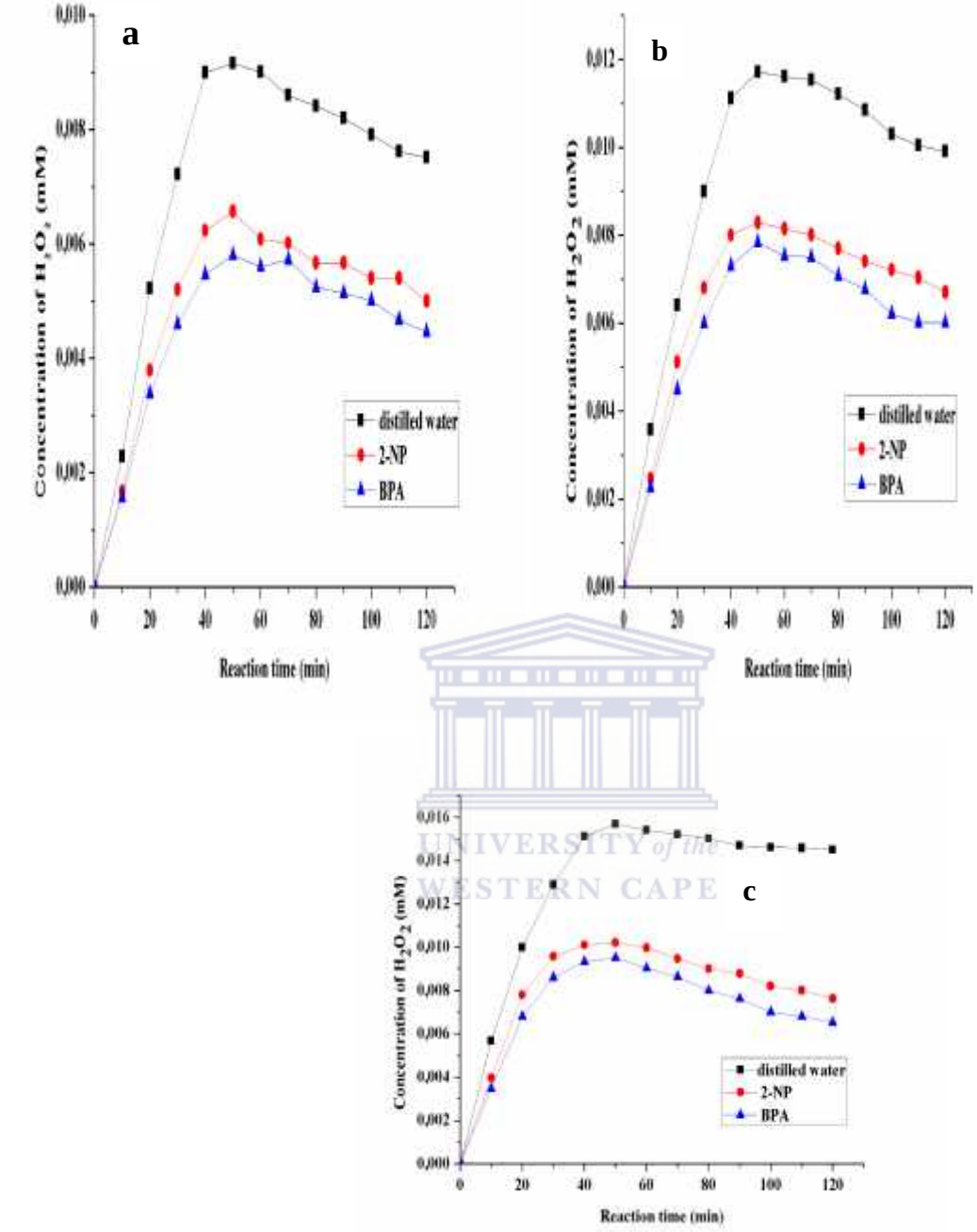

Figure 5.40: Concentration of H_2O_2 produced by (a) DBD alone (b) DBD/JT14 (c) DBD/photo-Fenton induced reaction (JT17) in distilled water or BPA or 2-NP solution (Conditions: solution pH 3, dosage of JT17, 0,06 g, mass of catalyst JT14 (0,8 g), discharge voltage 8 kV, concentration of BPA or 2-NP 10 ppm, solution volume 1.5 L)

As demonstrated in Figure 5.40 (a) – (c), it can be seen that the concentration of H_2O_2 increased linearly with increasing discharge time in distilled water until 50 min. Beyond 50

min, a deviation from linearity was noticed and was common to all the three systems. In the DBD system within 10 minutes, the concentration of H_2O_2 in distilled water was 0.00228 mM, and reduced to 0.00157 or 0.00166 mM in BPA or 2-NP solution respectively. In the case of DBD/supported Ag doped TiO_2 nanocomposites, the yield of H_2O_2 in distilled water was 0.00357 mM, which however reduced to 0.00227 or 0.00247 mM in BPA or 2-NP solution respectively. In the same vein, the concentration of H_2O_2 generated by DBD/photo-Fenton induced process in distilled water was 0.00567 mM and declined to 0.0039 or 0.0025 mM in 2-NP or BPA solution respectively. The concentration of H_2O_2 was higher in the distilled water than BPA or 2-NP solution and this trend was consistently observed till 120 minutes. The order of production rate of H_2O_2 in distilled water or BPA or 2-NP solution at every treatment time was DBD/photo-Fenton induced process > DBD/supported photocatalyst > DBD alone. This indicates the highest yield of H_2O_2 in the combined systems than in the case of the DBD alone. It also indicates higher concentration of H_2O_2 in the combined DBD/photo-Fenton induced process than others. The slight improvement in the concentration of H_2O_2 in the combined systems may be attributed to the additional OH^o provided by the supported Ag doped titania photocatalyst or nZVI via the interaction with the intense UV light produced by the DBD as shown in equation 5.19-5.21.

$$TiO_2 + UV \rightarrow h^+ + e^- \quad \text{.....(5.19)}$$

$$h^+ + H_2O \rightarrow H^+ + {}^{\circ}OH \quad \text{.....(5.20)}$$

$$Fe^0 + 2H_2O + UV \rightarrow Fe^{2+} + H_2 + 2OH^- \quad \text{.....(5.21)}$$

These additional OH radicals recombined and formed H_2O_2, thus enhanced H_2O_2 concentration in the combined system.

$$\cdot OH + \cdot OH \rightarrow H_2O_2 \quad \text{.....(5.22)}$$

Besides the recombination of OH^o (equation 5.22), other plausible sources for the slight increase in the H_2O_2 concentration includes:

i) Reaction between high energy electrons and water molecules in the plasma zone as shown in equation 5.23.

$$2H_2O \rightarrow H_2O_2 + H_2 \quad \text{..... (5.23)}$$

ii) The attack of molecular oxygen by energetic electrons produced from singlet oxygen as shown in equation (5.24)

$$O_2 + e^- \rightarrow {}^{\circ}O + {}^{\circ}C \quad \text{..... (5.24)}$$

Further reaction of the singlet oxygen with oxygen molecules produced ozone (O_3) (equation 5.25)

$^{o}O + O_2 \rightarrow O_3$…….. (5.25)

O_3 under intense UV-light may reacted with water molecules to produce H_2O_2 (equation 5.26).

$O_3 + UV + H_2O \rightarrow H_2O_2 + O_2$…….(5.26)

Thus the higher concentration of H_2O_2 in the distilled water or modelled solution in the combined systems confirmed the existence of a synergistic effect between the DBD and various catalysts. The synergy between the two combinedsystems contributed to the enhanced BPA or 2-NP removal efficiency. It is also noteworthy mentioning that the concentration of H_2O_2 generated via the combined DBD/photo-Fenton induced process was greater than that obtained with the DBD/supported TiO_2 photocatalyst. The reasons for such increment in the H_2O_2 yield upon the addition of nZVI is similar to the enhancement of BPA or 2-NP removal efficiency discussed in Figure 5.12 and 5.13. The higher H_2O_2 yields with other reactive species possibly OH^o may perhaps be responsible for complete removal of BPA or 2-NP molecules within 40 minutes using DBD/photo-Fenton induced process (JT17) (see Figure 5.12 and 5.13).

Furthermore, at every treatment time the concentration of H_2O_2 formed in the distilled water was greater than the amount measured in BPA or 2-NP solution by an order magnitude of 1.5 in all the three systems. This was expected since there was no competition in the distilled water between these reactive species and organic pollutants, except the interconversion reaction among species such as O_3, OOH and OH^o. For instance, O_3 reacted with hydroxyl ion (OH^-) in solution under intense UV light to generate hydroxyl radicals, and the recombination reaction of OH^o formed H_2O_2 and enhanced its yield. Whereas in the solution containing BPA or 2-NP, a lower yield of H_2O_2 was detected compared to distilled water. In the BPA or 2-NP solution, there was a strong competition between the BPA or 2-NP molecules and the intermediate compounds for the reactive species. As a matter of fact, BPA or 2-NP molecules and intermediates consumed the OH^o or perhaps H_2O_2 itself. The consumption of OH^o affected the recombination reaction thus limited H_2O_2 concentration. Beyond 60 min, the concentration of H_2O_2 in the BPA or 2-NP solution reduced, which may again be linked to consumption of the reactive species by the intermediates. The deviation from linearity or decrease in H_2O_2 after 60 minutes may equally be explained in terms of over saturation of H_2O_2 in the solution. The decline in H_2O_2 concentration at a longer treatment time may also be due to the reaction of H_2O_2 with O_3 which liberated more OH^o.

Comparing the rate of formation of H_2O_2 in the two combined systems for the pollutants, it was found that the concentration of H_2O_2 was slightly higher in 2-NP solution than in the BPA solution, suggesting that BPA consumed more H_2O_2 than 2-NP. This behaviour was observed in all the three systems. The obtained concentration of H_2O_2 obtained in this study either in the presence or absence of a catalyst is lower than 0.3 mM and 1.76 mM reported by Manoj Kumar Reddy et al. (2013) and Zhang et al., (2013). The differences in the H_2O_2 yield may be attributed to the type of discharge system, experimental conditions and the nature of the catalyst. In this study the power source only delivered 8 kV discharge voltage whereas the pulsed discharge system used by Manoj Kumar Reddy et al., (2013) and Zhang et al., (2013) provided 18 kV and 20 kV respectively. According to Sein et al., (2012) over saturation of H_2O_2 leads to decomposition of H_2O_2 in the plasma discharge zone to OH^{o} (Sein et al. 2012). Magureanu et al., (2013) argued that the slight deviation in yield of H_2O_2 at a longer treatment time may be attributed to increased electrical conductivity and solution temperature. However, in this study the electrical conductivity of the solution was not measured but the solution pH was determined during the oxidation process and decreased with treatment time (see Figure 5.1 (b) and 5.2 (b). Thus, the decreased in solution pH served as an evidence of increased electrical conductivity, which may perhaps responsible for the decreased in H_2O_2 yield (Magureanu et al., 2013). Conversely, Garcia-Araya et al., (2010) reported a higher concentration of H_2O_2 at a longer treatment in the diclofenac solution treated via TiO_2 photocatalytic process. It was found that the diclofenac decomposed to hydroxylated aromatic rings which enhanced the formation of H_2O_2. As reported in the literature, the concentration of free reactive species depends on the applied discharge or input voltage, the higher the input voltage the greater the formation and concentration of reactive species in the plasma zone.

5.8.3 *Quantification of OH radicals*

In the present study, hydroxyl radicals produced by the DBD and DBD in the presence of catalyst was quantified by disodium salt of terephthalic acid (NaTA) chemical dosimetry described in Section 3.2.9.8 and 3.2.9.9 respectively. The disodium salt of terephthalic acid (NaTA) was selected as a chemical probe owing to its non-reactivity with other active species such as H_2O_2 and O_3. It is reacted directly with OH^{o} and forms 2-hydroxylterephthalic acid (2-HTA). The detailed of the quantification technique and instrumental conditions by fluorescence at 425 nm have been described in Section 3.4.15. Figure 5.41 (a) illustrates the

amount of OHº produced by the DBD system in the distilled water or BPA or 2-NP solution as a function of the treatment time. While Figure 5.41 (b) and (c) represent the formation of hydroxyl radicals in the presence of either supported 2.4% Ag loaded carbon doped titania nanocomposites (JT14) or 0.06 g polyethylene glycol stabilised nano zero valent iron (JT17) respectively. Figure 5.41 (d) represents one of the fluorescence intensity spectra of the 2-HTA observed during the oxidation process.

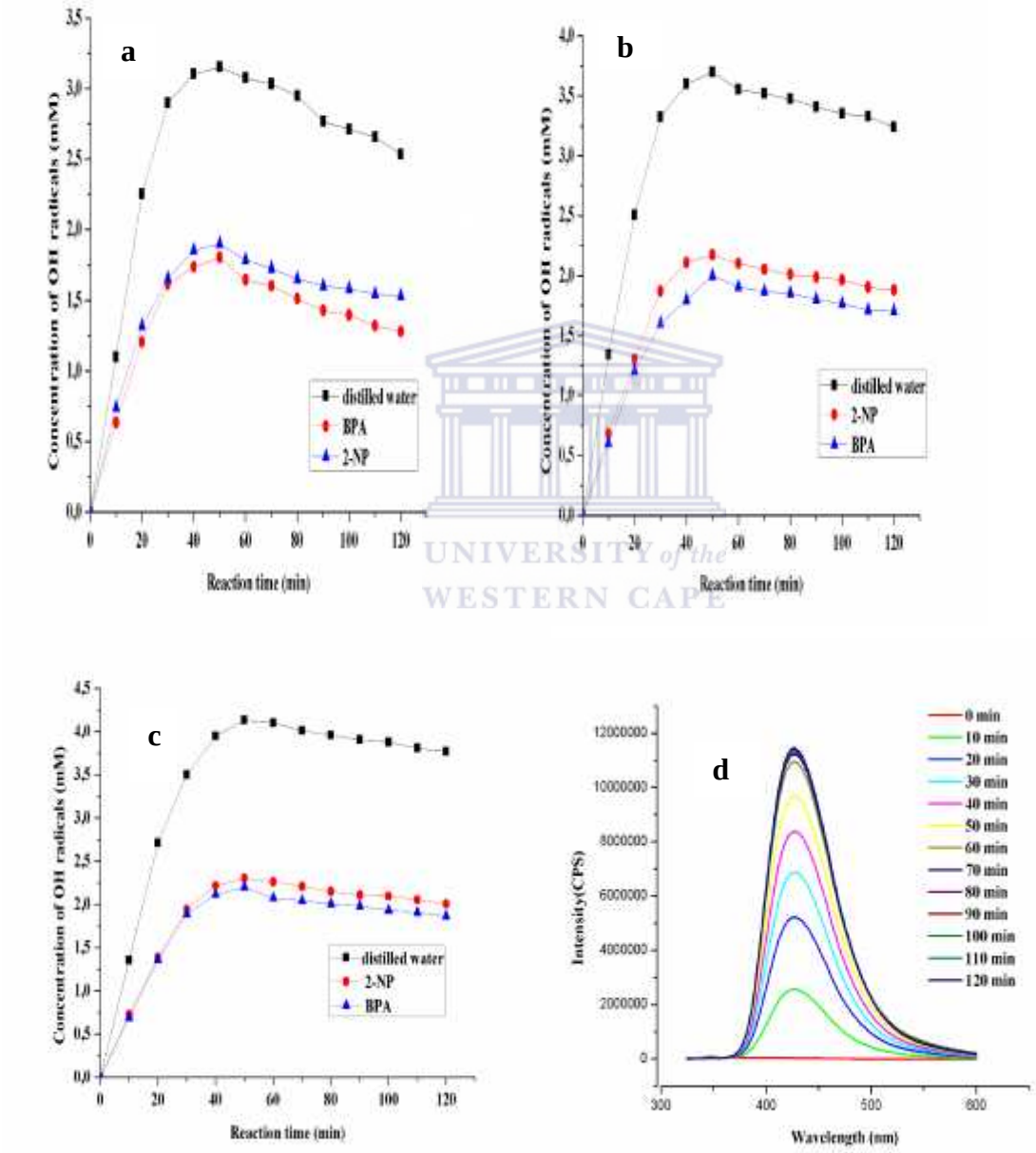

Figure 5.41: Concentration of OH radicals produced by (a) DBD alone (b) DBD/JT14 (c) DBD/photo-Fenton induced reaction (JT17) in distilled water and BPA or 2-NP solution (d) Changes in photolumiscence intensity at different reaction time

According to Figure 5.41 (a), OHº concentration measured in distilled water, 2-NP or BPA solution at 10 min was 1.096 mM, 0.632 mM and 0.74 mM respectively. While Figure 5.41 (b) shows that OH radicals slightly increased in distilled water, 2-NP or BPA solution to 1.338 mM, 0.684 mM and 0.652 mM within the same treatment time using DBD/JT14. In the case of DBD/photo-Fenton induced process (Figure 5.41 (c)), the OHº yield in distilled water, 2-NP or BPA solution were 1.355 mM, 0.72 mM and 0.68 mM respectively. The increment in OHº yield in the distilled water, BPA or 2-NP solution was consistent untill 50 minutes in all the three systems. The OHº production rate which corresponded to the fluorescence intensity of 2-HTA formed from the reaction between OHº in the solution and NaTA probes increased linearly with increasing plasma exposure time in the distilled water for 50 min in all the three systems. Similar trends were observed for BPA or 2-NP solution and no appreciable increase in the OHº concentrations was observed beyond 50 min. Instead the amount of OHº slightly reduced and deviated from linearity. It can be seen that the combined systems produced more OHº than the DBD system alone and the production rate was higher in the distilled water than the aqueous solutions of BPA or 2-NP. The increment in OHº by the combined systems over the DBD alone may be due to additional OH sources provided by the catalyst. The greater yield of OH radical as well as H_2O_2 concentration in the combined DBD/supported Ag doped TiO_2 nanocomposites (JT14) compared to the DBD alone can be explained as follows: the intense UV light produced by the DBD activated the TiO_2 catalyst prompting the excitation of electrons from the valence band to conduction band to create electron-hole pairs. However the positive holes on the valence band reacted further with the hydroxyl ions in the water and formed OHº. Similarly, the reaction between the electron on the conduction band and O_2 from air reacted and produced the superoxide radical (O_2^-) which further reacted with H_2O and liberated OHº. The recombination reaction of OHº produced H_2O_2. The reaction mechanism is represented in equations 5.27 – 5.30

$$OH + h^+ \rightarrow \cdot OH \quad \text{.....(5.27)}$$

$$O_2^{\cdot -} + 2H_2O_2 \rightarrow H_2O_2 + 2\,^{\circ}OH + O_2 \quad \text{.....(5.28)}$$

$$TiO_2 - + H_2O \rightarrow H^+ + {}^{\circ}OH \quad \text{.....(5.29)}$$

$$TiO_2 - + {}^{-}OH \rightarrow {}^{\circ}OH \quad \text{.....(5.30)}$$

Also, in the case of DBD/photo-Fenton-induced process, apart from the Fe^0/Fe^{2+} reaction with UV/H_2O_2 to produce OHº, the additional increase in OHº may be linked to the oxidation of Fe^0/Fe^{2+} by O_3 in the plasma zone thus producing FeO^{2+}, which reacted with H_2O and liberated OH radicals. The reaction mechanism is shown in equation 5.31 - 5.33

$Fe^{0} + 2H^{+} \rightarrow Fe^{2+} + H_2$ ……(5.31)

$O_3 + Fe^{2+} \rightarrow FeO^{2+} + O_2$ ……(5.32)

$FeO^{2+} + H_2O \rightarrow Fe^{3+} + {}^{\circ}OH + {}^{-}OH$…… (5.33)

The reaction between O_3 and H_2O_2 (peroxone process) under intense UV-light in the plasma discharge zone also produced OH radicals as shown in equation (5.34)

$O_3 + H_2O_2 + UV \rightarrow 2OH^{\cdot} + 3O_2$……(5.34)

Therefore, the summation of all the chemically active species, O_3, OHº and molecular species (H_2O_2) produced by the two combined system were responsible for the higher mineralization rate of BPA and 2-NP especially in the case of DBD/photo-Fenton induced process(JT17). The order of concentration of OHº was combined DBD/photo-Fenton induced process (JT17) > DBD/supported Ag doped TiO_2 nanocomposites (JT14) > DBD. The production rate of OHº followed a similar trend to that observed for H_2O_2. However the concentration of OHº in the system was far greater than H_2O_2 or O_3, which confirmed that OHº contributed significantly to the formation of H_2O_2. It is also clear that the OHº produced by the DBD system as well as the DBD with catalysts was the dominant species responsible for the degradation of BPA and 2-NP in water.

Beyond 50 minutes, the OHº concentration declined, which was similar to the trend observed with H_2O_2. The deviation from linearity or decrease in OHº at higher treatment time may be due to the decomposition of the chemical probe (HTA) formed as a result of reaction of OHº and NaTA. Additionally, the lower concentration of OHº in BPA or 2-NP solution compared to distilled water indicates consumption of OHº by both BPA or 2-NP and their intermediates. The decrease in the OHº equally affected the formation of H_2O_2 in the plasma zone. The OHº consumption rate of the two pollutants in the three systems expressed in percentage was evaluated by subtracting the amount consumed by the pollutants from the amount generated in the distilled water. It was found that BPA consumed close to 58% OHº while 2-NP consumption rate ranged between 42-45% at every treatment time in all the three systems. This higher consumption rate of OHº and other species by BPA compared to 2-NP in all the systems might be the reason for the higher degradation rate observed for BPA.

The 4.09 mM (0.00409 mol/L) produced by the combined DBD/photo-Fenton induced process at 70 minutes is greater than 6.8 μmol/L reported by Tang et al., (2013) on phenol degradation via combined DBD with granular activated carbon containing TiO_2. The difference can be attributed to the nature of the catalysts. The TiO_2 photocatalyst used in this study was on a support material and purely anatase in nature. Anatase TiO_2 has been reported

to be more active than other TiO_2 phases. Not only was the catalyst was doped with Ag, which it also contained carbon both probably reduced the electron-hole recombination rate on TiO_2 and enhanced the formation of more OH^o. Whereas, the catalyst used by Tang et al., (2013) was purely in powder form which possibly obscured the formation of more OH^o in the plasma zone.

5.9 Chapter summary

In this chapter, the removal and degradation of BPA and 2-NP in aqueous solution by the DBD plasma system on its own and in combination was investigated. It was found that an increase in solution pH and initial concentration of the pollutants as well as radical scavengers have a negative effect on the removal efficiency of the two compounds. The removal efficiency of BPA or 2-NP was mostly favoured in acidic conditions and at lower concentrations. Maximum BPA or 2-NP removal efficiency occurred at low pH (3) at an optimum concentration of 10 mg/L. The BPA or 2-NP degradation yield at 30 mg/L concentration of BPA or 2-NP, at 8 kV discharge voltage, solution pH (3), after 80 min treatment time was 3.73×10^{-4} g/kWh or 2.48×10^{-4} g/kWh respectively. The incorporation of supported 2.4% Ag loaded carbon doped TiO_2 nanocomposites enhanced the BPA or 2-NP removal efficiency by 21.8% and 24.2% in relation to DBD alone. It was found that the 2.4% Ag loaded carbon doped TiO_2 nanocomposites were photochemical stable even after four repeated applications in combination with the DBD system.

100% removal efficiency of BPA or 2-NP was achieved using combination of DBD with 0.06 g stabilized nZVI at BPA or 2-NP concentration of 10 ppm, discharge voltage 8 kV, solution pH (3), in less than 40 min, which indicated the existence of a synergetic effects. The TOC reduction value by the two combined systems was however rather low due to formation of recalcitrant transformation products. The degradation of BPA proceeded via ozonation, hydroxylation, dimerization, and decarboxylation and nitration steps were proposed. While 2-NP proceeded via hydroxylation, nitration and denitration steps respectively. Five and three new oxidation products such as (BP5, BP11 - BP14) and (OBP2-OBP4) of BPA or 2-NP which have not been previously reported in the literature were identified. The DBD alone and combined DBD with catalyst produced more of the OH^o than H_2O_2 and O_3. While the combined DBD/photo-Fenton induced process demonstrated the highest yield of H_2O_2 and OH^o rather than O_3. The OH^o that readily formed in acidic medium were the most significant species responsible for the degradation of BPA and 2-NP. The results presented in this study

have clearly demonstrated that the combination of the DBD system with JT14 or JT17 can applied as a pre or post treatment method to decompose recalcitrant pollutantS such as BPA or 2-NP in water.

However, as mentioned in Chapter one, the problem with DBD is high energy consumption, and difficulty in scaling-up, thus affecting industrial utilization, despite being successful at laboratory scale. Therefore, the next chapter focuses on the application of the jet loop reactor based on the principle of impingement to decompose BPA and 2-NP in water. Jet loop reactor has the capacity to treat 60 L of wastewater, and can be easily scaled for industrial applications.

CHAPTER SIX

DEGRADATION OF BPA OR 2-NP BY JET LOOP REACTOR: INFLUENCE OF ULTRA-VIOLET LIGHT AND HYDROGEN PEROXIDE

6 INTRODUCTION

The chapter focuses on the application of the jet loop reactor (JLR) which is based on the impingement principle to degrade bisphenol-A (BPA) and 2-nitrophenol (2-NP) in water. The effect of input applied pressure, solution pH, initial pollutant concentration and radical scavengers on the removal efficiency of BPA or 2-NP are investigated and presented accordingly. The efficiency of the combined JLR with UV-light, JLR with H_2O_2, UV/H_2O_2 and JLR/UV/H_2O_2 on the degradation rate of bisphenol-A and 2-nitrophenol are compared and discussed. The results of the synergetic index value of the various combined treatment options are also presented and discussed in this chapter.

6.1 Background

As mentioned in the introductory chapter, endocrine disrupting compounds such as bisphenol-A and 2-nitrophenol remain a great threat in drinking and wastewater thus different treatment techniques need to be developed for their removal. Conventional treatment technologies are not effective nor ecologically safe for complete degradation of complex bio-refractory organic contaminants. Besides, the advanced treatment technologies (AOTs) such as ultrasonic irradiation, dielectric barrier discharge system are also difficult to scale up for industrial and commercial purposes. Among the AOTs considered in this study is the jet loop reactor (JLR) system based on impingement. The JLR can be scaled-up easily for industrial uses compared to dielectric barrier discharge system or ultrasonic irradiation and also consumes less energy. Therefore, jet loop reactor system alone or in combination of JLR with UV-light and H_2O_2 is proposed in this section to decompose BPA or 2-NP in aqueous solution. The survey of the literature indicated that little or no information exists on the removal and degradation of BPA or 2-NP via jet loop reactor combined UV-light and H_2O_2. Thus, this chapter focuses on utilization of integrating the jet loop reactor with various combined advanced oxidation strategies to decompose BPA and 2-NP in water. The influence of the operating parameters such as input applied pressure, solution pH, and initial concentration of the pollutants and radical scavengers on the degradation of BPA or 2-NP were investigated and discussed.

6.2 Optimization of the operating parameters in the jet loop reactor

The overall performance of a jet loop reactor depends on its ability to operate at the optimum conditions. The next section focuses on the operating parameters which determine the efficiency of a jet loop reactor system.

6.2.1 *Effect of inlet pressure*

The inlet pressure is one of the fundamental physical operating parameters which determine the amount of OH radicals formed within the reactor chamber during impingement and extent of oxidation of pollutants by jet impingement process. Based on this, the removal efficiency of BPA or 2-NP in water was investigated by varying inlet pressure from 2 – 6 bar at natural solution pH of 4.5 (BPA) and 3.8 (2-NP) respectively. The detailed experimental procedure and analytical techniques used for determination of residual concentration of BPA or 2-NP were outlined in Section 3.3.2.2 (i) and 3.4.12. The obtained results of the effect of inlet applied pressure were expressed in term of pollutants removal efficiency represented in Figure 6.1 and apparent rate constants are shown in Table 6.1. Figure 6.1 illustrates the removal efficiency and degradation kinetics plots of BPA or 2-NP at different inlet applied pressure.

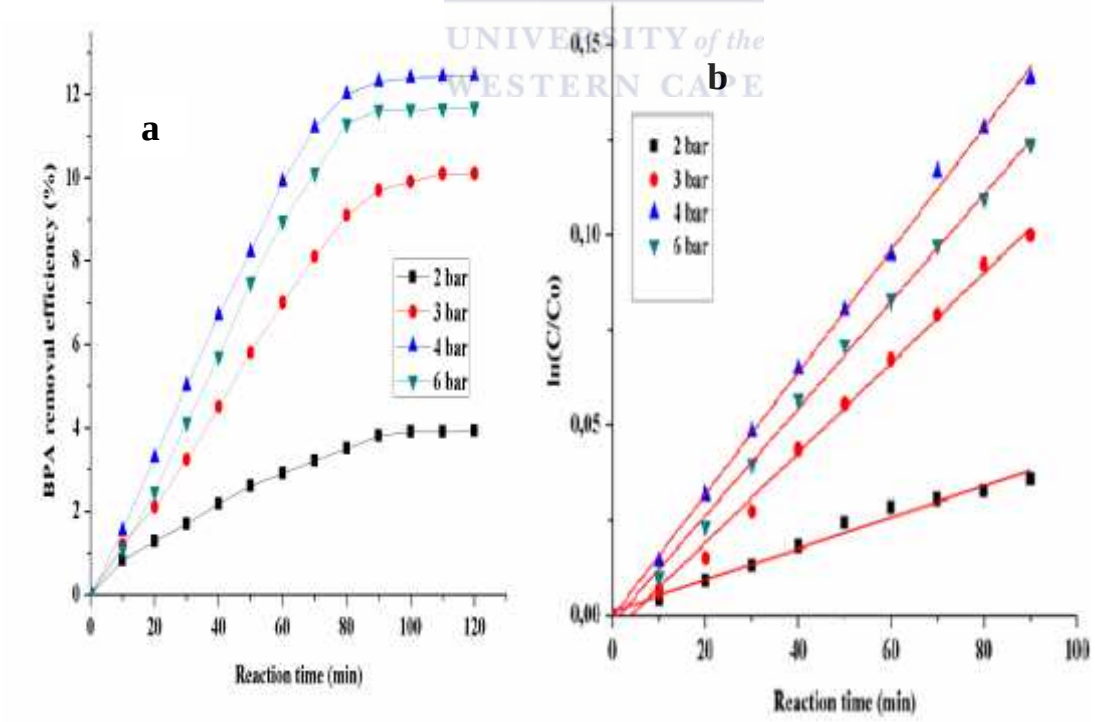

Figure 6.1: Effect of (a) inlet applied pressure on the BPA removal efficiency (b) degradation kinetics of bisphenol-A at different inlet pressure of the jet loop reactor. Experimental conditions (BPA concentration (10 ppm), volume of BPA or 2-NP, 60 L, natural pH of BPA (4.75), flow rate (0.7 L/s).

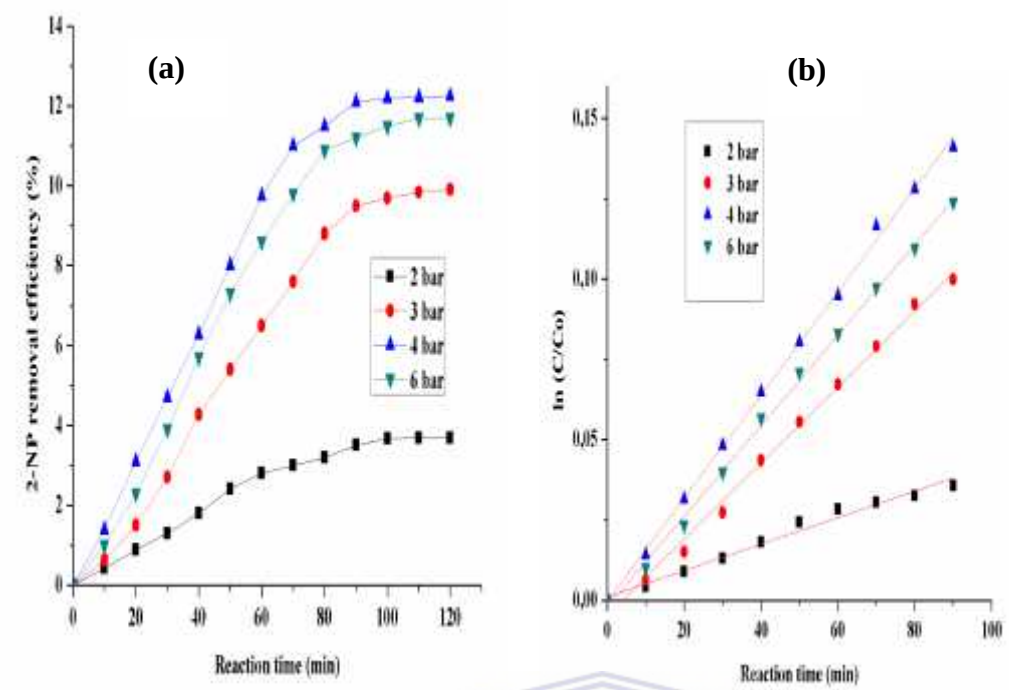

Figure 6.2: Effect of (a) inlet applied pressure on the 2-NP removal efficiency (b) degradation kinetics of 2-NP at different inlet pressure of the jet loop reactor. (Experimental conditions, 2-NP concentration (10 ppm), volume of BPA or 2-NP, 60 L, natural pH of 2-NP (3.87), flow rate (0.7 L/s).

As shown in Figure 6.1 (a) and 6.2 (a), it can be seen that the removal efficiency of BPA or 2-NP increases with an increase in inlet applied pressure from 2 bar to 4 bar. The maximum removal efficiency of BPA or 2-NP at 4 bar using the JLR was 12.4 % and 12.1 % respectively. The BPA or 2-NP removal efficiency slightly reduced to 11.6 % and 11.2 % respectively at higher inlet pressure of 6 bar. Since the results obtained at 6 bar did not improve the extent of pollutant removal as compared to that obtained at 4 bar, 4 bar was selected as the optimum inlet pressure. It was also found that after 90 min, there was no significance increase in the BPA or 2-NP removal efficiency, thus the experimental data from 10 – 90 min were fitted into pseudo-first order kinetic model shown in Figure 6.1 (b) and 6.2 (b) respectively. The rate constant (k), correlation coefficient (R^2) and maximum BPA or 2-NP removal efficiency at different inlet applied pressure at 90 min reaction time are presented in Table 6.1.

Table 6.1: Effect of inlet applied pressure on the removal efficiency of BPA or 2-NP at 90 min maximum (experimental conditions as in Figure 6.1 and 6.2)

Pollutants	Inlet applied pressure (bar)	Pollutant removal efficiency (%)	Pseudo-first order rate constant × 10^{-3} (min^{-1})	Correlation coefficient (R^2)
BPA	2	3.80	0.4	0.9791
	3	9.71	1.2	0.9968
	4	12.4	1.7	0.9977
	6	11.6	1.5	0.9981
2-NP	2	3.50	0.4	0.9822
	3	9.50	1.2	0.9983
	4	12.1	1.5	0.9912
	6	11.2	1.4	0.9981

The rate constants (k) of BPA as shown in Table 6.1 increased from 0.4×10^{-3} min^{-1} at 2 bar to 1.7×10^{-3} min^{-1} at 4 bar and thereafter decreased to 1.5×10^{-3} min^{-1} at 6 bar. Similarly, the apparent rate constant of 2-NP increases from 0.4×10^{-3} min^{-1} to 1.7×10^{-3} min^{-1} with an increase in the inlet pressure from 2 bar to 4 bar and however slightly reduced to 1.4×10^{-3} min^{-1} at 6 bar. The removal efficiency and apparent rate constant of the two pollutants were similar, which was an indication of the pollutants being attacked by the same species of similar magnitude. The observed trend of increasing BPA or 2-NP removal efficiency or rate constant (k) with an increase in inlet pressure can be attributed to the rapid or effective mixing, which enhanced the impingement of water molecules from both sides of the jet cavity. At 2 bar, the rate of mixing or collision of water molecules was slow compared to 3 or 4 bar, which was possibly responsible for the lower removal rate. With increasing inlet pressure from 3 bar to 4 bar, the collision rate of water molecules within the jet reactor chamber and the liquid flow rate or velocity increased, which in turn enhanced the impingement rate. Under the continuous flow system especially at 4 bar, heat was produced which eventually increased the solution temperature from 19ºC to 63ºC within 90 minutes. The increase in solution temperature at higher pressure (and possibly generation of vapour) caused cleavage of water molecules and formation of OH radicals as shown in equation (6.1)

$$H_2O \xrightarrow{Impingement} OH^{\cdot} + H^{\cdot} \quad \text{.....(6.1)}$$

The generated OH radicals and other free active species within the jet zone attacked the pollutants and degradation occurred and hence enhanced the removal efficiency. While, the decreased in the pollutant removal efficiency and apparent rate constant (k) beyond 4 bar may be attributed to excessive or indiscriminate growth of bubbles, which reduced the impingement intensity, which in turn lowered the formation of OH radicals (Gogate and Patil, 2015). The other possibility for the decrease in the removal efficiency and rate constant at 6 bar may be ascribed to formation of individual bubbles or vaporous cloud that escaped the jet reactor without necessarily collapsing. Based on the fact that no further increment in the removal efficiency or rate constant was observed beyond an inlet pressure of 4 bar, 4 bar was selected as the optimum inlet pressure for the next experiments. Comparison of the results obtained in this study with the previous studies reported in the literature would be difficult. This is because very little information exists in the literature on the application of jet impingement process to decompose persistent organic pollutants. Nevertheless, there are several reports on the decomposition of organic pollutants by hydrodynamic cavitation. Therefore, the results obtained in this study (Table 6.1) would be compared with previous studies done using hydrodynamic cavitation process. The establishment of an optimum inlet pressure in this study corroborated previous studies reported in the literature on the decomposition of organic pollutants via hydrodynamic cavitation: rhodamine B, 4 bar (Mishra and Gogate, 2010), imidacloprid, 4 bar (Raut-Jadhav et al. 2013), orange-G, 4 bar (Saharan et al., 2013). Gogate and Patil, (2015) demonstrated that degradation efficiency of triazophos via hydrodynamic cavitation increases with an increase in inlet pressure from 1-5 bar and decreased beyond 5 bar after 120 min. They reported maximum degradation efficiency of 35.77 % and a rate constant of 4.01×10^{-3} min^{-1} for an optimum inlet pressure of 5 bar. Very recently, Bagal and Gogate, (2014a) also reported 20.81 % and 2.1×10^{-3} min^{-1} as the maximum degradation efficiency and apparent rate constant of diclofenac degradation by hydrodynamic cavitation at optimum pressure of 3 bar after 150 min. They observed that further increase in inlet pressure to 4 bar resulted in a decrease in the degradation rate. The decrease was attributed to choking of the cavitational chamber with large bubbles which reduced the cavitational intensity. Similarly, Bagal and Gogate, (2013) also established an optimum inlet pressure of 4 bar during the decomposition of 2,4-dinitrophenol by hydrodynamic cavitation, with maximum removal efficiency and rate constant of 12.4 % and 1.2×10^{-3} min^{-1} after 150 min respectively. It was found that a further increase in inlet pressure to 6 bar led to cloudiness of the cavity chamber which reduced the cavitational

intensity and degradation rate of the pollutant. Conversely, Wang and Zhang, (2009) established no optimum pressure during the degradation of alachlor by swirling jet cavitation. They found that degradation rate constant increased from 2.92×10^{-2} min^{-1} to 4.90×10^{-2} min^{-1} with increasing inlet pressure from 2 to 6 bar. While in this study, maximum removal efficiency of 12.4 and 12.1 % were obtained within 90 minutes for BPA or 2-NP respectively. The maximum rate constant for BPA or 2-NP was 1.7×10^{-3} min^{-1} and 1.5×10^{-3} min^{-1} respectively. In spite of the differences in the mode of generation of free radicals and the nature of the pollutants, the removal efficiency reported in this study is the same as 12.4 % reported by Bagal and Gogate, (2013) for 2, 4-dinitrophenol by hydrodynamic cavitation.

6.2.2 *Effect of solution pH*

The pH of a solution is one of the important operating parameters that influence the degradation efficiency of organic pollutants during the jet impingement process. The oxidative strength of most free reactive species, especially OH radicals, depends on the solution pH range and directly or indirectly influences the solution physico-chemical properties. Based on this background, the influence of solution pH on the removal efficiency of BPA or 2-NP was investigated at different pH in the range of 3-12 using the jet loop reactor. The desired solution pH value was adjusted by 0.5 M NaOH or 0.5 M H_2SO_4 solution (experimental procedure and conditions have been described in section 3.2.8.1). The experiment was conducted using 10 ppm initial concentration of BPA or 2-NP, 60 L tank, and two jets as an impingement device, optimum applied pressure (4 bar) for 120 minutes. The detailed experimental procedure and instrumental analysis was outlined in Section 3.3.2.2 (ii) and 3.4.12 respectively. The results of the effects of solution pH on the BPA or 2-NP removal efficiency by the jet loop reactor are illustrated in Figure 6.3. Figure 6.3 (a) and (b) shows BPA removal efficiency and the pseudo-first order kinetics plot at different operating solution pH as a function of treatment time. While Figure 6.4 (a) and (b) depicts the 2-NP removal efficiency and pseudo-first order kinetics plot at different solution pH as a function of treatment time. The apparent rate constant (k), pollutant conversion rate and correlation coefficient at different solution pH at 90 minutes treatment time are given in Table 6.2. Beyond 90 minutes, no significant increase in the BPA or 2-NP removal efficiency was observed.

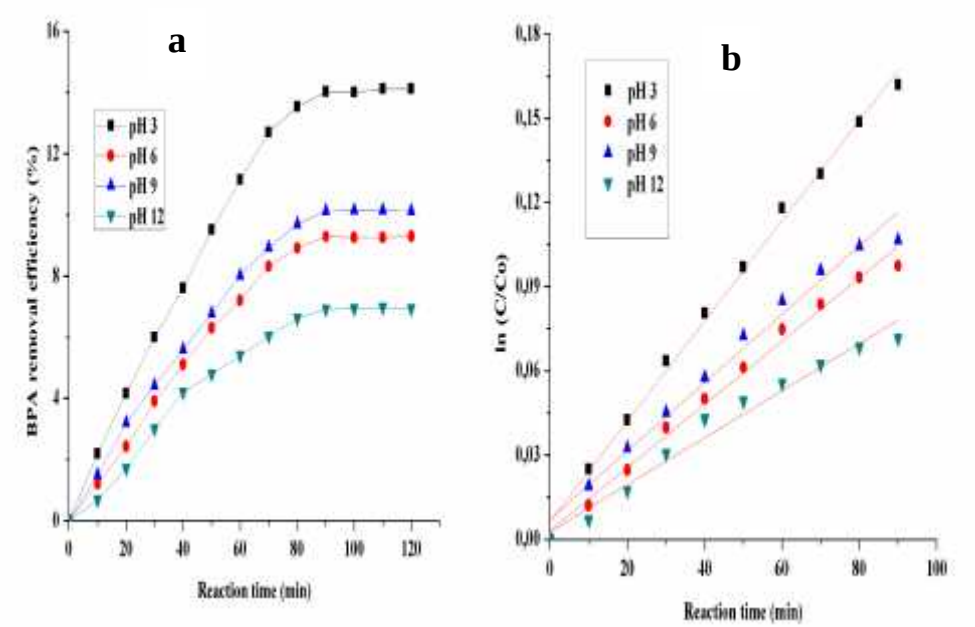

Figure 6.3: Effect of (a) solution pH on the BPA removal efficiency (b) degradation kinetics of bisphenol-A at different solution pH of the jet loop reactor. (Experimental conditions, BPA of concentration (10 ppm), volume of BPA or 2-NP solution in the tank tank (60 L), inlet applied pressure (4 bar), flow rate (0.7 L/s).

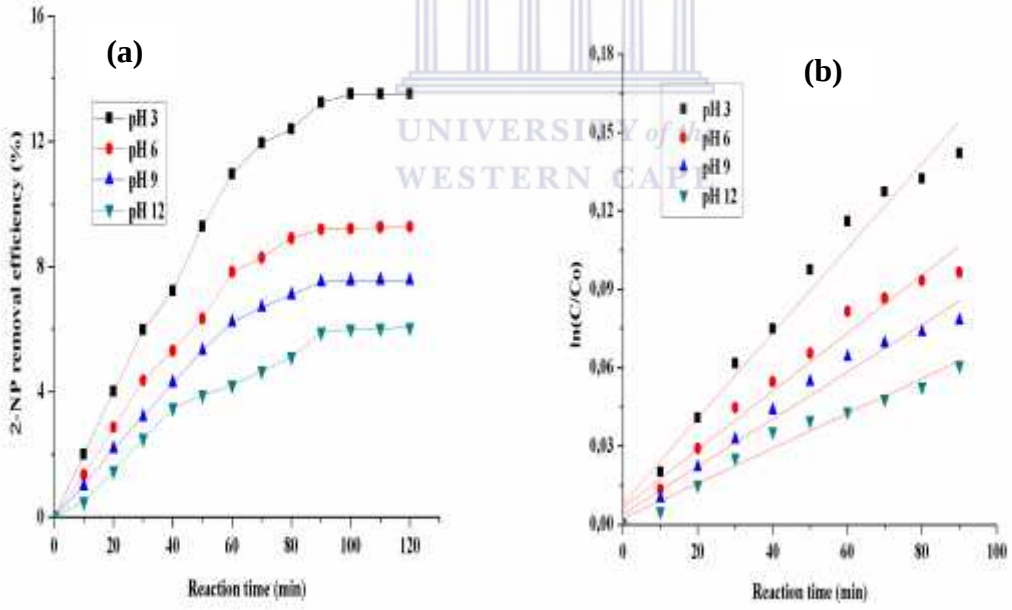

Figure 6.4: Effect of (a) solution pH on the 2-NP removal efficiency (b) degradation kinetics of 2-NP at different solution pH of the jet loop reactor. (Experimental conditions, 2-NP concentration (10 ppm), volume of BPA or 2-NP solution in the tank (60 L), inlet applied pressure (4 bar), flow rate (0.7 L/s).

Table 6.2: Effect of solution pH on the removal efficiency and rate constant of BPA or 2-NP at 90 min maximum (experimental conditions as in Figure 6.3 and 6.4)

Pollutants	Solution pH	Pollutant removal efficiency (%)	Pseudo-first order rate constant × 10^{-3} (min^{-1})	Correlation coefficient (R^2)
BPA	3	14.0	1.8	0.9958
	6	10.10	1.2	0.9829
	9	9.28	1.1	0.9905
	12	6.90	0.8	0.9801
2-NP	3	13.2	1.6	0.9777
	6	9.19	1.1	0.9725
	9	7.51	0.9	0.9757
	12	5.89	0.7	0.9724

As demonstrated in Figure 6.3 (a) and 6.4 (a), it can be seen that the removal efficiency of BPA or 2-NP decreases with an increase in solution pH from 3-12. Maximum removal efficiency of 14.0 % (BPA) or 13.2 % (2-NP) was observed at pH 3. While the minimum removal efficiency at pH 12 were 6.90 and 5.89 % respectively. In other words, acidic conditions favoured the removal of the pollutants more than neutral or alkaline medium. Similarly, the experimental data were fitted to pseudo-first order kinetic model to obtain the reaction rate constant (k) of BPA and 2-NP (Figure 6.3 (b) and 6.4 (b). As shown in Table 6.2, the rate constant of BPA increases from 8.0×10^{-4} min^{-1} to 1.8×10^{-3} min^{-1} as solution pH decreases from 12 to 3. A similar trend of increasing apparent rate constant with a decrease in pH from 12 to 3 was observed for 2-NP. This means that apparent rate constant (k) at pH 3 for both pollutants was two to three times greater than the rate constant obtained at pH 12. The increased conversion rate of BPA or 2-NP at lower solution pH value can be explained in term of the acid dissociation constant value and thermal degradation of the pollutants trapped within the jet impinging zone. The observed phenomenon can equally be elucidated with respect to the formation of OH radicals, which either reacted with the pollutants inside the jet reactor zone or within the bulk solution. For instance, BPA dissociated in solution into two

forms and existed as either an anionic species with acid dissociation constant (pKa1) value of 9.59 or as dianionic with pKa2 of 10.2 as shown in Figure 6.5.

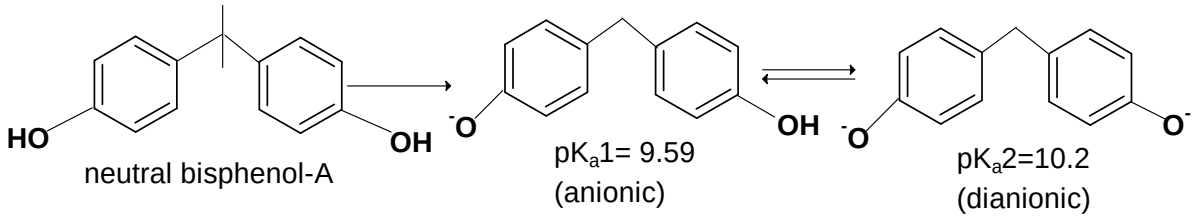

Figure 6.5: Dissociation of BPA in aqueous solution

While, the dissociation constant value of 2-NP is 6.80. At lower pH, when the solution pH value was less than the dissociation constant of the pollutants (pH<pKa), BPA or 2-NP existed as a molecular species and due to their hydrophobic nature, they penetrated or diffused into the jet cavity zone very easily, and were subjected to direct attack by OH radicals, thus responsible for higher removal rate. Another reason for the increment at lower pH may be attributed to the temperature effect due to continuous mixing of the pollutant molecules trapped within the jet reactor zone. It was found during the experiment that the solution temperature increased from 19ºC to 63ºC as the treatment time increased from 0-90 minutes. Although the temperature effect cannot be generalized, this was observed for all pH levels studied. As mentioned earlier at low pH, the pollutants existed as a molecular and hydrophobic species and as such the bond rupture phenomenon dominated relative to higher pH in which the pollutants existed in ionic or hydrophilic state. The other possibility may be due to the fact that acidic conditions were more favourable to the formation of OH radicals than the basic medium and lower recombination of the generated OH radicals predominate. Therefore, the obtained higher removal rate under acidic conditions (low pH) can be linked two reaction mechanisms taking place concurrently: thermal degradation and direct formation of OH radicals inside the jet reactor zone.

Whereas, at higher pH (pH >pKa) (under basic conditions), the pollutants exist as ionic species in the bulk solution and was less susceptible to OH radicals in the bulk solution or outside the jet reactor chamber, thus resulting in the lower removal rate. It should be noted that the recombination reaction of the generated OH radicals to form H_2O_2 predominate at higher pH, which reduced the amount of OH radicals and thus could be responsible for the lower pollutant conversion rate and apparent rate constant (k) obtained in alkaline medium. Since the removal rate and reaction rate constant were higher at lower pH (3), pH 3 was

chosen as the optimum value and was used for the remaining set of experiments. Similar findings on the influence of solution pH on the removal efficiency of pollutants have been reported in the literature. Gogate and Patil, (2015) studied the influence of solution pH on the degradation of triazophos using hydrodynamic cavitation. The authors revealed that maximum degradation efficiency of 49.7 % and corresponding first order rate constant of 5.87×10^{-3} min^{-1} was observed at pH 3 relative to 33.65 % and 3.39×10^{-3} min^{-1} obtained at pH 8. The slight or marginal difference in the removal efficiency or apparent rate constant was ascribed to the fact that at low pH (acidic conditions), the reaction was more rapid than under alkaline conditions, where H_2O_2 formation predominates. Joshi and Gogate, (2012) demonstrated that acidic conditions favoured the decomposition of dichlorvos using hydrodynamic cavitation and maximum degradation efficiency of 16 % was obtained at pH 3. In the same vein, Gore et al., (2014) found that the maximum removal efficiency of reactive orange 4 at pH 2 was 37.23 % and thereafter declined abruptly to 4.6 % at pH 10. The authors concluded that acidic conditions favoured the removal efficiency due to the formation of highly electrophilic OH radicals of higher oxidation potentials and decomposition of H_2O_2.

6.2.3 *Effect of initial concentration of BPA or 2-NP*

The overall performance of the jet impingement process is often dependent on the optimum concentration of organic pollutant to be treated. The determination of the optimal concentration is a function of solution pH, inlet pressure and available free radicals in the jet reactor cavity zone. Thus, the influence of the initial pollutant concentration in the range of 10 – 30 mg/L on the removal efficiency of BPA or 2-NP using the jet impingement process at optimal solution pH of 3 and inlet applied pressure of 4 bar was investigated. The detailed experimental procedure under the optimised conditions of inlet applied pressure and solution pH have been outlined in Section 3.3.2.2 (iii). The obtained results are expressed in terms of removal efficiency and pseudo-first order reaction rate constant depicted in Figure 6.6 and Table 6.3 respectively. Figure 6.6 (a) illustrates the removal efficiency of BPA and (b) pseudo-first order kinetics plot at different initial concentration of BPA. While Figure 6.7 (a) represents the conversion rate of 2-NP (b) degradation first-order kinetic plot over the concentration range of 10-30 ppm.

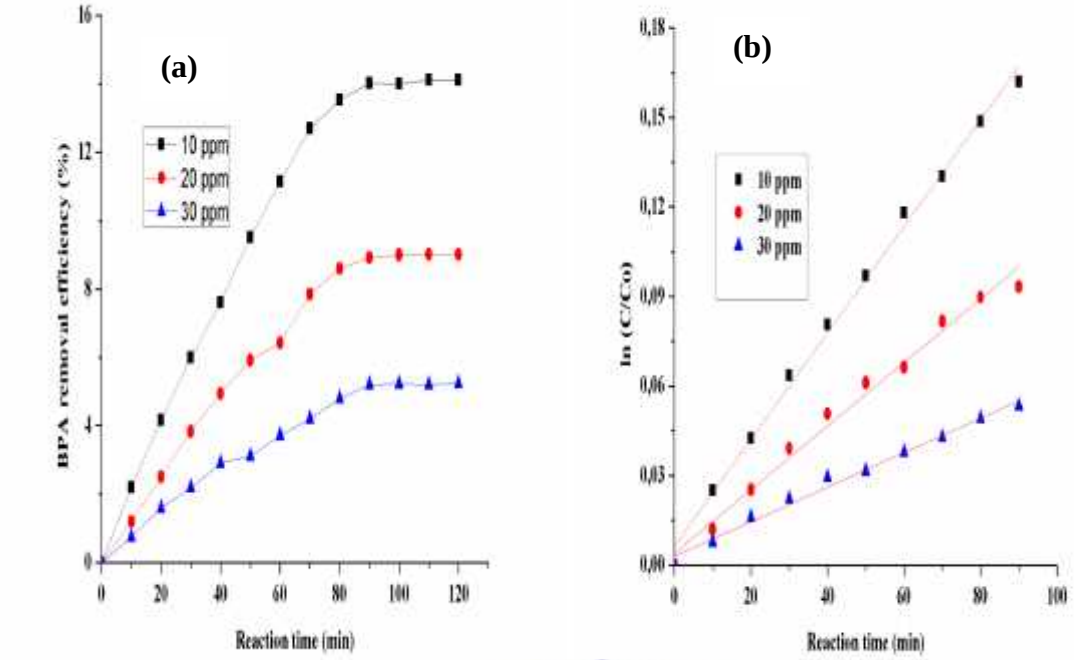

Figure 6.6: Effect of (a) initial concentration of BPA on the BPA removal efficiency (b) degradation kinetics of bisphenol-A at different concentration of the jet loop reactor (Experimental conditions solution pH (3), volume of BPA solution in the tank (60 L), inlet applied pressure (4 bar), flow rate (0.7 L/s)

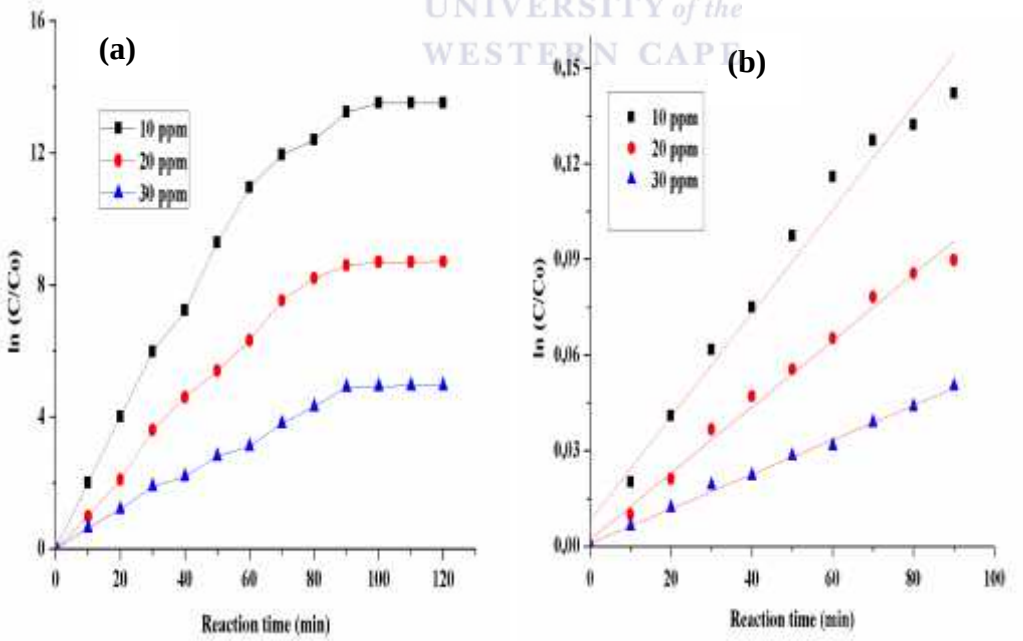

Figure 6.7: Effect of (a) initial concentration of 2-NP on 2-NP removal efficiency (b) degradation kinetics of 2-NP at different initial concentration of the jet loop reactor. Experimental conditions solution pH (3), volume of 2-NP solution in the tank (60 L), inlet applied pressure (4 bar), flow rate (0.7 L/s)

Table 6.3:Effect of initial concentration on the removal efficiency and rate constant of BPA or 2-NP at 90 min maximum (experimental conditions as in Figure 6.6 and 6.7)

Pollutants	Initial concentration of the pollutants (ppm)	Pollutant removal efficiency (%)	Pseudo-first order rate constant × 10^{-3} (min^{-1})	Correlation coefficient (R^2)
BPA	10	14.0	1.8	0.9958
	20	8.59	1.1	0.9875
	30	5.2	0.6	0.9891
2-NP	10	13.2	1.6	0.9887
	20	8.09	1.0	0.9905
	30	4.9	0.5	0.9961

It can be seen from Figure 6.6 (a) and 6.7 (a) that the removal efficiency reduced with an increase in the initial concentration of the pollutants from 10 – 30 ppm. For instance, as the BPA concentration increased from 10 – 30 ppm, the removal efficiency decreased from 14.0 % to 5.2 % within 90 minutes. Similarly, the 2-NP removal efficiency at 10 ppm was 13.2 %, which was approximately three times higher than the removal efficiency obtained at 30 ppm (see Table 6.3). This indicated that the conversion rate or removal efficiency was inversely proportional to the initial concentration of the pollutant. The kinetic study also revealed the rate constant value decreased with an increase in initial concentration of the pollutants. Notably, the apparent rate constant of BPA reduced from 1.8×10^{-3} min^{-1} to 6.0×10^{-4} min^{-1} as the initial concentration increased from 10 – 30 ppm. In the same vein, the apparent rate constant of 2-NP under the optimum solution pH (3) and inlet pressure of 4 bar, decreased from 1.6×10^{-3} min^{-1} to 5.0×10^{-4} min^{-1} over the same concentration range as BPA. The observed trend in Table 6.3 can be explained in terms of the number of BPA or 2-NP molecules against the available OH radicals in the jet cavity zone. With an increase in the concentration of the pollutants, the number of BPA or 2-NP molecules present in the solution increased while the concentration of OH radicals still remained the same. At higher concentration of BPA or 2-NP, complete oxidation cannot be achieved due to stronger

competition between the intermediates and original compounds for the available OH radicals. Owing to the limited amount of OH radicals at higher concentration of the pollutants, the removal efficiency and reaction rate constant decreased. The obtained results in this study is similar to the outcome of the investigation conducted by Basiri Parsa and Zonouzian, (2013) on the degradation of Rhodamine B using hydrodynamic cavitation. The authors observed that the extent of decolourization and apparent rate constant at 2 mg/L solution was 87 %, and 9.0×10^{-3} min^{-1}, which however declined to 34 %, and 1.6×10^{-3} min^{-1} at 14 mg/L. The observed decrease was attributed to low concentration of OH radicals at higher concentration of the pollutants.

6.2.4 *Effect of radical scavengers*

As mentioned in Chapter five Section 5.1.3, it was established that addition of radical scavengers such as NaCl and Na_2CO_3 to solutions containing BPA or 2-NP reduced the removal efficiency of a dielectric barrier discharge system due to consumption of the generated free OH radicals. While the BPA or 2-NP degradation was slightly improved with addition of Na_2SO_4. In this section, the influence of addition of Na_2CO_3, NaCl and Na_2SO_4 at a fixed concentration (60 mg/L) on the BPA or 2-NP removal efficiency via jet impingement process were evaluated under the optimal conditions of solution pH (3), inlet applied pressure (4 bar). The detailed experimental procedure has been described in Section 3.3.2.2 (iv). The obtained results on the effect of the addition of different radical scavengers expressed in terms of removal efficiency of BPA or 2-NP are depicted in Figure 6.8 and 6.9 respectively. While the pseudo-first order rate constant of BPA or 2-NP at 90 min maximum are shown in Table 6.4.

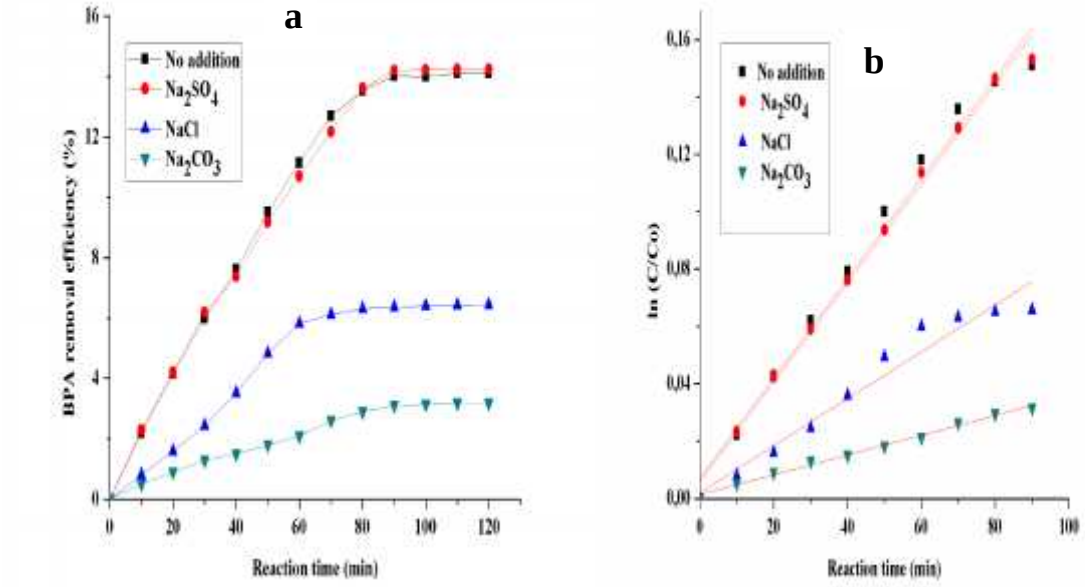

Figure 6.8: Effect of (a) radical scavengers addition on the BPA removal efficiency (b) degradation kinetics of bisphenol-A with different radical scavengers of the jet loop reactor Experimental conditions solution pH (3), concentration of BPA (10 ppm), volume of BPA solution in the tank (60 L), inlet applied pressure (4 bar), flow rate (0.7 L/s), 60 mg/L of Na_2SO_4, NaCl or Na_2CO_3.

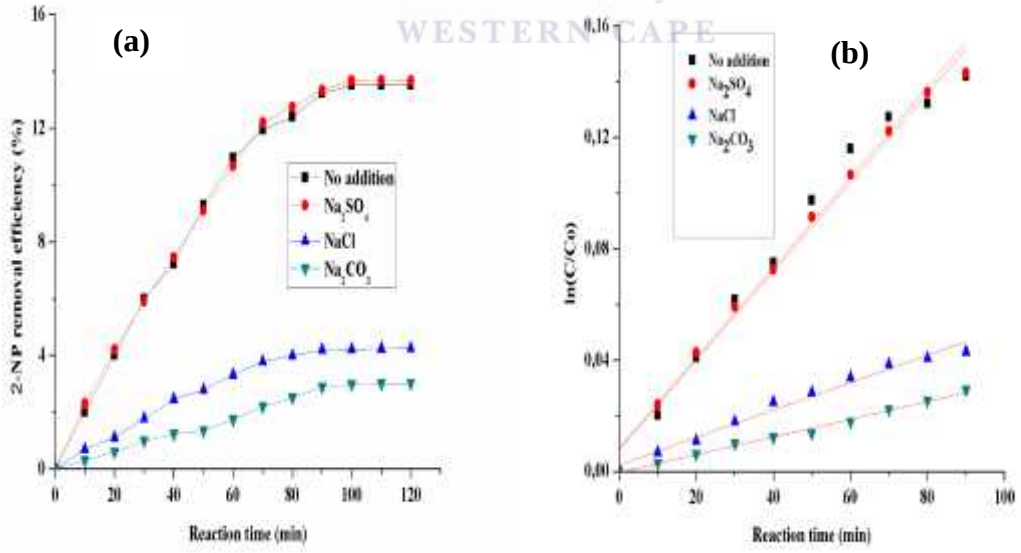

Figure 6.9: Effect of (a) radical scavengers on the 2-NP removal efficiency (b) degradation kinetics of 2-NP with different radical scavengers of the jet loop reactor. Experimental conditions solution pH (3), concentration of 2-NP (10 ppm), volume of 2-NP solution in the tank (60 L), inlet applied pressure (4 bar), flow rate (0.7 L/s), 60 mg/L of Na_2SO_4, NaCl or Na_2CO_3.

Table 6.4: Effect of addition of different radical scavengers on the conversion rate and rate constant of BPA or 2-NP at 90 min maximum (experimental conditions as in Figure 6.8 and 6.9)

Pollutants	Radical scavengers (ppm)	Pollutant removal efficiency (%)	Pseudo-first order rate constant (min^{-1})	Correlation coefficient (R^2)
BPA	No addition	14.0	0.0018	0.9953
	Na_2SO_4	14.2	0.0018	0.9943
	NaCl	6.36	0.0008	0.9549
	Na_2CO_3	3.1	0.0003	0.9928
2-NP	No addition	13.2	0.0016	0.9777
	Na_2SO_4	13.3	0.0016	0.9914
	NaCl	4.21	0.0005	0.9810
	Na_2CO_3	2.88	0.0003	0.9919

According to Figure 6.8 (a) and 6.9 (a), it can be seen that addition of NaCl and Na_2CO_3 inhibited the pollutants removal efficiency siginificantly. For instance, BPA removal efficiency decreased to 6.36 % and 3.1 % in the presence of NaCl and Na_2CO_3 compared to 14.0 % in the absence of the two scavengers. In the same vein, 2-NP removal efficiency was considerably reduced to 4.21 % and 2.88 % respectively with addition of NaCl and Na_2CO_3 compared to 13.2 % without the addition of scavengers. On the other hand, the BPA or 2-NP conversion rate was slightly enhanced by 0.2 or 0.1 % upon the addition of Na_2SO_4. According to Table 6.4, the apparent rate constant of BPA found in the absence of a scavenger decreased significantly from 1.8×10^{-3} min^{-1} to 8.0×10^{-4} and 3.0×10^{-4} min^{-1} upon the addition of NaCl and Na_2CO_3 respectively. A similar trend in terms of reduction in the rate constant was observed for 2-NP in the presence of NaCl and Na_2CO_3. In contrast, there was no differences in the rate constants of BPA or 2-NP with or without addition of Na_2SO_4. This indicated that BPA or 2-NP removal efficiency and rate constant was not inhibited with addition of Na_2SO_4. From Table 6.4, it is obvious that the BPA or 2-NP removal efficiency and apparent rate constant was slightly enhanced or similar with addition of Na_2SO_4 and but lowest in the presence of Na_2CO_3. This showed that Na_2CO_3 consumed more of the available OH radicals in the jet cavity zone or bulk solution than other scavengers. The possible reasons for the decrease in the BPA or 2-NP degradation upon the addition of the radical

scavengers are similar to the argument proposed in Chapter five, Section 5.2.3. The outcome of this study supports the findings of Bagal and Gogate, (2014 a) who demonstrated a decreased in diclofenac removal efficiency from 95 % to 31 % upon the addition of 2 g/L Na_2CO_3 to 5 L solution containing 20 ppm diclofenac.

The implication of the effect of radical scavengers would be that when pollutants are dispersed in effluents that contain salts, it can be expected that the decomposition rate would be reduced. This most likely also means that if these pollutants end up in natural salty waters such as the ocean they would degrade more slowly, as naturally occurring oxidants formed by solar irradiation and oxygen interaction would be scavenged by salts or photolytic dissociation of water. This initial optimization of inlet pressure, solution pH and pollutant concentration of the jet loop reactor was investigated in order to establish the optimum operating conditions at which the maximum degradation rate of the pollutants occurred. The next set of experiments involved the combination of the jet loop reactor with UV-light or hydrogen peroxide or with both UV and H_2O_2 under the optimised conditions

6.2.5 *Blank or control experiments*

Prior to the application of the combined Jet loop reactor/UV-light/H_2O_2 to decompose BPA or 2-NP in water, different blank experiments were conducted under the optimised condition of solution pH (3) and inlet applied pressure (4 bar) in the absence of the jet loop reactor. This was done in order to properly evaluate the removal efficiency of the individual treatment options (UV, H_2O_2) or the combined UV/H_2O_2 system towards BPA or 2-NP in water. The detailed experimental procedures that were followed to evaluate the capacity of UV-light, H_2O_2 or the combination of UV/H_2O_2 to decompose or perhaps remove BPA or 2-NP in water have been described in Section 3.3.3 subsection i-iii. The residual concentration of BPA or 2-NP was determined using analytical technique described in section 3.4.12. The results obtained after 120 minutes reaction time expressed in terms of pollutant removal efficiency and pseudo-first order kinetic plot of BPA or 2-NP are illustrated in Figure 6.10 and Figure 6.11 respectively. The removal efficiency and apparent rate constant of BPA or 2-NP at 90 min maximum is also represented in Table 6.5.

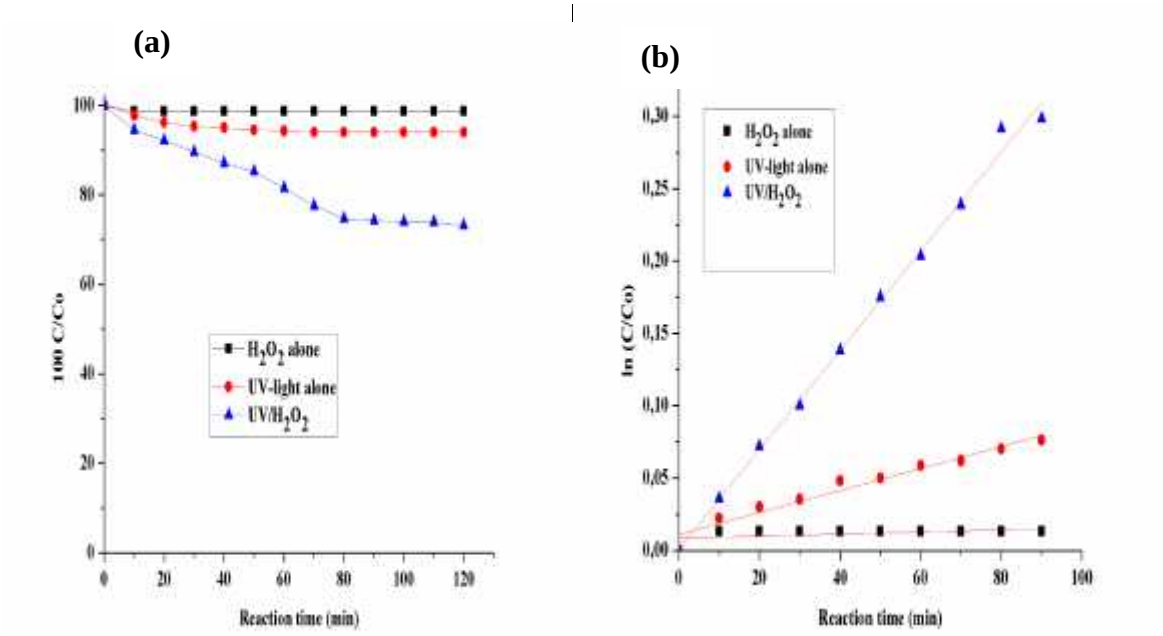

Figure 6.10: Blank experiment for the removal of BPA in water by (a) H_2O_2 alone, UV light alone, and UV/H_2O_2 (b) pseudo-first order kinetic plots of BPA removal (Concentration of BPA (10 ppm), concentration of H_2O_2 (0.34 g/L, solution pH (3), volume of BPA (60 L))

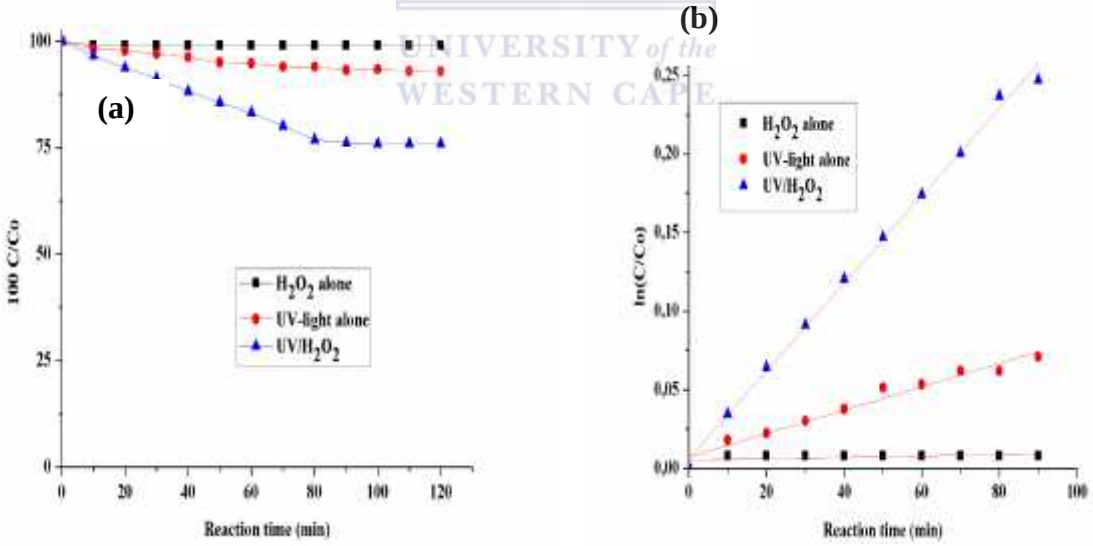

Figure 6.11: Blank experiment for the removal of 2-NP in water by (a) H_2O_2 alone, UV light alone and UV/H_2O_2 (b) pseudo-first order kinetic plots of 2-NP removal (Concentration of 2-NP (10 ppm), concentration of H_2O_2 (0.34 g/L, solution pH (3), volume of BPA (60 L))

Table 6.5: Effect of addition of H_2O_2, UV-light and UV/H_2O_2 on the conversion rate and rate constant of BPA or 2-NP at 90 min maximum (experimental conditions as in Figure 6.10 and Figure 6.11)

Pollutants	Treatment processes	Pollutant removal efficiency (%) at 90 min	Pseudo-first order rate constant (min^{-1})	Correlation coefficient (R^2)
BPA	H_2O_2	1.3	0.00007	0.2727
	UV-light	6.8	0.0008	0.9555
	UV/H_2O_2	25.8	0.0034	0.9955
2-NP	H_2O_2	1.0	0.00004	0.2727
	UV-light	6.3	0.0007	0.9671
	UV/H_2O_2	23.9	0.0028	0.9967

According to Figure 6.10 (a) and 6.11 (a), it can be observed that there was little or no removal of BPA or 2-NP with the addition of H_2O_2 alone. Whereas, a slight removal of 6.8 % (BPA) and 6.3 % (2-NP) was noticed in the presence of in-line UV light on its own. More so, with combination of in-line UV-light and H_2O_2, the BPA or 2-NP conversion rate increased considerably. Maximum BPA or 2-NP removal efficiency of 25.8 and 23.9% were obtained within 90 minutes respectively (see Table 6.5). Additionally, the experimental data on the BPA or 2-NP removal rate were fitted into pseudo-first order kinetic plot and illustrated in Figure 6.10 (b) and 6.11 (b). As shown in Table 6.5, it was found that that the apparent rate constant of BPA via combined UV/H_2O_2 was 3.4×10^{-3} min^{-1} compared to 8.0×10^{-4} min^{-1} and 7.0×10^{-5} min^{-1} obtained via the UV and H_2O_2 alone. In the same vein, the apparent rate constant of 2-NP using combined UV/H_2O_2 was four and seventy times greater than that obtained with UV and H_2O_2 alone. With H_2O_2 alone, the pollutant conversion rate was less than 1.5 % in spite of peroxide having a high oxidation potential of 1.78 V. This is because the dissociation rate of H_2O_2 into OH radicals was low especially when used alone under such a conventional flowing system. The H_2O_2 was passed through the bypass line without the JLR. It is possible to conclude that addition of H_2O_2 alone did not significantly influence the pollutant removal efficiency. The obtained 6.8 or 6.3 % removal rate due to direct photolysis with UV light only can be explained on the basis of photolytic dissociation of water molecules into OH radicals. The attack on the pollutants by the low quantum of OH

radicals was responsible for the low removal rate. However, the increase in the pollutant removal efficiency and higher apparent rate constant of the combined UV/H_2O_2 over each individual process (UV or H_2O_2) was probably due to the dual generation of OH radicals in the combined system. Firstly, because of the photolytic cleavage of water molecules (equation 6.2) and secondly because of the dissociation of H_2O_2 under UV-light irradiation (equation 6.3). Both processes increased the yield of the OH radicals in the solution.

$$H_2O + UV \rightarrow OH^{\cdot} + H^{+} \quad \text{.....(6.2)}$$

$$H_2O_2 + UV \rightarrow 2OH^{\cdot} \quad \text{.....(6.3)}$$

Thus, the combined effect of the generated OH radicals was considered to be responsible for the higher removal rate and reaction rate constant. The 23-26 % pollutant removal rate obtained via UV/H_2O_2 system showed that the extent of removal of BPA or 2-NP depended on both the UV and H_2O_2. This suggests the existence of a synergetic effect between the two processes. It is noted that hydrid system of UV/H_2O_2 gave a higher removal rate than the jet loop system alone but individually (UV and H_2O_2) were not effective.

6.3 Degradation of BPA or 2-NP using JLR alone or combining JLR/H_2O_2

The mechanism of decomposition of BPA or 2-NP via the jet impingement process is either by thermal pyrolysis of the pollutant molecules trapped within the jet reactor cavity or usually by the generated OH radicals. However, the concentration of OH radicals produced by the jet loop reactor may be enhanced by adding a process intensifier such as hydrogen peroxide. In the present investigation, the integrated system of JLR with different dosages of H_2O_2 was studied. The concentration of H_2O_2 was varied from 0.17 g/L to 2.04 g/L and separately added to 60 L aqueous solution of 10 mg/L BPA or 2-NP in the holding tank under the optimum conditions of inlet pressure (4 bar), flow rate (0.9 L/min) and solution pH (3). The pollutants and H_2O_2 mole ratio in the 60 L tank was in the range of 1:17 to 1: 204. Before H_2O_2 was added, the solution pH was 3 which was however reduced to 1.9 when the peroxide solution was added to the aqueous solution of BPA or 2-NP. The detailed experimental procedure has been provided in Section 3.3.3, subsection iv. The residual concentration of BPA or 2-NP was determined using HPLC described in section 3.4.12. The pollutant removal efficiency at every treatment time was calculated using the formula given in Chapter three Section 3.2.6. The results of the removal of BPA or 2-NP and pseudo-first order kinetic plots using JLR/H_2O_2 system are provided in Figure 6.12 (a-b) and Figure 6.13 (a-b) respectively.

The apparent rate constant (k) and maximum removal rate at 90 min for all the different treatment approaches are shown in Table 6.6 and 6.7 respectively.

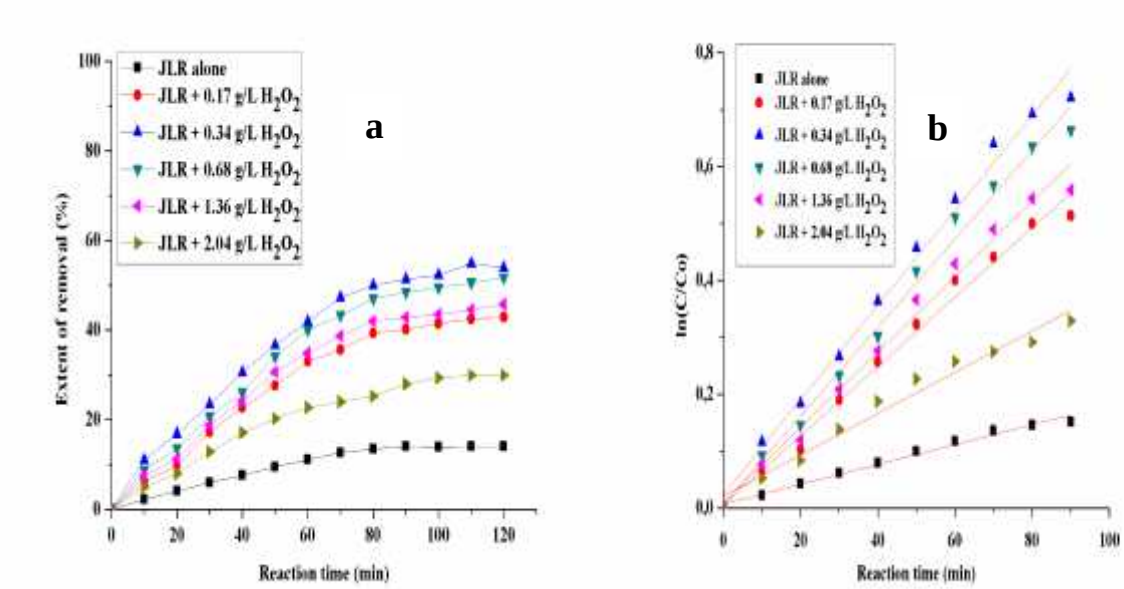

Figure 6.12: Effect of (a) addition of different concentrations of H_2O_2 on the extent of BPA removal and (b) pseudo-first order kinetics plots of BPA, using JLR/H_2O_2 system. Experimental conditions: initial concentration of BPA, 10 ppm, solution pH (3), inlet applied pressure (4 bar), flow rate 0.7 L/s, volume of aqueous BPA, 60 L.

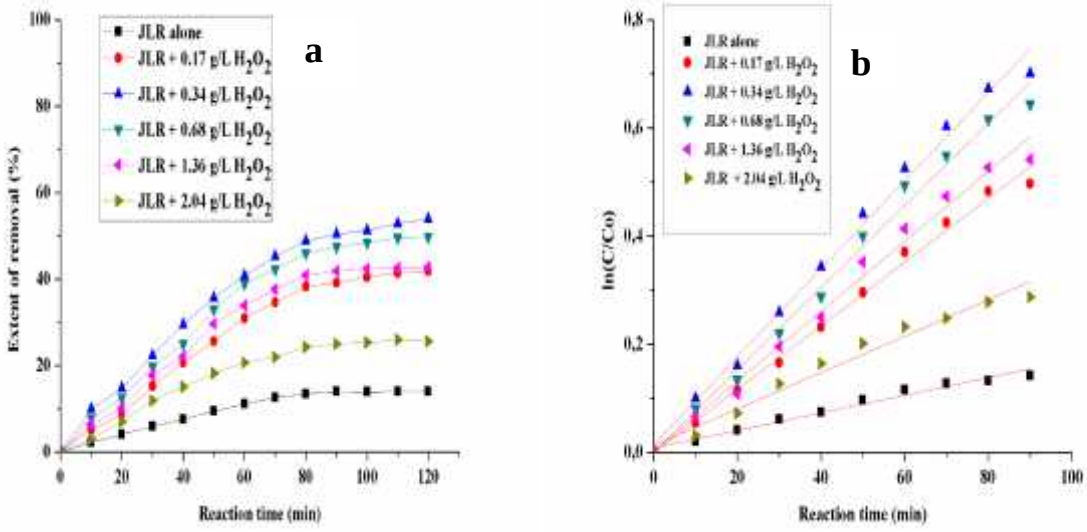

Figure 6.13: Effect of (a) addition of different concentrations of H_2O_2 on the extent of 2-NP removal in water (b) pseudo-first order kinetic plot of 2-NP using JLR/H_2O_2 system. (Experimental conditions: initial concentration of 2-NP, 10 ppm, solution pH (3), inlet applied pressure (4 bar), flow rate 0.7 L/s, volume of 2-NP solution, 60 L.

Table 6.6: Extent of BPA removal efficiency and rate constant using a combination of JLR with different concentrations of H_2O_2 (experimental conditions as in Figure 6.12)

Treatment processes	Maximum extent of removal after 90 min (%)	Pseudo-first order rate constant ($k \times 10^{-3}$)(min^{-1})	Correlation coefficient (R^2)	Synergistic index (f)
H_2O_2 alone	1.3	0.07	0.2727	-
JLR alone	14.0	1.8	0.9862	-
JLR + 0.17 g/L H_2O_2	40.1	6.1	0.9889	3.26
JLR + 0.34 g/L H_2O_2	51.3	8.3	0.9908	4.44
JLR + 0.68 g/L H_2O_2	48.5	7.8	0.9909	4.17
JLR + 1.36 g/L H_2O_2	42.8	6.6	0.9885	3.52
JLR + 2.04 g/L H_2O_2	28.1	3.6	0.9749	1.93

Table 6.7: Removal efficiency and rate constant of 2-NP using a combination of JLR with different concentrations of H_2O_2 (experimental conditions as in Figure 6.13)

Treatment processes	Maximum extent of removal after 90 min (%)	Pseudo-first order rate constant ($k \times 10^{-3}$) (min^{-1})	Correlation coefficient (R^2)	Synergistic index (f)
H_2O_2 alone	1.0	0.04	0.2727	-
JLR alone	13.2	1.6	0.9862	-
JLR + 0.17 g/L H_2O_2	39.1	5.9	0.9936	3.60
JLR + 0.34 g/L H_2O_2	50.1	8.1	0.9928	4.94
JLR + 0.68 g/L H_2O_2	47.2	7.6	0.9908	4.63
JLR + 1.36 g/L H_2O_2	41.5	6.5	0.9882	3.93
JLR + 2.04 g/L H_2O_2	25.2	3.4	0.9749	2.07

It can be observed from Figure 6.12 (a) and 6.13 (a) that the BPA or 2-NP removal efficiency by JLR alone at optimum inlet pressure (4 bar), solution pH (3) increases with an increasing reaction time till 90 min. The maximum removal efficiency of BPA or 2-NP at 90 min was 14 % and 13.2 % respectively. With the addition of 0.17 g/L H_2O_2 to JLR, the maximum removal efficiency for BPA at 90 minutes was 40.1 %, which was higher than 14 % obtained using JLR alone. Similarly, 2-NP removal efficiency which was 13.2 % in the absence of

0.17 g/L H_2O_2 increased to 39.1 % in the presence of 0.17 g/L H_2O_2 at 90 min. With an increase in H_2O_2 dosage to 0.34 g/L, the extent of removal of BPA or 2-NP was rapid and more than 50 % removal rate was achieved for both pollutants under the same applied reaction conditions. Thus, the increase in the concentration of H_2O_2 from 0.17 g/L to 0.34 g/L resulted in an increase in the pollutant removal efficiency from 13.2 or 14 % to 50 %. With further increases in H_2O_2 dosage to 0.68 g/L, BPA or 2-NP removal efficiency slightly reduced to 48.5 % and 47.2 % respectively. Conversely, when 1.36 g/L H_2O_2 was introduced to the holding tank containing the pollutants, the BPA or 2-NP removal rate decreased to 42.8 % and 41.5 % respectively. Similarly, with addition of 2.04 g/L H_2O_2 to the holding tank, the BPA or 2-NP removal efficiency significantly reduced to 28.1 % and 25.2 %. It can be seen that the extent of removal of BPA or 2-NP in water increased with an increase in the concentration of H_2O_2 till 0.34 g/L and beyond this value, the pollutant removal efficiency was reduced. This indicates an optimum dosage of H_2O_2 to be 0.34 g/L under the applied conditions.

Furthermore, the data obtained of all the combinations of JLR with different concentrations of H_2O_2 were fitted into a pseudo-first order kinetic model. It was found that all the experimental data obeyed the pseudo first order kinetic model, irrespective of the amount of H_2O_2 added to the JLR which suggests that the increasing loading of H_2O_2 did not essentially result in the alteration of the degradation mechanism. According to Table 6.6, the apparent rate constant increased with an increase in H_2O_2 dosage and the maximum reaction rate constant of 8.3×10^{-3} min^{-1} was obtained with JLR combined with 0.34 g/L H_2O_2 at 90 min. The rate constant value of 8.3×10^{-3} min^{-1} was however higher than 7.0×10^{-5} min^{-1} and 1.6×10^{-3} min^{-1} obtained for H_2O_2 and JLR alone. Similarly, the degradation rate constant of 2-NP increased from 5.9×10^{-3} min^{-1} to 8.1×10^{-3} min^{-1} as the concentration of H_2O_2 added to the JLR increased from 0.17 g/L to 0.34 g/L (Table 6.7). On the contrary, the degradation rate constant decreased with a further increase in the H_2O_2 dosage. It is obvious that higher amounts of H_2O_2 beyond the optimal value (0.34 g/L) resulted in lower removal efficiency and reaction rate constant. The increase in the removal efficiency and apparent rate constant with an increase in the concentration of H_2O_2 up to the optimum value of 0.34 g/L can be attributed to the dissociation reaction of H_2O_2 to OH radicals, which predominates over the scavenging and recombination reactions. The dissociation reaction of H_2O_2 occurred under the applied conditions of high temperature and pressure within the jet reactor cavity that generated OH radicals. The generated OH radicals attacked the pollutants causing bonds to

rupture and thus enhanced the degradation rate. Besides, the initial increase in the removal rate and apparent rate constant can equally be linked to the role played by the generated OH radicals via the thermal decomposition of water molecules trapped inside the jet reactor cavity (Bagal and Gogate, 2013), as can be seen by values obtained with JLR on its own.

On the other hand, at higher dosages of H_2O_2 beyond the optimum value, scavenging and consumption of the generated OH radicals by the undissociated H_2O_2 predominated, and lowered the observed pollutants degradation rate. The reduction in the pollutants removal rate can equally be explained in terms of the recombination reaction of the generated OH radicals as illustrated in equation 8. It should be noted that, the pollutants removal efficiency and apparent rate constant (k) using combined JLR and optimum dosage of H_2O_2 was 3.5 and 5.0 times greater than that obtained with JLR alone irrespective of the pollutants. This showed that jet loop reactor combined with the optimum amounts of H_2O_2 is better and faster to remove the two pollutants compared to JLR alone, which suggests the existence of a synergetic effect between the two individual processes. The synergetic index value (f) between the two integrated processes was estimated by substituting the individual treatment rate constant into equation 6.4.

Synergetic index (f) $= \frac{k(JLR+H_2O_2)}{k(JLR)+k(H_2O_2)}$ …… (6.4)

The synergetic index value of JLR combined with different concentrations of H_2O_2 is shown in Table 6.6 and 6.7 respectively. Detailed determination of the synergetic index value is provided in Appendix 6. It was noticed that the synergetic index value of the combined system was higher relative to the individual process such as JLR or H_2O_2, and however reduced with an increase in H_2O_2 dose. At the obtained optimum dosage of H_2O_2, (0.34 g/L), the synergetic index value for BPA or 2-NP was 4.44 and 4.94. This suggests that in order to effectively mineralize the two pollutants, H_2O_2 would be more effectively applied when integrated with the JLR. Furthermore, the synergetic coefficient value was an indication of an additional source of OH radicals apart from the JLR, which can be linked to the dissociation reaction of H_2O_2 under intense mixing and the impingement process. Thus, the higher yields of OH radicals was deemed responsible for the observed extent of removal and apparent rate constant by the JLR/H_2O_2 system. It is noteworthy that the two pollutants exhibited similar removal/degradation patterns, which was evidence of being attacked by the same reactive species (OH radicals or H_2O_2). Since there was no further increase in the removal efficiency of BPA or 2-NP after the optimal value, 0.34 g/L H_2O_2 was selected as the optimal concentration. Zupanc et al., (2014) reported a similar optimum value of 0.34 g/L during the

degradation of selected pharmaceuticals by shear-induced hydrodynamic process. Several other authors have equally demonstrated an optimium concentration of H_2O_2 during the degradation of organic pollutants by the combination of hydrodynamic cavitation (HC) and hydrogen peroxide namely: Bagal and Gogate, (2013), (2,4-dinitrophenol, 100 mg/L); Bagal and Gogate, (2014 a), (diclofenac, 0.2 g/L); Gore et al., (2014), (60 mg/L, reactive orange 4); Raut-Jadhav et al., (2013), imidacloprid, 3.90 mmol/L); Pradhan and Gogate, (2010), p-nitrophenol, 5 g/L. All the authors concluded that the observed intensification in the pollutant removal efficiency and reaction rate constant at optimium dosage of H_2O_2 was due to the dissociative effect of H_2O_2 to OH radicals as well as the existence of a synergetic effect between the hybrid system (HC/H_2O_2) over the individual process such as HC and H_2O_2. Furthermore, the synergetic index value of 4.44 or 4.94 obtained in this study for BPA or 2-NP (see Table 6.6 and 6.7) is greater than 1.4, 2.5, 3.87 reported by Bagal and Gogate, (2013), Bagal and Gogate, (2014a) and Gore et al., (2014) during the decomposition of diclofenac, 2,4-dinitrophenol and reactive orange 4 by combined HC/H_2O_2. The differences in the removal efficiency, apparent rate constant and synergetic index value and even the establishment of an optimum H_2O_2 dosage is dependent on several factors. Some of the factors include, nature and reactivity of the pollutants, volume of the aqueous solution in the holding tank, inlet pressure, solution pH, concentration of the pollutants, and concentration of H_2O_2 and mode of generation of OH radicals either by impingement or cavitation.

6.4 Degradation of BPA or 2-NP using JLR alone, JLR/UV and JLR/UV/H_2O_2

In order to increase the yield of OH radicals and enhance the pollutant removal efficiency, the in-line UV lamp was integrated with the jet loop reactor. Furthermore, the optimum concentration of H_2O_2 (0.34 g/L) was added to the combined JLR/UV to increase the concentration of OH radicals and to improve the mineralization rate. Thus, the efficiency of the individual (JLR alone) and combined processes (JLR/UV, JLR/UV/H_2O_2) were investigated and compared accordingly on the extent of removal of BPA or 2-NP in aqueous solution. The detailed experimental procedure under the optimised conditions of inlet applied pressure (4 bar), solution pH (3), concentration of H_2O_2 (0.34 g/L) was outlined in Chapter three Section 3.3.3 subsection (v) and (vi). Figure 6.14 and 6.15 represents the extent of removal and pseudo-first kinetic plot of BPA or 2-NP using combined JLR/UV and JLR/UV/H_2O_2. The maximum extent of removal and degradation rate constant of BPA or 2-NP via the different treatment approaches at 90 minutes are depicted in Table 6.8.

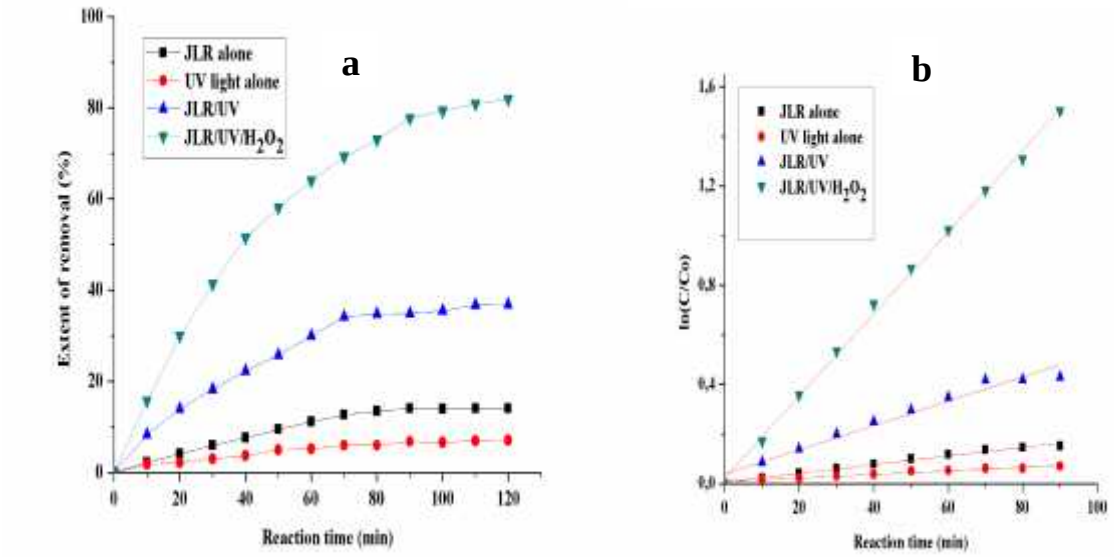

Figure 6.14: Extent of (a) removal of BPA (b) pseudo-first order kinetic plot of BPA using JLR/UV and JLR/UV/H_2O_2 system. (Experimental conditions: initial concentration of BPA, 10 ppm, solution pH (3), inlet applied pressure (4 bar), concentration of H_2O_2 (0.34 g/L), flow rate 0.7 L/s, volume of aqueous BPA solution, 60 L.

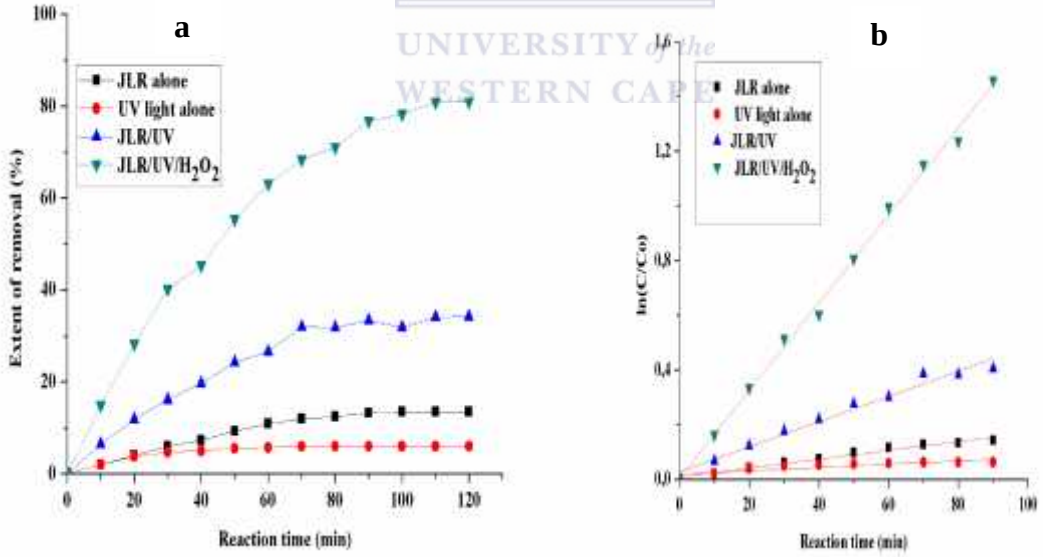

Figure 6.15: Extent of (a) removal of 2-NP (b) pseudo-first order kinetic plot of 2-NP by JLR/UV and JLR/UV/H_2O_2 system. (Experimental conditions: initial concentration of 2-NP, 10 ppm, solution pH (3), inlet applied pressure (4 bar), concentration of H_2O_2 (0.34 g/L), flow rate (0.7 L/s), volume of aqueous 2-NP solution, (60 L).

According to Figure 6.14 (a) and 6.15 (a), it can be seen that the removal efficiency of BPA or 2-NP by UV-light alone without passing through the jet cavity increased linearly, and a low removal efficiency of BPA (6.8 %) and 2-NP (6.3 %) at 90 min reaction time was obtained. Similarly, removal efficiency of BPA and 2-NP by JLR alone under the optimised inlet pressure of 4 bar and solution pH 3 increased with an increase in reaction time till 90 min. Maximum removal efficiency of BPA or 2-NP by JLR under the optimised applied conditions was 14 % and 13.2 % respectively within 90 min. With the utilization of combined JLR and in-line-UV light, the maximum removal of BPA and 2-NP observed only increased to 34.9% and 33.2% respectively. It can be seen that incorporation of in-line UV light with JLR enhanced the pollutants removal efficiency by 14.1 % or 13.7 %. Furthermore, when the optimum dosage of the process intensifier such as H_2O_2 was integrated with JLR/UV, the extent of removal of BPA or 2-NP was rapid compared to other individual treatment processes (JLR/UV, JLR, or UV irradiation). In fact, the pollutant removal efficiency increase with an increased in the treatment time and a maximum of 77.7 % (BPA) or 76.6 % (2-NP) removal was obtained respectively. It should be noted that the BPA or 2-NP removal efficiency obtained via combined JLR/UV/H_2O_2 was twice more than that obtained with JLR/UV system under similar conditions at a reaction time of 90 min. This means that addition of 0.34 g/L H_2O_2 to JLR/UV system enhanced BPA or 2-NP removal efficiency by 32.8% or 33.4% respectively under the optimised operating conditions of inlet pressure (4 bar) and solution pH (3) (see Table 6.8). This indicates that addition of H_2O_2 to JLR/UV was beneficial by augmenting the OH radicals in the system and hence improved the pollutants removal rate. Besides the pollutant removal efficiency, the experimental data of all the treatment processes were further fitted into pseudo-first order kinetic models. The obtained apparent rate constant values and the correlation coefficient (R^2) of BPA or 2-NP including synergetic index value are displayed in Table 6.8.

Table 6.8: Removal efficiency and rate constant of BPA or 2-NP using combined JLR/UV and JLR/UV/H_2O_2 (experimental conditions as in Figure 6.14 and 6.15)

Pollutants	Treatment processes	Conversion rate	Pseudo-first order rate constant ($k \times 10^{-3}$) (min^{-1})	Correlation coefficient (R^2)	Synergetic index value (f)
BPA	H_2O_2 alone	1.3	0.07	0.2727	-
	UV alone	6.8	0.8	0.9555	-
	JLR alone	14.0	1.7	0.9862	-
	JLR/UV	34.9	4.9	0.9688	1.96
	JLR/UV/H_2O_2	77.7	16.5	0.9980	6.42
2-NP	H_2O_2 alone	1.0	0.04	0.2727	-
	UV alone	6.3	0.7	0.9671	-
	JLR alone	13.2	1.6	0.9862	-
	JLR/UV	33.2	4.6	0.9771	2.0
	JLR/UV/H_2O_2	76.9	16.0	0.9968	6.84

According to Table 6.8, the pseudo-first order rate constant (k) obtained using combined JLR/UV/H_2O_2 was approximately 10 and 3.5 times more than that obtained using the JLR alone or the combined JLR/UV system respectively. The significant increase in the apparent rate constant of the former above that obtained with the latter may be attributed to the crucial role played by H_2O_2. Thus, the existence of a synergetic index in the combined JLR/UV and JLR/UV/H_2O_2 system was confirmed using equation 6.5 and 6.6 respectively.

Synergetic index value (f) $= \frac{k(JLR+UV)}{k(JLR)+k(UV)}$ ……...(6.5)

Synergetic index value (f) $= \frac{k(JLR+UV+H_2O_2)}{k(JLR)+k(UV)+k(H_2O_2)}$ ……(6.6)

By substituting the individual rate constant shown in Table 6.8 into equation 12, the (f) for degradation of BPA by JLR/UV is 1.96 while that of 2-NP is 2.0. The detailed determination of synergetic index value of each treatment process can be found in Appendix 4. The calculated synergetic index value for each process is depicted in Table 6.8. It is evident that the synergetic index value of the combined JLR/UV/H_2O_2 was 3.3 or 3.4 times higher than that obtained via JLR/UV system. It is also 6.42 or 6.84 times greater than JLR alone, which

suggests that UV/H_2O_2 should be combined with JLR in order to achieve greater mineralization efficiency at a short reaction time.

A possible explanation for the increase in pollutant removal efficiency and reaction rate constant observed with JLR/UV compared to the individual processes (JLR or UV irradiation) can be perhaps attributed to the slight increment in the yield of OH radicals. The increase in the quantum of OH radicals can be ascribed to the photolytic cleavage of water molecules in the presence of UV irradiation or thermal pyrolysis of trapped molecules under the continuous impingement process. In the case of JLR/UV/H_2O_2, it is clearly seen that integration of UV/H_2O_2 with JLR was responsible for a very substantial enhancement and removal efficiency or apparent rate constant compared to single processes. It has been established or reported in the literature that H_2O_2 readily decomposed into OH radicals in the presence of UV light (see equation 3). Besides the photolytic cleavage of H_2O_2 in the presence of UV light, thermal pyrolysis of H_2O_2 under conditions of high temperature and pressure may also produce OH radicals. Therefore, the enhanced quantum of the generated OH radicals in the combined JLR/UV/H_2O_2 may be responsible for such higher synergetic index value and pollutant removal rate as shown in Table 6.8 compared to the other tested combinations processes. The observed trend in the JLR/UV system reported in this study substantiates the findings reported by Bagal and Gogate, (2014a) on the degradation of diclofenac by combined HC/UV. Bagal and Gogate, (2014a) found that maximum removal efficiency of diclofenac by combined HC/UV was 65.53 % compared to 26.85 % and 49.75 % obtained separately via HC or UV process alone. According to the authors the obtained increment was attributed to higher yields of OH radicals in the hybrid system of HC/UV than the individual process of HC or UV, which was further supported with a synergetic index value of 1.4. Similar observations were reported by Bagal and Gogate, (2014a) on the degradation of diclofenac using combined hydrodynamic cavitation and ultraviolet light. The authors found that the synergetic index value of combined HC/UV process was almost twice that of the individual process of HC or UV, and was attributed to higher yields of OH radicals in the combined system compared to HC or UV alone. In this present study, the synergetic index value obtained was 6 – 7 times higher than JLR alone. This synergetic index value obtained in the study was two times greater than 3.03 reported by Gore et al., (2014) during the degradation of reactive orange dye 4 via combined hydrodynamic cavitation and ozone.

6.5 Mineralization studies

The results presented so far in other sections were expressed in terms of removal efficiency of the pollutants based on HPLC results, which did not represent the extent of degradation of the pollutants. This may be due to the formation of transformation by-products which were not detected by HPLC due to lack of standards, so TOC as an indicator parameter helped to confirm complete degradation. In order to establish the actual degree of mineralization of the pollutants and compare the efficiency of each treatment processes (JLR, H_2O_2, UV, UV/H_2O_2, JLR/H_2O_2, JLR/UV and JLR/UV/H_2O_2), the degradation of BPA or 2-NP was measured and expressed in terms of Total organic carbon (TOC) value. Prior to the treatment, the initial TOC value was measured and after treatment, the final TOC value from each process was recorded accordingly. The detailed experimental procedure under different conditions can be found in Chapter Three Section 3.3.3. subsection (i-v). The percentage reduction in the TOC value as estimated using the formula stated in Chapter Three Section 3.2.9.3. The obtained results expressed in terms of the differences between initial and final TOC value via different processes for BPA and 2-NP are represented in Figure 6.16.

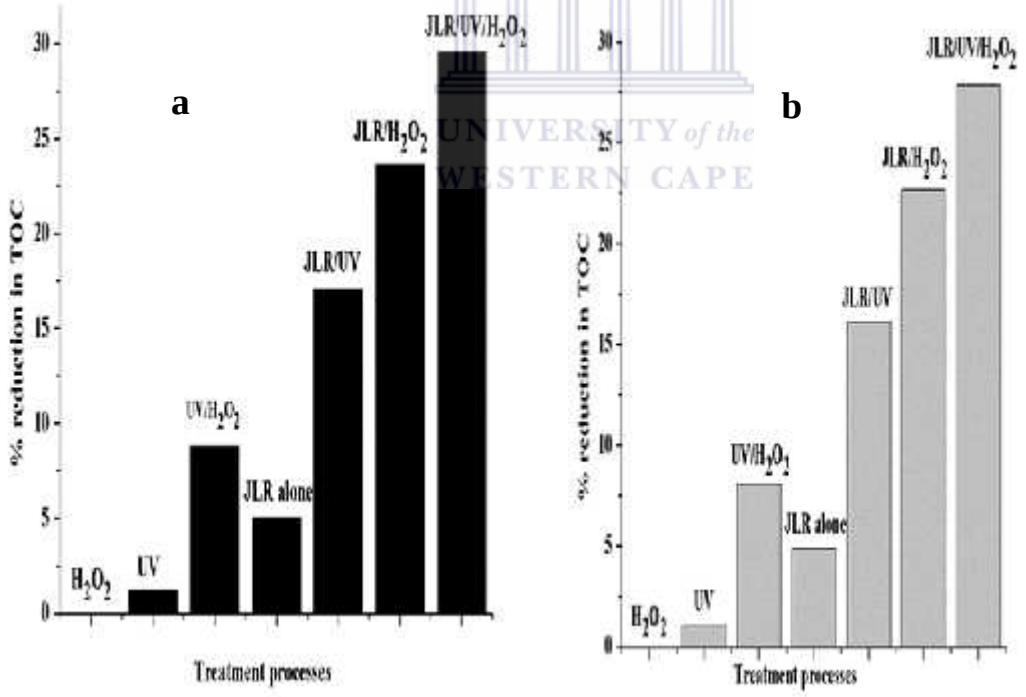

Figure 6.16: % reduction in TOC value of (a) BPA and (b) 2-NP via various advanced oxidation technologies. (Experimental conditions: volume of BPA or 2-NP, (60 L), initial concentration of BPA or 2-NP, (10 ppm), solution pH (3), inlet pressure (4 bar), concentration of H_2O_2, (0.34 g/L), reaction time, (90 min), liquid flow rate, (0.7 L/min), number of replicates=2

As shown in Figure 6.16 (a) and (b), it can be seen that there was no reduction in TOC value via H_2O_2 alone after 90 minutes. With UV alone, only 1.26 or 1.0 % TOC reduction was noticed for BPA or 2-NP under the same treatment time as H_2O_2. With combination of UV and H_2O_2, the TOC reduction value for BPA or 2-NP increased to 8.86 % and 8.03 % respectively. Also, when the two pollutants were subjected to JLR treatment alone for 90 min, the TOC reduction value was 5.0 and 5.2 %. In addition, the TOC reduction value of BPA or 2-NP was higher when JLR was coupled individually with UV and H_2O_2. For instance, with JLR/UV system, the extent of mineralization of BPA or 2-NP was 17.1 % and 15.9 % whereas with the hybrid system of JLR/H_2O_2, 23.6 % and 21.9 % TOC reduction was noticed. More so, it was found that the extent of degradation of BPA or 2-NP by combined JLR/UV/H_2O_2 increased to 29.6 % and 27.86 % after 90 min. The obtained %TOC reduction values demonstrated that effective mineralization of BPA or 2-NP can only be achieved via the combinatory approach of advanced oxidation technologies and not with individual processes. It can be see that in spite of 77.7 % or 76.9 % BPA or 2-NP removal efficiency obtained by combined JLR/UV/H_2O_2 (see Table 6.8), only 29.6 % or 27.8 % TOC reduction was noticed. This indicates that the rate of degradation or destruction of carbon-carbon framework on exposure to OH radicals was a relatively slow process compared to the removal rate. The degree of mineralization may be attributed to the formation of unidentified intermediate compounds which would strongly compete with the original compounds for the available OH radicals. These intermediates sometimes are refractory and resistant to further degradation as evident in the case of dielectric barrier discharge treatment (see Table 5.4 and 5.5). A similar trend in the degree of mineralization versus degradation of organic pollutants by individual and combined treatment processes based on hydrodynamic cavitation have been reported in the literature (Raut-Jadhav et al., 2013; Saharan et al., 2012). Raut-Jadhav et al., (2013) have investigated the degradation of imidacloprid by a combination of hydrodynamic cavitation (HC) and H_2O_2 and reported TOC reduction of 36.1 % for HC/H_2O_2 but 9.65 % for HC alone. Saharan et al., (2012) studied the degradation of acid red 88 dye using combined HC/H_2O_2 and found that the % TOC reduction for HC/H_2O_2 was 72 % whereas that obtained with HC alone was 35 %. Raut-Jadhav et al., (2013) and Saharan et al., (2012) attributed the obtained increment in % TOC reduction via HC/H_2O_2 to an increase in the quantum of OH radicals generated during the dissociation reaction of H_2O_2 under cavitation conditions.

Comparison of the efficiency of the JLR alone with other combined treatment processes with respect to TOC value, made it clear that the rate of degradation of BPA or 2-NP via JLR alone was small due to low yields of OH radicals. However, the increased efficiency in the combined JLR/UV/H_2O_2 could be ascribed to dual enhancement of OH radical formation via dissociation of hydrogen peroxide in the presence of UV and also its generation under the impingement conditions. It thus possible to conclude that there was an existence of a synergetic effect among the three combined systems (JLR, UV, H_2O_2) compared to the individual processes as indicated in Table 6.8.

6.6 Energy efficiency of JLR alone and combined JLR with UV/H_2O_2 based on TOC value

The performance of the JLR in combination with other AOTs were measured in terms of the amount of energy consumed to decompose BPA or 2-NP under the optimum conditions of solution pH (3), inlet pressure (4 bar) and reaction time 90 min. Energy efficiency of a system simply referred to the extent of degradation achieved per unit of energy supplied. During the degradation experiment, it was found that maximum TOC reduction was obtained at 90 minutes and no significant reduction was noticed beyond 90 min. Thus, the energy efficiency of all the treatment processes were computed using differential TOC reduction value obtained at 90 minutes. The TOC reduction values presented in section 6.4 was used to evaluate the energy efficiency of the each system. It should be mentioned that the power rating of the displacement pump connected to the JLR which supplied the electrical energy was 2.5 kW while that of the in-line UV lamp was 55 W. Detailed calculation of the energy efficiency of JLR, JLR/UV, JLR/H_2O_2 and JLR/UV/H_2O_2 can be found in Appendix 4. The results of the energy efficiency of each process is shown in Figure 6.17.

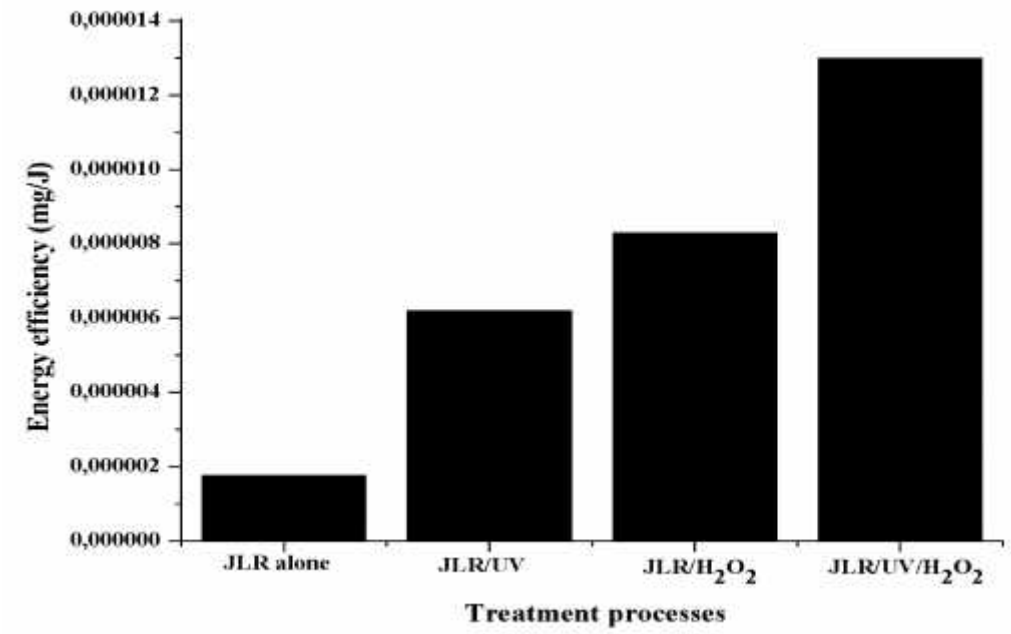

Figure 6.17: Comparison of the energy efficiency of each process (Experimental conditions same as in Figure 6.16), number of replicates=2

According to Figure 6.17, the energy efficiency expressed in mg/J for JLR alone at 90 min was 1.77×10^{-6} and that of JLR/UV was 6.2×10^{-6}. Similarly, the energy efficiency value of JLR/H_2O_2 and JLR/UV/H_2O_2 were 8.3×10^{-6} and 1.3×10^{-5} mg/J respectively. It can be seen that combined JLR/UV/H_2O_2 was 7.3 and 2.0 times more energy efficient and faster than JLR alone and JLR/UV system in the decomposition of either BPA or 2-NP. This may be attributed to the dual enhancement of OH radicals in the solution via photolytic cleavage of water molecules and dissociation of H_2O_2 respectively. The increase in the yield of OH radicals contributed to overall performance of the system compared to other processes.

6.7 Chapter summary

In this chapter, the degradation of BPA or 2-NP by JLR, in-line UV light and H_2O_2 operated individually or in combination was investigated. The influence of the following operating parameters such as applied inlet pressure, solution pH, initial concentration of BPA or 2-NP and addition of radical scavengers on the extent of degradation were studied accordingly. The effect of combining of JLR with in-line UV light and H_2O_2 on the extent of degradation of BPA or 2-NP was also investigated and the existence of a synergetic effect using the various combined system was established. Based on the results obtained, the following important conclusions can be drawn.

- The extent of removal of BPA or 2-NP by JLR was dependent on the applied inlet pressure, and solution pH. Maximum pollutants removal efficiency occurred in acidic medium at around pH 3 and inlet pressure 4 bar. In the JLR, the maximum extent of removal of BPA or 2-NP as a result of impingement of the cavitating jet within the JLR zone alone under the optimised condition of inlet pressure (4 bar) and solution pH (3) was 14.0 % or 13.2 % respectively. There was no significant difference in the removal efficiency of the two pollutants, which suggested that the two compounds were equally prone to attack by the same reactive species, possibly highly electrophilic OH radicals.
- In the JLR, the addition of radical scavengers such as NaCl or Na_2CO_3 inhibited the extent of removal of BPA or 2-NP with the exception of Na_2SO_4 which did not affect enhanced the pollutant conversion rate.
- A three-fold enhancement of the removal efficiency of BPA or 2-NP using JLR/H_2O_2 at optimum value of 0.34 g/L compare to JLR alone was due to both impingement and dissociative effect of H_2O_2 The synergetic index value of of JLR/H_2O_2 for BPA or 2-NP removal was 4.44 or 4.94.
- The combination of JLR with in-line UV light improved the BPA or 2-NP removal efficiency by 14.1 % or 13.7 %. The difference between the amounts removed by hybrid system of JLR/UV over JLR alone was BPA (14.1%) and 2-NP (13.7 %). The combination of JLR/UV/H_2O_2 was found to be the most energy efficient to degrade BPA or 2-NP compared to the JLR, JLR/UV or JLR/H_2O_2 system. The obtained high synergetic index value of 6.42 or 6.84, indicates that JLR is most effective when combined with UV and H_2O_2 to achieve greater mineralization efficiency instead of using H_2O_2 and/or UV separately. The obtained experimental data of all the treatment processes fitted well to the pseudo-first order kinetic models. The pseudo-first rate constant (k) obtained using combined JLR/UV/H_2O_2 was approximately 10 and 3.5 times more than that obtained using JLR alone or combined JLR/UV or JLR/H_2O_2 system respectively. TOC value provide better understanding of mineralization than removal efficiency, removal does not mean removal to everything but rather transformation of secondary pollutants. Generally, the present investigation has clearly demonstrated that a novel combination of JLR/UV/H_2O_2 can be effectively utilised to decompose BPA or 2-NP in water and achieve high mineralization of the target compound.

CHAPTER SEVEN

CONCLUSION AND RECOMMENDATIONS

7 INTRODUCTION

This chapter summarizes the major findings and achievements of this study. It also gives an overview of the previous chapters and to what extent the research objectives outlined in the introductory chapter were accomplished and the research questions answered. This was followed by contributions of the research to knowledge, scientific community and recommendations for future work.

7.1 Overview

In the introductory chapter, research hypothesis were formulated that:

- Dielectric Barrier Discharge (DBD) system will degrade bisphenol-A and 2-nitrophenol through free reactive species produced by the system.

- The incorporation of supported TiO_2 nanocrystals or stabilized nano zero valent iron particles into DBD system will improve the removal efficiency and degradation rate of the target pollutants.

- The jet loop reactor can degrade the target pollutants effectively due to impingement and effective mixing. The integration of the jet loop system with in-line UV lamp and hydrogen peroxide, can enhance the degradation rate due to an increase in the concentration of hydroxyl radicals under the applied impingement conditions.

On the basis of the research hypothesis, the aim of this study was conceived, which was to develop novel combined Advanced Oxidation Technologies (AOTs) among the following: DBD/supported photocatalyst, DBD/photo-Fenton induced process, JLR/UV/H_2O_2 for the degradation of BPA or 2-NP in water as well as improve the efficiency of the DBD and JLR. Based on the overall aims, the following specific objectives were achieved. (i) synthesis of supported TiO_2 nanocrystals, Ag doped TiO_2 nanocomposites and stabilised nano zero valent iron particles (ii) investigation of the influence of various prepared catalysts on the extent of removal/degradation of the model compounds by DBD. (iii) optimization of jet loop reactor

and determination of the removal efficiency of BPA or 2-NP in water using the jet loop hybrid system integrated with in-line UV light and H_2O_2. (iv) identification of the possible intermediate compounds from bisphenol-A or 2-nitrophenol using different AOTs and proposing the degradation pathways or routes. (v) identification of the reactive species responsible for the degradation of BPA or 2-NP (vi) quantification of the amount of free radicals produced by various combined AOTs considered in this study.

To accomplish the set objectives as well as prove or disprove the hypothesis and answer the research questions, different experimental procedures were employed. Based on the results obtained as presented in the previous chapters, the research questions summarily were answered as follows:

Q1. Is it possible to synthesis TiO_2 photocatalysts supported on a stainless steel mesh?

TiO_2 photocatalysts supported on a stainless steel mesh was successfully prepared using a sol-gel solution of 8 % PAN/DMF/$TiCl_4$. Twelve different supported TiO_2 photocatalysts (JT1-JT12) at different pyrolysis temperature and holding time were prepared and characterized. Among the prepared catalysts, JT7 was selected as the best catalyst due to high BET surface area, uniformity distribution of nanocrystals, strong adherence to the stainless steel mesh after 3 h, and polycrystalline nature. The optimum pyrolysis conditions for obtaining stable and active supported TiO_2 nanocrystals was 350 ºC for 3 h holding time in N_2. Besides, the selectivity of sample JT7 was also based on its higher activity under UV-light compared to others due to higher surface area and good crystallinity as shown by BET and XRD analysis. The most influential parameter which played a crucial role during the photocatalytic studies was pyrolysis temperature and not holding time. XRD analysis complemented by HRSEM, HRTEM, EDS, SAED, and XPS confirmed the formation of a pure anatase TiO_2 photocatalyst. This study for the first time in the field of photocatalysis discovered that the PAN precursor could be used as a durable binder between the stainless steel mesh and TiO_2 nanocrystals and that it also acts as a carbon doping source of the formed TiO_2 nanocomposites. The XPS confirmed that the supported carbon doped TiO_2 nanocrystals were made in one step by pyrolysis.

Q2. Does the deposition of plasmonic Ag reduce the band gap energy of TiO_2 and improve its photocatalytic activity?

- Carbon doped TiO_2 photocatalysts prepared via a sol-gel method were modified with different Ag contents by a thermal evaporation method. HRTEM, XRD and XPS analysis confirmed the deposition of Ag nanoparticles and attachment onto the TiO_2 layer without distorting the anatase phase of TiO_2 photocatalyst. Optimal or maximum Ag content of 2.4 % at 60 sec deposition time on the carbon doped TiO_2 layers enhanced the photocatalytic activity under UV light more than the carbon doped TiO_2 nanocomposites by 10.8%. Ag nanoparticles acted as electron trappers and prevented photoelectron-hole recombination on the TiO_2 layers, thus improved the photocatalytic activity. Besides, the deposition of 2.4 % Ag on the TiO_2 layer was responsible for the reduction of band gap energy from 3.18 eV to 2.94 eV. This study has demonstrated, for the first time the successful preparation of Ag loaded carbon doped TiO_2 nanocomposites via a combination of sol-gel and thermal evaporation technique.

Q3. Is the DBD system on its own capable of decomposing bisphenol-A and 2-nitrophenol? To what extent could UV and other reactive species generated by DBD enhance degradation?

- The present DBD system alone partially decomposed bisphenol-A and 2-nitrophenol in water leading to formation of different, recalcitrant intermediate compounds. Bisphenol-A degraded more than 2-nitrophenol under the optimum conditions of solution pH (3), initial pollutant concentration (10 ppm), applied discharge voltage (8 kV), air flow rate (3 L/min). The decomposition of bisphenol-A was initiated by UV and O_3, H_2O_2, OH radicals whereas 2-nitrophenol was refractory towards O_3. The substantial amount of O_3 generated by the DBD escaped from the surface of the solution because the DBD was not a closed system. The open DBD system reduced the concentration of O_3 competing with the target compounds compared to OH radicals. It was demonstrated that UV light, OH radicals, H_2O_2 and possibly O_3 in the acidic solution played an important role in removal of BPA or 2-NP in water. This study demonstrated that the present configuration of DBD used in this study cannot

achieved complete mineralization of the target compounds but % removal efficiency was obtained.

Q4. Is the removal efficiency of the two compounds improved in the DBD system by incorporation of supported TiO_2 photocatalyst or Ag doped TiO_2 nanocomposites or stabilized nano zero valent iron (nZVI)?

- The removal efficiency of BPA or 2-NP by the DBD alone at 80 minutes of reaction time was 67.22 % and 56.8 % respectively. With the incorporation of the stainless steel mesh supported carbon doped TiO_2 photocatalyst (JT7) into the DBD reactor, the BPA removal efficiency improved to 80 % while 77.5 % of 2-NP was removed under the same experimental conditions. Furthermore, with the additional combination of 2.4 % Ag on the carbon doped TiO_2 photocatalysts (JT14) supported on stainless steel in the DBD system, BPA or 2-NP removal efficiency at 80 min was increased to 89.02 % or 81 % respectively. This shows that the incorporation of supported Ag doped TiO_2 photocatalysts (JT14), improved BPA or 2-NP removal efficiency by 21.8 % and 24.2 % respectively, compared to DBD alone. The supported Ag loaded carbon doped catalyst could be reused and maintained high activity of the crystalline TiO_2 anatase polymorph after four repeated applications with no leaching of either TiO_2 or Ag.
- Additionally, when 0.06 g stabilized polyethylene glycol nano zero valent iron (nZVI) particles were added to the DBD system containing aqueous solution of BPA or 2-NP, complete removal of the target compounds was achieved within 40 minutes under the same conditions as combined DBD/supported photocatalyst. The BPA or 2-NP removal efficiency obtained via DBD/photo-Fenton induced process was 11 % or 19 % greater than what was obtained using combined DBD/supported photocatalyst.
- These results further corroborates the initial hypothesis that incorporation of supported photocatalysts or stabilized nano zero valent iron particles into the DBD reactor will improve the removal efficiency of BPA or 2-NP. The major shortcoming of the supported Ag doped TiO_2 photocatalyst was the leaching of metallic species such as Fe, Cr and Ni from the stainless steel mesh. The leaching of Fe, Cr, and Ni into the solution may have deactivated or coated the TiO_2 nanocrystals based on the proximity of the ionic radii of these elements with Ti. The instability of the stainless steel mesh to oxidative corrosion was deemed responsible for the lower conversion rate of BPA or 2-NP achieved by combined DBD/supported photocatalyst than the

combined DBD/nZVI system. However, the removal efficiency does not mean complete mineralization of the target pollutants

Q5. Are the OH radicals increased in the combined advanced system under optimised conditions?

- The concentration of OH radicals produced by the DBD plasma system alone in BPA or 2-NP solution at 60 min was 1.64 mM and 1.78 mM respectively under the optimum conditions of solution pH 3, discharge voltage 8 kV, air flow rate 3 mL/min. Combination of DBD and supported 2.4% Ag loaded carbon doped titania nanocomposites generated 2.10 mM and 1.90 mM OH radicals in BPA or 2-NP solution at 80 min. The concentration of OH radicals in BPA or 2-NP using combined DBD with 0.06 g polyethylene glycol stabilized nano zero valent iron particles at 80 min was 2.26 mM and 2.07 mM. The quantification of OH radicals, H_2O_2 and O_3 produced by the DBD was easy because of the small volume of water used. The point of production of these reactive species in the DBD system is also the point of sampling. It was found that the concentration of OH radicals and H_2O_2 was higher in the combined DBD/supported photocatalyst and DBD/photo-Fenton-induced process than DBD alone under the optimised conditions.

Q6. Can the jet loop reactor alone remove and mineralize the target pollutants due to impingement effect and effective mixing?

- The mineralization rate (TOC value) of BPA or 2-NP under intense mixing in a jet impinging reactor at optimum inlet pressure of 4 bar, solution pH 3, flow rate 0.7 L/s reaction time 90 min, was only 5.2 % and 5 % respectively. The results shows that the present jet loop reactor configuration based on impingement cannot be used effectively by itself to achieve complete mineralization of the two compounds.

Q7. Does the JLR combined with in-line UV lamp, and hydrogen peroxide enhance the degradation rate?

- The integration of in-line UV lamp and addition of optimum dosage of H_2O_2 to JLR system improved the degradation rate of BPA or 2-NP more than 5 times compared to JLR alone. This was due to effective mixing, photolytic cleavage of water molecules and dissociation of H_2O_2 as evident in the synergetic index value of 6.42 or 6.84. The

TOC reduction value of BPA or 2-NP using JLR alone under the optimum conditions of solution pH 3, inlet pressure 4 bar, flow rate 0.7 L/s was 5.2 % and 5.0 % respectively. The extent of degradation of BPA or 2-NP by combined JLR/UV/H_2O_2 was 29.6 % and 27.86 % after 90 min. However, the obtained %TOC reduction value was relatively small which suggests formation of refractory intermediates that were resistant to further oxidation. Combination of JLR/UV/H_2O_2 was considered the most energy efficient technique required to achieve complete degradation of the target compounds relative to the individual processes (namely UV or H_2O_2 or JLR). The quantification of OH radicals in BPA or 2-NP using combined JLR/UV/H_2O_2 was not successful. The amount of OH radicals produced by the jet reactor was probably small compared to the volume of water in the holding tank (60 L). High volume of the aqueous solution in the tank was not proportionate to the available radicals in the bulk solution. Besides, the long distance between the sampling point (holding tank) and jet reactor chamber where the radicals were being produced may also be a contributing factor. Thus due to their short-life nature, instant disappearance and collapse of the radicals could not be ruled out. The issue of distance between the reactor and the sampling point as in the case of JLR did not arise in the DBD. No intermediate compounds were identified using combined JLR/UV/H_2O_2, which may be due to the low yield of OH radicals.

Q8. Are any intermediate compounds of bisphenol-A and 2-nitrophenol in either the single or combined AOTs formed?

Generally, advanced oxidation technologies are used to achieve complete mineralization of recalcitrant organic pollutants. This however depends on the concentration of the pollutants. Sometimes, AOTs are applied to achieve partial decomposition and obtain lower molecular weight compounds that are biodegradable and can be easily removed by conventional treatment. In this study, the second scenario was observed in both the single or combined AOTs. With DBD alone, BPA decomposed into eight different intermediate compounds including oligomers while that of 2-NP was nine. Degradation of BPA by combined DBD with supported 2.4% Ag loaded carbon doped TiO_2 nanocomposites or DBD/photo-Fenton induced process generated lower molecular weight intermediates. The intermediate compounds formed by the two combined system were similar except at 120 min. Decomposition of 2-NP by combined DBD in the presence of supported 2.4% Ag loaded

carbon doped titania nanocomposites or combined DBD/photo-Fenton induced process also produced intermediates. It was found that the intermediate compounds of 2-NP with or without catalyst were similar except at 80 min. The degradation mechanism of the intermediate compounds of BPA or 2-NP was proposed. The degradation of BPA proceeded via ozonation, hydroxylation, dimerization, and decarboxylation and nitration steps was proposed. Whereas, decomposition of 2-NP in the radical environment proceeded via hydroxylation, nitration and denitration steps respectively. Five and three new oxidation products such as (BP3-BP5, BP11, BP14) and (OBP2-OBP4) of BPA or 2-NP which have not been previously reported in the literature were identified.

Q9. Which of the free reactive species are responsible for decomposition of the target compounds?

The degradation of BPA by DBD alone was mainly due to UV light, OH radicals and possibly O_3. However, 2-nitrophenol was refractory towards O_3. In the case of the combined system namely: DBD/supported photocatalysts, DBD/photo-Fenton induced process, JLR/UV/H_2O_2, the decomposition of the target compounds was due to a direct photolytic effect and highly oxidative OH radicals. Overall, OH radicals and UV light played crucial roles and OH remains the major species responsible for the decomposition of BPA or 2-NP as evident in this study.

7.2 Novel findings of the study

The novel findings of this study are listed as follows:

- It was found that carbonaceous species derived from PAN during the pyrolysis process played a role in the formation and adhesion of TiO_2 nanocrystals and did not only bond the TiO_2 nanocrystals onto the stainless steel but equally acted as a carbon doping source of the TiO_2 layers. This means that the synthesised TiO_2 photocatalyst was actually carbon doped TiO_2 nanocomposites and PAN could simultaneously serve as a carbon dopant and stabilizing agent.

- It was demonstrated that a stable, highly active supported Ag doped TiO_2 nanocomposite can be synthesised by the combination of the sol-gel and thermal evaporation technique.

- It was shown under the studied conditions that the combined advanced system based on supported 2.4 % Ag doped TiO_2 nanocomposites and dielectric barrier discharge system which produced UV light, was more effective for the removal BPA or 2-NP in aqueous solution than DBD alone. 2.4 % Ag doped TiO_2 nanocomposites was photochemical stable even after four successful applications, thus making the catalyst a potential candidate in wastewater treatment.

- It was established for the first time that the addition of polyethylene glycol stabilised nZVI particles to the DBD system can induced photo-Fenton like reaction resulting in complete removal of BPA or 2-NP in aqueous solution within 30 min. Thus, the combined DBD/photo-Fenton induced process can be included as a novel advanced oxidation technology.

- Five new transformation products namely: 4-nitrophenol ($C_6H_5NO_3$), 4-nitrosophenolate ($C_6H_4NO_2$), 4-(prop-1-en-2-yl) cyclohexa-3,5-diene-1,2-dione, ($C_9H_8O_2$), 4-(2-hydroxylpropan-2-yl)cyclohexane-3,5-diene-1,2-dione ($C_9H_{10}O_3$), and 1,2-dimethyl-4-(2-nitropropan-2-yl)benzene ($C_9H_{10}NO_4$) which have not been previously reported in the literature were identified during the oxidative process of BPA. In the case of 2-NP, three new aromatic intermediate compounds such as 2-nitro-1,3,5-benzenetriolate ($C_6H_2NO_5$), 2-nitro-1,4-benzoquinone ($C_6H_3NO_4$), and 2,5-dihydroxyl-1,4-benzoquinone ($C_6H_4O_4$) respectively were identified during the degradation of 2-NP for the first time using LC-MS.

- It was demonstrated for the first time that mineralization rate of BPA or 2-NP in aqueous via UV light and optimal dose of H_2O_2 can be enhanced using jet loop reactor system based on ordinary impingement and continuous mixing. Considering the volume of water treated using combined JLR/UV/H_2O_2 and the extent of degradation of BPA or 2-NP, this hybrid system offers an energy efficient process and can be scaled-up for municipal and industrial applications as a recommendation.

7.3 Significance of the study to the scientific and industrial community

The specific findings which are important to scientific and industrial community are enumerated below;

- The chemistry of the degradation of aqueous solution of BPA or 2-NP in a radical environment using DBD alone and combined DBD with catalyst including the operating parameters that influences the performance of the system have been fully established. Additionally, quantitative determination of free reactive species such as O_3, H_2O_2 and OH radicals produced by the DBD and combined DBD with supported photocatalyst was conducted. This study reported for the first time simultaneous quantification of O_3, H_2O_2 and OH radicals in DBD system and found that interconversion reaction between O_3 and H_2O_2 in the presence of UV light enhanced the concentration of OH radicals in the system.

- This study has shown that apart from ozonation and hydroxylation steps mostly reported in the literature for BPA degradation. BPA can also decompose via dimerization, decarboxylation and nitration steps. While 2-NP proceeded via hydroxylation, nitration and denitration steps respectively. Contrary to most studies in the literature which established denitration as the first step during the oxidative process of 2-NP, this study established that the first step during the oxidation of 2-NP is hydroxylation followed by denitration.

- Five new transformation products namely: 4-nitrophenol ($C_6H_5NO_3$), 4-nitrosophenolate ($C_6H_4NO_2$), 4-(prop-1-en-2-yl) cyclohexa-3,5-diene-1,2-dione, ($C_9H_8O_2$), 4-(2-hydroxylpropan-2-yl)cyclohexane-3,5-diene-1,2-dione ($C_9H_{10}O_3$), and 1,2-dimethyl-4-(2-nitropropan-2-yl)benzene ($C_9H_{10}NO_4$) were identified during the degradation of BPA. While, three aromatic intermediate compounds such as 2-nitro-1,3,5-benzenetriolate ($C_6H_2NO_5$), 2-nitro-1,4-benzoquinone ($C_6H_3NO_4$), and 2,5-dihydroxyl-1,4-benzoquinone ($C_6H_4O_4$) were identified during the degradation of 2-NP for the first time using LC-MS. These intermediate compounds have never been reported in the literature, thereby expanding the number of BPA or 2-NP intermediates in the existing data-base.

- It was also shown that addition of nZVI to DBD plasma technology induced photo-Fenton like reaction gave 100% removal within 30 min and enhanced removal efficiency of BPA or 2-NP in aqueous solution. This novel combined advanced technology has great potential for environmental remediation in the area of wastewater purification.

7.4 Conclusions

In conclusion, the degradation of BPA and 2-NP in aqueous solution using DBD/supported photocatalyst, DBD/photo-Fenton induced process and JLR/UV/H_2O_2 was investigated. Based on the results obtained the following conclusions are drawn:

- This study has shown that carbon doped TiO_2 nanocrystals supported on a stainless steel mesh can be synthesised via sol-gel method comprising 8 g PAN, 92 g DMF and 6 mL of 0.09 M $TiCl_4$ at 350 °C temperature and holding time 3 hr under N_2 flow at 50 mL/min.

- The optimum synthesis conditions to synthesis highly crystalline, homogeneously grown and stable supported TiO_2 photocatalyst with high specific surface area according to HRSEM and BET analysis was 350 ºC for 3 hr. It was also established that PAN precursor which served as a binder acted as a carbon doping source on the TiO_2 layer according to FTIR, TGA-DSC, EDS, XRD and XPS results. XRD results showed that the prepared supported TiO_2 photocatalyst was purely anatase. The crystallite sizes, shapes, degree of crystalline, specifics surface area and photocatalytic activity were greatly influenced by temperature and holding time, allowing control of the product characteristics.

- A novel and simple combined method based on sol-gel and thermal evaporation was successfully applied to prepare supported Ag doped TiO_2 nanocomposites. The anchoring of different amount of metallic Ag on the TiO_2 layer did not affect the crystalline and anatase characteristics of TiO_2. The novel supported carbon doped TiO_2 nanocrystals with Ag at an optimal loading of 2.4 % exhibited higher photocatalytic activity than supported carbon doped TiO_2 photocatalysts. The good photocatalytic activity was ascribed to the plasmonic effect of Ag, which possibly

prevented the electron-hole recombination rate as well as narrowing of band gap energy from 3.18 eV to 2.94 eV. It was established that the obtained metal-semiconductor nanocomposites may be a good candidate in the field of wastewater treatment especially in terms of colour removal.

- DBD only or DBD with commercial powder TiO_2 resulted in a slow removal and degradation of BPA or 2-NP in aqueous solution. In the case of combined DBD with supported Ag doped TiO_2 nanocomposites, this study found that coupling of the stainless steel mesh supported 2.4 % Ag carbon doped TiO_2 nanocomposites with the DBD system enhanced the removal efficiency and the degradation rate of both BPA and 2-NP in aqueous solution significantly more than DBD alone or DBD with commercial powder TiO_2 nanoparticles under the applied conditions. The stainless steel mesh supported Ag carbon doped TiO_2 photocatalyst was stable and reusable. Under the studied conditions, increasing solution pH, initial pollutant concentration and addition of radical scavengers resulted in a decrease of pollutant removal efficiency and degradation rate.

- On the other hand, the removal efficiency and degradation rate of BPA or 2-NP in aqueous solution was faster using combination of DBD with photo-Fenton like induced process than DBD with supported Ag doped TiO_2 nanocomposites. Complete removal of BPA or 2-NP was achieved in 30 min, which showed that addition of stabilized nZVI particles induced photo-Fenton like process and enhanced the concentration of OH radicals.

- The OH radicals produced by the combined system played a crucial role in the removal and degradation of BPA and 2-NP in aqueous solution than H_2O_2 and O_3. The results obtained for the change of TOC indicated that the intermediates were quite refractory to further mineralization, leading to ineffective mineralization.

- The degradation of BPA proceeded via ozonation, hydroxylation, dimerization, and decarboxylation and nitration steps. While 2-NP proceeded via hydroxylation, nitration and denitration steps. Five new oxidation products of BPA such as (BP5, BP11 - BP14) were identified using LC-MS. While three new transformation products

of 2-NP (OBP2-OBP4) which have not been previously reported in the literature were identified.

- The removal and degradation of BPA or 2-NP in aqueous solution by combination of JLR/UV/H_2O_2 was found to be much more energy efficient than using JLR alone, or JLR/UV or JLR/H_2O_2 system. Inlet pressure, solution pH, initial concentration of pollutants and radical scavengers influenced the removal efficiency of the two pollutants. The obtained high synergetic index value of 6.42 or 6.84, indicated that JLR is most effective when used with UV and H_2O_2 to achieve greater mineralization efficiency instead of using H_2O_2 and/or UV separately. The obtained experimental data of all the treatment processes fitted well to the pseudo-first order kinetic models.

- Lastly, combination of advanced oxidation technologies (DBD/supported photocatalyst, DBD/photo-Fenton process, JLR/UV/H_2O_2) produced better results at a short reaction time than DBD or JLR alone. The findings emanating from these investigation on the application of combined advanced oxidation technologies is recommended for implementation to address the shortcomings and growing challenge of single advanced oxidation technologies.

7.5 Recommendations for further study

Despite achieving the research aims and objectives, further work can still be done to improve the performance of the TiO_2 photocatalyst, DBD plasma system and jet impinging reactor.

The following recommended areas need further investigation:

- The DBD system should be redesigned and reconfigured to prevent loss of ozone. A closed new DBD system is recommended as this will reduce loss of ozone, increase the concentration of free reactive species and enhance the performance of the system. Also, the total energy consumption and holistic cost implications of the DBD system for practical implementation either for municipal or industrial uses should be carried out.

- The degradation mechanism of BPA or 2-NP either by DBD alone or combined DBD with catalyst is a complex phenomenon due to the presence of different reactive atomic and molecular species in the system. The concentration and the contribution

of OH radicals, H_2O_2 and O_3 during the oxidation of BPA or 2-NP have been established in this study. Future study should include quantification of other active species such as, H●, HO_2^-●, O_2^-● produced by the DBD. The roles played during the oxidation process of organic pollutants' interaction need further investigation.

- In view of the leaching of Fe, Cr, Ni from the stainless steel mesh, which reduced the efficiency of the TiO_2 photocatalyst based on inactivation or interference or immobilization of TiO_2 photocatalyst on a less corrosion prone support material such as Ti-mesh should be considered. This will enhance the mineralization rate of the organic pollutants and will prevent leaching of metallic ions.
- Optimization of the jet impinging jets and orifice plate device vis-a-viz size and diameter will increase the yield of OH radicals and the reactor performance. The free reactive species such as $OH^{\bullet}$ radicals, $H^{\bullet}$ and H_2O_2 produced by JLR should be properly quantified and their life times established.
- The possibility of incorporating the cavitation chamber immediately after the jet reactor should be explored to create both hydrodynamic cavitation and impinging jet system.
- Dosing of hydrogen peroxide directly inside the jet reactor or cavitation chamber and not inside the holding tank should lead to significant enhancement of the process.
- The DBD system should be integrated with JLR as a single system followed by process optimization of the combined system.
- The various combined AOTs investigated in this study should be tested using real environmental samples.

References

Abdo HS, Khali KA, Al-Deyab SS, Altaleb H and Sherif EM. (2013). Antibacterial effect of carbon nanofibers containing Ag nanoparticles. *Fibers and Polymers*, 14(12): 1985-1992

Ahmed S, Rasul MG, Brown R, and Hashib MA. (2011). Influence of parameters on the heterogeneous photocatalytic degradation of pesticides and phenolic contaminants in wastewater: a short review. *Journal of Environmental Management*, 92(3):311-30

Ahmed E, Nagaoka K, Fayez M, Abdel-Daim MM, Samir H and Watanabe G. (2015). Suppressive effects of long-term exposure to p-nitrophenol on gonadal development, hormonal profile with disruption of tissue integrity, and activation of caspase-3 in male Japanese quail (*Coturnix japonica*). *Environmental Science and Pollution Research*, 22(14):10930-42

Álvarez PM, Jaramillo J, López-Piñero F, and Plucinski PK. (2010). Preparation and characterization of magnetic TiO_2 nanoparticles and their utilization for the degradation of emerging pollutants in water. *Applied Catalysis B: Environmental*, 100: 338–345

Amin MT, Ryu S and Park H. (2007). Degradation of phenol and Bisphenol-A using discharge water generating system. *Journal of Water Supply: Research and Technology—AQUA*, 56(3): 203 - 216

Ammar S, Oturan N and Oturan MA. (2007). Electrochemical oxidation of 2-nitrophenol in aqueous medium by electro-Fenton technology. *Journal of Environmental Engineering and Management*, 17(2): 89-96

Anouzla A, Abrouki Y, Souabi S, Safi M. and Rhbal H. (2009). Color and COD removal of disperse dye solution by a novel coagulant: Application of statistical design for the optimization and regression analysis. *Journal of Hazardous Materials*, 166: 1302–1306

Arrojo S. and Benito Y. (2008). A theoretical study of hydrodynamic cavitation. *Ultrasonics Sonochemistry*, 15: 203–211

Ayob A, Ismail N, Tow TT, Abdullah ZA, and Siddique BM. (2012). Characterization of Polymer-Stabilized Nano Zero-valent Iron Particle by Ultrasonic Irradiation-assisted Method. *Journal of Polymer Materials*, 29(1): 167-179.

Aziz AA, Puma GL, Ibrahim S, and Saravan P. (2013). Preparation, characterization and solar photoactivity of titania supported strontium ferrite nanocomposite photocatalyts. *Journal of Experimental Nano Science,* 3: 295-310

Ba-Abbad MM, Kadhum AH, Mohamed AB, Takriff MS and Sopian K. (2012). Synthesis and catalytic activity of TiO_2 nanoparticles for photochemical oxidation of concentrated chlorophenols under direct solar radiation. *International Journal of Electrochemical Science*, 7: 4871-4888.

Bader H and Hoigné J. (1981). Determination of ozone in water by the indigo method. *Water Research*, 15(4): 449–456

Bahnemann W, Muneer M, and Haque MM. (2007). Titanium dioxide-mediated photocatalysed degradation of few selected organic pollutants in aqueous suspensions, *Catalysis Today,* 124:133-148

Bagal MV. and Gogate PR. (2013). Degradation of 2, 4-nitrophenol using a combination of hydrodynamic cavitation, chemical and advanced oxidation processes. *Ultrasonic Sonochemistry,* 20: 1226-1235

Bagal MV. and Gogate PR.(2014a). Degradation of diclofenac sodium using combined processes based on hydrodynamic cavitation and heterogeneous photocatalysis. *Ultrasonic Sonochemistry,* 21(3):1035-43

Bagal MV. and Gogate PR. (2014b). Wastewater treatment using hybrid treatment schemes based on cavitation and Fenton chemistry. A review. *Ultrasonics Sonochemistry,* 21:1-14

Bagheri S, Julkapli, NM and Abd Hamid, SB. (2014). Titanium Dioxide as a Catalyst Support in Heterogeneous Catalysis. *The Scientific World Journal*, Article ID 727496, 21 pages

Baker DR. and Kasprzyk-Horden, B. (2013). Spatial and temporal occurrence of pharmaceuticals and illicit drugs in the aqueous environment and during wastewater treatment: New developments. *Science of the Total Environment*, 454 (455): 442-456

Baroch P, Saito N. and Takai, O. (2008). Special type of plasma dielectric barrier discharge reactor for direct ozonisation of water and degradation of organic pollution. *Journal of Physics. D: Applied. Physics*. 41: 1-6

Basiri Parsa J. and Zonouzian SAE. (2013). Optimization of a heterogeneous catalytic hydrodynamic cavitation reactor performance in decolorization of Rhodamine B: Application of scrap iron sheets. *Ultrasonics Sonochemistry*, 20: 1442–1449

Bassioni G, Korin A. and Salama AE. (2015). Stainless Steel as a Source of Potential Hazard due to Metal Leaching into Beverages. *International. Journal of Electrochemical Science,* 10: 3792 - 3802

Behnajady MM. (2008). Enhancement of photocatalytic activity of TiO_2 nanoparticles by silver doping: Photodeposition versus Liquid impregnation methods. *Global NEST Journal,* 10(1): 1-7.

Behnajady MA, Eskandarloo H, Modirshahla N, Shokri, M. (2011). Investigation of the effect of sol-gel synthesis variables on structural and photocatalytic properties of TiO_2 nanoparticles. *Desalination*, 278: 10-17

Belgiorno V, Rizzo L, Fatta D, Rocca CD, Lofrano G, Nikolaou A, Naddeo V, and Meric S. (2007). Review on endocrine disrupting-emerging compounds in urban wastewater: Occurrence and removal by photocatalysis and ultrasonic irradiation for wastewater reuse. *Desalination*, 215:166–176.

Bell KY, Wells MJM, Traexler KA, Pellegrin M, Morse A, and Bandy J. (2011). Emerging Pollutants. *Water Environment Research*, 83: 1906-1984

Bestetti M, Sacco D, Brunella MF, Franz S, Amadelli R, and Samiolo L. (2010). Photocatalytic degradation activity of titanium dioxide sol–gel coatings on stainless steel wire meshes. *Materials Chemistry and Physics*, 124: 1225–1231

Boehncke, A, Koennecker, G, Mangelsdorf, I, and Wibbertmann, A. (2000). Mononitrophenols: World Health Organization, Concise International Chemical Assessment Document 20. Published under the joint sponsorship of the United Nations Environment Programme, the International Labour Organisation, and the World Health Organization, and produced within the framework of the Inter-Organization Programme for the Sound Management of Chemical. ISSN 1020-6167, Pp. 5

Boithias L, Acuña V, Vergoñós L, Ziv G, Marcé R, and Sabater S. (2014). Assessment of the water supply: demand ratios in a Mediterranean basin under different global change scenarios and mitigation alternatives. *Science of the Total Environment*, 470-471: 567-577

Bokhale NB, Bomble SD, Daldhanjan RR, Mahale DD, Hinge SP, Barnerjee BS, Mohod, AV, and Gogate PR. (2014). Sonocatalytic and sonophotocatalytic degradation of rhodamine 6G containing wastewaters. *Ultrasonics Sonochemistry*, 21: 1797-1804

Bonefeld-Jorgensen EC, Long M, Hofmeister MV, and Vinggaard AM. (2007). Endocrine-disrupting potential of bisphenol-A, bisphenol-A dimethacrylate, 4- n-nonylphenol, and 4-n-octylphenol in vitro: new data and a brief review. *Environmental Health Perspectives*, 115 (Suppl. 1): 69–76

Boparai HK, Joseph M, and O'Carroll DM. (2013). Cadmium (Cd^{2+}) removal by nano zerovalent iron: Surface analysis, effects of solution chemistry and surface complexation modelling. *Environmental Science and Pollution Research*, 20: 6210–6221

Bruggeman PJ, and Locke BR. (2013). Assessment of Potential Applications of Plasma with Liquid Water, in Low Temperature Plasma Technology: Methods and Applications, P. Chu, and X. Lu (Eds.), Taylor and Francis Group, 368–369

Brunauer S, Deming LS, Deming WE, and Teller E, (1940). On a theory of the van der Waals adsorption of gases. *Journal of American Chemical Society*, 62 (7): 1723–1732

Burger AEC. and Nel A (2008) Scoping study to determine the potential impacts of agricultural chemical substances (pesticides) with Endocrine Disruptor properties on water resources of South Africa. WRC Report No. 1774/1/08. Water Research Commission (WRC), Pretoria. ISBN 978-1-77005-714-2. Pp 1.

Byranvand MM, Kharat AN, Fatholahi L. and Beiranvand ZM (2013). A review on the synthesis of nano-TiO_2 via different methods. *Journal of Nanoscience*, 3: 1-9

Cao Y, Tan H, Shi T, Tang T and Li J. (2008). Preparation of Ag-doped TiO_2 nanoparticles for photocatalytic degradation of acetamiprid in water. *Journal of Chemical Technolology and Biotechnology*, 83: 546–552

Cao T, Li Y, Wang C, Shao C and Liu Y. (2011). One-Step Nonaqueous Synthesis of Pure Phase TiO_2 Nanocrystals from $TiCl_4$ in Butanol and Their Photocatalytic Properties. *Journal of Nanomaterials*, Article ID 267415, 6 pages doi:10.1155/2011/267415

Caputo GA, and London E. (2003). Cumulative effects of amino acid substitutions and hydrophobic mismatch upon the transmembrane stability and conformation of hydrophobic alpha-helices. *Biochemistry*, 42(11): 3275-85.

Cardoso da Silva JC, Reis Teodoro JA, Franco Afonso RJC, Aquino SF, and Augusti R. (2014). Photodegradation of bisphenol Ain aqueous medium: Monitoring and identification of by-products by liquid chromatography coupled to high-resolution mass spectrometry. *Rapid Communication in. Mass Spectrometry*, 28: 987–994

Carlucci C, Xu H, Scremin BF, Giannini C, Altamura D, Carlino E, Videtta V, Conciauro F, Gigli G and Ciccarella G. (2014). Selective synthesis of TiO_2 nanocrystals with morphology control with the microwave-solvothermal method. *CrystEngComm*, 16: 1817–1824

Cañizares P, Saez C, Lobato J, and Rodrigo MA. (2004). Electrochemical treatment of 2,4-dinitrophenol aqueous wastes using boron-doped diamond anodes, *Electrochimical Acta*, 49: 4641–4650.

Chang JA, Vithal M, Baek IC, and Seok SII (2009). Morphological and phase evolution of TiO_2 nanocrystals prepared from peroxotitanate complex aqueous solution: Influence of acetic acid. *Journal of Solid State Chemistry*, 182: 749–756

Chang BV, Yuan SY, and Chiou CC. (2011) Biodegradation of bisphenol-A in river sediment. *Journal of Environmental Science Health A*, 46(9):931–937

Chanathaworn J, Bunyakan C, Wiyaratn W. and Chungsiriporn J. (2012). Photocatalytic decolorization of basic dye by TiO_2 nanoparticle in photoreactor. *Songklanakarin Journal Science and Technology*, 34(2): 203–210

Chen H, Yao S, Lecheng L, Ye Z, Hailin C, Ruizhuang Y. and Yabin Z. (2009). Catalysis-assisted Decomposition of Aqueous 2, 4, 6-Trinitrotoluene by Pulsed High Voltage Discharge Process. *11th International Conference on Electrostatic Precipitation, Hangzhou*, 661-664

Chen TC, Shue MF, Yeh YL, and Kao TJ. (2010). Bisphenol A occurred in Kao-Pin River and its tributaries in Taiwan. *Environmental Monitoring and Assessment*, 161:135–45.

Chen D, Du G, Zhu Q and Zhou F. (2013). Synthesis and characterization of TiO2 pillared montmorillonites: Application for methylene blue degradation. *Journal of Colloid and Interface Science*, 409: 151-157

Chicgoua N, Sabine C, and Richard C. (2012). Nanoscale metallic iron for environmental remediation: Prospects and limitations. *Water, Air, and Soil Pollution*, 223 (3): 1363-1382

Choi J, Park H, and Hoffmann MR. (2010). Effects of Single metal-ion doping on the visible light photo-reactivity of TiO_2. *Journal of Physical Chemistry*, C, 114 (2):783–792

Chong MN, Lei S, Jin B, Saint C, and Chow CWK. (2009b). Optimisation of an annular photoreactor process for degradation of Congo red using a newly synthesized Titania impregnated kaolinite nano-photocatalyst. *Separation and Purification Technology*, 67: 355-363.

Chong MN, Jin B, Zhu HY, Chow CWK, Saint C. (2009c). Application of H-titanate nanofibers for degradation of Congo red in an annular slurry photoreactor. *Chemical Engineering Journal*, 150: 49-54.

Chong MN, Jin B, Chow CWK, and Saint CP. (2010). Recent developments in photocatalytic water treatment technology: a review. *Water Resources*, 44: 2997–3027.

Chong MN, Sharma AK, Burn S. and Saint CP. (2012). Feasibility study on the application of advanced oxidation technologies for decentralised wastewater treatment. *Journal of Cleaner Production*, 35: 230-238

Colombo A, Cappelletti G, Ardizzone S, Biraghi I, Bianchi CL, Meron D, Pirola C, and Spadavecchia F. (2012). Bisphenol A endocrine disruptor complete degradation using TiO_2 photocatalysis with ozone. *Environmental Chemistry Letters*: 10: 55–60

Cong Y, Li X, Qin Y, Dong Z, Yuan G, Cui Z. and Lai X. (2011). Carbon-doped TiO_2 coating on multiwalled carbon nanotubes with higher visible light photocatalytic activity. *Applied Catalysis B: Environmental*, 107:128–134

Corbari L. (2008). "Iron oxide deposits associated with the ectosymbiotic bacteria in the hydrothermal vent shrimp Rimicaris exoculata". *Biogeosciences*, 5: 1295–1310.

Crane RA, Dickinsona M, Popescub IC and Scott TB (2011). Magnetite and zero-valent iron nanoparticles for the remediation of uranium contaminated environmental water. *Water Research*, 45: 2931-2942

Cullity BD. and Stock SR. (2001). Elements of X-ray Diffraction, 3rd Edition, Prentice Hall. Upper Saddle River, New Jersey, 664.

Dalrymple, OK, Yeh H. and Trotz MA. (2007). Removing pharmaceuticals and endocrine-disrupting compounds from wastewater by photocatalysis, *Journal of Chemical Technology and Biotechnology*, 82 (2): 121-134

Dhabbe RS, Kokate MR, Kadam AN, Garadkar KM, and Suwarnkar MB (2014). Enhancement in the photocatalytic activity of Ag loaded N-doped TiO_2 nanocomposite under sunlight. *Journal of Material Science: Material Electron*, 25:3179–3189

Deborde M, Rabouana S, Mazelliera P, Duguet JP and Legube B. (2008). Oxidation of bisphenol A by ozone in aqueous solution. *Water Research*, 42: 4299–4308

Department of Water Affairs (DWA) (2012). The Annual National State of water resources for the hydrological year 2012/2013. Published by Department of Water Affairs. Pretoria, South Africa.

Diamanti-Kandarakis E, Bourguignon JP, Giudice LC, Hauser R, Prins GS, Soto AM, Zoeller RT, and Gore AC (2009). "Endocrine-disrupting chemicals: an Endocrine Society scientific statement". *Endocrine Review*, 30 (4): 293–342

Dmitruk U, Piascik M, Taboryska B. and Dojlido J (2008). Persistent organic pollutants (POPs) in bottom sediments of the Vistula River, Poland. *Clean*, 36: 222-229

Dobrin D, Bradu C, Magureanu M, Mandache NB, and Parvulescu VI. (2013). Degradation of diclofenac in water using a pulsed corona discharge. *Chemical Engineering Journal*, 234: 389–396

Dolat NQ, Kusiak-Nejman E, Morawski AW. and Li PG. (2012). One step, hydrothermal synthesis of nitrogen, carbon co-doped titanium dioxide (N, C TiO_2) photocatalyst. Effects of alcohol degree and chain length as carbon dopant precursors on photocatalytic activity and catalyst deactivation. *Applied Catalysis B: Environment*, 115–116: 81–89

Dong F, Guo S, Wang H, Li X and Wu Z. (2011). Enhancement of the Visible Light Photocatalytic Activity of C-Doped TiO_2 Nanomaterials Prepared by a Green Synthetic Approach. *Journal of Physical Chemistry. C*, 115: 13285–13292

Dussubieux L. and Van Zelst L. (2004). LA-ICP-MS analysis of platinum group elements and other elements of interest in ancient gold, *Applied Physics A79: Materials Science and Processing*, 353-356.

Egertton RF. (2005), —Physical principles of electron microscopy: An introduction to TEM, SEM and AEM, Springer, USA.

Elmolla ES and Chaudhuri M. (2010). Comparison of different advanced oxidation process for treatment of antibiotics aqueous solution. *Desalination*, 256: 43-47

Fabiola MA, Gimenez J, and Esplugas S. (2008). Photolysis and TiO_2 photocatalytic treatment of naproxen: Degradation, mineralization, intermediates and toxicity. *Journal of Advanced Oxidation Technology*, 11(3): 436–445

Fan MD, Yuan P, Chen TH, He HP, Yuan AH, Chen KM, Zhu JX and Liu D. (2010). Synthesis, characterization and size control of zerovalent iron nanoparticles anchored on montmorillonite. *Materials Science*, 55(11): 1092-1099

Fan Z, Hu J, An W. and Yan M. (2013). Detection and Occurrence of Chlorinated Byproducts of Bisphenol A, Nonylphenol, and Estrogens in Drinking Water of China: Comparison to the Parent Compounds. *Environmental Science and Technology*. 47: 10841−10850

Fang X, Mark G. and von Sonntag C. (1996). “OH radical formation by ultrasound in aqueous solutions Part I: chemistry underlying the tereophthalae dosimeter,” *Ultrasonic. Sonochemistry,* 3: 57-63

Farbod M. and Khademalrasool M. (2011). Synthesis of TiO_2 nanoparticles by a combined sol–gel ball milling method and investigation of nanoparticle size effect on their photocatalytic activities. *Powder Technology*, 214: 344–348

Farahany S, Ali O, and Mohd Hasbullah I. (2012). "The usage of computer-aided cooling curve thermal analysis to optimise eutectic refiner and modifier in Al–Si alloys". *Journal of Thermal Analysis and Calorimetry,* 109 (1): 105–111.

Fawell J, and Ong CN. (2012). Emerging contaminants and the implications for drinking water. *International Journal of Water Resources Development*, 28(2): 247–263

Fenoll J, Garrido I, Hellín P, Flores P, and Navarro S. (2015). Photodegradation of neonicotinoid insecticides in water by semiconductor oxides. *Environmental Science and Pollution Research,* 22: 15055–15066

Fernandez M. (2010). Endocrine disruptors and semen quality. Presentation at European Society of Human Reproduction and Embryology (ESHRE) Annual Meeting, Rome, Italy.

Fernández A, Lassaletta G, Jimknez VM, Justo A, GonzSlez-Elipe AR, Herrmann JM, Tahiri H. and Ait-Ichou Y. (1995). Preparation and characterization of TiO_2 photocatalysts supported on various rigid supports (glass, quartz and stainless steel). Comparative studies of photocatalytic activity in water purification. *Applied Catalysis B: Environmental,* 7: 49-63

Ferrer I and Thurman EM. (2009). Liquid chromatography-Time of Flight Mass Spectrometry: Principles, Tools and Applications for Accurate Mass Analysis. John Wiley and Sons: New York, ISBN 978-0-470-13797-0.

Field JA, Johnson CA and Rose JB. (2006). What is “emerging contaminants”? *Environmental Science and Technology,* 40:7105

Flint S, Markle T, Thompson S, and Wallace E. (2012). Bisphenol A exposure, effects, and policy: A wildlife perspective. *Journal of Environmental Management*, 104: 19–34.

Friedmann D, Mendive C, and Bahnemann D. (2010). TiO_2 for water treatment: parameters affecting the kinetics and mechanisms, of photocatalysis. *Applied Catalysis B,* 99: 398–406.

Fukushima M, Tatsumi K, and Moimoto K. (2000). Influence of Fe (III) and humic acid on the phototodegradation of pentachlorophenol. *Environmental Toxicology and. Chemistry*. 19, 1711–1716

Fung YS, Wu Z. and Dao KL. (1996). Determination of Total Organic Carbon in Water by Thermal Combustion-Ion Chromatography. *Analytical Chemistry*, 68:2186-2190

Gao L, Sun L, Wan S, Yu Z, and Li M. (2013). Degradation kinetics and mechanism of emerging contaminants in water by dielectric barrier discharge non-thermal plasma: The case of 17b-Estradiol. *Chemical Engineering Journal*, 228: 790–798

Garcia-Araya JF, Beltran FJ, and Aguinaco A. (2010). Diclofenac removal from water by ozone and photolytic TiO_2 catalysed processes. *Journal of. Chemical Technology and Biotechnology*, 85: 798–804

Gaya UI, and Abdullah AH. (2008). Heterogeneous photocatalytic degradation of organic contaminants over titanium dioxide: a review of fundamentals, progress and problems. *Journal of Photochemistry and Photobiology C*, 9(1): 1–12.

Geens T, Goeyens L. and Covaci A., (2011). Are potential sources for human exposure to bisphenol-A overlooked? *International Journal of Hygiene and Environmental Health*, 214: 339–347

Gerrity D, Stanford BD, Trenholm RA, and Snyder SA. (2010). An evaluation of a pilot-scale non-thermal plasma advanced oxidation process for trace organic compound degradation. *Water Research*, 44: 493–504.

Gogate PR (2008). Treatment of wastewater streams containing phenolic compounds using hybrid techniques based on cavitation: a review of the current status and the way forward. *Ultrasonics Sonochemistry*, 15: 1-15

Gogate PR. (2011). Hydrodynamic Cavitation for Food and Water Processing. *Food Bioprocess Technology*, 4: 996–1011

Gogate PR and Patil PN. (2015). Combined treatment technology based on synergism between hydrodynamic cavitation and advanced oxidation processes. *Ultrasonics Sonochemistry*, 25: 60–69

Goi A and Trapido M. (2002). Hydrogen peroxide photolysis, Fenton reagent and photo-Fenton for the degradation of nitrophenols: a comparative study. *Chemosphere*, 46: 913–922

Gore MM, Saharan VK, Pinjari DV, Chavan, PV, and Pandit, AB. (2014). Degradation of reactive orange 4 dye using hydrodynamic cavitation based hybrid techniques. *Ultrasonics Sonochemistry*, 21:1075–1082

Grabowski LR, van Veldhuizen EM, Pemen AJM, and Rutgers WR. (2006). Corona above water reactor for systematic study of aqueous phenol degradation. *Plasma Chemistry and Plasma Processing*, 26: 3-17.

Grabowski LR, van Veldhuizen EM, Pemen AJM, and Rutgers WR. (2007). Breakdown of methylene blue and methyl orange by pulsed corona discharge. *Plasma Sources Science and. Technology*, 16: 226-232.

Gupta SB. (2007). Investigation of a Physical Disinfection Process Based on Pulsed Underwater Corona Discharges. Unpublished PhD thesis submitted to Forschungszentrum Karlsruhe, Institute for Pulsed Power and Microwave Technology (IHM), Karlsruhe, Germany

Gupta SM and Tripathi M. (2012). A review on the synthesis of TiO_2 nanoparticles by solution route. *Central European Journal of Chemistry*, 10(2): 279-294

Gupta K, Singh RP, Pandey A and Pandey A. (2013). Photocatalytic antibacterial performance of TiO_2 and Ag-doped TiO_2 against *S. aureus*. *P. aeruginosa* and *E. coli. Beilstein Journal of. Nanotechnology*, 4: 345–351.

Habibi S, Fatemi S, Izadyar S. and Mousavand T. (2012). TiO_2 nanoparticle layer formation on ceramic support, a statistical approach to control influential synthesis parameters. *Powder Technology*, 229:51–60

Hänel A, Moreń P, Zaleska A, and Hupka J. (2010). Photocatalytic activity of TiO_2 immobilized on glass beads. *Physicochemical Problem of Mineral Processing*, 45: 49-56

Hao XL, Zhou MH, and Lei, LC. (2007). Non-thermal plasma-induced photocatalytic degradation of 4-chlorophenol in water, *Journal of Hazardous Material,* 141: 475–482.

He F, Ma F, Li J, Li T, and Li G. (2014). Effect of calcination temperature on the structural properties and photocatalytic activities of solvothermal synthesized TiO_2 hollow nanoparticles. *Ceramic International*, 40: 6441-6446

Hintsho N, Petrik L, Alexander N, Salam T, and Patrick, N. (2014). Photo-catalytic activity of titanium dioxide carbon nanotube nano-composites modified with silver and palladium nanoparticles. *Applied Catalysis B: Environmental*, 156–157: 273–283

Hoeben WFLM, van Veldhuizen EM, Classens HA, and Rutgers WR. (1997). Degradation of Phenol and Atrizine in Water by Pulsed Corona Discharges. 13th International Symposium on Plasma Chemistry, August 18-22, Beijing, China.

Hou F, Deng T. and Jiang X. (2013). Dispersive liquid-liquid microextraction of phenolic compounds using solidified floating organic droplets, and their determination by HPLC. *Microchimical Acta*, 180: 341–346

Houtman CJ. (2010). Emerging contaminants in surface waters and their relevance for the production of drinking water in Europe. *Journal of Integrative Environmental Sciences*, 7(4): 271–295.

Huang YQ, Wong CKC, Zheng JS, Bouwman H, Barra R, Wahlstro¨m B, Neretin L, and Wong MH. (2012). Bisphenol A (bisphenol A) in China: a review of sources, environmental levels, and potential human health impacts. *Environmental International*, 42, 91–99

Huang DL, Chen GM, Zeng GM, Xu P, Yan M, Lai C, Zhang C, Li NJ, Cheng M, He XX, and He Y. (2015). Synthesis and Application of Modified Zero-Valent Iron Nanoparticles for Removal of Hexavalent Chromium from Wastewater. *Water Air and Soil Pollution*, 226:375

Hussain S, Shaikh S and Farooqui M. (2013). COD reduction of waste water streams of active pharmaceutical ingredient – Atenolol manufacturing unit by advanced oxidation-Fenton process. *Journal of Saudi Chemical Society*, 17: 199-202

Iwuoha EI. (2012). Smart nano-dimensional dendritic aptasensor for real-time determination of estrogenic 17β-estradiol. *International conference and exhibition on 'Biosensors and Bioelectronics"*. May 14–16, 2012 Embassy Suites Las Vegas, USA

Jabeen H, Kemp KC and Chandra V. (2013). Synthesis of nano zerovalent iron nanoparticles -Graphene composite for the treatment of lead contaminated water. *Journal of Environmental Management*, 130: 429-435

Jen JF, Leu MF and Yang TC. (1998). Determination of hydroxyl radicals in an advanced oxidation process with salicylic acid trapping and liquid chromatography. *Journal of Chromatography A*, 796: 283–288

Jia C, Wang Y, Zhang C, Kong S, Qin Q, and Yao SK. (2012). Photocatalytic Degradation of Bisphenol A in Aqueous Suspensions of Titanium Dioxide. *Environmental Engineering Science*, 29(7): 630 – 637

Jiang X, Wu Y, Wang P, Li H and Dong W. (2013). Degradation of bisphenol-A in aqueous solution by persulfate activated with ferrous ion. *Environmental Science and Pollution Research*, 20: 4947–4953

Jiang B, Qiu JZS, Mingbo W, Yan QZZ, and Xue Q. (2014). Review on electrical discharge plasma technology for wastewater remediation. *Chemical Engineering Journal*, 236: 348–368.

Jo JO and Mok YS. (2009). In-situ production of ozone and ultraviolet light using a barrier discharge reactor for wastewater treatment. *Journal of Zhejiang University SCIENCE A*, 10(9):1359-1366

Joshi RK and Gogate PR. (2012). Degradation of dichlorvos using hydrodynamic cavitation based treatment strategies. *Ultrasonics Sonochemistry,* 19: 532-539

Joshi RP, and Thagard SM. (2013). Streamer-like electrical discharges in water: part II. Environmental applications. *Plasma Chemistry and Plasma Processing*, 33: 17–49

Joshi AA, Locke BR, Arce P and Finney WC. (1995). "Formation of Hydroxyl Radicals, Hydrogen Peroxide and Aqueous Electrons by Pulsed Streamer Corona Discharge in Aqueous Solution." *Journal of Hazardous Materials*, 41: 3-30.

Kavitha V. and Palanivelu K. (2005). Degradation of nitrophenols by Fenton and photo-Fenton processes. *Journal of Photochemistry and Photobiology A: Chemistry*, 170: 83-95

Kerkez Ö and Boz İ. (2013). Efficient removal of methylene blue by photocatalytic degradation with TiO_2 nanorod array thin films. *Reaction Kinetic and Mechanical Catalysts*, 110: 543–557

Khan MM, Ansari SA, Amal MI, Lee J. and Cho MH. (2013). Highly visible light active Ag@TiO_2 nanocomposites synthesized using an electrochemically active biofilm: a novel biogenic approach. *Nanoscale*, 5: 4427-4435.

Kirkpatrick M. and Locke BR. (2005). Hydrogen, Oxygen, and Hydrogen Peroxide Formation in Electrohydraulic Discharge. *Industrial and Engineering Chemistry Research* 44: 4243-4248.

Klavarioti M, Mantzavinos D, and Kassinos D. (2009). Removal of residual pharmaceuticals from aqueous systems by advanced oxidation processes. *Environment International*, 35: 402–417.

Klauson D, Babkina J, Stepanova K, Krichevskaya M, and Preis S. (2010). Aqueous photocatalytic oxidation of amoxicillin. *Catalysis Today*, 151: 39-45.

Kolle SN, Ranmirez T, Kamp HG, Buesen R, Flick B, and Strauss V. (2013). A testing strategy for the identification of mammalian, systemic endocrine disruptors with particular focus on steroids. *Regulation and Toxicology Pharmacology*, 63:259–78

Kondo Y, Yoshikawa H, Awaga K, Murayama M, Mori T, Sunada K, Bandow S, and Iijima S. (2008). Preparation, photocatalytic activities, and dye-sensitized solar-cell performance of submicron-scale TiO_2 hollow spheres. *Langmuir*, 24: 547–550.

Kostedt WL, Ismail AA, and Mazyck DW. (2008). Impact of Heat Treatment and Composition of $ZnO–TiO_2$ Nanoparticles for Photocatalytic Oxidation of an Azo Dye, *Industrial Engineering and Chemical Research*, 47: 1483–1487.

Krause H, Schweiger B, Schuhmacher J, Scholl S, and Steinfeld U. (2009). Degradation of the endocrine disrupting chemicals (EDCs) carbamazepine, clofibric acid, and isopromide by corona discharge over water. *Chemosphere*, 75(2): 163-168.

Kümmerer K. (2011). Emerging Contaminants versus Micro-pollutants. *Clean – Soil, Air, Water*, 39 (10): 889–890

Kuriechen SK, and Murugesan S. (2013). Carbon-Doped Titanium Dioxide Nanoparticles Mediated Photocatalytic Degradation of Azo Dyes Under Visible Light. *Water Air and Soil Pollution*, 224:1671-5

Kushwaha AK, Gupta N, and Chattopadhyaya MC. (2014). Enhanced adsorption of methylene blue on modified silica gel: equilibrium, kinetic, and thermodynamic studies. *Desalination and Water Treatment*, 52 (22-24): 4527-4537.

Ku, Y, Hung, JJ and Wang, WY. (2006). Decomposition of 2-Nitrophenol in Aqueous Solution by Ozone and UV/Ozone Processes. *Water Environment Research*, 78(9): 901-908

Lee J, Park H. and Yoon J. (2003). Ozonation characteristics of bisphenol-A in water. *Environmental Technology*, 24(2): 241-248

Lei LC, Zhang Y, Zhang XW, Du YX, Dai QZ, and Han S. (2007). Degradation performance of 4-chlorophenol as a typical organic pollutant by a pulsed high voltage discharge system. *Industrial and Engineering Chemistry Research*, 46: 5469–5477.

Leong KH, Monash P, Ibrahim S, and Saravanan P. (2014). Solar photocatalytic activity of anatase TiO_2 nanocrystals synthesised by non-hydrolitic sol-gel method. *Solar Energy*, 101: 321-332

Lesage O, Falk L, Tatoulian M, Mantovani D, and Ognier S. (2013). Treatment of 4-chlorobenzoic acid by plasma-based advanced oxidation processes. *Chemical Engineering and Processing: Process Intensification*, 72: 82-89

Li W, Ismat Shah S, Sung M and Huang CP. (2002). Structure and size distribution of TiO_2 nanoparticles deposited on stainless steel mesh. *Journal of Vacuum Science and Technology*, B 20(6): 2303-8

Li Y, Zhang S, Yu Q, and Yin W. (2007). The effects of activated carbon supports on the structure and properties of TiO_2 nanoparticles prepared by a sol-gel method. *Applied Surface Science*, 253: 9254-9258

Li D, Quing D, Wu T, Miao M, Wang J, Weng X, Ferber J, Herrinton L, Zhu Q, Gao E, Checkoway H, and Yuan W. (2010a). Occupational exposure to bisphenol A and risk of self-reported male sexual dysfunction. *Human Reproduction*, 25: 519–527.

Li S, Ma X, Jiang Y and Cao X. (2014). Acetamiprid removal in wastewater by the low-temperature plasma using dielectric barrier discharge. *Ecotoxicology and Environmental Safety,* 106:146–153

Liu Y, Mei S, Iya-Sou D, Cavadias S and Ognier S. (2012). Carbamazepine removal from water by dielectric barrier discharge: Comparison of ex situ and in situ discharge on water. *Chemical Engineering and Processing*, 56: 10–18

Locke BR, Sato M, Sunka P, Hoffmann MR, and Chang JS. (2006). Electrohydraulic discharge and non-thermal plasma for water treatment. *Industrial and Engineering Chemistry Research*, 45(3): 882–905.

Luiz DB, Genena AK, José HJ, Moreira RF, and Schröder HF. (2009). Tertiary treatment of slaughterhouse effluent: degradation kinetics applying UV radiation or H_2O_2/UV. *Water Science and Technology*, 60(7): 1869–1874

Lukes P. and Locke BR (2004). Degradation of Substituted Phenols in Hybrid Gas-Liquid Electrical Discharge Reactor. *Industrial and Engineering Chemistry Research*, 44(9): 2921-2930.

Lukes P, Clupek M, and Babicky V. (2011). Discharge filamentary patterns produced by pulsed corona discharge at the interface between a water surface and air. *Institute of Electrical and Electronics Engineers (IEEE) Transactions on Plasma Science,* 39(11): 2644–2645.

Luo Q, Li X, Li X, Wang D, An J and Li X. (2012). Visible light photocatalytic activity of TiO_2 nanoparticles modified by pre-oxidized polyacrylonitrile. *Catalysis Communications,* 26: 239-243

Machulek JA, Oliveira SC, Osugi ME, Ferreira VS, Quina FH, Dantas RF, Oliveira SL, Casagrande GA, Anaissi FJ, Silva VO, Cavalcante RP, Gozzi F, Ramos DD, da Rosa APP, Santos APF, de Castro DC, and Nogueira JA. (2013). Application of different advanced oxidation processes for the degradation of organic pollutants. Chapter 6 in organic pollutants—monitoring, risk and treatment. InTech, Croatia. 142-146 doi: 10.5772/53188

Madhavi V, Prasad TNVKV, and Madhavi G. (2013). Synthesis and Spectral Characterization of Iron Based Micro and Nanoparticles. *Iranica Journal of Energy and Environment,* 4 (4): 385-390

Madhu GM, Ashly Thomas, Deepak S, Preetham HS, and Rajanandam KS (2014). Escalation of degradation of malachite green and Methyl violet using hydrodynamic cavitations using different orifice geometry. International *Journal of Environmental Sciences,* 5(3): 644-651

Madzivire G, Gitari W, Vadapalli V. and Petrik L. (2015). Jet loop reactor application for mine water treatment using fly ash, lime and aluminium hydroxide. *International Journal of Environmental Science and Technology,* 12(1): 173

Magureanu M, Piroi D, Gherendi F, Mandache N, and Parvulescu V. (2008). Decomposition of Methylene Blue in Water by Corona Discharges. *Plasma Chemistry and. Plasma Processing*. 28 (6): 677−688

Magureanu M, Piroi D, Mandache NB, David V, Medvedovici A, and Parvulescu VI (2010). Degradation of pharmaceutical compound pentoxifylline in water by non-thermal plasma treatment. *Water Research,* 44: 3445–3453

Magureanu M, Piroi D, Mandache NB, David V, Medvedovici A, Parvulescu VI, and Bradu C. (2011). Degradation of antibiotics in water by non-thermal plasma treatment. *Water Research*, 45: 3407-3416

Magureanu M, Bogdan N, Piroi D, Mandache NB, and Parvulescu V. (2013). Pulsed Corona Discharge for Degradation of Methylene Blue in Water. *Plasma Chemistry and Plasma Processing*, 33: 51–64

Malato S, Fernandez-Ibanez P, Maldonado MI, Blanco J, and Gernjak W. (2009). Decontamination and disinfection of water by solar photocatalysis: recent overview and trends. *Catalysis Today*, 147: 1–59.

Malik MA. (2010). Water purification by plasmas: which reactors are most energy efficient? *Plasma Chemistry and Plasma Processing*, 30: 21–31

Manickum T and John W (2014). Occurrence, fate and environmental risk assessment of endocrine disrupting compounds at the wastewater treatment works in Pietermaritzburg (South Africa). *Science of the Total Environment*, 468–469: 584–597

Manoj Kumar Reddy P. and Subrahmanyam C. (2012). Green Approach for Wastewater Treatment - Degradation and Mineralization of Aqueous Organic Pollutants by Discharge Plasma. *Industrial Engineering and Chemical Research*, 51: 11097−11103

Manoj Kumar Reddy P, Rama Raju B, Karuppiah J, Linga Reddy E, and Subrahmanyam, C. (2013). Degradation and mineralization of methylene blue by dielectric barrier discharge non-thermal plasma reactor. *Chemical Engineering Journal*, 217: 41–47

Marinov IL, Guaitella O, Rousseau A, and Starikovskaia SM. (2011). Successive nanosecond discharges in water. *Institute of Electrical and Electronics Engineers (IEEE) Transactions on Plasma Science*, 39(11): 2672-2673

Miao G, Chen L. and Qi Z. (2012). Facile Synthesis and Active Photocatalysis of Mesoporous and Microporous TiO_2 Nanoparticles. *European Journal of Inorganic Chemistry*, 35: 5864–5871

Michałowicz J. (2014). Bisphenol A – Sources, toxicity and biotransformation. *Environmental Toxicology and Pharmacology*, 37: 738–758

Mishra KP. and Gogate PR. (2010). Intensification of degradation of Rhodamine B using hydrodynamic cavitation in the presence of additives, *Separation and Purification Technology*, 75: 385–391

Mok YS, Jo JO, Lee HJ, Ahn HT, and Kim JT. (2007). Application of Dielectric Barrier Discharge Reactor Immersed in Wastewater to the Oxidative Degradation of Organic Contaminant. *Plasma Chemistry and Plasma Processing*, 27: 51–64

Monreal HA, Chacon-Nava, Arce-Colunga U, Martinez CA, Casillas PG, Martınez-Villafane A. (2009). Sol–gel preparation of titanium dioxidenanoparticles in presence of a linear polysaccharide. *Micro and Nano Letters*, 4(4): 187-191

Mouele ESM. (2014). Water treatment using electrohydraulic discharge system. Unpublished Msc thesis to the Department of Chemistry, University of the Western Cape, South Africa. Pp. 63-66

Nainani R, Thakur P, and Chaskar M. (2012). Synthesis of Silver Doped TiO_2 Nanoparticles for the Improved Photocatalytic Degradation of Methyl Orange. *Journal of Materials Science and Engineering B*, 2 (1): 52-58

Nam HJ, Amemiya T, Murabayashi M, and Itoh K. (2004). Photocatalytic activity of sol-gel TiO_2 thin films on various kinds of glass substrates: the effects of Na^+ and primary particle size, *The Journal of Physical Chemistry B*, 108: 8254-8259,

National Institute of Health, (2008). National Toxicology Program - Center for the Evaluation of Risks to Human Reproduction (NTP-CERHR) Monograph on the Potential Human Reproductive and Developmental Effects of Bisphenol-A. NIH Publication No. 08–5994 National Toxicology Program, US

Neng NR and Nogueira JMF. (2014).Determination of Phenol Compounds in Surface Water Matrices by Bar Adsorptive Microextraction-High Performance Liquid Chromatography-Diode Array Detection. *Molecules*, 19: 9369-9379

Nie Y, Qiang Z, Zhang H, and Ben W. (2012). Fate and seasonal variation of endocrine-disrupting chemicals in a sewage treatment plant with A/A/O process. *Separation and Purification Technology*, 84: 9–15.

Ochuma IJ, Fishwick RP, Wood J, and Winterbottom JM. (2007). Optimisation of degradation conditions of 1,8-diazabicyclo[5. 4.0]undec-7-ene in water and reaction kinetics analysis using a cocurrent downflow contactor photocatalytic reactor. *Applied Catalysis. B: Environment*, 73: 259-268.

Oehlmann J, Schulte-Oehlmann U, Kloas W, Jagnytsch O, Lutz I, Kusk KO, Wollenberger L, Santos EM, Paull GC, Van Look KJ, and Tyler CR. (2009). A critical analysis of the biological impacts of plasticizers on wildlife. *Philosophical Transaction of Royal Society, B*, 364: 2047-2062.

Okolo B, Lamparter P, Welzel U, and Mittemeijer EJ. (2004). Stress, texture, and microstructure in niobium thin films sputter deposited onto amorphous substrates. *Journal of Applied Physics*, 95: 466-476

Olson TM, and Higgens MR. (2009). Life-Cycle Case Study Comparison of Permeable Reactive Barrier versus Pump-and-Treat Remediation. *Environmental Science and Technology*, 43(24): 9432–9438.

Oller I, Malato S, and Sánchez-Pérez JA. (2011) Combination of Advanced Oxidation Processes and biological treatments for wastewater decontamination - A review: *Science of The Total Environment*, 409 (20): 4141–4166

Olujimi OO, Fatoki OS, Odendaal JP, and Okonkwo JO. (2010). Endocrine disrupting chemicals (phenol and phthalates) in the South African environment: A need for more monitoring. Review. *Water SA*, 36(5): 671–682.

Olujimi OO, Fatoki OS, Odendaal JP, Daso AP. (2012) Chemical monitoring and temporal variation in levels of endocrine disrupting chemicals (priority phenols and phthalate esters)

from selected wastewater treatment plant and freshwater systems in Republic of South Africa. *Microchemical Journal*, 101: 11–23

Omri A, Benzina M. and Bennour F. (2015). Industrial application of photocatalysts prepared by hydrothermal and sol–gel methods. *Journal of Industrial and Engineering Chemistry*, 21: 356–362

Palominos R, Freer J, Mondaca MA, and Mansilla HD. (2008). Evidence for hole participation during photocatalytic oxidation of the antibiotic flumequine. *Journal of Photochemistry and. Photobiology.* A 193: 139-145

Pham TD, and Lee KB. (2014). Feasibility of Silver Doped TiO_2 /Glass Fiber Photocatalyst under Visible Irradiation as an Indoor Air Germicide. *International Journal of Environmental Research and Public Health*, 11: 3271-3288

Pardeshi SK. and Patil AB. (2009). Effect of morphology and crystallite size on solar photocatalytic activity of zinc oxide synthesized by solution free mechanochemical method. *Journal of Molecular Catalysis A: Chemical*, 308: 32–40

Park J, Han Y, and Kim H. (2012). Formation of mesoporous materials from silica dissolved in various NaOH concentrations: Effect of pH and ionic strength. *Journal of Nanomaterials*. vol. 2012, Article ID 528174, 10 pages, 2012. doi:10.1155/2012/528174

Patil PN, Bote SD, and Gogate PR. (2014a). Degradation of imidacloprid using combined advanced oxidation processes based on hydrodynamic cavitation. *Ultrasonics Sonochemistry*. 21(5):1770-7

Patil PN, and Gogate PR. (2012). Degradation of methyl parathion using hydrodynamic cavitation: Effect of operating parameters and intensification using additives. *Separation and Purification Technology*, 95: 172-179

Pattanayak M and Nayak PL. (2013a). Green Synthesis and Characterization of Zero Valent Iron Nanoparticles from the Leaf Extract of Azadirachta indica (Neem). *World Journal of Nano Science and Technology*, 2(1): 06-09

Pattanayak M and Nayak PL. (2013b). Ecofriendly green synthesis of iron nanoparticles from various plants and spices extract. *International Journal of Plants, Animal and Environmental Sciences*, 3(1): 68-78

Petrie B, Barden R. and Kasprzyk-Hordern B. (2015). A review on emerging contaminants in wastewaters and the environment: Current knowledge, understudied areas and recommendations for future monitoring. *Water Research*, 72: 3-27

Pradhan AA, and Gogate PR. (2010). Removal of p-nitrophenol using hydrodynamic cavitation and Fenton Chemistry at pilot scale. *Chemical Engineering Journal*, 156: 77-82

Prati S, Joseph E, Sciutto G, and Mazzeo R. (2010). New Advances in the Application of FTIR Microscopy and Spectroscopy for the Characterization of Artistic Materials. *Accounts of Chemical Research*, 43 (6): 792–801.

Poursaberi T, Konoza E, Mohsen Sarrafi H, Hassanisadi M. and Hajifathli F. (2012). Application of Nanoscale Zero-Valent Iron in the Remediation of DDT from Contaminated Water. *Chemical Science Transactions*, 1(3): 658-668

Qu G, Liang D, Qu D, Huang Y, Liu T, Mao H, Ji P, and Huang D. (2013). Simultaneous removal of cadmium ions and phenol from water solution by pulsed corona discharge plasma combined with activated carbon, *Chemical Engineering Journal*, 228:28–35

Quiroz M, Sánchez-Salas JL, Reyna S, Bandala ER, Peralta-Hernández JM, and Martínez-Huitle CA. (2014). Degradation of 1-hydroxy-2,4-dinitrobenzene from aqueous solutions by electrochemical oxidation: Role of anodic material. *Journal of Hazardous Materials*, 268: 6–13

Rahaman MSA, Ismail AF, and Mustafa A. (2007). A review of heat treatment on polyacrylonitrile fiber. *Polymer Degradation and Stability*, 92: 1421-1432

Rahman MF, Yanful EK. and Jasim SY.(2009). Occurrences of endocrine disrupting compounds and pharmaceuticals in the aquatic environment and their removal from drinking water: Challenges in the context of the developing world. *Desalination*, 248:578–585.

Raut-Jadhav S, Saharan VK, Pinjari D, Sonawane S, Saini D, and Pandit A. (2013). Synergetic effect of combination of AOP's (hydrodynamic cavitation and H_2O_2) on the degradation of neonicotinoid class of insecticide. *Journal of Hazardous Materials*, 261:139–147

Ray S. and Shard AG. (2011). Quantitative Analysis of Adsorbed Proteins by X-ray Photoelectron Spectroscopy. *Analytical Chemistry*, 83(22): 8659-8666.

Ren W, Ai Z, Jia F, Zhang L, Fan X, and Zou Z. (2007). Low temperature preparation and visible light photocatalytic activity of mesoporous carbon-doped crystalline TiO_2. *Applied Catalysis B: Environmental*, 69: 138–144

Ribeiro RS, Silva AMT, Figueiredo JL, Faria JL, and Gomes HT. (2013). Removal of 2-nitrophenol by catalytic wet peroxide oxidation using carbon Materials with different morphological and chemical properties. *Applied Catalysis B: Environmental*, 140– 141: 356–362

Richardson SD. and Ternes TA, (2011). Water analysis: emerging contaminants and current issues. *Analytical Chemistry*, 83 (12): 4614-4648.

Richardson SD. (2012). Environmental Mass Spectrometry: Emerging Contaminants and Current Issues. *Analytical Chemistry*, 84: 747–778

Rocha S, Domingues VF, Fernandes VC, Gameiro P, Pinho C, Delerue-Matos C, and Mansilha C. (2013). Occurrence of Bisphenol A, Estrone, 17β-Estradiol and 17α-

Ethinylestradiol in Portuguese Rivers. *Bulletin Environmental Contamination and Toxicology*, 90:73–78

Rodríguez-González V, Obregón Alfaro S, Torres-Martínez LM, Cho SH and Lee SW. (2010). Silver–TiO_2 nanocomposites: Synthesis and harmful algae bloom UV-photoelimination. *Applied Catalysis B: Environmental*, 98: 229–234

Rogers JA, Metz L, and Wee Yong V. (2013). Review: Endocrine disrupting chemicals and immune responses: A focus on bisphenol-A and its potential mechanisms. *Molecular Immunology*, 53:421–430.

Rong SP, Sun YB, and Zhao ZH. (2014). Degradation of sulfadiazine antibiotics by water falling film dielectric barrier discharge. *Chinese Chemical Letters*, 25: 187-192

Rong S, and Sun Y. (2013). Wetted-wall corona discharge induced degradation of sulfadiazine antibiotics in aqueous solution. *Journal of Chemistry Technology and Biotechnology*, 89: 1351–1359

Rouquerol J, Llewellyn PL, Rouquerol F. (2007). Is the BET equation applicable to microporous adsorbents? Characterization of porous solids VII. Studies in surface science and catalysis. 160: 49–56

Saharan VK, Pandit AB, Kumar PSS, and Anandan S. (2012). Hydrodynamic cavitation as an advanced oxidation technique for the degradation of acid red 88 dye. *Industrial Engineering Chemical Research*, 51: 1981-1989

Saharan, VK, Rizwani, MA, Malani, AA, and Pandit, AB (2013). Effect of geometry of hydrodynamically cavitating device on degradation of orange-G. *Ultrasonics Sonochemistry*, 20: 345–353

Sahni M and Locke BR. (2006). Quantification of Hydroxyl Radicals Produced in Aqueous Phase Pulsed Electrical Discharge Reactors. *Industrial Engineering and Chemical Research*, 45: 5819-5825

Salehi M, Hashemipour H, and Mirzaee M. (2012). Experimental Study of Influencing Factors and Kinetics in Catalytic Removal of Methylene Blue with TiO_2 Nanopowder. *American Journal of Environmental Engineering*, 2(1): 1-7

Sanchez-Avila J, Bonet J, Velasco G, and Lacorte S. (2009). Determination and occurrence of phthalates, alkylphenols, bisphenol A, PBDEs, PCBs and PAHs in an industrial sewage grid discharging to a municipal wastewater treatment plant. *Science of The Total Environment*, 407: 4157–67

Sato M, Tokutake T, Ohshima T. and Sugiarto AT. (2008). Aqueous phenol decomposition by pulsed discharges on the water surface. *Institute of Electrical and Electronics Engineers (IEEE) Transactions on Industry Applications*, 44 (5): 1397-1402.

Scott JP, and Ollis DF. (1995). Integration of chemical and biological oxidation processes for water treatment: review and recommendations. *Environmental Progress*, 14(2):88–103

Sein MM, Nasir ZB, Telgheder U. and Schmidt TC. (2012). Studies on a non-thermal pulsed corona plasma between two parallel-plate electrodes in water. *Journal of Physics D and Applied Physics*. 45: 225203-225212

Sellin MK, Snow DD, Schwarz M, Carter BJ, Kolok AS. (2009). Agrichemicals in Nebraska, USA, watersheds: occurrence and endocrine effects. *Environmental Toxicology and Chemistry (SETAC)* 28: 2443–2448

Senthilnathan J. and Philip L. (2010). Photocatalytic Degradation of Lindane under UV and Visible Light Using N-doped TiO_2. *Chemical Engineering Journal*, 1(2): 83-92.

Shahwana T, Abu Sirriah S, Nairat M, Boyaci E, Eroglu AE, Scott TB, and Hallam KR. (2011). Green synthesis of iron nanoparticles and their application as a Fenton-like catalyst for the degradation of aqueous cationic and anionic dyes. *Chemical Engineering Journal*, 172: 258–266

Shameli K, Bin Ahmad M, Jazayeri SD, Sedaghat S, Shabanzadeh P, Jahangirian H, Mahdavi M, and Abdollahi Y. (2012). Synthesis and Characterization of Polyethylene Glycol Mediated Silver Nanoparticles by the Green Method. *International Journal of Molecular Science*, 13: 6639-6650

Sharma, S, Ruparelia, JP, and Patel, ML. (2011). A general review on advanced oxidation processes for waste water treatment. Institute of Technology, Nirma University, Ahmedabad, 382-481, 08-10

Sheikhnejad-Bishe O, Zhao F, Rajabtabar-Darvishi A, Khodadad E, Mostofizadeh A, and Huang Y. (2014). Influence of temperature and surfactant on the photocatalytic performance of TiO_2 Nanoparticles. *International Journal of Electrochemical Science*, 9: 4230 – 4240

Shen C, Wang YJ, Xu JH. and Luo GS. (2012). Facile synthesis and photocatalytic properties of TiO_2 nanoparticles supported on porous glass beads. *Chemical Engineering Journal*, 209: 478–485

Shi J, Bian W, and Yin X. (2009). Organic contaminants removal by the technique of pulsed high-voltage discharge in water. *Journal of Hazardous Materials*, 171: 924–931.

Shirke BS, Korake PV, Hankare PP, Bamane SR and Garadkar KM. (2011). Synthesis and characterization of pure anatase TiO_2 nanoparticles. *Journal of Material Science and Material Electronic*, 22: 821–824

Singh R, Misra V, and Singh RP. (2011). Synthesis, characterization and role of zero-valent iron nanoparticle in removal of hexavalent chromium from chromium-spiked soil. *Journal of Nanoparticle Research*, 13(9): 4063-4073

Skoog DA, Holle FJ, and Crouch SR. (2007). Principles of Instrumental Analysis (6th ed.). Belmont, CA: Thomson Brooks/Cole. Pp. 169–173. ISBN 9780495012016.

Stieber M, Putschew A, and Jekel M. (2011). Treatment of Pharmaceuticals and Diagnostic Agents Using Zero-Valent Iron – Kinetic Studies and Assessment of Transformation Products Assay. *Environmental Science and Technology*, 45 (11): 4944–4950

Steffen W, Persson Å, Deutsch L, Zalasiewicz J, Williams M, and Richardson K (2011). The Anthropocene: from global change to planetary stewardship. *Ambiology* A *Journal of the Human Environment*, 40: 739–61.

Stuart M, Lapworth D, Crane E, and Hart A. (2012). Review of risk from potential emerging contaminants in UK groundwater. *Science of The Total Environment*, 416: 1–21

Subrahmanyam A, Biju KP, Rajesh P, Jagadeesh Kumar K, and Raveendra Kiran M. (2012). Surface modification of sol gel TiO_2 surface with sputtered metallic silver for sun light photocatalytic activity: Initial studies. *Solar Energy Materials and Solar Cells*, 101: 241-248

Sun YP, Li XQ, Cao J, Zhang WX, and Wang HP (2006). Characterization of zero-valent iron nanoparticles. *Advances in Colloid and Interface Science*, 120: 47–56

Sun T, Liu L, Sun Y, Tan C, Yao F, Liang X, Wang Y, Yang Y, Hu X and Fan J. (2012). Synthesis and characterization of TiO_2 Nanoparticles: Applications in Research on the Interaction of colloidal TiO_2 with Human Serum Albumin by Fluorescence Spectroscopy. *Analytical Sciences*, 28: 491- 496

Suwarnkar MB, Dhabbe RS, Kadam AN, and Garadkarn KM. (2014). Enhanced photocatalytic activity of Ag doped TiO_2 nanoparticles synthesized by a microwave assisted method. *Ceramic International*, 40: 5489-5496

Tahara M. and Okubo M. (2012). Detection of Free Radicals Produced by a Pulsed Streamer Corona Discharge in Solution Using Electron Spin Resonance. Proceeding 2012 Joint Electrostatics Conference held on June 12-14, 2012 at Cambridge, ON, Canada. Pp.1-12

Tai C, Peng JF, Liu JF, Jiang GB, and Zou H. (2004). Determination of hydroxyl radicals in advanced oxidation processes with dimethyl sulfoxide trapping and liquid chromatography. *Analytica Chimica Acta*, 527: 73–80

Tamimi M, Qourzal S, Barka N, Assabbane A, Ait-Ichou Y. (2008). Methomyl degradation in aqueous solutions by Fenton's reagent and the photo-Fenton system. *Separation and Purification Technology*, 61: 103-108

Tang S, Lu N, Li J, Shang K, and Wu Y. (2013). Improved phenol decomposition and simultaneous regeneration of granular activated carbon by the addition of a titanium dioxide catalyst under a dielectric barrier discharge plasma. *Carbon*, 53: 380– 390

Tao Z, Jin J, Yang S, Hu D, Li G, and Jiang J. (2009). "Synthesis and Characterization of Fluorinated PBO with High Thermal Stability and Low Dielectric Constant". *Journal of Macromolecular Science, Part B*, 48: 1114–1124

Tay KS, Abd.Rahman N and Radzi Bin Abas M. (2012). Degradation of bisphenol A by ozonation: rate constants, influence of inorganic anions, and by-products. *Maejo International Journal of Science and Technology*, 6(01): 77-94

Teppala S, Madhavan S, and Shankar A, (2012). Bisphenol A and metabolic syndrome: results from NHANES http://dx.doi.org/10. 1155/2012/598180.

Tijani JO, Fatoba OO and Petrik LF (2013). A review of pharmaceuticals and endocrine disrupting compounds: Sources, effects, removal and detections. *Water, Air and Soil Pollution*. 224:1770 DOI 10.1007/s11270-013-1770-3

Tijani JO, Fatoba OO, Madzivire G. and Petrik LF (2014). A Review of Combined Advanced Oxidation Technologies for the Removal of Organic Pollutants from Water. *Water Air Soil Pollut*, 225:2102, DOI 10.1007/s11270-014-2102-y

Totito TC. (2014). Photocatalytic activity of supported TiO_2 nanocrystals. Unpublished Msc thesis to the Department of Chemistry, University of the Western Cape, South Africa. Pp. 53-54

Trapido M, Epold I, Bolobajev J and Dulova N. (2014). Emerging micropollutants in water/wastewater: growing demand on removal technologies. *Environmental Science and Pollution Research*, 21(21):12217-22

Trovo AG, Melo SAS, and Nogueira RFP. (2008). Photodegradation of the pharmaceuticals amoxicillin, bezafibrate and paracetamol by the photo-Fenton processed application to sewage treatment plant effluent. *Journal of Photochemistry and Photobiology. A*: Chemistry. 198: 215- 220

Tsai WT, Leeb MK, Suc TY, and Yuan MC. (2009). Photodegradation of bisphenol-A in a batch TiO_2 suspension reactor. *Journal of Hazardous Materials*, 168: 269–275.

Tsai WT. (2006). Human health risk on environmental exposure to Bisphenol-A: a review. *Journal of Environmental Science and Health C Environmental Carcinogenesis and Ecotoxicology Reviews*, 24: 225–55.

USEPA (2010). Bisphenol A Action Plan. Washington D.C., USA. [CA Index Name: Phenol, 4,4'-(1-methylethylidene)bis-] Accessed at http://www2.epa.gov/sites/production/files/2015-09/documents/bpa_action_plan.pdf.

US Environmental Protection Agency, (2007). Memorandum to EDSTAC Members RE: Definition of “Endocrine Disruptor”. Washington D.C., USA. http://www.epa.gov/endocrine (accessed on 20 Feb 2007)

USGS (US Geological Survey). (2014). Emerging Contaminants In the Environment: Accessed October 2014. http://toxics.usgs.gov/regional/emc/

Üzüm C, Shahwan T, Eroğlu AE, Lieberwirth I, Scott TB, and Hallam KR. (2008). Application of zero-valent iron nanoparticles for the removal of aqueous Co^{2+} ions under various experimental conditions. *Chemical Engineering Journal*, 144: 213–220

Vandenberg LN, Hauser R, Marcus M, Olea N, and Welshons WV. (2007): Human exposure to bisphenol A (BPA). *Reproductive Toxicology*, 24: 139-177

Vivian JT and Callis PR. (2001). Mechanisms of tryptophan fluorescence shifts in proteins. *Biophysics Journal.* 80 (5): 2093–109.

Verlicchi P, Al Aukidy M, and Zambello E. (2012). Occurrence of pharmaceutical compounds in urban wastewater: removal, mass load and environmental risk after a secondary treatment — A review. *Science of The Total Environment*, 429:123–55

Wang H, Li J, Quan X, Wu Y, Li G and Wang F. (2007). Formation of hydrogen peroxide and degradation of phenol in synergistic system of pulsed corona discharge combined with TiO_2 photocatalysis. *Journal of Hazardous Materials*, 141: 336–343

Wang J, Sun W, Zhang Z, Li XZR, Ma T, Zhang P, and Li Y. (2007). Sonocatalytic degradation of methyl parathion in the presence of micron-sized and nano-sized rutile titanium dioxide catalysts and comparison of their sonocatalytic abilities. *Journal of Molecular Catalysis A: Chemical*, 272: 84–90

Wang H, Li J, Quan X, and Wu Y. (2008). Enhanced generation of oxidative species and phenol degradation in a discharge plasma system coupled with TiO_2 photocatalysis. *Applied Catalysis B: Environmental*, 83: 72–77

Wang L, Jiang X and Liu Y. (2008). Degradation of bisphenol A and formation of hydrogen peroxide induced by glow discharge plasma in aqueous solutions. *Journal of Hazardous Materials*, 154: 1106–1114

Wang X, Wang J, Guo P, Guo W, and Li G. (2008). Chemical effect of swirling jet-induced cavitation: Degradation of rhodamine B in aqueous solution. *Ultrasonics Sonochemistry*, 15: 357-363

Wang H, Chu J, Ou H, Zhao R, and Han J. (2009). Analysis of TiO_2 photocatalysis in a pulsed discharge system for phenol degradation. *Journal of Electrostatic,* 67: 886–889.

Wang X, and Zhang Y. (2009). Degradation of alachlor in aqueous solution by using hydrodynamic cavitation. *Journal of Hazardous Materials,* 16: 202-207

Wang T, Li M, Chen B, Xu M, and Xu Y, (2012) Urinary Bisphenol A (BPA) Concentration Associates with Obesity and Insulin Resistance. *Journal of Clinical Endocrinology Metabolism*, 97: E223–E227.

Wang Y, Sun H, Duan X, Ang HM, Tadé MO, and Wang S. (2015). A new magnetic nano zero-valent iron encapsulated in carbon spheres for oxidative degradation of phenol. *Applied Catalysis B: Environmental*, 172: 73–81

Wang C, Shi H, and Li Y. (2015). Synthesis and characterization of natural zeolite supported Cr-doped TiO_2 photocatalysts. *Applied Surface Science*, 258: 4328–4333

Wankhade AV, Gaikwad GS, Dhonde MG, Khaty NT, and Thakare SR. (2013). Removal of Organic Pollutant from Water by Heterogenous Photocatalysis: A Review. *Research Journal of Chemistry and Environment*, 17 (1): 84-94

Wei L, Shifu C, Wei Z, and Sujuan Z. (2009). Titanium dioxide mediated photocatalytic degradation of methamidophos in aqueous phase. *Journal of Hazardous Materials*, 164: 154–160

Wei L, Zhu H, Mao H. and Gan F. (2011). Electrochemical oxidation process combined with UV photolysis for the mineralization of nitrophenol in saline wastewater. *Separation and Purification Technology*, 77:18–25

WHO/UNEP. (2013). State of the science of endocrine disrupting chemicals – 2012. An assessment of the state of the science of endocrine disruptors prepared by a group of experts for the United Nations Environment Programme (UNEP) and WHO. Accessed at http://www.who.int/ceh/publications/endocrine/en/

Wilfried MA, Niessen W, and Niessen M (2006). Liquid Chromatography-Mass Spectrometry, Third Edition (Chromatographic Science). Publisher: Taylor and Francis, Boca Raton: CRC. Press. ISBN 0-8247-4082-3.

Wu L, Deng D, Jin J, Lu X, and Chen J. (2012). Nanographene-based tyrosinase biosensor for rapid detection of bisphenol A. *Biosensors and Bioelectronics*, 35: 193–199

Wu X, Yin S, Dong Q, Guo C, Li H, Kimura T, and Sato T. (2013). Synthesis of high visible light active carbon doped TiO_2 photocatalyst by a facile calcination assisted solvothermal method. *Applied Catalyst B. Environmental*, 142-143: 450-457

Xu B, Gao N, Rui M, Wang H, and Wu H. (2007). Degradation of endocrine-disruptor Bisphenol-A in drinking water by ozone oxidation. *Front Environmental Science and Engineering. China*, 1(3): 350-356

Xi Y, Mallavarapu M and Naidu R. (2010). Reduction and adsorption of Pb2+ in aqueous solution by nano-zero-valent iron—A SEM, TEM and XPS study. *Material Research Bulletin*, 45: 1361-1367

Xu J, Xiao X, Ren F, Wu W, Dai Z.,Cai G, Zhang S, Zhou J, Mei F, and Jiang C. (2012). Enhanced photocatalysis by coupling of anatase TiO_2 film to triangular Ag Nanoparticle Island. *Nanoscale Research Letters*, 7: 239

Yildiz E, Keskinler B, Pekdemir T, Akay G, and Nuhoğlu A. (2005). High strength wastewater treatment in a jet loop membrane bioreactor: kinetics and performance evaluation. *Chemical Engineering Science*, 60(4): 1103–1116

Yu B, Leung KM, Guo Q, Lau WM and Yang J. (2011). Synthesis of Ag–TiO_2 composite nano thin film for antimicrobial application. *Nanotechnology* 22: 115603-115612

Zhang W, Xiao X, An T, Song Z, Fu J, Sheng G, and Cui M, (2003). Kinetics, degradation pathway and reaction mechanism of advanced oxidation of 4-nitrophenol in water by a UV/H_2O_2 process. *Journal of Chemistry Technology Biotechnol*ogy, 78:788–794

Zhang C, Ren Z, Yin Z, Jiang L, and Fang, S. (2011). Experimental FTIR and simulation studies on H-bonds of model polyurethane in solutions I: In dimethylformamide (DMF). *Spectrochimica Acta Part A: Molecular and Biomolecular Spectroscopy,* 81(1): 598-603

Zhang Y, Xu H, and Xin Q. (2012). Enhanced Phenol Degradation by Pulsed Plasma Cooperated with TiO_2 Nanotubes Film. *2012 Asia Pacific Conference on Environmental Science and Technology, Advances in Biomedical Engineering*, 6: 376-379

Zhang TH, Piao LY, Zhao SL, Xu Z, Wu Q, and Kong C. (2012). Application of TiO_2 with different structures in solar cells. *Chinical Physics. B*. 21(11): 118401-5

Zhang Y, Zhang R, Ma W, Zhang X, Wang L, and Guan Z. (2013). Purification of water by bipolar pulsed discharge plasma combined with TiO_2 catalysis. *Journal of Physics: Conference Series,* 418, 121-25

Zhang Y, Xin Q, Cong Y, Wang Q and Jiang B. (2013). Application of TiO_2 nanotubes with pulsed plasma for phenol degradation. *Chemical Engineering Journal*, 215–216: 261–268

Zhao D, Wang J, Zhang Z, Zhao X, and Zhang J. (2009). TiO_2 /NaY composite as photocatalyst for degradation of omethoate. *Chemical Research Chinese Universities* 25(4): 543-549

Zhu B. and Zou L. (2009). Trapping and decomposing of color compounds from recycled water by TiO_2 coated activated carbon. *Journal of Environmental Management.* 90: 3217–3225.

Zhu L, Ma J, and Yang S. (2007). Removal of phenol by activated alumina bed in pulsed high-voltage electric field. *Journal of Environmental Sciences*, 19: 409–415

Zhu Y, Cai Y, Xu L, Zheng L, Wang L, Qi B, and Xu C. (2015). Building An Aptamer/Graphene Oxide FRET Biosensor for One-Step Detection of Bisphenol-A. *ACS Applied Material Interfaces*, 7: 7492−7496

Ziv-Gal A, Zelieann C, Wang W, and Flaws J. (2013). Bisphenol A inhibits cultured mouse ovarian follicle growth partially via the aryl hydrocarbon receptor signaling pathway. *Reproductive Toxicology*, 42: 58–67.

Zupanc M, Kosjek T, Petkovsek M, Dular M, Kompare B, Sirok B, Strazar M, and Heath E. (2014). Shear-induced hydrodynamic cavitation as a tool for pharmaceutical micropollutants removal from urban wastewater. *Ultrasonics Sonochemistry*, 21: 1213–1221.

Appendix 1: Effect of solution pH on BPA removal efficiency by the DBD alone

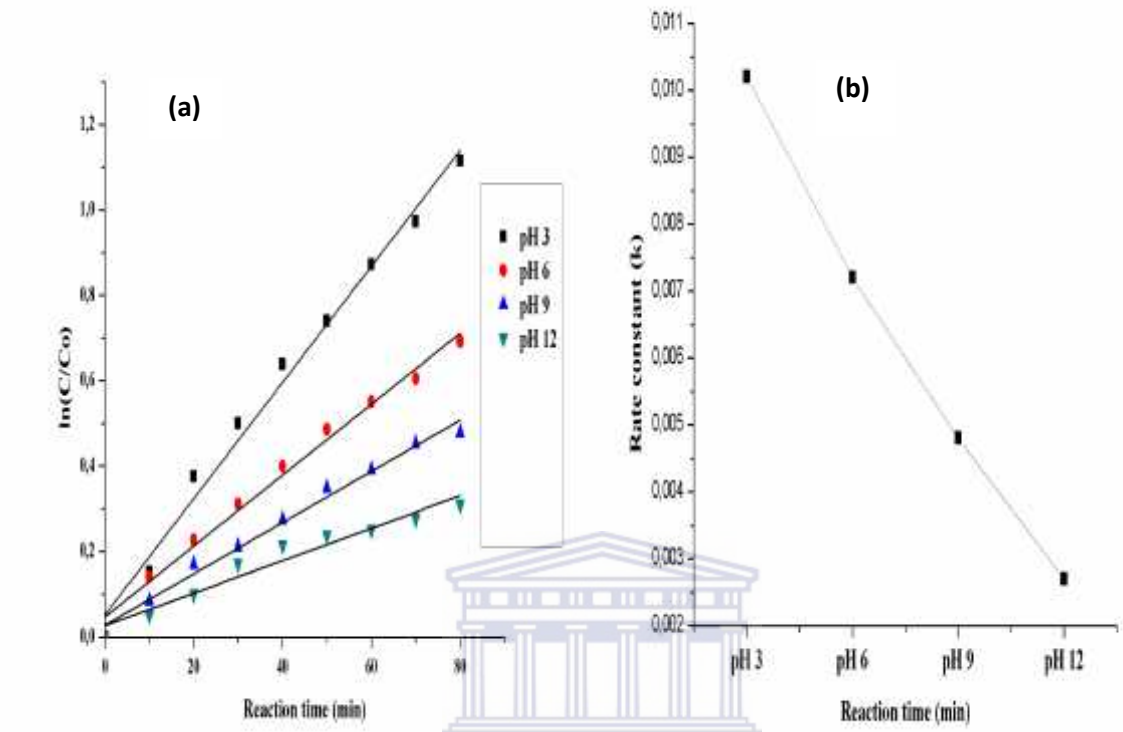

(a) Pseudo-first order kinetics plot of the experimental data (b) reaction rate constant against as a function of the pH values for BPA

Appendix 2: Effect of solution on 2-NP removal efficiency by the DBD alone

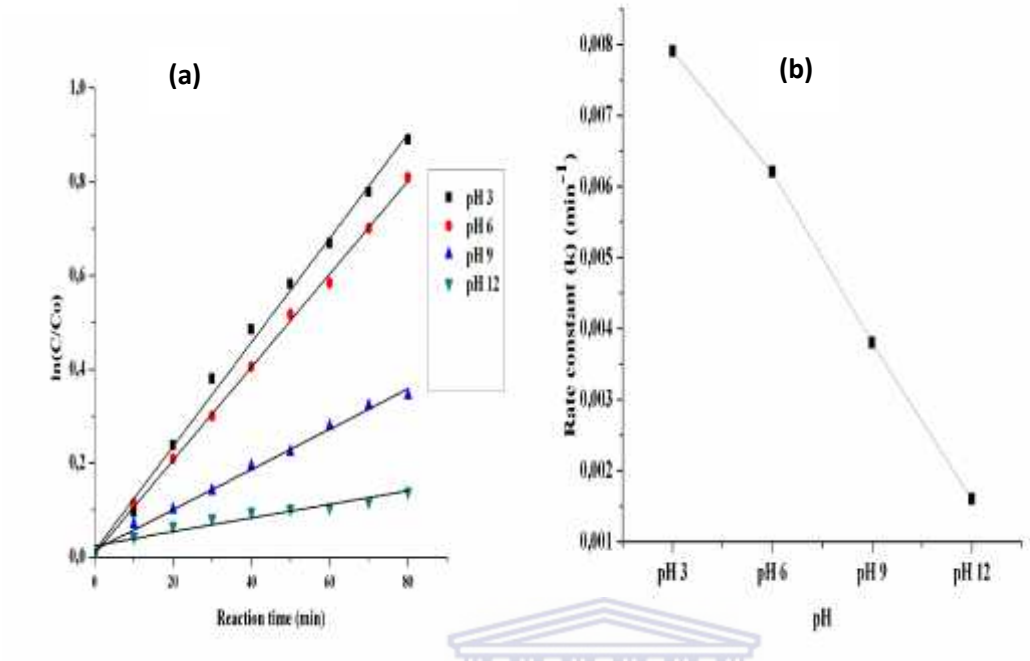

(a) pseudo-first order kinetics plot of the experimental data, (b) reaction rate constant against as a function of the pH values for 2-NP

Appendix 3: Concentration of metallic elements in aqueous solution of BPA or 2-NP prior to introduction of JT14 into the DBD

Concentration of elements (ug/L)					
Time (min)	**Ti**	**Cr**	**Fe**	**Ni**	**Ag**
0	BDL	BDL	BDL	BDL	BDL
10	BDL	BDL	BDL	BDL	BDL
20	BDL	BDL	BDL	BDL	BDL
30	BDL	BDL	BDL	BDL	BDL
40	BDL	BDL	BDL	BDL	BDL
50	BDL	BDL	BDL	BDL	BDL
60	BDL	BDL	BDL	BDL	BDL
70	BDL	BDL	BDL	BDL	BDL
80	BDL	BDL	BDL	BDL	BDL
90	BDL	BDL	BDL	BDL	BDL
100	BDL	BDL	BDL	BDL	BDL
110	BDL	BDL	BDL	BDL	BDL
120	BDL	BDL	BDL	BDL	BDL

Appendix 4: Formula for determining the energy efficiency of JLR and combined JLR/UV/H_2O_2

The energy efficiency was estimated using the relationship below:

(Initial TOC value – final TOC value) (mg/L) × volume of the BPA or 2-NP solution (60 L).

The initial and final TOC value obtained via each process at 90 min is shown in Table 6.19.

Table 6.19: TOC value of each treatment at 90 min maximum

Treatment process	Initial TOC value (mg/L)	Final TOC value (mg/L)	Differences in TOC value (mg/L)
JLR alone	7.9	7.5	0.4
JLR/UV	7.9	6.55	1.35
JLR/H2O2	7.9	6.03	1.87
JLR/UV/H_2O_2	7.9	4.85	3.05

The extent of TOC reduction in 90 minutes using JLR alone = 0.4 (mg/L) × 60 L

= 24 mg

The energy supplied using JLR in 90 min = (Energy input) Watt × time (s)

The power rating of the pump = 2.5 kW = 2500 W (J/s), time = 90 min = 5400 sec

The energy supplied using JLR alone = 2500 × 5400

= 13500000 J

Energy efficiency = $\frac{TOC\ reduction\ in\ 90\ min(mg)}{Energy\ supplied\ using\ JLR}$

$= \frac{24}{13500000}$

$= 1.777 \times 10^{-6}$ mg/J

JLR/UV system

(Initial TOC-final TOC) mg/L × 60 L = 1.35 × 60 =86.4 mg

Energy supplied using JLR/UV = Energy input (Watt) = 2500 W (JLR) + 55 W(UV) = 2555 W, time = 5400 sec

Energy supplied by the combined system = 2555 × 5400 = 13797000 J

Energy efficiency of JLR/UV = $\frac{86.4}{13797000}$ = 6.3×10^{-6} mg/J

For JLR/H_2O_2 system

(Initial TOC-final TOC) mg/L × 60 L = 1.87 × 60 =112.3 mg

Energy supplied using JLR/H_2O_2 = Energy input (Watt) = 2500 W (JLR), time = 5400 sec

Energy supplied by the combined system = 2500 × 5400 = 13500000 J

Energy efficiency of JLR/UV = $\frac{112.2}{13500000}$ = 8.3×10^{-6} mg/J

For JLR/UV/H_2O_2 system

(Initial TOC-final TOC) mg/L × 60 L = 3.05 × 60 =183 mg

Energy supplied using JLR/UV/H_2O_2 = Energy input (Watt) = 2500 W (JLR), 55 W (UV), time = 5400 sec

Energy supplied by the combined system = 2555 × 5400 = 13797000 J

Energy efficiency of JLR/UV = $\frac{183}{13797000}$ = 1.3×10^{-5} mg/J

Appendix 5: Synergetic index value for BPA

$$(f)=\frac{0.0049}{0.0008+0.0017}$$

$$(f) = \frac{0.0049}{0.0025}$$

$$(f)= 1.96$$

While that of 2-NP was $(f) = \frac{0.0046}{0.0007+0.0016}$

$$(f)= \frac{0.0046}{0.0023}$$

$$(f)= 2.0$$

Synergetic index value (f) for BPA = $\frac{k(JLR+UV+H_2O_2)}{k(JLR)+k(UV)+k(H_2O_2)}$……(6)

$$(f)= \frac{0.0165}{0.0017+0.0008+0.00007}$$

$$(f)= \frac{0.0165}{0.00257}$$

$$(f)= 6.42$$

And 2-NP was $(f)= \frac{0.0160}{0.0016+0.0007+0.00004}$

$$(f)= \frac{0.0160}{0.00234}$$

$$(f)= 6.84$$